ABSTRACT

Title of dissertation: HELICOPTER FLIGHT DYNAMICS SIMULATION WITH A TIME-ACCURATE FREE-VORTEX WAKE MODEL

Maria Ribera, Doctor of Philosophy, 2007

Dissertation directed by: Professor Roberto Celi
Department of Aerospace Engineering

This dissertation describes the implementation and validation of a coupled rotor-fuselage simulation model with a time-accurate free-vortex wake model capable of capturing the response to maneuvers of arbitrary amplitude. The resulting model has been used to analyze different flight conditions, including both steady and transient maneuvers.

The flight dynamics model is based on a system of coupled nonlinear rotor-fuselage differential equations in first-order, state-space form. The rotor model includes flexible blades, with coupled flap-lag-torsion dynamics and swept tips; the rigid body dynamics are modeled with the non-linear Euler equations. The free wake models the rotor flow field by tracking the vortices released at the blade tips. Their behavior is described by the equations of vorticity transport, which is approximated using finite differences, and solved using a time-accurate numerical scheme. The flight dynamics model can be solved as a system of non-linear algebraic trim equations to determine the steady state solution, or integrated in time in response

to pilot-applied controls. This study also implements new approaches to reduce the prohibitive computational costs associated with such complex models without losing accuracy.

The mathematical model was validated for trim conditions in level flight, turns, climbs and descents. The results obtained correlate well with flight test data, both in level flight as well as turning and climbing and descending flight. The swept tip model was also found to improve the trim predictions, particularly at high speed. The behavior of the rigid body and the rotor blade dynamics were also studied and related to the aerodynamic load distributions obtained with the free wake induced velocities.

The model was also validated in a lateral maneuver from hover. The results show improvements in the on-axis prediction, and indicate a possible relation between the off-axis prediction and the lack of rotor-body interaction aerodynamics. The swept blade model improves both the on-axis and off-axis response. An axial descent though the vortex ring state was simulated. As the"vortex ring" goes through the rotor, the unsteady loads produce large attitude changes, unsteady flapping, fluctuating thrust and an increase in power required. A roll reversal maneuver was found useful in understanding the cross-couplings effects found in rotorcraft, specifically the effect of the aerodynamic loading on the rotor orientation and the off-axis response.

Helicopter Flight Dynamics Simulation With a Time-Accurate Free-Vortex Wake Model

by

Maria Ribera

Dissertation submitted to the Faculty of the Graduate School of the
University of Maryland, College Park in partial fulfillment
of the requirements for the degree of
Doctor of Philosophy
2007

Advisory Commmittee:

Professor Roberto Celi, Chair/Advisor
Professor James Baeder
Professor Inderjit Chopra
Professor J. Gordon Leishman
Professor Tobias von Petersdorff

To my parents, for giving me wings,
and to my husband, for flying with me.

A mis padres por darme alas,
y a mi marido, por volar a mi lado.

ACKNOWLEDGMENTS

I am indebted to my advisor, Dr. Roberto Celi, for the opportunity that he gave me to come study at the University of Maryland. He offered me his support, but he also opened my mind to the possibility of rotorcraft, a field both challenging and exciting, and now I cannot understand why I never thought of it before.

I would like to express my sincere gratitude to my advisory committee, Dr. James Baeder, Dr. Inderjit Chopra and Dr. von Petersdorff for the guidance and support. Particularly, to Dr. J. Gordon Leishman, for sharing with me with the wake model and his invaluable experience in wake aerodynamics.

To my colleagues in the flight dynamics group, Rendy Cheng, Dario Fusato and Carlos Malpica, I owe them much for their help and useful discussions. They offered me a warm welcome and their friendship. Our many years sharing the cubicle and the code have made Carlos and I much more than coworkers, he and his wife are true friends and I will miss them very much.

I have formed many other friendships in the Rotorcraft Center, the list is too long, but I particularly want to remember Anne, for her laughs, Tracy, for being a girlfriend among all the boys, and Felipe, for the fun conversations and gossip. They have all made my time here much more pleasant and easy to endure, and I thank them for that. Most specially, I am forever indebted to Shreyas Ananthan. He has taught me much about aerodynamics and wake models, but also about perseverance

and confidence. I would not be were I am today without his help, and this work would not be what it is without his.

The friends I have made at the University of Maryland have opened my eyes to a world of diversity, without borders, and have, during these seven years, become my extended family. I truly consider Alice Lapuerta, Magdalena Pasztaleniec and Sandra Pereira my sisters, I love them and thank them for sticking by me through the thick and thin, in the good and the bad moments. We have had so much fun together, and they truly helped me lead a balanced life. Their families have become my family as well, and I particularly like to show my appreciation to Cesar Lapuerta, the Pereira family, Gustavo, Isabel, Frederico and Olga, who have adopted me and cared for me all these years, and Linda Curtis, for her extreme kindness in giving me a home and a listening ear in the most difficult times of this PhD, the writing year. My good friend Wendy Abi Assali and her daughter Sabrina have also opened her heart and her home to me towards the end of this degree. I am thankful for her trust, her friendship and her support. She has understood like noone else the frustrations and hardships of a long PhD, and I wish her the best of luck to complete hers soon as well. And last, but not least, I want to thank Igor Alonso, one of my oldest and dearest friends. We shared our college years and embarked in the graduate adventure together. He has always been there, and I know he will always be.

To my parents and my brother, this dissertation has felt longer and more painful than even to myself. They have endured my absence with patience and understanding, with constant reminders of their love and support, and have never failed in believing in my capabilities to complete this challenging task. I know

I have made them proud, and somehow that makes all the low points of this PhD worthwhile. I love them and I will never have words to thank them enough, although perhaps a grandchild or two will do.

And I leave my husband Luis for the end, but he is indeed the beginning. The end of this PhD has been marked by our wedding and first months of married life. I am blessed to have such a loving, patient, understanding partner. We have survived the hardest tests and our love has come out stronger. And I cannot wait to discover what life has in store for us.

TABLE OF CONTENTS

LIST OF TABLES

LIST OF FIGURES

NOMENCLATURE

a	Lift-curve slope
$\mathbf{a}$	Acceleration vector
$\mathbf{A}$	State matrix
b	Semi-chord length
$\mathbf{B}$	Control matrix
c	Blade section chord length
C_L, C_D, C_M	Blade section lift, drag and pitching moment coefficients
C_Γ	Ratio of tip vortex strength to maximum bound circulation
E	Young's Modulus, acceleration coupling matrix
e_1	Hinge offset of main rotor blade
$\mathbf{e}_T$, $\mathbf{e}_P$, $\mathbf{e}_R$	Unit vectors of local airflow velocity reference frame
$\hat{\mathbf{e}}_x$, $\hat{\mathbf{e}}_y$, $\hat{\mathbf{e}}_z$	Unit vectors of undeformed preconed blade reference frame
$\hat{\mathbf{e}}'_x$, $\hat{\mathbf{e}}'_y$, $\hat{\mathbf{e}}'_z$	Unit vectors of deformed blade reference frame
g	Acceleration due to gravity
G	Shear modulus
$\mathbf{G}$	Blade deformed section basis vectors
$\mathbf{H}$	Hermite interpolation polynomials
i_θ, i_ϕ	Longitudinal and lateral shaft tilt angles
$\mathbf{i}, \mathbf{j}, \mathbf{k}$	Unit vectors of hub rotating reference frame
$\mathbf{i}_\mathrm{B}, \mathbf{j}_\mathrm{B}, \mathbf{k}_\mathrm{B}$	Unit vectors of body-fixed reference frame
$\mathbf{i}_\mathrm{F}, \mathbf{j}_\mathrm{F}, \mathbf{k}_\mathrm{F}$	Unit vectors of rotating blade reference frame

$\mathbf{i}_{\mathrm{G}}, \mathbf{j}_{\mathrm{G}}, \mathbf{k}_{\mathrm{G}}$	Unit vectors of global wake reference frame
$\mathbf{i}_{\mathrm{H}}, \mathbf{j}_{\mathrm{H}}, \mathbf{k}_{\mathrm{H}}$	Unit vectors of the undeformed tip coordinate system
$\mathbf{i}_{\mathrm{I}}, \mathbf{j}_{\mathrm{I}}, \mathbf{k}_{\mathrm{I}}$	Unit vectors of inertial reference frame
$\mathbf{i}_{\mathrm{P}}, \mathbf{j}_{\mathrm{P}}, \mathbf{k}_{\mathrm{P}}$	Unit vectors of free wake blade preconed reference frame
$\mathbf{i}_{\mathrm{S}}, \mathbf{j}_{\mathrm{S}}, \mathbf{k}_{\mathrm{S}}$	Unit vectors of shaft reference frame
$\mathbf{i}_{\mathrm{T}}, \mathbf{j}_{\mathrm{T}}, \mathbf{k}_{\mathrm{T}}$	Unit vectors of the deformed tip coordinate system
$\mathbf{i}_{\mathrm{W}}, \mathbf{j}_{\mathrm{W}}, \mathbf{k}_{\mathrm{W}}$	Unit vectors of wind reference frame
$\mathbf{i}$	Unit vector
I_b	Influence coefficient matrix for bound circulation
I_{NW}	Influence coefficient matrix for near-wake circulation
I_{xx}, I_{yy}, I_{zz}	Aircraft mass moments of inertia about body axes
I_{xy}, I_{xz}, I_{yz}	Aircraft products of inertia
$\mathbf{j}$	Unit vector
$\mathbf{k}$	Unit vector
$\mathbf{K}$	Linear portion of stiffness matrix
K_R	Wake distortion parameter
L, M, N	Components of total applied moments about body axes
m_o	Reference blade mass per unit length
M	Mach number
$\mathbf{M}$	Linear portion of mass matrix
n	Load factor
N_{b}	Number of blades

N_{e}	Number of finite elements
N_{h}	Number of harmonics of each blade mode
N_{m}	Number of blade modes
p	Roll rate of aircraft
$\mathbf{p}$	Blade section applied force vector
q	Pitch rate of aircraft, blade generalized coordinate, dynamic pressure
$\mathbf{q}$	Blade section applied moment vector
r	Yaw rate of aircraft
r_c	Viscous core radius
R	Main rotor radius
$\mathbf{B}$	Position vector
t	Time (sec)
$T_{\mathrm{A}P}$	Transformation matrix from undeformed preconed frame to blade section aerodynamic frame
$T_{\mathrm{B}I}$	Transformation matrix from inertial frame to body-fixed frame
$T_{\mathrm{D}P}$	Transformation matrix from undeformed preconed frame to deformed blade frame
$T_{\mathrm{F}G}$	Transformation matrix from global wake-fixed frame to rotating blade frame
$T_{\mathrm{G}B}$	Transformation matrix from body-fixed frame to global wake-fixed frame

$T_{\mathrm{P}G}$	Transformation matrix from global wake-fixed frame to undeformed preconed frame
$T_{\mathrm{P}R}$	Transformation matrix from hub-rotating frame to undeformed preconed frame
$T_{\mathrm{R}S}$	Transformation matrix from shaft-fixed frame to hub-rotating frame
$T_{\mathrm{S}B}$	Transformation matrix from body-fixed frame to shaft-fixed frame
$T_{\mathrm{T}S}$	Transformation matrix from shaft-fixed frame to tip path plane
$T_{\mathrm{W}B}$	Transformation matrix from body-fixed frame to wind reference frame
$[T_\Lambda]$	Transformation matrix from blade undeformed preconed coordinate system to the tip undeformed preconed frame.
u	Forward speed of the aircraft, axial deflection of a point on the blade
$\mathbf{u}$	Control vector
v	Lateral speed of the aircraft, lagwise elastic deflection of a point on the blade
v_h	Hover induced velocity, $\sqrt{C_T/2}$
$\mathbf{V}$	Velocity vector, modal coordinate transformation matrix
$\mathbf{y}$	State vector
$\mathbf{y}_n$	Finite element degrees of freedom vector

w	Vertical speed of the aircraft, flapwise elastic deflection of a point on the blade
X, Y, Z	Components of total applied forces along body axes
$\mathbf{x}$	Trim vector
x_0, y_0, z_0	Location of a point on the blade in local coordinates
x_A	Aerodynamic center offset from elastic axis
x_H, y_H, z_H	Location of the hub with respect to the center of gravity
x_J	Spanwise coordinate of the junction between the straight portion of the blade and the swept tip
x_t	Spanwise coordinate of point on the swept tip from the junction

Greek Symbols

α_F	Aircraft angle of attack
α_S	Longitudinal shaft tilt
α_Y	Blade section angle of attack
β	Local flap slope of blade elastic axis
β_F	Fuselage sideslip angle
β_0	Blade coning angle
β_{1c}, β_{1s}	Tip path plane longitudinal and lateral tilt angles
β_p	Blade precone angle
Γ	Tail rotor cant angle, circulation
γ	Flight path angle

γ_{xy}	Coherence
γ_I	Blade section local flow yaw angle
ϵ	Component of strain
Δ_{SP}	Swashplate phase angle
$\Delta\psi$	Azimuth discretization resolution, wake resolution
$\Delta\zeta$	Vortex filament discretization resolution
δ	Perturbation size, turbulent velocity coefficient
ζ	Local lag slope of the blade elastic axis
η	Coordinates of a point on a blade section in local coordinates
θ	Aircraft pitch attitude Euler angle, blade pitch angles associated with geometric rotation
$\theta_0, \theta_{1c}, \theta_{1s}, \theta_{0t}$	Collective, lateral, longitudinal cyclic pitch and tail rotor collective
θ_B	Built-in twist of the straight portion of the blade
θ_{BJ}	Value of θ_B at junction with swept tip
θ_{BT}	Pre-twist of swept tip with respect to the junction to the straight portion of the blade
θ_G	Total geometric pitch of blade section
θ_{TW}	Build-in blade twist
ζ	vortex age
κ_y, κ_z	Beam curvature
$\lambda_0, \lambda_c, \lambda_s$	Steady, cosine and sine portions of main rotor inflow

λ_t	Tail rotor inflow
μ	Main rotor advance ratio
ν	Kinematic viscosity
ρ	Air density
σ	Stress components
τ	Elastic twist of deformed blade section
ϕ	Aircraft roll attitude Euler angle, blade section elastic deformation
ϕ_{FW}	Induced angle of attack at a point in the blade due to the far wake
χ	Wake skew angle
ψ	Aircraft yaw attitude Euler angle, rad, blade azimuth angle, rad
ω	Vector of angular rates
Ω	Main rotor speed

Superscripts and Subscripts

$\dot{(\ )}$	Derivative with respect to time
$\ddot{(\ )}$	Second partial derivative with respect to time
$(\ )^\top$	Transpose
$(..)_{,x}$	Partial derivative with respect to x spatial coordinate
$(\ )_{\mathrm{A}}$	Aerodynamic

$(..)^{\mathrm{b}}$	Straight blade finite element
$(..)_{\mathrm{B}}$	Body-fixed reference frame
$(..)_{CG}$	Center of mass
$(..)_{\mathrm{D}}$	Lag damper
$(..)_{\mathrm{F}}$	Fuselage reference frame, fuselage
$(..)_{\mathrm{G}}$	Global wake reference frame
	Global blade reference frame
$(\ )_{\mathrm{H}}$	Horizontal tail
$(..)_{h}$	Harmonics
$(..)_{\mathrm{I}}$	Inertial reference frame, inertia
$(..)_{\mathrm{L}}$	Local blade reference frame
$(\ )_{MR}$	Main rotor
$(..)_{\mathrm{P}}$	Free wake blade preconed reference frame
$(..)_{\mathrm{S}}$	Shaft reference frame, structural
$(..)^{\mathrm{t}}$	Tip finite element
$(..)_{\mathrm{T}}$	Tension
$(..)_{TPP}$	Tip path plane
$(\ )_{tr}$	Tail rotor
$(\ )_{\mathrm{V}}$	Vertical tail
$(..)_{\mathrm{W}}$	Wind reference frame

Abbreviations

BVI	Blade-Vortex Interaction

ODE	Ordinary Differential Equation
$PC2B$	Predictor-Corrector 2^{nd}-order Backward difference
PDE	Partial Differential Equation
$PIPC$	Pseudo-Implicit Predictor-Corrector
TWS	Turbulent Wake State
TPP	Tip Path Plane
VRS	Vortex Ring State

Chapter 1

Introduction

1.1 Motivation

Ever since the dawn of civilization, design and innovation have been a trial-and-error process. Advancement in technology, whether it was the wheel or the pulley, the light bulb or the steam engine, occurred as a result of test and failure, and learning from one's earlier mistakes. The history of aviation contains many examples of ingenuity and disaster in the road to the first flight of the Wright Brothers, and for many years after that inventiveness walked hand in hand with great achievements but also catastrophic mistakes (Ref. 2). Aviation pioneers often tested their ideas personally, risking, and sometimes losing, their own lives.

The development of the helicopter was not free of failures and mistakes. Indeed, the complexity of rotating-wing aircraft delayed the first successful flight of a helicopter more than 30 years after the first flight of a fixed-wing aircraft, a period in which many ideas and configurations were built and tested (Ref. 3). Many of these ended in crashes, some leading to better understanding of the physics of rotorcraft, some discarded. In any case, these early inventors had no means to validate

their ideas but to build them and test them, and build them again iterating until a successful design was found.

It is for this reason that having accurate simulation models is vital in the design process to avoid unnecessary redesigns due to poor predictions (Ref. 4). Such redesigns not only are expensive, but also delay the overall production process. Simulation models can be used to validate new technologies before they are built. Proper understanding of the theory behind rotorcraft flight can therefore help construct better and more accurate simulation models to build better helicopters more efficiently.

Improved modeling capabilities are also necessary to meet the increasingly more demanding handling qualities requirements. Today's military helicopters are expected to perform missions that require more maneuverability and agility. Such maneuvers often involve high rates and rapid changes, and accurate simulation requires high resolution models to capture the transient dynamics (Ref. 5). Civil helicopters are also being put through more demanding mission task elements, such as steep approaches to land in order to minimize the noise signature over populated areas, which involve risks such as high vibration or power settling. The availability of high fidelity simulation models provides the means to study such phenomena without any material or human losses.

Design of advanced flight control systems can also greatly benefit from accurate modeling of helicopters. Flight dynamics simulation can be used for the verification of new control system designs before they are implemented in real helicopters, specially if the model can rigorously replicate the real life conditions in a more varied

range of flight conditions, without relying extensively on empirical data that might not always be available.

Recent flight dynamics simulation models have achieved levels of sophistication that allow for increasingly more accurate predictions in a broader range of flight conditions (Ref. 6). While many of such models are too complex and computationally expensive to be used for real time simulation, they have demonstrated their utility by helping design better and more maneuverable helicopters and reliable flight control systems.

Helicopter simulation is a multi-disciplinary field, that involves flight dynamics, aerodynamics and structural dynamics. Building a comprehensive simulation model involves the coupling of many sub-systems, such as the aeroelastic rotor, the rotor wake, the fuselage, etc, which are not independent of each other and interact between themselves, adding another level of complexity to the behavior of the helicopter model (Ref. 4). These comprehensive models can then be used to calculate the steady-state trim equilibrium solution under any prescribed flight condition, to obtain a linearized model that can be used for stability and frequency response calculations, or to determine the transient response of the helicopter to arbitrary pilot inputs.

An important aspect of the flight dynamics simulation is the type of aerodynamics model used to predict the main rotor induced velocities. The existing flight dynamics simulation models, both in industry and in academia, utilize a wide spectrum of aerodynamic models to provide the main rotor inflow. Simple inflow models, such as those based on momentum theory or dynamic inflow, have been

widely used in comprehensive flight dynamics simulation models because of their low computational cost and their relatively easy implementation and solution with the rest of the rotor-fuselage model. However, they are limited in that they are based on a rigid and undistorted representation of the rotor wake structure and cannot capture the dynamics of the wake flow field. Free wake models overcome such limitations. By modeling the wake vortices as they are released from the blade and allowing them to distort freely under the influence of their mutual interactions as well as the blade circulation and the free stream and maneuvering velocities, it is possible to obtain an accurate description of the flow field and the induced velocities on the rotor without *a priori* assumptions (Ref. 7).

The aeroelastic modeling of the rotor blades is also of importance in the quest to accurately describe the behavior of helicopters for flight dynamics applications (Ref. 8). Modeling the non-linear coupling in flap, lag and torsion of the rotor blades is critical to obtain accurate results.

The present study aims to improve a comprehensive flight dynamics simulation model developed over the years at the University of Maryland (Ref. 6), commonly referred to as HeliUM, in two specific areas, namely the modeling of the rotor wake and the aeroelastic blade model. Regarding the rotor wake, this study will couple the Bhagwat–Leishman time-marching maneuvering free wake model (Ref. 9) with the rest of the rotor-fuselage model. This free wake model can capture maneuvering flight accurately in time, and therefore can be used to determine the response of the helicopter to transient pilot inputs. It can also be used for the calculation of equilibrium flight conditions, both periodic (straight and level flight, coordinated

turns) and aperiodic (steep descents). Since most modern helicopters have swept tips, as they reduce noise and vibrations and improve the overall performance of rotors (Ref. 8), it is important to include tip sweep in the aeroelastic modeling of the blade as well, therefore it is part of the present study to expand the blade model to account for the swept tip of the UH-60A helicopter.

Although the problem of obtaining a free-flight trim equilibrium solution has received considerable attention through the years, most often it has been limited to straight and level flight. Few studies have attempted to model steady coordinated turns (Refs. 6, 10, 11), or steady climbs and descents (Refs. 10, 11), of which only Ref. 6, the preceding work to the present study, includes the effect of maneuvering on the free wake (Ref. 12). Most comprehensive flight dynamics models have the capability to calculate the transient response of the helicopter to arbitrary maneuvers. Unsteady turning flight has often been considered, although traditional comprehensive codes did not have the capability to include the effect of maneuvering in their modeling of the wake. The ability to capture maneuvering flight, not limited to small excursions from trim, expanding the range of flight conditions that can be modeled with a flight dynamics simulation model, must therefore be the goal of comprehensive flight dynamics models.

A particularly challenging problem is the prediction of rotor flow fields in descending flight conditions, in which the rotor wake is unsteady and aperiodic. Whether it is in shallow descents, where the increased closeness of the rotor vortices makes their interaction more pronounced, or in steep descents, where the vortices cross over the rotor plane, modeling descending flight is a challenging problem.

Several of the most interesting problems that face aerodynamicists and flight dynamicists, such as BVI, autorotation modeling and the VRS, fall within this flight condition. Accurate modeling of descending flight is, therefore, indispensable.

When the rotor descents into its own wake, the increased proximity of the vortices creates a strongly unsteady flow close to the rotor. As the rate of descent increases, the upward flow pushes the vortices through the rotor, which enters the vortex ring state (VRS), a flight condition characterized by the accumulation of vorticity in the form of a ring at the tip of the rotor. The VRS manifests in strong thrust fluctuations, an increase in the rotor torque, highly unsteady blade airloads, aperiodic blade flapping and loss of control, which makes it a significantly dangerous flight condition when the helicopter is near the ground. The vortex ring state is not a condition exclusive of axial flight. In steep descents at low speed the VRS manifests in a condition called power settling, which consists in an increase in the power required to continue to increase the rate of descent (Refs. 4, 13). As the rate of descent increases, the power first decreases. Eventually, the power required to fly at the same speed reaches a minimum and any increase in rate of descent requires more power. When power settling occurs, the helicopter continues to descend even after applying additional power. Since recovery from power settling usually involves a significant loss in altitude, knowing the boundaries for this condition becomes extremely important, particularly when it occurs upon approach to landing.

The vortex ring state is characterized by largely unsteady flow. In the incipient stages of VRS, the degree of unsteadiness is mild and therefore the conditions encountered by the rotor blades over successive revolutions do not change consid-

erably and a trim solution is possible and represents the real flight conditions well. However, as the rotor enters into deep VRS, the flow is highly unsteady and the flight conditions encountered by the rotor blades over successive revolutions, as well as the different blades in the same revolution, are considerably different. Under these conditions, assumptions of periodicity enforced by a trim algorithm are invalid and cannot be applied. The proper approach under these flight conditions is to use a time-marching solution to simulate the unsteady transient evolution of the wake dynamics and the resulting flight dynamic response.

Another important standing problem that still draws a lot of attention is the prediction of the off-axis response. By off-axis, one refers to the response in a different axis to that related to the control perturbed, i.e., the pitch response to lateral cyclic or the roll response to a longitudinal cyclic. For years, the helicopter community was at loss at why many simulation models did not capture the direction of the off-axis response correctly. It was not until the nineties that some explanation was found. Rosen and Isser (Ref. 14) demonstrated that the distortion of the wake, up until then ignored, played an important role in the accuracy of the prediction of the off-axis response. Since then, the importance of the effect of maneuvering on accurately predicting both on-axis and off-axis responses has lead to many studies to account for maneuvering effects in the calculation of the main rotor inflow distribution.

The main objective of the work in this dissertation is to develop a flight dynamics model that can be used to calculate equilibrium and transient conditions in steady and unsteady maneuvers, including steep and axial descents. The present

study starts with the model developed by Theodore (Ref. 6), which is a flight dynamics model that consists of a coupled rotor-fuselage model, with flexible blades modeled with a finite element analysis, and the ability to calculate the induced velocities on the rotor both with dynamic inflow or with the Bagai–Leishman relaxation maneuvering free wake model (Ref. 12). The present study will expand that model to include a time-marching free wake model, the Bhagwat–Leishman free wake (Ref. 15), and incorporate the swept tip into the modeling of the flexible blade. The new model will then be used to simulate both steady and unsteady flight conditions on a UH-60 helicopter.

1.2 Literature review

This section presents a review of the current state of the art of those topics relevant to the present study. It is divided in the following sections: first, a review of existing comprehensive flight dynamics simulation models is presented, followed by a review of the different methods for determining the rotor inflow, with particular attention to free wake models, specially those which can capture maneuvering flight. Next, the problem of the off-axis response in maneuvering flight is covered. The state of the art in the modeling of descending flight continues, with special emphasis in the vortex ring state. Finally, a review of the evolution of aeroelastic models with swept tips is included.

1.2.1 Helicopter simulation models

In recent years, several comprehensive flight dynamics simulation models have been developed, in industry, academia, research institutions or for commercial use. These models have achieved high levels of sophistication, allowing for very accurate predictions of the helicopter behavior under many different flight conditions.

Theodore (Ref. 6) includes a comprehensive review of the diferent flight dynamics codes and their inflow modeling characteristics, and a summary is presented here, together with some updates and newer models that have been made public since then. A point made by Theodore and worth reinforcing is the difficulty to obtain details of the methodology or solution techniques used by these models, which are not often made available, particularly with the commercial models. Each of these models is described next, presented in alphabetical order.

The CAMRAD family of models (Ref. 11), which include CAMRAD, CAMRAD/JA and CAMRAD II has been developed by Johnson Aeronautics. Like all the models presented here, CAMRAD includes a coupled rotor/fuselage system. The fuselage model is rigid, but the blades are modeled with a finite element analysis that allows for both rigid and flexible blade models with coupled flap, lag and torsion degrees of freedom. The induced velocities can be calculated with simple uniform inflow based on momentum theory or with the Johnson free wake model (Ref. 16), which is a modification of the Scully wake model (Ref. 17). The model can be used to obtain a trimmed solution, both as free-flight and wind tunnel trim, and is not limited to level flight but includes coordinated turns and climbing and descending

flight. Moreover, the model can be used to obtain a linearized model using a perturbation analysis from a trim condition and to obtain the transient response to pilot inputs, both with the linear and the non-linear models. CAMRAD has been extensively used and validated.

The CHARM model (Refs. 18, 19), developed at Continuum Dynamics Inc. (CDI), is a general rotor/airframe model that includes the Constant Vorticity Contour wake model combined with a fuselage aerodynamic model using fast vortex and fast panel methods. The result is a model that can be used in real time while keeping the advantages of free vortex models, and that can capture rotor-wake-fuselage interactions. The blades are modeled with a finite element analysis that includes flap and lag bending, twist and extension. This model has been coupled with Sikorsky's GenHel flight dynamics simulation model providing a platform to perform trim and dynamic response calculations.

The COPTER model at Bell (Ref. 20), which stands for Comprehensive Program for Theoretical Evaluation of Rotorcraft, includes both a rigid and a NASTRAN-based flexible representation of the fuselage. The blades are modeled with fully coupled flap, lag and torsion, and the induced velocities are obtained with the Scully (Ref. 17) free wake model. It can be used for both free-flight and wind-tunnel trim calculations, to extract a linear representation of the equations of motion and to determine the response to pilot inputs. However, not much validation has been published.

FLIGHTLAB (Ref. 21), together with CAMRAD, is a commercially available simulation model. It contains a rigid fuselage model and the flexible blade includes

coupled flap and lag, but uncoupled torsional degree of freedom. To calculate the induced velocities, FLIGHTLAB uses a three state version of the Peters and He Finite State Dynamic inflow model (Ref. 22). Like most other models, it can be used to obtain trim, linear models and transient response calculation, being the only one that can do so in real time by means of parallel processing.

Several European companies and research centers, mainly Eurocopter, ONERA and DLR, have joined forces in the development of their own comprehensive model for flight dynamics, the Helicopter Overall Simulation Tool, or HOST (Ref. 23). The HOST model can be used to do trim calculations, to perform time domain and inverse simulations, and to obtain an equivalent linear system. Both a rigid and an elastic model can be used for the blades. The inflow can be calculated with several simple models, with the Pitt–Peters dynamic inflow (Ref. 24), although a model to account for the wake distortions has been included (Ref. 25), with a vortex rings method and with a prescribed wake model (only in trim).

The Second Generation Comprehensive Helicopter Analysis System (2GCHAS) (Ref. 26) has evolved and been renamed as the Rotorcraft Comprehensive Analysis System (RCAS) (Ref. 27). RCAS has both a rigid and elastic NASTRAN modal representation of the fuselage. The blades are modeled with a finite element analysis and include coupled flap, lag and torsional degrees of freedom. For the calculation of the induced velocities, RCAS provides several options: momentum theory, Peters–He finite state wake (Ref. 22), a prescribed wake model, and three free wake models: the Scully-Johnson wake (Ref. 16), the Bagai–Leishman relaxation free wake model (Ref. 28) and the Bhagwat–Leishman time-marching free

wake model (Ref. 7). Like most of the comprehensive models, it can calculate trim, linear and integrated solutions.

The model developed at Boeing, known as the Technology One program (TECH-01) (Ref. 29), also includes a flexible fuselage model in addition to the rigid one, but the flexible blades have only coupled flap and pitch degrees of freedom, while the lag dynamics are uncoupled. Both the Drees (Ref. 30) and Pitt–Peters (Ref. 24) dynamic inflow models can be used to determine the induced velocities, but no free wake models are available. Like with the Bell model, TECH-01 can be used for trim, linearization and integration calculations, but little validation has been published.

Developed also at the University of Maryland, the UMARC model (Ref. 31) can use both rigid and flexible fuselage and blades, with fully coupled flap, lag and torsion. UMARC has several options to calculate the induced velocities, including simple momentum theory uniform inflow, Pitt–Peters dynamics inflow (Ref. 24), the Scully (Ref. 17) and Johnson (Ref. 16) wakes and the Bagai–Leishman relaxation free wake model (Ref. 28). UMARC can be used to calculate an algebraic trim solution and a linearized model, but can only obtain the response to pilot inputs with the linear model.

In addition to these models, the present study is based on a model developed over the years, called HeliUM in its current implementation, that derived from the original GenHel (Ref. 32). This model includes flexible blades with coupled flap, lag and torsion dynamics, a rigid fuselage with aerodynamic data obtained from look-up tables, several dynamic inflow options and two free wake models, the Bagai–Leishman relaxation free wake (Ref. 28) and the Bhagwat–Leishman time-marching

model (Ref. 7). The model can obtain trim equilibrium conditions, linearized models and integrate the equations of motion to obtain the response to arbitrary pilot inputs. A detailed description of history and development of the model is presented in Section 1.3.

1.2.2 Wake and inflow models

An important aspect of the flight dynamics simulation is the type of aerodynamics model used to predict the main rotor induced velocities. The existing flight dynamics simulation models, both in industry and in academics, utilize a varied set of aerodynamic models to provide the main rotor inflow.

Simple inflow models

The simplest inflow models are those based on momentum theory or a combination of momentum theory with blade element theory (BET) (Ref. 3). Being computationally inexpensive and reliable, these models are still extensibly used today as a preliminary analysis tool. Linear models, such as that of Drees and Mangler and Squire improve the previous methods with variations of the longitudinal and lateral inflow with forward speed (Ref. 3).

Dynamic inflow models are some of the most popular and extensively used inflow models in comprehensive flight dynamics models. They have the general advantage of being formulated in first order form, which simplifies their integration in the formulation of most existing fight dynamics mathematical models. In short, the formulation of dynamic inflow models consists of a set of ordinary differential

equations in state-space form with an equal number of states representing the inflow coefficients. The matrices associated with such formulation represent mass and gain functions and can be obtained with different methods, from actuator disc to vortex theory. The different dynamic inflow models available were reviewed by Gaonkar and Peters (Refs. 33, 34) and Chen (Ref. 35).

One of the most widely used dynamic inflow models in the literature is the Pitt–Peters model (Ref. 24), which derives the inflow equations using unsteady-actuator disc theory, relating the rotor transient loads to the induced velocity field.

More recently, finite state wake models, like that of Peters and He (Refs. 22, 36), have allowed for a formulation with multiple states which permit both radial and higher harmonic azimuthal variations of the rotor inflow. A more realistic approximation to the induced velocity field can be obtained with such a method by increasing the number of states, while maintaining the formulation in first order.

The basic dynamic inflow models have been extended through the development of sets of coefficients that allow the application of such models to specific flight conditions. One example is that of Prasad *et al.* (Refs. 37, 38), which includes the dynamic wake distortion effects due to maneuvering, and which obtains the time constants of the model using a vortex tube analysis. Another extension is that of He *et al.* to allow the finite state wake model to be used for such problems as the prediction of the off-axis response or flight through the vortex ring state (Ref. 39).

As it has been mentioned already, dynamic inflow models benefit from their formulation being in a form that is easy to couple with comprehensive flight dynamics codes and from their inexpensive cost of computation. However, there are some

practical disadvantages associated with the use of such models, particularly the fact that they are defined with a set of coefficients associated with a particular flight condition, and cannot be applied to another problem without *a priori* determination of the constant parameters associated with their mathematical representation. Moreover, dynamic inflow models are based on a rigid and undistorted representation of the wake structure, and cannot account for the dynamics of the wake flow field.

Free-vortex wake models

Vortex models describe the rotor wake as a series of vortex filaments released from the blade and that are discretized in time and space, and once the position of each filament segment is known (depending if it is part of the problem, as in free wake models, or assumed rigid, as in prescribed wakes), the induced velocities on the rotor can be calculated from the influence of each vortex segment in the flow field (Ref. 3). The studies of Bhagwat (Ref. 15) and Ananthan (Ref. 40) contain a detailed review of the different types of vortex models of the rotor wakes and the different attempts that have been made at modeling them. Therefore, only a summary is included here.

Prescribed wake models are the simplest of all the vortex wake models. The geometry of the wake is described with undistorted helical vortex filaments, the influence of which on the rotor can be calculated with Biot-Savart law to obtain the induced velocities. Prescribed wake models have been used successfully to model both hovering (Landgrebe (Ref. 41), Kocurek & Tangler (Ref. 42)) and forward

flight (Egolf & Landgrebe (Ref. 43), Beddoes (Ref. 44)), but they need to rely on empirical data to model the distortions of the wake structure. For this reason, and because the wake is assumed rigid, prescribed wake models provide little advantage over dynamic inflow models.

Free vortex models represent the next level of sophistication in the calculation of the induced velocities. Unlike prescribed wake models, free wake models include the geometry and strength of the vortex filaments as part of the problem. The vortex filaments are allowed to distort freely under their self and mutual influence, including the influence of the blade bound vortex and the velocities due to translation and rotation of the helicopter.

Free wake models can be categorized according to the method used to discretize the flow field or the numerical scheme used to solve them. The vortex filaments are usually approximated with straight line segments, although they can also be modeled with curved vortex segments (Ref. 45) or vortex blobs (Ref. 46). Regarding the solution scheme used, the models are either relaxation or time-marching methods.

Relaxation methods assume that the wake solution is periodic and obtain a solution through an iterative process until the wake geometry does not change between successive iterations. Because relaxation methods are numerically efficient and free of the instabilities that are associated with time-marching schemes, they have been widely used in the field.

The first attempt at using an iterative method to model the rotor wake was done by Clark & Leiper (Ref. 47), who modeled two turns of the tip vortex and used ring vortices for the far wake and obtained successful results for hover performance.

The wake model of Scully (Ref. 48), which he developed as a relaxation scheme after failing to obtain a time-marching model without numerical instabilities, is one of the most recognized and widely used today. The induced velocities were calculated with a weighted average using a relaxation parameter, which gives name to this family of models. It used an azimuthal step of 15 degrees, and was used successfully both in hover, with 6 to 12 free wake turns and a vortex cylinder for the far wake, and in forward flight, for which 2 to 4 free wake turns were deemed sufficient. Its success is traced to the fact that it was later adapted by Johnson and used in CAMRAD (Ref. 49), a commercially available comprehensive flight dynamics model. Miller (Ref. 50) developed a model for hover with vortex sheets or a vortex cylinder to model the far wake boundary, and included the Weissinger-L lifting surface model (Ref. 51) to calculate the bound circulation. Bliss *et al.* followed with a family of relaxation models (Refs. 52, 53) characterized by curved vortex segments, which allowed for larger discretization, a predictor-corrector iterative scheme and a large core radius (5% of the rotor radius). Miller & Bliss (Ref. 54) developed an interative scheme which differed in that the non-linear equations of the wake were linearized and then solved with a predictor-corrector scheme.

Closer to the present work is the wake model of Crouse & Leishman (Ref. 55), which precedes the Bagai–Leishman free wake model (Ref. 28). The Bagai–Leishman wake model uses a pseudo-implicit predictor-corrector scheme to solve the wake geometry, a five point central differencing scheme to approximate the derivatives both in time and space and a Weissinger-L model to solve the blade bound circulation-lift problem. This wake model, capable of capturing the effects of maneuvering,

was coupled successfully with several flight dynamics models, including that of Theodore (Ref. 6), the starting point of the present study.

Time-marching free wake models do not enforce periodicity of the rotor wake solution. Instead, the solution is obtained from an impulsive start by advancing in time and allowing the wake to distort freely until a solution is found.

Several of the earliest attempts at solving the wake problem with time-marching method were unsuccessful due to their choice of numerical scheme leading to numerical instabilities (Refs. 17, 56, 57). Landgrebe (Ref. 58) overcame some of the numerical instabilities in forward flight with an explicit time-marching scheme and a coarse discretization to reduce the high cost of the method. He obtained good correlation with experimental data for forward flight, but in hover he could not overcome the numerical instabilities. Similarly, Sadler (Ref. 59) used an explicit Euler scheme for multiple rotor configurations, which worked well in forward flight but was too unstable in hovering flight. A method with curved filaments and a predictor corrector scheme was used by Bliss *et al.* (Refs. 60, 61), but only used for forward flight conditions. Also for forward flight use only was the time-marching wake model of Egolf (Ref. 62), which used a vortex lattice to represent the wake.

The CHARM wake model (Refs. 19, 45) uses a constant vorticity contour (CVC) method, which follows lines of constant strength vortex elements, with curved vortex filaments.A vortex lattice lifting surface model is used for the blade, which uses a finite element structural analysis to determine the mode shapes. The fuselage body and blade surface are modeled with panel methods, and can therefore be used to study the interaction between the rotor wake and the helicopter body.

Fast computational methods and a reduced wake resolution are used to reduce the computational cost and run in real time.

A different approach has been taken more recently by Brown *et al.* (Refs. 63, 64), which use a vorticity transport method to solve the wake, which is solved in an Eulerian frame using Toro's Weighted Average Flux algorithm (Ref. 65) to march the equation in time, which provides the advantage over other CFD methods of maintaining more control over the dissipation of vorticity in the wake. The model can therefore capture both blade-wake and wake-body interactions.

The Bhagwat–Leishman free wake model (Ref. 15) is a maneuvering, time-marching free wake model developed from the Bagai-Leishman model (Ref. 12). This is the model used in the present study. The Bhagwat model uses a second-order, predictor corrector two-step backward (PC2B) algorithm to integrate the equations of the wake in time, while the space derivative is approximated with a five-point central difference scheme. This model has been tested and validated over many flight conditions. In addition, Ananthan (Ref. 40) has added vortex filament stretching and has demonstrated the validity of the model in unsteady maneuvers (Ref. 5).

1.2.3 Maneuvering models and the off-axis response

The level of sophistication of the aerodynamics in flight dynamic simulation models has increased rapidly in the last decade, especially for nonreal-time, research type simulation models. One of the drivers in the research community has been the problem of predicting the off-axis response (e.g., the pitch response to lateral cyclic).

The problem remained unresolved until Rosen and Isser (Ref. 14) demonstrated the role played by the distortion of the wake geometry, due to the maneuver, using a prescribed wake approach. Since then, several approaches have been followed to account for maneuvering effects in the calculation of the main rotor inflow distribution, though most use a dynamic inflow type model. Basset and Tchen-Fo (Ref. 25) developed a set of coefficients using a dynamics vortex model to couple the angular rates to the inflow distribution, and used them in a dynamic inflow model. The popular Pitt–Peters dynamic inflow model has also been extended to capture the dynamic distortion of the wake due to maneuver and transition flight. The work by Prasad, Peters *et al.* (Refs. 37, 38), where the appropriate time constants are extracted from a vortex tube analysis, is one of the latest developments of the model. Simple but accurate state-space inflow models suitable for maneuver analyses have also been extracted using frequency domain system identification, either from experimental (Ref. 66) or simulation (Refs. 67, 68) data.

A free vortex wake model to account for the effects of maneuvering from first principles, has been developed by Bagai and Leishman (Ref. 69). Note that, in the context of the present paper, "from first principles" is limited to meaning that no *a priori* assumptions are made on the distortion of the wake geometry caused by the maneuver, that is, the wake geometry is free to evolve from the time history of the motion of the rotor blades, and that no empirical or semi-empirical correction coefficients are used in the definition of the rotor inflow or wake geometry. The model of Ref. 69 is based on the solution of the vorticity transport equations, and uses a relaxation technique to solve numerically the governing equations (as mentioned

earlier). Therefore, it is rigorously appropriate only for a steady trimmed flight condition, and not for transient conditions. The limitations of the relaxation wake have been subsequently removed in the time-accurate free wake model of Bhagwat and Leishman (Ref. 9), which is therefore suitable for analyzing unsteady maneuvers of arbitrary amplitude.

Another free wake model capable of modeling maneuvering flight has been developed by Wachspress *et al.* (Ref. 19) as part of the simulation model CHARM (mentioned earlier), and successfully applied to the analysis of flight in vortex ring state and to the prediction of off-axis response. This wake has been coupled with the Sikorsky GenHel simulation code, and used for the modeling of free wake-empennage aerodynamic interaction, with improvements in the correlation with flight test data (Ref. 70). The wake has also been coupled with the NASA version of the GenHel code (Ref. 71), giving results similar to those of the Pitt–Peters dynamic inflow model. The same simulation code has also been used to obtain aircraft and blade motion data for wake dynamics and acoustics studies (Refs. 72, 73). In this case, aircraft and blade motion data were provided as input to the time-accurate free wake model of Ref. 9 in an "open loop" fashion, as the NASA GenHel model is based on linear inflow, and rigid flap and lag motion with an empirical correction for torsion (Ref. 32).

The relaxation wake of Ref. 69 was coupled with a flight dynamic simulation that included a flexible blade model, and the resulting model was used to study the dynamics of the Eurocopter BO-105, with a special focus on the prediction of the off-axis response (Ref. 74). One of the conclusions of the study was that an

accurate prediction of the off-axis response from first principles was indeed possible, but it required the simultaneous modeling of: (i) blade flexibility in flap, lag, and torsion, and (ii) distortion of the wake geometry caused by the maneuver. The off-axis predictions with the correct wake distortions but with elastic flap only, and those with fully coupled flap-lag-torsion but with a conventional free wake without maneuver distortion, exhibited the traditional "wrong direction" error (Ref. 74). On the other hand, accurate predictions of the on-axis response did not require such a sophisticated modeling. Although the relaxation free wake was not rigorously applicable to transient maneuvers, it performed well, probably because the flight test maneuvers were of small amplitude.

1.2.4 Descending flight and vortex ring state

Experimental investigations of the VRS started in the 1950s with the wind-tunnel work of Drees & Hendal (Ref. 1) who, via smoke-flow visualization, showed the recirculation of the flow in the rotor plane and the toroidal shape of the vortex ring around the tips of the rotor blade (Fig. 1.1). Refs. 75 and 76 provide a fairly comprehensive analysis and comparison of the experimental data available.

Numerical analysis of the VRS has not been very abundant. It was necessary that the technology matured and provided the capability to accurately model the vortex flow field. Simple models, such as those based on momentum theory, can be used when the descent angles are not very large. Several early works, such as those in Refs. 77 and 78, used momentum theory to map the boundaries of the

vortex ring state. The model in Ref. 13 explains power settling and autorotation, and provides contour maps for the power required by the rotor as a function of glide speed, glide angle and rotor pitch angle. More recently, several studies have proposed simple inflow models (Refs. 39, 76, 79–82) to work in steep or axial descent flight, including operation in the VRS. These parametric extensions of momentum theory can be adequate with the appropriate selection of tuning parameters, however they are not based on first principles and are unable to capture the dynamics of the flow field of the rotor wake. The most accurate numerical approaches to model the VRS are those based on free wake models and computational fluid dynamics. Leishman *et al.* (Refs. 83, 84) studied the instabilities associated with the onset of the VRS using a time-accurate free wake model (Ref. 9). This model can capture the formation and development of the vortex ring state and can be used both to obtain steady state solutions as well as the time-integrated response to maneuvers in descending flight. Brown *et al.* (Refs. 75, 85) developed a vorticity transport model of the rotor wake, which they successfully applied to both axial and forward flight descents. Their results allowed for a numerical mapping of the VRS boundary that complements that obtained through experiments and flight test. Moreover, the interference effects between the rotor wake and the fuselage and tail during the descent cases were also investigated.

Not much work has been done to implement such computational models capable of accurately describing descending flight and VRS into comprehensive flight dynamics simulation models. Descent flight and autorotation are the drivers behind the implementation of coupled advanced wake and flight dynamics models such as

Ref. 86, which compares the results for finite-state induced inflow methods with the vorticity transport wake model. Their results show that, while for shallow descents the differences are small, for steeper descents, such as those required for autorotation, there were some discrepancies between the two models and the higher accuracy of the inflow predicted by the vorticity transport method is essential to correctly predict autorotation performance.

A very loose coupling of a flight dynamics model with the Bhagwat–Leishman free wake (Ref. 9) is used in Ref. 73 to perform aeroacoustics calculations for pop-up maneuvers starting from a shallow descent.

1.2.5 Swept tip modeling

In the early eighties, several studies investigated the effects of swept blade tips on rotor aerodynamics (Refs. 87–89). These early studies showed the importance of proper modeling of the blade tip sweep, which introduces flap-torsion and lag-axial coupling effects. Moreover, because elastic displacements and dynamic pressure are the largest at the tip, proper dynamic and aerodynamic modeling becomes necessary for accurately modeling the rotor loads.

Tarzanin & Vlaminck (Ref. 90) conducted the first analytical study of the effect of swept tips on hub loads. Their approach to model the swept tip consisted of displacing the shear, aerodynamic and mass center of cross sections on the tip. They concluded that tip sweep affects both vibration and stability.

The first systematic aeroelastic model of rotor blades with swept tips was

developed by Celi & Friedmann (Refs. 91–93). This model was based on the formulation of the rotor blades equations of motion presented in Refs.94–96, which use a finite element approach based on the Galerkin Method of Weighted Residuals, and a special finite element model for the tip was developed. The main conclusions of their study are that the flap-torsion and lag-axial couplings introduced by the tip sweep may produce aeroelastic instabilities related to frequency coalescence, but when frequency coalescence does not occur, tip sweep has a stabilizing effect. This model's main limitations were the assumption that the transformation at the joint between the straight and swept part of the blade is linear and that only tip sweep is considered, neglecting the modeling of anhedral or other advance geometry parameters.

The nonlinear nature of the transformation at the joint between the tip element and the straight part of the blade was derived by Panda in Ref. 97. For sweep angles greater than 20 degrees, he demonstrated that the nonlinearities are significant and should not be neglected.

Benquet & Chopra (Ref. 98) developed an aeroelastic analysis of rotor blades with both sweep and anhedral using a finite element method based on Hamilton's principle, to calculate the loads and response in forward flight. Kim & Chopra (Ref. 99) developed the model of Ref. 98 further by including the nonlinear transformation of Ref. 97 at the junction between the straight blade and the tip. In addition to this, Bir & Chopra (Ref. 100) developed the model for advance geometry tips with variable sweep, anhedral, pretwist and planform.

Some more recent studies by Yuan & Friedmann (Refs. 101, 102) considered the

aeroelastic behavior of composite blades with swept tips and examined the structural couplings of such blades. The blade model included arbitrary cross-sectional shape, generally anisotropic material behavior, transverse shears and out-of-plane warping. A structural optimization study was performed, with the composite ply orientations, tip sweep and anhedral as the design variables, with the objective of minimizing vibratory hub loads in forward flight. Posterior studies (Ref. 103) combined this model with a free wake analysis to reduce BVI induced vibrations.

1.3 History of the flight dynamics model

The origin of the model used in the present study is traced back to the GENHEL helicopter model developed by Howlett in Ref. 32. The rotor in this model was limited to rigid blades hinged in both flap and lag. Torsion was accounted for by means of an empirically-based dynamic twist model. A rigid body model was used for the fuselage, with its aerodynamics obtained from look-up tables containing aerodynamic coefficients obtained experimentally. The modeling of the fuselage, empennage and tail rotor in the present study are based mostly in this original model.

Ballin (Ref. 104) extended the model, his primary contribution being the engine modeling. Further improvement to the model, now called UM-GENHEL, was carried out by Kim (Ref. 105), who can be credited with two important contributions. First of all, he added the Pitt–Peters dynamic inflow model (Refs. 24, 106) to calculate the main rotor inflow. In addition, he reformulated the trim process

to represent the equations of motion in rigorous first-order form, which allowed the calculation of linear, constant coefficient equations of motion that describe the small perturbation dynamics about an equilibrium position.

The modeling of the rotor was improved by Turnour (Ref. 107), who included a fully numerical structural formulation (Ref. 108) with coupled elastic flap, lag and torsional degrees of freedom, plus a finite element analysis and a modal coordinate transformation to reduce the number of blade degrees of freedom. In addition, he also improved the aerodynamic modeling with a new higher order dynamic inflow model (Refs. 22, 36), which includes the effects of trailed as well as shed wake, and added the Leishman–Nguyen (Ref. 109) state-space unsteady aerodynamics model. This model, referred to as FLEXUM, was specialized for the UH-60 helicopter and could be used to calculate trim, linearize the equations of motion as well as time integrate them to obtain the response of the helicopter to pilot inputs.

Theodore (Ref. 6) made a significant contribution to the way the model, that he termed HeliUM, computed the inflow, with the addition of the maneuvering free wake model of Bagai and Leishman (Ref. 110). In addition, he included Keller's extended momentum theory for inflow model and a quasi-steady aerodynamic model for blade section aerodynamics. The model, which allowed for more accurate predictions of the off-axis response, was also modified for a hingeless rotor, and a full new BO-105 implementation was added.

Besides an optimization and sensitivities study, the work of Fusato (Ref. 111) provided a new implicit formulation of the equations of motion, which makes the simulation model more flexible and modular. The last improvements to the model

before the present work were carried on by Cheng (Ref. 112), who modified and applied the model for the study of Higher Harmonic Control, extracted a high-order linear model including the HHC characteristics in rotor states and hub loads and extended the vibration prediction capabilities. Presently, the model evolves through the work of Malpica (Ref. 113), who has performed a closed-loop HHC and time periodic stability analysis and has incorporated a trailing-edge flap model for flight and rotor control analysis and a state-space formulation for compressible unsteady aerodynamic forces.

1.4 Objective of this dissertation

The objectives of the present study are:

1. To develop a flight dynamics simulation model that includes a time-accurate maneuvering free vortex model, the Bhagwat–Leishman, wake model, that can be used for the calculation of the response of the helicopter to maneuvers of arbitrary amplitude. A new approach for the trim and integration calculation need to be developed, in particular to adapt the Weissinger-L method to calculate the bound circulation to the rest of the flight dynamics model.

2. To improve the fidelity of the aeroelastic blade model with the inclusion of the modeling of the swept tip. The implementation of the swept tip has been developed and validated in previous works, and therefore the investigation of the details of such an implementation or the structural properties of such a model are not really a specific objective of the present study. However,

the effect of including the blade with tip sweep on the trim solution and the dynamic response of the helicopter will be investigated.

3. To optimize the model to eliminate unnecessary computations and reduce the overall cost while keeping the same level of accuracy.

4. To use the developed model to study the physical mechanisms behind steady and transient helicopter flight. In particular, steady level flight, turning flight and descending flight equilibrium conditions will explored, and the response of the helicopter to lateral maneuvers and in axial descents, paying special attention to the helicopter cross-couplings and the vortex ring state.

5. To validate the proposed mathematical model with flight test data when available, both in steady and transient conditions.

1.5 Principal contributions

1. The most significant contribution of the present study is the incorporation of a time-accurate free wake model to the trim solution and to the integration of the equations of motion of the helicopter. The Bhagwat–Leishman free wake model can be used both to obtain the steady-state equilibrium conditions of trim and to integrate the response of the helicopter to pilot inputs accurately in time.

   In addition, the following are also original contributions in this study:

2. Optimized the trim procedure to reduce the overall cost of computation. Unnecessary calls to the free wake model were eliminated, and the circulation-inflow dependance was solved in a more efficient manner than in the previous implementation of the simulation model.

3. Introduced the modeling of the swept tip into the aeroelastic blade model. This adds one more level of sophistication to the modeling of the blade, which is an important asset of the current rotor-fuselage model.

4. Replaced the previous methodology to calculate the bound circulation with a new approach that makes use of the Weissinger-L model available with the free wake model, which not only provides a more accurate value of the vortex strength, but also allows the inclusion of the near wake model as well as permits a frequent series of updates of the bound vortex with every new value of the induced velocities within the free wake model.

1.6 Outline of the thesis

In Chapter 2, a description of the mathematical model used for this dissertation is presented. This description is not complete, but illustrates the model and its capabilities.

Chapter 3 describes the free wake model used for this study in detail.

Chapter 4, discusses the different solution methods used in the model, namely the calculation of the blade mode shapes, the trim solution and the determination

of the response of the helicopter to pilot inputs. In addition, the coupling of the wake model with the trim and integration methodologies is discussed, and a solution offered.

In Chapter 5, the helicopter model used to obtained the results presented in this dissertation is described, and the natural frequencies and blade mode shapes are shown.

In Chapter 6, results are presented for the calculation of trim with the new additions to the model. These are compared to experimental data. Results are obtained for level flight, turning flight, descending flight and descending turning flight.

In Chapter 7, the results of applying the model for integrating the equations of motion are described. The response is obtained for different maneuvers at different speeds, and the model is compared to flight test data when available.

Chapter 8 provides the conclusion to the thesis.

Additional material is provided in the Appendices for completeness.

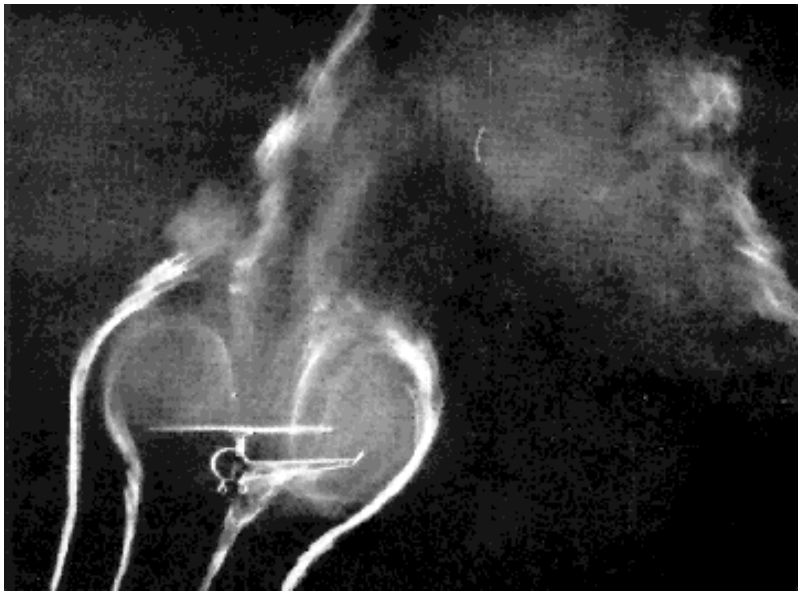

Figure 1.1: Smoke-flow visualization of the vortex ring state (Ref. 1).

Chapter 2

Mathematical Model

This chapter contains a description of the mathematical model of the helicopter used in this study. The chapter starts with an overview of the main features of the model, followed by a description of the aircraft, rotor and free wake coordinate systems. Next, the formulation of the main rotor equations of motion and the rigid fuselage, empennage and tail equations are presented. This is followed by a description of the inflow models available in the model, particularly the free wake model used in the present study. The transformation of the equations of motion into rigorous first order, state space form is presented next. Finally, a list of the main assumptions taken in the formulation and solution of the mathematical model is provided.

2.1 Overview

Except for the free wake, the mathematical model is formulated as a system of first order, coupled, non-linear ordinary differential equations of the form:

$$\dot{\mathbf{y}} = \mathbf{g}(\mathbf{y}, \mathbf{u}; t) \tag{2.1}$$

or of the equivalent implicit form:

$$\mathbf{f}(\dot{\mathbf{y}}, \mathbf{y}, \mathbf{u}; t) = \mathbf{0} \tag{2.2}$$

where $\mathbf{y}$ is a vector of states, $\mathbf{u}$ is a vector of controls and t is time.

The maneuvering free wake model is implemented as a set of finite difference equations, which result from the discretization in space and time of a vector partial differential equation (PDE), the vorticity transport equation (Ref. 15). These finite difference equations need to be solved with a time marching method separately from the main flight dynamics model because of the different mathematical form. Therefore, the wake model does not explicitly contribute any additional states to the basic flight dynamics model, nor does it change the basic first order form of the equations of motion.

When the inflow distribution over the main rotor is calculated using the free wake model, the state vector $\mathbf{y}$ takes the form (for a four-bladed rotor):

$$\begin{aligned} \mathbf{y}(\psi_i) \;=\; & [u_F \; v_F \; w_F \; p \; q \; r \; \phi_F \; \theta_F \; \psi_F \; \lambda_t \; q_1^1 \; q_2^1 \; q_3^1 \; q_4^1 \; \dot{q}_1^1 \; \dot{q}_2^1 \; \dot{q}_3^1 \; \dot{q}_4^1 \\ & \ldots q_1^{N_h} \; q_2^{N_h} \; q_3^{N_h} \; q_4^{N_h} \; \dot{q}_1^{N_h} \; \dot{q}_2^{N_h} \; \dot{q}_3^{N_h} \; \dot{q}_4^{N_h}] \end{aligned} \tag{2.3}$$

where u_F, v_F, w_F, p, q, and r are the velocities and rates in the body fixed coordinate system; ϕ_F, θ_F, and ψ_F are the Euler angles of the fuselage; λ_t is the tail rotor inflow; and q_i^k and $\dot{q}_i^k$ are the generalized displacement and velocity coordinates for the i-th blade and the k-th normal mode in the rotating frame at the azimuth angle ψ_i.

If dynamic inflow is used instead to calculate the induced velocities, three additional states are used to describe the main rotor inflow, and the state vector $\mathbf{y}$

becomes:

$$\begin{aligned}\mathbf{y}(\psi_i) &= [u_F\ v_F\ w_F\ p\ q\ r\ \phi_F\ \theta_F\ \psi_F\ \lambda_0\ \lambda_c\ \lambda_s\ \lambda_t\ q_1^1\ q_2^1\ q_3^1\ q_4^1\ \dot{q}_1^1\ \dot{q}_2^1\ \dot{q}_3^1\ \dot{q}_4^1 \\ &\quad \ldots q_1^{N_h}\ q_2^{N_h}\ q_3^{N_h}\ q_4^{N_h}\ \dot{q}_1^{N_h}\ \dot{q}_2^{N_h}\ \dot{q}_3^{N_h}\ \dot{q}_4^{N_h}] \end{aligned} \tag{2.4}$$

where λ_0, λ_c, and λ_s are the uniform, cosine and sine coefficients of the dynamic inflow model respectively.

The control vector, $\mathbf{u}$ is defined as:

$$\mathbf{u} = [\theta_0\ \theta_{1c}\ \theta_{1s}\ \theta_t\ \dot{\theta}_0\ \dot{\theta}_{1c}\ \dot{\theta}_{1s}] \tag{2.5}$$

where θ_0 and θ_t are the main and tail rotor collective controls, θ_{1c} and θ_{1s} are the lateral and longitudinal cyclic controls and $\dot{\theta}_0$, $\dot{\theta}_{1c}$ and $\dot{\theta}_{1s}$ are the time derivatives of the pitch controls, which are used only in a few occasions in the model, such as in the modeling of the lag damper (Refs. 32, 105).

2.2 Coordinate systems

Several different coordinate systems are used throughout the present study, for the body as a whole, for the rotor and for the free wake. This section defines the different coordinate systems used and the transformation between them.

2.2.1 Body coordinate systems

The overall motion of the helicopter is described in three main body coordinate systems: the inertial coordinate system, the body-fixed coordinate system and the

wind coordinate system. All three frames of reference have their origin at the center of mass of the helicopter, but their axes have different orientation.

Inertial coordinate system

The inertial coordinate system has its origin at the helicopter CG, and its z_I axis is vertical, and therefore it has the same direction as the weight vector. The x_I and y_I axes can have an arbitrary direction. They are usually taken pointing North and East, respectively, but the precise orientation is not important for the present study. This coordinate system is depicted in Fig. 2.1.

Body-fixed coordinate systems

The body-fixed coordinate system, shown in Fig. 2.1, is also centered at the CG, and its axes rotate with the fuselage. The x_B and z_B axes point forward and downward respectively, and define the vertical plane of symmetry (or quasi-symmetry) of the helicopter. The y_B axis is perpendicular to both and points starboard.

The transformation between the inertial and body-fixed coordinate systems is based on the Euler angles ϕ, θ and ψ, which represent the roll, pitch and yaw attitudes of the aircraft. The sequence and rotation of these angles is shown in

Fig. 2.2. The resultant transformation matrix is:

$$[T_{\mathrm{B}I}] = \begin{bmatrix} \cos\theta\cos\psi & \sin\psi\cos\theta & -\sin\theta \\ \sin\phi\sin\theta\cos\psi - \cos\phi\sin\psi & \sin\phi\sin\theta\sin\psi + \cos\phi\cos\psi & \sin\phi\cos\theta \\ \cos\phi\sin\theta\cos\psi + \sin\phi\sin\psi & \cos\phi\sin\theta\sin\psi - \sin\phi\cos\psi & \cos\phi\cos\theta \end{bmatrix} \tag{2.6}$$

Therefore:

$$\begin{Bmatrix} \mathbf{i}_{\mathrm{B}} \\ \mathbf{j}_{\mathrm{B}} \\ \mathbf{k}_{\mathrm{B}} \end{Bmatrix} = [T_{\mathrm{B}I}] \begin{Bmatrix} \mathbf{i}_{\mathrm{I}} \\ \mathbf{j}_{\mathrm{I}} \\ \mathbf{k}_{\mathrm{I}} \end{Bmatrix} \tag{2.7}$$

Wind coordinate system

The wind coordinate system has its center at the CG and its orientation is determined by the freestream airflow. The x_W axis points forward, aligned with the freestream velocity. The y_W and z_W axes are perpendicular to x_W and point to the right and downwards respectively. The relation between the wind axes and the body-fixed frame is determined by the fuselage angle of attack α_F and the fuselage sideslip angle β_F, and it is shown in Fig. 2.3. The transformation between both systems is given by the following matrix:

$$[T_{\mathrm{W}B}] = \begin{bmatrix} \cos\alpha_F\cos\beta_F & -\cos\alpha_F\sin\beta_F & -\sin\alpha_F \\ \sin\beta_F & \cos\beta_F & 0 \\ \sin\alpha_F\cos\beta_F & -\sin\alpha_F\sin\beta_F & \cos\alpha_F \end{bmatrix} \tag{2.8}$$

Thus:

$$\left\{ \begin{array}{c} \mathbf{i}_{\mathrm{W}} \\ \mathbf{j}_{\mathrm{W}} \\ \mathbf{k}_{\mathrm{W}} \end{array} \right\} = [T_{\mathrm{W}B}] \left\{ \begin{array}{c} \mathbf{i}_{\mathrm{B}} \\ \mathbf{j}_{\mathrm{B}} \\ \mathbf{k}_{\mathrm{B}} \end{array} \right\} \tag{2.9}$$

In the present study, this coordinate system is used only to obtain the aerodynamic characteristics of fuselage and empennage, which are defined in tabular form with respect to it.

2.2.2 Main rotor coordinate systems

Shaft coordinate system

The rotor shaft is not usually aligned with the z_B body axis, but tilted a small amount to help alleviate the steady loads it sustains in flight. The shaft coordinate system, which has its origin at the hub and is a body-fixed axis system, has its z_S component in the shaft direction, the x_S axis pointing forward, and the y_S axis pointing to starboard.

The angles i_θ and i_ϕ are, respectively, the lateral and longitudinal tilt angles of the shaft. The transformation matrix between the shaft and the body-fixed coordinate systems is given by:

$$[T_{SB}] = \begin{bmatrix} \cos i_\theta & \sin i_\theta \sin i_\phi & \sin i_\theta \cos i_\phi \\ 0 & \cos i_\phi & -\sin i_\phi \\ -\sin i_\theta & \cos i_\theta \sin i_\phi & \cos i_\theta \cos i_\phi \end{bmatrix} \tag{2.10}$$

so that:

$$\left\{ \begin{array}{c} \mathbf{i}_S \\ \mathbf{j}_S \\ \mathbf{k}_S \end{array} \right\} = [T_{SB}] \left\{ \begin{array}{c} \mathbf{i}_B \\ \mathbf{j}_B \\ \mathbf{k}_B \end{array} \right\} \tag{2.11}$$

Hub rotating coordinate system

The hub rotating coordinate system has its origin at in the hub, with its z axis is aligned with the shaft, and it rotates about the shaft at the rotor speed. The z axis points upwards, the x axis lies on a vertical plane containing the elastic axis of the undeformed blade and is positive outwards, and the y axis is perpendicular to them and positive in the forward (i.e., lead) direction. The transformation between the shaft fixed and the hub rotating frames is illustrated in Fig. 2.4, and determined by the following transformation matrix:

$$[T_{RS}] = \begin{bmatrix} -\cos\psi & \sin\psi & 0 \\ \sin\psi & \cos\psi & 0 \\ 0 & 0 & -1 \end{bmatrix} \tag{2.12}$$

where ψ is the azimuth angle of the reference blade.

Thus:

$$\begin{Bmatrix} \mathbf{i} \\ \mathbf{j} \\ \mathbf{k} \end{Bmatrix} = [T_{RS}] \begin{Bmatrix} \mathbf{i}_S \\ \mathbf{j}_S \\ \mathbf{k}_S \end{Bmatrix} \tag{2.13}$$

Undeformed preconed blade coordinate system

The undeformed preconed blade coordinate system is the result of rotating the hub rotating coordinate system by the blade precone angle β_p. This rotating frame has its center at the blade root; the $\hat{\mathbf{e}}_x$ unit vector is positive outwards, the $\hat{\mathbf{e}}_y$ vector is oriented in the blade lead direction and the $\hat{\mathbf{e}}_z$ is perpendicular to the undeformed elastic axis and is positive upwards. Figure 2.5 shows the relation between the hub rotating and the undeformed preconed coordinate systems.

The transformation from the hub rotating frame and the blade undeformed preconed system is defined by:

$$[T_{\mathrm{P}R}] = \begin{bmatrix} \cos\beta_p & 0 & \sin\beta_p \\ 0 & 1 & 0 \\ -\sin\beta_p & 0 & \cos\beta_p \end{bmatrix} \tag{2.14}$$

so that:

$$\begin{Bmatrix} \hat{\mathbf{e}}_x \\ \hat{\mathbf{e}}_y \\ \hat{\mathbf{e}}_z \end{Bmatrix} = [T_{\mathrm{P}R}] \begin{Bmatrix} \mathbf{i} \\ \mathbf{j} \\ \mathbf{k} \end{Bmatrix} \tag{2.15}$$

Deformed blade coordinate system

The deformed blade coordinate system is a rotating coordinate system whose origin is at the point on the deformed elastic axis of the blade corresponding to the cross section being analyzed. The $\hat{\mathbf{e}}'_x$ unit vector points outboard along the tangent to the elastic axis at the origin, the $\hat{\mathbf{e}}'_y$ axis is aligned with the blade chord perpendicular to the elastic axis and is positive in the blade lead direction and the $\hat{\mathbf{e}}'_z$ is completes the orthonormal trio and is defined as positive up. This coordinate system is depicted in Fig. 2.5.

The transformation from the undeformed preconed to the deformed blade coordinate systems is determined by the following matrix:

$$[T_{\mathrm{D}P}] = \begin{bmatrix} S_{11} & S_{12} & S_{13} \\ S_{21} & S_{22} & S_{23} \\ S_{31} & S_{32} & S_{33} \end{bmatrix} \tag{2.16}$$

where

$$
\begin{aligned}
S_{11} &= \cos\theta_y \cos\theta_z \\
S_{12} &= \cos\theta_y \sin\theta_z \\
S_{13} &= -\sin\theta_y \\
S_{21} &= \sin\theta_x \sin\theta_y \cos\theta_z - \cos\theta_x \sin\theta_z \\
S_{22} &= \cos\theta_x \cos\theta_z + \sin\theta_x \sin\theta_y \sin\theta_z \\
S_{23} &= \sin\theta_x \cos\theta_y \\
S_{31} &= \cos\theta_x \sin\theta_y \cos\theta_z + \sin\theta_x \sin\theta_z \\
S_{32} &= -(\sin\theta_x \cos\theta_z - \cos\theta_x \sin\theta_y \sin\theta_z) \\
S_{33} &= \cos\theta_x \cos\theta_y
\end{aligned}
$$

and where,

$$
\begin{aligned}
\theta_x &= \phi \\
\sin\theta_y &= -\frac{w_{,x}}{\sqrt{1 + 2u_{,x} + {u_{,x}}^2 + {v_{,x}}^2 + {w_{,x}}^2}} \\
\cos\theta_y &= \frac{\sqrt{1 + 2u_{,x} + {u_{,x}}^2 + {v_{,x}}^2}}{\sqrt{1 + 2u_{,x} + {u_{,x}}^2 + {v_{,x}}^2 + {w_{,x}}^2}} \\
\sin\theta_z &= \frac{v_{,x}}{\sqrt{1 + 2u_{,x} + {u_{,x}}^2 + {v_{,x}}^2 + {w_{,x}}^2}} \\
\cos\theta_z &= \frac{1 + u_{,x}}{\sqrt{1 + 2u_{,x} + {u_{,x}}^2 + {v_{,x}}^2 + {w_{,x}}^2}}
\end{aligned}
$$

After substituting all the terms and simplifying, the transformation matrix becomes:

$$
[T_{\mathrm{D}P}] = \begin{bmatrix} 1 & v_{,x} & w_{,x} \\ -v_{,x} - \phi w_{,x} & 1 - \phi v_{,x} w_{,x} & \phi \\ -w_{,x} - \phi v_{,x} & -\phi - v_{,x} w + , x & 1 \end{bmatrix} \tag{2.17}
$$

The deformed and undeformed frames are related by the following equation:

$$\left\{ \begin{array}{c} \hat{\mathbf{e}}'_x \\ \hat{\mathbf{e}}'_y \\ \hat{\mathbf{e}}'_z \end{array} \right\} = [T_{\mathrm{D}P}] \left\{ \begin{array}{c} \hat{\mathbf{e}}_x \\ \hat{\mathbf{e}}_y \\ \hat{\mathbf{e}}_z \end{array} \right\} \tag{2.18}$$

Tip path plane coordinate system

The tip path plane coordinate system is required for the formulation of the dynamic inflow model. This system is a nonrotating frame, and its z_{TPP} axis is perpendicular to the plane defined by the first harmonic of the flapping motion of the blade tips, defined positive upwards.

The transformation between the shaft and the tip path plane coordinate systems is described by:

$$[T_{\mathrm{T}S}] = \left[\begin{array}{ccc} \cos\beta_{1c} & \sin\beta_{1c}\sin\beta_{1s} & \sin\beta_{1c}\cos\beta_{1s} \\ 0 & \cos\beta_{1s} & -\sin\beta_{1s} \\ -\sin\beta_{1c} & \cos\beta_{1c}\sin\beta_{1s} & \cos\beta_{1c}\cos\beta_{1s} \end{array} \right] \tag{2.19}$$

where β_{1c} and β_{1s} are multiblade coordinates defined as follows:

$$\beta_{1c} = \frac{2}{N_{\mathrm{b}}} \sum_{j=1}^{N_{\mathrm{b}}} \frac{w_{tipj}}{R-e} \cos\psi_j \tag{2.20}$$

$$\beta_{1s} = \frac{2}{N_{\mathrm{b}}} \sum_{j=1}^{N_{\mathrm{b}}} \frac{w_{tipj}}{R-e} \sin\psi_j \tag{2.21}$$

The relation between the unit vectors of the two involved systems is:

$$\left\{ \begin{array}{c} \mathbf{i}_{\mathrm{T}PP} \\ \mathbf{j}_{\mathrm{T}PP} \\ \mathbf{k}_{\mathrm{T}PP} \end{array} \right\} = [T_{\mathrm{T}S}] \left\{ \begin{array}{c} \mathbf{i}_{\mathrm{S}} \\ \mathbf{j}_{\mathrm{S}} \\ \mathbf{k}_{\mathrm{S}} \end{array} \right\} \tag{2.22}$$

Blade sectional aerodynamics coordinate system

The blade sectional aerodynamics coordinate system is needed for the calculation of the section aerodynamic loads at any point along the blade. Its origin is at the point of the elastic axis corresponding to the cross section being analyzed. Its unit vectors determining are defined such that $\mathbf{e}_T$ points in the lag direction, $\mathbf{e}_R$ is tangent to the elastic axis and points outwards and $\mathbf{e}_P$ is perpendicular to both and is considered positive for airflow moving downwards.

The velocity in the undeformed preconed coordinate system is given by:

$$\mathbf{V}_T F = V_x \hat{\mathbf{e}}_x + V_y \hat{\mathbf{e}}_y + V_z \hat{\mathbf{e}}_z \tag{2.23}$$

For the aerodynamic calculations, this velocity needs to be represented as:

$$\mathbf{V}_A = U_T \mathbf{e}_T + U_P \mathbf{e}_P + U_R \mathbf{e}_R \tag{2.24}$$

To convert the velocity from undeformed preconed coordinate system to the airflow velocity system, the following transformation is required:

$$[T_{\mathrm{AP}}] = \begin{bmatrix} \sin\zeta & -\cos\zeta & 0 \\ \sin\beta\cos\zeta & \sin\beta\sin\zeta & -\cos\beta \\ \cos\beta\cos\zeta & \cos\beta\sin\zeta & \sin\beta \end{bmatrix} \tag{2.25}$$

where β and ζ are the local flap and lag slopes of the blade elastic axis with reference to the undeformed preconed blade coordinate system and are given by:

$$\beta = w_{,x} \tag{2.26}$$

$$\zeta = v_{,x} \tag{2.27}$$

where w and v are the flap and lag displacements of the elastic axis.

The relationship between the two systems is therefore:

$$\left\{ \begin{array}{c} \mathbf{e}_T \\ \mathbf{e}_P \\ \mathbf{e}_R \end{array} \right\} = [T_{\mathrm{A}P}] \left\{ \begin{array}{c} \hat{\mathbf{e}}_x \\ \hat{\mathbf{e}}_y \\ \hat{\mathbf{e}}_z \end{array} \right\} \tag{2.28}$$

Undeformed tip coordinate system

If the swept tip is being included in the modeling of the blade, additional coordinate systems are required to formulate the aerodynamic forces and moments locally at the tip.

The undeformed tip coordinate system has its origin at the junction between the straight portion of the blade and the swept tip, as shown in Fig. 2.6. The $\mathbf{i}_H$ axis points outwards of the swept tip, the $\mathbf{j}_H$ axis is parallel to the chord of the tip portion of the blade and perpendicular to the elastic axis, and the $\mathbf{k}_H$ is perpendicular to both and coincident with the blade undeformed $\hat{\mathbf{e}}_z$ axis.

The conversion between the blade and the tip undeformed coordinate systems is:

$$\left\{ \begin{array}{c} \mathbf{i}_H \\ \mathbf{j}_H \\ \mathbf{k}_H \end{array} \right\} = [T_\Lambda] \left\{ \begin{array}{c} \hat{\mathbf{e}}_x \\ \hat{\mathbf{e}}_y \\ \hat{\mathbf{e}}_z \end{array} \right\} \tag{2.29}$$

The geometric, linear transformation between the two coordinate systems is given by matrix $[T_\Lambda]$, which is:

$$[T_\Lambda] = \left[\begin{array}{ccc} \cos\Lambda & -\sin\Lambda & 0 \\ \sin\Lambda & \cos\Lambda & 0 \\ 0 & 0 & 1 \end{array} \right] \tag{2.30}$$

The transformation between the vectors of nodal degrees of freedom, however, is non-linear, as shown by Ref. 97. The non-linear transformation is described in Section 4.2.1.

Deformed tip coordinate system

The origin of the deformed tip coordinate system is at the point of the elastic axis of the swept part of the blade corresponding to the section being considered. The $\mathbf{i}_T$ axis of this coordinate system, shown in Fig. 2.6, is tangent to the elastic axis at the origin, with the $\mathbf{j}_T$ parallel to the chord and perpendicular to the elastic axis and and positive forward and the $\mathbf{k}_T$ orthonormal to both and positive upwards.

The relation between the deformed and the undeformed tip coordinate systems is:

$$\begin{Bmatrix} \mathbf{i}_T \\ \mathbf{j}_T \\ \mathbf{k}_T \end{Bmatrix} = [T_{\mathrm{D}P}]_L \begin{Bmatrix} \mathbf{i}_H \\ \mathbf{j}_H \\ \mathbf{k}_H \end{Bmatrix} \tag{2.31}$$

where the subscript L refers to the local tip frame. The transformation matrix $[T_{\mathrm{D}P}]_L$ is then:

$$[T_{\mathrm{D}P}]_L = \begin{bmatrix} 1 & v_{,x} & w_{,x} \\ -v_{,x} - \phi w_{,x} & 1 - \phi v_{,x} w_{,x} & \phi \\ -w_{,x} - \phi v_{,x} & -\phi - v_{,x} w + , x & 1 \end{bmatrix} \tag{2.32}$$

with the elastic deformations in the local tip coordinate system.

2.3 Main assumptions

The following list is a summary of the main assumptions that are used in the formulation and solution of the mathematical model used in this study.

2.3.1 Aerodynamic assumptions

1. The wind velocity is zero.

2. The effects of dynamic stall are not included. Quasi-steady stall and compressibility effects are modeled through tables of lift, drag and moment coefficients. The unsteady aerodynamic effects include circulatory effects and the acceleration type non-circulatory effects are neglected with the exception of the pitch damping.

3. Aerodynamic forces and moments on the blade section are based on the airflow velocity at the elastic axis of the blade.

4. The effect of the downwash of the rotor on the fuselage and empennage is not included.

5. The pitch angle of the horizontal stabilizer (for the UH-60 helicopter used in this dissertation) is fixed for a given flight condition, and the control logic for the automatic positioning of the stabilizer is not modeled.

6. The aerodynamic loads on the swept tip are calculated for a cross section perpendicular to the swept elastic axis, rather than for a sheared airfoil perpendicular to the straight blade elastic axis.

7. Independence principle is assumed, such that sweep does not cause a cross flow.

2.3.2 Inertial and structural assumptions

1. The airframe is a rigid body with a constant mass and the x_B-z_B plane is a plane of symmetry.

2. The undeformed blade has no droop or torque offsets. The baseline blade is straight, unless it is specified that the swept tip is used.

3. The blade is rigid in flap, lag and torsion, and generates no aerodynamic loads, inboard of the flap and lag hinges.

4. The flap, lag and pitch hinges (when they are present) are coincident.

5. The blade cross sections are symmetric with respect to the major principal axes.

6. The blade cross-sectional area centroid and elastic axes are coincident, which means that the tension center is coincident with the elastic axis. However, cross-sectional centers of gravity (CG), aerodynamic centers (AC), and elastic axes (EA) need not be coincident.

7. Blade chord, built-in twist, stiffness and mass properties, and cross-sectional offsets are defined at discrete spanwise stations, and vary linearly in between.

8. The blade is built of an isotropic, linearly elastic material.

9. All blades have identical mass, stiffness, and geometric properties.

10. Bernoulli-Euler beam theory is used, implying that plane cross sections remain plane and perpendicular to the elastic axis during deformations. The effects of shear deformation are neglected.

11. The blade undergoes moderate deflections in bending and torsion, implying small strains and finite rotations.

12. The blades rotate at a constant angular speed, Ω. Engine and engine control system dynamics are neglected.

13. The blade pitch control system, including the actuators, is infinitely stiff. Freeplay in the control linkages is not modeled. The swashplate and tail rotor collective control are attached rigidly to the pilot controls.

2.4 Main rotor equations of motion

2.4.1 Overview

This section describes the mathematical model of the main rotor used in the present study. An extended description of the model can be found in Refs. 107, 6. Only a summary is presented in this dissertation, except for those topics that are of special relevance for this study, or that have not been included in previous references.

The main rotor blade dynamics are calculated in the rotating frame and separately for each blade, allowing the model to be used for dissimilar blades, although

the present study will assume identical blades. Each blade is considered a flexible beam undergoing coupled flap, lag, torsion, and axial motion and is attached to a hub that may have large amplitude linear and angular motions. The resultant equations of motion are nonlinear, coupled, *partial* differential equations with periodic coefficients. A finite element discretization, based on Galerkin's method of weighted residuals, is used to transform these equations into a system of nonlinear, coupled, *ordinary* differential equations. To reduce the total number of degrees of freedom, a modal coordinate transformation is used. The resultant mathematical model of the rotor is a system of nonlinear, coupled, second order ordinary differential equations with time-varying coefficients, which is converted to first-order form and is coupled to the rest of the mathematical model.

2.4.2 Main rotor aerodynamic loads

The calculation of the distributed aerodynamic forces, $\mathbf{p}_{\mathrm{A}}$, and moments, $\mathbf{q}_{\mathrm{A}}$, requires the knowledge of the absolute velocity seen by each point along the blade elastic axis. This velocity is the derivative with respect to time of the position vector of a point P on the elastic axis of the blade relative to a fixed point, given by:

$$\mathbf{R}_P = \mathbf{R}_{CG} + \mathbf{R}_H + \mathbf{R}_B \tag{2.33}$$

where $\mathbf{R}_{CG}$ is the position vector of the body center of gravity with respect to a fixed point, $\mathbf{R}_H$ is the position of the hub relative to the center of gravity and $\mathbf{R}_B$ is the position vector of the point P, located on the elastic axis of the blade, with

respect to the hub.

The position vector of the hub in reference to the center of gravity is given by:

$$\mathbf{R}_H = x_H \mathbf{i}_\mathrm{B} + y_H \mathbf{j}_\mathrm{B} + z_H \mathbf{k}_\mathrm{B} \tag{2.34}$$

The position vector of the point on the elastic axis with respect to the hub is given by:

$$\mathbf{R}_B = e\mathbf{i} + (x_0 + u)\hat{\mathbf{e}}_x + v\hat{\mathbf{e}}_y + w\hat{\mathbf{e}}_z \tag{2.35}$$

where e is the offset of the blade flap, lag and pitch hinges from the axis of rotation (if present), which are assumed coincident. The elastic portion of the blade starts at the hinge, and inboard from this point the blade is assumed rigid. The term x_0 is the distance from the start of elastic portion to the point P on the elastic axis of the undeformed section and u, v and w are the elastic deflections of the point from the undeformed blade coordinate system. Using the coordinate transformation presented in Eq. (2.14), Eq. (2.35) can be rewritten in the undeformed preconed coordinate system as

$$\mathbf{R}_B = (e\cos\beta_p + x_0 + u)\hat{\mathbf{e}}_x + v\hat{\mathbf{e}}_y + (w - \sin\beta_p)\hat{\mathbf{e}}_z \tag{2.36}$$

where β_p is the blade precone angle.

The absolute velocity of the point on the elastic axis is:

$$\mathbf{V}_P = \frac{d\mathbf{R}_P}{dt} = \frac{d\mathbf{R}_{CG}}{dt} + \frac{d\mathbf{R}_H}{dt} + \frac{d\mathbf{R}_B}{dt} \tag{2.37}$$

The velocity of the center of gravity is given by:

$$\frac{d\mathbf{R}_{CG}}{dt} = u_F \mathbf{i}_\mathrm{B} + v_F \mathbf{j}_\mathrm{B} + w_F \mathbf{k}_\mathrm{B} \tag{2.38}$$

where u_F, v_F and w_F are the linear velocity components in the body-fixed axes system.

The other derivatives are:

$$\frac{d\mathbf{R}_H}{dt} = \frac{\partial \mathbf{R}_H}{\partial t} + \boldsymbol{\omega} \times \mathbf{R}_H \tag{2.39}$$

$$\frac{d\mathbf{R}_B}{dt} = \frac{\partial \mathbf{R}_B}{\partial t} + \boldsymbol{\omega} \times \mathbf{R}_B \tag{2.40}$$

where $\boldsymbol{\omega}$ is the angular velocity vector of the body and is given by

$$\boldsymbol{\omega} = p\mathbf{i}_\mathrm{B} + q\mathbf{j}_\mathrm{B} + r\mathbf{k}_\mathrm{B} \tag{2.41}$$

in which p, q and r are the roll, pitch and yaw rates, respectively.

The term $\partial \mathbf{R}_H/\partial t$ in Eq. (2.37) is zero because the fuselage is rigid. The partial derivative $\partial \mathbf{R}_B/\partial t$ is the velocity vector of the point as seen in the body-fixed axes, and it is

$$\frac{\partial \mathbf{R}_B}{\partial t} = \left(\frac{\partial \mathbf{R}_B}{\partial t}\right)_R + \boldsymbol{\Omega} \times \mathbf{R}_B \tag{2.42}$$

where the first term represents the velocity vector of the point relative to the hub in the rotating frame and $\boldsymbol{\Omega}$ is the angular velocity vector of the main rotor

$$\boldsymbol{\Omega} = \Omega \mathbf{k}_\mathrm{S} \tag{2.43}$$

where Ω is the rotor speed.

The absolute velocity $\mathbf{V}_P$ (from Eq. 2.37) is therefore given by:

$$\mathbf{V}_P = \frac{d\mathbf{R}_{CG}}{dt} + \left(\frac{\partial \mathbf{R}_B}{\partial t}\right)_R + \boldsymbol{\Omega} \times \mathbf{R}_B + \boldsymbol{\omega} \times [\mathbf{R}_H + \mathbf{R}_B] \tag{2.44}$$

The total local velocity at the blade section is obtain by adding the contribution of the induced velocity by the rotor wake, $\mathbf{V}_I$:

$$\mathbf{V}_T = \mathbf{V}_P - \mathbf{V}_I \tag{2.45}$$

where the induced velocity $\mathbf{V}_I$ is subtracted because it represents the velocity of the flow with respect to the blade, rather than that of the blade with respect to the flow. In the undeformed preconed blade coordinate system, the velocity $\mathbf{V}_P$ can be written in the form

$$\mathbf{V}_P = V_{11}\hat{\mathbf{e}}_x + V_{12}\hat{\mathbf{e}}_y + V_{13}\hat{\mathbf{e}}_z \tag{2.46}$$

where V_{11}, V_{12} and V_{13} are the velocity components in the direction of $\hat{\mathbf{e}}_x$, $\hat{\mathbf{e}}_y$ and $\hat{\mathbf{e}}_z$, the unit vectors of the undeformed preconed blade coordinate system. The second term in Eq. (2.45) is

$$\mathbf{V}_I = \lambda_x\hat{\mathbf{e}}_x + \lambda_y\hat{\mathbf{e}}_y + \lambda_z\hat{\mathbf{e}}_z \tag{2.47}$$

where λ_x, λ_x and λ_x are the x, y and z components in the undeformed preconed blade coordinate system of the induced velocity.

The total velocity, expressed in the undeformed preconed rotating coordinate system, is therefore

$$\mathbf{V}_T \;=\; V_{11}\hat{\mathbf{e}}_x + V_{12}\hat{\mathbf{e}}_y + (V_{13} - \lambda_z)\hat{\mathbf{e}}_z \tag{2.48}$$

where V_{11}, V_{12} and V_{13} are the components of the velocity $\mathbf{V}_P$, and λ_z is the induced velocity in the z direction (the components of the induced velocity in the x and y directions could be included, but are not used in the present study).

The total velocity $\mathbf{V}_T$ in Eq.(2.48) is the velocity of the blade as it moves in the air. The relative velocity of the flow with respect to the blade, $\mathbf{V}_{TF}$, is therefore the negative of this expression, i.e.,

$$\mathbf{V}_{TF} = -\mathbf{V}_T \tag{2.49}$$

which expressed in the same undeformed preconed coordinate system is

$$\mathbf{V}_{TF} = V_x\hat{\mathbf{e}}_x + V_y\hat{\mathbf{e}}_y + V_z\hat{\mathbf{e}}_z \tag{2.50}$$

with

$$V_x = -V_{11} \tag{2.51}$$

and so on.

For the aerodynamic calculations, however, the more traditional airflow velocity components in the blade sectional aerodynamics coordinate system is desired. Using the transformation in Eq. (2.25) one obtains

$$\mathbf{V}_A = U_T\mathbf{e}_T + U_P\mathbf{e}_P + U_R\mathbf{e}_R \tag{2.52}$$

where $\mathbf{V}_A$ is the resultant velocity of the airflow at the 1/4-chord location. U_T is considered positive for an airflow coming toward the leading edge of the airfoil, U_R is positive for an outboard flow and U_P is defined as positive for a flow coming from above.

The local velocity components can be used to calculate the local angle of attack, α_y, and yaw angle, γ_I, which are shown in Fig. 2.7, and which are

$$\cos\gamma_I = \frac{|U_T|}{\sqrt{U_T^2 + U_R^2}} \tag{2.53}$$

$$\alpha_Y = \tan^{-1}\left[\frac{(U_T\tan\theta_G - U_P)\cos\gamma_I}{U_T + U_P\tan\theta_G\cos^2\gamma_I}\right] \tag{2.54}$$

where θ_G is the total geometric pitch of the blade section

$$\theta_G = \theta_0 + \theta_{1c}\cos(\psi + \Delta_{SP}) + \theta_{1s}\sin(\psi + \Delta_{SP}) + \theta_{TW} + \phi \tag{2.55}$$

in which ψ is the blade azimuth angle, θ_{TW} is the built-in twist, Δ_{SP} is the swash-plate phasing angle, and ϕ is the elastic rotation of the blade section about the elastic axis. The sectional aerodynamic angle of attack, α_Y, defined in Eq.(2.54), can be approximated as the difference between the geometric and induced angles

$$\alpha_Y \approx \theta - \phi = \theta - \tan^{-1}\left(\frac{U_P}{U_T}\right) \tag{2.56}$$

With the angle of attack and the Mach number at any blade section, the sectional lift, drag and moment coefficients (C_L, C_D, and C_M respectively) can be obtained from look-up tables.

Two-dimensional quasi-steady aerodynamics (Ref. 94) are used for the blade section force and moment calculations. The current implementation is described in detail in Ref. 6, but a summary is included here for convenience. The basic expressions for the distributed lift L and pitching moment M are (with the acceleration terms $\ddot{h}$ and $\ddot{\alpha}$ neglected for simplification purposes; therefore, the $\dot{\alpha}$ term is the only non-circulatory term that remains in the lift expression):

$$L = L_Q + \frac{1}{2}a\rho(bR)^2 V_0 \dot{\alpha} \tag{2.57}$$

$$M = L_Q x_A - \frac{1}{2}a\rho V_0 \dot{\alpha}(bR - x_A)(bR)^2 \tag{2.58}$$

where a is the lift-curve slope obtained from look-up tables as a function of the angle of attack α_Y and the Mach number M, ρ is the air density, b is the non-dimensional semi-chord length, R is the blade radius, α is the total pitch angle of the blade section, which is $\theta_G - \phi$, where θ_G is the geometric pitch angle and ϕ is the rotation of the cross section of the blade around the elastic axis, V_0 is the oncoming

freestream flow defined as

$$V_0 = \sqrt{U_P^2 + U_T^2 + U_R^2} \tag{2.59}$$

x_A is the blade cross-sectional aerodynamic center offset from the elastic axis (positive for aerodynamic center forward of the elastic axis) and $\dot{\alpha}$ is the time rate of change of the total blade pitch angle, which corresponds to $\dot{\theta}_G - \dot{\phi}$.

The quasi-steady lift L_Q is given by:

$$L_Q = \frac{1}{2}\rho V_0^2 c \left[C_L + \frac{a\dot{\alpha}}{V_0}\left(\frac{c}{2} - x_A\right)\right] \tag{2.60}$$

where c is the local blade chord.

The lift equation (Eq. (2.57)), with the chord c substituted for the semi-chord b, becomes

$$L = L_Q + \frac{1}{8} a \rho_A V_0 c^2 \dot{\alpha} \tag{2.61}$$

The aerodynamic drag is given by:

$$D = \frac{1}{2}\rho_A V_0^2 c C_D \tag{2.62}$$

where C_D is the steady drag coefficient obtained from look-up tables as a function of angle of attack α_Y and Mach number M.

The aerodynamic lift L and drag D forces have to be transformed to the local blade sectional aerodynamics coordinate system. The aerodynamic force components in this coordinate system are

$$f_P = \frac{1}{V_0}\left[-L\frac{U_T}{\cos\gamma_I} + DU_P \right] \tag{2.63}$$

$$f_T = \frac{1}{V_0}\left[DU_T + LU_P \cos\gamma_I \right] \tag{2.64}$$

$$f_R = \frac{1}{V_0}\left[DU_R + L\frac{U_P \cos\gamma_I U_R}{U_T} \right] \tag{2.65}$$

along the $\mathbf{e}_P, \mathbf{e}_T$ and $\mathbf{e}_R$ unit vectors, respectively.

The distributed aerodynamic loads are transformed to the undeformed preconed blade coordinate system by converting the force components in the blade sectional aerodynamics coordinate system f_P, f_T and f_R using the inverse of the coordinate transformation matrix presented in Eq. (2.25). The distributed aerodynamic forces are

$$\begin{aligned}
\mathbf{p}_{\mathrm{A}} &= \left(f_P \cos\zeta \sin\beta - f_T \sin\zeta - f_R \cos\zeta \cos\beta\right) \hat{\mathbf{e}}_x \\
&\quad + \left(f_P \sin\zeta \sin\beta + f_T \cos\zeta - f_R \sin\zeta \cos\beta\right) \hat{\mathbf{e}}_y \\
&\quad + \left(-f_P \cos\beta - f_R \sin\beta\right) \hat{\mathbf{e}}_z \\
&= p_{\mathrm{A}x}\hat{\mathbf{e}}_x + p_{\mathrm{A}y}\hat{\mathbf{e}}_y + p_{\mathrm{A}z}\hat{\mathbf{e}}_z
\end{aligned} \tag{2.66}$$

The distributed aerodynamic moments are

$$\begin{aligned}
\mathbf{q}_{\mathrm{A}} &= -M \cos\zeta \cos\beta \hat{\mathbf{e}}_x - M \sin\zeta \cos\beta \hat{\mathbf{e}}_y - M \sin\beta \hat{\mathbf{e}}_z \\
&= q_{\mathrm{A}x}\hat{\mathbf{e}}_x + q_{\mathrm{A}y}\hat{\mathbf{e}}_y + q_{\mathrm{A}z}\hat{\mathbf{e}}_z
\end{aligned} \tag{2.67}$$

2.4.3 Main rotor inertial loads

The main rotor integrated inertial forces and moments are

$$\begin{aligned}
\mathbf{p}_{\mathrm{I}} &= -\int_A \rho(\mathbf{a}_P + g\mathbf{k}_{\mathrm{I}}) dA \\
&= p_{\mathrm{I}x}\hat{\mathbf{e}}_x + p_{\mathrm{I}y}\hat{\mathbf{e}}_y + p_{\mathrm{I}z}\hat{\mathbf{e}}_z
\end{aligned} \tag{2.68}$$

$$\begin{aligned}
\mathbf{q}_{\mathrm{I}} &= -\int_A \rho \left[(y_0 \hat{\mathbf{e}}'_x + z_0 \hat{\mathbf{e}}'_y) \times (\mathbf{a}_P + g\mathbf{k}_{\mathrm{I}})\right] dA \\
&= q_{\mathrm{I}x}\hat{\mathbf{e}}_x + q_{\mathrm{I}y}\hat{\mathbf{e}}_y + q_{\mathrm{I}z}\hat{\mathbf{e}}_z
\end{aligned} \tag{2.69}$$

where ρ is the mass density of the blade, y_0 and z_0 are the coordinates of the generic mass point of the cross section A (see Fig. 2.5) and $g\mathbf{k_I}$ is the contribution due to gravity.

The inertia loads depend on the absolute acceleration of a point on the rotor blade, $\mathbf{a}_P$, which is calculated by taking derivatives from the position vector of the point, $\mathbf{R}_P$.

The position vector of a point on the blade, which is not necessarily on the elastic axis, is given by

$$\mathbf{R}_B = e\mathbf{i} + (x_0 + u)\hat{\mathbf{e}}_x + v\hat{\mathbf{e}}_y + w\hat{\mathbf{e}}_z \underline{+ y_0\hat{\mathbf{e}}'_y + z_0\hat{\mathbf{e}}'_z} \tag{2.70}$$

where the underlined terms represent the distance of the point from the elastic axis.

This position vector can be expressed in the undeformed preconed coordinate system by using the coordinate transformations presented in Eqs. (2.14) and (2.16), as

$$\begin{aligned} \mathbf{R}_B &= \left[(e\cos\beta_p + u) + x_0 \underline{+ S_{21}y_0 + S_{31}z_0}\right]\hat{\mathbf{e}}_x + \\ &\quad \left[v \underline{+ S_{22}y_0 + S_{32}z_0}\right]\hat{\mathbf{e}}_y + \left[w - \sin\beta_{\mathrm{P}} \underline{+ S_{23}y_0 + S_{33}z_0}\right]\hat{\mathbf{e}}_z \end{aligned} \tag{2.71}$$

The absolute velocity of the point is the same as that in Eq. (2.37), with the exception of the $\mathbf{R}_B$ vector which is defined in Eq. (2.71). The acceleration of the point on the blade relative to a fixed point is

$$\begin{aligned} \mathbf{a}_P &= \frac{d^2\mathbf{R}_{CG}}{dt^2} + \frac{\partial^2\mathbf{R}_B}{\partial t^2} + 2\boldsymbol{\omega}\times\frac{\partial\mathbf{R}_B}{\partial t} + \dot{\boldsymbol{\omega}}\times(\mathbf{R}_B + \mathbf{R}_H) + \\ &\quad \boldsymbol{\omega}\times[\boldsymbol{\omega}\times(\mathbf{R}_B + \mathbf{R}_H)] \end{aligned} \tag{2.72}$$

where

$$\frac{\partial^2 \mathbf{R}_B}{\partial t^2} = \left(\frac{\partial^2 \mathbf{R}_B}{\partial t^2}\right)_R + \dot{\mathbf{\Omega}} \times \mathbf{R}_B + 2\mathbf{\Omega} \times \left(\frac{\partial \mathbf{R}_B}{\partial t}\right)_R + \mathbf{\Omega} \times (\mathbf{\Omega} \times \mathbf{R}_B) \tag{2.73}$$

The acceleration of the center of gravity is given by

$$\frac{d^2 \mathbf{R}_{CG}}{dt^2} = \dot{u}_F \mathbf{i}_\mathrm{B} + \dot{v}_F \mathbf{j}_\mathrm{B} + \dot{w}_F \mathbf{k}_\mathrm{B} \tag{2.74}$$

where $\dot{u}_F$, $\dot{v}_F$ and $\dot{w}_F$ are the linear acceleration components in the body fixed axes system.

From the above expressions, one can obtain an expression for the absolute acceleration of a point on the blade

$$\begin{aligned} \mathbf{a}_P \;=\; & \frac{d^2 \mathbf{R}_{CG}}{dt^2} + \dot{\boldsymbol{\omega}} \times \mathbf{R}_H + \boldsymbol{\omega} \times (\boldsymbol{\omega} \times \mathbf{R}_H) + \left(\frac{\partial^2 \mathbf{R}_B}{\partial t^2}\right)_R + \dot{\mathbf{\Omega}} \times \mathbf{R}_B + \\ & 2\mathbf{\Omega} \times \left(\frac{\partial \mathbf{R}_B}{\partial t}\right)_R + \mathbf{\Omega} \times (\mathbf{\Omega} \times \mathbf{R}_B) + \dot{\boldsymbol{\omega}} \times \mathbf{R}_B + \\ & 2\boldsymbol{\omega} \times \left[\left(\frac{\partial \mathbf{R}_B}{\partial t}\right)_R + \mathbf{\Omega} \times \mathbf{R}_B\right] + \boldsymbol{\omega} \times (\boldsymbol{\omega} \times \mathbf{R}_B) \end{aligned} \tag{2.75}$$

A more detailed expression of the acceleration terms can be found in Ref. 114.

2.4.4 Main rotor structural loads

The calculation of the structural loads on the main rotor blade is based on the equations of the Bernoulli-Eurler theory of isotropic beams undergoing moderate deflections in flap and lag bending, and torsion. A detailed derivation of the structural terms is provided by Turnour (Ref. 114).

The resultant loads, expressed as operators on the first and second derivatives

with respect to the spanwise coordinate of the mode shapes, are

$$p_{Sy}^{II} = M_z - S_{32}M_y \tag{2.76}$$

$$p_{Sz}^{II} = -(M_y - S_{23}M_z) \tag{2.77}$$

$$p_{Sx}^{I} = T \tag{2.78}$$

$$p_{Sy}^{I} = -S_{13,x}M_x - (S_{23,x} - S_{13}S_{21,x})M_y - S_{32,x}M_y \tag{2.79}$$

$$p_{Sz}^{I} = S_{12,x}M_x + (S_{32,x} - S_{12}S_{31,x})M_y + S_{23,x}M_y \tag{2.80}$$

$$q_{Sx}^{I} = M_x \tag{2.81}$$

where the terms S_{12}, S_{13}, S_{23} and S_{32} are elements of transformation matrix from undeformed to deformed coordinates given in Eq.2.16, and the terms $S_{12,x}$, $S_{13,x}$, $S_{21,x}$, $S_{23,x}$, $S_{31,x}$ and $S_{32,x}$ are their derivatives.

The terms T, M_x, M_y and M_z are obtained from the stress-force relationship:

$$\mathbf{F} = T\hat{\mathbf{e}}'_x + V_y\hat{\mathbf{e}}'_y + V_z\hat{\mathbf{e}}'_z = \int\int_A \mathbf{t}dA \tag{2.82}$$

$$\mathbf{M} = M_x\hat{\mathbf{e}}'_x + M_y\hat{\mathbf{e}}'_y + M_z\hat{\mathbf{e}}'_z = \int\int_A \mathbf{d}\times\mathbf{t}dA \tag{2.83}$$

where

$$\mathbf{d} = y_0\hat{\mathbf{e}}'_y + z_0\hat{\mathbf{e}}_z \tag{2.84}$$

$$\mathbf{t} = \sigma_{xx}\hat{\mathbf{e}}'_x + \tau_{xy}\hat{\mathbf{e}}'_y + \tau_{xz}\hat{\mathbf{e}}'_y \tag{2.85}$$

with the stresses σ_{xx}, τ_{xy} and τ_{xz} being defined in detail in Ref. 114.

2.4.5 Main rotor tension-induced loads

The calculation of the tension-induced loads is based on the equations of equilibrium of a deformed rod (Ref. 115). The tension loads are derived in Refs. 6 and 114, and

in the blade preconed undeformed coordinate system they are

$$\begin{aligned} P_{\mathrm{T}}^{I} &= TS_{12}\hat{\mathbf{e}}_y + TS_{13}\hat{\mathbf{e}}_z \\ &= p_{\mathrm{T}y}^{I}\hat{\mathbf{e}}_y + p_{\mathrm{T}z}^{I}\hat{\mathbf{e}}_z \end{aligned} \tag{2.86}$$

where T is the tension along the $\hat{\mathbf{e}}_x$ direction and S_{12} and S_{13} are elements of transformation matrix from undeformed to deformed coordinates given in Eq.2.16. Since the current study does not include axial degrees of freedom, axial dynamics along the $\hat{\mathbf{e}}_x$ direction are not considered.

2.4.6 Lag damper loads

If a lag damper is included, the moment it generates about the hinge, $\mathbf{M}_{\mathrm{D}}$, is given by

$$\mathbf{M}_{\mathrm{D}} = M_{\mathrm{D}x}\hat{\mathbf{e}}_x + M_{\mathrm{D}y}\hat{\mathbf{e}}_y + M_{\mathrm{D}z}\hat{\mathbf{e}}_z \tag{2.87}$$

The details of the implementation are found in Ref. 114.

2.4.7 Loads on a point on the swept tip

The procedure to compute the aerodynamic, inertial, structural and tension loads for the swept tip is similar to that used for the straight portion, but with the following modifications:

- The loads on the swept tip are calculated in the local tip coordinate system. For the calculation of the hub loads, they are transformed later to the blade

coordinate system before being added to the loads of the straight portion of the blade. For the calculation of the blade natural frequencies and mode shapes, these are not transformed, and the mass and stiffness matrices are calculated for the tip element in this coordinate system.

- The elastic displacements of the points on the tip need to be in the local tip coordinate system.

- The structural properties of a point in the swept tip need not be the same as in the equivalent straight blade radial positions. The properties used for the straight blade are approximations, since the actual blade of the UH-60 is sheared. The original UH-60 data is used for the swept blade.

The position vector of a point on the tip section of the blade is given by:

$$\mathbf{R}_P = e_1\mathbf{i} + x_J\hat{\mathbf{e}}_x + (x_t + u)\,\mathbf{i}_H + v\mathbf{j}_H + w\mathbf{k}_H + y_0\mathbf{j}_T + z_0\mathbf{k}_T \tag{2.88}$$

where e_1 is the blade root offset, x_t is the point along the tip of the blade in local axes, starting from the joint between the straight and swept portions of the blade, which is given by x_J. The unit vectors $\mathbf{i}_H$, $\mathbf{j}_H$, $\mathbf{k}_H$ represent the tip undeformed preconed coordinate system while $\mathbf{j}_T$, $\mathbf{i}_H$ correspond to the tip deformed coordinate system, defined in Section 2.2.2.

This expression needs to be written entirely in the swept undeformed coordinate system, which is the frame used for the calculation of the loads on the swept tip. Using the transformations presented in Eqs.(2.14), (2.30) and (2.32), the position

vector becomes:

$$\mathbf{R}_P = [(x_J + e_1)\cos\Lambda + x_t + u + y_0 v_{,x} + z_0 w_{,x}]\,\mathbf{i}_H \tag{2.89}$$

$$+ \; [(x_J + e_1)\sin\Lambda + v + y_0 + z_0\phi]\,\mathbf{j}_H \tag{2.90}$$

$$+ \; [w - \beta_P e_1 - y_0\,(\phi + v_{,x} w_{,x}) + z_0]\,\mathbf{k}_H \tag{2.91}$$

where β_P is the precone angle and Λ is the sweep angle.

The velocity and acceleration are calculated by taking derivatives of the position vector $\mathbf{R}_P$ of Eq.(2.91) in the same way as for the straight blade, Eqs.(2.37) and (2.75). The only difference is that the linear and angular velocities and accelerations are transformed to the tip preconed undeformed coordinate system using Eq.(2.29).

Total geometric pitch angle of a point on the tip:

$$\theta_G = (\theta_0 + \theta_{1c}\cos(\psi + \Delta_{SP}) + \theta_{1s}\sin(\psi + \Delta_{SP}) + \theta_{BJ})\cos\Lambda + \theta_{BT}\,(x_t) \tag{2.92}$$

where θ_{BJ} is the value of the built-in twist at the junction of the straight and swept portions of the blade, θ_{BT} is the pretwist of the swept tip with respect to the junction to the straight portion of the blade, Δ_{SP} is the swashplate phasing angle, and x_t is the spanwise coordinate of the point from that junction.

2.4.8 Main rotor equations of motion

The equations representing the motion of the rotor blades are a system of coupled non-linear partial differential equations with time varying coefficients. These equations are transformed into a system of nonlinear, coupled, ordinary differential equations using a finite element discretization (see Section 4.2). Moreover, a modal

coordinate transformation is performed in order to reduce the number of degrees of freedom as well as the number of equations for the dynamics of each rotor blade (see Section 4.4). The result is a system of nonlinear, coupled, second order ordinary differential equations with time-varying coefficients, which can be expressed in the symbolic form

$$\ddot{\mathbf{q}} = \mathbf{f}_q(\dot{\mathbf{q}}, \mathbf{q}) \tag{2.93}$$

where $\mathbf{q}$ is the vector of generalized coefficients.

This set of equations is then converted to first-order form and is coupled to the rest of the mathematical model.

2.5 Fuselage equations of motion

The main assumption in the formulation of the fuselage equations of motion is that the body of the helicopter is rigid.

The non-linear force and moment equilibrium equations, which are expressed in the body-fixed coordinate system (Section 2.2.1), are formulated as follows:

$$X\frac{R}{m_0} = m\dot{u}_F + m(qw_F - rv_F) + mg\sin\theta_F \tag{2.94}$$

$$Y\frac{R}{m_0} = m\dot{v}_F + m(ru_F - pw_F) - mg\cos\theta_F\sin\phi_F \tag{2.95}$$

$$Z\frac{R}{m_0} = m\dot{w}_F + m(pv_F - qu_F) - mg\cos\theta_F\cos\phi_F \tag{2.96}$$

$$\begin{aligned} L\frac{R^3}{m_0} &= I_{xx}\dot{p} - I_{xy}\dot{q} - I_{xz}\dot{r} - I_{yz}(q^2 - r^2) - I_{xz}pq + I_{xy}pr \\ &\quad -(I_{yy} - I_{zz})qr \end{aligned} \tag{2.97}$$

$$\begin{aligned} M\frac{R^3}{m_0} &= I_{yy}\dot{q} - I_{xy}\dot{p} - I_{yz}\dot{r} - I_{xz}(r^2 - p^2) - I_{xy}qr + I_{yz}pq \\ &\quad -(I_{zz} - I_{xx})pr \end{aligned} \tag{2.98}$$

$$\begin{aligned} N\frac{R^3}{m_0} &= I_{zz}\dot{r} - I_{xz}\dot{p} - I_{yz}\dot{q} - I_{xy}(p^2 - q^2) - I_{yz}pr + I_{xz}qr \\ &\quad -(I_{xx} - I_{yy})pq \end{aligned} \tag{2.99}$$

In Eqs. (2.94)-(2.99), the mass and inertia terms have been non-dimensionalized with respect to the main rotor radius R and a reference blade mass m_0.

The force and moment components on the left hand side of Eqs. (2.94)-(2.99) are the externally applied loads at the center of gravity of the body, described below. The right hand side represents inertia forces and moments due to the rigid body motion of the fuselage in response to the applied loads.

The total applied forces and moments are the sum of contributions from the

main rotor, tail rotor, fuselage and empennage, that is:

$$X = X_{MR} + X_{TR} + X_F + X_V + X_H \tag{2.100}$$

$$Y = Y_{MR} + Y_{TR} + Y_F + Y_V + Y_H \tag{2.101}$$

$$Z = Z_{MR} + Z_{TR} + Z_F + Z_V + Z_H \tag{2.102}$$

$$L = L_{MR} + L_{TR} + L_F + L_V + L_H \tag{2.103}$$

$$M = M_{MR} + M_{TR} + M_F + M_V + M_H \tag{2.104}$$

$$N = N_{MR} + N_{TR} + N_F + N_V + N_H \tag{2.105}$$

where the subscript MR denotes the main rotor, TR the tail rotor, F the fuselage, H and V the horizontal and vertical tail.

The fuselage rigid body equations are completed with three equations that relate the aircraft angular rates p, q, r, and the rates of change of the Euler angles ϕ_F, θ_F, ψ_F. These equations are:

$$\dot{\phi}_F = p + q \tan\theta_F \sin\phi_F + r \tan\theta_F \cos\psi_F \tag{2.106}$$

$$\dot{\theta}_F = q \cos\phi_F - r \sin\phi_F \tag{2.107}$$

$$\dot{\psi}_F = r \frac{\cos\psi_F}{\cos\theta_F} + q \frac{\sin\phi_F}{\cos\theta_F} \tag{2.108}$$

The following subsections describe the components of the external forces and moments applied to the center of gravity of the body that appear in Eqs.(2.100) through (2.105).

2.5.1 Main rotor loads

The contributions from the main rotor to the fuselage loads consists of the sum of the distributed aerodynamic and inertial loads, integrated along the span of the blade to obtain the loads at the hinge. The integrated loads are formulated in the undeformed preconed coordinate system (Section 2.2.2). These forces and moments are given by

$$\mathbf{F}_R = \int_e^1 (\mathbf{p}_\mathrm{A} + \mathbf{p}_\mathrm{I}) dx_0 \tag{2.109}$$

$$\mathbf{M}_R = \int_e^1 (\mathbf{q}_\mathrm{A} + \mathbf{q}_\mathrm{I}) dx_0 + \int_e^1 \mathbf{R}_C \times (\mathbf{p}_\mathrm{A} + \mathbf{p}_\mathrm{I}) dx_0 + \mathbf{M}_\mathrm{D} \tag{2.110}$$

where $\mathbf{p}_\mathrm{A}$, $\mathbf{p}_\mathrm{I}$, $\mathbf{q}_\mathrm{A}$, $\mathbf{q}_\mathrm{I}$ and $\mathbf{M}_\mathrm{D}$ are defined by Eqs. (2.66), (2.68), (2.67), (2.69) and (2.87), respectively, and e is the hinge offset. $\mathbf{R}_C$ is the position vector of a point on the deflected elastic axis from the hub in the undeformed preconed coordinate system, and it is:

$$\mathbf{R}_C = x_0 \hat{\mathbf{e}}_x + u \hat{\mathbf{e}}'_x + v \hat{\mathbf{e}}'_y + w \hat{\mathbf{e}}'_z \tag{2.111}$$

The main rotor loads are transformed to equivalent loads at the center of gravity of the body in the body fixed axes system (x_B, y_B, z_B).

For an articulated rotor configuration, the flap and lag aerodynamic or inertial blade moments are not transferred through the hinge. The forces generated by the rotor are obtained by integrating the aerodynamic and inertial distributed loads over the elastic portion of the blade. For a single rotor blade, these forces are

$$\mathbf{F}_{MR} = \begin{Bmatrix} X_{MR} \\ Y_{MR} \\ Z_{MR} \end{Bmatrix} = [T_{SB}]^{-1}[T_{RS}]^{-1}[T_{PR}]^{-1} \begin{Bmatrix} \int_e^1 (p_{\mathrm{A}x} + p_{\mathrm{I}x}) dx_0 \\ \int_e^1 (p_{\mathrm{A}y} + p_{\mathrm{I}y}) dx_0 \\ \int_e^1 (p_{\mathrm{A}z} + p_{\mathrm{I}z}) dx_0 \end{Bmatrix} \tag{2.112}$$

where the coordinate transformation matrices $[T_{SB}], [T_{RS}]$ and $[T_{PR}]$ are defined, respectively, by Eqs.(2.10), (2.12) and (2.14).

The moment vector at the center of gravity of the body, for a single blade, is

$$\begin{aligned} \mathbf{M}_{MR} = \left\{ \begin{array}{c} L_{MR} \\ M_{MR} \\ N_{MR} \end{array} \right\} &= [T_{SB}]^{-1}[T_{RS}]^{-1}[T_{PR}]^{-1} \left\{ \begin{array}{c} M_{\mathrm{D}x} \\ M_{\mathrm{D}y} \\ \int_0^1 (q_{\mathrm{A}z} + q_{\mathrm{I}z}) dx_0 + M_{\mathrm{D}z} \end{array} \right\} \\ &+ [T_{SB}]^{-1}[T_{RS}]^{-1}[T_{PR}]^{-1} \{\mathbf{R}_C \times \mathbf{F}_R\} \\ &+ \mathbf{R}_H \times \mathbf{F}_{MR} \end{aligned} \tag{2.113}$$

The first term indicates that the lag damper moments are all transferred through the hinge, but only the pitching moments of the distributed inertial and aerodynamic loads are. The second term transforms the forces at the blade hinge into moments at the hub, where $\mathbf{R}_C$ is the position vector from the hub to the hinge in the rotating frame

$$\mathbf{R}_C = e\hat{\mathbf{e}}_x \tag{2.114}$$

The third term transforms the forces at the hub into moments at the center of gravity of the body; the moment arm, $\mathbf{R}_H$, is the distance of the hub from the aircraft center of gravity, Eq. (2.34).

Loads on the swept tip

If the swept tip model is included, the loads calculated in the tip local coordinate system, both of aerodynamic and inertial origin, need to be transformed to the global blade coordinate system before they can be integrated with the loads on the straight portion of the blade (Ref. 91).

The local aerodynamic forces and moments for a point in the swept tip, $p^L_{\mathrm{A}x}$, $p^L_{\mathrm{A}y}$ and $p^L_{\mathrm{A}z}$, and $q^L_{\mathrm{A}x}$, $q^L_{\mathrm{A}y}$ and $q^L_{\mathrm{A}z}$, are calculated as described in Sections 2.4.2 and 2.4.7.

Using the inverse of the transformation in Eq.(2.30), the aerodynamic forces and moments in the global coordinate system are:

$$p^G_{\mathrm{A}x} = p^L_{\mathrm{A}x}\cos\Lambda + p^L_{\mathrm{A}y}\sin\Lambda \tag{2.115}$$

$$p^G_{\mathrm{A}y} = p^L_{\mathrm{A}y}\cos\Lambda - p^L_{\mathrm{A}x}\sin\Lambda \tag{2.116}$$

$$p^G_{\mathrm{A}z} = p^L_{\mathrm{A}z} \tag{2.117}$$

and

$$q^G_{\mathrm{A}x} = q^L_{\mathrm{A}x}\cos\Lambda + q^L_{\mathrm{A}y}\sin\Lambda \tag{2.118}$$

$$q^G_{\mathrm{A}y} = q^L_{\mathrm{A}y}\cos\Lambda - q^L_{\mathrm{A}x}\sin\Lambda \tag{2.119}$$

$$q^G_{\mathrm{A}z} = q^L_{\mathrm{A}z} \tag{2.120}$$

Similarly, for the inertial forces and moments, the transformation becomes:

$$p^G_{\mathrm{I}x} = p^L_{\mathrm{I}x}\cos\Lambda + p^L_{\mathrm{I}y}\sin\Lambda \tag{2.121}$$

$$p^G_{\mathrm{I}y} = p^L_{\mathrm{I}y}\cos\Lambda - p^L_{\mathrm{I}x}\sin\Lambda \tag{2.122}$$

$$p^G_{\mathrm{I}z} = p^L_{\mathrm{I}z} \tag{2.123}$$

and

$$q^G_{\mathrm{I}x} = q^L_{\mathrm{I}x}\cos\Lambda + q^L_{\mathrm{I}y}\sin\Lambda \tag{2.124}$$

$$q^G_{\mathrm{I}y} = q^L_{\mathrm{I}y}\cos\Lambda - q^L_{\mathrm{I}x}\sin\Lambda \tag{2.125}$$

$$q^G_{\mathrm{I}z} = q^L_{\mathrm{I}z} \tag{2.126}$$

2.5.2 Fuselage aerodynamic loads

The aerodynamic forces and moments acting on the body of the fuselage are extracted from non-linear data tables of aerodynamic coefficients. These aerodynamic loads are based on the freestream velocity at the fuselage aerodynamic reference point (Ref. 32), with a correction factor to take into account the interference of the main rotor

$$u_F = u_B + y_f r_B - z_f q_B + u_{in_f} \tag{2.127}$$

$$v_F = v_B + z_f p_B - x_f r_B + v_{in_f} \tag{2.128}$$

$$w_F = w_B + x_f q_B - y_f p_B + w_{in_f} \tag{2.129}$$

where x_f, y_f and z_f represent the components of the position vector from the center of gravity of the body to the aerodynamic reference point of the fuselage in the body axis system. The components u_{in_f}, u_{in_f} and u_{in_f} are the interference velocities based on the main rotor downwash, tip speed and wake skew angle, and are based on experimental results (Ref. 32):

$$u_{in_f} = v_0 \nu_{x_{wf}}(\beta_{1c}, \chi) \tag{2.130}$$

$$v_{in_f} = 0 \tag{2.131}$$

$$w_{in_f} = v_0 \nu_{z_{wf}}(\beta_{1c}, \chi) \tag{2.132}$$

with β_{1c} being the longitudinal tilt of the tip path plane, given in Eq. (2.20); v_0 is the main rotor average downwash, which is taken as the constant inflow coefficient λ_0 when dynamic inflow is used to calculate the induced velocities; and χ is the

rotor wake skew angle, which is

$$\chi = \tan^{-1} \frac{u_S}{|v_0 - w_S|} + \beta_{1c} \tag{2.133}$$

where u_S and w_S are the freestream velocity components taken in the shaft fixed coordinate system, $\mathbf{i}_S, \mathbf{j}_S, \mathbf{k}_S$, defined in Eq.(2.11). The functions $\nu_{x_{wf}}(\beta_{1c}, \chi)$ and $\nu_{z_{wf}}(\beta_{1c}, \chi)$ are obtained from look-up tables (Ref. 32).

The angles of attack and sideslip of the fuselage are defined as:

$$\alpha_F = \tan^{-1} \frac{w_F}{|u_F|} \tag{2.134}$$

$$\beta_F = \tan^{-1} \frac{v_F}{\sqrt{v_F^2 + w_F^2}} \tag{2.135}$$

where α_F is defined as positive nose up and β_F is defined as positive nose right.

The dynamic pressure is

$$\bar{q}_F = \frac{1}{2}\rho \frac{R^2}{m_0}(u_F^2 + v_F^2 + w_F^2) \tag{2.136}$$

For the UH-60A, the non-linear fuselage aerodynamic coefficients are defined in the wind-axes system (Ref. 32)

$$C_{Df} = C_{D_\alpha f}(\alpha_F) + C_{D_\beta f}(\beta_F) \tag{2.137}$$

$$C_{Yf} = C_{Yf}(|\beta_F|) \tag{2.138}$$

$$C_{Lf} = C_{L_\alpha f}(\alpha_F) + C_{L_\beta f}(-\beta_F) \tag{2.139}$$

$$C_{Rf} = -\frac{\beta_F}{|\beta_F|} C_{Rf}(|\beta_F|) \tag{2.140}$$

$$C_{Mf} = C_{M_\alpha f}(\alpha_F) - \frac{\beta_F}{|\beta_F|} C_{Mf}(|\beta_F|) \tag{2.141}$$

$$C_{Nf} = C_{Nf}(-\beta_F) \tag{2.142}$$

The non-dimensional fuselage aerodynamic loads in the wind axes system are

$$\mathbf{F}_{wF} = -\bar{q}_F C_{Df}\mathbf{i}_{\mathrm{F}} - \bar{q}_F C_{Yf}\mathbf{j}_{\mathrm{F}} - \bar{q}_F C_{Lf}\mathbf{k}_{\mathrm{F}} \tag{2.143}$$

$$\mathbf{M}_{wF} = \bar{q}_F C_{Rf}\mathbf{i}_{\mathrm{F}} - \bar{q}_F C_{Mf}\mathbf{j}_{\mathrm{F}} + \bar{q}_F C_{Nf}\mathbf{k}_{\mathrm{F}} \tag{2.144}$$

These loads need to be transformed from the wind axes system to the body axes system, using the angles of attack and sideslip at the aerodynamic reference point of the fuselage. The transformation is similar to the transformation from wind axes system to body fixed system, Eq. (2.8), and is

$$T_{\mathrm{F}B} = \begin{bmatrix} \cos\alpha_F \cos\beta_F & \cos\alpha_F \sin\beta_F & -\sin\alpha_F \\ \sin\beta_F & \cos\beta_F & \\ \sin\alpha_F \cos\beta_F & -\sin\alpha_F \sin\beta_F & \cos\alpha_F \end{bmatrix} \tag{2.145}$$

so that

$$\begin{Bmatrix} \mathbf{i}_{\mathrm{B}} \\ \mathbf{j}_{\mathrm{B}} \\ \mathbf{k}_{\mathrm{B}} \end{Bmatrix} = [T_{\mathrm{F}B}]^{-1} \begin{Bmatrix} \mathbf{i}_{\mathrm{F}} \\ \mathbf{j}_{\mathrm{F}} \\ \mathbf{k}_{\mathrm{F}} \end{Bmatrix} \tag{2.146}$$

Once resolved at the center of gravity of the body, the forces and moments due to the aerodynamics of the fuselage are:

$$\mathbf{F}_F = \begin{Bmatrix} X_F \\ Y_F \\ Z_F \end{Bmatrix} = [T_{FB}]^{-1}\mathbf{F}_{wF} = [T_{FB}]^{-1} \begin{Bmatrix} -\bar{q}_F C_{Df} \\ -\bar{q}_F C_{Yf} \\ -\bar{q}_F C_{Lf} \end{Bmatrix} \tag{2.147}$$

and

$$\mathbf{M}_F = \begin{Bmatrix} L_F \\ M_F \\ N_F \end{Bmatrix} = [T_{FB}]^{-1}\mathbf{M}_{wF} + \mathbf{x}_F \times \mathbf{F}_F \tag{2.148}$$

where $\mathbf{x}_F$ is the position vector of the fuselage aerodynamic reference point from the center of gravity of the body

$$\mathbf{x}_F = x_f\mathbf{i}_{\mathrm{B}} + y_f\mathbf{j}_{\mathrm{B}} + z_f\mathbf{k}_{\mathrm{B}} \tag{2.149}$$

In the body axes system, the non-dimensional aerodynamic forces at the center of gravity are:

$$\mathbf{F}_F = \left\{ \begin{array}{c} X_F \\ Y_F \\ Z_F \end{array} \right\} = \left\{ \begin{array}{c} \bar{q}_F C_{Xf} \\ \bar{q}_F C_{Yf} \\ \bar{q}_F C_{Zf} \end{array} \right\} \tag{2.150}$$

And the fuselage aerodynamic moment vector is

$$\mathbf{M}_F = \left\{ \begin{array}{c} L_F \\ M_F \\ N_F \end{array} \right\} = \left\{ \begin{array}{c} \bar{q}_F C_{Lf} \\ \bar{q}_F C_{Mf} \\ \bar{q}_F C_{Nf} \end{array} \right\} + \mathbf{x}_F \times \mathbf{F}_F \tag{2.151}$$

2.5.3 Empennage aerodynamic loads

The aerodynamic loads acting on the horizontal and vertical tail surfaces contribute to the total loads on the helicopter. The loads are calculated with velocities at the horizontal and vertical tail aerodynamic reference points:

$$\mathbf{u}_H = K_H \mathbf{u}_B + \mathbf{x}_H \times \omega + \mathbf{u}_{in_H} \tag{2.152}$$

$$\mathbf{u}_V = K_V \mathbf{u}_B + \mathbf{x}_V \times \omega + \mathbf{u}_{in_V} \tag{2.153}$$

K_H and K_V, which are obtained empirically, determine the dynamic pressure losses at the horizontal and vertical tail (Ref. 32); the vector products $\mathbf{x}_H \times \omega$ and $\mathbf{x}_V \times \omega$ are the velocity components due to the rotation of the body, and $\mathbf{u}_{in_H}$ and $\mathbf{u}_{in_V}$ are the interference velocity components due to the downwash of the main rotor and fuselage, based on wind tunnel test data (Ref. 32).

The dynamic pressures at the tail surfaces are

$$\bar{q}_H = \frac{1}{2}\rho \frac{R^2}{m_0}(u_H^2 + v_H^2 + w_H^2) \tag{2.154}$$

$$\bar{q}_V = \frac{1}{2}\rho \frac{R^2}{m_0}(u_V^2 + v_V^2 + w_V^2) \tag{2.155}$$

The interference velocities are a function of the main rotor downwash, tip speed and rotor wake skew angle (Ref. 32):

$$\mathbf{u}_{in_H} = v_0 \nu_{x_w H}(\beta_{1c}, \chi)\mathbf{i}_{\mathrm{H}} + v_0 \nu_{z_w H}(\beta_{1c}, \chi)\mathbf{k}_{\mathrm{H}} \tag{2.156}$$

$$\mathbf{u}_{in_V} = v_0 \nu_{x_w V}(\beta_{1c}, \chi)\mathbf{i}_{\mathrm{V}} + v_0 \nu_{z_w V}(\beta_{1c}, \chi)\mathbf{k}_{\mathrm{V}} \tag{2.157}$$

where v_0 is the main rotor downwash (which, like in the case of the fuselage loads, is equal to the constant inflow coefficient when dynamic inflow is used, but zero when the free wake model calculates the induced velocities), β_{1c} is the longitudinal tilt of the tip path plane, given in Eq. (2.20), and χ is the rotor wake skew angle Eq.(2.133). The functions $\nu_{x_w H}(\beta_{1c}, \chi)$, $\nu_{z_w H}(\beta_{1c}, \chi)$, $\nu_{x_w V}(\beta_{1c}, \chi)$ and $\nu_{z_w V}(\beta_{1c}, \chi)$ are obtained from look-up tables (Ref. 32).

The angles of attack and sideslip at the horizontal and vertical tail are:

$$\alpha_H = \tan^{-1}\frac{w_H}{|u_H|} + \theta_{0\mathrm{H}} \tag{2.158}$$

$$\beta_H = \tan^{-1}\frac{v_H}{\sqrt{v_H^2 + w_H^2}} \tag{2.159}$$

$$\alpha_V = \tan^{-1}\frac{w_V}{|u_V|} \tag{2.160}$$

$$\beta_V = \tan^{-1}\frac{v_V}{\sqrt{v_V^2 + w_V^2}} \tag{2.161}$$

The angles of attack are positive nose up, the angle of sideslip are defined as positive nose right and $\theta_{0\mathrm{H}}$ is the variable pitch angle of the horizontal tail, which depends on the flight speed and is adjusted by the flight control system (Ref. 32).

The empennage aerodynamic loads acting of the UH-60A are defined in the local wind axes system, the lift and drag aerodynamic coefficients at the tail surfaces

being:

$$C_{LH} = C_{LH}(\alpha_H) \tag{2.162}$$

$$C_{DH} = C_{DH}(|\alpha_H|) \tag{2.163}$$

$$C_{LV} = C_{LV}(\beta_V) \tag{2.164}$$

$$C_{DV} = C_{DV}(|\beta_V|) \tag{2.165}$$

The total aerodynamic loads in the local wind axes systems of the empennage are:

$$\mathbf{F}_{wH} = -C_{DH}\bar{q}_H S_H \mathbf{i}_{\mathrm{H}} - C_{LH}\bar{q}_H S_H \mathbf{k}_{\mathrm{H}} \tag{2.166}$$

$$\mathbf{F}_{wV} = -C_{DV}\bar{q}_V S_V \mathbf{i}_{\mathrm{V}} + C_{LV}\bar{q}_V S_V \mathbf{j}_{\mathrm{V}} \tag{2.167}$$

where S_H and S_V are the surface areas of the horizontal and vertical tail respectively.

A transformation is necessary to convert these forces, from the local wind axes system of the horizontal ($\mathbf{i}_{\mathrm{H}}$, $\mathbf{j}_{\mathrm{H}}$, $\mathbf{k}_{\mathrm{H}}$) and vertical ($\mathbf{i}_{\mathrm{V}}$, $\mathbf{j}_{\mathrm{V}}$, $\mathbf{k}_{\mathrm{V}}$) tails, into the body fixed system. The coordinate transformation matrix is:

$$T_{\mathrm{H}B} = \begin{bmatrix} \cos(\alpha_H - \theta_{0\mathrm{H}})\cos\beta_H & \cos(\alpha_H - \theta_{0\mathrm{H}})\sin\beta_H & -\sin(\alpha_H - \theta_{0\mathrm{H}}) \\ \sin\beta_H & -\cos\beta_H & 0 \\ \sin(\alpha_H - \theta_{0\mathrm{H}})\cos\beta_H & \sin(\alpha_H - \theta_{0\mathrm{H}})\sin\beta_H & \cos(\alpha_H - \theta_{0\mathrm{H}}) \end{bmatrix} \tag{2.168}$$

so that:

$$\begin{Bmatrix} \mathbf{i}_{\mathrm{B}} \\ \mathbf{j}_{\mathrm{B}} \\ \mathbf{k}_{\mathrm{B}} \end{Bmatrix} = [T_{\mathrm{H}B}]^{-1} \begin{Bmatrix} \mathbf{i}_{\mathrm{H}} \\ \mathbf{j}_{\mathrm{H}} \\ \mathbf{k}_{\mathrm{H}} \end{Bmatrix} \tag{2.169}$$

The aerodynamic forces and moments of the horizontal tail, transformed to

the body axis at the center of gravity of the body are

$$\mathbf{F}_H = \left\{ \begin{array}{c} X_H \\ Y_H \\ Z_H \end{array} \right\} = [T_{\mathrm{H}B}]^{-1} \mathbf{F}_{wH} \tag{2.170}$$

and

$$\mathbf{M}_H = \left\{ \begin{array}{c} L_H \\ M_H \\ N_H \end{array} \right\} = \mathbf{x}_H \times \mathbf{F}_H \tag{2.171}$$

with $\mathbf{x}_H$ being the position vector of the horizontal tail aerodynamic reference point with respect to the center of gravity of the body, defined as

$$\mathbf{x}_H = x_H \mathbf{i}_{\mathrm{B}} + y_H \mathbf{j}_{\mathrm{B}} + z_H \mathbf{k}_{\mathrm{B}} \tag{2.172}$$

For the vertical tail, the coordinate transformation matrix is

$$T_{\mathrm{V}B} = \left[\begin{array}{ccc} \cos\alpha_V \cos\beta_V & \cos\alpha_V \sin\beta_V & -\sin\alpha_V \\ \sin\beta_V & -\cos\beta_V & 0 \\ \sin\alpha_V \cos\beta_V & \sin\alpha_V \sin\beta_V & \cos\alpha_V \end{array} \right] \tag{2.173}$$

so that

$$\left\{ \begin{array}{c} \mathbf{i}_{\mathrm{B}} \\ \mathbf{j}_{\mathrm{B}} \\ \mathbf{k}_{\mathrm{B}} \end{array} \right\} = [T_{\mathrm{V}B}]^{-1} \left\{ \begin{array}{c} \mathbf{i}_{\mathrm{V}} \\ \mathbf{j}_{\mathrm{V}} \\ \mathbf{k}_{\mathrm{V}} \end{array} \right\} \tag{2.174}$$

And the forces and moments at the center of gravity of the body are:

$$\mathbf{F}_V = \left\{ \begin{array}{c} X_V \\ Y_V \\ Z_V \end{array} \right\} = [T_{\mathrm{V}B}]^{-1} \mathbf{F}_{wV} \tag{2.175}$$

and:

$$\mathbf{M}_V = \left\{ \begin{array}{c} L_V \\ M_V \\ N_V \end{array} \right\} = \mathbf{x}_V \times \mathbf{F}_V \tag{2.176}$$

where $\mathbf{x}_V$ is the position vector from the center of gravity of the body to the vertical tail aerodynamic reference point

$$\mathbf{x}_V = x_V \mathbf{i}_\mathrm{B} + y_V \mathbf{j}_\mathrm{B} + z_V \mathbf{k}_\mathrm{B} \tag{2.177}$$

2.5.4 Tail rotor loads

The tail rotor model is based on a modification of the simplified closed-form Bailey solution (Ref. 116). At the tail rotor, the velocity of the airflow in the body fixed axes system is

$$\mathbf{u}_{TR} = \mathbf{u}_B + \mathbf{x}_{TR} \times \omega + \mathbf{u}_{in_{TR}} \tag{2.178}$$

where $\mathbf{u}_{in_{TR}}$ is the interference velocity caused by the fuselage and main rotor wake and is a function of the main rotor downwash, tip speed and wake skew angle:

$$\mathbf{u}_{in_{TR}} = v_0 \nu_{x_w TR}(\beta_{1c}, \chi)\mathbf{i}_{\mathrm{TR}} + v_0 \nu_{z_w TR}(\beta_{1c}, \chi)\mathbf{k}_{\mathrm{TR}} \tag{2.179}$$

where the functions $\nu_{x_w TR}(\beta_{1c}, \chi)$ and $\nu_{z_w TR}(\beta_{1c}, \chi)$ are read from look-up tables (Ref. 32).

The position vector from the hub of the tail rotor to the center of gravity of the body, $\mathbf{x}_{TR}$, is given by:

$$\mathbf{x}_{TR} = x_{TR}\mathbf{i}_\mathrm{B} + y_{TR}\mathbf{j}_\mathrm{B} + z_{TR}\mathbf{k}_\mathrm{B} \tag{2.180}$$

The velocity components at the tail rotor hub in the body fixed coordinate system are

$$u_{TR} = u_B + y_{TR} r_B - z_{TR} q_B + u_{in_{TR}} \tag{2.181}$$

$$v_{TR} = v_B + z_{TR} p_B - x_{TR} r_B + v_{in_{TR}} \tag{2.182}$$

$$w_{TR} = w_B + x_{TR} q_B - y_{TR} p_B + w_{in_{TR}} \tag{2.183}$$

These velocities need to be expressed in the local tail rotor coordinate system. For this transformation, two rotations are necessary, one about the x_B axis by the tail rotor cant angle, Γ_{TR}, and the second about the new z axis by the tail rotor yaw angle, Λ_{TR}. The resultant coordinate transformation is:

$$T_{\mathrm{T}B} = \begin{bmatrix} \cos\Lambda_{TR} & -\sin\Gamma_{TR}\sin\Lambda_{TR} & \cos\Gamma_{TR}\sin\Lambda_{TR} \\ 0 & \cos\Gamma_{TR} & \sin\Gamma_{TR} \\ -\sin\Lambda_{TR} & -\sin\Gamma_{TR}\cos\Lambda_{TR} & \cos\Gamma_{TR}\cos\Lambda_{TR} \end{bmatrix} \tag{2.184}$$

The velocity components in the local tail rotor coordinate system become:

$$\begin{Bmatrix} u_{\mathrm{t}l} \\ v_{\mathrm{t}l} \\ w_{\mathrm{t}l} \end{Bmatrix} = [T_{\mathrm{T}B}] \begin{Bmatrix} u_{TR} \\ v_{TR} \\ w_{TR} \end{Bmatrix} \tag{2.185}$$

The expression for the non-dimensional tail rotor thrust is:

$$T_{\mathrm{t}l} = 2\rho \left(\pi \bar{R}_{\mathrm{t}}\right)^2 \nu_{\mathrm{t}} v_{T\mathrm{t}} \left(\bar{\Omega}_{\mathrm{t}} \bar{R}_{\mathrm{t}}\right)^2 K_{blk} \left[\frac{R^2}{m_0}\right] \tag{2.186}$$

where $\bar{R}_{\mathrm{t}}$ and $\bar{\Omega}_{\mathrm{t}}$ are the non-dimensional tail rotor radius and rotational speed respectively, non-dimensionalized with respect to the main rotor radius and rotational speed each; ν_{t} is the tail rotor induced velocity, K_{blk} is an empirical tail rotor blockage factor to account for the presence of the vertical tail (Ref. 32) and $v_{T\mathrm{t}}$ is the total speed of the airflow at the tail rotor hub, which is given by:

$$v_{T\mathrm{t}l} = \sqrt{\mu_{\mathrm{t}}^2 + \lambda_{\mathrm{t}}^2} \tag{2.187}$$

where

$$\mu_{\mathrm{t}l} = \sqrt{u_{\mathrm{t}l}^2 + v_{\mathrm{t}l}^2} \tag{2.188}$$

$$\lambda_{\mathrm{t}} = w_{\mathrm{t}l} - \nu_{\mathrm{t}} \tag{2.189}$$

The non-dimensional torque produced by the tail rotor is:

$$Q_{\mathrm{t}l} = \frac{1}{2}\rho \left(\bar{\Omega}_{\mathrm{t}} \bar{R}_{\mathrm{t}}\right)^2 \pi \bar{R}_{\mathrm{t}}^3 \left[\frac{R^2}{m_0}\right] \tag{2.190}$$

The thrust and torque loads in the local tail rotor coordinate system are:

$$\mathbf{F}_{\mathrm{t}l} = -T_{\mathrm{t}l}\mathbf{j}_{\mathrm{t}} \tag{2.191}$$

$$\mathbf{M}_{\mathrm{t}l} = -Q_{\mathrm{t}l}\mathbf{j}_{\mathrm{t}} \tag{2.192}$$

After transforming these loads at the center of gravity of the body obtained using the transformation from tail rotor coordinate system to body fixed system, the resultant forces and moments at the center of gravity due to the tail rotor are:

$$\mathbf{F}_{TR} = \left\{ \begin{array}{c} X_{TR} \\ Y_{TR} \\ Z_{TR} \end{array} \right\} = [T_{\mathrm{T}B}]^{-1}\mathbf{F}_{\mathrm{t}l} \tag{2.193}$$

and

$$\mathbf{M}_{TR} = \left\{ \begin{array}{c} L_{TR} \\ M_{TR} \\ N_{TR} \end{array} \right\} = [T_{\mathrm{T}B}]^{-1}\mathbf{M}_{\mathrm{t}l} + \mathbf{x}_{TR} \times \mathbf{F}_{TR} \tag{2.194}$$

2.6 Tail rotor dynamic inflow

The tail rotor inflow dynamics are calculated with a 1-state Pitt–Peters dynamic inflow model (Ref. 24). Therefore, only one constant inflow state is used, the sine and cosine terms are zero, and only one equation is needed to represent the inflow

$$\frac{1}{\Omega_t}\tau_t\dot{\nu}_t + \nu_t = L_t C_{T_t} \tag{2.195}$$

where (Ref. 24)

$$\tau_t = \frac{1}{v_{T_t}}\frac{4}{3\pi} \tag{2.196}$$

$$Ł_t = \frac{1}{2v_{T_t}} \tag{2.197}$$

v_{T_t} is the total induced velocity at the tail rotor, given by:

$$v_{T_t} = \sqrt{(u_t^2 + \lambda_t^2)} \tag{2.198}$$

The tail rotor thrust coefficient, C_{T_t}, is given by:

$$C_{T_t} = \frac{T_{tl} m_0 \Omega^2 R^2}{\rho\pi\Omega_t^2 R_t^4} \tag{2.199}$$

where Ω_t is the tail rotor rotational speed, R_t is the tail rotor radius and T_{tl} is the non-dimensional tail rotor thrust, Eq. (2.186).

2.7 Assembly of equations of motion

The previous sections have described the different components necessary to build the complete equations of motion of the helicopter. These equations are formulated in the form of first-order ODEs:

$$\dot{\mathbf{y}} = \mathbf{g}(\dot{\mathbf{y}}, \mathbf{y}, \mathbf{u}\,; t) \tag{2.200}$$

where $\mathbf{y}$ and $\dot{\mathbf{y}}$ are the state vector, Eq.(2.4), and its derivative, respectively, $\mathbf{u}$, Eq.(2.5), is the vector of controls and t is the time.

The equations of motion can be grouped in the following categories:

1. The nonlinear, rigid body equations of motion for the helicopter, known as the Euler equations. These are a set of 9 equations representing the force and moment equilibrium, given in Eqs.(2.94) through (2.99), and the kinematic relationship between the angular rates and the derivatives of the Euler angles, Eq.(2.108), described in Section 2.5.

2. The rotor equations, Eq.(2.93), described in Section 2.4.8.

3. An equation for the tail rotor inflow, as described in Section 2.6.

4. If dynamic inflow is used to calculate the main rotor induced velocities, the equations of the Peters–He dynamic inflow model are provided (Ref. 36). If instead the inflow is calculated with the free wake model, the free wake equations are solved separately.

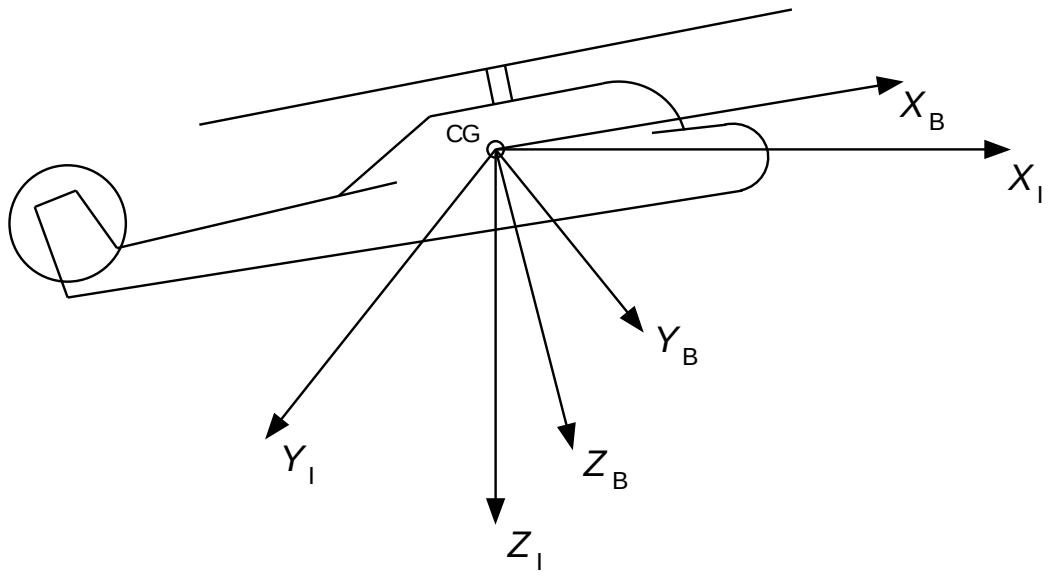

Figure 2.1: Inertial and body-fixed coordinate systems.

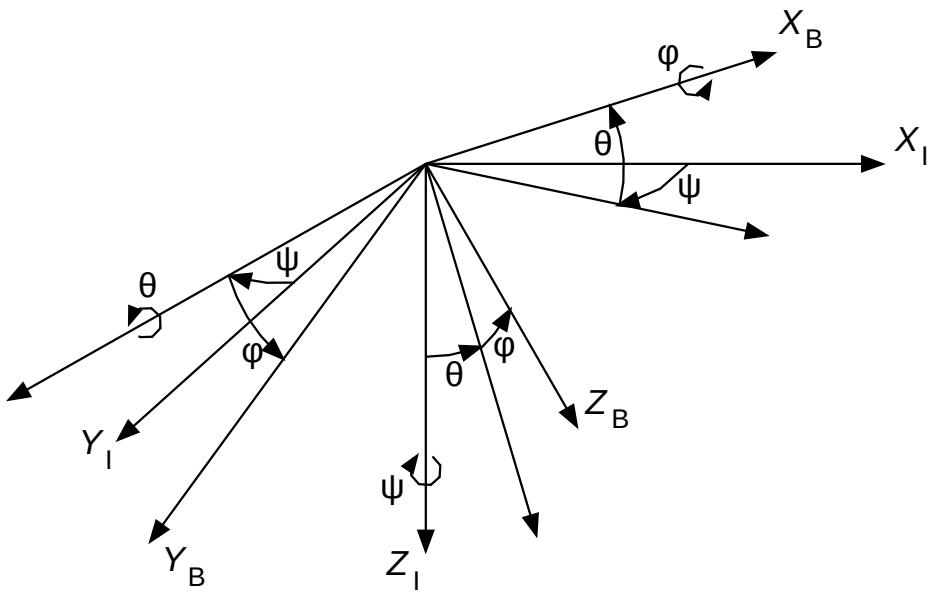

Figure 2.2: Euler angles and rotations from the inertial to fuselage coordinate systems. The sequence of rotations is $\psi \longrightarrow \theta \longrightarrow \phi$.

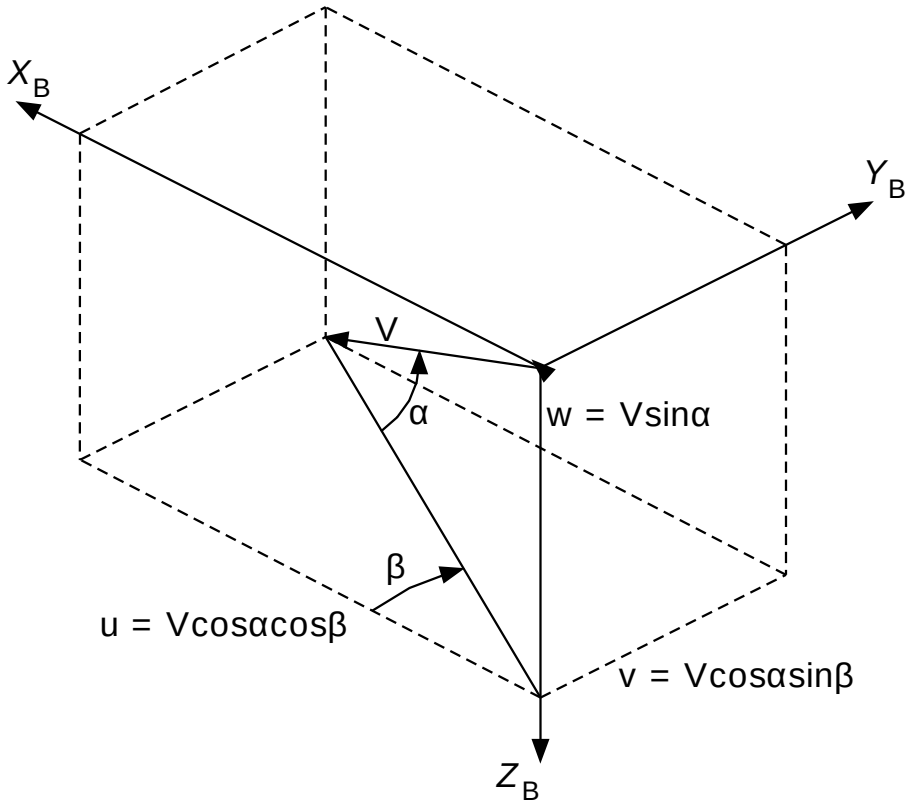

Figure 2.3: Relationship between velocity vector defining the wind coordinate system and the body-fixed coordinate system.

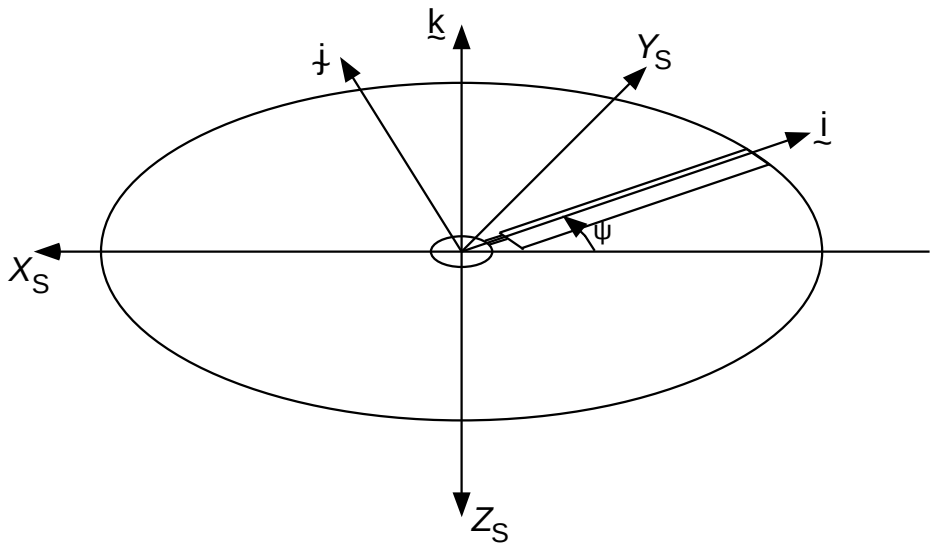

Figure 2.4: Hub-fixed rotating and shaft-fixed non-rotating coordinate systems.

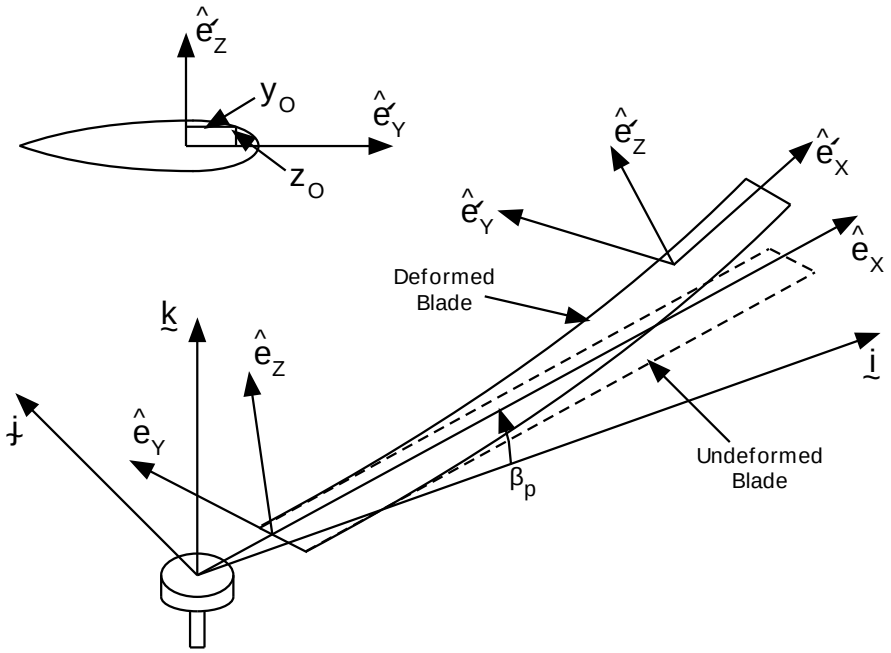

Figure 2.5: Blade deformed and undeformed coordinate systems.

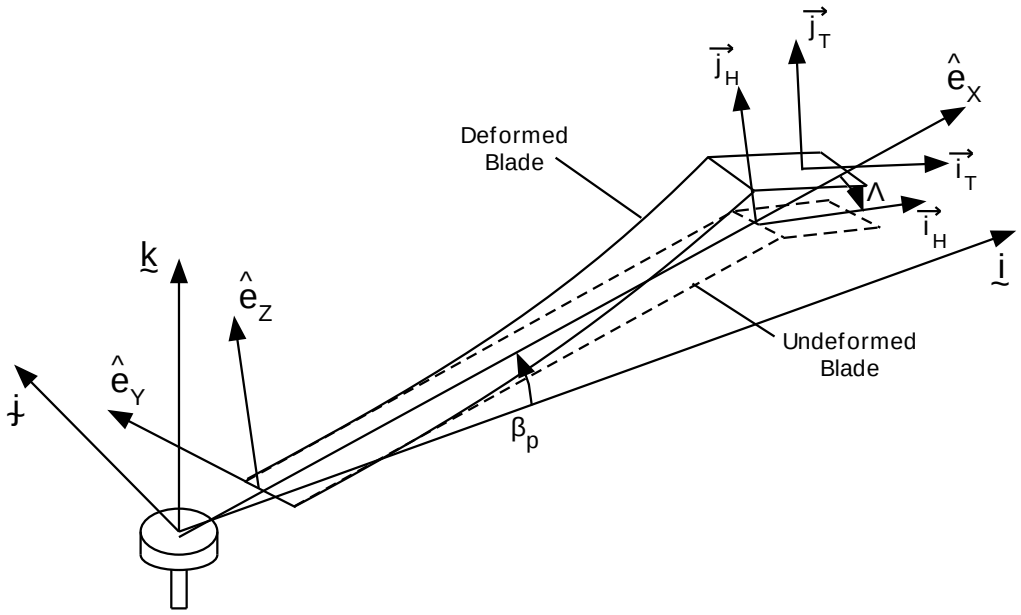

Figure 2.6: Tip deformed and undeformed coordinate systems.

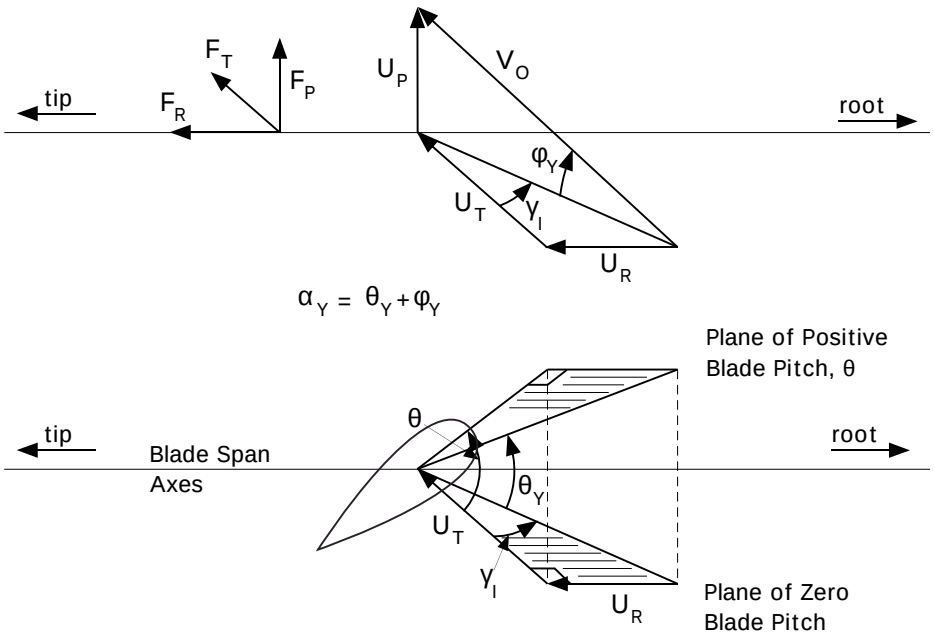

Figure 2.7: Definition of the sectional aerodynamic angles, the yaw angle γ_I and the induced angle of attack ϕ_Y (Ref. 32).

Chapter 3

Free wake model

3.1 Overview

The wake of a helicopter rotor is comprised mostly of the strong vortices that are released from the tips of its blades. These vortices form quickly behind the rotor blades and are convected below the rotor in a helical structure in hover, and are skewed back with increasing forward speeds (Ref. 3). Numerical vortex models describe the rotor wake by tracking the tip vortices through the flow field (Ref. 3). While there are several approaches to modeling the tip vortices, the free wake models used in the present study discretize the vortex filaments with straight segments, whose strength and location constitutes part of the problem being solved. By virtue of the vorticity transport theorem, each vortex filament can be modeled and its location determined. With the position and strength of the vortex filaments known, one can compute the induced velocity field at the rotor by means of the Biot–Savart law. Free wake models are a particular type of vortex model in which the vortex filaments are allowed to distort freely under their self and mutual interaction, as well as the bound circulation, rather than follow a predetermined trajectory as in

rigid or prescribed wakes. The exact position of each filament is calculated as part of the problem (Ref. 3).

There are two main categories of free wake methodologies: relaxation (or iterative) methods, and time-marching schemes. Relaxation methods assume periodicity, which makes them more appropriate for steady-state solutions. Time-marching schemes are potentially subject to numerical instabilities, but are not restricted by the flight condition (Ref. 3).

The free wake model used in this study is the time-accurate maneuver free wake initially developed by Bhagwat and Leishman (Ref. 9) and subsequently improved by Ananthan and Leishman (Refs. 5, 117). The distortions of the wake geometry due to maneuvers are taken into account without *a priori* assumptions on the geometry. In this section, a brief description of these wake models is presented.

The free wake model used in the present study is comprised of two parts: the near wake, which is assumed planar and with a fixed angular length, and the tip vortex that constitutes the free wake and which extends beyond the near wake constituting the far wake.

3.2 Assumptions

The following assumptions are associated with the free wake model and the coupling the free wake model to the rest of the flight dynamic model.

The intrinsic assumptions in the free wake model are:

1. The free-vortex wake analysis is based on the assumption of irrotational in-

compressible flow (i.e., a potential flow).

2. The vorticity is assumed to be concentrated in a finite number of vortex filaments. For the present study, blade trailed vorticity is characterized by a single vortex released from the blade elastic axis at the blade tip. This assumption may be questionable at high speeds or through the vortex ring state, but those are aerodynamic issues, and for flight dynamics considerations, the present assumption will suffice.

3. The bound circulation and lift are assumed constant over each blade segment with the Weissinger-L model.

4. Thin airfoil theory is assumed in the relation between lift and circulation in the formulation of the Weissinger-L model.

5. The initial tip vortex strength is taken to be the maximum bound circulation along the blade.

Additionally, the following assumptions are taken in the coupling of the free wake model to the flight dynamics model:

1. Within the free wake model, it is assumed that the blade is rigid and straight with a single flap hinge at the axis of rotation. An "equivalent" flap angle is defined as indicated in Section 3.3.3.

2. The free wake model provides all three spatial components of the induced velocity in the free wake blade preconed coordinate system (see Section 3.3.2),

however the x and y components are set to zero and only the z component (i.e., the component along the z_P axis) is used for the calculation of the aerodynamic loads. This assumption can be safely done for most flight conditions, for which the x and y components are negligible in comparison with the z component. However, for the vortex ring state conditions this may not be true and this assumption may need reconsideration.

3. No lag and torsion motion is included in the free wake model. However, the effect of flap, lag and torsion is included in the blade sectional velocities that are provided by the flight dynamics model to the free wake model.

4. The effect of the downwash of the rotor on the fuselage and empennage is not included.

5. Fuselage aerodynamics does not affect the rotor wake.

3.3 Free wake coordinate systems

The free wake model is formulated in a wind coordinate system (Refs. 12, 15, 40), and the necessary coordinate systems are defined in this section.

3.3.1 Global wake coordinate system

In the global wake coordinate system, in which the free wake model is formulated, the x-axis is aligned with the freestream flow and is positive aft, the y-axis points to starboard and the z-axis points up. For a wind tunnel trim problem, the x-axis is

aligned with the longitudinal axis of the wind tunnel. In hover, where the freestream velocity is zero, the x-axis is assumed to point along the longitudinal axis of the helicopter.

Figure 3.1 illustrates this coordinate system. The longitudinal shaft tilt angle, α_S, is the angle that the z-axis makes with the rotor shaft, and also indicates the angle of attack of the rotor hub with respect to the freestream flow. α_S is defined as positive with the shaft tilted aft so that the thrust vector is also tilted in the aft direction. The axes of the global coordinate system are x_{GW}, y_{GW}, z_{GW}, with corresponding unit vectors $\mathbf{i}_{GW}$, $\mathbf{j}_{GW}$, $\mathbf{k}_{GW}$.

3.3.2 Free wake blade preconed coordinate system

The free wake blade preconed coordinate system is the system in which the free wake calculates the induced velocities. It has its origin at the hub and its unit vectors are $\mathbf{i}_{\mathrm{P}}$, $\mathbf{j}_{\mathrm{P}}$, $\mathbf{k}_{\mathrm{P}}$ with the x-axis pointing outboard along the blade, the y-axis pointing in the blade lead direction and the z-axis pointing up.

The transformation from the global-fixed frame to the free wake blade preconed rotating frame requires first a rotation of the longitudinal shaft tilt α_S about the global fixed y_GW-axis, followed by a rotation of the azimuth angle ψ about the new z-axis (aligned with the rotor shaft), and a rotation of the precone angle β_P about the new y-axis (normal to the rotor shaft and pointing in the blade lead direction). The resultant transformation matrix is:

$$[T_{PG}] = \begin{bmatrix} \cos\alpha_S \cos\psi \cos\beta_p & \sin\psi \cos\beta_p & -\sin\alpha_S \cos\psi \cos\beta_p \\ +\sin\alpha_S \sin\beta_p & & +\cos\alpha_S \sin\beta_p \\ -\cos\alpha_S \sin\psi & \cos\psi & \sin\alpha_S \sin\psi \\ -\cos\alpha_S \cos\psi \sin\beta_p & -\sin\psi \sin\beta_p & \sin\alpha_S \cos\psi \sin\beta_p \\ +\sin\alpha_S \cos\beta_p & & +\cos\alpha_S \cos\beta_p \end{bmatrix} \tag{3.1}$$

so that:

$$\begin{Bmatrix} \mathbf{i}_P \\ \mathbf{j}_P \\ \mathbf{k}_P \end{Bmatrix} = [T_{PG}] \begin{Bmatrix} \mathbf{i}_{GW} \\ \mathbf{j}_{GW} \\ \mathbf{k}_{GW} \end{Bmatrix} \tag{3.2}$$

3.3.3 Coupling of the flight dynamic and the free wake coordinate systems

The flight dynamics model and the free wake model are each formulated in a slightly different frame of reference. At the interface between both models, the necessary transformations must take place, in both directions, in order to ensure the data transmitted between them are in the right coordinate system.

There are four sets of information that are exchanged between the two models, and for each the appropriate transformation is needed:

Body velocities and rates The freestream velocity and the body angular rates, which are in the body axis system $\mathbf{i}_B$, $\mathbf{j}_B$, $\mathbf{k}_B$, in the flight dynamics model (Eq.(2.7)), need to be converted to the global wake axis system $\mathbf{i}_{GW}$, $\mathbf{j}_{GW}$, $\mathbf{k}_{GW}$ (Eqs.(3.5) and (3.6)).

Flap angle The flap angle at the tip of the blade needs to be provided by the

flight dynamics model to the free wake model. Both the rotor-fuselage model and the free wake model consider the flapping angle β positive for an upward deflection, therefore no transformation is required (only an "equivalent rigid blade flap" approximation is necessary, as explained in Section 4.5.5).

Blade velocities The velocity of the flow seen by the blade at the different sections along the blade span needs to be provided by the flight dynamics model to the free wake model. This velocity includes the freestream velocities at the blade section, the velocities due the angular rotation of the helicopter and the blade and the velocities due to the elastic deformation of the blade (see Section 4.5.5 for further details). In the flight dynamics model, these velocities are calculated in the blade undeformed preconed coordinate system, $\hat{\mathbf{e}}_x$, $\hat{\mathbf{e}}_y$, $\hat{\mathbf{e}}_z$ (Eq.(2.15)). In the free wake model, these velocities are required in the free wake blade preconed coordinate system, $\mathbf{i}_\mathrm{P}$, $\mathbf{j}_\mathrm{P}$, $\mathbf{k}_\mathrm{P}$ (Eq.(3.2)). Since both coordinate systems are equivalent, no transformation is necessary.

Induced velocities The inflow distribution calculated in the free wake model needs to be provided to the rest of the flight dynamic model, and therefore needs to be converted from the free wake blade preconed coordinate system, $\mathbf{i}_\mathrm{P}$, $\mathbf{j}_\mathrm{P}$, $\mathbf{k}_\mathrm{P}$ (Eq.(3.2)), to the flight dynamics blade preconed coordinate system, $\hat{\mathbf{e}}_x$, $\hat{\mathbf{e}}_y$, $\hat{\mathbf{e}}_z$ (Eq.(2.15)). These two coordinate systems are coincident, so no transformation is required.

3.3.4 Body-fixed to global wake coordinate systems

The transformation from the body-fixed to the wake global wake reference frames is simply given by:

$$T_{GB} = \begin{bmatrix} -1 & 0 & 0 \\ 0 & 1 & 0 \\ 0 & 0 & -1 \end{bmatrix} \tag{3.3}$$

so that:

$$\begin{Bmatrix} \mathbf{i}_{GW} \\ \mathbf{j}_{GW} \\ \mathbf{k}_{GW} \end{Bmatrix} = [T_{GB}] \begin{Bmatrix} \mathbf{i}_{B} \\ \mathbf{j}_{B} \\ \mathbf{k}_{B} \end{Bmatrix} \tag{3.4}$$

Therefore, the velocity components and the angular rates of the body can be converted from the body-fixed system to the global wake axis system as follows:

$$\begin{Bmatrix} u_{GW} \\ v_{GW} \\ w_{GW} \end{Bmatrix} = \begin{Bmatrix} -u_B \\ v_B \\ -w_B \end{Bmatrix} \tag{3.5}$$

and:

$$\begin{Bmatrix} p_{GW} \\ q_{GW} \\ r_{GW} \end{Bmatrix} = \begin{Bmatrix} -p_B \\ q_B \\ -r_B \end{Bmatrix} \tag{3.6}$$

3.4 The far wake problem

The behavior of the vortex filaments is described by the equation of vorticity transport (Ref. 7)

$$\frac{d\mathbf{r}(\psi,\zeta)}{dt} = \mathbf{V}(\mathbf{r}(\psi,\zeta)) \tag{3.7}$$

which can be rewritten as

$$\frac{\partial \mathbf{r}(\psi,\zeta)}{\partial \psi} + \frac{\partial \mathbf{r}(\psi,\zeta)}{\partial \zeta} = \frac{1}{\Omega}\mathbf{V}(\mathbf{r}(\psi,\zeta)) \tag{3.8}$$

where $\mathbf{r}(\psi, \zeta)$ defines the position of a point on the vortex filament and $\mathbf{V}(\mathbf{r}(\psi, \zeta))$ is the local velocity at that point.

The derivatives on the left hand side of Eq. (3.8) are calculated using finite difference approximation (Ref. 7). For this purpose, the wake is discretized both in space and time. A schematic of the wake discretization is shown in Fig. 3.3. In the time domain, ψ, the rotor azimuth is divided into N_ψ angular steps, each of size $\Delta\psi$. Since there is one filament released at each time step, the total number of vortex filaments representing the tip vortex geometries at the entire set of azimuth angles is

$$N_\psi = \frac{2\pi}{\Delta\psi} \tag{3.9}$$

Each vortex filament is discretized into N_ζ straight segments, whose angular resolution is $\Delta\zeta$. The total number of straight line vortex segments in each filament is

$$N_\zeta = \frac{\zeta_{max}}{\Delta\zeta} \tag{3.10}$$

and the total number of collocation points for each vortex filament is $N_\zeta + 1$.

In Fig. 3.3, the index j in the collocation points is used as a reference to the azimuth angle ψ and the index k references the location of the collocation point in the vortex filament ζ.

The right hand side of Eq. (3.8) is determined by the total velocities at the collocation point, which comprise the free-stream velocity, the velocities induced by all the other vortex filaments and the blades, plus the velocities due to maneuvering.

3.4.1 The time marching scheme

The time-marching free wake model is based on the solution of the governing partial differential equations at the midpoints of the grid cell defined by the discretizations in ψ and ζ, that is at $(\psi + \Delta\psi/2, \zeta + \Delta\zeta/2)$.

A five-point central difference scheme is used to describe the spatial derivative (Ref. 7), D_ζ, given by

$$D_\zeta \approx \frac{\partial \mathbf{r}(\psi + \Delta\psi/2, \zeta + \Delta\zeta/2)}{\partial \zeta} = \frac{\mathbf{r}(\psi + \Delta\psi, \zeta + \Delta\zeta) - \mathbf{r}(\psi, \zeta + \Delta\zeta) + \mathbf{r}(\psi + \Delta\psi, \zeta) - \mathbf{r}(\psi, \zeta)}{2\Delta\zeta} \tag{3.11}$$

The time derivative, D_ψ, is approximated with a predictor-corrector with second order backward (PC2B) scheme:

$$D_\psi \approx \frac{\partial \mathbf{r}(\psi + \ \Delta\psi/2, \zeta)}{\partial \psi} = \frac{3\mathbf{r}(\psi + \ \Delta\psi, \zeta) - \mathbf{r}(\psi, \zeta) - 3\mathbf{r}(\psi - \ \Delta\psi, \zeta) - \mathbf{r}(\psi - 2\Delta\psi, \zeta)}{4\Delta\psi} \tag{3.12}$$

Both schemes are second order accurate (Ref. 118).

3.5 Velocity field at the vortex filament

The velocity field at each segment of the vortex filament is composed of the free-stream velocity, the velocities self and mutually induced by all the vortex filaments and the blades, plus any additional velocities due to maneuvering (Ref. 7).

The velocity term in the RHS of Eq. (3.8) is therefore given as

$$\mathbf{V}\left(\mathbf{r}(\psi,\zeta)\right) = \mathbf{V}_{\infty} + \mathbf{V}_{ind}\left(\mathbf{r}(\psi,\zeta)\right) + \mathbf{V}_{man}\left(\mathbf{r}(\psi,\zeta)\right) \tag{3.13}$$

The free-steam velocity can be simply written as

$$\mathbf{V}_{\infty} = V_{\infty x}\mathbf{i} + V_{\infty y}\mathbf{j} + V_{\infty z}\mathbf{k} \tag{3.14}$$

The velocities due to the maneuvering of the helicopter are calculated with the cross product of the angular rates by the position vector of the given point from the center of gravity (Ref. 40):

$$\mathbf{V}_{man} = \omega \times \mathbf{r}_{CG} = (r_G y - q_G z)\mathbf{i}_{\mathrm{G}} + (p_G z - r_G x)\mathbf{j}_{\mathrm{G}} + (q_G x - p_G y)\mathbf{k}_{\mathrm{G}} \tag{3.15}$$

where the subscript G denotes the global wake coordinate system described in Section 3.3.1.

The most difficult and expensive term to compute is the one corresponding to the induced velocities. The Biot–Savart law is used to calculate the velocity induced at a point located at position $\mathbf{r}$ relative to the vortex element $d\mathbf{l}$, for each filament segment in the wake (Ref. 7):

$$\mathbf{V}_{ind} = \frac{\Gamma_j}{4\pi}\int \frac{d\mathbf{l}_j \times \mathbf{r}_i}{|\mathbf{r}_i - \mathbf{r}_j|^3} \tag{3.16}$$

Two aspects of the vortex model that are important in the calculation of the induced velocities are the tangential velocity profile and the diffusion of the vortex along its length.

The vortex model is characterized by an inner viscous region which consists of a "solid-body" rotation and an outer region that simulates a potential vortex profile.

Ref. 15 shows that the tangential velocity v_θ of the rotor tip vortices can be closely approximated by

$$v_\theta(r) = \frac{\Gamma r}{2\pi\sqrt{r_c^4 + r^4}} \tag{3.17}$$

where Γ is the vortex circulation strength, r is the distance at which the tangential velocity is evaluated and r_c is the vortex viscous core radius.

The diffusion of the vortex is incorporated as a variation in the viscous core radius r_c in which the core radius grows as function of the vortex age (Ref. 40)

$$r_c(\zeta) = \sqrt{r_{c_0}^2 + \frac{4\alpha\delta\nu\zeta}{\Omega}} \tag{3.18}$$

where α is the Oseen parameter and has a value of 1.25643, ν is the kinematic viscosity of air, ζ is the vortex age in radians, Ω is the rotational speed of the rotor, and δ is an "eddy" or turbulent velocity coefficient that determines the rate at which the vortex core grows with time, which is determined empirically (Ref. 15).

Including the tangential velocity profile model, Eq. (3.17), and vortex diffusion, Eq. (3.18), into the Biot–Savart law, the induced velocity due to the vortex element is

$$\mathbf{V}_{ind} = \frac{\Gamma_j h}{2\pi\sqrt{r_c^4 + h^4}} \int \frac{d\mathbf{l}_j \times \mathbf{r}}{|\mathbf{r}_i - \mathbf{r}_j|^3} \tag{3.19}$$

where h is the perpendicular distance of the evaluation point from the influencing vortex element. The total induced velocity at a point in the flow field results of combining effect of all of the influencing vortices.

The present model uses realistic values for the vortex core growth obtained from experiments (Ref. 119) rather than an arbitrary core value to improve convergence of the numerical method.

3.6 Bound circulation and the near wake problem

The bound circulation is obtained using a Weissinger-L lifting surface model (Ref. 51), which is a type of lifting surface model that relates the blade lift to the bound circulation through the Kutta–Joukowski theorem. The bound circulation along the blade determines the strength of the trailed wake vortices, which in turn influence the velocity field at the rotor blades.

In this model, the blade is discretized into N_S spanwise segments and only one chordwise segment, as shown in Fig. 3.4 (Refs. 15, 40). At each segment, a control point is located at 3/4 of the chord, while the bound circulation is located at the quarter-chord location and is assumed constant along the segment. The difference in circulation between consecutive segments is trailed behind the blade at segment endpoints, with a vortex strength equal to the difference between the two segments bound vortex strengths. These trailed vortices comprise the near wake, which is assumed planar and with a fixed angular length. The tip vortex that constitutes the free wake extends beyond the near wake with a strength equal to the maximum bound circulation along the blade.

To solve for the strength of the bound circulation, one must satisfy the flow tangency condition (Ref. 120), which means that the flow cannot go through the rotor blade, at least at the 3/4-chord point. Therefore, the component of the incident velocity normal to the spanwise segment must be zero at that point (Ref. 40):

$$\mathbf{V}_i \cdot \mathbf{n}_i = 0 \tag{3.20}$$

The total velocity at any point in the blade, $\mathbf{V}_i$, is composed of the free-

stream velocities at the given point, the velocities due to the blade motion and flexibility, the local velocities due to the maneuvering of the helicopter and the induced velocities, which have three sources, the bound circulation, the near wake and the far wake (Ref. 40) :

$$\mathbf{V}_i = \mathbf{V}_\infty + \mathbf{V}_{BM} + \mathbf{V}_{man} + \mathbf{V}_B + \mathbf{V}_{NW} + \mathbf{V}_{FW} \tag{3.21}$$

The bound and near wake velocities can be expressed in terms of the strength of the bound circulation (Ref. 40)

$$\begin{aligned} \mathbf{V}_{B_i} &= \sum_{j=1}^{N_S} I_{b_{i,j}} \Gamma_j \\ \mathbf{V}_{NW_i} &= \sum_{j=1}^{N_S} I_{NW_{i,j}} \Gamma_j \end{aligned} \tag{3.22}$$

with i going from 1 to N_S. The terms $I_{b_{i,j}}$ and $I_{NW_{i,j}}$ are the bound and near wake influence coefficient matrices, respectively.

Substituting $\mathbf{V}_{B_i}$ and $\mathbf{V}_{NW_i}$ into Eq.(3.21), reorganizing Eq.(3.20) and expressing in the form of a linear system of equations, yields the governing equation for the Weissinger-L method (Ref. 40)

$$\sum_{j=1}^{N_S} \left[I_{b_{i,j}} + I_{NW_{i,j}} \right] \Gamma_j = \{ (\mathbf{V}_\infty + \mathbf{V}_{BM} + \mathbf{V}_{man} + \mathbf{V}_{FW}) \cdot \mathbf{n} \}_i \tag{3.23}$$

The velocity induced by the trailed vortices, $\mathbf{V}_{FW}$, is calculated by the free wake model. Since this velocity depends of the strength of the bound vortex itself, the the circulation is updated with the new inflow at each iteration of the solving process until both converge to a solution. The stream velocities at the control point, $\mathbf{V}_\infty$, are provided by the flight dynamics model and include the velocity due to the translation

of the helicopter. The velocity due to the blade motion and flexibility $\mathbf{V}_{BM}$ and the velocities due to the rotation of the helicopter $\mathbf{V}_{man}$, to account for the effect of maneuvering, are also provided by the rotor-fuselage model.

3.7 The free wake model with swept tip blades

In order to account for the tip sweep in the blade, several modifications need to be done to the free wake model.

The blade control points on the free wake model, which are located at the center of each blade segment, need to be moved backwards in the lag direction for those points located on the swept tip. The distance they are displaced is an amount equal to the product of the distance from the joint between the straight and swept parts of the blade, $x_{i_{JT}}$, and the tangent of the sweep angle, Δ, i.e.,

$$h_i = x_{i_{JT}} \tan \Delta \tag{3.24}$$

The near wake, which extends for a fixed angular length behind the blade, needs to be extended further in the region of the swept tip. For this purpose, the location of the end points of the near wake at each radial station in the tip is extended with the same approach as that used for the blade control points.

The release point of the vortex filament occurs at the end of the swept portion of the blade.

The velocities seen by each blade section, used for the computation of the circulation with the Weissinger-L model, are provided in a reference frame perpendicular to the blade at the swept tip.

The induced velocities are provided back to the rotor-fuselage model at the swept points, which is where they are required. No transformation is therefore needed for the induced velocities.

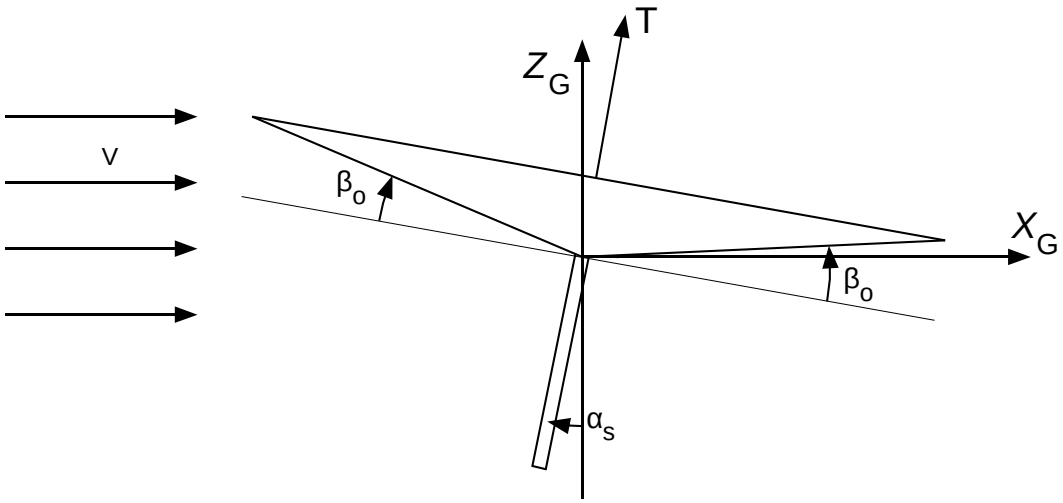

Figure 3.1: Global-fixed coordinate system for free wake model.

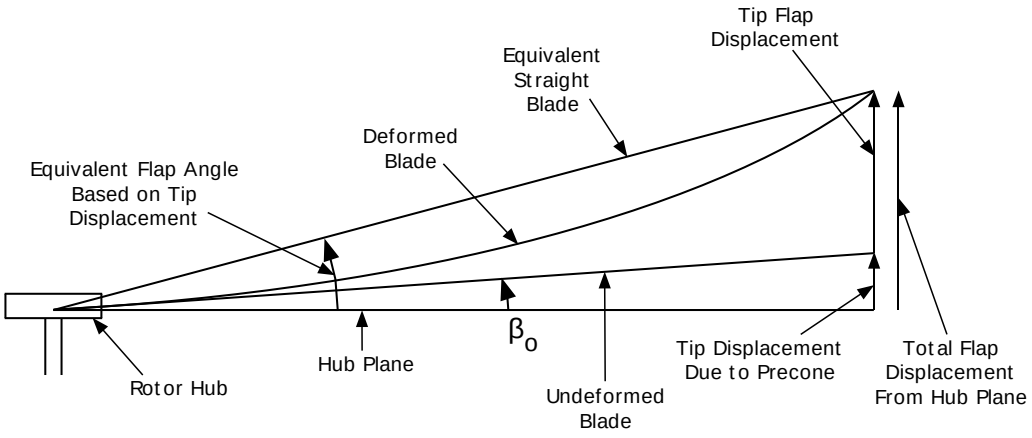

Figure 3.2: Definition of equivalent tip flapping angles for the free wake model.

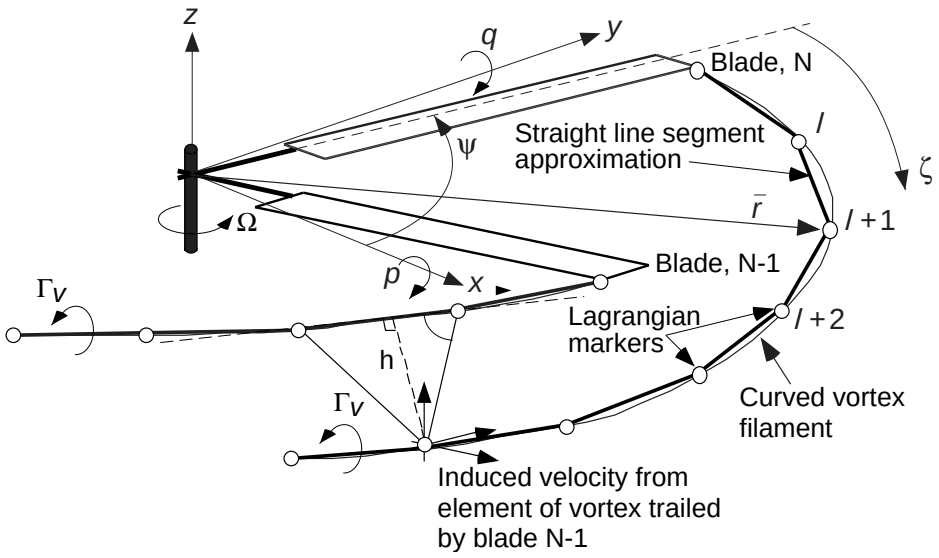

Figure 3.3: Schematic of the free wake discretization (Ref. 15).

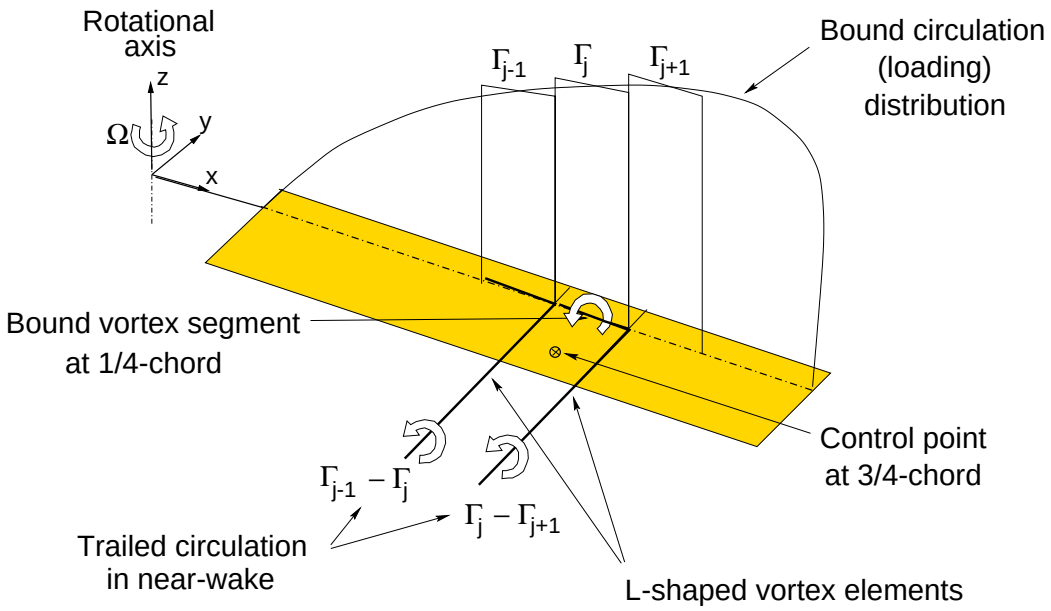

Figure 3.4: Schematic of the Weissinger-L circulation model (Ref. 15).

Chapter 4

Solution methods

This chapter describes the different solution methodologies and techniques used in the present study. The chapter starts with the procedure to solve the equations of motion. Next is the description of the finite element method used to model the blade, both in its straight and swept configurations. Following is the approach for the calculation of the blade mode shapes and natural frequencies of these two blade configurations, straight and swept. The modal coordinate transformation used to reduce the number of degrees of freedom is explained next.

The last two sections describe, respectively, the trim methodology to obtain the steady state solution of the helicopter, with the inclusion of the time marching free wake model, and the method for the integration of the equations of motion.

4.1 Solution of the equations of motion

In Eq.(2.200), the derivative terms, which are primarily associated with the main rotor inertia, appear both on the right- and the left-hand-side of Eq.(2.200). This requires that the derivative terms on the right-hand-side be identified and moved to the left-hand-side, or that the equations be solved as an implicit system of ODEs in

the form

$$\mathbf{f}(\dot{\mathbf{y}}, \mathbf{y}, \mathbf{u}\,; t) = \mathbf{0} \tag{4.1}$$

With suitable manipulations and appropriate ODE solvers, the two approaches are essentially equivalent. Both have been used to obtain the results of this dissertation.

The first approach is based on rewriting the equations of motion in the form

$$\dot{\mathbf{y}} = \mathbf{g}_I(\dot{\mathbf{y}}\,; t) + \mathbf{g}_N(\mathbf{y}, \mathbf{u}\,; t) \tag{4.2}$$

From a careful examination of the acceleration dependent terms (Ref. 114) it can be seen that, with the exception of some very small terms, they are linear in the acceleration, and therefore it is possible to write:

$$\mathbf{g}_I(\dot{\mathbf{y}}\,; t) = \mathbf{E}_C \dot{\mathbf{y}} \tag{4.3}$$

where $\mathbf{E}_C$ is an inertial coupling matrix that can be obtained numerically using finite difference approximations and $\mathbf{g}_N$ are the equations of motion without the acceleration-dependent terms, which can be computed by simply letting $\dot{\mathbf{y}} = \mathbf{0}$ in Eq.(2.4). Substituting this into Eq.(4.2) gives

$$\dot{\mathbf{y}} = \mathbf{E}_C \dot{\mathbf{y}} + \mathbf{g}_N(\mathbf{y}, \mathbf{u}\,; t) \tag{4.4}$$

from which a rigorous first order form can be determined:

$$\dot{\mathbf{y}} = (I - \mathbf{E}_C)^{-1} \mathbf{g}_N(\mathbf{y}, \mathbf{u}\,; t) \tag{4.5}$$

or

$$\dot{\mathbf{y}} = \mathbf{f}_1(\mathbf{y}, \mathbf{u}\,; t) \tag{4.6}$$

Alternatively, the model can be simply expressed in implicit form (Ref. 111):

$$\mathbf{f}(\dot{\mathbf{y}}, \mathbf{y}, \mathbf{u}\,; t) = \mathbf{0} \tag{4.7}$$

Because Eq.(4.7) does not require any preliminary manipulations, this is the recommended approach.

4.2 Finite element discretization

The blade equations of motion, are a set of partial differential equations and need to be transformed to ordinary differential equations to be coupled with the rest of the flight dynamic model. This is obtained through a finite element approach, which removes the spanwise coordinate. The following finite element analysis is based on the Galerkin method of weighted residuals (Ref. 95).

For each finite element in the analysis, there are 11 degrees of freedom: the flap and lag bending displacement and their slope at each end of the element, and the torsional rotations at the two ends of the element and at the element mid-point. Figure 4.1 depicts the nodal degrees of freedom in each element, in which ϕ, v and w represent respectively the torsion, lag and flap degrees of freedom.

The lag, flap, and torsion degrees of freedom for each element are, respectively

$$\mathbf{y}_v = \{\, v_0 \; v_{x,0} \; v_1 \; v_{x,1} \}^{\mathrm{T}} \tag{4.8}$$

$$\mathbf{y}_w = \{\, w_0 \; w_{x,0} \; w_1 \; w_{x,1} \}^{\mathrm{T}} \tag{4.9}$$

$$\mathbf{y}_\phi = \{\, \phi_0 \; \phi_1 \; \phi_2 \,\}^{\mathrm{T}} \tag{4.10}$$

where v_0, $v_{x,0}$, w_0, $w_{x,0}$ are the lag and flap displacement and rotation at the inboard end, v_1, $v_{x,1}$, w_1 and $w_{x,1}$ are the lag and flap displacement and rotation at the outboard end, ϕ_0 is the torsional rotation at the inboard end, ϕ_1 is that at the center and ϕ_2 at the outboard end of the element. The complete vector of degrees of freedom for the i-th finite element is arranged as:

$$\mathbf{y}_i = \{ \mathbf{y}_v \ \mathbf{y}_w \ \mathbf{y}_\phi \}^{\mathrm{T}} \tag{4.11}$$

Figure 4.2 shows how the local degrees of freedom of each finite element are assembled to build the entire blade, for the case of the straight blade configuration. The global degrees of freedom for the blade with the swept tip element are shown in Fig. 4.3. The total number of degrees of freedom is $5+6N_e$ where N_e is the number of finite elements used.

The degrees of freedom for the entire blade are assembled into the vector, $\mathbf{y}_n$:

$$\mathbf{y}_n = [\mathbf{v}_n \ \mathbf{w}_n \ \boldsymbol{\phi}_n]^{\mathrm{T}} \tag{4.12}$$

where

$$\mathbf{v}_n = [v_0 \ v_{0,x} \ v_1 \ v_{1,x} \ \ldots \ v_{N_e} \ v_{N_e,x}]^{\mathrm{T}} \tag{4.13}$$

$$\mathbf{w}_n = [w_0 \ w_{0,x} \ w_1 \ w_{1,x} \ \ldots \ w_{N_e} \ w_{N_e,x}]^{\mathrm{T}} \tag{4.14}$$

$$\boldsymbol{\phi}_n = [\phi_0 \ \phi_1 \ \ldots \ \phi_{2N_e}]^{\mathrm{T}} \tag{4.15}$$

The flap, lag and torsion displacements at any point within each element are reconstructed from the nodal degrees of freedom using Hermite interpolation

polynomials. For flap and lag, the polynomials are

$$\mathbf{H}_v(x_e) = \mathbf{H}_w(x_e) = \left\{ \begin{array}{c} 1 - 3\eta^2 + 2\eta^3 \\ \eta(1 - 2\eta + \eta^2)l \\ 3\eta^2 - 2\eta^3 \\ \eta(-\eta + \eta^2)l \end{array} \right\}^{\mathrm{T}} \tag{4.16}$$

and for torsion

$$\mathbf{H}_\phi(x_e) = \left\{ \begin{array}{c} 1 - 3\eta + 2\eta^2 \\ 4\eta - 4\eta^2 \\ -\eta + 2\eta^2 \end{array} \right\}^{\mathrm{T}} \tag{4.17}$$

where l is the length of the element, and $\eta = x_e/l$, where x_e is the distance from the inboard node of the element. Therefore $\eta = 0$ represents the inboard node and $\eta = 1$ represents the outboard node.

Using the Hermite polynomials, the flap, lag and torsion deflections at any point in the element are given by

$$v(x_e, t) = \mathbf{H}_v(x_e)\mathbf{y}_v(t) \tag{4.18}$$

$$w(x_e, t) = \mathbf{H}_w(x_e)\mathbf{y}_w(t) \tag{4.19}$$

$$\phi(x_e, t) = \mathbf{H}_\phi(x_e)\mathbf{y}_\phi(t) \tag{4.20}$$

To calculate the derivatives of the displacements with respect to spanwise location, only the derivatives of the Hermite polynomials are required.

The derivatives of the displacements with respect to time are given by

$$\dot{v}(x_e) = \mathbf{H}_v(x_e)\dot{\mathbf{y}}_v(t) \tag{4.21}$$

and similarly for the other degrees of freedom.

With the displacement quantities and their derivatives known at any point in the blade, the distributed aerodynamic, inertial, tensile and structural loads can be calculated (Ref. 95).

The element inertia load vector for the i-th element is

$$\mathbf{p}_{\mathrm{I}i}(t) = \int_0^{l_i} \left\{ \begin{array}{c} p_{\mathrm{I}y}(x_e,t)\,\mathbf{H}_v(x_e) \\ p_{\mathrm{I}z}(x_e,t)\,\mathbf{H}_w(x_e) \\ q_{\mathrm{I}x}(x_e,t)\,\mathbf{H}_\phi(x_e) \end{array} \right\} dx_i = \left\{ \begin{array}{c} \mathbf{p}_{\mathrm{I}i_v}(t) \\ \mathbf{p}_{\mathrm{I}i_w}(t) \\ \mathbf{p}_{\mathrm{I}i_\phi}(t) \end{array} \right\} \tag{4.22}$$

where $p_{\mathrm{I}y}$, $p_{\mathrm{I}z}$ and $q_{\mathrm{I}x}$ are components of the distributed inertial loads (Eqs.(2.68) and (2.69) in Section 2.4.3). The terms $\mathbf{p}_{\mathrm{I}i_v}$, $\mathbf{p}_{\mathrm{I}i_w}$ and $\mathbf{p}_{\mathrm{I}i_\phi}$ are the nodal load vectors for the lag, flap and torsional degrees of freedom.

Similarly, the aerodynamic nodal loads, $\mathbf{p}_A$ for the ith element can be calculated:

$$\mathbf{p}_{\mathrm{A}i}(t) = \int_0^{l_i} \left\{ \begin{array}{c} p_{\mathrm{A}y}(x_e,t)\,\mathbf{H}_v(x_e) \\ p_{\mathrm{A}z}(x_e,t)\,\mathbf{H}_w(x_e) \\ q_{\mathrm{A}x}(x_e,t)\,\mathbf{H}_\phi(x_e) \end{array} \right\} dx_i = \left\{ \begin{array}{c} \mathbf{p}_{\mathrm{A}i_v}(t) \\ \mathbf{p}_{\mathrm{A}i_w}(t) \\ \mathbf{p}_{\mathrm{A}i_\phi}(t) \end{array} \right\} \tag{4.23}$$

where $p_{\mathrm{A}y}$, $p_{\mathrm{A}z}$ and $q_{\mathrm{A}x}$ are the components of the blade section aerodynamic loads (Eqs.(2.66) and(2.67) in Section 2.4.2).

The structural nodal load vector for the i-th element is given as

$$\mathbf{p}_{\mathrm{S}i}(t) = \int_0^{l_i} \left\{ \begin{array}{c} p^I_{\mathrm{S}y}(x_e,t)\,\mathbf{H}_{v,x}(x_e) + p^{II}_{\mathrm{S}y}(x_e,t)\,\mathbf{H}_{v,xx}(x_e) \\ p^I_{\mathrm{S}z}(x_e,t)\,\mathbf{H}_{w,x}(x_e) + p^{II}_{\mathrm{S}z}(x_e,t)\,\mathbf{H}_{w,xx}(x_e) \\ q_{\mathrm{S}x}(x_e,t)\,\mathbf{H}_\phi(x_e) + q^I_{\mathrm{S}x}(x_e,t)\,\mathbf{H}_{\phi,x}(x_e) \end{array} \right\} dx_i = \left\{ \begin{array}{c} \mathbf{p}_{\mathrm{S}i_v}(t) \\ \mathbf{p}_{\mathrm{S}i_w}(t) \\ \mathbf{p}_{\mathrm{S}i_\phi}(t) \end{array} \right\} \tag{4.24}$$

where the structural operators $p^I_{\mathrm{S}y}$, $p^{II}_{\mathrm{S}y}$, $p^I_{\mathrm{S}z}$, $p^{II}_{\mathrm{S}z}$, $q_{\mathrm{S}x}$ and $q^I_{\mathrm{S}x}$ are defined in the undeformed blade coordinate system (Eqs.(2.76) through(2.81) in Section 2.4.4).

The tension load vector for the i-th finite element is given by:

$$\mathbf{p}_{\mathrm{T}i}(t) = \int_0^{l_i} \left\{ \begin{array}{c} p^I_{\mathrm{T}y}(x_e,t)\,\mathbf{H}_{v,x}(x_e) \\ p^I_{\mathrm{T}z}(x_e,t)\,\mathbf{H}_{w,x}(x_e) \\ 0 \end{array} \right\} dx_i = \left\{ \begin{array}{c} \mathbf{p}_{\mathrm{T}i_v}(t) \\ \mathbf{p}_{\mathrm{T}i_w}(t) \\ \mathbf{p}_{\mathrm{T}i_\phi}(t) \end{array} \right\} \tag{4.25}$$

where the distributed tension-induced loads are defined in Eq.(2.86) in Section 2.4.5.

In addition, the contribution of the moments produced by the lag damper to the elemental nodal load vector needs to be computed . The lag damper applies a moment, $\mathbf{M}_{\mathrm{D}}$, to the inboard end of the blade, which is applied directly to the nodal load vector in the undeformed blade coordinate system

$$\mathbf{p}_{\mathrm{D}_1} = \{\, 0\ M_{\mathrm{D}y}\ 0\ 0\ 0\ M_{\mathrm{D}z}\ 0\ 0\ M_{\mathrm{D}x}\ 0\ 0 \,\}^{\mathrm{T}} \tag{4.26}$$

The quantities $M_{\mathrm{D}x}$, $M_{\mathrm{D}y}$ and $M_{\mathrm{D}z}$ are the components of the lag damper moment (Eq.(2.87)).

4.2.1 Local-to-global coordinate transformation

The transformation from preconed undeformed rotating blade coordinate system to the tip local undeformed coordinate system is given by Eq.(2.29), where the transformation matrix, $[T_\Lambda]$, is given by Eq.(2.30).

The local-to-global coordinate transformation for the vector of nodal degrees of freedom of the swept-tip element can be written in the form:

$$\left\{\mathbf{y}^t_L\right\} = [\Lambda_{LG}]\left\{\mathbf{y}^t_G\right\} \tag{4.27}$$

where the superscript t indicates that these quantities correspond to the tip element; the subscripts L and G denote the local and global coordinate system, respectively.

The vectors of degrees of freedom in both coordinate systems are:

$$\left\{\mathbf{y}_L^t\right\} = \left[\begin{array}{cccccccccccc} v_1 & v_{,x1} & v_2 & v_{,x2} & w_1 & w_{,x1} & w_2 & w_{,x2} & \phi_1 & \phi_2 & \phi_3 \end{array}\right]^{\mathrm{T}} \tag{4.28}$$

and

$$\left\{\mathbf{y}_G^t\right\} = \left[\begin{array}{cccccccccccc} v_J & v_{,xJ} & v_T & v_{,xT} & w_J & w_{,xJ} & w_T & w_{,xT} & \phi_J & \phi_M & \phi_T & u_J \end{array}\right]^{\mathrm{T}} \tag{4.29}$$

The axial displacement, u_J appears temporarily in Eq.(4.29) for completeness of the transformation, but is later dropped as the blade is assumed to be inextensional (Ref. 91).

The transformation matrices between the global and the local coordinate systems are nonlinear, as shown by Ref. 97. The derivation in Ref. 97 is for a blade tip with sweep, anhedral and pretwist rotations. The result of Ref. 97 for sweep only (as no anhedral and pretwist are used in the present study) follows.

The transformation of the translational degrees of freedom is linear:

$$\left\{\begin{array}{c} u_L \\ v_L \\ w_L \end{array}\right\} = [T_\Lambda] \left\{\begin{array}{c} u_G \\ v_G \\ w_G \end{array}\right\} \tag{4.30}$$

where the transformation matrix T_Λ is given by Eq.(2.30).

The nonlinear elements of the transformation are due to the rotational degrees of freedom, $[\phi_G, w_{,xG}, v_{,xG}]^T$ in the global coordinate system and $[\phi_L, w_{,xL}, v_{,xL}]^T$ in the local coordinate system.

The transformation of the rotational degrees of freedom is given by

$$\left\{\begin{array}{c} \phi_L \\ w_{,xL} \\ v_{,xL} \end{array}\right\} = \left([T_\Lambda]^T + \left[T_\Lambda^K\right] \right) \left\{\begin{array}{c} \phi_G \\ w_{,xG} \\ v_{,xG} \end{array}\right\} \tag{4.31}$$

The matrix $\left[T_\Lambda^K\right]$ contains the nonlinear elements of the transformation between the rotational degrees of freedom in both frames. For the case of sweep only, the only nonlinear terms appear in the lag equation, and the only non-zero element of nonlinear transformation matrix is $T_\Lambda^K(3,1)$, given by:

$$T_\Lambda^K(3,1) = w_{,xG}\left(\sin^2\Lambda + v_{,xG}\sin\Lambda\cos\Lambda\right) \tag{4.32}$$

With the transformation of both the translational and rotational degrees of freedom known, the total transformation matrix $[\Lambda_{LG}]$ can be assembled:

$$[\Lambda_{LG}] = \begin{bmatrix} [\Lambda_{LL}] & [0] & [\Lambda_{NL}] \\ [0] & [\Lambda_{FF}] & [\Lambda_{FT}] \\ [0] & [\Lambda_{TF}] & [\Lambda_{TT}] \end{bmatrix} \tag{4.33}$$

With the nonzero submatrices given by:

$$[\Lambda_{LL}] = \begin{bmatrix} \cos\Lambda & 0 & 0 & 0 \\ 0 & 1 & 0 & 0 \\ 0 & 0 & \cos\Lambda & 0 \\ 0 & 0 & 0 & 1 \end{bmatrix} \tag{4.34}$$

$$[\Lambda_{FF}] = \begin{bmatrix} 1 & 0 & 0 & 0 \\ 0 & \cos\Lambda & 0 & 0 \\ 0 & 0 & 1 & 0 \\ 0 & 0 & 0 & \cos\Lambda \end{bmatrix} \tag{4.35}$$

$$[\Lambda_{FT}] = \begin{bmatrix} 0 & 0 & 0 \\ -\sin\Lambda & 0 & 0 \\ 0 & 0 & 0 \\ 0 & 0 & -\sin\Lambda \end{bmatrix} \tag{4.36}$$

$$[\Lambda_{TF}] = \begin{bmatrix} 0 & \sin\Lambda & 0 & 0 \\ 0 & \frac{1}{2}\sin\Lambda & 0 & \frac{1}{2}\sin\Lambda \\ 0 & 0 & 0 & \sin\Lambda \end{bmatrix} \tag{4.37}$$

$$[\Lambda_{TT}] = \begin{bmatrix} \cos\Lambda & 0 & 0 \\ 0 & \cos\Lambda & 0 \\ 0 & 0 & \cos\Lambda \end{bmatrix} \tag{4.38}$$

$$[\Lambda_{NL}] = \begin{bmatrix} 0 & 0 & 0 \\ w_{,xJ}\left(\sin^2\Lambda + \sin\Lambda\cos\Lambda v_{,xJ}\right) & 0 & 0 \\ 0 & 0 & 0 \\ 0 & 0 & 0 \end{bmatrix} \tag{4.39}$$

The transformation between the local and the global coordinate systems of the velocity and acceleration of the rotational degrees of freedom is given in Appendix A.

4.3 Blade natural frequencies and mode shapes

The blade mode shapes and corresponding natural frequencies are calculated using the rotating blade *in vacuo* with no damping. The problem of finding the mode shapes and natural frequencies is written as

$$[M]\,\ddot{\mathbf{y}}_n + [K]\,\mathbf{y}_n = \mathbf{0} \tag{4.40}$$

where $[M]$ is the linear portion of the mass matrix, $[K]$ is the linear portion of the stiffness matrix and $\mathbf{y}_n$ is the vector of nodal displacements from the finite element model. Because the mass and stiffness matrices are non-linear, they are never built explicitly, and therefore they must be calculated using a finite difference approximation.

The mass and stiffness matrices are constructed by successively perturbing the different components of the nodal acceleration vector. Details on the calculation of the mass and stiffness matrices can be found in Ref. 6.

The calculation of the blade mode shapes involves the solution of the eigen problem

$$\omega^2 [M] \bar{\mathbf{y}}_n + [K] \bar{\mathbf{y}}_n = 0 \tag{4.41}$$

where $\bar{\mathbf{y}}_n$ are the eigenvectors which form the columns of the modal transformation matrix, $[V]$.

The natural frequencies of vibration of the system, ω, are the square roots of the eigenvalues. ω_i is the natural frequency corresponding to the i^{th} mode shape, described by the i^{th} eigenvector.

With the exception of the two lowest mode shapes, which represent the rigid flap and lag modes for an articulated rotor, all eigenvectors contain a combination of flap, lag and torsion. The reason for this is found in the coupled nature of the flexible blade modes. However, in this study each mode will be referred as a flap, lag or torsion mode, depending on which is the dominant tip response.

4.3.1 Assembly of mass and stiffness matrices with swept tip model

If the tip sweep is modeled, the mass and stiffness matrices need to be built separately for the straight and swept portions of the blade.

The vector of nodal degrees of freedom for the blade needs to be split in two subvectors, one containing the degrees of freedom of the straight portion of the blade, and one for the degrees of freedom corresponding to the swept tip elements. The degrees of freedom corresponding to the node connect the straight and swept

parts of the blade appear in both vectors. The global degrees of freedom for a blade with four finite elements for the straight blade and one finite element for the swept tip element are shown in Fig. 4.3.

For a general case with N_e total final elements and N_t finite elements in the swept tip, the assembled vector of degrees of freedom for the straight portion of the blade is given by:

$$\mathbf{y}_S = [\ \mathbf{v}_S\ \mathbf{w}_S\ \boldsymbol{\phi}_S]^{\mathrm{T}} \tag{4.42}$$

where

$$\mathbf{v}_S = \left[\ v_0\ v_{0,x}\ v_1\ v_{1,x}\ \ldots\ v_{N_e-N_t}\ v_{(N_e-N_t),x}\right]^{\mathrm{T}} \tag{4.43}$$

$$\mathbf{w}_S = \left[\ w_0\ w_{0,x}\ w_1\ w_{1,x}\ \ldots\ w_{N_e-N_t}\ w_{(N_e-N_t),x}\right]^{\mathrm{T}} \tag{4.44}$$

$$\boldsymbol{\phi}_S = \left[\ \phi_0\ \phi_1\ \ldots\ \phi_{2(N_e-N_t)}\right]^{\mathrm{T}} \tag{4.45}$$

Similarly, the vector of degrees of freedom for the swept part of the blade is given by

$$\mathbf{y}_T = [\ \mathbf{v}_T\ \mathbf{w}_T\ \boldsymbol{\phi}_T]^{\mathrm{T}} \tag{4.46}$$

where

$$\mathbf{v}_T = \left[\ v_{N_e-N_t}\ v_{(N_e-N_t),x}\ \ldots\ v_{N_e}\ v_{(N_e),x}\right]^{\mathrm{T}} \tag{4.47}$$

$$\mathbf{w}_T = \left[\ w_{N_e-N_t}\ w_{(N_e-N_t),x}\ \ldots\ w_{N_e}\ w_{N_e,x}\right]^{\mathrm{T}} \tag{4.48}$$

$$\boldsymbol{\phi}_T = \left[\ \phi_{2(N_e-N_t)}\ \ldots\ \phi_{2N_e}\right]^{\mathrm{T}} \tag{4.49}$$

For the particular case of 4 straight-blade elements and 1 swept-tip element, these vectors become

$$\mathbf{v}_S = [\ v_0\ v_{0,x}\ v_1\ v_{1,x}\ \ldots\ v_5\ v_{5,x}]^{\mathrm{T}} \tag{4.50}$$

and

$$\mathbf{v}_T = [\ v_5\ v_{5,x}\ v_6\ v_{6,x}]^{\mathrm{T}} \tag{4.51}$$

and similarly for $\mathbf{w}_S, \mathbf{w}_T, \boldsymbol{\phi}_S$ and $\boldsymbol{\phi}_T$.

The construction of the straight portion of the blade mass and stiffness matrices, M_S and K_S respectively, is performed as in the unswept model, but with the total number of finite elements and the number of degrees of freedom limited to those corresponding to the straight portion of the blade only.

Similarly, the mass and stiffness matrices corresponding to the swept blade, M_T and K_T, are built separately but in the same manner as the rest of the blade, only limited to the number of finite elements and degrees of freedom of the tip portion of the blade. For the swept tip element, the mass and stiffness matrices need to be obtained in the local tip coordinate system described in Section 2.2.2.

Once calculated in the swept coordinate system, the tip mass and stiffness matrices need to be transformed to the blade undeformed preconed coordinate system (Ref. 91), such that:

$$[M_T]_G = [\Lambda_{LG}]^T [M_T]_L [\Lambda_{LG}] \tag{4.52}$$

for the mass and

$$[K_T]_G = [\Lambda_{LG}]^T [K_T]_L [\Lambda_{LG}] \tag{4.53}$$

for the stiffness matrix, where the substript $(...)_G$ indicates that the matrix is in the global (blade undeformed preconed) coordinate system and $(...)_L$ refers to the local (tip undeformed) coordinate system. The transformation matrix Λ_{LG} is that defined in Eq.(4.33).

Like for the unswept case, described in Section 4.3, the calculation of the blade mode shapes involves the solution of the eigen problem

$$\omega^2 \left[M_S + M_T\right] \bar{\mathbf{y}}_n + \left[K_S + K_T\right] \bar{\mathbf{y}}_n = 0 \tag{4.54}$$

The assembly of the straight and swept portions of the mass and stiffness matrices must include the reordering of the degrees of freedom (Ref. 121). A simplified description of the assembly procedure is shown in Fig. 4.4, in which M_S and K_S represent the mass and stiffness matrices of the straight unswept part of the blade, and M_T and K_T represent the mass and stiffness matrices of the swept part of the bade, after they have been transformed to the global coordinate system (Fig. 4.4 is an over-simplification of the process, and the actual assembly has to separate the flap, lag and torsion degrees of freedom).

4.4 Modal coordinate transformation

The blade motion is represented by $N_D = 5 + 6N_e$ degrees of freedom, which results in N_D second order, non-linear ordinary differential equations for the dynamics of each rotor blade.

A modal coordinate transformation is used to reduce the number of total degrees of freedom. The vector of finite element degrees of freedom, $\mathbf{y}_n$, defined in Eq.(4.46) is written as:

$$\mathbf{y}_n = [V]\, \mathbf{q} \tag{4.55}$$

where $[V]$ is a modal coordinate transformation matrix and $\mathbf{q}$ is a vector of modal coefficients.

The matrix $[V]$ is formed with the normal modes of the blade, columnwise. Therefore, if N_m modes are used in the modal coordinate transformation, the matrix $[V]$ has N_D rows and N_m columns, usually with $N_m \ll N_D$. The vector $\mathbf{q}$ becomes the vector of blade generalized coordinates for the problem.

The nodal load vectors for each element, defined in Eqs.(4.22) and(4.23) through(4.26) are transformed into modal load vectors using the same modal coordinate transformation used to reduce the number of degrees of freedom. The transformations are as follows:

$$\mathbf{F}_{\mathrm{A}} = \sum_{i=1}^{N_e} [V_i]^{\mathrm{T}} \mathbf{p}_{\mathrm{A}i} \tag{4.56}$$

$$\mathbf{F}_{\mathrm{I}} = \sum_{i=1}^{N_e} [V_i]^{\mathrm{T}} \mathbf{p}_{\mathrm{I}i} \tag{4.57}$$

$$\mathbf{F}_{\mathrm{S}} = \sum_{i=1}^{N_e} [V_i]^{\mathrm{T}} \mathbf{p}_{\mathrm{S}i} \tag{4.58}$$

$$\mathbf{F}_{\mathrm{T}} = \sum_{i=1}^{N_e} [V_i]^{\mathrm{T}} \mathbf{p}_{\mathrm{T}i} \tag{4.59}$$

$$\mathbf{F}_{\mathrm{D}} = \sum_{i=1}^{N_e} [V_i]^{\mathrm{T}} \mathbf{p}_{\mathrm{D}i} \tag{4.60}$$

The blade dynamics are then represented by the ordinary differential equations resulting from adding the contribution of all the modal load vectors:

$$\mathbf{0} = \mathbf{F}_{\mathrm{A}} + \mathbf{F}_{\mathrm{I}} + \mathbf{F}_{\mathrm{S}} + \mathbf{F}_{\mathrm{T}} + \mathbf{F}_{\mathrm{D}} \tag{4.61}$$

where the total number of modal equations is obtained by multiplying the number of blades, N_b, by the number of mode shapes in the modal coordinate transformation, N_m.

4.5 Trim

4.5.1 The trim flight condition

The generic trim flight condition is a steady, coordinated, helical turn. The flight condition is defined by three parameters: the velocity V along the trajectory, the flight path angle γ, which is positive for climbing flight, and the rate of turn $\dot{\psi}$, positive for a right turn (Refs. 122, 123). The geometry of the trim problem and the defining parameters are illustrated in Fig. 4.5.

Straight and level flight becomes then a particular case in which both the flight path angle and the rate of turn are zero. In climbing and descending flight, the flight path angle would be nonzero, while in turning flight it is the turn rate that is nonzero. In a diving turn, all three variables are nonzero.

Hover is a particular case in which the velocity is also zero. However, if $V = 0$, some singularities appear in the model (in those equations in which the velocity is the denominator). To avoid this problem, a very small value of V in the forward direction is used to represent hover.

4.5.2 The trim unknowns

The vector of trim unknowns is composed of three parts:

$$\mathbf{X} = \{ \mathbf{X}_B \, \mathbf{X}_R \, \mathbf{X}_I \}^{\mathrm{T}} \tag{4.62}$$

where $\mathbf{X}_B$, $\mathbf{X}_R$ and $\mathbf{X}_I$ contain, respectively, the trim unknowns associated with body, rotor and inflow. If the free wake is used to compute the induced velocities,

the inflow unknowns are not necessary, and therefore the vector of trim unknowns becomes:

$$\mathbf{X} = \{ \mathbf{X}_B \; \mathbf{X}_R \}^{\mathrm{T}} \tag{4.63}$$

The total number of trim unknowns is $12 + N_{\mathrm{m}}(2N_{\mathrm{h}} + 1)$ if dynamic inflow is used, or $9 + (1 + 2N_{\mathrm{h}})N_{\mathrm{m}}$ if the free wake model is included, of which 9 correspond to $\mathbf{X}_B$, $N_{\mathrm{m}}(2N_{\mathrm{h}} + 1)$ to $\mathbf{X}_R$, and 3 to $\mathbf{X}_I$.

The body trim unknowns, $\mathbf{X}_B$, are:

$$\mathbf{X}_B = [\; \theta_0 \; \theta_{1c} \; \theta_{1s} \; \theta_t \; \alpha_F \; \beta_F \; \phi_F \; \theta_F \; \lambda_t \;]^{\mathrm{T}} \tag{4.64}$$

where $\theta_0, \theta_{1c}, \theta_{1s}$ and θ_{0t} are the collective, cyclic and tail pitch settings, respectively, and $\alpha_F, \beta_F, \theta_F$ and ϕ_F are angle of attack, sideslip, pitch angle and bank angle of the fuselage; λ_t is the constant tail rotor inflow, and is included in the $\mathbf{x}_B$ partition for convenience, as it is present both when dynamic inflow and the free wake models are used.

The angle of attack α_F and the sideslip β_F, together with the velocity along the trajectory V, are used to calculate the velocities u, v, and w along the body axes

$$u_F = V \cos\alpha_F \cos\beta_F \tag{4.65}$$

$$v_F = V \sin\beta_F \tag{4.66}$$

$$w_F = V \sin\alpha_F \cos\beta_F \tag{4.67}$$

The angular velocities p, q, and r about the body axes can be calculated from the

Euler angles θ_F and ϕ_F and the turn rate $\dot{\psi}$:

$$p = -\dot{\psi}\sin\theta_F \tag{4.68}$$

$$q = \dot{\psi}\sin\phi_F\cos\theta_F \tag{4.69}$$

$$r = \dot{\psi}\cos\phi_F\cos\theta_F \tag{4.70}$$

The blade motion, which is periodic in trim, is approximated by a truncated Fourier series. The Fourier expansions of the coefficients of the generalized coordinate of each of the blade modes become the unknowns of the trim problem:

$$q^k(\psi) \approx q^k_{app}(\psi) = q^k_0 + \sum_{j=1}^{N_\mathrm{h}} (q^k_{jc}\cos j\psi + q^k_{js}\sin j\psi) \tag{4.71}$$

where q^k_0 is the constant coefficient in the expansion of the k-th mode, and q^k_{jc} and q^k_{js} are the coefficients of the j-th harmonic cosine and sine for the k-th mode; N_h is the number of harmonics included in the expansion for each mode, and N_m is the number of main rotor modes retained for the trim procedure after the modal coordinate transformation (Section 4.4). Therefore, the vector of rotor trim unknowns, $\mathbf{X}_R$, is defined as

$$\begin{aligned}\mathbf{X}_R = \; [\;\; & q^1_0 \; q^1_{1c} \; q^1_{1s} \; q^1_{2c} \; q^1_{2s} \ldots q^1_{N_h c} \; q^1_{N_h s} \ldots \\ & \ldots q^{N_\mathrm{m}}_0 \; q^{N_\mathrm{m}}_{1c} \; q^{N_\mathrm{m}}_{1s} \; q^{N_\mathrm{m}}_{2c} \; q^{N_\mathrm{m}}_{2s} \ldots q^{N_\mathrm{m}}_{N_\mathrm{h} c} \; q^{N_\mathrm{m}}_{N_\mathrm{h} s} \;]^\mathrm{T}\end{aligned} \tag{4.72}$$

Assuming that the blades are identical, and perform identical motions in trim, only one blade needs be taken into account.

If a dynamic inflow model is used (Refs. 6, 36), the $\mathbf{X}_I$ partition contains the values of the dynamic inflow coefficients representing the main rotor inflow:

$$\mathbf{X}_I = [\; \lambda_0 \; \lambda_s \; \lambda_c \;]^\mathrm{T} \tag{4.73}$$

where λ_0 is the uniform inflow component, and λ_s and λ_c are the sine and cosine inflow components, respectively.

4.5.3 The trim equations

The trim equations make up a system of non-linear algebraic equations, which can be written as

$$\mathbf{F}(\mathbf{X}) = \mathbf{0} \tag{4.74}$$

The vector $\mathbf{F}$ of equations can be divided as

$$\mathbf{F} = \{\ \mathbf{F}_B\ \mathbf{F}_R\ \mathbf{F}_I\ \}^{\mathrm{T}} \tag{4.75}$$

if dynamic inflow is used, or

$$\mathbf{F} = \{\ \mathbf{F}_B\ \mathbf{F}_R\ \}^{\mathrm{T}} \tag{4.76}$$

with the free wake model, where $\mathbf{F}_B$ represents the equations of the body, $\mathbf{F}_R$, those of the main rotor, and $\mathbf{F}_I$ those for inflow.

Body equations $\mathbf{F}_B$

A set of nine algebraic equations is used to describe the trim state of the entire aircraft and the tail rotor inflow. These equations are the following:

1. *Force and moment equilibrium*

   Force and moment equilibrium is enforced by requiring that the linear and angular accelerations of the aircraft be equal to zero when averaged over one rotor revolution, e.g.,

$$\int_0^{2\pi} \dot{u}_F\, d\psi = 0 \tag{4.77}$$

and similarly for $\dot{v}_F, \dot{w}_F, \dot{p}, \dot{q}$ and $\dot{r}$.

2. *Turn coordination equation*

   The condition for turn coordination is that the Y force component be zero when averaged over one rotor revolution, that is (Ref. 6):

$$\int_0^{2\pi} \left[\sin\phi_F - \frac{\dot{\psi} V}{g} (\cos\alpha_F \cos\phi_F + \sin\alpha_F \tan\theta_F) \cos\beta_F \right] d\psi = 0 \qquad (4.78)$$

3. *Relationship between angle of attack and Euler pitch angle*

   The flight path angle, γ, and angle of attack, sideslip angle, roll angle, and pitch angle, need to satisfy the following equation (Ref. 6):

$$\int_0^{2\pi} [\cos\alpha_F \cos\beta_F \sin\theta_F - (\sin\beta_F \sin\phi_F + \sin\alpha_F \cos\beta_F \cos\phi_F) \cos\theta_F - \sin\gamma] \, d\psi = 0 \qquad (4.79)$$

4. *Tail rotor inflow*

   The tail rotor equation enforces that the tail rotor inflow be constant on average over one rotor revolution:

$$\int_0^{2\pi} \dot{\nu}_t \, d\psi = 0 \qquad (4.80)$$

Rotor equations $\mathbf{F}_R$

The ordinary differential equations governing the blade motion, which is assumed to be periodic, are transformed to a set of non-linear algebraic equations using Galerkin technique (Ref. 95). The generalized coordinates and their derivatives are obtained

from their truncated Fourier series expansions, Eq.(4.71):

$$q^k(\psi) \approx q^k_{app}(\psi) = q^k_0 + \sum_{j=1}^{N_\mathrm{h}} (q^k_{jc} \cos j\psi + q^k_{js} \sin j\psi) \tag{4.81}$$

$$\dot{q}^k(\psi) \approx \dot{q}^k_{app}(\psi) = \Omega \sum_{j=1}^{N_\mathrm{h}} (-q^k_{jc} \sin j\psi + q^k_{js} \cos j\psi) \tag{4.82}$$

$$\ddot{q}^k(\psi) \approx \ddot{q}^k_{app}(\psi) = -\Omega^2 \sum_{j=1}^{N_\mathrm{h}} (q^k_{jc} \cos j\psi + q^k_{js} \sin j\psi) \tag{4.83}$$

where the superscript k refers to the k-th mode in the modal coordinate transformation and N_h is the highest harmonic in the truncated Fourier series for the approximation to the generalized coordinates.

The vector containing the generalized coordinates for each mode is

$$\mathbf{q} = \left\{ \, q^1 \; q^2 \; \ldots \; q^{N_\mathrm{m}} \, \right\}^\mathrm{T} \tag{4.84}$$

The approximations to $\mathbf{q}$ and its derivatives from the Fourier series expansions are denoted by:

$$\mathbf{q}_{app} = \left\{ \, q^1_{app} \; q^2_{app} \; \ldots \; q^{N_\mathrm{m}}_{app} \, \right\}^\mathrm{T} \tag{4.85}$$

and similarly for $\dot{\mathbf{q}}_{app}$ and $\ddot{\mathbf{q}}_{app}$.

If the approximate solution $\mathbf{q}_{app}$ is substituted into Eq.(2.93) described in Section 2.7, there will be a nonzero residual vector $\boldsymbol{\varepsilon}$, defined as:

$$\boldsymbol{\varepsilon}(\psi) = \ddot{\mathbf{q}}_{app} - \mathbf{f}_\mathrm{q}(\dot{\mathbf{q}}_{app}, \mathbf{q}_{app}) \tag{4.86}$$

Galerkin method states that the choice of q^j_0, q^j_{kc}, and q^j_{ks} that minimizes on average the residual vector $\boldsymbol{\varepsilon}$ is the one which satisfies the following equations (Ref. 122)

$$\int_0^{2\pi} \boldsymbol{\varepsilon}^k(\psi)\, d\psi = 0$$

$$\int_0^{2\pi} \boldsymbol{\varepsilon}^k(\psi) \cos j\psi\, d\psi = 0 \quad j = 1, \ldots, N_\mathrm{h} \tag{4.87}$$

$$\int_0^{2\pi} \boldsymbol{\varepsilon}^k(\psi) \sin j\psi\, d\psi = 0 \quad j = 1, \ldots, N_\mathrm{h}$$

The result is a set of $1 + 2N_\mathrm{h}$ vector algebraic equations, and a total of $(1 + 2N_\mathrm{h})N_\mathrm{m}$ scalar equations (N_m is the number of modes used in the modal coordinate transformation), which make up the partition $\mathbf{F}_R$ of Eq.(4.76).

Dynamic inflow equations $\mathbf{F}_I$

The dynamic inflow trim equations require that the average of the derivative of each dynamic inflow coefficient over one rotor revolution be zero, that is:

$$\int_0^{2\pi} \dot{\lambda}_0\, d\psi = 0 \tag{4.88}$$

$$\int_0^{2\pi} \dot{\lambda}_s\, d\psi = 0 \tag{4.89}$$

$$\int_0^{2\pi} \dot{\lambda}_c\, d\psi = 0 \tag{4.90}$$

When used to determine the induced velocities, these three equations make up the partition $\mathbf{F}_I$ of the vector of trim equations, Eq.(4.76).

4.5.4 Solution of baseline trim equations

The widely used, nonlinear algebraic equation solver HYBRD (Ref. 124) is used to obtain a solution to the system of rotor-fuselage equations. The solver uses

a modified Powell hybrid method (Ref. 125), which is described here briefly as a preliminary to the description of the trim process with the free wake.

In the code , the trim equations are implemented in the form

$$\mathbf{F}(\mathbf{x}) = \mathbf{r} \tag{4.91}$$

where $\mathbf{r}$ is the vector of residual obtained by substituting a tentative trim solution $\mathbf{x}$ into the system of equations $\mathbf{F}$. The equation solver then adjusts the values of $\mathbf{x}$ to reduce the norm of $\mathbf{r}$ below a certain tolerance, and therefore solve the trim problem. HYBRD begins the solution process by building a Jacobian matrix using forward difference, that is, by perturbing each of the elements of the $\mathbf{x}$ vector. The Jacobian is used to compute a direction along which the residuals are minimized, and the residuals are recomputed along this direction until the residual stops decreasing. Then the Jacobian is recalculated and the process is continued until convergence.

4.5.5 Coupling of the free wake and rotor-fuselage models in trim

When the time-marching free wake model is included in the trim calculation, the main rotor inflow coefficients and the dynamic inflow equations corresponding to the main rotor are not included in the vectors of trim unknowns and trim equations respectively. The induced velocities are instead provided by the free wake model, which is solved separately at every step of the trim iteration.

In the coupling of the flight dynamics model with the free wake, the former must provide the following input:

1. *The hub linear and angular velocities,* $u_{GW}, v_{GW}, w_{GW}, p_{GW}, q_{GW}, r_{GW}$.

   The hub linear velocities, u_{GW}, v_{GW}, w_{GW}, Eqs.(2.38,3.5), and angular velocities, p_{GW}, q_{GW}, r_{GW}, Eq.(2.41,3.6), in the global wake coordinate system described in Section 3.3.4, are required to calculate the velocity field at the vortex filament, as described in Section 3.5. The total velocity at any point in the filament is described by Eq.(3.13), which is repeated here for completeness:

$$\mathbf{V}\left(\mathbf{r}(\psi,\zeta)\right) = \underline{\mathbf{V}_{\infty}} + \mathbf{V}_{ind}\left(\mathbf{r}(\psi,\zeta)\right) + \underline{\mathbf{V}_{man}\left(\mathbf{r}(\psi,\zeta)\right)} \quad (3.13) \text{ repeated}$$

   The freestream velocity $\mathbf{V}_{\infty}$ is comprised of the freestream velocities u_{GW}, v_{GW} and w_{GW}, as shown in Eq.(3.14):

$$\mathbf{V}_{\infty} = V_{\infty x}\mathbf{i} + V_{\infty y}\mathbf{j} + V_{\infty z}\mathbf{k} \quad (3.14) \text{ repeated}$$

   with $V_{\infty x} = u_{GW}$ and so on.

   The velocity distribution over the rotor due to the maneuver, p_{GW}, q_{GW} and r_{GW} is calculated with Eq.(3.15):

$$\mathbf{V}_{man} = (r_G y - q_G z)\mathbf{i}_{\mathrm{G}} + (p_G z - r_G x)\mathbf{j}_{\mathrm{G}} + (q_G x - p_G y)\mathbf{k}_{\mathrm{G}} \quad (3.15) \text{ repeated}$$

2. *The distribution of the velocities at all points in the blade around the azimuth,* not including the induced velocities from the free wake model, in all three directions, $V_x(\psi, r), V_y(\psi, r), V_z(\psi, r)$, Eq.(2.50), which are computed as described in Section 2.4.2.

   The calculation of the bound circulation with the Weissinger-L model is de-

scribed in Eq.(3.23) in Section 3.6:

$$\sum_{j=1}^{N_S} \left[I_{b_{i,j}} + I_{NW_{i,j}} \right] \Gamma_j = \{ (\underline{\mathbf{V}_\infty + \mathbf{V}_{BM} + \mathbf{V}_{man}} + \mathbf{V}_{FW}) \cdot \mathbf{n} \}_i \quad \text{(3.23) repeated}$$

This calculation requires a knowledge of the velocities seen at the blade section, both those of translational (free stream and blade motion) and rotational (maneuvering) origin, underlined in Eq.(3.23). These velocities are calculated in the rotor-fuselage model and are provided to the free wake model to be used in the computation of the circulation, contained in the velocities $V_x(\psi, r), V_y(\psi, r)$ and $V_z(\psi, r)$ which are the components of the total velocity at each blade section. This velocity contains the linear translational velocities of the helicopter in global wake axes, u_{GW}, v_{GW} and w_{GW}, the velocities due to the angular rates, p_{GW}, q_{GW} and r_{GW}, described above, and the velocities due to the blade motion and blade elastic deformations, given by Eq.(2.40):

$$\frac{d\mathbf{R}_B}{dt} = \frac{\partial \mathbf{R}_B}{\partial t} + \boldsymbol{\omega} \times \mathbf{R}_B \quad \text{(2.40) repeated}$$

Note, however, that the Weissinger-L model needs these velocities at the 3/4 chord location, not at the elastic axis (located in the quarter-chord location), which is the point at which they are required in the rotor-fuselage model for the rest of the aerodynamic load calculation. To account for that, the velocities due to the blade motion are computed as in Eq.(2.40), but using the the position vector from Eq.(2.70),

$$\mathbf{R}_B = e\mathbf{i} + (x_0 + u)\hat{\mathbf{e}}_x + v\hat{\mathbf{e}}_y + w\hat{\mathbf{e}}_z \underline{+ y_0\hat{\mathbf{e}}'_y + z_0\hat{\mathbf{e}}'_z} \quad \text{(2.70) repeated}$$

which is the position vector of a point which is not necessarily on the elastic

axis and where the underlined terms represent the distance of the point from the elastic axis. This way, the velocities can be calculated at the 3/4 chord location.

3. *The equivalent rigid blade flapping angles, $\beta(\psi)$.*

   The flapping angles, $\beta(\psi)$, are necessary to determine the relative positions of the blade points with respect to the wake filaments in the flow field, which need to be known to solve the Biot-Savart law, Eq.(3.16). A subset of this requirement is the determination of the release point of the vortex filament that is released at the tip of the blade. In addition, the motion of the blade affects the sectional velocity seen at each blade point (Refs. 15, 40), Eq.(2.50), needed for the calculation of the bound circulation. The latter requirement is met with the inclusion of the blade motion in the velocities provided by the rotor-fuselage model to the free wake (described earlier in this section), therefore the velocities used for the calculation of the bound circulation account for blade flexibility.

   However, the flap angle at the tip of the blade still needs to be provided by the flight dynamics model to the free wake model. The free wake model assumes the blade to be straight, with a flap hinge at the axis of rotation. In the flight dynamics model, the blades are flexible and have hinges that need not be in the axis of rotation. For this reason, an "equivalent" blade flap angle is defined. Figure 3.2 illustrates the definition of this flap angle β, which represents the angle between the hub plane and a straight blade hinged at the axis of rotation

that has the same tip flap displacement as the elastic blade. The "equivalent" blade flapping angle is given by the following equation:

$$\beta(\psi) = \frac{w_{tip}(\psi)}{R} + \beta_p \tag{4.92}$$

w_{tip} is the flapping displacement of the elastic blade from the undeformed preconed blade coordinate system in the flight dynamics model. This displacement is calculated from Eq.(2.36) and it represents the component of that vector in the z-direction of the free wake blade preconed coordinate system at the tip of the blade. The angle β_p is the blade precone angle, which relates the hub rotating coordinate system (Section 2.2.2) to the preconed undeformed coordinate system (Section 2.2.2). The blade flapping angle $\beta(\psi)$ therefore includes contributions from both the blade precone angle and the elastic deformation of the blade.

The product of the free wake is the distribution of the induced velocities over the rotor, $\lambda(\psi, r)$. The present model makes use of the z-component of these induced velocities at the rotor plane, even though the free wake model calculates the induced velocities at the control points on the rotor in all three directions. This assumption can be made safely for the majority of flight conditions, since the x and y components are much smaller than the z component and the inflow can be assumed to be unidirectional. However, the results presented in Chapter 7 seem to indicate that, for very extreme flight conditions such as the vortex ring state, these velocities might be significant enough to be accounted for.

The induced velocities are used in Eq.(2.47) and can then added to the ve-

locity of the blade section, Eq.(2.44), to obtain the total local velocities required to compute the aerodynamic rotor loads, as shown in Eq.(2.48) (Section 2.4.2).

For the flight dynamics model and the free wake model to interact correctly, several other details need to be taken into account, such as proper transformation between the coordinate systems used by both models, as described in Section 3.3.3.

The trim procedure with the free wake model is described schematically in Fig. 4.6. This procedure can be summarized as follows:

1. The process starts with a guess of the trim solution, $\mathbf{X}_0$, which is provided to the non-linear algebraic equation solver, as described in detail in Section 4.5.4.

2. For each guess, $\mathbf{X}_K$, the velocities seen by the blade, $V_x(\psi, r), V_y(\psi, r), V_z(\psi, r)$, Eq.(2.50), are calculated, as well as the equivalent flapping angles, $\beta(\psi)$, Eq.(4.92). These, together with the body rates and velocities, u_F, v_F, w_F, p, q, r, Eqs.(2.38,3.52.41 and 3.6), are converted to the appropriate wake coordinate system and passed to the free wake model.

3. The free wake model adds the inflow, $\lambda(\psi, r)$ (from a previous solution, the previous iteration or, in the case of starting without an initial wake solution, from a prescribed wake), to the blade velocities to calculate the circulation distribution, $\Gamma(\psi, r)$, with the Weissinger-L method, Eq.(3.23).

4. With this circulation, $\Gamma(\psi, r)$, the free wake geometry is calculated (Section 3.4.1) and the corresponding updated induced velocities, $\lambda(\psi, r)$, are determined.

5. With the newly calculated induced velocities, steps 3 and 4 are repeated, until the inflow converges.

6. The converged inflow, $\lambda(\psi, r)$, is returned to the flight dynamics model, which uses it to evaluate the equations of motion and determine the residual with the methodology described in Section 4.5.4.

7. Steps 2 to 6 are repeated until the residual falls below a certain tolerance and a trim solution is reached as in Section 4.5.4.

There are two important aspects in the above approach that significantly reduce the overall computational cost of obtaining a trim solution:

1. First of all, the computational cost has been cut down by not updating the inflow during the calls to build the Jacobian matrix. To calculate the Jacobian, the non-linear algebraic equation solver firsts calls the function that evaluates the right hand side of the equations of motion in Eq.(4.91), $\mathbf{F}(\mathbf{x})$, once to get the baseline solution with which to build the forward difference approximation of the derivatives, and then it perturbs each element of the vector of trim unknowns $\mathbf{x}$ to build the derivatives. The perturbation is very small, of the order of 0.01% of the value of each element of $\mathbf{x}$. The free wake model, however, was almost insensitive to such a small perturbation of one of it's inputs. For that reason, the induced velocities obtained when calculating the baseline for each Jacobian matrix are fixed for the entire process of building each derivative by the perturbation approach. Once the Jacobian is calculated, and in each

attempted solution along the new direction determined by the Jacobian, the free wake geometry and inflow are calculated normally, as described in Fig. 4.6.

2. The present study takes advantage of the Weissinger-L method included with the free wake model, which offers the possibility of updating the bound vortex strengths for each step of the free wake loop, reducing the overall cost of converging the induced velocities.

4.5.6 Extraction of the state vector from the trim solution

The vector of trim unknowns used to obtain a trim solution, $\mathbf{X}$, does not correspond exactly with the state vector, $\mathbf{y}$. However, the vectors of states and controls can be reconstructed from the information contained in the vector of trim unknowns and the information about the flight condition at which the trim solution is obtained.

The state vector needs to be calculated in the rotating frame, which is the frame in which the equations of motion are formulated, and it is defined at a reference azimuth angle, ψ_{REF}, which is the reference azimuth location of a reference blade (the locations of all other blades can be determined from this reference azimuth angle).

For the baseline case without the free wake mode, the state vector is as follows:

$$\mathbf{y} = \left\{ \begin{array}{c} \mathbf{y}_B \\ \mathbf{y}_I \\ \mathbf{y}_R \end{array} \right\} \tag{4.93}$$

with the partitions referring to a rigid body part, an inflow part and a main rotor part.

When the free wake is used to provide the vortex wake geometry and main rotor inflow, the state vector does not contains the inflow part:

$$\mathbf{y} = \left\{ \begin{array}{c} \mathbf{y}_B \\ \mathbf{y}_R \end{array} \right\} \tag{4.94}$$

The vector $\mathbf{y}_B$ contains the state variables associated with the motion of the rigid body of the aircraft, which are independent on the reference azimuth angle at which the state vector is defined. This rigid body part takes the form (the tail rotor inflow is included in the rigid body portion of the state vector for convenience):

$$\mathbf{y}_B = [u\ v\ w\ p\ q\ r\ \phi_F\ \theta_F\ \psi_F\ \lambda_t]^{\mathrm{T}} \tag{4.95}$$

These components are determined from the rigid body part of the trim vector, $\mathbf{X}_R$, Eq.(4.64), and the velocity, V, the flight path angle, γ, and the turn rate, $\dot{\psi}$, which define the flight condition for which the trim solution was calculated. The velocity components along the body axes are obtained from the velocity V and the fuselage angle of attack and sideslip angle, α_F and β_F respectively:

$$\begin{aligned} u_F &= V \cos\alpha_F \cos\beta_F \quad \text{(4.65) repeated} \\ v_F &= V \sin\beta_F \quad \text{(4.66) repeated} \\ w_F &= V \sin\alpha_F \cos\beta_F \quad \text{(4.67) repeated} \end{aligned}$$

The angular velocities p, q, and r about the body axes can be obtained turn rate $\dot{\psi}$ and the Euler angles θ_F and ϕ_F:

$$\begin{aligned} p &= -\dot{\psi} \sin\theta_F \quad \text{(4.68) repeated} \\ q &= \dot{\psi} \sin\phi_F \cos\theta_F \quad \text{(4.69) repeated} \\ r &= \dot{\psi} \cos\phi_F \cos\theta_F \quad \text{(4.70) repeated} \end{aligned}$$

The pitch and roll Euler angles of the fuselage in the state vector, θ_F, ϕ_F, are the same as those in the trim vector, as is the tail rotor inflow, λ_t. The Euler yaw angle, ψ_F, is taken arbitrarily, since it is defined with respect to the inertial coordinate system; in the present study it is taken to be zero.

The vector $\mathbf{y}_R$ contains modal coefficients for the individual main rotor blades and their time derivatives, which are dependent on the azimuth angle. For a four-bladed rotor, $\mathbf{y}_R$ takes the form:

$$\begin{aligned} \mathbf{y}(\psi_i)_R &= [q_1^1\ q_2^1\ q_3^1\ q_4^1\ \dot{q}_1^1\ \dot{q}_2^1\ \dot{q}_3^1\ \dot{q}_4^1 \\ &\quad \ldots q_1^{N_\mathrm{m}}\ q_2^{N_\mathrm{m}}\ q_3^{N_\mathrm{m}}\ q_4^{N_\mathrm{m}}\ \dot{q}_1^{N_\mathrm{m}}\ \dot{q}_2^{N_\mathrm{m}}\ \dot{q}_3^{N_\mathrm{m}}\ \dot{q}_4^{N_\mathrm{m}}]^\mathrm{T} \end{aligned} \tag{4.96}$$

where q_i^k and $\dot{q}_i^k$ are the generalized displacement and velocity coefficients of the i-th blade for the k-th normal mode in the rotating frame at azimuth angle, ψ_i. They are reconstructed from the Fourier series expansions at trim. Eq.(4.71):

$$q_i^k = q_0^k + \sum_{j=1}^{N_\mathrm{h}} (q_{jc}^k \cos j\psi_i + q_{js}^k \sin j\psi_i) \quad k = 1, 2, \ldots, N_m \tag{4.97}$$

$$\dot{q}_i^k = \Omega \sum_{j=1}^{N_\mathrm{h}} (-q_{jc}^k \sin j\psi_i + q_{js}^k \cos j\psi_i) \quad k = 1, 2, \ldots, N_m \tag{4.98}$$

with the superscript k referring to the k-th mode in the modal coordinate transformation and the subscript i being the blade number.

The azimuth angle of the current blade, the i-th blade, is calculated with respect to the reference azimuth angle using:

$$\psi_i = \psi_{REF} + \frac{2\pi(i-1)}{N_\mathrm{b}} \tag{4.99}$$

where N_b is the number of main rotor blades.

The vector $\mathbf{y}_I$ contains the inflow coefficients for the dynamic inflow model, which are independent of the azimuth angle at which the state vector is defined, therefore it is identical to the inflow portion of the trim vector $\mathbf{X}_I$ (Eq.(4.73)).

The vector of controls is as follows:

$$\mathbf{u} = [\theta_0 \; \theta_{1c} \; \theta_{1s} \; \theta_t \; \dot{\theta}_0 \; \dot{\theta}_{1c} \; \dot{\theta}_{1s}]^{\mathrm{T}} \tag{4.100}$$

where the main and tail rotor controls in the control vector are the same as those in the rigid body portion of the trim vector, Eq.(4.64). The derivatives of the controls in the control vector are taken to be zero for trim since the controls themselves are fixed for trim.

4.6 Integration of the equations of motion

This section describes the procedure to integrate the equations of motion to determine the response of the helicopter to arbitrary pilot inputs.

4.6.1 Baseline integration procedure

As described in Section 2.7, the equations of motion can be expressed in first-order state space form, both in the explicit form

$$\dot{\mathbf{y}} = \mathbf{g}(\mathbf{y}, \mathbf{u}; t) \tag{4.101}$$

or in the implicit form

$$\mathbf{f}(\dot{\mathbf{y}}, \mathbf{y}, \mathbf{u}; t) = 0 \tag{4.102}$$

and integrated numerically using an ordinary differential equation solver.

In the case of the explicit formulation, a variable step, variable order Adams-Bashforth ordinary differential equation solver is used. For the implicit formulation (as seen in Ref. 126), the solver DASSL, a variable step, variable order method in which the derivatives are approximated by backward differentiation formulae is used (Ref. 127).

The baseline integration procedure is as follows. An integration simulation must start from an initial trim solution. From this trimmed helicopter state, the non-linear equations of motion are integrated in time for the prescribed duration of the simulation. The result is a set of time histories of all the states of the model following the pilot-prescribed input controls. The controls prescribed by the pilot are included in the form of time histories of at least one of the four controls, i.e., the collective, longitudinal and lateral cyclic and pedal (in addition to prescribing the controls, the time histories of one or more of the state variables themselves can be specified).

4.6.2 Integration with a time-marching free wake model

When dynamic inflow is used to obtained the induced velocities over the main rotor, the equations of motion include the Peters–He dynamic inflow equations (Ref. 36). If the free wake model is used instead, these equations are removed from the model and the induced velocities are instead provided by the free wake.

The time-marching free wake model used in the present study can be advanced in time with arbitrary time step sizes $\Delta\psi$, and therefore can be coupled with the

rotor-fuselage model at any desired point in the integration of the equations of motion. Unlike in Ref. 6, in which a steady state relaxation free wake model was used, there is no need to assume that each time the free wake is evaluated represents a steady-state condition. And since no assumption of periodicity is necessary, the induced velocities do not need to be converged and evaluated for the entire rotor at each call of the wake. Instead, the time-marching free wake is only advanced from the previous to the new time in the integration procedure, resulting in highly reduced computational costs in addition to the accurate-in-time induced velocities.

The input required by the free wake model to obtained a time-accurate inflow during the integration are the same as during trim (Section 4.5.5), i.e.

1. *The hub linear and angular velocities,* u_F, v_F, w_F, p, q, r.

   The hub linear velocities, u_{GW}, v_{GW}, w_{GW}, Eqs.(2.38,3.5), and angular velocities, p_{GW}, q_{GW}, r_{GW}, Eq.(2.41,3.6) are required to calculate the velocity field at the vortex filament, Eq.(3.13), (as described in Section 3.5):

$$\mathbf{V}\left(\mathbf{r}(\psi,\zeta)\right) = \underline{\mathbf{V}_{\infty}} + \mathbf{V}_{ind}\left(\mathbf{r}(\psi,\zeta)\right) + \underline{\mathbf{V}_{man}\left(\mathbf{r}(\psi,\zeta)\right)} \quad \text{(3.13) repeated}$$

   where

$$\mathbf{V}_{\infty} = V_{\infty x}\mathbf{i} + V_{\infty y}\mathbf{j} + V_{\infty z}\mathbf{k} \quad \text{(3.14) repeated}$$

   with $V_{\infty x} = u_{GW}$ and so on. The velocity distribution over the rotor due to the maneuver, $\mathbf{V}_{man}$, is calculated with Eq.(3.15):

$$\mathbf{V}_{man} = (r_G y - q_G z)\mathbf{i}_{\mathrm{G}} + (p_G z - r_G x)\mathbf{j}_{\mathrm{G}} + (q_G x - p_G y)\mathbf{k}_{\mathrm{G}} \quad \text{(3.15) repeated}$$

2. *The velocities at all points in the blade*, not including the inflow, in all three directions, $V_x(\psi, r), V_y(\psi, r), V_z(\psi, r)$, computed as described in Section 2.4.2. These velocities are necessary for the calculation of the bound circulation with the Weissinger-L model described in Eq.(3.23) in Section 3.6:

$$\sum_{j=1}^{N_S} \left[I_{b_{i,j}} + I_{NW_{i,j}} \right] \Gamma_j = \{ (\underline{\mathbf{V}_\infty + \mathbf{V}_{BM} + \mathbf{V}_{man}} + \mathbf{V}_{FW}) \cdot \mathbf{n} \}_i \quad \text{(3.23) repeated}$$

3. *The equivalent rigid blade flapping angles*, $\beta(\psi)$, given by the following equation:

$$\beta(\psi) = \frac{w_{tip}(\psi)}{R} + \beta_p \quad \text{(4.92) repeated}$$

The free wake model returns the inflow distribution for that particular flight condition, $\lambda(\psi, r)$.

The main difference is that only the new updated values of the flap and the blade velocities are required at the new azimuth position at which the free wake must be evaluated for each blade, rather than the values over the entire rotor.

The methodology used in the present study is shown schematically in Fig. 4.7. Although the solver used for the simulation is a variable-step solver, it is necessary to choose a step size $\Delta\psi$ at which to synchronize the flight dynamics simulation and the free wake, which is solved separately. The simulation is advanced in steps of variable size chosen by the solver algorithm, but the solver stops every $\Delta\psi$, at which time the wake is advanced to the new position and the induced velocities updated. The step used to advance the free wake model needs not be the same as the time step of the simulation, $\Delta\psi$. If the free wake azimuthal discretization, $\Delta\psi_{FW}$, is smaller than $\Delta\psi$, several free wake time steps take place to advance to $\Delta\psi$. The present

study, however, uses the same wake azimuthal discretization $\Delta\psi_{FW}$ and time step $\Delta\psi_{FW}$ (10 degrees), and thus only one free wake step is taken for each time step of the simulation.

The process is as follows:

1. The simulation starts from a trimmed flight condition that is represented by the trim vector $\mathbf{X}_{trim}$ (Eq.(4.63)), which is calculated using the method presented in Section 4.5. The state vector in the rotating frame, at a reference azimuth angle of zero, $\mathbf{y}(\psi_{REF} = 0)$, needs to be extracted from the trim solution, as described in Section 4.5.6.

2. At $t = 0$, besides the trimmed states and unknowns, the following information is also available from the trim solution: the trimmed condition induced velocities, $\lambda(\psi, r)$, the corresponding distribution of circulation over the rotor, $\Gamma(\psi, r)$, and the wake filaments geometry at this baseline flight condition.

3. With the inflow held fixed, the non-linear equations of motion can be integrated in time using a variable step until it reaches the point where it synchronizes with the wake, at a new time $t_i = t_{i-1} + \Delta\psi$. The vector with the updated states, $\mathbf{y}$, and the updated flap angles, $\beta(\psi)$, and blade velocities, $V_x(\psi, r), V_y(\psi, r), V_z(\psi, r)$, at the new time step t_i for all blades are stored.

4. The current states and controls of the helicopter, $\mathbf{y}$ and $\mathbf{u}$, the blade flapping distribution updated for the new time step, $\beta(\psi)$, and updated blade section velocities, $V_x(\psi, r), V_y(\psi, r), V_z(\psi, r)$, are provided to the free wake model. Together with the current distribution of induced velocities, $\lambda(\psi, r)$, they are used

to evaluate the circulation $\Gamma(\psi, r)$ at the new time in the simulation with the Weissinger-L method (Section 3.6).

5. The newly-calculated circulation, $\Gamma(\psi, r)$, is used to advance in time the free wake geometry until the new time step in the simulation, t_i (Section 3.4.1). If the size of the free wake time step $\Delta\psi_{FW}$ is the same as the simulation $\Delta\psi$, only one free wake step is needed. If the free wake azimuthal discretization $\Delta\psi_{FW}$ is smaller than the time step of the simulation (the simulation time step needs to be a multiple of the free wake $\Delta\psi$), several free wake steps take place to reach t_i. In that case, the induced velocities at each new step are used to recalculate the circulation, and the process is repeated until the new time is reached. The induced velocities for this new geometry, $\lambda(\psi, r)$, are calculated and stored.

6. The updated induced velocities, $\lambda(\psi, r)$, are used to integrate the equations of motion to the new time in the simulation, t_{i+1}. Steps 3, 4 and 5 are repeated for each time step in the simulation until it is complete.

Both the variable step Adams-Bashforth algorithm and the DASSL method need to evaluate the equations of motion at any azimuth angle between each time step of the integration. The specific values of azimuth angle used are selected by the integration algorithm itself and are not known prior to the integration. The free wake model only provides the inflow at specific azimuth angles. For that reason, a linear interpolation of the inflow is performed as a function of the azimuth angle during the evaluations of the solver between the azimuth points in which the inflow

is available.

4.6.3 Response after trimming with a relaxation free wake model

In the earlier stages of the present study (Refs. 128, 129), the trim solution was obtained with a relaxation free wake model (Ref. 12) because it was thought that it would be more appropriate for the calculation of steady-state conditions. However, this approach was later dropped in favor of the present methodology for the benefits obtained from using the same free wake model for both trimming and integrating the equations of motion, and, specially, because the trim formulation with the time-accurate wake showed better numerical characteristics (speed of convergence, accuracy, stability). A summary of that earlier approach with a relaxation free wake model for the trim calculation is presented in Appendix B for completeness.

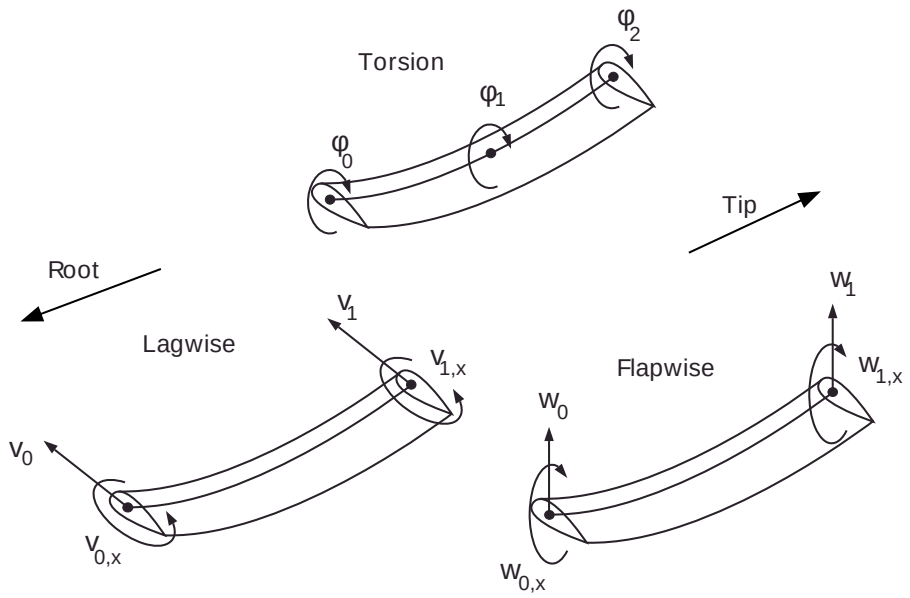

Figure 4.1: Finite element nodes and degrees of freedom.

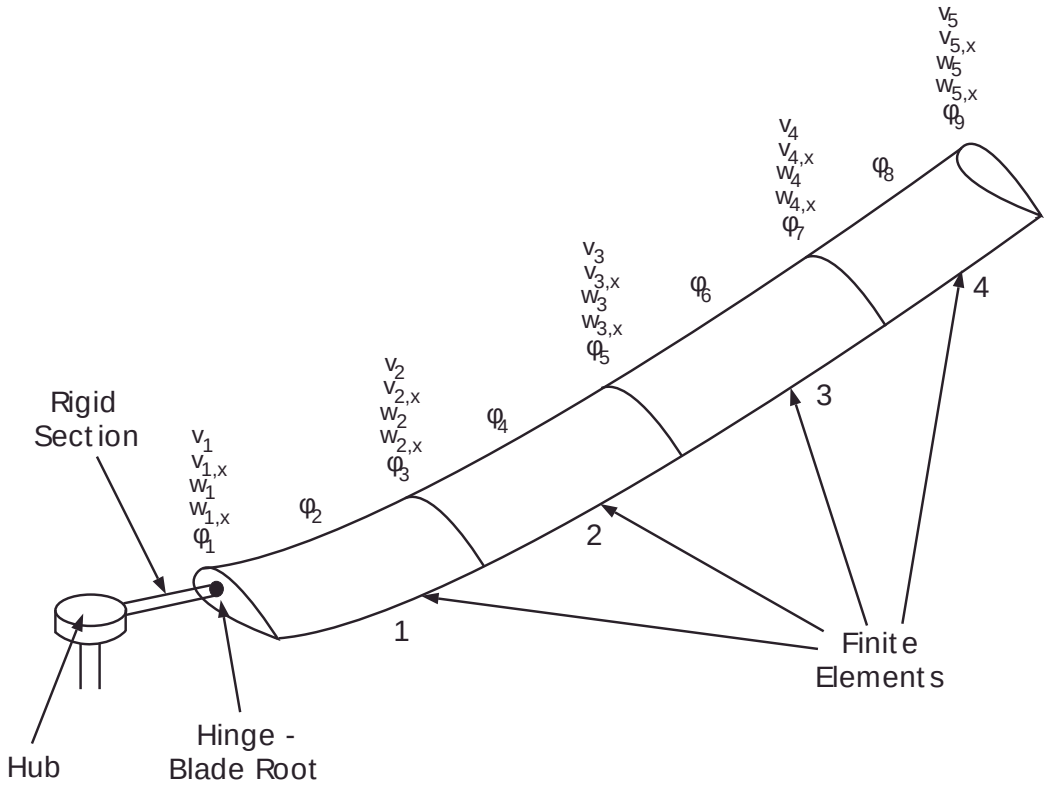

Figure 4.2: Blade degrees of freedom for the complete blade using four finite elements.

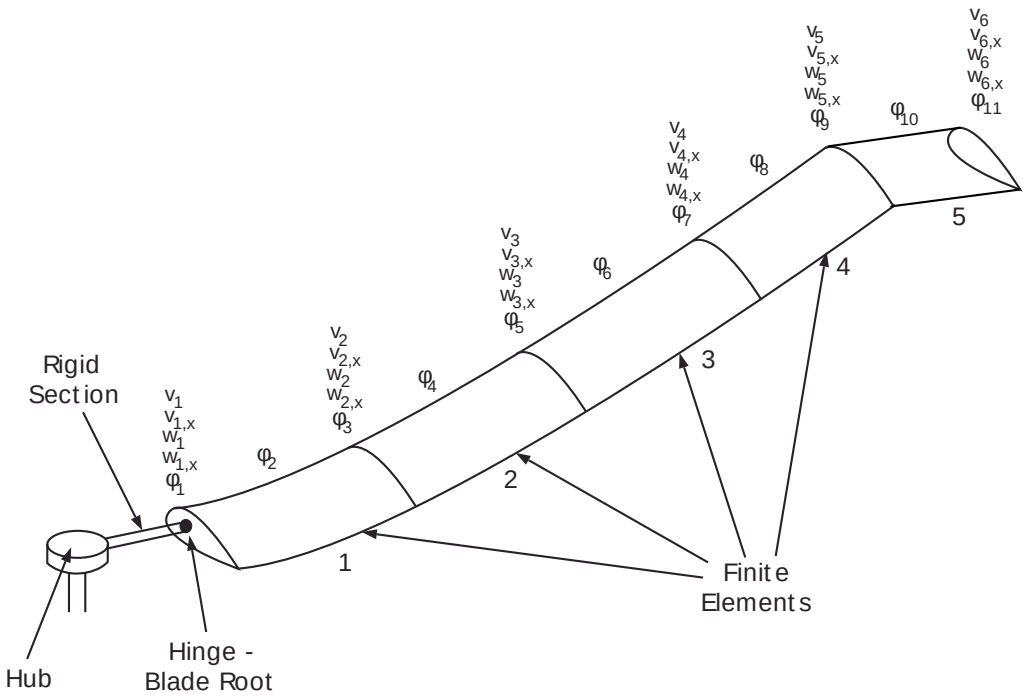

Figure 4.3: Blade degrees of freedom for the complete blade using four finite elements for the straight portion of the blade and one for the swept tip.

$$\left[\ M\ \right] = \left[\begin{array}{cc} \left[\begin{array}{ccc} M_S & \cdots & M_S \\ \vdots & & \vdots \\ M_S & \cdots & M_S + M_T \end{array}\right] & \begin{array}{c} \\ \\ M_T \end{array} \\ \begin{array}{ccc} & & M_T \end{array} & M_T \end{array}\right]$$

$$\left[\ K\ \right] = \left[\begin{array}{cc} \left[\begin{array}{ccc} K_S & \cdots & K_S \\ \vdots & & \vdots \\ K_S & \cdots & K_S + K_T \end{array}\right] & \begin{array}{c} \\ \\ K_T \end{array} \\ \begin{array}{ccc} & & K_T \end{array} & K_T \end{array}\right]$$

Figure 4.4: Schematic of the assembly of the straight and swept portions of the mass and stiffness matrices.

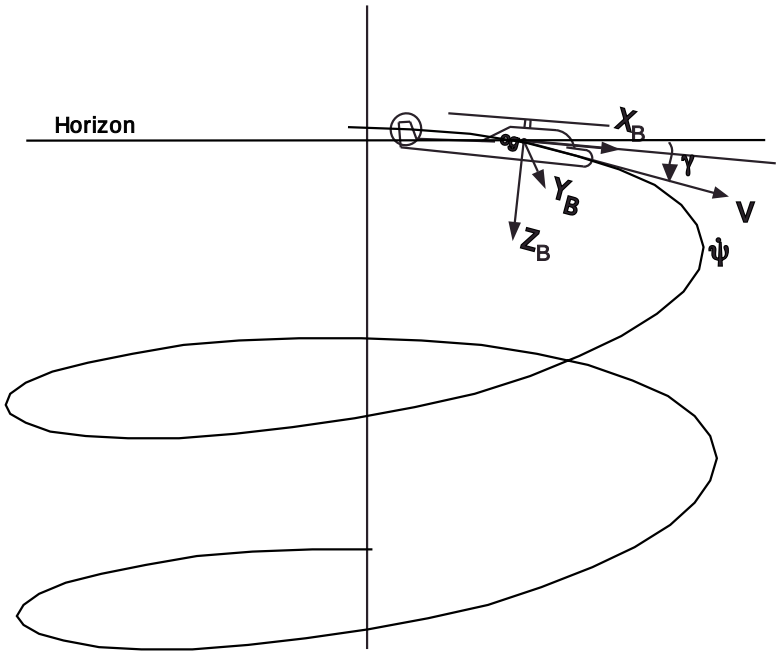

Figure 4.5: Coordinated turn.

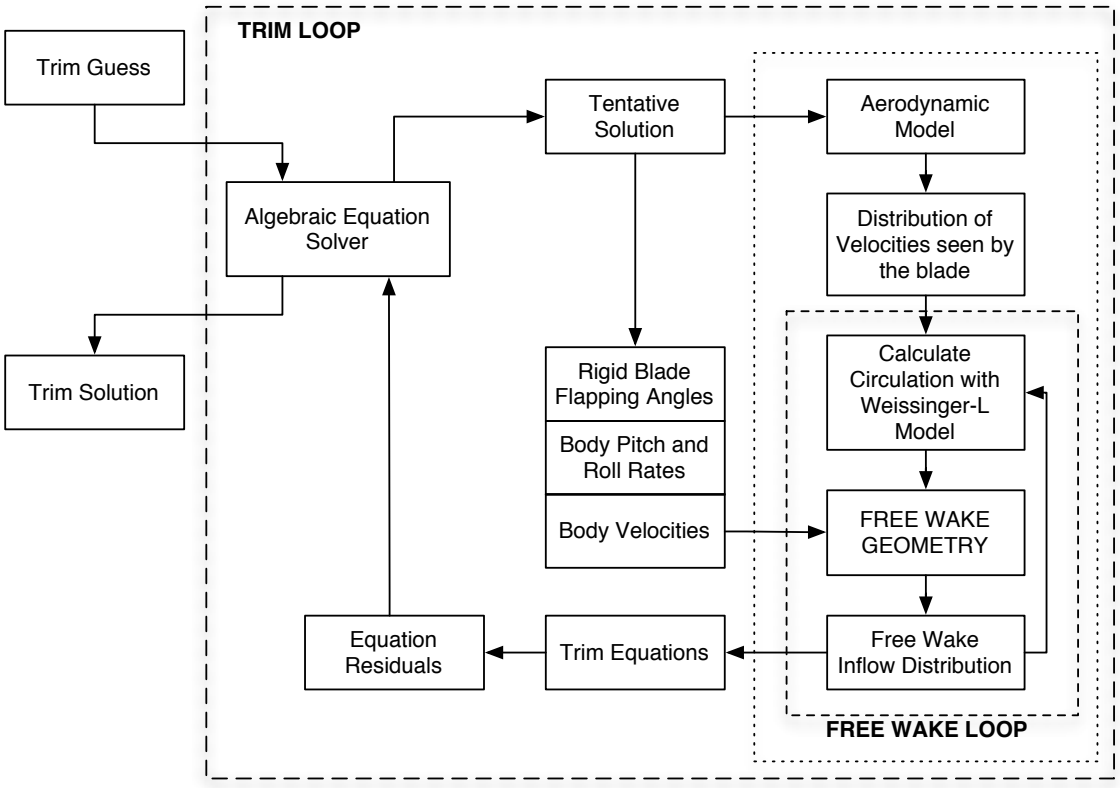

Figure 4.6: Scheme of the trim procedure with a time-marching free wake model coupled to the rotor-fuselage model.

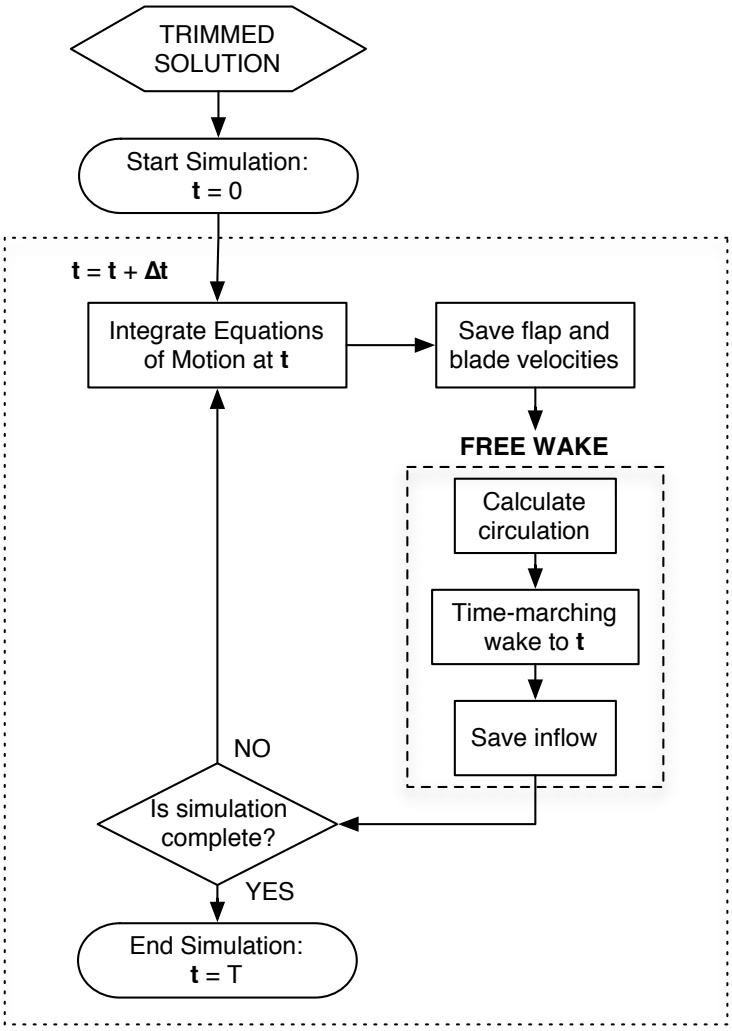

Figure 4.7: Integration scheme procedure with a time-marching free wake model coupled to the rotor-fuselage model.

Chapter 5

Helicopter configuration and blade mode shapes

5.1 UH-60 Helicopter configuration

This section describes the general characteristics of the helicopter and the model configuration used in the current study.

The helicopter configuration is based on the Sikorsky UH-60A, which has a fully-articulated rotor system with 4 blades of 26.83 feet radius rotating at 27 rad/sec or 260 RPM and a forward shaft tilt of 3 degrees. The blade airfoil section is the SC 1095, for which aerodynamic data is extracted from look-up tables. The tip of the blade is swept by 20 degrees over the outboard 1.90 feet of the radius, and the present study includes results both with the swept tip and assuming a straight blade tip. The hinge offset is 1.25 feet and the cuff extends outboard for another 3.83 feet. The blade has a chord length of 1.75 feet and an equivalent linear twist of about -18 degrees, although the blade is twisted only outboard of the cuff. The actual blade twist from the root to tip is -14 degrees (without the inclusion of the swept tip).

The tail rotor has a cant angle of 20 degrees, and therefore it generates relatively strong couplings between longitudinal and lateral directional dynamics. It has the same airfoil section and blade twist as the main rotor, although with a smaller radius and chord (5.5 feet and 0.81 feet, respectively).

The horizontal stabilizer uses the NACA 0014 airfoil and has an area of 45 square feet and an aspect ratio of 4.6. Its incidence is adjustable by the flight control system as a function of speed. The vertical stabilizer, which uses the NACA 0021 airfoil, has a surface area of 32.3 square feet and an aspect ratio of 1.92.

Table 5.1 summarizes the configuration of the UH-60A articulated rotor helicopter used in this study. Unless specified otherwise, the results in this study are for a gross weight of 16,000 lbs, corresponding to a $C_T/\sigma = 0.074$, and at an altitude of 5250 feet.

The majority of the UH-60 parameters and non-linear functions and data tables have been adapted from an existing UH-60 simulation model (Ref. 32). Further details of the implementation of the fuselage, empennage and tail rotor models for the UH-60A helicopter can be found in the GENHEL theory manual (Ref. 32). Figures 5.1, 5.2 and 5.3 show the lift, drag and moment coefficients, C_L, C_D and C_M respectively, as a function of angle of attack α and Mach number M for the airfoil of the U-60A as obtained from the data in Ref.32.

The results included in the present study have been generated with a blade model that includes the five lowest blade modes, which represent the two rigid modes in flap and lag plus the first elastic flap, lag and torsion modes.

5.1.1 Flight dynamics model details

For the straight blade configuration, four finite elements of equal length are used to model the blade. When the swept tip is modeled, the blade is discretized into five finite elements, four equidistant elements for the straight portion of the blade, and one element for the entire swept tip.

The total number of degrees of freedom is $5 + 6N_e$ where N_e is the number of finite elements used. Therefore, for the four-element straight blade $N_e = 29$ and for the swept five-element blade model $N_e = 35$. With the root constraints, the root flap, lag and torsional displacement for an articulated rotor are zero, and therefore the total number of degrees of freedom is reduced by 3, to 26 for the straight blade and 32 for the blade with tip sweep.

For each finite element, 8 Gaussian (therefore, not equally spaced) points are considered. Therefore, there are 32 points along the blade at which structural, inertial and aerodynamic loads are calculated. In the case of the swept tip blade, there are 5 finite elements, for a total of 40 spanwise points.

The effect of the main rotor downwash on the fuselage and empennage is not included in the present study. The model is not used because of numerical convergence issues. However, the model itself is just a parametric extension developed early in the history of the legacy model to help fit experimental data, but not based on first principles. Therefore, the effect was turned off until a better modeling of the influence of the downwash on the helicopter can be implemented.

5.1.2 Free wake parameters

The free wake of each blade has been modeled with only the tip vortex, whose length is 4 free turns downstream of the rotor. A 10-degree discretization is used for both the time and space derivatives, unless otherwise noted. The near wake extends for 20 degrees behind the blade, and beyond it extends the tip vortex.

For the purpose of calculating the bound vortex and the circulation, the blade is divided into 32 equidistant spanwise sections.

5.2 Blade mode shapes

This section presents the results of the free vibration analysis of the UH-60A rotor blade, both for the straight blade configuration and for the effect of tip sweep. The natural frequencies and mode shapes are calculated using the finite element method as described in Sections 4.2 and 4.3, using four finite elements for the straight blade and five for the swept model.

5.2.1 Straight blade

The blade mode shapes corresponding to the six lower natural frequencies for the straight blade configuration are shown in Figs. 5.4 and 5.5. The modes corresponding to the two lowest natural frequencies are the rigid lag and flap mode, respectively. The next two lowest frequencies represent the first elastic (and second overall) flap and lag modes. The first torsion mode corresponds to the sixth lowest natural frequency. These figures show that there is some coupling between the flap and

torsion modes due to the structural twist built into the blade. Note that the modes are normalized with respect to the tip value of the highest magnitude, although the difference between the displacements in bending and the angles in torsion are of different magnitude; thus, the plot the second flap mode may appear of smaller magnitude than the torsion mode, although in reality this does not determine the nature of the mode shape.

The numerical results for the UH-60A presented in this study have been generated using a flexible blade model, unless otherwise stated.

5.2.2 Swept tip blade

The influence of tip sweep on the natural frequencies is shown in Table 5.2. Results are shown for the baseline straight four-element blade model, for a straight five-element model with the same spanwise node distribution as the swept tip model, and for a swept five-element blade configuration. Table 5.2 shows that increasing the number of finite elements does not significantly affect the natural frequencies and mode shapes for the straight blade. The inclusion of the swept tip affects mostly the torsional frequency, which increases from 5.25 to 5.35 /rev, due to the increase in the torsional stiffness (tennis racket effect). The inherent coupling between the flap and lag degrees of freedom is reflected in a slight decrease of the flap modes, the first of which goes from 1.035 to 1.022 /rev with the inclusion of a 20-degree sweep at the blade tip. The increase in torsional frequency is observed in some of the studies in the literature (Refs. 98, 101), while in others the opposite effect is observed (Ref. 93).

All these models use different aircraft with different blade properties. Therefore, the reason for the different results is the tip sweep increases both the torsional stiffness and the torsional inertia, and depending on which of these quantities increases more, the torsional frequency will increase or decrease (Ref. 101). The results in the present study present the same tendency as those in Ref. 130, in which the same helicopter is used.

Figure 5.6 shows the variation of the lowest six natural frequencies with increasing sweep angle, ranging from 0 to 25 degrees. As the sweep angle Λ increases, the lag frequencies stay the same, the flap frequencies decrease slightly, while the largest effect is the torsional frequency increase.

The blade mode shapes corresponding the the six lowest natural frequencies for the swept tip configuration are presented in Figs. 5.7 and 5.8. As for the case of the straight blade, the coupling between the flap and torsional degrees of freedom is clearly visible, but the couplings are stronger with the swept tip, including the second lag mode, which is significantly affected despite the corresponding natural frequency not changing.

MAIN ROTOR	
Number of blades	4
Radius R, ft	26.83
Blade chord c, ft	1.75
Rotational speed Ω, rad/sec	27.0
Tip speed V_{tip}, ft/sec	724.41
Longitudinal mast tilt i_θ, deg	-3.0
Airfoil section	SC 1095
First airfoil section, ft	5.08
Blade precone β_P, deg	0.0
Linear blade twist θ_{TW}, deg	-18.0
Solidity σ	0.083
Lock number γ	5.11
Control phase shift Δ_{SP},deg	-9.7
FUSELAGE	
Gross weight w, lbs	16000.00
Pitch inertia I_{yy}, lbs-ft^2	38512.0
Roll inertia I_{xx}, lbs-ft^2	4659.0
Yaw inertia I_{zz}, lbs-ft^2	36796.0
I_{xz}, lbs-ft^2	1882.0
Horizontal tail surface area (ft^2)	45.00
TAIL ROTOR	
Number of blades	4
Radius R_{tr}, ft	5.5
Blade chord c_{tr}, ft	0.81
Rotational speed Ω_{tr}, rad/sec	124.62
Tip speed, ft/sec	685.41
Rotor shaft cant angle, deg	20.0

Table 5.1: Main parameters of the UH-60A Black Hawk helicopter configuration.

Mode Number	Mode Type	Frequency (/rev)		
		4 FEM straight	5 FEM straight	5 FEM swept
1	1st lag	0.2680	0.2679	0.2688
2	1st flap	1.0352	1.0352	1.0225
3	2nd flap	2.8160	2.8157	2.7684
4	2nd lag	4.6504	4.6551	4.6543
5	3rd flap	5.1744	5.1792	5.1073
6	1st torsion	5.2486	5.2531	5.3534

Table 5.2: Blade natural frequencies.

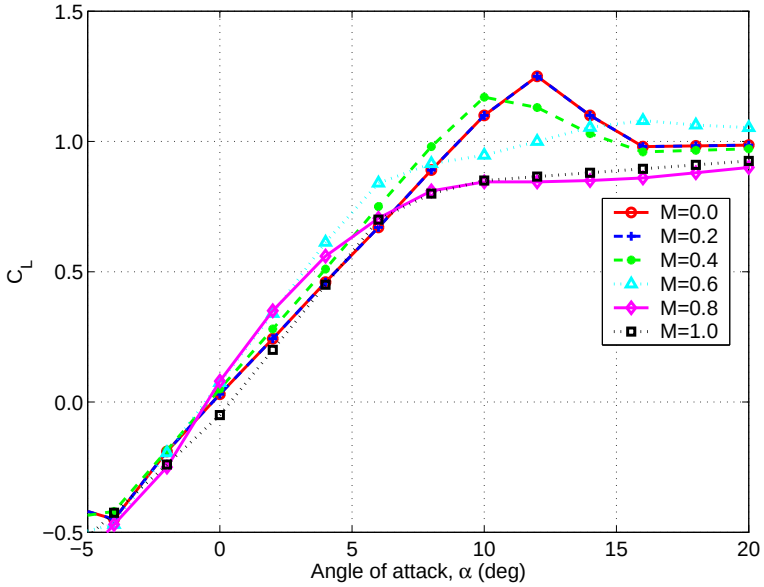

Figure 5.1: Lift coefficient C_L as a function of the angle of attack α and Mach number M for the SC 1095 airfoil (Ref. 32).

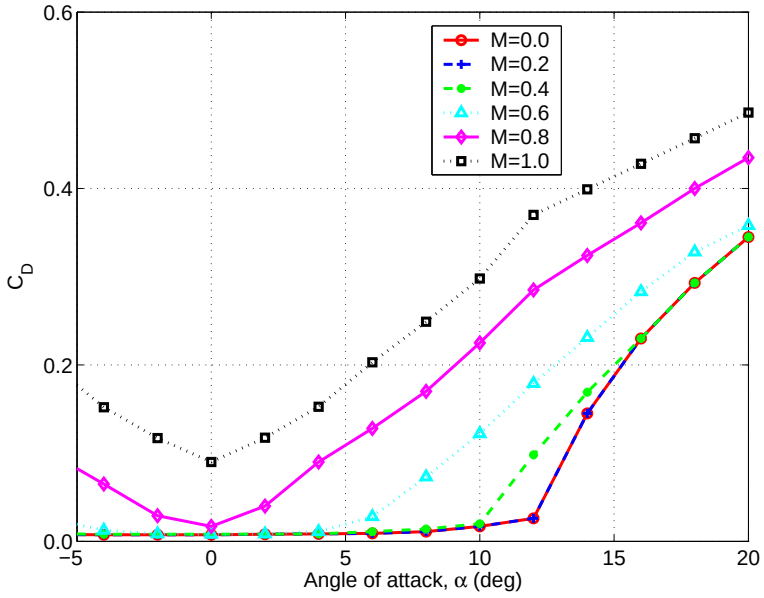

Figure 5.2: Drag coefficient C_D as a function of the angle of attack α and Mach number M for the SC 1095 airfoil (Ref. 32).

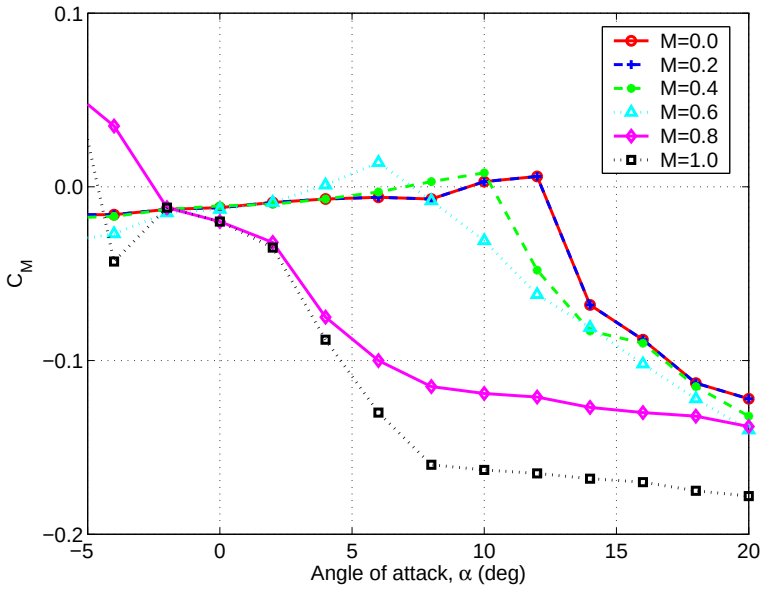

Figure 5.3: Moment coefficient C_M as a function of the angle of attack α and Mach number M for the SC 1095 airfoil (Ref. 32).

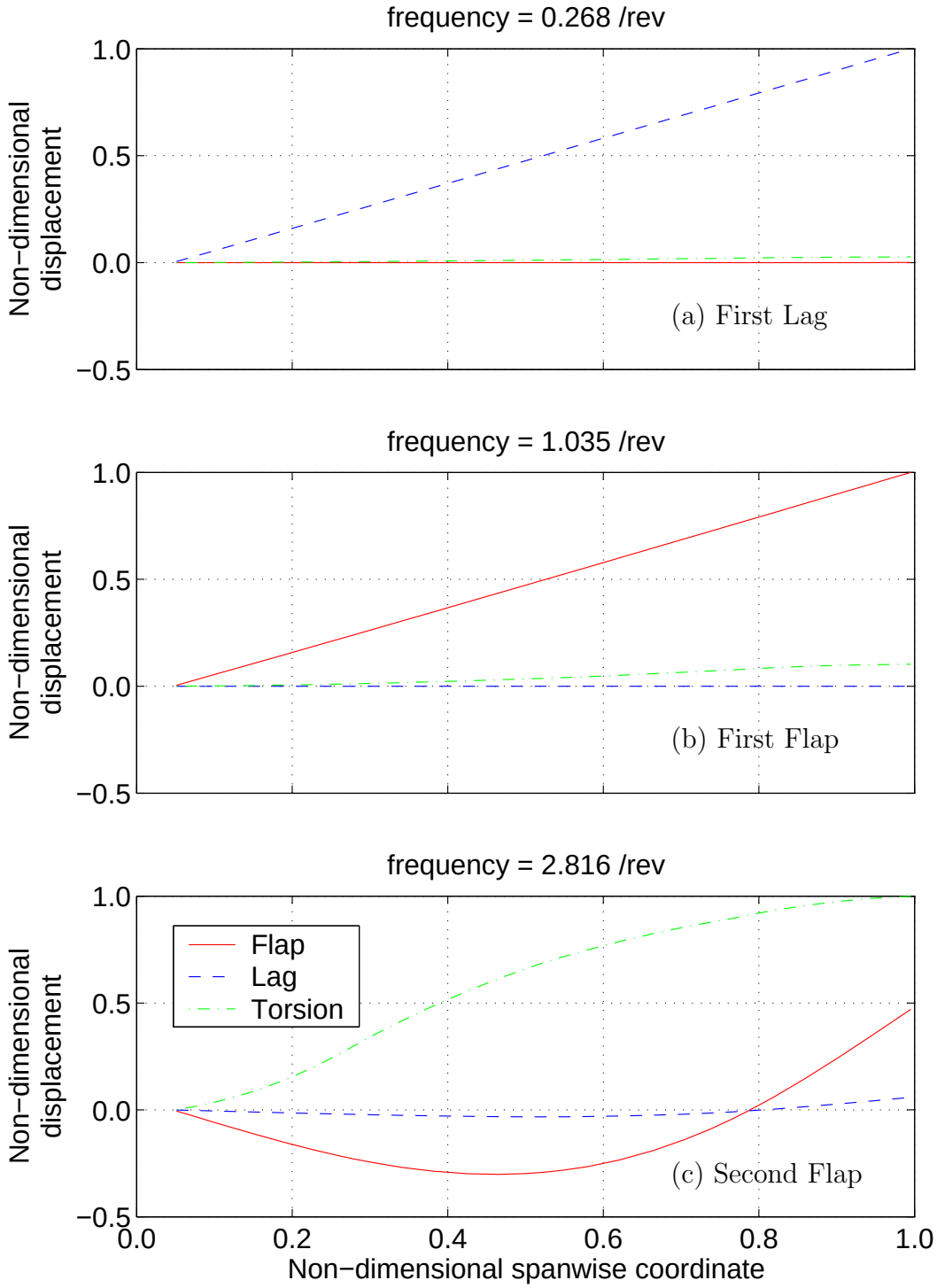

Figure 5.4: First, second and third natural mode shapes for the baseline model with a straight blade; frequency=0.268/rev (top), frequency=1.035/rev (middle) and frequency=2.816/rev (bottom).

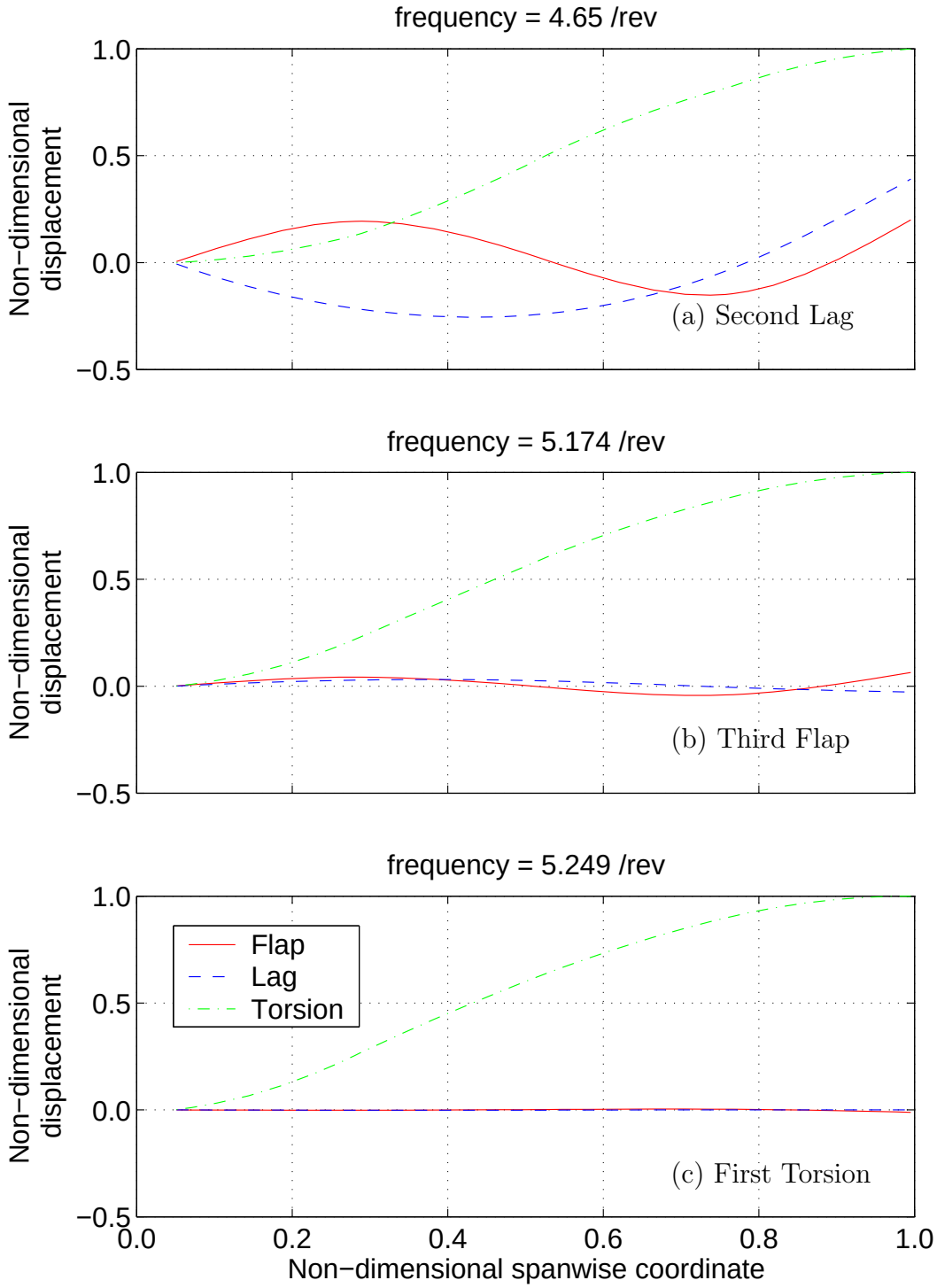

Figure 5.5: Fourth, fifth and sixth natural mode shapes for the baseline model with a straight blade; frequency=4.650/rev (top), frequency=5.174/rev (middle) and frequency=5.249/rev (bottom).

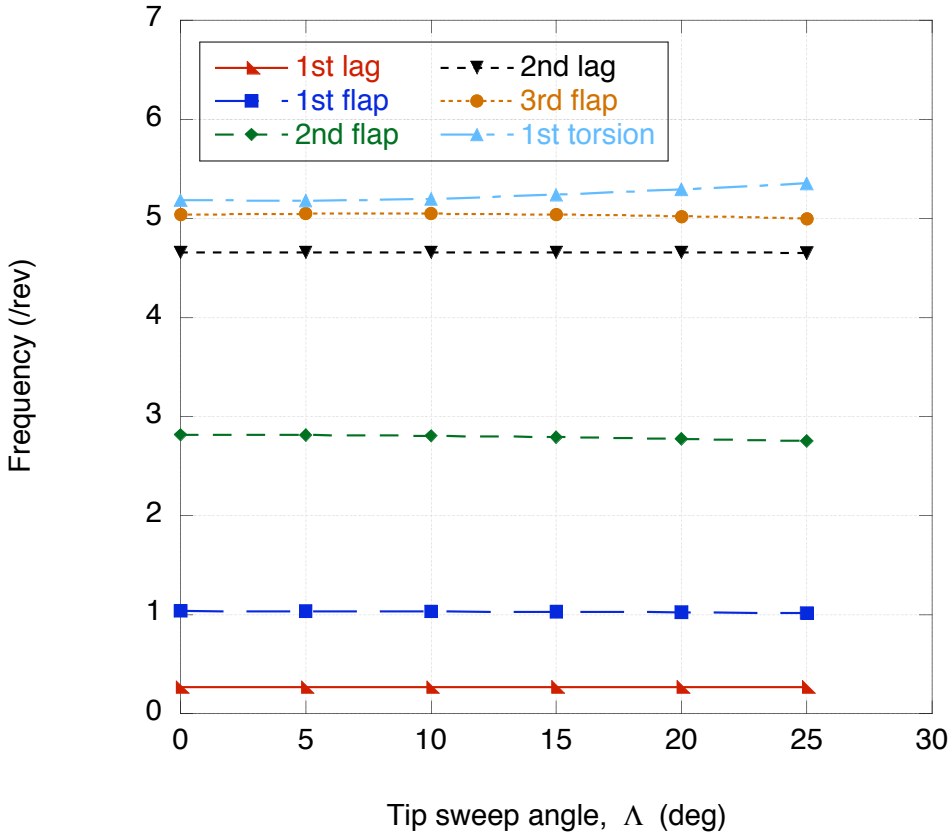

Figure 5.6: First six natural frequencies with varying tip sweep angle.

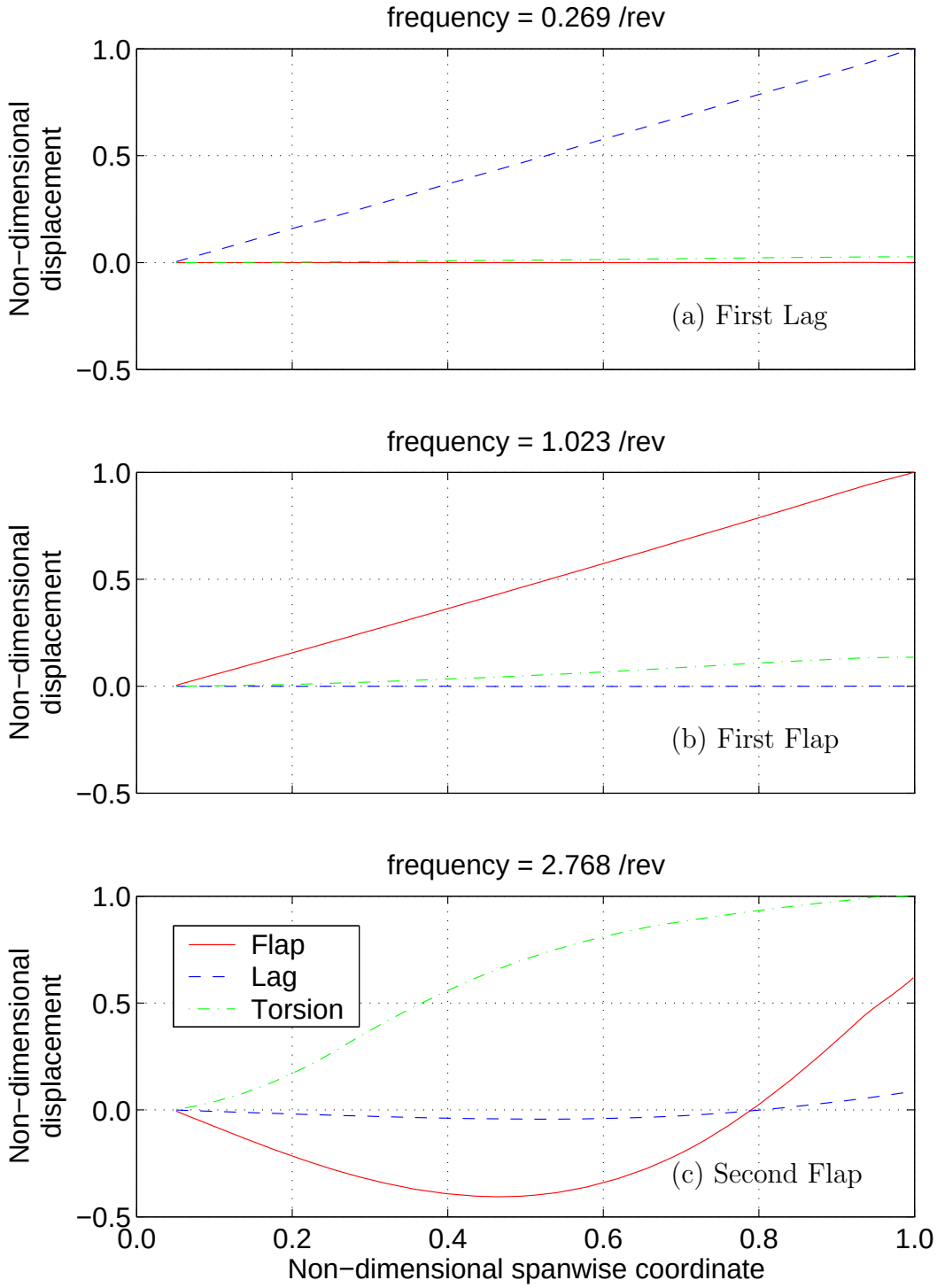

Figure 5.7: First, second and third natural mode shapes for the model with swept tip; frequency=0.269/rev (top), frequency=1.023/rev (middle) and frequency=2.768/rev (bottom).

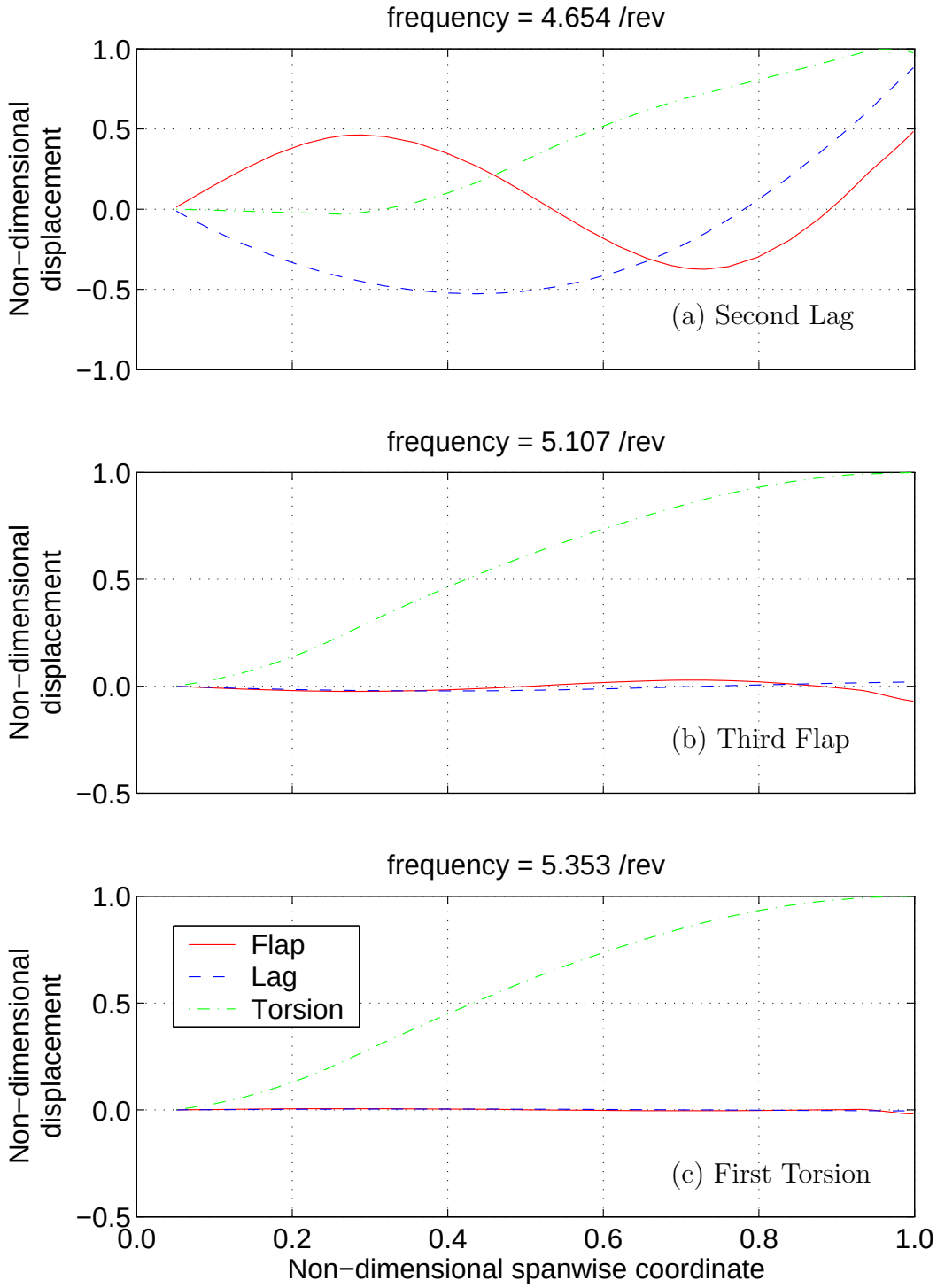

Figure 5.8: Fourth, fifth and sixth natural mode shapes for the model with swept tip; frequency=4.654/rev (top), frequency=5.107/rev (middle) and frequency=5.353/rev (bottom).

Chapter 6

Trim results

6.1 Overview

This chapter describes the trim results for a variety of flight conditions. The first section presents trim results obtained at different speeds in straight and level flight. The simulation results are also compared to flight test data. Both the trim results and the blade dynamics are studied, as well as the rotor loading and the effect that the free wake inflow prediction has on it. The effect of blade flexibility, the level of discretization of the free wake geometry and the inclusion of the swept tip are discussed. The second section contains results for coordinated turns, with different values of the turn rate, both to the right and the left. Special attention is paid to the influence of the wake geometry and the induced velocities it produces on the rotor. The third section presents results for straight climbing and descending flight. For a range of flight path angles, the behavior of both the fuselage and rotor is studied. Additionally, some high rate of descent conditions are to determine the highest rate of descent in incipient Vortex Ring State for which a trim solution can be obtained. The fourth section presents results for coordinated turns, including steep descents.

6.2 Straight and level flight

6.2.1 Comparison with flight test data

This section presents a comparison between the trim results and the flight test data from Ref. 10, which was obtained with a gross weight of 16,000 lbs at an altitude of 5,250 ft.

Figure 6.1 shows the power required by the main rotor, in horsepower (hp), as a function of speed. The values predicted by the model show excellent correlation with the experimental values for most of the flight speed range considered. The power is underpredicted below 30 kts (data below 20 kts was not available), although some uncertainty in the accuracy of the flight test data also plays a role at those speeds. Above 100 kts, the main rotor power required is slightly overpredicted, between 10% and 12% approximately. This may be caused by a combination of factors, including stall modeling and fuselage aerodynamics.

The collective stick value is shown in Fig. 6.2, and shows a very similar type of agreement with the experimental results.

The longitudinal cyclic stick position, presented in Fig. 6.3, has a good agreement with experimental values above 60 kts. At lower speeds, the predictions are less accurate, and the trend with speed is in the opposite direction than in the flight test data. This discrepancy might be caused by the fact that the effect of the downwash of the rotor on fuselage and empennage is not included in the model. At low speed this effect can significantly alter the predicted orientation of the helicopter fuselage and the rotor. A better treatment of the rotor/fuselage aerodynamic interaction is

necessary to accurately predict the longitudinal cyclic at low speed.

The fuselage pitch attitude as a function of speed is shown in Fig. 6.4. The values predicted are good at high speed flight, but overpredicted at low speed. This overprediction can also be attributed to the lack of a rotor/fuselage aerodynamic interaction model.

Figure 6.5 shows a comparison of the lateral cyclic stick position predictions with the experimental results. Except for the two data points at around 30 kts, the agreement is good at all speeds.

Figure 6.6 shows the correlation for the fuselage bank angle. The agreement is good for flight speeds between 30 and 100 kts. Below 30 kts, the comparison is inconclusive because of the scatter of the flight test data, but the trend seems correct. At high speed flight, the roll attitude is underpredicted, perhaps because the power overprediction results in an increased tail rotor thurst and slightly more roll to the right, but the trend is captured correctly.

Finally, the pedal correlation is shown in Fig. 6.7. The results obtained with the model show a consistent overprediction of about 10%. This overprediction of the pedal setting has been observed in other studies (Refs. 10, 6). Ref. 6 uses a similar rotor-fuselage model with both a relaxation free wake model (Ref. 28) and the Pitt–Peters dynamic inflow model (Ref. 24) to simulate the same flight conditions. Both inflow models predict very similar results, which indicates that the reasons for the discrepancy with the experimental data are not to be found in the inflow model, but elsewhere, possibly in the modeling of the body of the helicopter (fuselage and empennage).

The values of the pitch and roll attitudes predicted with the time marching free wake model are also similar to those obtained with dynamic inflow, as shown in Ref. 6. Again, any discrepancies with the flight test data are unlikely to be related to the inflow model.

6.2.2 Analysis of trim results

This section presents the trim results obtained at speeds of $V = 1, 40$ and 100 kts, corresponding to advance ratios of $\mu = 0.002, 0.093$ and 0.233 respectively, with a straight blade configuration. The three cases are representative, respectively, of hover, low speed and high speed conditions. In the first two cases there is considerable mutual interaction between rotor and wake, and between the vortices trailed by the four blades. These interactions are less strong in the third case, where the wake is quickly swept away behind the rotor.

The side view of the wake geometry as a function of speed is shown in Fig. 6.8. In hover, the wake presents a helical structure that only breaks far downstream of the rotor due to the instability of the wake vortices in hover, a behavior that has been observed both experimentally (Refs. 131–133) and numerically (Refs. 134, 7). The helical pattern of the geometry is clearly appreciated, and it contracts as it convects downstream of the rotor. As the speed increases, the wake begins to skew, and the vortices begin to interact as their proximity increases. The rollup of the lateral edges of the wake geometry that characterizes the wake in forward flight, due to the formation of vortex bundles or "super vortices" (Ref. 15), becomes visible at

$V = 40$ kts. At $V = 100$ kts, the wake is convected fast behind the rotor, and the influence of the vortices at the rotor plane is much reduced. The wake geometry is highly skewed at this speed, and the filaments are quickly left behind, decreasing their effect over the rotor plane with increasing distance.

Figure 6.9 shows the rear view of the wake geometry at $V = 1, 40$ and 100 kts. In hover, the rear view is very similar to the view from the side, with the same helical pattern observed. The helicopter in hover has a negative roll attitude of $-2.7°$, which is appreciated in the orientation of the rotor. At $V = 40$ kts, the rollup of the wake on the lateral edges becomes apparent, particularly on the advancing side. This effect becomes more pronounced as the speed increases.

The wake view from the top is shown in Fig. 6.10. In hover, the filaments appear nearly concentric with filament age. At $V = 40$ kts, the wake is convected behind the rotor, but the tip vortices still remain close. The rollup on both sides of the wake is also visible from the top. At $V = 100$ kts, the tip vortices are convected far behind the rotor.

The induced velocity as a function of speed is shown in Fig. 6.11. Figure 6.11(a) shows the inflow distribution obtained with the time-marching free wake model for $V = 1$ kt. In near hover conditions, the inflow distribution looks almost axisymmetric. The symmetry is not perfect because the tip path plane is slightly tilted forward and some cyclic pitch is necessary to compensate for the tail rotor thrust. This near-symmetry corresponds to the helical structure depicted in Figs. 6.8(a), 6.9(a) and 6.10(a). The norm of the inflow, $\|\lambda\|$, at this flight condition is 0.0803 (58.20 ft/sec).

As the speed increases, the wake begins to skew, and the vortices begin to interact between themselves as their proximity to each other increases. Figure 6.11(b) presents the induced velocities at a speed of 40 kts. The overall induced velocities are lower than in hover, with $\|\lambda\| = 0.0534$ (38.65 ft/sec). The geometry of the free wake at this speed, shown in Figs. 6.8(b), 6.9(b) and 6.10(b), has a great influence in this distribution of induced velocities. The wake filaments start to convect behind the rotor plane, and the area where they exert their greatest influence shifts towards the rear of the rotor. The rollup that characterizes the wake in forward flight is already present at this speed, and affects the inflow, which has a higher downwash in the tip region in the advancing and retreating side, close to the formation of the rollup on the lateral edges of the wake.

Figure 6.11(c) shows the induced velocities at 100 kts. The corresponding geometry is shown in Figs. 6.8(c), 6.9(c) and 6.10(c). At this speed, the wake is convected fast behind the rotor, and the influence of the vortices at the rotor plane is much reduced. A region of upwash flow develops in the front of the rotor, while the rear of the rotor, closer to the wake trailed behind, contains the larger downwash. The overall norm of the induced velocities at this speed is even farther reduced in comparison with the inflow at $V = 40$ kts, with $\|\lambda\| = 0.0269$ (19.48 ft/sec), as the vortices move farther away from the rotor plane.

The changes in induced velocities translate to changes in angle of attack. According to Eq.(2.56), an increase in inflow λ would increase the perpendicular component of the airflow at the section, U_P, and therefore decrease the angle of attack. Figure 6.12(a) show the distribution of angle of attack for $V = 1$ kt. At near hover

conditions, when the induced velocities are almost uniformly distributed and at their highest value, the aerodynamic angle of attack α, which includes both the geometric pitch (which is the sum of the pitch due to the controls, the built in twist and the elastic twist, as seen in Eq.(2.55) and the induced angle of attack, is also almost uniform with a small variation between 3 and 5 degrees. Because of the 3-degree forward tilt of the rotor and the azimuthal and radial variations in the geometric pitch θ_G, the distribution is slightly biased and higher in the front of the rotor than in the rear, while the angle of attack presents the opposite distribution. The lower induced velocities seen in the front of the rotor at 40 kts (Fig. 6.11(b)) translate into a region of higher angle of attack, seen in Fig. 6.12(b). The areas of higher inflow, similarly, translate into lower values of the angle of attack there. The region of upward flow in the front of the rotor produces some areas of higher angle of attack in the front and retreating side, while the higher induced velocities in the rear of the rotor reduce the angle of attack seen in the rear and advancing sides (Fig. 6.12(c)).

The relation between the angle of attack and the induced inflow is, however, not as simple, as other factors come into play, such as the perpendicular component of the airstream that results from the orientation of the rotor or change in the tangential component U_T, which has a sinusoidal variation over the azimuth with increasing magnitude as forward speed increases, and the changes in the elastic deformation of the blade around the azimuth (Fig. 6.26). However, it serves as an indication of how the changes in the inflow modeling affect the flight dynamics of the helicopter.

Figure 6.13 shows the distribution of lift coefficient, C_L, over the rotor for

all three speeds considered, $V = 1$ kt, 40 kts and 100 kts. The lift coefficient is a function of both the angle of attack, α, and the Mach number, M (Fig. 5.1). In hover, the Mach number varies radially in the same way over the whole azimuth. Therefore, the only variation around the azimuth for a given radial location in the C_L distribution in hover is due to the changes in the angle of attack. Figure 6.13(a) shows the lift coefficient at $V = 1$ kt, which is higher in the same areas of the rotor where the angle of attack is higher, and similarly lower in the areas where α is lower. As the speed increases, the effect of the Mach number on C_L should be accounted, as the changes are not solely due to variations in the angle of attack distribution. However, the influence of the angle of attack α on the lift coefficient C_L is still very direct. Figure 6.13(b) shows the lift coefficient distribution at $V = 40$ ks. There are two areas of higher lift coefficient, with values of C_L up to 0.75, in the front-retreating side (between $\psi = 200°$ and $\psi = 270°$), and at the rear of the rotor disk (between $\psi = 340°$ and $\psi = 20°$), which occur precisely in the regions where the angle of attack α is the highest, reaching values up to 7 to 8 degrees. The same can be observed at $V = 100$ kts, shown in Fig. 6.13(c), speed at which the higher areas of angle of attack in the retreating side reaching values up to 10 degrees produce values of C_L of 1.

The corresponding elemental lift distribution, $C_L M^2$, is shown in Fig. 6.14. The square of the Mach number, M, increases radially outwards, uniformly around the azimuth in hover and increasingly more biased to the advancing side as the speed increases. In hover, Fig. 6.14(a), the distribution appears nearly axisymmetric, due to the influence of the square of the Mach number, which increases radially

outboard of the blade in the same proportion in all directions in hover. A close examination (the scale used in Fig. 6.14(a) was chosen to be consistent with all the speeds represented in Fig. 6.14) reveals that the influence of the angle of attack that was clearly visible on the lift coefficient C_L (Fig. 6.13(a)) is still present, although the effect of the square of the Mach number is dominant. At $V = 40$ kts, $C_L M^2$ increases in the same regions where the angle of attack α and thus the lift coefficient C_L increase, as seen in Fig. 6.14(b), and decreases similarly where the angle of attack decreases. However, these regions are a bit more biased towards the tip, and a new region of higher values appears in the advancing side, both effects resulting from the higher values of the square of the Mach number towards the tips and particularly in the advancing side (where M nears values of 0.7 at this speed). At $V = 100$ kts, the elemental lift distribution (Fig. 6.14(c)), like at 40 kts, varies as a function of the angle of attack, α. The effect of the square of the Mach number M, however, becomes more pronounced, and as a consequence the values of higher $C_L M^2$ shift towards slightly towards the advancing side, where M^2 is the highest. At this speed, spanwise gradients can be observed, particularly on the second quadrant of the rotor. These gradients indicate that the single vortex model might not be the best way to model the wake aerodynamics especially if accurate predictions of the spanwise inflow is necessary (for aeroacoustic purposes) but in the case where only integral loads are necessary (for helicopter dynamics) this assumption is still valid.

Figure 6.15 shows the local flap moment distribution, $rC_L M^2$, over the rotor disk, for the cases of $V = 1$ kt, $V = 40$ kts and $V = 100$ kts. This value serves as an indicative of the influence of the lift at a given point on the blade on the

flapping motion. At $V = 1$ kt, the factor of the non-dimensional radius r, between 0 and 1, reduces the value of $C_L M^2$ inboard of the blade, while increasing it towards the tip, where the highest contribution to the flapping motion occurs (due to the larger moment arm). The values may appear at first sight axisymmetric, although a slight bias towards the rear of the rotor is present. As the speed increases, the same effect is appreciated. The lower moment arm inboard of the blade (lower value of r) reduces the values of $C_L M^2$ both at $V = 40$ kts, Fig. 6.15(b), and $V = 100$ kts, Fig. 6.15(c), which therefore become biased towards the tip of the blade, however the areas where these higher values occur are the same as for $C_L M^2$.

The drag coefficient, C_D, like the lift coefficient C_L, is also a function of angle of attack, α, and Mach number, M (Fig. 5.2). For low Mach numbers, up to $M = 0.6$, and angles of attack, up to $\alpha = 5°$, the drag coefficient is almost constant, but it increases for all angles of attack for $M > 0.6$ and for angles of attack beyond $\alpha = 5°$ otherwise. Figure 6.16 shows the distribution of drag coefficient over the rotor disk for $V = 1, 40$ and 100 kts. In hover, Fig. 6.16(a), the drag coefficient is almost axisymmetric, almost constant for the inboard 3/4 of the blade, and increasing towards the tip, where the angle of attack is higher. A small region of higher drag occurs in the back of the rotor about the $0.5R$ where the angle of attack also is higher. However, closer to the tip, the drag is higher near the front of the rotor. At $V = 40$ kts, shown in Fig. 6.16(b), two areas of higher drag are observed, coincident with the areas of higher angle of attack in the front-retreating side and at the rear of the rotor. At high speed, Fig. 6.16(c), the high speeds reached near the tip in the advancing side bring the blades into the transonic flow region, and compressibility

effects translate into areas of very high drag values.

The elemental drag distribution, $C_D M^2$ is shown in Fig. 6.17. In hover, Fig. 6.17(a), the factor of the square of the Mach number, M, makes the distribution slightly more axisymmetric. The local drag is, in general, fairly low at this speed. At $V = 40$ kts, Fig. 6.17(b), the values of the local drag are still low, with areas slightly larger where the angle of attack, α, and thus the drag coefficient, C_D, are higher. At 100 kts, the Mach number at the tip on the advancing side exceeds $M = 0.75$. The local elemental drag, shown in Fig. 6.17(c), clearly shows the effect of high Mach number and high compressibility drag caused by this same high M, with values of $C_D M^2$ reaching 0.02.

The variations in angle of attack affect, therefore, both the induced and profile torque generated by the rotor. Figures 6.18 and 6.19 show the distributions of elemental induced torque, $rC_L M^2 \sin\phi$, and elemental profile torque, $rC_D M^2 \cos\phi$ for $V = 1$ kt, $V = 40$ kts and $V = 100$ kts. In near hover conditions, both the induced and profile torque are almost axisymmetric, as shown in Figs. 6.18(a) and 6.19(a). The slight asymmetry is primarily caused by the asymmetry of the distribution of $\phi = \tan^{-1}(\frac{U_P}{U_T})$, which in turn depends on the slight forward speed of 1 kt and the longitudinal flapping $\beta_{1c} = 3$ degrees. The induced torque reaches values of 0.02 towards the tip for almost the entire azimuth, which combined with moderately high values of profile torque rear the tip for the entire azimuth, with values up to 0.008, contribute to high power required to hover, around 1724 hp, as seen in Fig. 6.1. At $V = 40$ kts, the overall induced torque goes down, Fig. 6.18(b), as the induced velocities are lower. Moreover, the higher values of local induced

torque move to the rear half of the rotor, where the induced velocities are higher. At this speed, the profile torque is still much lower than the induced torque. Both the induced and profile torque being lower than in hover, it follows that the power require to fly at 40 kts is also lower, around 1133 hp. As the speed increases, the Mach number on the advancing side increases. At $V = 100$ kts, the local profile torque distribution, in Fig. 6.19(c), shows an area of very high values near the tip of the advancing side, reaching values of 0.02 at the very tip, while it remains lower for the rest of the rotor. The induced torque continues to decrease as the induced velocities become lower with the highly skewed wake vortices, with maximum values of around 0.015 over a smaller region of the rotor than at lower speeds. The increase in torque due to the higher drag encountered at higher speeds in the advancing side increases the overall power required, while the decrease in induced torque reduces the power requirements, with values around 1063 hp, as shown in Fig. 6.1. As the speed continues to increase, the profile torque becomes dominant and the power required to fly at higher velocities increases further.

Figures 6.20 and 6.21 present the distribution of sectional pitching moment, C_M, and elemental pitching moment $C_M M^2$, for the same cases at $V = 1$ kt, $V = 40$ kts and $V = 100$ kts. In hover, both C_M and $C_M M^2$ appear almost axisymmetric, although it takes slightly higher values, even positive, at the front of the rotor, particularly towards the tips. At $V = 40$ kts, the highest, positive values occur at the rear of the rotor, although two other regions of high, albeit negative, C_M occur around $\psi = 100°$ and $\psi = 250°$. The case at $V = 100$ kts is characterized by a region of low, nose-down pitching moments throughout the advancing side, and

higher values in the front-retreating side. The variation in the pitching moment can be related to the changes in the lift distribution. The regions where the maximum pitching moment occurs are also those where the local lift coefficient is greater (Figs. 6.14(a) through 6.14(c)). Since the lift coefficient shown is located at the quarter chord, an increase in lift produces a nose up pitching moment, and similarly lower lift is reflected in more negative or nose down pitching moment over the elastic axis.

6.2.3 Blade dynamics

This section presents an analysis of the blade dynamics during straight and level flight, for the baseline model with 4 finite elements and a straight blade configuration.

Figure 6.22 shows the variation of the equivalent flapping angle at the tip of the blade β as a function of the azimuth angle ψ at $V = 1$ kt, 40 kts and 100 kts. In hover, the induced velocities and angle of attack distributions are almost axisymmetric (Figs. 6.11(a) and 6.12(a)), with slightly higher values of the angle of attack in the rear of the rotor, as described in Section 6.2.2. A close examination of the lift distribution (Fig. 6.14(a)) and the contribution of lift to the flapping moment, rC_LM^2 (Fig. 6.15(a)), as previously explained, reveals that the lift distribution is slightly biased, with values moderately larger in the rear of the rotor, producing a sinusoidal flapping response, rather than simple coning only. Figure 6.23(a) shows that the magnitude of the higher harmonics is really insignificant compared to the

first harmonic. The phase of the flapping response in hover is 35 degrees, as shown in Fig. 6.23(b). The presence of some longitudinal and lateral flapping ($\beta_{1c} = 1.5°$, $\beta_{1s} = 1.1°$) is necessary to orient the rotor for equilibrium with the fuselage, which is slightly oriented with a pitch attitude of $\theta = 4.7°$ and roll attitude of $\phi = -2.8°$ (Figs. 6.4 and 6.6). The longitudinal and lateral flapping coefficients respond to the cyclic controls in Fig. 6.3 and 6.5: a longitudinal cyclic of $\theta_{1s} = -1.7°$ producing a forward longitudinal tilt of the rotor by 1.5° and a lateral cyclic of $\theta_{1c} = 0.7°$ causing the lateral tilt of the rotor by 1.1°.

At $V = 40$ kts, the overall magnitude of the flapping response shown in Fig. 6.22 decreases, as fewer collective is necessary (Fig. 6.2), translating into a reduced coning angle ($\beta_0 = 3.1°$ down from $\beta_0 = 3.5°$ in hover) associated with the lower collective setting necessary for this flight condition (Fig. 6.2). The response over the azimuth, unlike the case of hover, indicates the presence of higher harmonics. Figure 6.23(a) shows that, while considerably smaller than the first harmonic, the magnitude of the second and third harmonic is significant. The cause for these higher harmonics can be found in the distribution of rC_LM^2 (Fig. 6.15(b)), the contribution of lift to the flapping moment has multiple regions where rC_LM^2 is higher, producing a 2/rev and a 3/rev variation in the flapping response. Figure 6.23(b) shows that the phase of the first and principal harmonic corresponds to the region of higher angle of attack around $\psi = 0°$, while the second and third harmonics, of much lower magnitude, are excited by the areas of higher rC_LM^2 found in the advancing and front-retreating sides.

The flapping response at $V = 100$ kts, depicted in Figs. 6.22 and 6.23 as

well, shows a decrease in the overall magnitude of the flapping angle ($\beta_0 = 2.7°$), with respect to the case of $V = 40$ kts. However, at this higher speed the cause is not the lower collective, which, after decreasing to a minimum at about 70 kts, starts to increase again; instead, it is the overall lower magnitude of the angle of attack over the rotor (Fig. 6.12(c)), which as shown in Section 6.2.2 produces lower magnitude rC_LM^2 (Fig. 6.15(c)). Some signs of the presence of higher harmonics are also visible in the flapping response at this speed. The dominant first harmonic is excited by the area of higher magnitude rC_LM^2 found in the rear of the rotor, while 2/rev and 3/rev variation in rC_LM^2, of smaller magnitude, excite the higher harmonics.

The equivalent lag angle at the blade tip, ζ, is shown in Fig. 6.24, for the cases of $V = 1$, 40 and 100 kts, as a function of the azimuth angle ψ. In hover, the lag angle is almost constant around $\zeta = -6$ degrees (ζ is positive for angles in the lead direction), with a slight sinusoidal variation of about a quarter of a degree around the rotor azimuth. The higher drag seen in the front of the rotor towards the tip, shown in Figs. 6.16(a) and 6.17(a), slightly increases the lag between $\psi = 90°$ and $\psi = 270°$, while the reduction in the drag force in the rear of the rotor allows the blade to lag less. At 40 kts, the overall drag over the rotor, shown in Figs. 6.16(b) and 6.17(b), decreases, and therefore the mean lag over the azimuth also decreases in magnitude, with an average value of around $\zeta = -4.2$ degrees, as seen in Fig. 6.24. The drag distribution, moreover, is not as close to axisymmetry as in hover, and higher drag occurs in the rear and advancing side of the rotor, while in the front and retreating side the drag is lower. As a consequence, the lag displacement increases

(becomes more negative) on the advancing side, while it decreases on the retreating side, with an overall variation over the azimuth of half a degree. At $V = 100$ kts, the drag increases considerably near the tip of the blade on the advancing side, although it decreases over the rest of the rotor (Figs. 6.16(c) and 6.17(c)). The overall reduction in drag reduces the average lag over the azimuth, Fig. 6.24, which at this speed has a mean around $\zeta = -4$ degrees, with an overall variation over the azimuth of half a degree. The higher drag on the advancing side increases the lag displacement, which reaches its maximum near the front of the rotor, while it decreases in the retreating side where the lower drag forces are found.

Figure 6.25 shows the magnitude and phase of the first three harmonics of the lag response at $V = 1$ kt, 40 kts and 100 kts. In all three cases, the presence of higher harmonics of similar magnitude indicate that the drag distribution excites a 1/rev, 2/rev and 3/rev variation in the lag displacement. In hover, the three first harmonics are similar in magnitude, although the constant lag coefficient ($\zeta_0 = -5.9$ degrees) is dominant and therefore the higher harmonics ($\zeta_{1c} = 0.1$, $\zeta_{1s} = 0.1$ and even lower second and third harmonic coefficients) are not clearly appreciated in Fig. 6.24. At $V = 40$ and 100 kts, the constant lag coefficient ζ_0 is lower than in hover, and the first harmonic is comparably larger, therefore the sinusoidal variation over the azimuth is more pronounced in Fig. 6.24.

The total elastic torsion deflection at the tip of the blade as a function of the azimuth is shown in Fig. 6.26, for speeds of $V = 1$ kt, 40 kts and 100 kts. The elastic twist in hover presents a sinusoidal distribution of a very moderate nose-down amplitude, with an overall twist variation over the rotor of around $\Delta\phi = 0.5$

degrees, with a mean value of around $\phi = -0.5$ degrees. At the $V = 40$ kt case, the overall peak-to-valley amplitude increases, and the torsion deflection is no longer negative for the entire range of the azimuth, with a variation in ϕ between -0.7 and 1.1 degrees. Moreover, the presence of higher harmonic excitations becomes evident. The increase in the magnitude of the peak-to-valley variation of the elastic twist continues with the $V = 100$ kt case, which now ranges between -1.2 and 1.0 degree. At this speed, the elastic twist also shows signs of the presence of higher harmonic excitations, although to a lesser extent that at $V = 40$ kts.

Figure 6.27 shows the magnitude and phase of the harmonics of the elastic torsion response at $V = 1$ kt, 40 kts and 100 kts. At $V = 1$ kt, the magnitude of the first harmonic is clearly dominant, with a value of 0.24 degrees over the almost negligible 0.03 and 0.02 of the second and third harmonic. At 40 kts, the magnitude of the first harmonic increases to 0.61 degrees. The second and third harmonic become significant, with magnitudes of 0.24 and 0.38 degrees respectively, i.e., approximately half the value of the first harmonic. At 100 kts, the magnitude of the first harmonic increases further to 0.97 degrees. The second and third harmonics have magnitudes comparable to those at 40 kts, 0.37 and 0.23 degrees respectively, but they are proportionally lower than the first harmonic than at $V = 40$ kts.

To understand the behavior of the torsion of the blade with speed, one must look at the distribution of pitching moment over the rotor, shown in Fig. 6.20, or the elemental pitching moment distribution, $C_M M^2$, in Fig. 6.21. The distribution seen at 1 kt appears almost axisymmetric, although the values of pitching moment are slightly larger at the front of the rotor than at the rear, which corresponds with

the simple low-magnitude, 1-harmonic twist distribution observed at this speed. At 40 kts, the pitching moment distribution shows three identifiable areas of low, nose-down values, which twist the blade nose-down, and three areas of higher, even positive values, which produce a nose-up torsional deflection. This is reflected in Fig. 6.26, in which the torsional deflection reaches a local minimum for each minimum of the pitching moment in Figs. 6.20(b) and 6.21(b), around $\psi = 80°, 180°$ and 300°, while the positive areas of the pitching moment, the highest at around $\psi = 0°$ and others around $\psi = 130°$ and 250°, produce the positive values of twist. A similar behavior is observed at 100 kts. On the advancing side, the pitching moments are low and produce a nose-down twist of the blade, as seen in Figs. 6.20(c) and 6.21(c), producing a minimum twist deflection of $\phi = -1.1$ degrees around $\psi = 100°$, depicted in Fig. 6.26. The maximum values of the pitching moment are found on the retreating side, twisting the blade up to $\phi = 1$ degree at the rear of the rotor.

6.2.4 Effect of blade modeling

This section studies the effect of modeling blade flexibility on the trim solution and compares the results obtained with the flexible blade model used throughout this thesis, which includes the five lowest natural frequencies and mode shapes, with a simpler rigid model, which only includes the two lowest frequencies, corresponding the the rigid flap and lag modes.

The predictions of main rotor power obtained using the two models are shown

in Fig. 6.28. The predictions of the simplified, rigid blade model is on average about 10% lower than those of the flexible blade model. In the lower speed range, this makes the rigid blade model under-predict the power required by the main rotor. In high speed, however, the flexible blade model over-predicts the experimental values available, while the rigid blade model captures them better.

Figure 6.29 shows the main rotor collective setting. As for the case of the power required, the rigid blade model predicts lower values of the collective by about 5%.

The differences in the predicted values for power and collective can be explained by looking both at the blade elastic torsion and the inflow distribution.

The elastic torsional tip displacement, shown in Fig. 6.26 indicates that with the elastic blade, an overall nose-down twist is present on the blade. This negative torsion reduces the geometric angle of attack of the blade. Therefore, to produce the same thrust, the rigid blade model needs less collective.

The induced velocities predicted by the rigid blade model are lower than with the flexible blade model, as seen in Fig. 6.30 for the case of near hover conditions. This can be explained as follows.The induced velocities depend, among others, on two parameters that are affected by the modeling of the blade, namely the flapping angle and the bound circulation. This lower flap angle is passed on the the free wake model and affects the induced velocities.

The time histories of the flapping angle at $V = 1$ kt, predicted using the two models, are shown in Fig. 6.31. The flap angle is smaller with the rigid blade model than with the flexible blade model.

If the elastic displacements are ignored, then the local airflow velocities will

be affected, and so will be the circulation and the inflow.

Figure 6.32 shows the x and z-components of the blade sectional velocity in the blade undeformed coordinate system along the blade span at $\psi = 0$ and $\psi = 180$ degrees at $V = 1$ kt. The plots show that the differences between the rigid and flexible blade models are significant, The bound circulation, which is calculated with the local airflow velocities (see Section 3.6), will therefore be also affected.

Figure 6.6 shows a longitudinal cross section of the bound circulation at $\psi = 0$ and $\psi = 180$ degrees. Except for the root of the blade, the flexible blade model predicts an overall higher bound circulation, which translates into stronger tip vortices and higher induced velocities over the rotor.

6.2.5 Effect of the swept tip

This section presents the results of including the swept tip in the blade modeling. Figure 6.34 shows the comparison of the main rotor power required with experimental values, both with the simplified straight blade and the swept tip blade, as a function of flight speed. For V less than 40 kts, the power required with the swept tip blade is lower than the equivalent straight blade configuration. Between 40 and 100 kts, the power predicted by the swept tip blade model is higher. For V greater than 100 kts, it becomes progressively lower. The difference in predictions can be better understood by considering the various components of the required power.

The collective setting as a function of speed, both with the straight and swept blade models, is shown in Fig. 6.35. At very low and very high speeds, both models

trim to a similar collective position. In the middle range of speeds, however, the swept tip blade model trims to higher values of collective, significantly overpredicting the experimental values. These higher collective angles increase the total geometric angle of attack and therefore affect the flapping response, the bound circulation and the overall induced velocities, and therefore, the power required. This higher values of collective are also seen in other studies in the literature, such as in Ref. 130.

The elemental induced and profile torque distributions at hover, 60 kts and 158 kts are shown in Figs. 6.36 through 6.37 (note that a different color range is used for the profile power at 158 kts because the values at that speed are a full order of magnitude higher than in the other speeds shown, and using the same color scheme for all would render the plots indistinguishable at the lower speeds), with a straight tip blade model (top) and with the swept blade model (bottom). Figure 6.37(b) shows that, at $V = 1$ kt, the elemental profile torque inboard of the swept tip junction is higher than in the corresponding straight blade model, but it decreases dramatically outboard of the junction because of the lower velocities perpendicular to the blade section. The elemental induced torque, $rC_L M^2 \sin\phi$, shown in Fig. 6.36(b), is very similar both with the straight and the swept tip blade models, although the swept blade model shows slightly higher values in the retreating side. The overall effect is that the power required to hover is slightly lower for the swept tip model. At 60 kts, the elemental profile torque for the swept tip blade is significantly lower, compared to the straight blade (Fig. 6.37(d)). This reduction, however, does not make up for the higher induced torque (Fig. 6.36(d)), which increases specially in the rear of the rotor. As a result, the overall power with

the swept tip is higher. At $V = 158$ kts, both the overall induced and profile torque distributions result in a lower power required for the swept tip blade, which is in a better agreement with the flight test data of Fig. 6.34.

Figures 6.38(b) through 6.38(f) show the distributions of induced velocities for $V = 1$ kt, 60 kts and 158 kts with a straight tip blade model and with the swept blade model. In hover, the induced velocities predicted by both blade models are very similar, although the swept tip model is slightly higher (the overall inflow norm is $\|\lambda\| = 0.0804$ with the straight tip, and $\|\lambda\| = 0.0822$ with the inclusion of the swept tip). At $V = 60$ kts, the swept tip model produces higher induced velocities in the rear of the rotor, which increases the overall inflow (from $\|\lambda\| = 0.0373$ for the straight blade model to $\|\lambda\| = 0.0464$ for the swept one). At $V = 158$ kts, the inflow over most of the rotor is lower with the swept tip model, although there is a thin region of very high values at the tip of the blade.

The bound circulation distributions for the same cases above is shown in Figs. 6.39(b) through 6.39(f). In hover, the circulations obtained are very similar, which explains the similar induced velocities observed earlier. At $V = 60$ kts, the swept tip blade has regions of higher induced velocity, particularly on the retreating side. This translates into a higher tip vortex strength, which explains the higher induced velocities seen in that region (Fig. 6.38(d)). At $V = 158$ kts, there is a region of very high circulation in the front of the rotor, which produces a strong tip vortex that in turn causes the very high values of inflow close to the tip observed in Fig. 6.38(f). Notice that the bound circulation at this high speed does now show signs of strong tip vortex on the advancing side. This may be an indication at at

these high speeds the single-tip vortex model might not be sufficient and multiple-trailed vortices might be necessary. The present study, however, will not address such aerodynamic issues, and the baseline wake model with a single tip vortex will be used throughout.

Notice that to include the effect of sweeping the blade tip in the free wake model, the only approach consisted of moving the collocation points in the blade sections of the tip backwards by distance corresponding to the difference between the straight and swept elastic axes at each given radial location. No further consideration has been made in the free wake to account for the swept tip. Given that there have not been any particular studies of the stand-alone free wake model with blades with swept tips, this was the only approach considered. A recommendation for the future would include the study of the free wake with swept tip blades to better understand the behavior seen in the present study, which might include multiple trailed vortices and dual-peak bound circulation calculation.

6.3 Steady level coordinated turns

Several turns are performed with a velocity along the trajectory of $V = 60$ kts and at rates of turn between $\dot{\psi} = -25$ and $\dot{\psi} = 25$ deg/sec.

6.3.1 Analysis of trim results

The experimental trim results (Ref. 10) are presented as a function of the roll attitude rather than the turn rate, therefore, the same representation will be used for

all the results presented in this section. The relation between the roll angle and the turn rate is given in Fig. 6.40. This relation is almost linear for the range of turn rates considered in this study. Therefore, for the sake of simplicity, both terms will be used interchangeably in this discussion.

A parameter that helps indicate the severity of the turn is the load factor. For the cases in the present study the values are shown in Fig. 6.41. For level flight, the load factor is zero, and it increases parabolically with the increase of bank angle, in the same manner for both left and right turns.

The predicted power required is compared with the experimental data in Fig. 6.42(a). Power is slightly overestimated for roll angles ϕ below about 40°. For higher values of ϕ, the predictions still follow the general trend of the flight test data, but because of the much higher slope of the curve, the overpredictions are higher. The right turns tend to require slightly higher power than the corresponding left turns.

The main rotor collective, δ_{col}, shows an excellent correlation with the flight test data, as seen in Fig. 6.42(b).

Figure 6.43(a) shows the lateral cyclic, δ_{lat} as a function of roll angle ϕ. While for straight and level flight ($\phi = 0°$) δ_{lat} is slightly underpredicted, the agreement improves in turns, both right and left.

The longitudinal cyclic, δ_{lon}, shown in Fig. 6.43(b), is not predicted very accurately, and the variations with ϕ show a different trend from the flight test data.

Figure 6.44(a) shows the pitch attitude, θ. Although the trend in the flight test data is somewhat captured in the left turns, the predictions are poor. Comparing

this figure with Fig. 6.43(b), it can be seen that wherever the longitudinal cyclic is underpredicted, producing a more forward tilt of the tip path plane, the body shows a larger nose-up pitch attitude θ. This suggests that the modeling of the fuselage and the rotor downwash-fuselage interaction, which is neglected in the theoretical results, might be a primary reason for the discrepancy with the flight test data.

The pitch rate q is shown in Fig. 6.44(b). The theoretical results are in excellent agreement with the flight test data, for the entire range of turn rates. No flight test data was available to correlate the roll rate predictions, shown in Fig. 6.44(c). The predicted results indicate that a negative mild roll rate needs to be applied for most turn cases. Right turns, in particular, need a more negative roll rate than the left turns.

Figure 6.45(a) presents the pedal setting, δ_{ped} The predictions are reasonably accurate. Note that for the higher turn rates, where the overall power required predicted by the model is much higher than the flight test data, the tail rotor predictions decrease well below the expected experimental values to counteract the additional torque (a decrease in percentage of the pedal setting means an increase in the tail rotor collective, with 0% corresponding to 2.69 in to the left, or 29.9 degrees of tail rotor collective, and 100% corresponding to 2.69 in to the right, or 0.1 degrees of tail rotor collective).

Finally, Fig. 6.45(b) shows the yaw rate r as a function of the roll angle ϕ. The yaw rate is an almost linear function of the roll angle, and is in an excellent agreement with the experimental values.

Figures 6.46, 6.47 and 6.48 show, respectively, the side, rear and top views

of the tip vortex geometry for turn rates of $\dot{\psi} = 0$, ± 5, ± 15 and ± 25 deg/sec. At $\dot{\psi} = 5$ deg/sec (right turn), the angular rates of the body, in roll, pitch and yaw, are still very small, with values of $p = -0.2$ deg/sec (Fig. 6.44(c)), $q = 1.3$ deg/sec (Fig. 6.44(b)) and $r = 4.8$ deg/sec (Fig. 6.45(b)). Such small angular rates do not deform the wake geometry significantly (the only appreciable difference is due to the orientation of the rotor). Similarly, at $\dot{\psi} = -5$ deg/sec (left turn), the angular rates are small and the wake geometry resembles that in level flight. As the turn rate increases to $\dot{\psi} = \pm 15$ deg/sec, the angular rates increase slightly, however not enough to produce major deformations on the geometry described by the tip vortices. The roll rate p is around 1.0 deg/sec or less, too small to have any effect on the wake geometry. The rear view, Fig. 6.47, shows a very small difference in the geometry due to the effect of the pitch and yaw rates (as the effect of the roll rate is negligible), particularly in the right turn, which shows that the far wake remains slightly closer to the plane of the rotor than it does in level flight. The pitch rate q is slightly larger, around 9.0 deg/sec for both left and right turns, and the side view, Fig. 6.46, shows that the vortex filaments are compressed closer together in the upper part of the wake (closer to the rotor), while the distance between them increases in the lower part of the wake. The yaw rate r is about ± 11.5 deg/sec for right and left turns respectively and the top view of the wake, Fig. 6.48, shows that the edges of the wake (as seen from the top) are more compressed that in level flight. For turns at $\dot{\psi} = \pm 25$ deg/sec, the angular rates are large enough to significantly deform the wake geometry. The pitch rate, q, takes values around 20 deg/sec for left and right turns and its effect is to contract the wake on the top, with vortex

filaments much closer together than at $\dot{\psi} = \pm 15$ deg/sec, while further increasing the distance between each filament at the bottom of the wake. This is seen as a "flattening" of the free wake geometry, particularly obvious at the top and in the advancing side as seen from the side, Fig. 6.46. The effect is similar on turns to both sides, although the different pitch attitude gives an apparently different appearance. The roll rate p is still small, -2.0 deg/sec for left turns and -4.2 deg/sec for right turns. Its effect, together with the effect of the higher pitch and yaw rates, can now be appreciated in the rear view of the vortex filaments, Fig. 6.47, which also shows signs of the "flattening" seen from the side, as well as increased bundling of the vortices on the advancing side for the turn to the right, and reciprocally on the retreating side for left turns. The effect of the yaw rate, r, with values of ± 14.5 deg/sec approximately, is to push the vortex filaments inwards into the wake structure in the advancing side in the right turns. In the left turns, however, the vortex filaments are not as changed in the advancing side as in the right turns, but in the retreating side they are pushed closer together by effect of the yaw rate.

The induced velocities λ at turn rates of $\dot{\psi} = 0, \pm 5, \pm 15$ and ± 25 deg/sec are shown in Fig. 6.49. With increasing turn rate, the pitch rate increases nose up for both left and right turns (see Fig. 6.44(b)). This brings the wake progressively closer to the plane of the rotor, particularly to the rear (see Fig. 6.46), and consequently the induced velocities increase over the entire rotor, less negative in the front and higher and positive in the rear of the rotor, but specially in the rear where the influence of the nearby vortex filaments is higher.

Figure 6.50 shows the distribution of angle of attack α over the rotor disk

for turn rates of $0, \pm 5, \pm 15$ and ± 25 deg/sec. For low turn rates, such as $\dot{\psi} = \pm 5$ deg/sec, the changes in the distribution of angle of attack from level flight are small and can barely be appreciated. However, as the turn rate $\dot{\psi}$ increases, the angle of attack α increases over the entire rotor by an average of 4 to 6 degrees, particularly around $\psi = 0^\circ$ and in the third quarter of the rotor, between $\psi = 180^\circ$ and $\psi = 270^\circ$, where it reaches values upward of 10 degrees. As described by Eq.(2.56), the angle of attack α depends on the geometric pitch θ_G, given by Eq.(2.55), and the velocities perpendicular and tangential to the airfoil section, U_P and U_T respectively. In level flight, the change in angle of attack is due mostly to the variation in U_P caused by changes in the inflow distribution λ. In turning flight, however, the orientation of the rotor with respect to the incoming airflow, which affect the distribution of U_P and U_T, and the azimuthal variation of the geometric pitch of the blade (Fig. 6.64), make the relationship less straightforward.

The lift coefficient, C_L, distribution for the turns at $\dot{\psi} = 0, \pm 5, \pm 15$ and ± 25 deg/sec is shown in Fig. 6.51. The lift coefficient is a function of both angle of attack α and Mach number M (Fig. 5.1). As for the angle of attack, the difference in the distribution in lift coefficient between level flight and turns at low rates such as $\dot{\psi} = \pm 5$ deg/sec. At larger turn rates, $\dot{\psi} = \pm 25$ deg/sec, the values of C_L over the rotor increase by about 0.6, with the largest values in the same areas where the angle of attack is maximum, i.e., around $\psi = 0^\circ$ and between $\psi = 180^\circ$ and $\psi = 270^\circ$, where it reaches values of 1.1.

Figure 6.52 shows the elemental lift distribution, $C_L M^2$, corresponding to the same turn cases at $\dot{\psi} = 0, \pm 5, \pm 15$ and ± 25 deg/sec. The factor of M^2, which

increases radially towards the tips and is larger on the advancing than on the retreating side, biases the local lift distribution towards the tip and to the advancing side, while the areas inboard of the blade, where the Mach number is low, become regligible. Although the lift coefficient does not significantly change between level flight and $\dot{\psi} = \pm 5$ deg/sec, a slightly larger Mach number at this turn rates translates into some minor but appreciable differences in the elemental lift values near the tips. As the turn rate increases, so do the values of $C_L M^2$ near the tips, particularly around $\psi = 0°$ and between $\psi = 180°$ and $\psi = 270°$ where C_L is larger, but also around $\psi = 90°$, where both C_L and M are of significance. At $\dot{\psi} = \pm 25$ deg/sec, the values of $C_L M^2$ in these areas become even larger, of particular importance in the advancing side where the effect of the maximum Mach number is dominant, and where the elemental lift reaches values around 0.35.

The local flap moment distribution, $rC_L M^2$, which indicates the contribution of the local lift to the flapping angle, is shown in Fig. 6.53 for the turns considered at $\dot{\psi} = 0, \pm 5, \pm 15$ and ± 25 deg/sec. The values of $rC_L M^2$ mimic those of the elemental lift $C_L M^2$ in Fig. 6.52, although slightly more biased towards the tip by the factor of the nondimensional radius r.

Figure 6.54 shows the drag coefficient, C_D, distribution for turns at $\dot{\psi} = 0, \pm 5, \pm 15$ and ± 25 deg/sec. At low turn rates, the drag coefficient over the rotor is very similar to the values at level flight. At $\dot{\psi} = \pm 25$ deg/sec, however, the high values of angle of attack α (Fig. 6.50) and Mach number that are found towards the tip of the blade increase the drag coefficient from an average of 0.01 in level flight to 0.03 and larger near the tips. Around $\psi = 90°$, particularly, the drag coefficient

reaches value of 0.08.

The distribution of elemental drag, $C_D M^2$, for turns at $\dot{\psi} = 0, \pm 5, \pm 15$ and ± 25 deg/sec, is shown in Fig. 6.55. As for the elemental lift, the effect of the square of the Mach number is to bias the values towards those areas where M is highest, i.e., the tips and mostly in the advancing side. The values of $C_D M^2$ mirror those of C_D with the biased described above, reaching values at $\dot{\psi} = \pm 25$ deg/sec of 0.035 towards the tip around $\psi = 90°$.

The elemental induced torque, $rC_L M^2 \sin\phi$, seen in Fig. 6.56 for turns at $\dot{\psi} = 0, \pm 5, \pm 15$ and ± 25 deg/sec, increases in the rear of the rotor with increasing turn rate. At low turn rates of $\dot{\psi} = \pm 5$ deg/sec, the change from level flight is insignificant. As the turn rate increases, particularly at $\dot{\psi} = \pm 25$ deg/sec, where at the rear of the rotor the values reach 0.04. The first part of the induced torque, $rC_L M^2$, seen in Fig. 6.53, is higher towards the tip, with values particularly high in the advancing side. However, the second term, $\sin\phi$, depends directly on the inflow, shown in Fig. 6.49. The induced velocities in the front of the rotor are particularly low, close to zero, negating the effect of the high $rC_L M^2$ near the tip at $\psi = 90°$. In the rear, however, it reaches values around 0.2, with the consequent effect of increasing the induced torque in this region of the rotor.

Figure 6.57 shows the elemental profile torque, $rC_D M^2 \cos\phi$, at turn rates of $\pm 5, \pm 15$ and ± 25 deg/sec. While the profile torque remains low for the low and moderate turn rates, at ± 25 deg/sec the profile drag increases considerably near the tip in the advancing side (see Fig. 6.55) increasing the values of the profile torque near the tips, particularly around $\psi = 90°$ where it reaches a value of 0.03.

For moderate turns, the primary change from level flight is in the induced power which is a function of the increased rotor thrust. The increase is higher in the right turns (as it is for in the induced velocities as well), and thus the power required is higher in right turns than in left turns (Fig. 6.42(a)). However, the higher induced torque is not the only cause for the increase in power required. Like in the induced torque, the profile torque is also higher in the right turns, contributing further to the higher power required to perform the right turns.

Figure 6.58 shows the pitching moment coefficient, C_M over the rotor disk for turns at $\dot{\psi} = 0, \pm 5, \pm 15$ and ± 25 deg/sec. The moment coefficient is a function of the angle of attack α and the Mach number M, as described by Fig. 5.3. For low positive values of α, the moment coefficient is almost constant and negative. For low Mach numbers, beyond $\alpha = 10°$, C_M increases into the positive realm before dropping with large nose-down values. For higher Mach numbers, the same behavior is observed, but it occurs for angles of attack higher than $\alpha = 5°$. For very high Mach numbers approaching unity, the moment coefficient quickly drops into large negative values even for very low angles of attack. At low turn rates, the moment coefficient looks very similar to level flight, i.e., a moderate negative value around -0.01 for much of the rotor disk, except for very negative values close to the tip on the advancing side, where the angle of attack is negative and the Mach number is large, and two regions of higher, close to positive values around $\psi = 0°$ and on the outer part of the third quadrant, between $\psi = 180°$ and $\psi = 270°$, where the angle of attack is higher. As the turn rate increases, both left and right, so does the angle of attack, and therefore the moment coefficient becomes positive in

the areas described above. Moreover, the angle of attack also increases over the advancing side, where the Mach number is also higher, and the moment coefficient increases overall, particularly in a pocket around $\psi = 90°$. For very high turn rates, $\dot{\psi} = \pm 25°$, much of the outer part of the rotor is operating at angles of attack and Mach numbers high enough to produce positive moment coefficients. In addition, the angle of attack at the tip around $\psi = 90°$ reaches values around 6° to 8° (higher on the right turns) at a point where the Mach number reaches $M = 0.7$. This brings the moment coefficient beyond the maximum positive value into the large negative drop, and therefore in this area C_M takes very low values around -0.03 (over a slightly larger area on the right turn than the left).

The elemental pitching moment, $C_M M^2$, is shown in Fig. 6.59 for the same cases at $\dot{\psi} = 0, \pm 5, \pm 15$ and ± 25 deg/sec. The factor M^2 makes only the values near the tips important, as inboard of the blade the Mach number tends to zero. The local moment, therefore, is almost uniform for the inner part of the rotor for almost all the turn cases, with negative values close to zero. Like C_M, the values of $C_M M^2$ increase into the positive range in the areas where the angle of attack is highest, on the third quadrant and at the rear of the rotor. And as for C_M, a pocket of very large negative local moment is found around $\psi = 90°$ where both α and M are high.

6.3.2 Blade dynamics

This section presents an analysis of the blade dynamics in turning flight.

Figure 6.60 shows the variation of the equivalent flapping angle β at the tip of the blade as a function of the azimuth angle ψ for turns at $\dot{\psi} = 0, \pm 5, \pm 15$ and ± 25 deg/sec. As the turn rate increases, both left and right, the equivalent flap angle β increases. For low turn rates, such as $\dot{\psi} = \pm 5$ deg/sec, the flap angle is only slightly larger than in level flight between $\psi = 270°$ and $\psi = 90°$, i.e., on the rear half of the rotor. For turn rates of $\dot{\psi} = \pm 15$ deg/sec, the flap angle is about 1 degree larger in the front half of the rotor, while in the rear the increase reaches about 2 degrees over the level flight flap angle. For much higher turn rates, $\dot{\psi} = \pm 25$ deg/sec, the same is observed, with an additional 2 degrees more flap angle that at $\dot{\psi} = \pm 15$ deg/sec turns. Moreover, for all turn rates, the flap angle in right turns is slightly higher than for the left counterpart. The magnitude and phase of the flap time histories are shown in Fig. 6.61. The first harmonic is much larger than the higher harmonics, with values increases from 0.8 degrees in level flight to about 1.7 in turns at $\dot{\psi} = \pm 25$ deg/sec.

The local flap moment shown in Fig. 6.53 contributes to understanding the flapping response in turning flight. As the turn rate increases, the overall value of $rC_L M^2$ increases, therefore increasing the magnitude of the flapping response around the azimuth. At the higher rates, it is possible to appreciate that the flap moment is slightly higher on the right turns, and thus the flap angle is also slightly higher. At the lower rates, the flap moment is very similar on both left and right

turns, although slightly higher around $\psi = 0°$ on the right turns, producing slightly larger flap angle in the rear of the rotor. In general, the lower values of rC_LM^2 on the advancing side, particularly on the second quadrant of the rotor, decrease the flap angle; the higher values on the third quadrant increase the flap on the blade, which increases between $\psi = 180°$ and $\psi = 270°$; on the third quadrant the local flap decreases significantly, and thus the flap goes down, before increasing again at the rear of the rotor due to the higher values of rC_LM^2 around $\psi = 0°$.

Figure 6.62 shows the the equivalent lag angle ζ at the tip as a function of azimuth angle ψ for the turn rates shown above. In level flight, the variation of the lag angle over the azimuth is almost flat, with very small amplitude, and a mean value about $\zeta = -3.5°$. For moderate turns at $\dot{\psi} = \pm 5$ deg/sec, the lag time history is very similar, although the lag is slightly larger (more negative) by about 0.5°. At $\dot{\psi} = \pm 15$ deg/sec, the lag angle increases over the entire azimuth, to a mean value around $\zeta = -4.5°$, with a slightly larger amplitude of about 0.7°. At $\dot{\psi} = \pm 25$ deg/sec, the lag increases considerably, doubling to an average value of about $\zeta = -8.5°$ to $-9°$. The amplitude of the response also increases to about 1.5°. In all cases, the lag angle is higher on the right turns than on the left ones, with the difference increasing with $\dot{\psi}$. The response at all turn rates is mostly a 1/rev variation, with the magnitude of the first harmonic much larger than the higher harmonics, as shown in Fig. 6.63.

The local drag distribution, shown in Fig. 6.55, explains the lag response obtain at different turn rates. In level flight and at low turn rates, the drag is very low and almost uniform (with values around 0.005), except for slightly larger values on the

advancing side. The lag, therefore, is low and has almost the same value around the azimuth, with slightly larger values on the advancing side where the drag is higher. As the turn rate increases to $\dot{\psi} = \pm 15$ deg/sec, a pocket of higher drag on the advancing side (close to 0.01) and overall slightly larger values around the azimuth increase both the average lag displacement around the azimuth as well as the difference between the values on the advancing and retreating side. At $\dot{\psi} = \pm 25$ deg/sec, the drag increases considerably, mostly on the advancing side and around $\psi = 0°$, specially at around $\psi = 90°$, where the local drag reaches values of 0.035. As a consequence, the lag displacement also increases considerably, specially on the advancing side where the drag is higher. At this turn rate, the difference between left and right turns is visible, with both larger values of $C_D M^2$ over slightly larger areas on the right turns.

Figure 6.64 shows the elastic torsional deflection ϕ at the tip of the blade as a function of azimuth angle. The magnitude and phase of the first three torsional harmonics are shown in Fig. 6.65. The elastic torsional response shows multiple local maxima and minima, particularly at the higher turn rates. In level flight and low turn rates of $\dot{\psi} = \pm 5$ deg/sec, ϕ is maximum a the rear of the rotor, then decreases up to $\psi = 100°$, and then increases slowly until it reaches the maximum at the rear of the rotor, with a small local peak around $\psi = 270°$. At these turn rates, the first harmonic, much larger than the higher harmonics in magnitude, dominates the response, although it is distorted by the presence of higher harmonics. At turn rates of $\dot{\psi} = \pm 15$ deg/sec, the magnitude of the first harmonics does not change, although the proportion between the first and the second and third harmonics decreases. The

response is similar to the one at lower rates in magnitude, although several local maxima are observed, at around $\psi = 0°$, $\psi = 120°$ and $\psi = 270°$, approximately. At much higher turn rates, $\dot{\psi} = \pm 25$ deg/sec, the magnitude of the first harmonic still remains the same, but the second and third harmonic increase in magnitude to about 2/3 of that of the first harmonic. The overall amplitude and mean value of the elastic torsion response increase, and the oscillations at the 2/rev and 3/rev frequencies dominate the response.

The moment coefficient distribution at different turn rates, shown in Fig. 6.58, is helpful in understanding the torsional behavior of the blade during turns. If C_M is positive, a nose-up deflection of the blade occurs, while negative values of the moment coefficient produce a nose-down twist. In level flight and at $\dot{\psi} = \pm 5$ deg/sec, there are two regions of mildly positive C_M, around $\psi = 0$ and on the third quadrant of the rotor, between $\psi = 180°$ and $\psi = 270°$, that cause the blade to twist up. At higher turn rates, $\dot{\psi} = \pm 15$ deg/sec, the pitching moment in these two areas increases, with another area of positive C_M appearing between $\psi = 90°$ and $\psi = 120°$; these three areas produce local maxima of the torsional response, which decreases in between. At very high turn rates, $\dot{\psi} = \pm 25$ deg/sec, there are regions of both large positive and negative ($\psi \approx 90°$), which excite the higher harmonic oscillations observed in the torsional response.

6.4 Climbing and descending flight

The results for the climb and descent cases presented in this section were obtained at a speed $V = 60$ kts. Results were calculated for a range of flight path angles, between $\gamma = -20°$ and $\gamma = 20°$.

6.4.1 Analysis of trim results

Figure 6.66(a) compares the predicted power required by the main rotor with the experimental values of Ref. 10. Only five experimental values are available. The point at $V_c = 500$ ft/min is well captured. For the three points at descent rates of $V_c = 1000$ ft/min and above, the predictions are in good agreement with the test data, taking into account the scatter in the measurements. For this range of V_c the power required by the rotor goes to zero, which can be interpreted as an autorotative flight condition. Finally, the power at $V_c = 3257$ ft/min is overpredicted.

Figure 6.66(b) shows the collective setting δ_{col} for the same flight conditions as in Fig. 6.66(a). The level of agreement with flight test data is mostly the same, except that at $V_c = 3257$ ft/min the correlation is greatly improved.

Figures 6.67(a) and 6.67(b) show the longitudinal and lateral stick positions δ_{lon} and δ_{lat}. The longitudinal cyclic is in reasonable agreement with the experimental data. In climbing flight, δ_{lon} remains fairly flat; in descents it decreases slightly. The lateral cyclic δ_{lat} is also fairly constant with flight path angle, both in climbs and descents, but it appears to be predicted less accurately.

The helicopter pitch attitude θ is shown in Fig. 6.68(a). The simulation over-

predicts θ by 1 to 3 degrees, although the predicted behavior has the same trend as the flight test data. Two factors need to be taken into account. First, extrapolating from Fig. 6.4, the level flight value at 60 kts appears to be overpredicted by nearly 2 degrees, and this offset probably affects the cases obtained at different climb and descents angles. Moreover, the longitudinal cyclic δ_{lon} (Fig. 6.67(a)) is underpredicted for the entire range of flight path angles, with higher deviation from the experimental values in climb than in descent, where the difference in the pitch attitude θ is higher. The trim solution seems to be compensating an additional nose up pitch of the fuselage with additional δ_{lon} to produce a forward tilt of the TPP (see Fig. 6.98). A possible explanation could be the lack of modeling of the rotor-fuselage aerodynamic interactions, which are not considered in the present study.

Finally, Fig. 6.68(b) shows the delta position, δ_{ped}. As the power decreases with increasing descent angle, the torque that the tail has to counteract is reduced, and therefore less tail rotor collective is needed. The reverse occurs in climbing flight. This trend is predicted correctly , however, the pedal is overpredicted by 10-15% of its total excursion, especially in descents.

The behavior of the wake in climbing flight is shown in Figs. 6.69 through 6.71. Figure 6.69 shows the side view of the wake geometry for climb angles from $\gamma = 0°$ to 18°. For low climb angles, the wake remains close to the rotor. As γ increases, the vortex filaments are convected farther down from the rotor, and their influence at the rotor plane is reduced. This is also clear in the rear view of the wake geometry, Fig. 6.70.The top view, Fig. 6.71, shows that with increasing γ the vortex filaments grow apart and the wake stretches farther downstream. Recall that all the wakes

are calculated with the same vortex length of 1440 degrees.

The side view of the wake geometry for descent angles from $\gamma = 0°$ to $-18°$ is shown in Fig. 6.72. For level flight, the wake is trailed behind and below the rotor, but as the flight path angle decreases beyond approximately $\gamma = -9°$ the vortex filaments start to get closer to the rotor and eventually cross above the rotor plane. For steeper descents, $\gamma < -18°$, the entire wake is above the plane of the rotor, organized again into a cleaner helical structure and the helicopter is in the windmill brake state. Figure 6.73 shows the rear views of the wake. In level flight, there is some roll up of the wake, mostly on the advancing side. As the angle of descent increases, the roll up becomes more pronounced, with the near rolled up bundles initially over the rotor plane and then progressively moving below the rotor plane. At high descent angles the wake is fully over the rotor plane and the roll up becomes less evident, eventually The top views are shown in Fig. 6.74. For low values of γ, the vortex filaments remain bundled and tight, but as the descent angle increases and the wake goes over the rotor plane, the distance between the vortex filaments increases and the interaction between filaments is reduced until it almost disappears.

The inflow distribution for the different climb cases is shown in Fig. 6.75. As the climb angle increases and the wake is washed farther down from the rotor plane, the influence of the vortex filaments decreases and so does their effect on the inflow at the rear of the rotor. With increasing climb, the wake skew angle is also reduced, the vortices become closer at the front of the rotor and the induced velocities become less negative there. In particular, it is observed that between $\gamma = 6°$ and $\gamma = 9°$,

the inflow barely changes in the rear of the rotor, while it becomes less negative in the front. Between $\gamma = 9°$ and $\gamma = 12°$, the increased proximity of the vortices to the front of the rotor increases the inflow there, while decreasing it in the rear of the rotor.

The inflow distribution in descending flight is shown in Fig. 6.76. For low angles of descent, the vortex filaments get closer to the rotor plane, and their effect becomes noticeable in the induced velocities. For flight path angles between $\gamma = -3°$ and $\gamma = -6°$, some ripples can be seen in the inflow distribution over the rotor disk. These are areas where blade-vortex interactions (BVI) are likely to occur. As the descent angle becomes steeper the upwash induced by the forward velocity decreases, while the effect of the wake vortices now crossing over the rotor plane is reflected in higher but irregular induced velocities in the rear half of the rotor. Eventually, these irregular patterns seen in the inflow disappear when the helicopter enters the windmill brake state and the wake reforms into a clean helical structure over the rotor.

The changes in the distribution of the induced velocities with climb angle are reflected in the angle of attack, and therefore in the lift distribution over the rotor. However, notice that, for climbing and descending flight, not only the inflow, but also the climb or descent velocities play an important role in determining the local blade angle of attack α, as well as the changes in the forward velocity due to the increasing flight path angle and any changes in the geometric pitch of the blade. Figure 6.77 shows the distribution of angle of attack α over the rotor for different climb angles. At low values of γ, the angle of attack α decreases slightly

almost uniformly over the rotor, i.e., the distribution looks very similar to the level flight angle of attack, only with slightly lower values of α, with lower values α on the advancing side than the retreating side, and two areas of large values of α particularly around $\psi = 0°$ and in the third quadrant of the rotor, between $\psi = 180°$ and $\psi = 270°$. At flight path angles between $\gamma = 6°$ and $\gamma = 9°$, the angle of attack continues to decrease on the advancing side and through the third quadrant; however, it increases slightly in the fourth quadrant, between $\psi = 270°$ and $\psi = 330°$, while the area of higher α around $\psi = 0°$ remains the same. As γ increases to 12° and beyond, the angle of attack remains constant on the advancing side, with values around 1°; on the retreating side, the value α decreases slightly in the areas where it was highest at $\psi = 0°$ and between $\psi = 180°$ and $\psi = 270°$, while it increases to the same value between $\psi = 270°$ and $\psi = 360°$, so that the angle of attack is almost uniformly at $5° - 6°$ on the retreating side. Notice that, as the flight path angle increases, so does the vertical component of the velocity of the helicopter. The incoming airflow, opposite in direction and therefore downward, increases the total value of U_P at each blade section almost uniformly over the rotor. At the same time, keeping the total speed constant while increasing the flight path angle decreases the forward speed by a factor of $\cos\gamma$. On the advancing side, the reduced forward speed decreases the tangential component of the velocity seen at the blade section, U_T, while on the advancing side U_T increases with lower forward velocities. According to the definition of the angle of attack in Eq.(2.56), increasing the ratio of U_P to U_T decreases the value of the angle of attack α, and vice-versa. On the advancing side, U_P increases and U_T decreases, therefore the ratio of the two

increases, and the angle of attack decreases slightly. On the retreating side, however, both U_P and U_T increase; U_T is much larger in magnitude than U_P, therefore the ratio decreases, increasing the angle of attack, particularly around $\psi = 270°$, where the maximum U_T occurs. The distribution of angle of attack α over the rotor in descending flight is shown in Fig. 6.78. With decreasing flight path angle, the angle of attack does not change significantly at the tips of the rotor. Inboard of the blade, the angle of attack increases, mostly on the retreating side, and becomes increasingly more axisymmetric as γ decreases. At high descent angles, high angles of attack occur near the root of the blade, specially on the retreating side around $\psi = 270°$, which decrease radially outward of the blade. In descents, the change that occurs in U_P is the opposite as in climbs, the incoming upward flow decreases the value of U_P, while the changes in the tangential component U_T mirror those during climbs, i.e., on the advancing side, the reduced forward speed decreases the tangential component of the velocity seen at the blade section, U_T, and the opposite happens on the retreating side. The closer to the root, the lower the value of U_T (as Ωr is low), and therefore the change in U_P is dominant and α increases. Towards the tips, however, the changes in the ratio of U_P to U_T are small and the angle of attack does not significantly change.

Figure 6.79 shows the lift coefficient distribution for climbing angles between $\gamma = 0°$ and $\gamma = 18°$. The lift coefficient, C_L, is a function of both the angle of attack, α, and the Mach number, M (Fig. 5.1). As explained in previous sections, The lift coefficient is highest in those areas where the angle of attack is higher, biased towards the tips where the Mach number, which increases the C_L for a given

α, is highest. As with the angle of attack, C_L has to areas of high values around $\psi = 0°$ and in the third quadrant of the rotor in level flight. As the flight path angle increases, the lower values of angle of attack decrease the C_L, particularly on the advancing side, and at higher values of the climb angle beyond $\gamma = 6°$, the lift increases on the retreating side. The lift coefficient for descending cases between $\gamma = 0°$ to $\gamma = -18°$ is shown in Fig. 6.80. With decreasing flight path angle γ, the lift coefficient increases inboard of the blade, like the angle of attack, reaching values near 0 towards the tip.

The elemental lift coefficient, $C_L M^2$, in climbing flight is shown in Fig. 6.81. The factor of M^2 biases the values of the local lift towards the tip of the blades, specially on the advancing side where M is higher. At low climb angles, up to $\gamma = 0°$, the local lift increases on the retreating side and around $\psi = 0°$, where α is highest, and around $\psi = 90°$, where the Mach number is maximum. For steeper climbs, however, as the forward speed decreases by a factor of $\cos\gamma$, the Mach number decreases on the advancing side, and therefore $C_L M^2$ decreases around $\psi = 90°$. In descents, Fig. 6.82, the areas where the lift coefficient is heavily biased towards the root of the blades, are now very small because of the factor of M^2, which is approaches zero towards the root. At the same time, M^2 brings forward the areas of higher local lift. In particular, at low rates of descents, two areas of high $C_L M^2$ can be identified in the first and third quadrant of the rotor, between $\psi = 0°$ and $\psi = 90°$ and between $\psi = 180°$ and $\psi = 270°$ respectively. As the descent angle increases, particularly beyond $\gamma = -9°$, the local lift on the first quadrant remains higher than over the rest of the rotor.

Figure 6.83 shows the contribution of the local flap moment, rC_LM^2, for the same climb angles used above. The factor of the nondimensional radius biases the values towards the tip even more. The highest values of rC_LM^2 are found in the front-retreating side and around $\psi = 0°$, in the outer quarter of the blade. In the descent cases, Fig. 6.84, the same is observed, i.e., the areas where C_LM^2 is higher are highlighted and biased the closer to the tips by the effect of the product of r.

Figure 6.85 shows the drag coefficient, C_D for different climb angles between $\gamma = 0°$ and $\gamma = 18°$. Like the lift coefficient, C_D is a function of angle of attack α and Mach number M (Fig. 5.2). As described earlier, for angles of attack lower than $\alpha = 5°$ and Mach numbers up to $M = 0.6$, the drag coefficient has an almost constant value around $C_D = 0.008$. At low climb angles, the drag coefficient distribution is almost constant at this value, except for the regions in the third quadrant of the rotor, between $\psi = 180°$ and $\psi = 270°$, and around $\psi = 0°$, where α reaches values between $7° - 8°$. At $\gamma = 9°$, there is a small region of very high drag coefficient, reaching values of around $C_D = 0.03$. In this area, the Mach number seen locally by the blade is between 0.6 and 0.7. The angle of attack, which is very low for the entire advancing side with values between $\alpha = 0°$ and $1°$ near the tips, becomes much larger for a small pocket around $\psi = 90°$, where it reaches values about $\alpha = 5°$. At this high Mach numbers and angles of attack, a small change in angle of attack increases the drag considerably (Fig. 5.2). For higher climb angles, the ares of higher angle of attack barely reach $5°$, and occur where the Mach number is low, and therefore the drag coefficient remains constant for the entire rotor at $C_D = 0.008$. The drag coefficient distribution in descents is shown in Fig. 6.86. Throughout the

descent cases, the regions of high angle of attack occur near the root, where the Mach number is low, and therefore the drag coefficient is only dependent on α. As shown in Fig. 6.78, the angle of attack increases near the root with increasing descent angle. Similarly, the drag coefficient C_D mirrors the areas of high α, becoming very high near the root, particularly on the retreating side.

Figure 6.87 shows the local drag coefficient, $C_D M^2$, in climbing flight. The effect of M^2 is to bias the local drag towards the tip, particularly on the advancing side, where the Mach number is highest, making the areas inboard of the blade, where M is low, negligible. The areas where the drag coefficient in climb is highest occur where the Mach number is low, making the local drag $C_D M^2$ negligible there. In descents, shown in Fig. 6.88, the same is observed: the high values of drag coefficient near the root become almost negligible when multiplied by M^2, and the maximum local drag is found near the tips on the advancing side, where the Mach number reaches its maximum values.

Figure 6.89 shows the elemental induced torque, $rC_L M^2 \sin\phi$, for climb angles between $\gamma = 0°$ and $\gamma = 18°$. The first part of the expression $rC_L M^2 \sin\phi$ has already been explained in Fig. 6.83. The second part, the sine of the induced angle $\phi = \tan^{-1}(\frac{U_P}{U_T})$, depends on several factors. On one side, the climb velocity increases the perpendicular velocity U_P over the whole rotor, while the climb angle also affects the tangential component U_T, which is slightly larger on the retreating side than on the advancing side, as previously explained. However, the induced velocities λ (Fig. 6.75) also affect the perpendicular velocity U_P. Therefore, the most significant variation in ϕ over the rotor is due to the changes in the inflow. The inflow is roughly

close to zero or negative in the front of the rotor disk, and positive and increasing towards the rear of the rotor. As a consequence, the induced torque is mostly zero (or slightly negative) in the front of the rotor, despite rC_LM^2 being large near the tips in the front of the rotor. The values of the induced torque increase towards the tips in the rear of the rotor, although biased towards the retreating side, reaching a maximum value of 0.025. In terms of climb angle, the induced velocities do not change a lot in climbs up to $\gamma = 9°$, and beyond this climb angle the inflow becomes slightly less negative in the front of the rotor, and lower in the rear of the rotor. In the meantime, as explained previously, rC_LM^2 increases with climb angles up to $\gamma = 9°$, and decreases slightly beyond this γ. As a result, the induced torque increases with increasing flight path angle up to $\gamma = 9°$, and the values decrease slightly for higher climb angles. The induced torque in descending flight is shown in Fig. 6.90. The induced velocities are much lower in descending flight than in climbs (Fig. 6.76), and thus the induced torque is also lower. As in climb, the inflow is close to zero or negative in the front of the rotor, and therefore the induced torque is also minimum there, and it increases towards the tips at the rear of the rotor.

Figure 6.91 shows the elemental profile torque, $rC_DM^2 \cos\phi$, in climbing flight. Since ϕ is a small angle, the main factor affecting the profile torque is the local drag. The distribution of profile torque follows that of the local drag shown in Fig. 6.87, although the factor of the local radius r biases the profile torque more towards the tips, while it becomes even more negligible closer to the root. In low climb angles, up to $\gamma = 9°$, the profile torque shows two distinctive areas where higher values occur, on the advancing side near the tips where the Mach number is maximum, and on

the third quadrant, between $\psi = 280°$ and $\psi = 270°$, also near the tip, where the drag is high due to the higher angle of attack. Win increasing climb angle, the angle of attack decreases, and so does the drag, therefore the local profile torque on the third quadrant diminishes. On the advancing side near the tips, the profile torque remains high, although the lower Mach number found as the climb angle increases reduced the maximum value of profile torque reached in that area. In descents, the profile torque Fig. 6.92 behaves the same way. As the local drag, shown in Fig. 6.88, the maximum profile torque is found where the Mach number is highest, near the tips on the advancing side.

The increase in power in climbing flight seen in Fig. 6.66(a) is clearly not associated with profile torque. The maximum profile torque found on a small band near the tip on the advancing side is half the magnitude of the maximum induced torque, which occurs over a much larger area of the rotor. Therefore, the higher induced torque seen as the climb angle increases is the cause for the higher power required in climb, and the decrease in induce torque has γ decreases therefore reduces the need for power in descending flight. Observe that the induced torque is larger for the case of $\gamma = 9°$ than it is at $\gamma = 12°$, which explains the higher power required to operate at that particular flight condition that it does at slightly higher climb angles.

Figure 6.93 shows the moment coefficient C_M over the rotor for different climb angles. In level flight, there are two areas where the moment coefficient is larger, i.e., around $\psi = 0°$ in the outboard half of the blade, and in the third quadrant of the rotor, between $\psi = 180°$ and $\psi = 270°$, also in the outer half of the blade.

At $\gamma = 3°$ the distribution looks very similar to that in level flight. At $\gamma = 6°$ to 9°, however, there is a significant increase in the values of C_M reached in the areas described above, while it remains similar in the rest of the rotor. For higher climb angles, the moment coefficient decreases in those localized areas, although it increases slightly in the rest of the retreating side. In all cases, at the very tip of the blade where the angle of attack is zero or negative, the moment coefficient becomes much more negative. Figure 5.3 is useful to understand the changes in C_M with increasing flight path angle. As stated before, the moment coefficient is a function of both the angle of attack α and the Mach number M. For very high Mach numbers, $M \approx 0.7$ and above, the moment coefficient C_M is negative for the entire range of positive angle of attack values, particularly low for $\alpha > 5°$. For very low Mach numbers, up to $M \approx 0.4$, C_M is almost constant at a slightly negative value for angles of attack up to 10°, then it increases till becoming slightly positive before plunging into large nose-down moments. For the Mach numbers in between, a similar behavior is observed as in the lowest values of M, although the increase and drop in C_M occurs at increasingly lower angles of attack, reaching also increasingly more positive values before dropping into very negative values. Figure 6.94 illustrates how the different values of angle of attack and Mach number affect the moment coefficient seen in Fig. 6.93. It shows the moment coefficient for two radial locations, $r = 0.85R$ and $r = 0.90R$, at several azimuth locations, as a function of the angle of attack, over-imposed over a section of Fig. 5.3, for two of the climb cases, $\gamma = 6°$ and $\gamma = 12°$. On the advancing side ($\psi = 92°$ in the figure.), the Mach numbers achieved are large at these outboard radial stations, however the

angle of attack is low in both climb cases, and therefore the moment coefficient is negative and moderate. The moment coefficient increases around the azimuth for both climb angles and radial stations, reaching a maximum at around $\psi = 233°$. In both climb cases, the Mach number is higher for the outer blade station, although the angle of attack is lower there, and therefore the moment coefficient is higher at the $r = 0.85R$ station than at $r = 0.90R$. Except for the outer blade station at $\gamma = 12°$, all cases produce a positive C_M at this point. At $\gamma = 6°$, the angle of attack is more than $1°$ larger than at $\gamma = 12°$, and this difference increases the moment coefficient considerably. The moment then goes down at all radial stations and climb cases for the rest of the azimuth locations, although it increases again at the rear of the rotor, at $\psi = 358°$. The increase, however, is not enough to make the moment coefficient positive in all cases but one, in the $r = 0.85R$ radial location at $\gamma = 6°$. Figure 6.95 shows the moment coefficient C_M at different descent angles. As in climb, the moment coefficient depends mostly on the angle of attack for except for at large values of α and M. As the descent angle increases, the angle of attack grows close to the root, and the moment coefficient is large, even positive, in that area. On the advancing side, the angle of attack is lower, but the Mach number is higher, and therefore an area of larger C_M can be found in the first quarter of the rotor.

Figure 6.96 shows the elemental moment coefficient $C_M M^2$ for the same climb cases as before. The product of the square of the Mach number biases the values of the local moment towards the tip, and more on the advancing side than the retreating side. The local moment is almost constant at a moderate negative value

around $C_M \approx -0.001$ for all the inner half of the rotor. On the outer half on the advancing side, some low negative values are reached, due to the negative angle of attack, while on the advancing side some areas of higher C_M are observed, specially on the third quadrant where the angle of attack is higher. In descents, shown in Fig. 6.97, the high values of C_M inboard of the blade are negated by the low Mach number inboard of the blade, and, similarly to the climb cases, $C_M M^2$ is mostly uniform in the inner half of the rotor. In the outer half, slightly higher values are reached on the third quadrant for the lower descent angles, and both on the first and third quadrant for the steeper descent cases.

6.4.2 Blade dynamics

The equivalent flapping angle β at the blade tip as a function of azimuth is shown in Fig. 6.98, for several climb and descent angles, including level flight for reference. As the flight path angle increases, the phase of the flapping response changes, but the magnitude is not significantly affected. Moreover, the presence of higher harmonics can be appreciated in the climbs at $\gamma = 6°$ and $\gamma = 12°$. In descents, as the angles increase, so does the magnitude of the flapping response, which for all the cases considered presents a clearly sinusoidal time history.

Figure 6.99 shows magnitude and phase of the first three harmonics of the flapping response. As can be seen from Fig. 6.98, the magnitudes of the harmonics are much larger in the descent than in the climb cases. Throughout the flight path range, the 1/rev response is dominant. In climbs, however, the ratio between the

1/rev and the 2/rev flapping is larger (particularly in the $\gamma = 6°$ and $\gamma = 12°$ climbs), and the presence of the 2/rev excitation is visible in the shape of the flap curves.

A possible explanation for the shape of the flap distribution at the different flight path angles can be obtained from Figs. 6.83 and 6.84, which shows the distribution of flapping moment, rC_LM^2, over the rotor disk for different values of γ. Areas of high rC_LM^2 contribute to increase the flap displacement, while low rC_LM^2 values decrease it. In level flight, the flap moment starts to decrease from $\psi = 0°$ onto the advancing side, with a slight perturbation around $\psi = 9°$. The equivalent flap angle at the tip, therefore, decreases on the advancing side. Around $\psi = 150°$, the flapping moment starts to increase again, reaching a maximum around $\psi = 270°$, then decreases considerably for almost the entire fourth quadrant of the rotor, before increasing again around $\psi = 0°$. The flap angle, therefore, increases on the third quadrant of the rotor, and then decreases towards the rear of the rotor. Because of this multiple variation around the azimuth, the flap higher harmonics are being excited. In climbing flight, the local flapping moment has has a similar distribution than in level flight, although the areas of high rC_LM^2 around $\psi = 0°$ and on the third quadrant are slightly higher in magnitude, affecting the flap history. In descents, the local maxima of rC_LM^2 do not reach as high values as in climbing flight. However, an area of negative contribution to the flap angle occurs on the second quadrant of the rotor, between $\psi = 90°$ and $\psi = 180°$. This large flap-down moment decreases the lag angle, which reaches a minimum during descents around $\psi = 180°$, while the high flap moment on the third quadrant increases again. The

negative dip increases with descent angle, which increases the amplitude of the flap time history. Although the mean flap value in climbs is higher, due to the higher average value of the local flap moment, the amplitude in descents is much higher caused by the larger variation in the values of rC_LM^2 around the azimuth.

Figure 6.100 shows the equivalent lag angle ζ at the tip as a function of azimuth angle ψ for the climb and descent cases being considered. All climb and descent cases look very similar in shape, although the mean value of each time history changes considerably with γ. The amplitude of the sinusoidal variation of the equivalent tip lag is also very similar in all cases. Increasing the climb angle, however, increases the mean value of the lag, which doubles by the time $\gamma = 18°$. Increasing the climb angle also changes the phase of the distribution slightly, with the maximum occurring slightly earlier as γ increases. In descents, the opposite occurs, as the flight path angle decreases, the average lag angle also decreases, and the point of maximum lag occurs later over the azimuth. Figure 6.101 shows the magnitude and phase of the first three harmonics of the equivalent lag angle. In climbing flight, the magnitude of all three harmonics is pretty similar, specially for the higher climb angles. However, these are much lower than the magnitude of the constant lag coefficient ($\zeta_0 = -6.6852$, $\zeta_{1c} = -0.083403$, $\zeta_{1s} = -0.11343$, $\zeta_{2c} = -0.14286$, etc., at $\gamma = 18°$), and therefore the lag time histories appear almost flat. In descents, the magnitude of the first harmonic is clearly dominant over the higher hamonics, and although smaller than the constant coefficient as in climb, the lag time histories appear slightly more sinusoidal in descents.

The azimuthal variation of lag displacement depends on the distribution of

elemental drag, shown in Figs. 6.87 and 6.88. The local drag in the outer quarter of the blade is much larger in climbs than in descents, which explains the much larger lag displacement in climbs than in descents. Particularly, it local drag increases in the outer part of the rotor with climb angle, mostly on the retreating side, which increases the lag displacement for the steeper climbs. The variation over the rotor is very moderate, and thus the lag displacement does not change considerably as a function of azimuth. On the advancing side, the higher drag found at the tip increases the lag, which increases again on the retreating side where the drag is lower. In descents, the difference between the advancing and retreating side is more defined, with higher drag on the advancing side increasing the lag displacement and lower drag on the retreating side that decreases the lag. The maximum drag on the advancing side decreases as the descent angle increases, and therefore the average lag decreases too. While in descents the variation in drag is clearly a 1/rev variation, perturbing mostly the first harmonic, in climbs the drag distribution exciting the higher harmonics as well.

Figures 6.102 and 6.103 show, respectively, the elastic torsional deflection ϕ at the blade tip as a function of azimuth angle, and the magnitude and phase of the first three torsional harmonics.The magnitude of the first harmonic increases progressively from almost 0.4 degrees at $\gamma = 18°$ to slightly more than 1 degree at $\gamma = -18°$. Its phase is almost constant with γ. The magnitude of the second harmonic also increases as γ goes from $18°$ to $-18°$, and remains below 0.2 degrees except at $\gamma = 6°$. Its phase has more noticeable variations, which determine the variations in azimuth position of the minima of ϕ.

The distribution of pitching moment over the rotor, shown in Figs. 6.93 and 6.95 for $\gamma = 0°, \pm 6°, \pm 12°$ and $\pm 18°$, helps understand the behavior of the torsion of the blade. In descents, the very negative pitching moment found on the advancing side excites the first harmonic, which is much larger than the higher harmonics; the elastic torsion response shows a large nose-down deflection on the advancing side corresponding to this negative pitching moment. In climbs, the advancing side does not show such large negative values, and the regions of positive C_M, which occur at $\psi = 0°$ and on the third quadrant of the rotor, excite the higher harmonics of the response. The overall variation in magnitude of C_M is lower in climbs as well, producing a response with lower amplitude than in descents.

6.4.3 High rates of descent

This section contains the results of simulations performed at high rates of descent and low speeds, for velocities $V = 20, 25$ and 30 kts and descent angles between $\gamma = -21°$ and $\gamma = -50°$. Several simulations were carried out progressively approaching the onset of VRS, with a combination of velocities and flight path angles. True vortex ring state (VRS) is an intrinsically unsteady phenomenon, and therefore it cannot be properly studied as a trim condition. However, the onset and incipient stages of VRS can be explored as trim states, both to understand the underlying physical mechanism, and to study the numerical behavior of the trim algorithm.

Figure 6.104 shows the VRS boundary as obtained from the experiments of Drees and Hendal (Ref. 1). The boundary is delimited by a combination of forward

speed ratios V_x/V_h and descent speeds V_z/V_h, where V_x, V_z and V_h are, respectively, the velocity in the plain of the rotor, the velocity perpendicular to the plane of the rotor and a velocity scale, namely the ideal inflow in hover from momentum theory $\sqrt{T/2\rho A}$. Within this boundary, signs of VRS were observed in the experiments. Superimposed are the cases analyzed in the present study, which approach or cross over the boundary that determines the onset of VRS. While the experimental data are not rigorously applicable for the full-scale helicopter configuration used in the present study, Fig. 6.104 is still used here to provide a general indication of the stage of each descent case. The different markers in the figure denote the flight conditions analyzed. In general, the slower and steeper the trajectory, the deeper the rotor enters into VRS conditions.

A subset of cases obtained at 20 kts is selected to see the effect of approaching VRS. Figure 6.105 shows the variation of main rotor power required and collective for flight path angles between $\gamma = 0°$ and $\gamma = -50°$ at $V = 20$ kts.The steeper the descent, the more difficult it becomes to obtain a trimmed solution, as indicated by the need for more iterations of the trim procedure, and a higher residual in the trim equations at the end of the procedure. Beyond $\gamma = -50°$, it became impossible to obtained a steady-state solution with the current model. The results show that the power required decreases almost linearly with γ (much steeper descents, outside the range of the present study, would be necessary for conditions of "power settling" to be observed). The collective also decreases linearly with γ.

Figure 6.106 shows the fuselage angle of attack, fuselage pitch angle and the longitudinal cyclic for the same cases between $\gamma = 0°$ and $\gamma = -50°$ at $V = 20$

kts. The aerodynamic angle of attack of the fuselage α_F increases linearly with the descent angle, while the pitch angle θ is almost constant with γ and increases by less than two degrees as the flight path angle goes from $\gamma = 0°$ to $\gamma = -50°$. The rotor responds by tilting forward, with a positive longitudinal flapping β_{1c} (Fig. 6.108(a)) that increases by about two degrees as the flight path angle decreases to $\gamma = -50°$. The longitudinal cyclic remains almost constant with γ.

Figure 6.107 shows the fuselage roll angle, lateral cyclic and pedal setting and Fig. 6.108(b) shows the lateral flapping, for $\gamma = 0°$ to $\gamma = -50°$ at $V = 20$ kts. Roll angle ϕ and lateral flapping β_{1s} are not significantly affected. The conditions in the present study are not severe enough to affect the lateral motion of the helicopter, although deep in the VRS both pitch and roll oscillations are usually observed. The pedal position increases by 10% (right) with γ to maintain heading due to the change in torque.

Figure 6.109 shows side and top views of the wake geometry for $\gamma = -30°$, $-40°$ and $-50°$ at $V = 20$ kts. The incipient stages of VRS are characterized by an initial convection of the vortex filaments over the rotor tip path plane, which are subsequently pulled back under the rotor, and some instability develops in the form of vortex "bundling" (Ref. 83) of the filaments downstream of the rotor. The bundling is clearly visible for all the values of γ in this figure. As the descents become steeper, the formation of these vortex rings occurs closer to the rotor and they are not convected as far from it. If the rate of descent were to increase any further, the accumulation of vorticity would reach the rotor plane and the rotor would be operating fully in the VRS.

Figure 6.110 shows the distribution of both the induced velocities λ and the perpendicular component of the sectional velocity U_P over the rotor for the same descent angles at $V = 20$ kts. For the lower values of γ, the upward flow starts convecting the vortex filaments over the rotor, but they stay close to the tip path plane and their proximity can be identified as regions of drastic changes in the induced velocities. With increasing descent rate, the vortices move closer to the rotor plane and the induced velocities increase towards the tip. In the meantime, the upward flow due to the high rates of descents significantly decrease the perpendicular velocity at the blade section, which is composed of the inflow, the velocities due to translation and rotation and the those due to blade flexibility. Figure 6.111 shows the angle of attack α and the lift coefficient C_L corresponding to these cases. In the stage where the vortex filaments are first convected above the rotor, a region of very high angle of attack appears, and stall occurs at that location. The increase in upward flow that reduces U_P increases the overall angle of attack, except for the region on the advancing side at $\gamma = -30^\circ$ where the tip vortex is crossing the rotor. The increase is slightly more pronounced on the retreating side, as the tangential component of the sectional velocity U_T is higher as a result of the higher flight path angle, than on the advancing side. The lift coefficient distribution, depicts the occurrence of stall inboard of the blade and some regions of negative lift close to the root (Refs. 83, 135).

Figure 6.112 shows the elemental lift and induced torque distributions for the above flight conditions. The figure also shows the distribution of induced torque, which is observed to decrease the steeper the descent. The lower U_P that occurs

with the lower values of γ decreases the value of the induced angle ϕ, decreasing the induced torque. As a consequence, the power required by the main rotor, shown in Fig. 6.105, decreases as well in these steep descents. In addition, the tangential component U_T increases on the retreating side, and decreases on the advancing side. Therefore, the decrease in ϕ is more pronounced on the retreating side than on the advancing side, as is its effect on the induced torque.

Figure 6.113 shows the local flap moment and the pitching moment coefficients at $\gamma = -30°$, $-40°$ and $-50°$. The flapping moment rC_LM^2 is similar to the elemental lift, C_LM^2, although the product of the non-dimensional radius r makes those values close to the root negligible, and those with a larger moment arm towards the tip are the only ones contributing to the flap motion. As for C_M^2, the flap moment is higher towards the tips in the rear of the rotor disk, between $\psi = 270°$ and $\psi = 90°$ approximately. The values of rC_LM^2 decrease in magnitude as the descent angle increases. However, the difference between the values in the rear and the rear of the rotor disk increases slightly with descent angle. The moment coefficient C_M, which is a function of angle of attack and Mach number, shows particularly high, even positive, values towards the tip, specially on the retreating side, but also around $\psi = 90°$. The Mach number, at this high descent angles and low speed, is almost axi-symmetric, with peak values around $M = 0.6$ at the tips. For such value of M, angles of attack higher than $4°$ produce positive C_M (Fig. 5.3, while for the slightly lower M found a bit more inboard, C_M is positive for $\alpha > 7° - 8°$.

The flapping response as a function of azimuth for the cases at $\gamma = -30°$, $-40°$ and $-50°$ and $V = 20$ kts is shown in Fig. 6.114. All three cases have the

same phase and similar average flap value as well, although the amplitude of the response increases with the steeper descent angles. The local flap moment, shown in Fig. 6.113, shows that the lift contributes to an increased flap in the rear of the rotor, while in the front the contribution is minimum reducing the flap angle. The higher difference between the local flap moment in the front and the rear of the rotor seen at the steeper descents causes the larger magnitude in the flap response.

The elastic torsional displacement for the same steep descent cases is shown in Fig. 6.115. Unlike the flapping response, the elastic twist decreases in amplitude with the higher descent angles. The response in all three cases looks similar, only slight off phase, with multiple harmonics being excited. The variation in the moment coefficient C_M (Fig. 6.113) produce these oscillations in the torsional response.

6.5 Steep descending turns

This section presents results for steep descending turns, with a speed $V = 40$ kts along the trajectory, flight path angle $\gamma = 40°$ and with turn rates from $\dot{\psi} = -40$ deg/sec to $\dot{\psi} = 40$ deg/sec. The trim results for turns at $V = 60$ kts and $\gamma = 0°$, described in Section 6.3, are shown for reference.

Figure 6.116(a) as a function of turn rate for turns from $\dot{\psi} = -40$ deg/sec to $\dot{\psi} = 40$ deg/sec. In straight flight at $\gamma = -40°$, the load factor is 1, and it increases with turn rate until it reaches values around 1.5 at $\dot{\psi} = \pm 40$ deg/sec, moderately larger on the left turns than on the right ones. The load factor increases slower in descending turns that in level turns due to the lower thrust required.

Figure 6.116(b) shows the main rotor power required as a function of turn rate. The power required increases with turn rate, both for left and right turns. For straight flight at $\gamma = 40°$ the power required is almost zero and the helicopter is operating close to autorotation conditions. As turn rate increases, increasingly more power and thrust are required to overcome the centrifugal force and perform the turns. For turn rates of up to $\dot{\psi} = 30$ deg/sec, the increment in the power required is similar for both left and right turns. At rates of $\dot{\psi} = \pm 40$ deg/sec the left turn requires about 100 hp more than the right turn.

Figure 6.116(c) shows the main rotor collective, δ_{col}, for the different turn rates. Unlike the power, the right turns show a higher requirement for collective than the left turns, as much as 5 % at the higher turn rates. The change in magnitude of the required collective with varying turn rate is similar to that of the turns at level flight (Fig. 6.42(b)), only about 20 % lower due to the descending flight condition and slightly lower speed.

The lateral cyclic, δ_{lat}, helicopter roll angle, ϕ, and roll rate, p, as a function of turn rate are shown in Fig. 6.117. The lateral cyclic, which in level fight turns decreased for turns to both left and right directions (Fig. 6.43(a)), presents a larger magnitude decrease in the port diving turns, although in the starboard dives it increases (although note that besides the flight path angle, the diving turns are also performed at lower speed, 40 kts vs. 60 kts for the level turns). The helicopter roll angle increases proportionally to the turn rate, both with left and right turns. While the helicopter is highly banked in the more severe cases, the angle does not change at a high rate. Up to turn rates of $\dot{\psi} = \pm 20$ deg/sec, the roll rate is around

0. On the right turns, it increases to around $p = 8$ deg/sec at $\dot{\psi} = 40$ deg/sec, while on the left turns it reaches values slightly higher in magnitude, but negative, around $p = -12$ deg/sec at $\dot{\psi} = -40$ deg/sec.

The longitudinal cyclic, δ_{lon}, helicopter pitch angle, θ, and pitch rate, q, are shown in Fig. 6.118. The longitudinal cyclic increases initially with the lower rates of turn, both left and right, which follows the trends of the experimental level flight turns (Fig. 6.43(b)), but at the highest turn rates computed, $\dot{\psi} = \pm 40$ deg/sec, the predicted value decreases. Because the helicopter continues to descent as it turns, it needs to continuously increase its nose-down pitch angle to maintain the flight path angle. Up to turn rates of $\dot{\psi} = \pm 30$ deg/sec, the pitch attitude is very similar in both the left and right turns. However, at $\dot{\psi} = \pm 40$ deg/sec the pitch attitude of the left turn is much lower than the right equivalent one. The pitch rate needed to turn is more than double the value in magnitude than the roll rate, increasing to zero in straight flight to around $q = 25$ deg/sec at $\dot{\psi} = \pm 40$ deg/sec, with slightly higher value on the right turns.

Figure 6.119 shows the pedal setting, δ_{ped}, and yaw rate, r, required for the different turn rates. Although no fight test data is available for this flight condition, a comparison with the level fight turn predictions for power and pedal (Figs. 6.42(a) and 6.45(a)) seems to indicate that also in the diving turns the power at the higher turn rates might be slightly overpredicted, and that the pedal setting for these extreme diving turns might be lower than the trends observed at more moderate turn rates to compensate for the additional torque (like mentioned before, a percentage decrease in the pedal setting indicates an increase in the pedal to the left, which

increases the tail rotor collective). The yaw rate, which controls the actual turn of the helicopter in the helical path of the coordinated turn, is the largest of the three angular rates, reaching values of $r = \pm 28$ deg/sec at $\dot{\psi} = \pm 40$ deg/sec.

Figures 6.120 through 6.125 show the resulting geometry side, rear and top views for the descending turns being studied at $V = 40$ kts, $\gamma = -40°$ and $\dot{\psi} = 0, \pm 10, \pm 20, \pm 30$ and ± 40 deg/sec. These turns take place at a very steep angle of descent, therefore the wake vortices are convected above the rotor disk, even as the rate of turn, and therefore rotor thrust, increases. Vortex bundling begins to appear for turn rates higher than about $\dot{\psi} = 30$ deg/sec. With increasing turn rate, both right and left, the tip path plane pitches down, bringing the wake vortices closer to the rear of the rotor. The main differences between left and right turns are noticed at the higher turn rates. Right turns vortex bundling is more evident on the advancing side, but almost disappears on the retreating side, while in the left turn the vortex bundle is more evident, and extends further, with a higher area of influence over the rear and advancing side of the rotor.

Figure 6.126 shows the induced velocities for turns at $\dot{\psi} = 0$ deg/sec, ± 20 deg/sec and ± 40 deg/sec. The induced velocities in the left turns are clearly higher than in the right turn at the same rate. While the inflow very near tip of the front and retreating side is slightly higher in the right turn, the left turn shows considerably larger in the rear of the rotor.

Figure 6.127 shows the angle of attack for the same turns at $\dot{\psi} = 0$ deg/sec, ± 20 deg/sec and ± 40 deg/sec. At these high rates of descent, the upward flow decreases the perpendicular component of the velocity at the blade section, U_P,

considerably. However, the high angular rates experienced at the higher turn rates also affect the perpendicular and tangential velocities U_P and U_T, and therefore the induced angle ϕ and the angle of attack, to a great extent. As a result, the angle of attack changes from an almost axi-symmetric (slightly higher on the retreating side) distribution in straight flight at $\gamma = -40°$ to a distribution with much higher values on the second quadrant of the rotor on the right turns, and on the first quadrant on the left turns. The maximum angle of attack reached is higher on the right turns, where it reaches 15° in a region close to the root between $\psi = 150°$ and $\psi = 180°$, while on the left turns the maximum values reached inboard of the blade are about 11°.

The lift coefficient C_L at $\dot{\psi} = 0$ deg/sec, ± 20 deg/sec and ± 40 deg/sec is shown in Fig. 6.128. In the regions where the angle of attack is highest, the Mach number is low, therefore the lift coefficient depends mostly on α. As the angle of attack, the lift coefficient is maximum close to the root and decreases radially for the low turn rates, although at high turn rates the higher values are found on the second quadrant of the rotor disk for the right turns and on the first quadrant for the left turns.

The elemental lift distribution, $C_L M^2$, is given in Fig. 6.129. The values close to the root become less important by the factor of M^2, which goes to zero at the root. Only the values in regions of high dynamic pressure, close to the tips and specially on the advancing side, are important. At low turn rates, the areas where the lift coefficient is slightly higher begin to be noticeable, and occur on the second quadrant for the right turn, where values of $C_L M^2 = 0.17$ are found, and on the first

quadrant for the left turns, where similar values are reached, although over a slightly smaller area and closer to $\psi = 0°$. At $\dot{\psi} = \pm 40$ deg/sec, the maximum values of elemental lift almost double, reaching $C_L M^2 = 0.3$, again in the same areas. At these rates, however, the region where $C_L M^2$ is highest is larger on the left turns, although over the entire rotor, the values are higher on the right turns.

Figure 6.130 shows the elemental drag distribution at $\dot{\psi} = 0$ deg/sec, ± 20 deg/sec and ± 40 deg/sec. At low turn rates, the combinations of angles of attack and Mach numbers experienced are low enough to produce an almost constant local drag. At the highest turn rates, however, the drag increases considerably, due to the large value of α encountered precisely on the advancing side, where M is highest. On the right turns, the elemental drag reaches $C_D M^2 = 0.012$ over the outer half of the second quadrant of the rotor, while on the left turns, similar values are reached over the outer third of the first quadrant.

The induced torque distribution, $rC_L M^2 \sin\phi$, at $\dot{\psi} = 0$ deg/sec, ± 20 deg/sec and ± 40 deg/sec, is shown in Fig. 6.131. While the right turn has higher induced torque requirements in the third quadrant of the rotor, between $\psi = 180°$ and $\psi = 270°$ approximately, the left turn has overall higher values, which translate into the higher power requirements in the left turn. The value of the induced torque depends both on the local lift at each point on the rotor and the induced angle, i.e., $\phi = U_P/U_T$. The induced angle, which changes considerably between the left and right turns due to the different angular rates, drives the main differences between the two cases. On the right turns, the induced angle is negative on the advancing side, which coupled with the large values of $C_L M^2$ found on the second quadrant,

produces very low negative values there. On the retreating side, the elemental lift was lower, but ϕ is larger, producing large positive values of the induced torque. On the left turns, $C_L M^2$ is not as large on the second quadrant of the rotor disk, therefore while negative, the induced torque is not as low. The highest value of the induced torque occurs on the rear of the rotor, increasing the induced torque, specially between $\psi = 330°$ and $\psi = 0°$, as both components are high there.

Figure 6.132 shows the elemental profile torque, $rC_D M^2 \cos\phi$ at $\dot{\psi} = 0$ deg/sec, ± 20 deg/sec and ± 40 deg/sec. The profile torque depends on the cosine of the induced angle, which is close to one, therefore the distribution resembles that of the elemental drag, with the torque increasing considerably at the higher turn rates due to areas of high drag on the second quadrant for the right turns and on the first quadrant for the left turns.

The slightly higher power required for the left turns is justified by the slightly higher values of the induced torque, as the overall profile torque is very similar (maximum value is slightly higher on the left turn, although the right turn has significant values over a larger portion of the rotor).

6.6 Numerical characteristics

The results in the present study were obtained using a 2.5 GHz Quad G5 (two dual core PowerPC processors) Macintosh computer with 1GB of RAM. The code is not currently designed to exploit parallelism and therefore the resultant effect from a computational point of view was that of running on a single processor.

Trim convergence is sensitive to the initial solution for both the model with dynamic inflow and that with the free wake. Even with the former, for which convergence is relatively easier, starting from a poor initial solution often leads to failure of convergence. Therefore, it is important to start with as good an estimate as possible.

The trim procedure is also sensitive to flight condition. At high speeds, i.e. for $\mu > 0.18$, it is relatively easy to achieve convergence. Hover and low speed conditions are usually more difficult and computationally expensive. The recommended procedure is to compute trim at moderately high speeds (e.g. $0.23 < \mu < 0.28$) and then progressively increase speed, or decrease it towards hover, increments or reduction of 10 kts at each step usually proved successful in this study. At each speed, the initial solution is the converged solution for the previous speed.

The overall CPU time required to achieve convergence was primarily driven by two factors, namely, the increased computational effort required to obtain a trim solution in hover and low speed, and the CPU time required to achieve convergence of the free wake geometry for each evaluation of the trim equations. Recall, however, that the function evaluations required to build the Jacobian matrix did not include a recalculation of the wake, as explain in Section 4.5.5). Convergence for the free wake model is determined by observing the L_2 norm of the induced velocities over the rotor. The root mean square (RMS) change in the inflow is calculated using,

$$RMS = \frac{1}{N_\psi N_r} \sqrt{\sum_{\psi:j=1}^{N_\psi} \sum_{r:k=1}^{N_r} (\lambda(\psi_j, r_k)^n - \lambda(\psi_j, r_k)^{n-1})^2} \tag{6.1}$$

where N_ψ is the number of blade azimuthal steps in one revolution and N_r is the

number of radial points used along the blade.

At lower speeds, the vortex filaments remain closer to the rotor and their influence is larger, whereas at higher speeds, the vortices are quickly washed away behind the rotor, and their influence is lessened. As a consequence, the inflow norm tends to converge more easily at higher speeds.

The figures that follow are representative of the computation time and the number of iterations necessary to trim at different speeds. At $V = 120$ kts, representative of high speed flight, obtaining a trim solution from an initial solution corresponding to $V = 100$ kts, requires 115 evaluations of the trim equations, of which 92 are required to build the Jacobian twice using one-sided finite differences. During those 92 evaluations, the free wake is not evaluated, but on each of the remaining 23, the free wake calculations are carried out until convergence. The complete trim calculation for the coupled rotor-fuselage-wake system requires approximately about 1.5 hours. At $V = 60$ kts, the process requires a similar effort, i.e., 120 evaluations of the trim equations of motion, of which 92 are needed to compute 2 Jacobians. At $V = 30$ kts, representative of the transition flight range, the cost increases considerably, as it the solver needs to compute a new Jacobian matrix 6 times, requiring 306 evaluations of the trim equations of motion. However, hover is the most difficult case, as it requires 316 evaluations of the equations of motion and 6 builds of the Jacobian to obtain a solution. In terms of time, the process takes longer, needing about 3 hours to obtain a trim solution.

In turning flight, the speed of convergence depends on the speed at which the turn takes place, and the same arguments apply. In addition, the higher the

turn rate, the more difficult achieving convergence becomes. As for the low speed cases, the approach to converge results at high turn rates consists in progressively incrementing the turn rate and using each solution as the starting estimate for the next turn rate.

Similarly, climbing and descending flight cases are susceptible to the speed at which the flight condition occurs, and for a given speed, the higher the flight path angle, the more difficult convergence becomes. Incremental progress is also used to achieve convergence at high flight path angles, either in climb or descent. Descending flight is particularly more difficult to converge, and smaller increments might be necessary.

Finally, a note on the accuracy of the converged solution. The algebraic equation solver tries to reduce the residual of the equations of motion by reducing the difference between the approximate present solution $\mathbf{X}$ and a previous solution $\mathbf{X}_{sol}$ below a certain tolerance TOL (Ref. 124), so that

$$\|\mathbf{X} - \mathbf{X}_{sol}\| \leq TOL \cdot \|\mathbf{X}_{sol}\| \tag{6.2}$$

The tolerance used in the present study is 10^{-6}. By meeting this criterion, the norm of the residuals of the equations of motion usually becomes very small. However, as the speed is decreased, not only it takes longer to obtain a trim solution, but the solver returns a solution with larger and larger residuals. The procedure used in the present study was the following: if a solution was returned with a overall residual norm greater than 10^{-3}, the accuracy was considered insufficient and therefore the solution was discarded and the trim solution process repeated. At high speeds,

this was not an issue, and he solutions obtained resulted in residual norms of the order of 10^{-8}. At hover and low speeds, however, poor convergence was frequently a problem, but solutions were found with residual norms of the order of 10^{-4}, which were deemed acceptable.

An important remark to be made regarding the convergence of the trim procedure is that speed and extent of convergence are very sensitive to the value of the vortex core growth parameter δ Eq.(3.18). The smaller the vortex core growth value, the smaller the core size and the higher the velocity field that each filament sees because of the other filaments. This increases the strength of their mutual interactions, and this results in a more difficult convergence of the free wake, and therefore of the entire trim procedure. Increasing that value would improve convergence, as has been found many times in the literature (Refs. 48, 52). However, in this study the vortex core growth was not used as a tuning parameter. A realistic value determined from experimental results (Ref. 119) was used instead, even if it could increase the difficulty of convergence.

Another important observation regarding the cost of computation for the trim calculation is that the present approach, described in Section 4.5.5, eliminates the calls to the free wake during the calculation of the Jacobian matrix. In early stages of the present study, as well as in the study that serves as a baseline for the present work (Ref. 6), the wake was used to calculate the inflow at each evaluation of the trim equations, whether these were to compute the Jacobian matrix or to advance the solution (see Appendix C for a schematic of the trim procedure in Ref. 6). Considering that a single Jacobian (in the present configuration, as its size depends on

the number of modes and other factors) requires 46 evaluations of the trim equations, converging the wake for each of those evaluations constituted a significantly large cost of computation. However, it was discovered that the free wake model is quite insensitive to the small perturbations used to obtain the derivatives that form the Jacobian (1% of the quantity being perturbed). Therefore, the solution attempted consisted on calculating the free wake inflow only on the iteration that establishes the baseline for the Jacobian calculations and on each trim calculation used to obtain a solution, but not in those evaluations of the trim equations required to build the Jacobian, for which the inflow from the last solution computed is used. The present study also simplifies the convergence of the inflow-circulation problem. Previous stages of this work and the earlier related studies (Ref. 6) used an assumed value of the inflow to calculate the bound vortex circulation (see Appendix C). The inflow was converged with this fixed value of Γ. But the inflow and circulation are mutually dependent, therefore the new inflow had to be used to re-evaluate the circulation, and this double-loop was repeated until the inflow converged. In the present study, the implementation of the time-marching wake with a Weissinger-L method for the calculation of the inflow has permitted that the inflow calculation be replaced by a single loop, which updates Γ for each new value of the inflow, therefore reducing the number of calls to the free wake dramatically. In terms of cost, this translates into a reduction of an order of magnitude, since the previous approach needed 24 to 30 hours for a simple solution (in the above mentioned machine, much more in earlier Powermacs with G4 PowerPC processors), while now it needs between 2 and 3 hours.

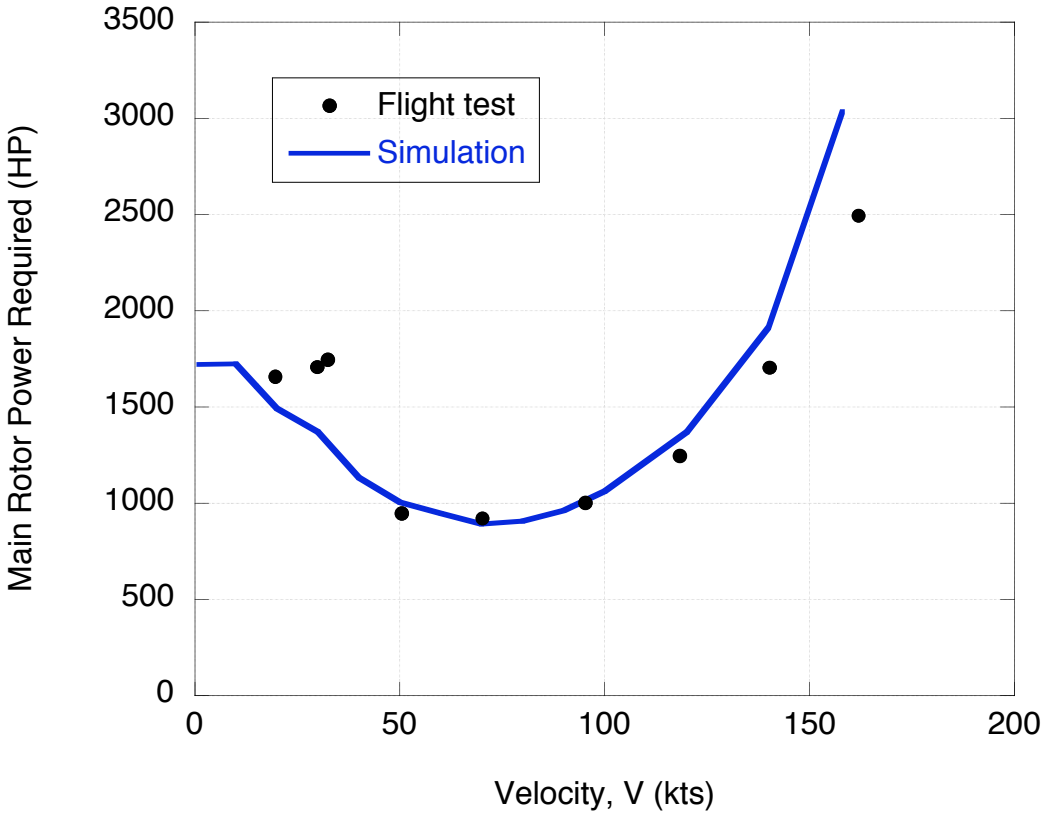

Figure 6.1: Main rotor power required, Q_{MR}, as a function of speed, for a straight blade configuration.

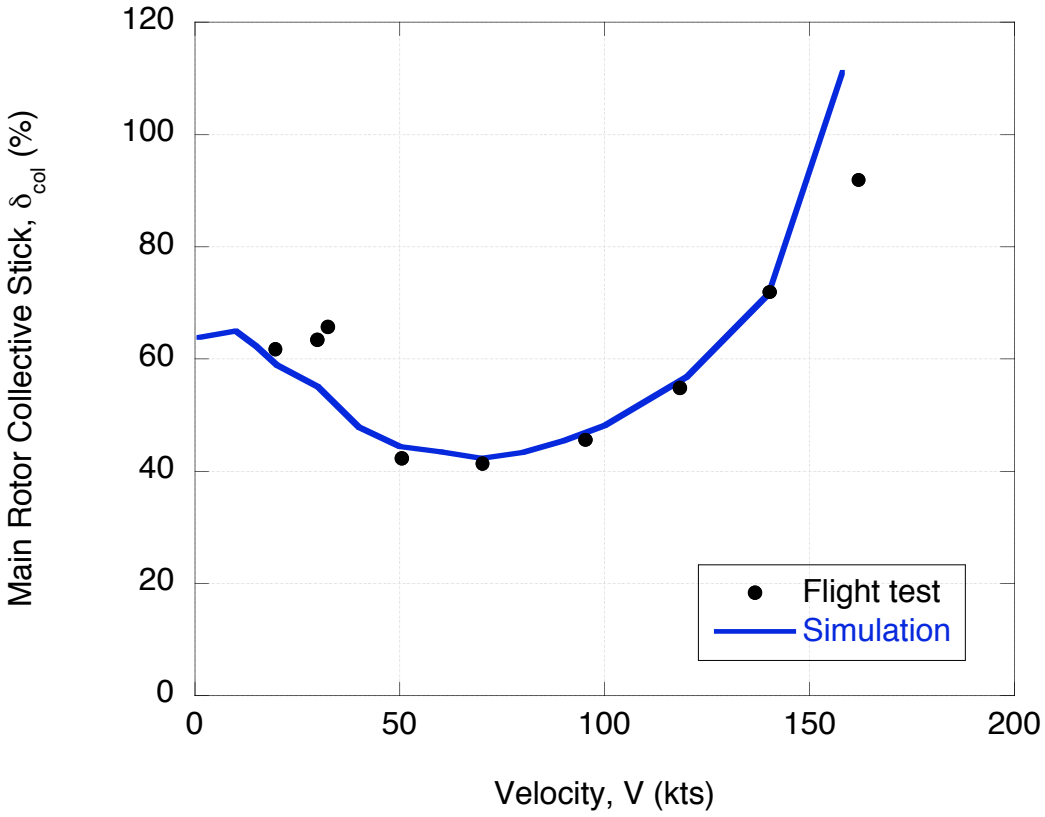

Figure 6.2: Main rotor collective required as a function of speed, for a straight blade configuration.

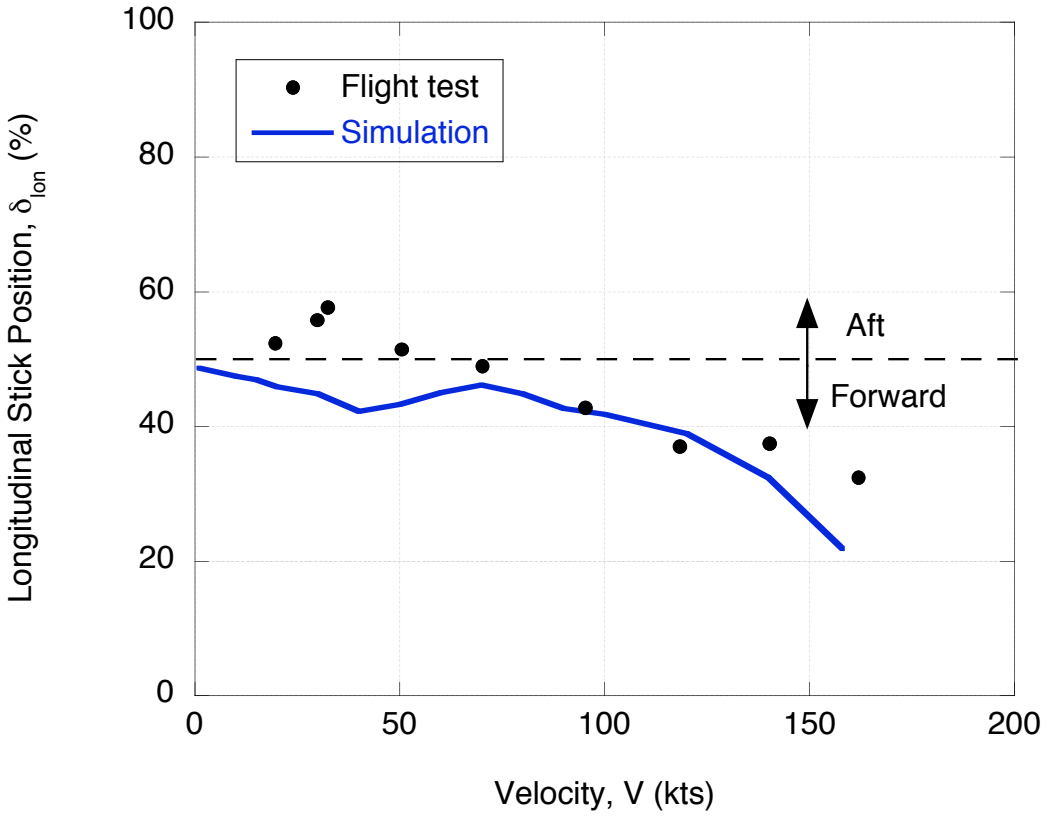

Figure 6.3: Main rotor longitudinal stick position as a function of speed, for a straight blade configuration.

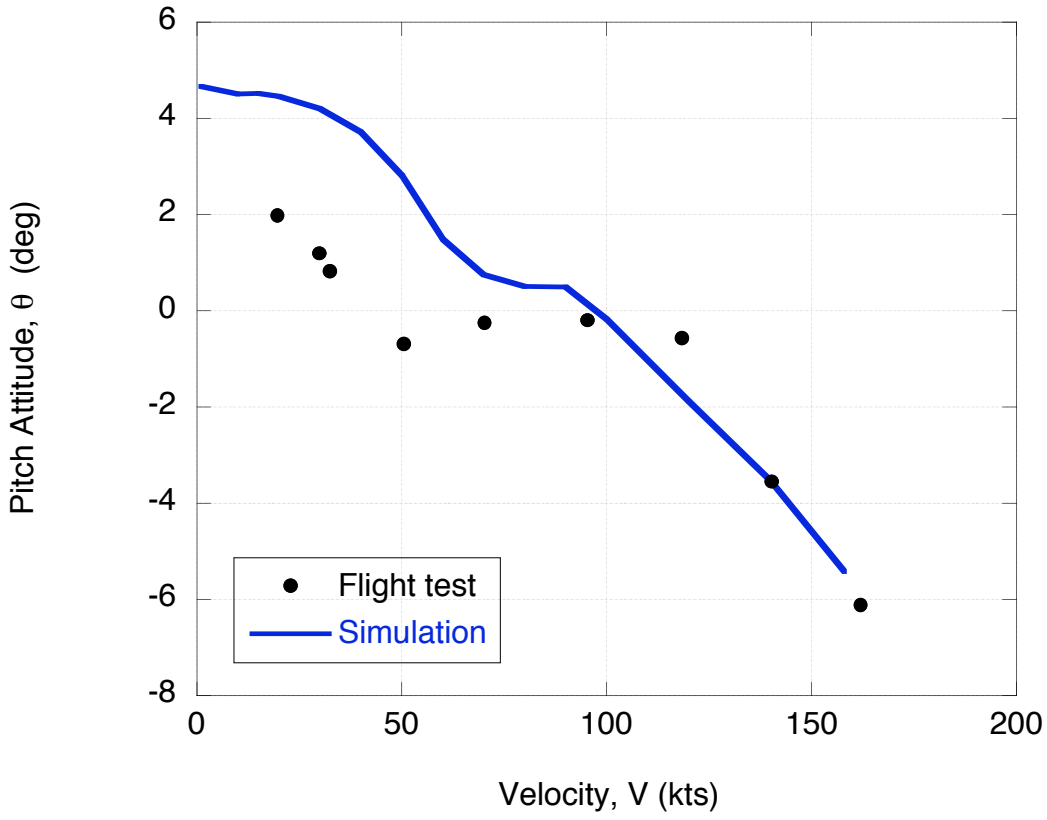

Figure 6.4: Helicopter pitch attitude as a function of speed, for a straight blade configuration.

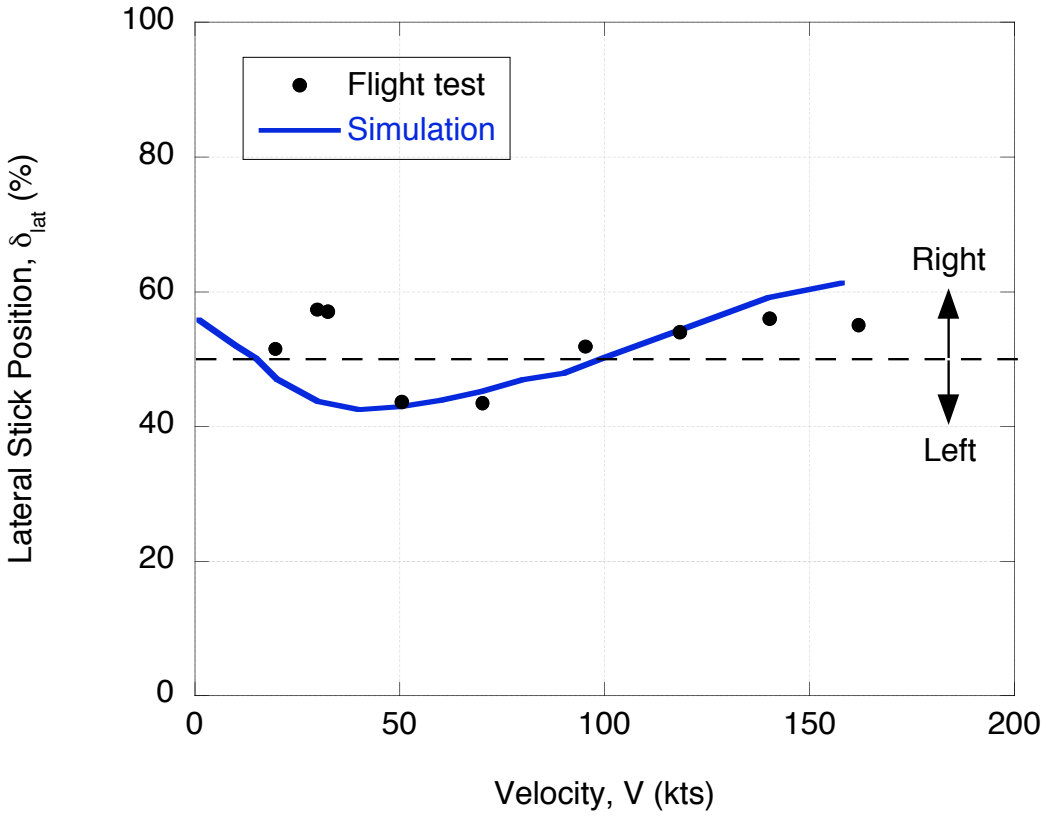

Figure 6.5: Main rotor lateral stick position as a function of speed, for a straight blade configuration.

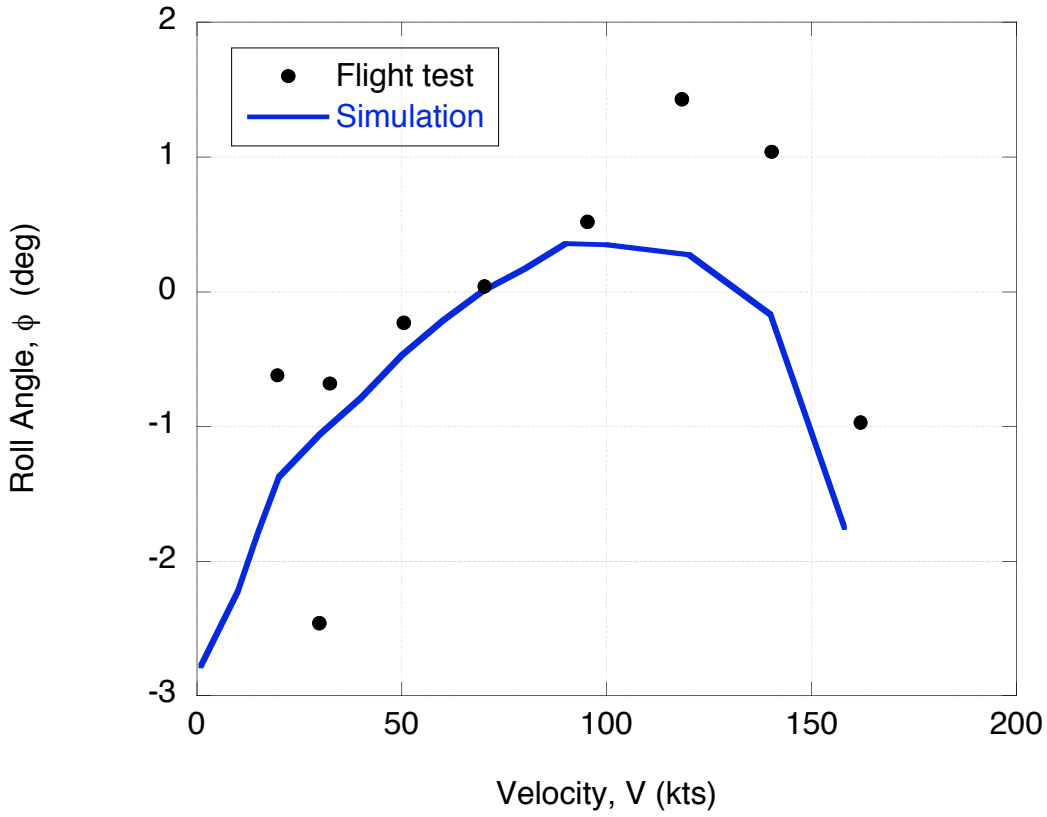

Figure 6.6: Helicopter bank angle as a function of speed, for a straight blade configuration.

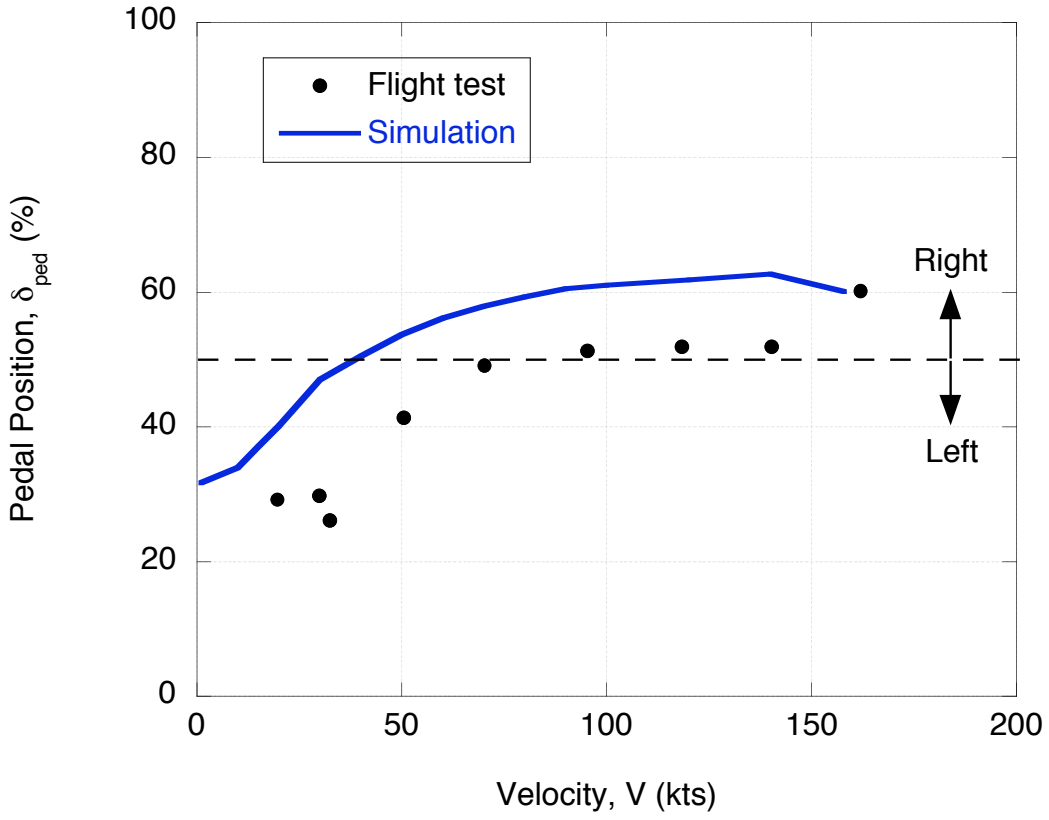

Figure 6.7: Pedal position as a function of speed, for a straight blade configuration.

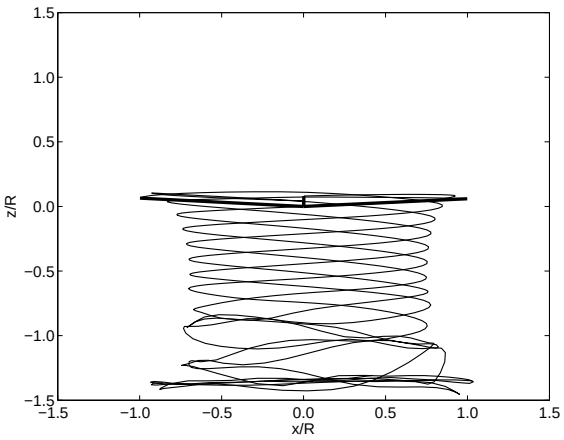

(a) $V = 1$ kts.

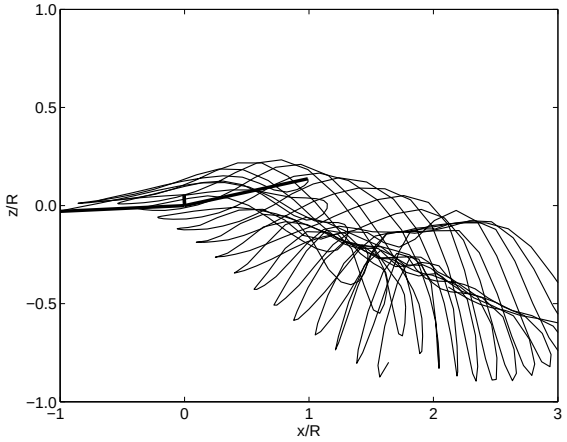

(b) $V = 40$ kts.

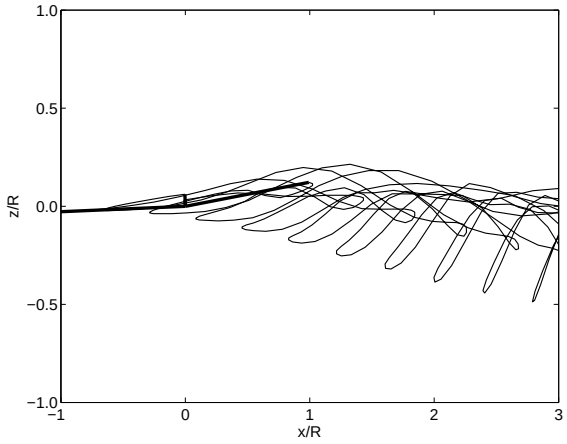

(c) $V = 100$ kts.

Figure 6.8: Side view of the wake geometry at $V = 1, 40$ and 100 kts.

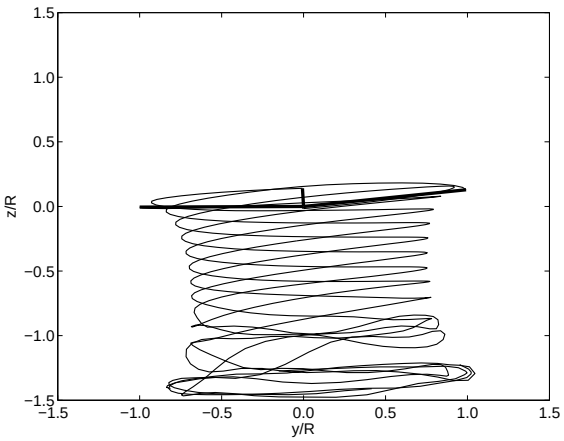

(a) $V = 1$ kts.

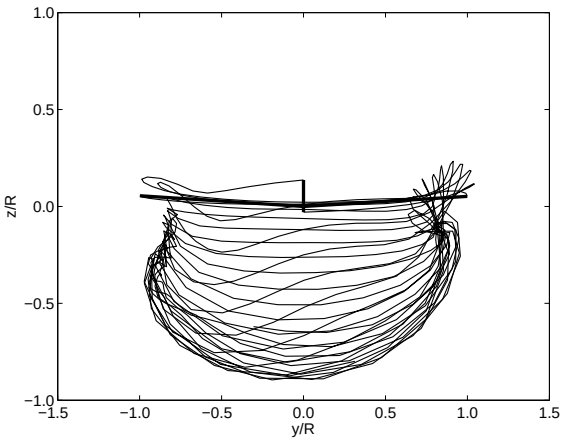

(b) $V = 40$ kts..

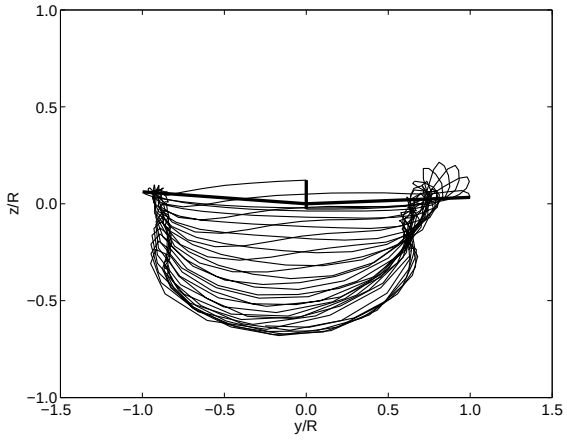

(c) $V = 100$ kts.

Figure 6.9: Rear view of the wake geometry at $V = 1, 40$ and 100 kts.

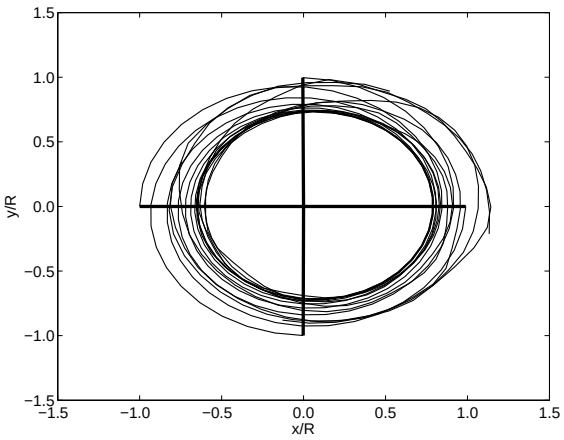

(a) $V = 1$ kts.

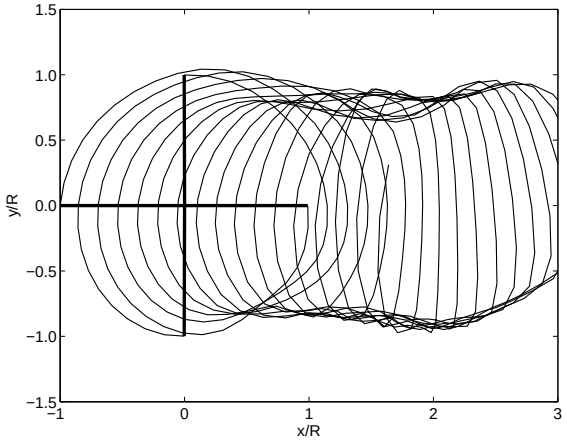

(b) $V = 40$ kts.

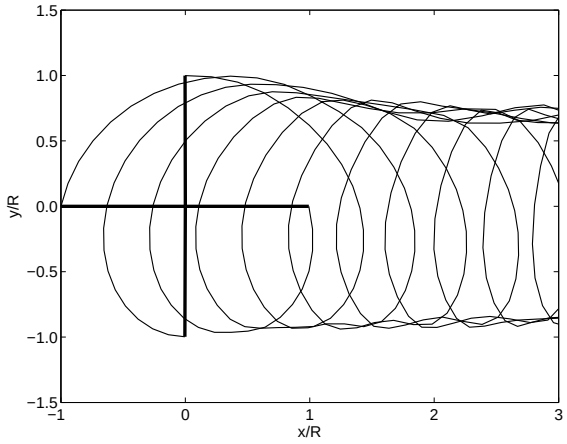

(c) $V = 100$ kts.

Figure 6.10: Top view of the wake geometry at $V = 1, 40$ and 100 kts.

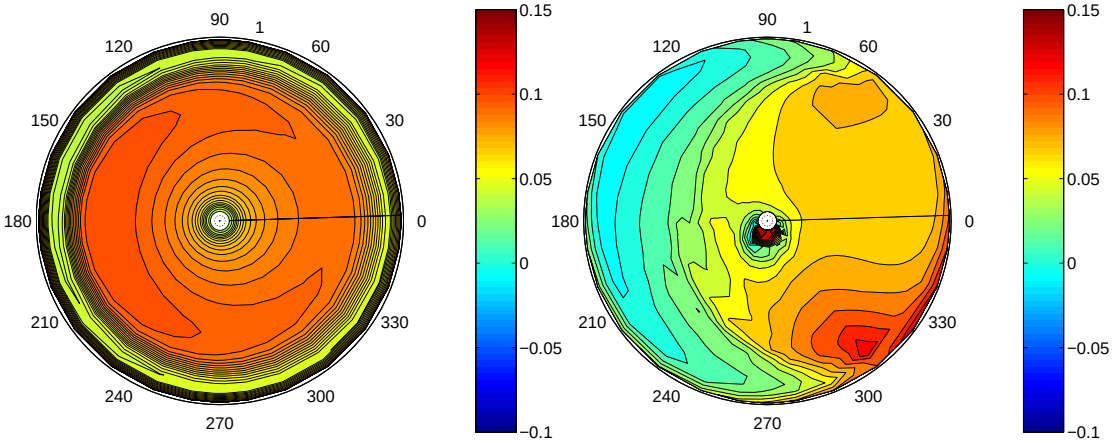

(a) Inflow, λ (N-D) $V = 1$ kt.

(b) Inflow, λ (N-D) $V = 40$ kts.

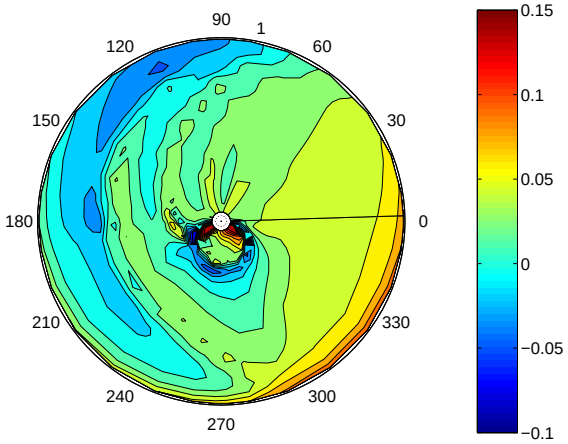

(c) Inflow, λ (N-D) $V = 100$ kts,

Figure 6.11: Distribution of induced velocities over the rotor disk.

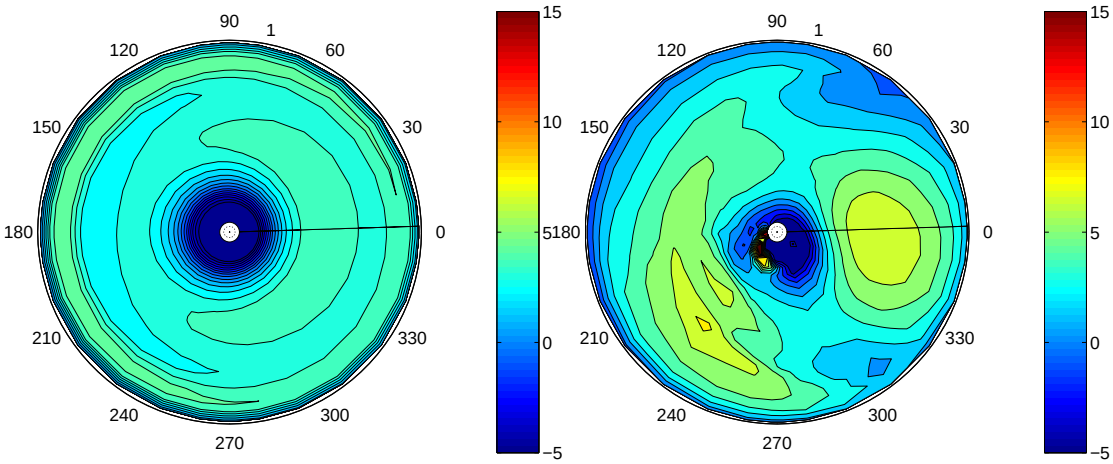

(a) Angle of attack, α (deg), $V = 1$ kt.

(b) Angle of attack, α (deg), $V = 40$ kts.

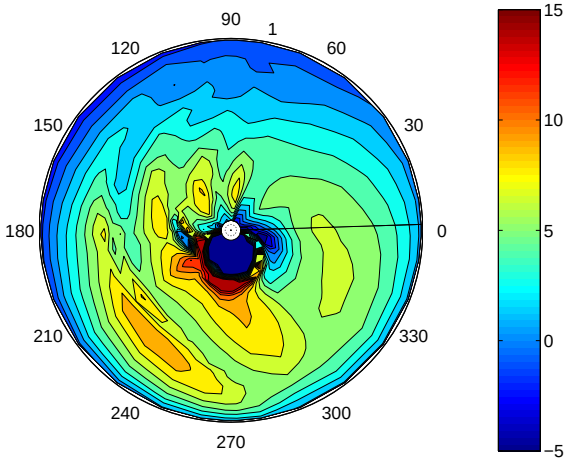

(c) Aangle of attack, α (deg), $V = 100$ kts,

Figure 6.12: Distribution of aerodynamic angle of attack over the rotor disk.

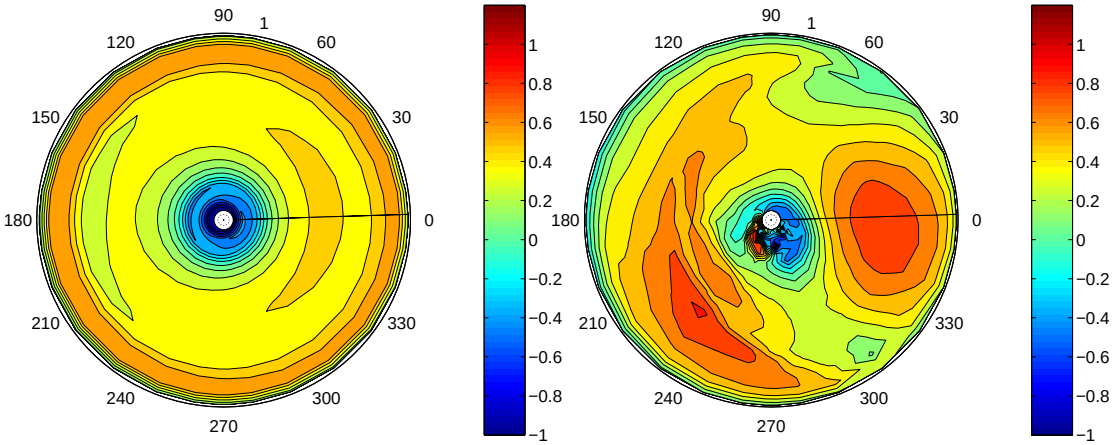

(a) C_L, (N-D), $V = 1$ kt.

(b) C_L, (N-D), $V = 40$ kts.

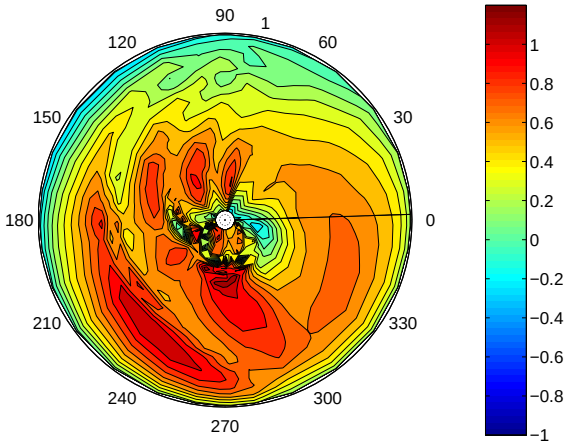

(c) C_L, (N-D), $V = 100$ kts,

Figure 6.13: Distribution of lift coefficient, C_L, over the rotor disk.

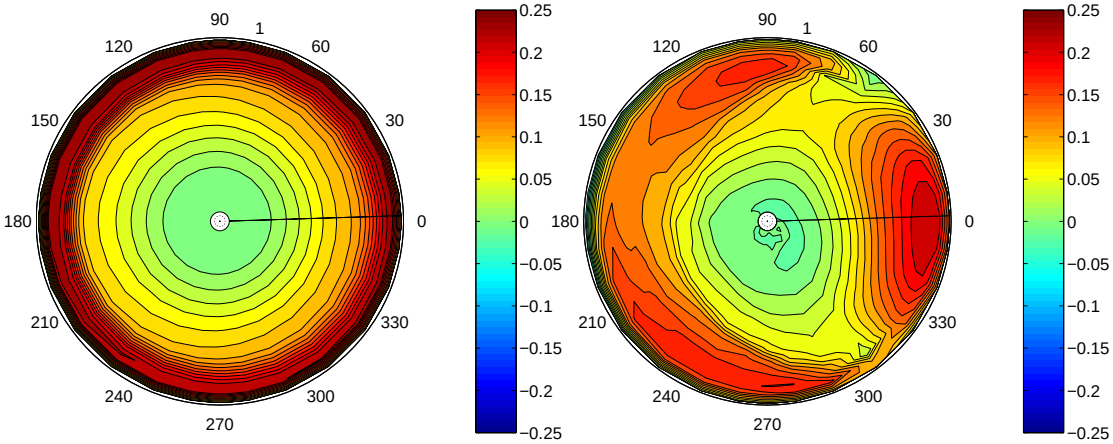

(a) $C_L M^2$, (N-D), $V = 1$ kt.

(b) $C_L M^2$, (N-D), $V = 40$ kts.

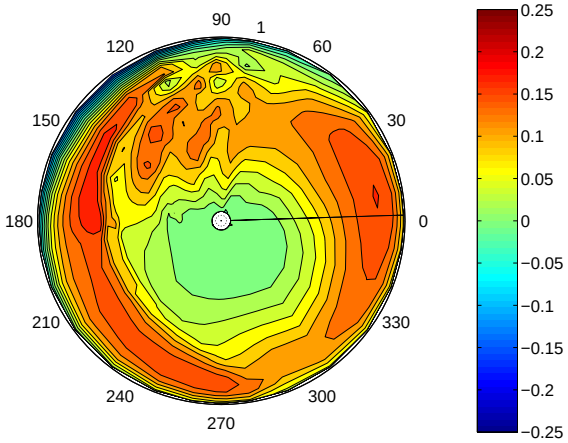

(c) $C_L M^2$, (N-D), $V = 100$ kts,

Figure 6.14: Distribution of elemental lift, $C_L M^2$, over the rotor disk.

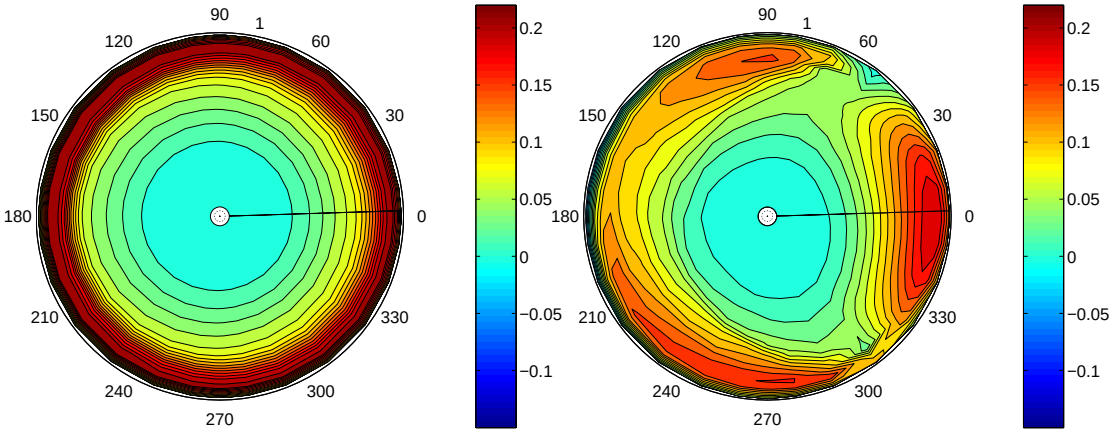

(a) rC_LM^2, (N-D), $V = 1$ kt.

(b) rC_LM^2, (N-D), $V = 40$ kts.

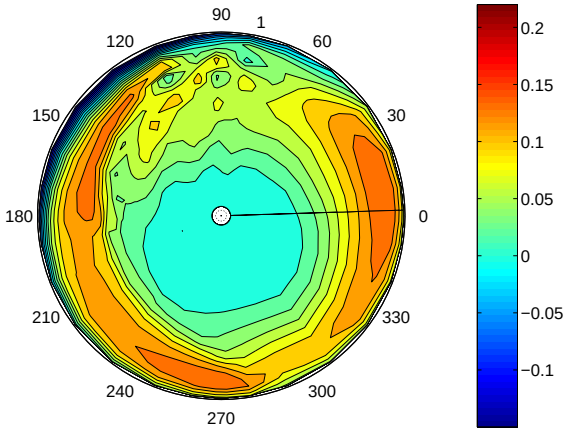

(c) rC_LM^2, (N-D), $V = 100$ kts,

Figure 6.15: Distribution of local flap moment, rC_LM^2, over the rotor disk.

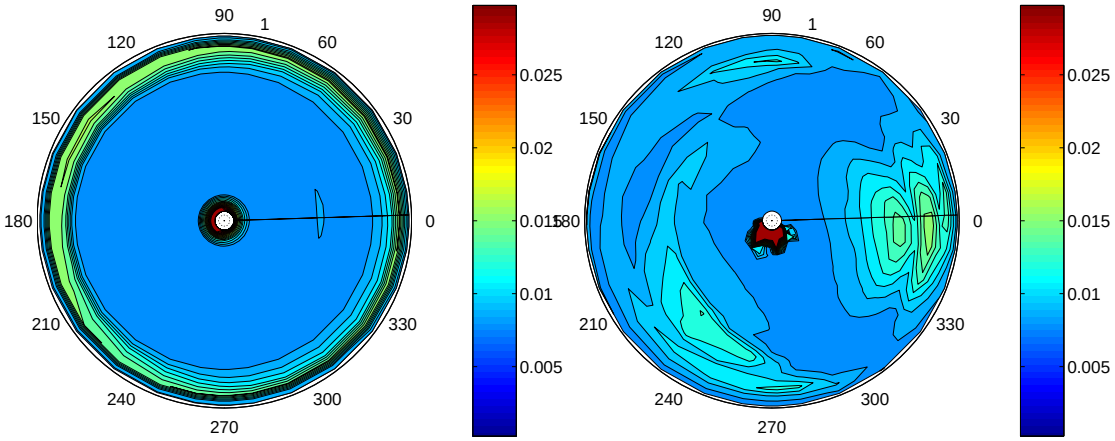

(a) C_D, (N-D), $V = 1$ kt.

(b) C_D, (N-D), $V = 40$ kts.

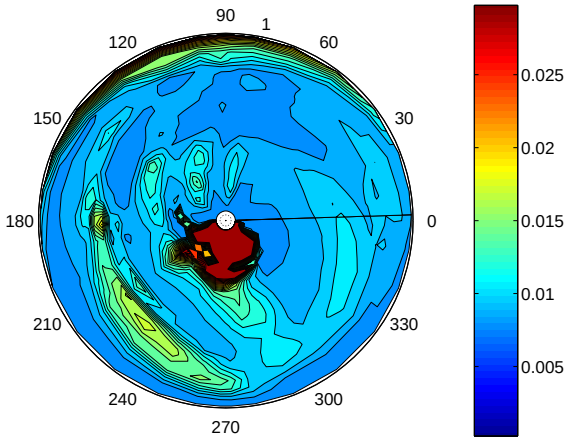

(c) C_D, (N-D), $V = 100$ kts,

Figure 6.16: Distribution of drag coefficient, C_D, over the rotor disk.

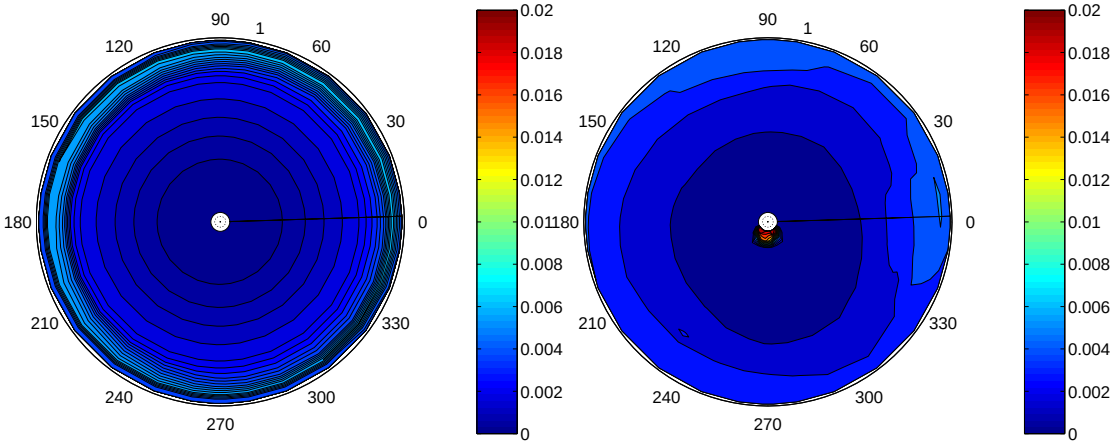

(a) $C_D M^2$, (N-D), $V = 1$ kt.

(b) $C_D M^2$, (N-D), $V = 40$ kts.

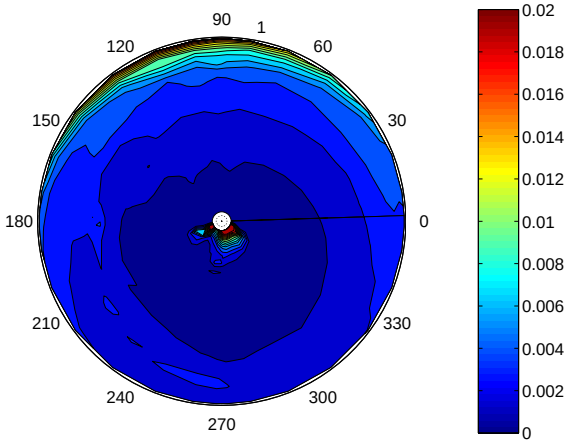

(c) $C_D M^2$, (N-D), $V = 100$ kts,

Figure 6.17: Distribution of elemental drag, $C_D M^2$, over the rotor disk.

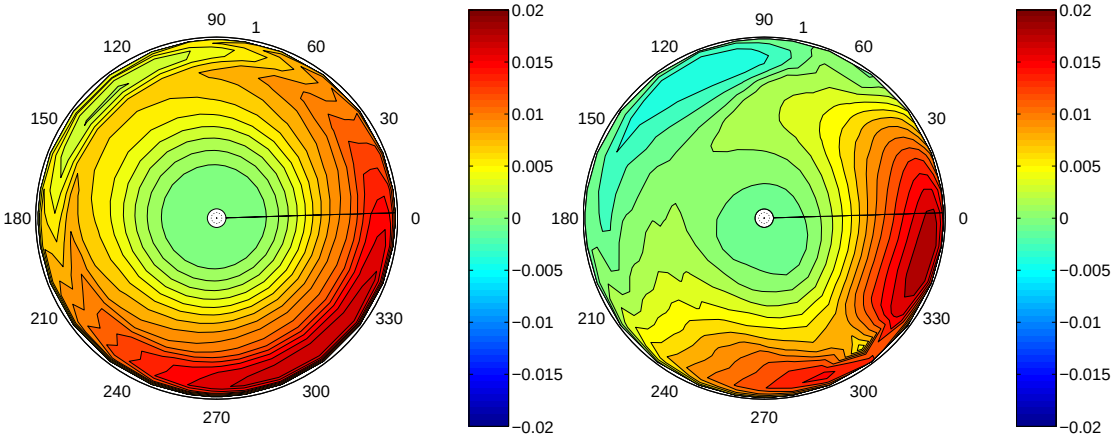

(a) $rC_L M^2 \sin\phi$ (N-D), $V = 1$ kt.

(b) $rC_L M^2 \sin\phi$ (N-D), $V = 40$ kts.

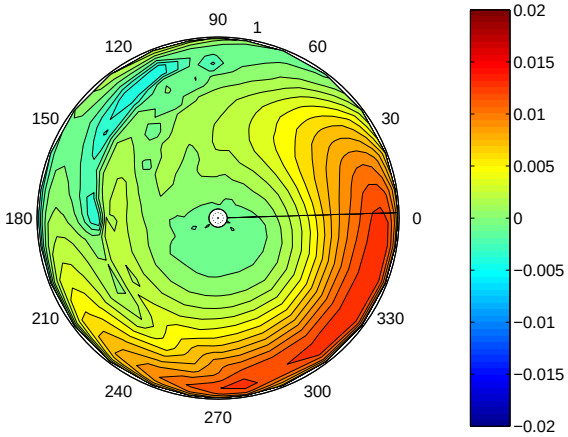

(c) $rC_L M^2 \sin\phi$ (N-D), $V = 100$ kts.

Figure 6.18: Elemental induced torque distribution, $rC_L M^2 \sin\phi$, over the rotor disk.

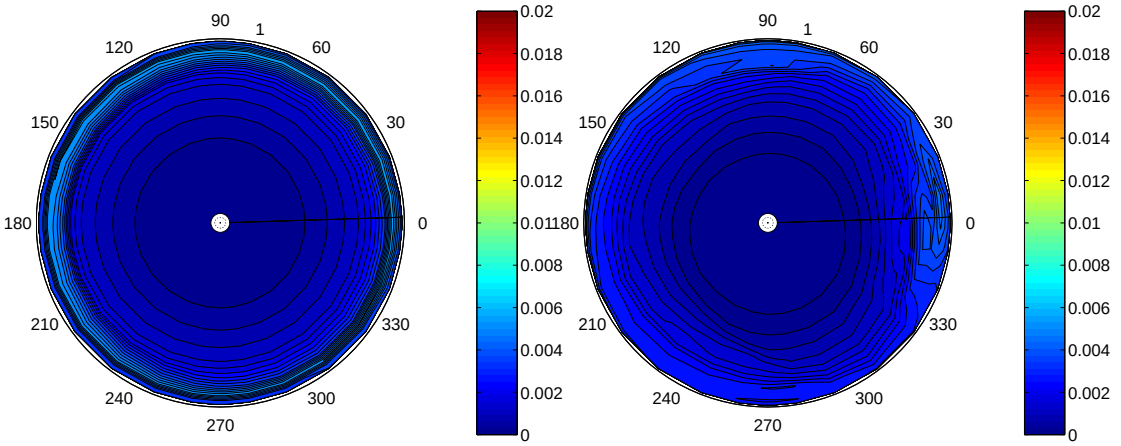

(a) $rC_D M^2 \cos\phi$ (N-D), $V = 1$ kt.

(b) $rC_D M^2 \cos\phi$ (N-D), $V = 40$ kts.

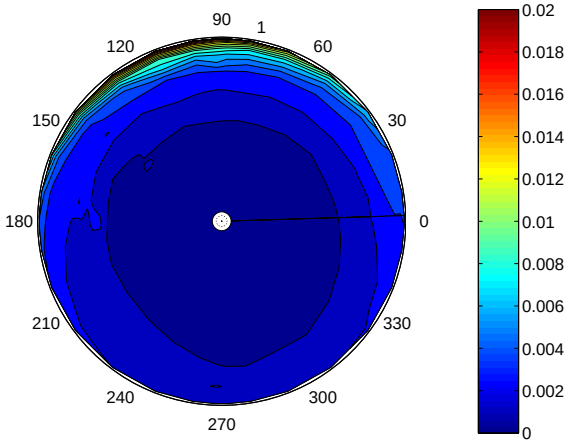

(c) $rC_D M^2 \cos\phi$ (N-D), $V = 100$ kts.

Figure 6.19: Elemental profile torque distribution, $rC_D M^2 \cos\phi$, over the rotor disk.

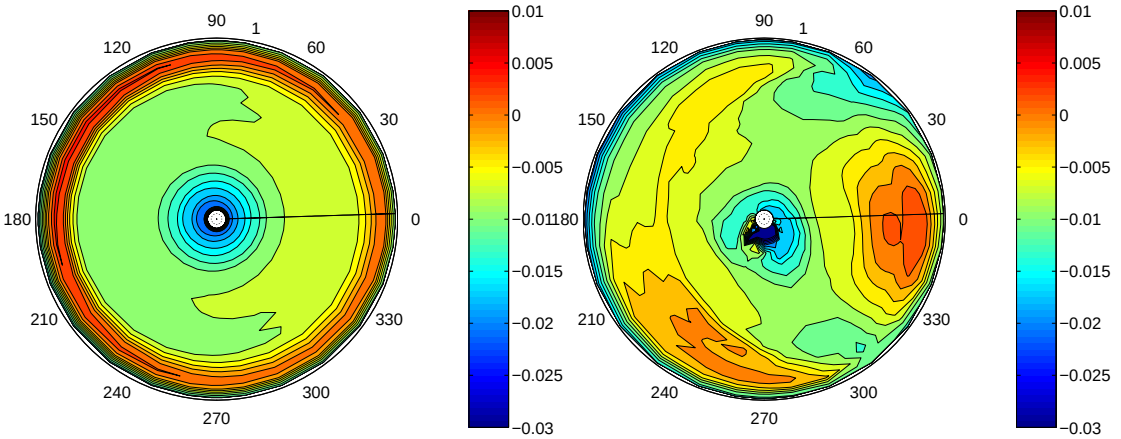

(a) C_M, (N-D), $V = 1$ kt.

(b) C_M, (N-D), $V = 40$ kts.

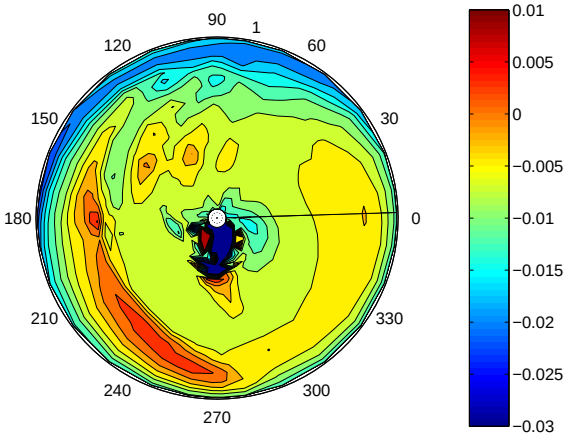

(c) C_M, (N-D), $V = 100$ kts,

Figure 6.20: Distribution of pitching moment coefficient, C_M, over the rotor disk.

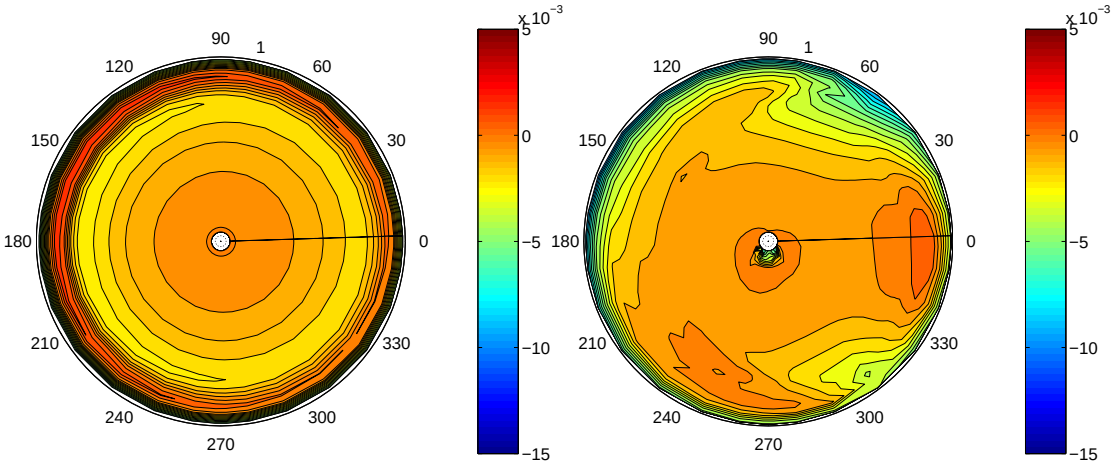

(a) $C_M M^2$, (N-D), $V = 1$ kt.

(b) $C_M M^2$, (N-D), $V = 40$ kts.

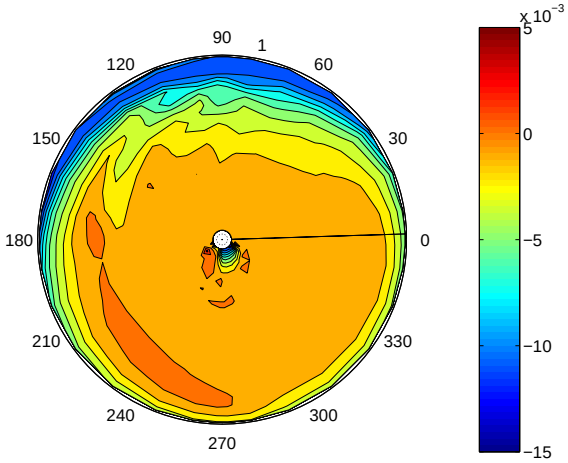

(c) $C_M M^2$, (N-D), $V = 100$ kts,

Figure 6.21: Distribution of elemental pitching moment, $C_M M^2$, over the rotor disk.

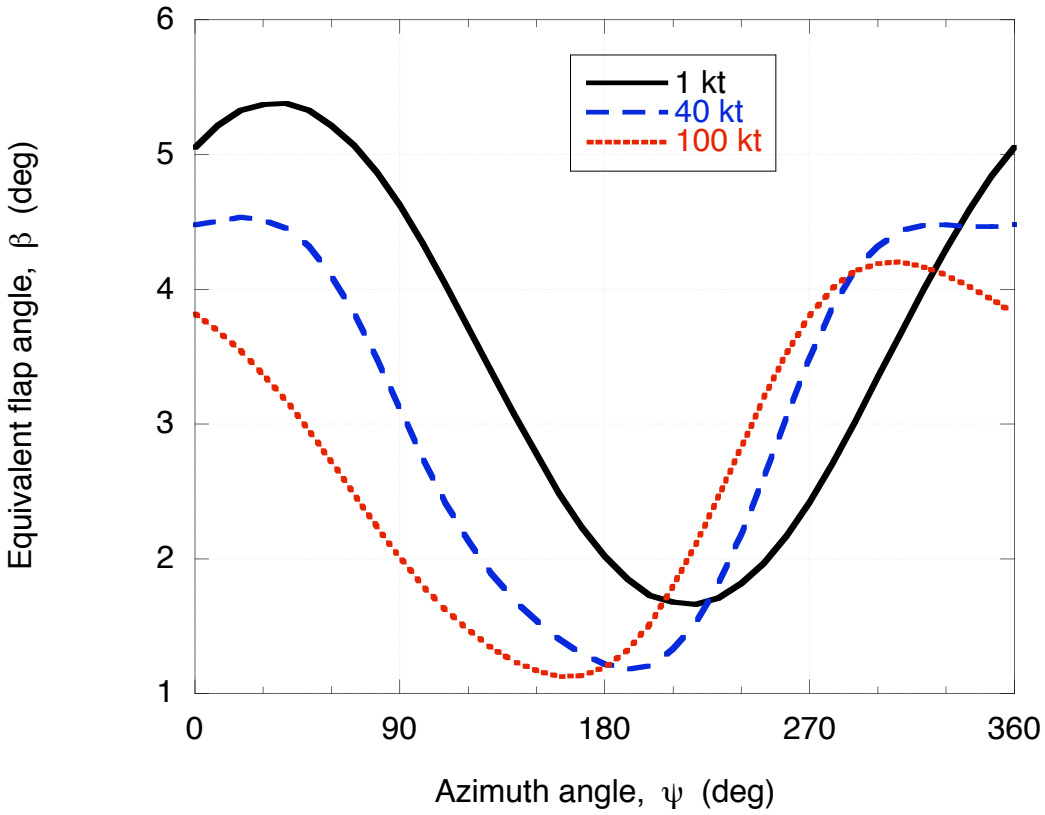

Figure 6.22: Equivalent flap angle distribution as a function of azimuth at $V = 1$ kt, 40 kts and 100 kts.

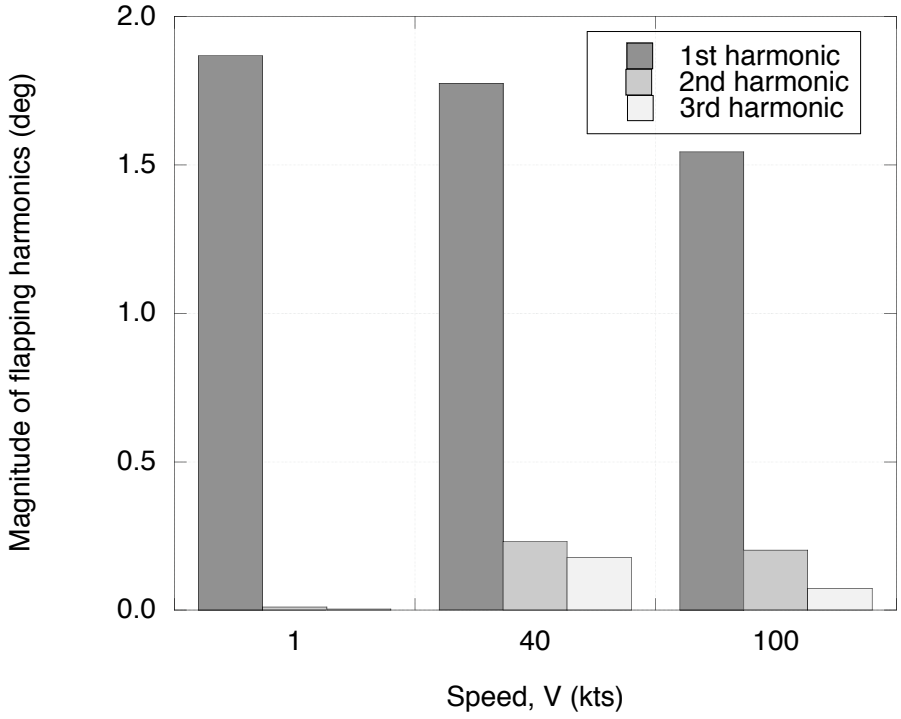

(a) Magnitude.

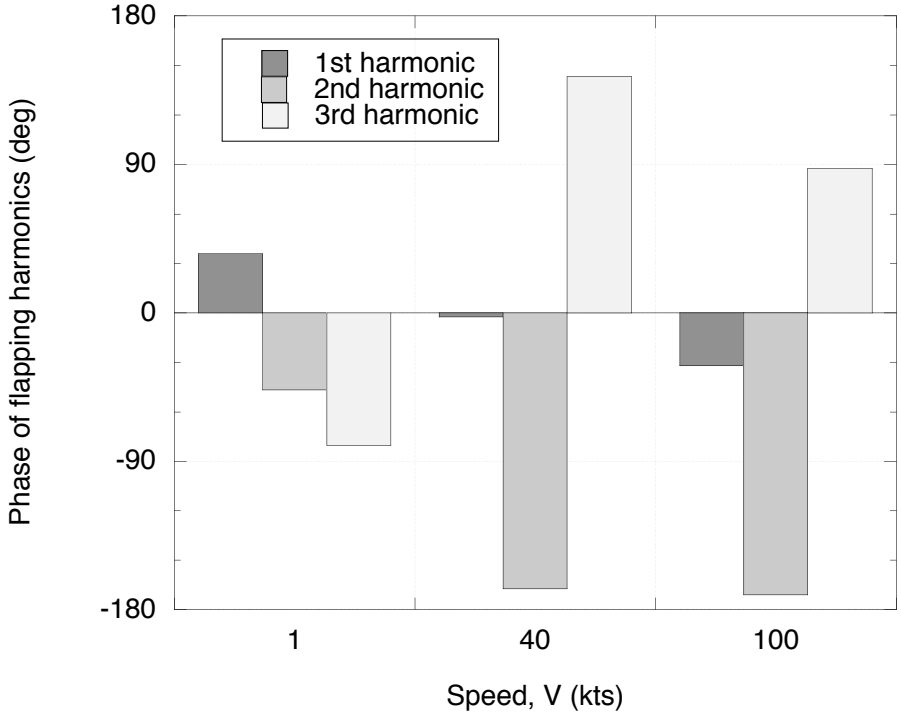

(b) Phase.

Figure 6.23: Magnitude and phase of the first three flapping harmonics at $V = 1$ kt, 40 kts and 100 kts.

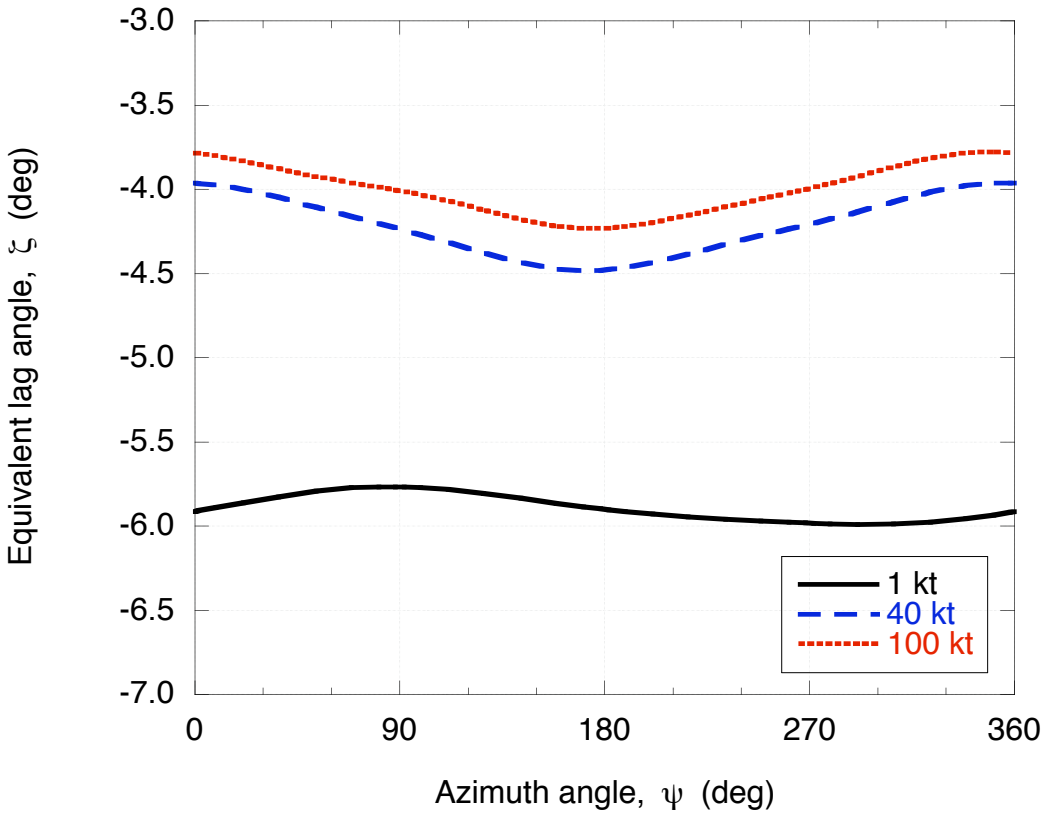

Figure 6.24: Equivalent lag angle distribution as a function of azimuth at $V = 1$ kt, 40 kts and 100 kts.

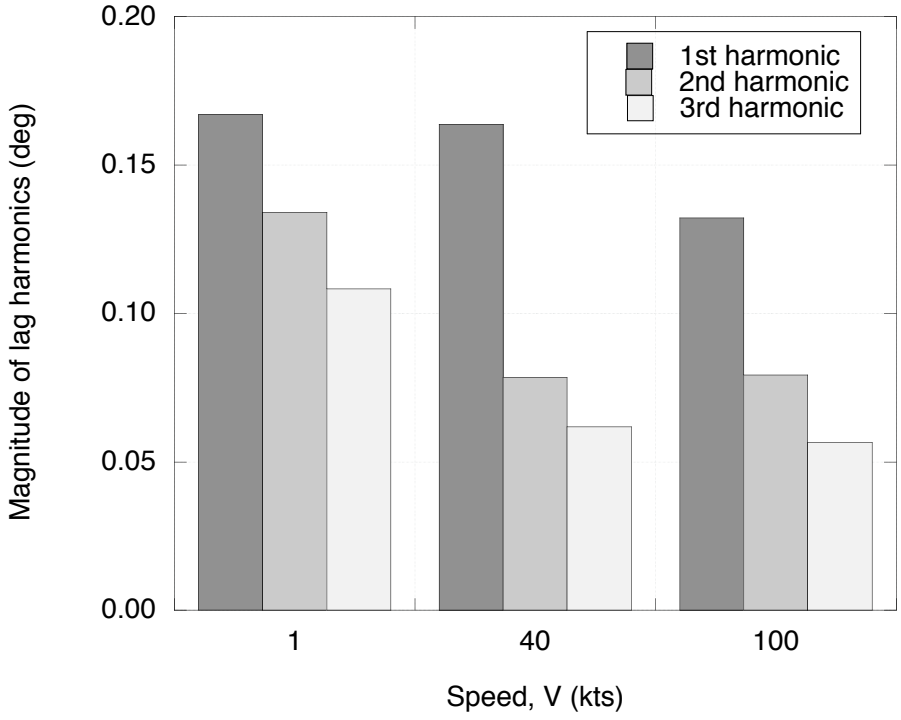

(a) Magnitude.

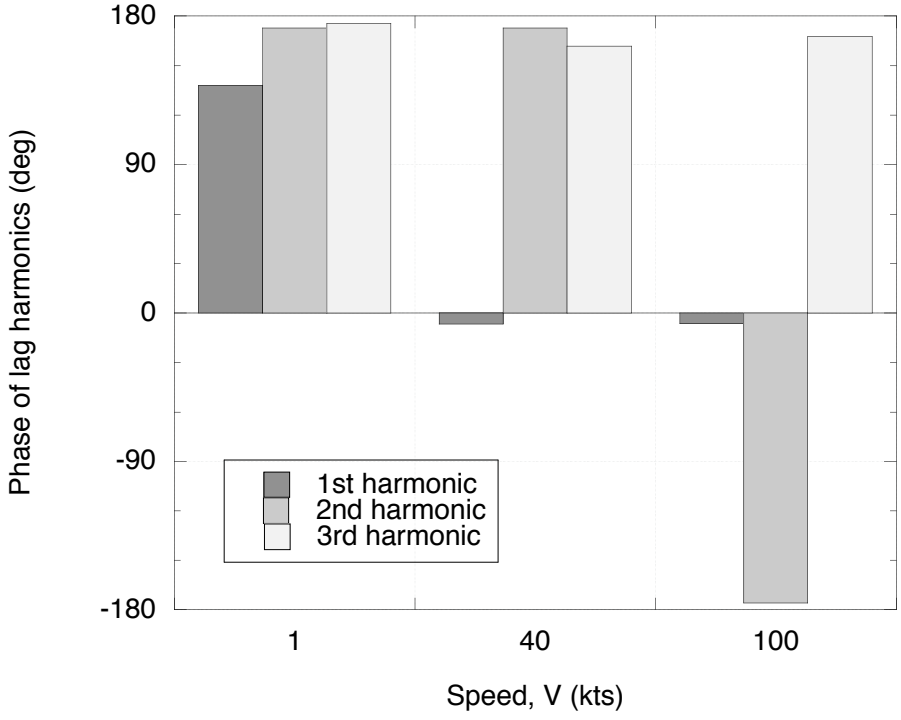

(b) Phase.

Figure 6.25: Magnitude and phase of the first three lag harmonics at $V = 1$ kt, 40 kts and 100 kts.

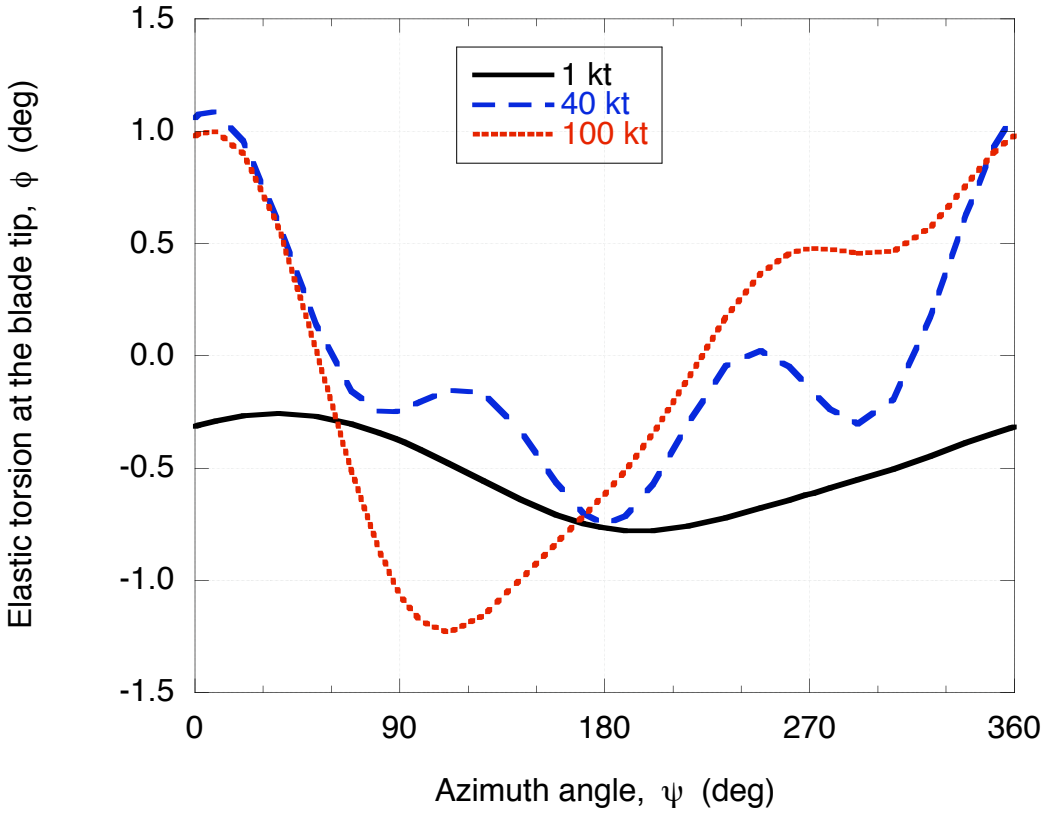

Figure 6.26: Blade tip elastic torsion as a function of azimuth at $V = 1$ kt, 40 kts and 100 kts.

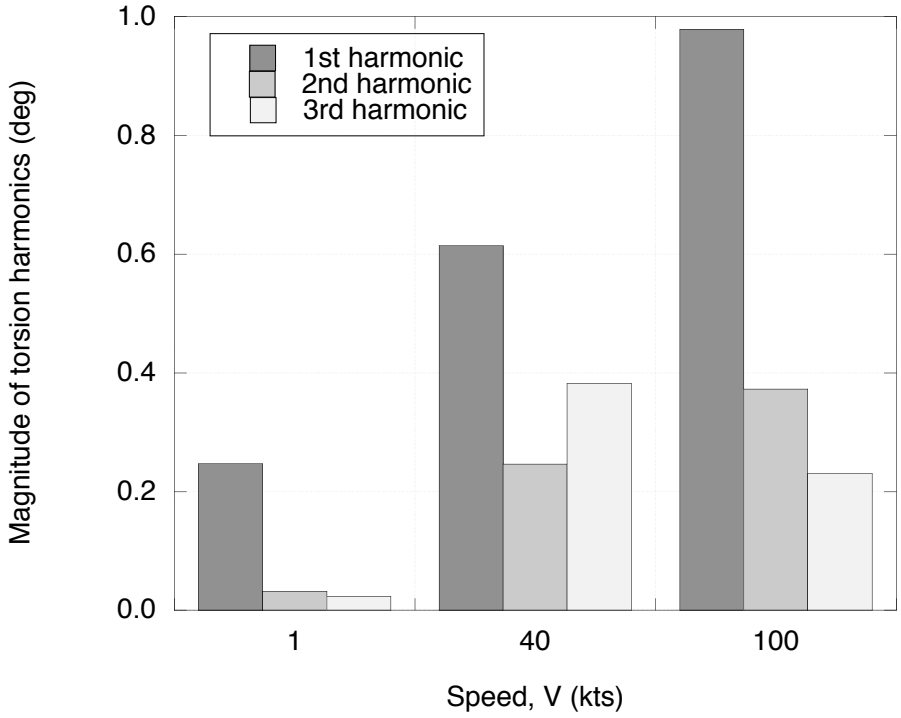

(a) Magnitude.

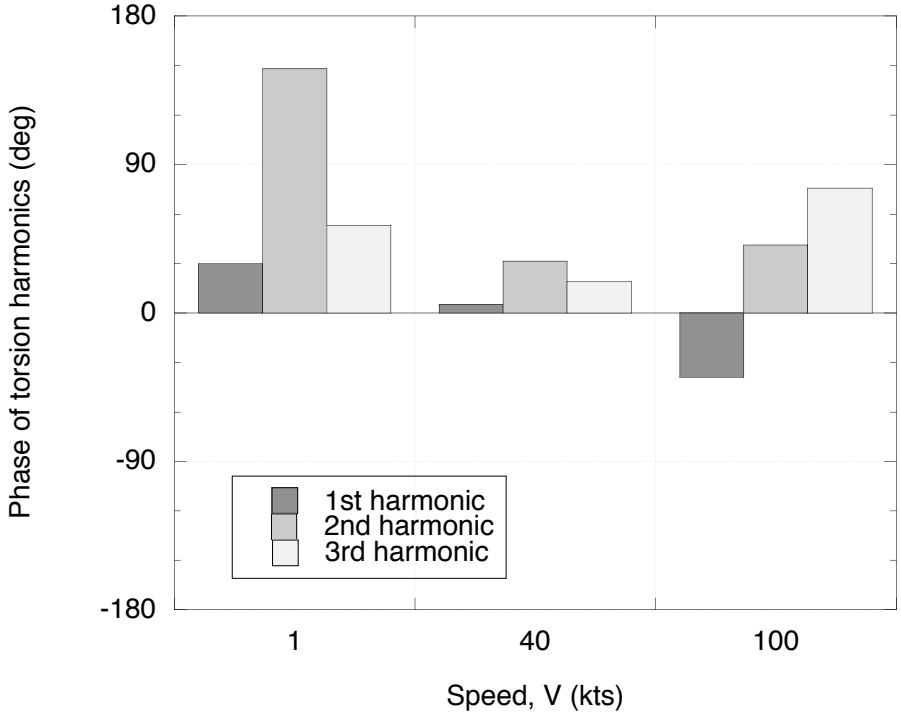

(b) Phase.

Figure 6.27: Magnitude and phase of the first three torsion harmonics at $V = 1$ kt, 40 kts and 100 kts.

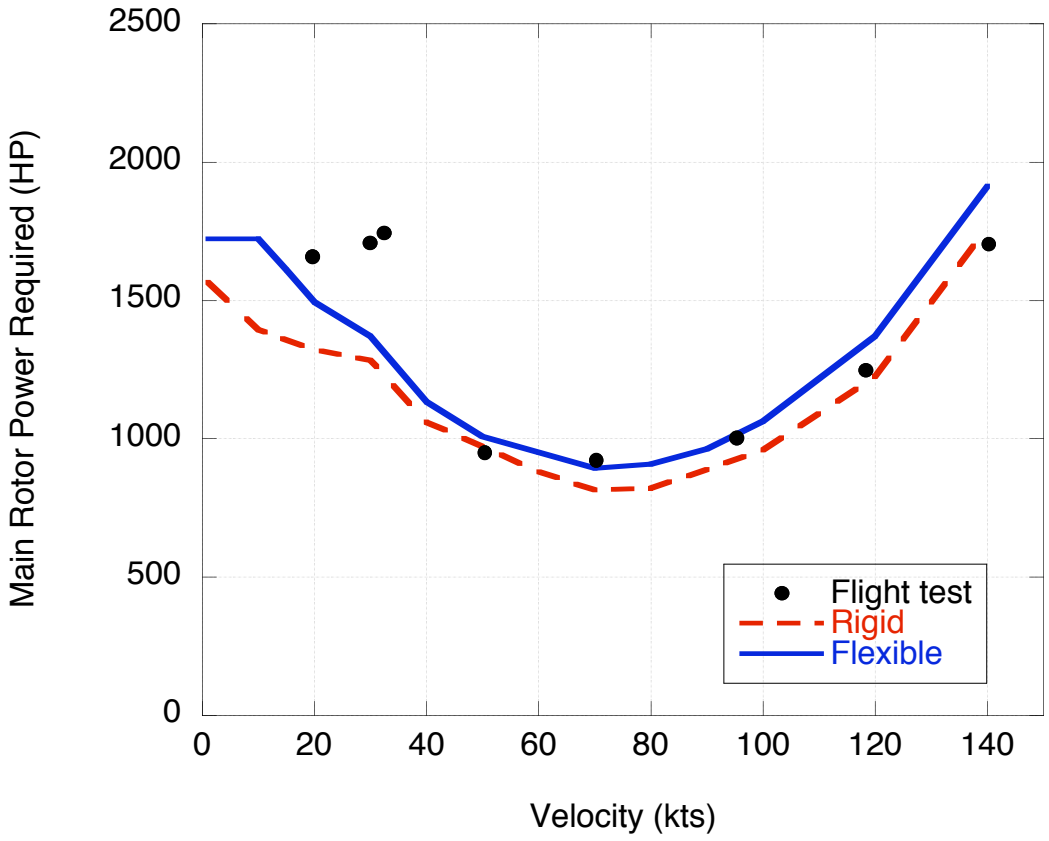

Figure 6.28: Main rotor power required, Q_{MR}, as a function of speed, with a rigid blade model and a flexible blade model.

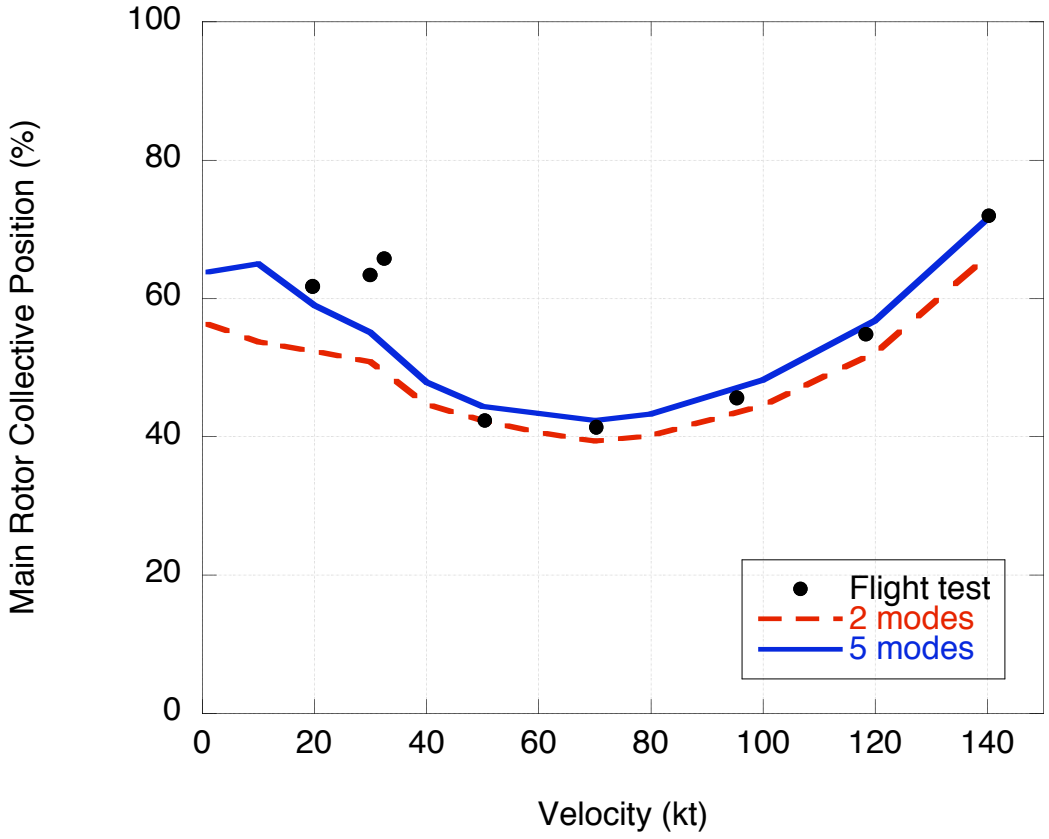

Figure 6.29: Main rotor collective as a function of speed, with a rigid blade model and a flexible blade model.

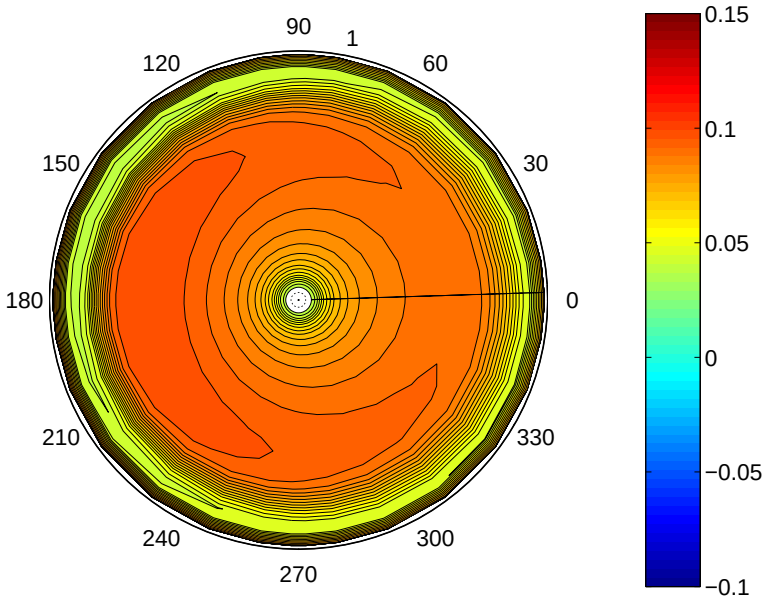

(a) Inflow, λ, flexible blade

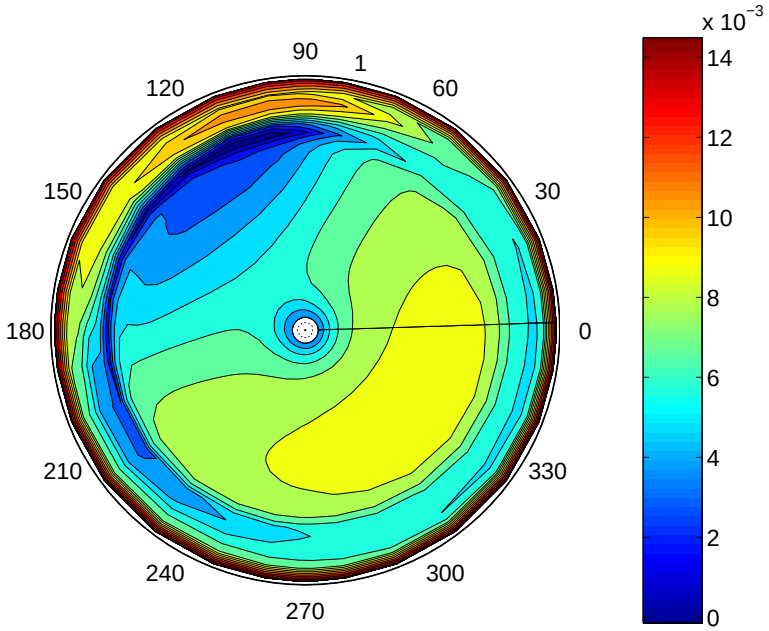

(b) Inflow difference, $\lambda_{flexible} - \lambda_{rigid}$

Figure 6.30: Comparison of the induced inflow distribution with the rigid and flexible blade models; $V = 1$ kt.

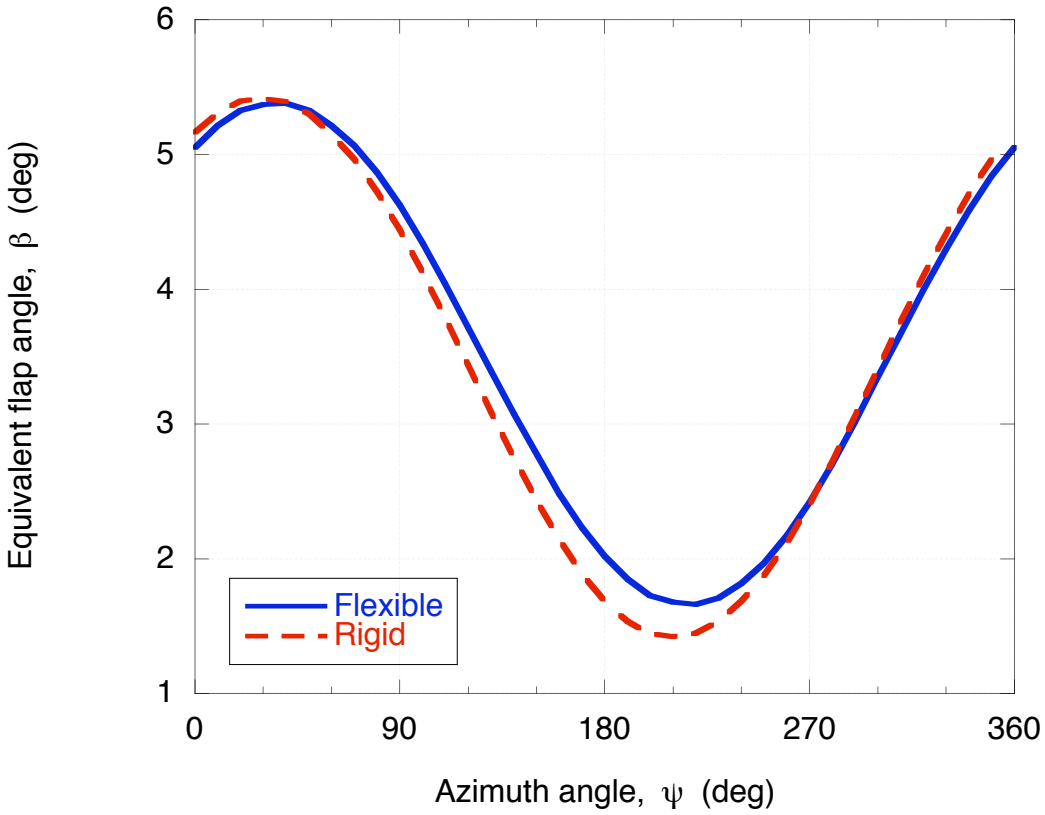

Figure 6.31: Equivalent flap angle as a function of azimuth azimuth at $V = 1$ kt, with a rigid blade model and a flexible blade model.

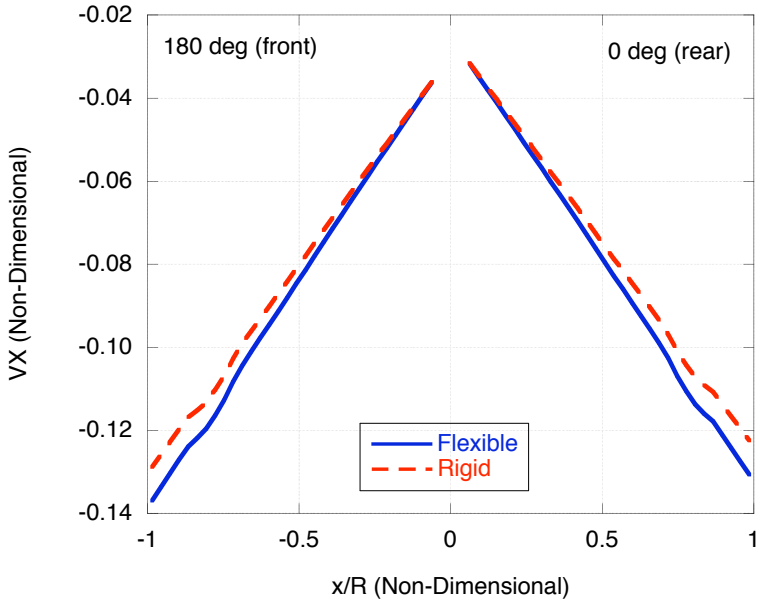

(a) V_x

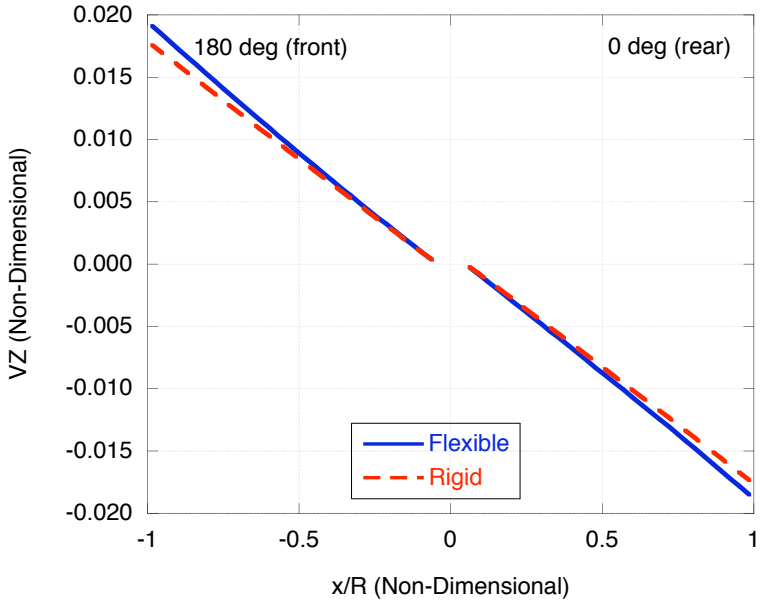

(b) V_z

Figure 6.32: Comparison of the x and z-components of the velocity seen by the blade section for a longitudinal cross section of the rotor, with the rigid and flexible blade models; $V = 1$ kt.

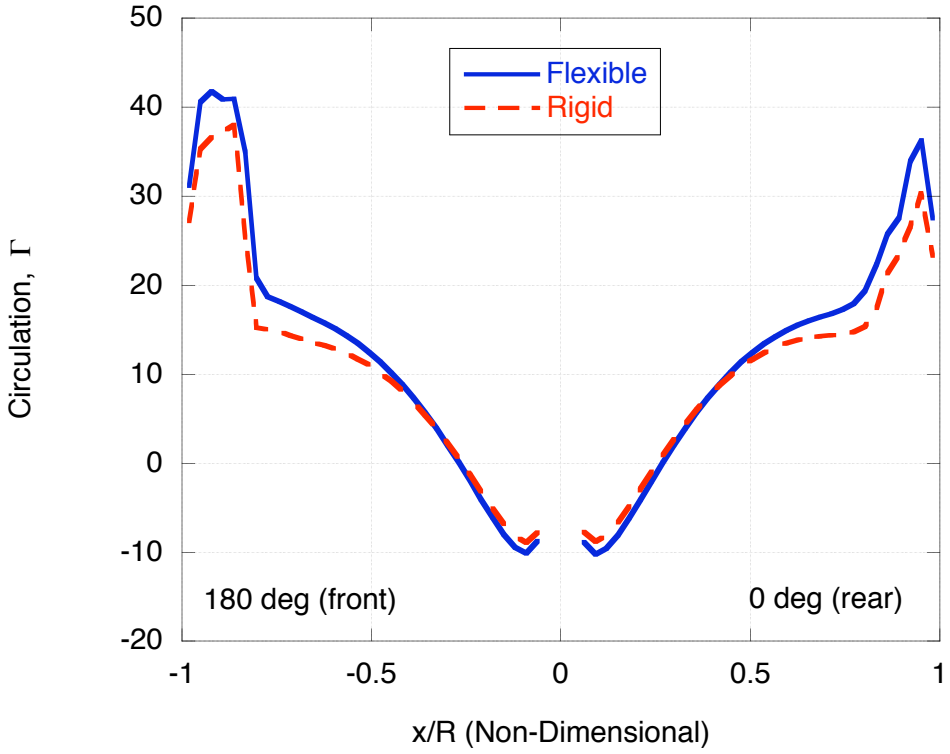

Figure 6.33: Comparison of the bound circulation for a longitudinal cross section of the rotor, with the rigid and flexible blade models; $V = 1$ kt.

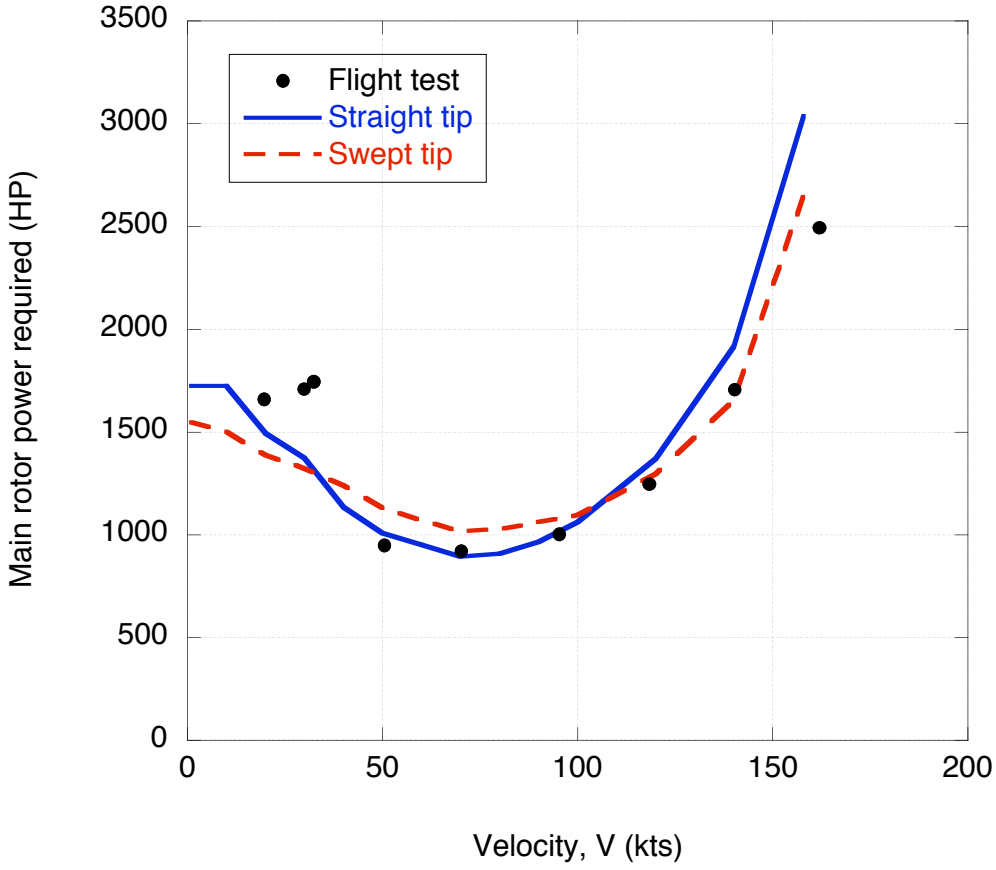

Figure 6.34: Main rotor power required, Q_{MR}, as a function of speed with a time-marching free wake model with a straight and swept tip blade models.

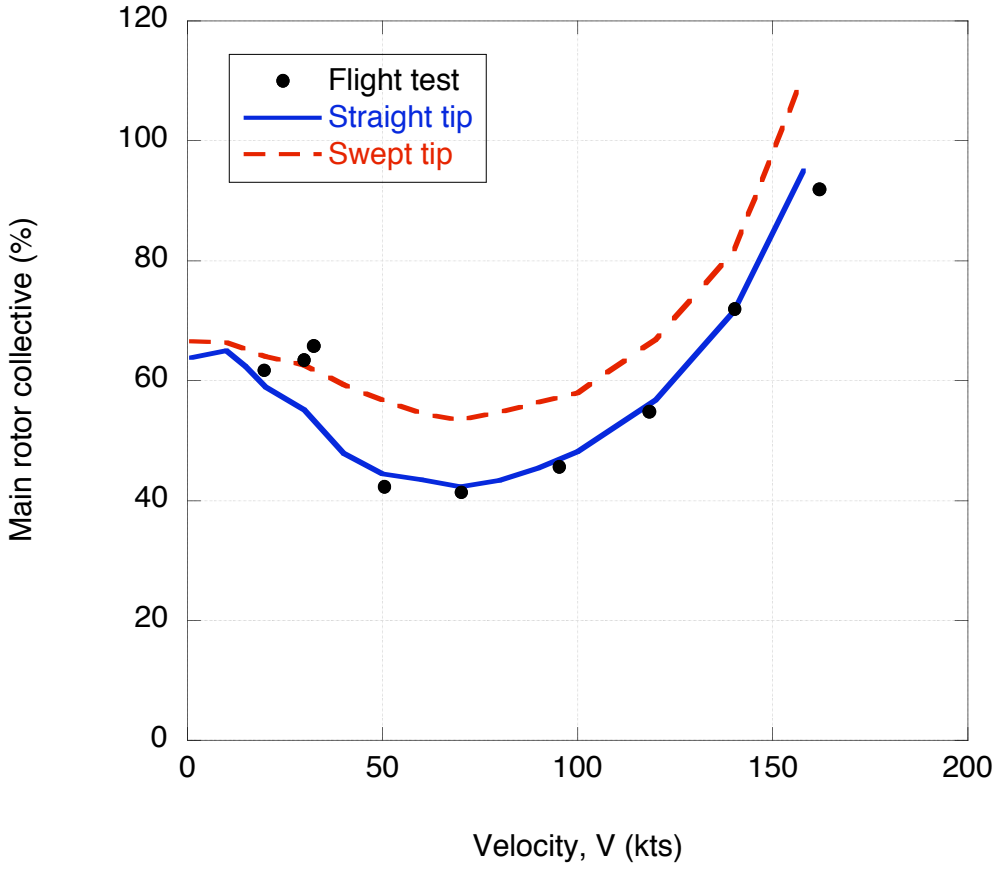

Figure 6.35: Main rotor collective as a function of speed with a straight and swept tip blade models.

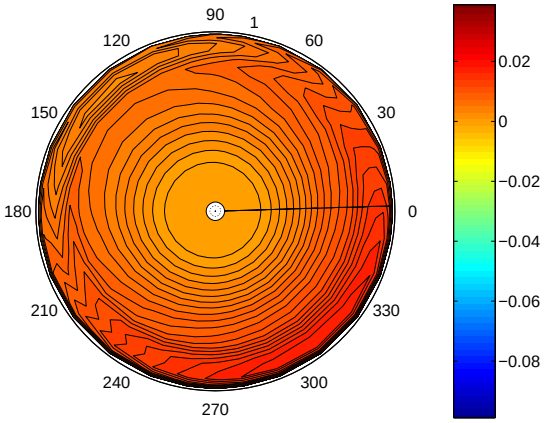

(a) $rC_L M^2 \sin\phi$, $V = 1$ kt, straight.

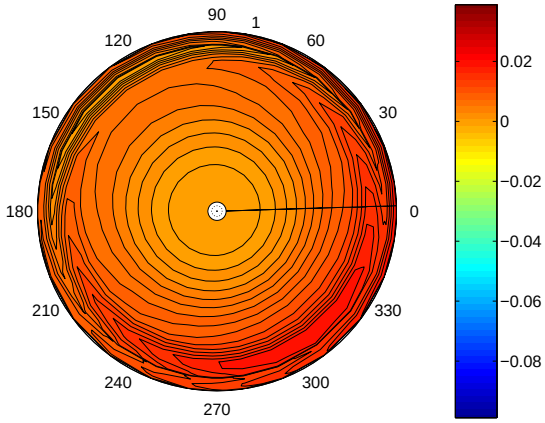

(b) $rC_L M^2 \sin\phi$, $V = 1$ kt, swept.

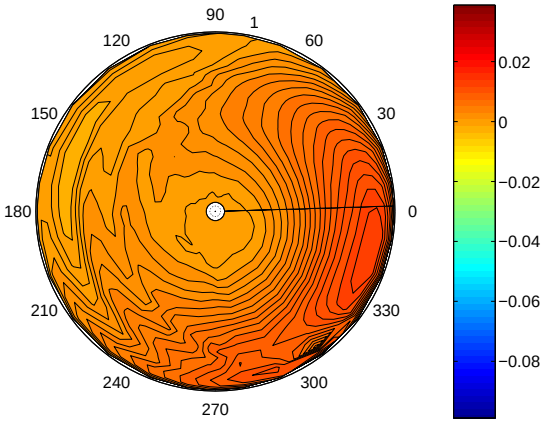

(c) $rC_L M^2 \sin\phi$, $V = 60$ kts, straight.

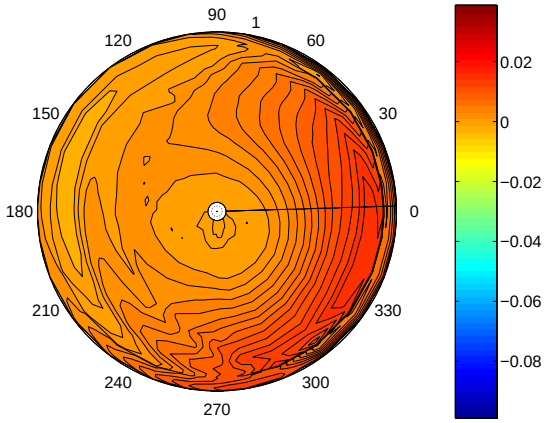

(d) $rC_L M^2 \sin\phi$, $V = 60$ kts, swept.

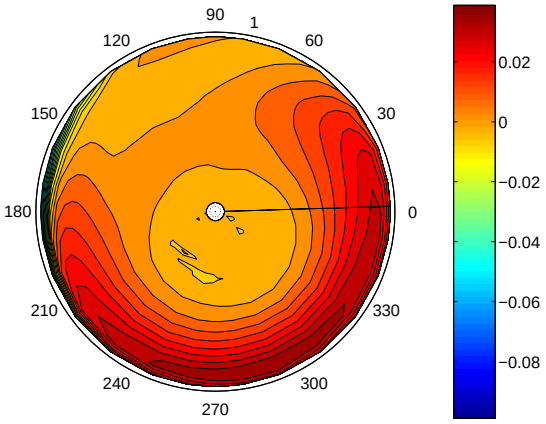

(e) $rC_L M^2 \sin\phi$, $V = 158$ kts, straight.

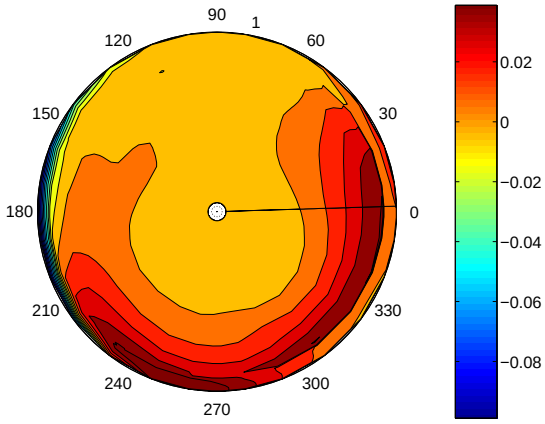

(f) $rC_L M^2 \sin\phi$, $V = 158$ kts, swept.

Figure 6.36: Elemental induced torque, $rC_L M^2 \sin\phi$, with a straight and swept tip blade models, at $V = 1, 60$ and 158 kts.

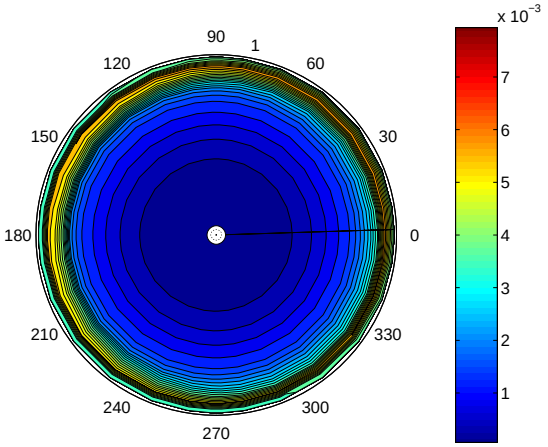

(a) $rC_DM^2 \sin\phi$, $V = 1$ kt, straight.

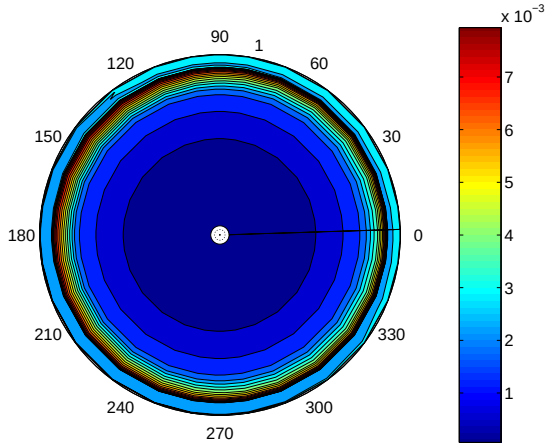

(b) $rC_DM^2 \sin\phi$, $V = 1$ kt, swept.

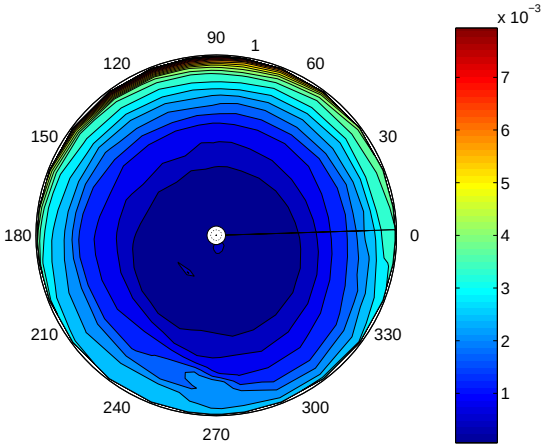

(c) $rC_DM^2 \sin\phi$, $V = 60$ kts, straight.

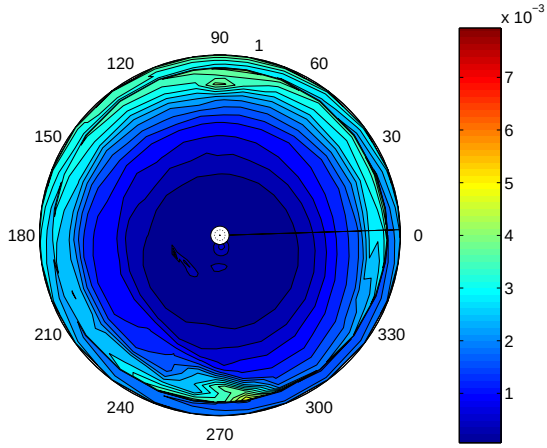

(d) $rC_DM^2 \sin\phi$, $V = 60$ kts, swept.

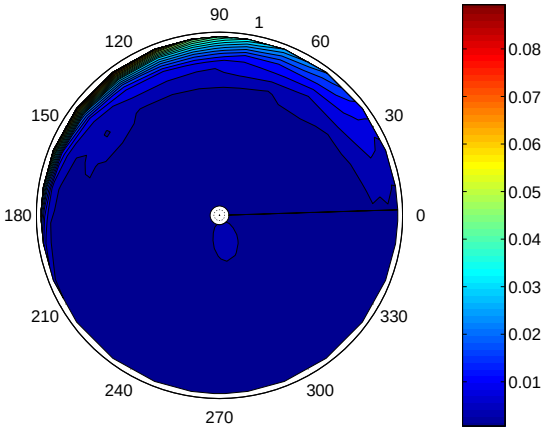

(e) $rC_DM^2 \sin\phi$, $V = 158$ kts, straight.

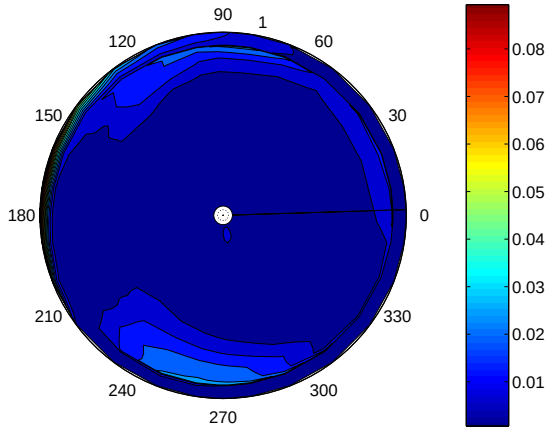

(f) $rC_DM^2 \sin\phi$, $V = 158$ kts, swept.

Figure 6.37: Elemental profile torque, $rC_DM^2 \cos\phi$, with a straight and swept tip blade models, at $V = 1, 60$ and 158 kts.

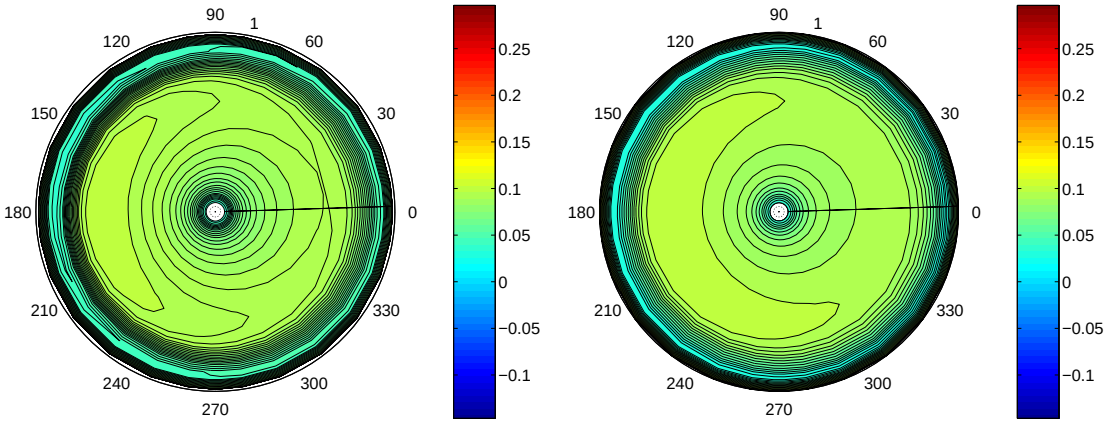

(a) λ, $V = 1$ kt, straight.

(b) λ, $V = 1$ kt, swept.

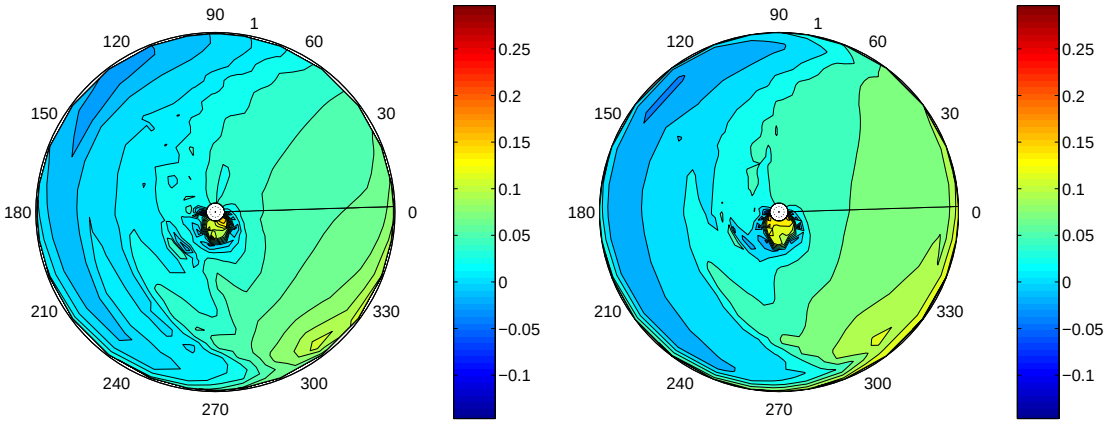

(c) λ, $V = 60$ kts, straight.

(d) λ, $V = 60$ kts, swept.

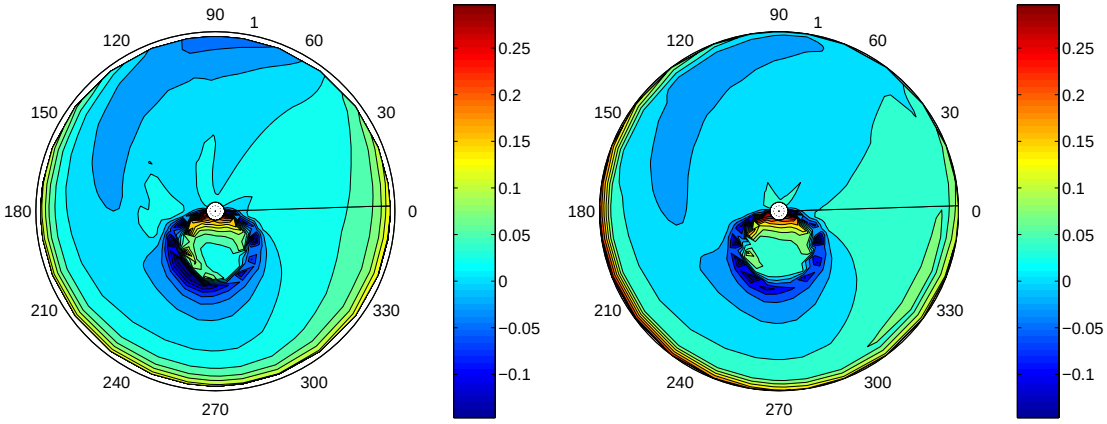

(e) λ, $V = 158$ kts, straight.

(f) λ, $V = 158$ kts, swept.

Figure 6.38: Induced velocities, λ, with a straight and swept tip blade models, at $V = 1, 60$ and 158 kts.

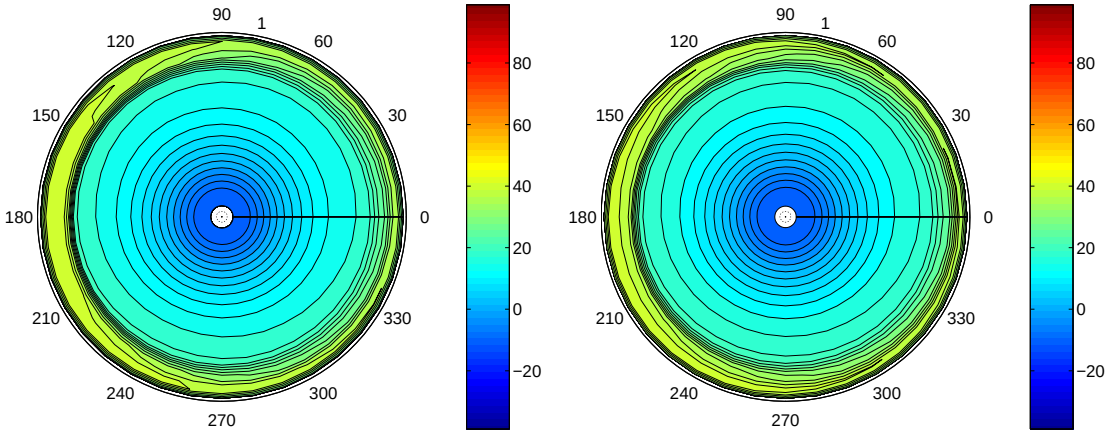

(a) Γ, $V = 1$ kt, straight.

(b) Γ, $V = 1$ kt, swept.

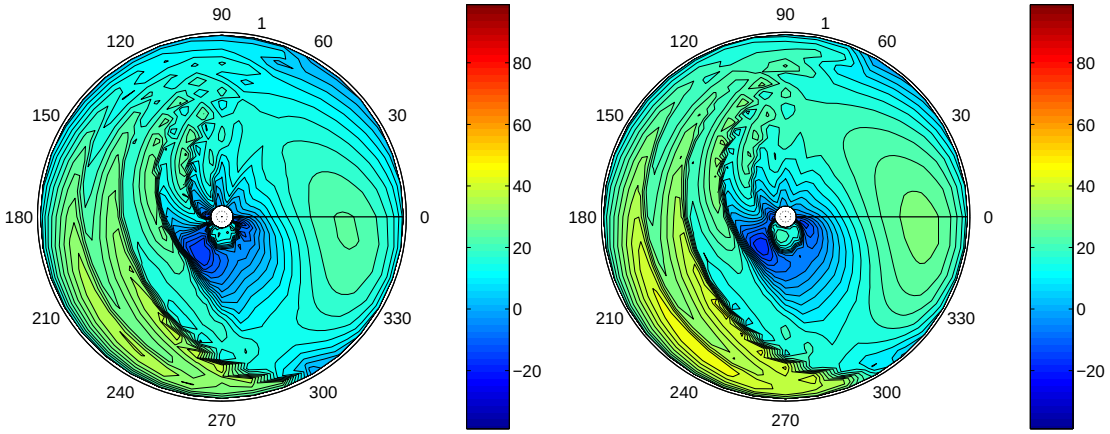

(c) Γ, $V = 60$ kts, straight.

(d) Γ, $V = 60$ kts, swept.

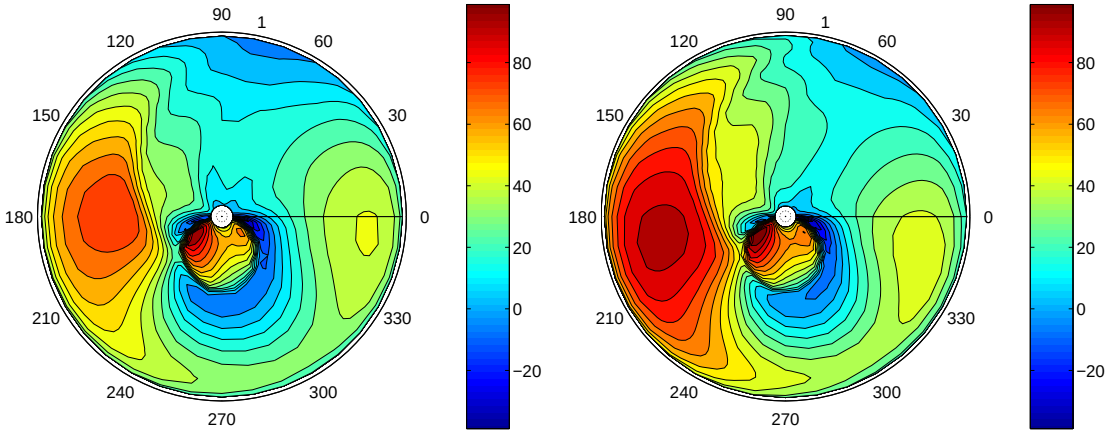

(e) Γ, $V = 158$ kts, straight.

(f) Γ, $V = 158$ kts, swept.

Figure 6.39: Bound circulation, Γ, with a straight and swept tip blade models, at $V = 1, 60$ and 158 kts.

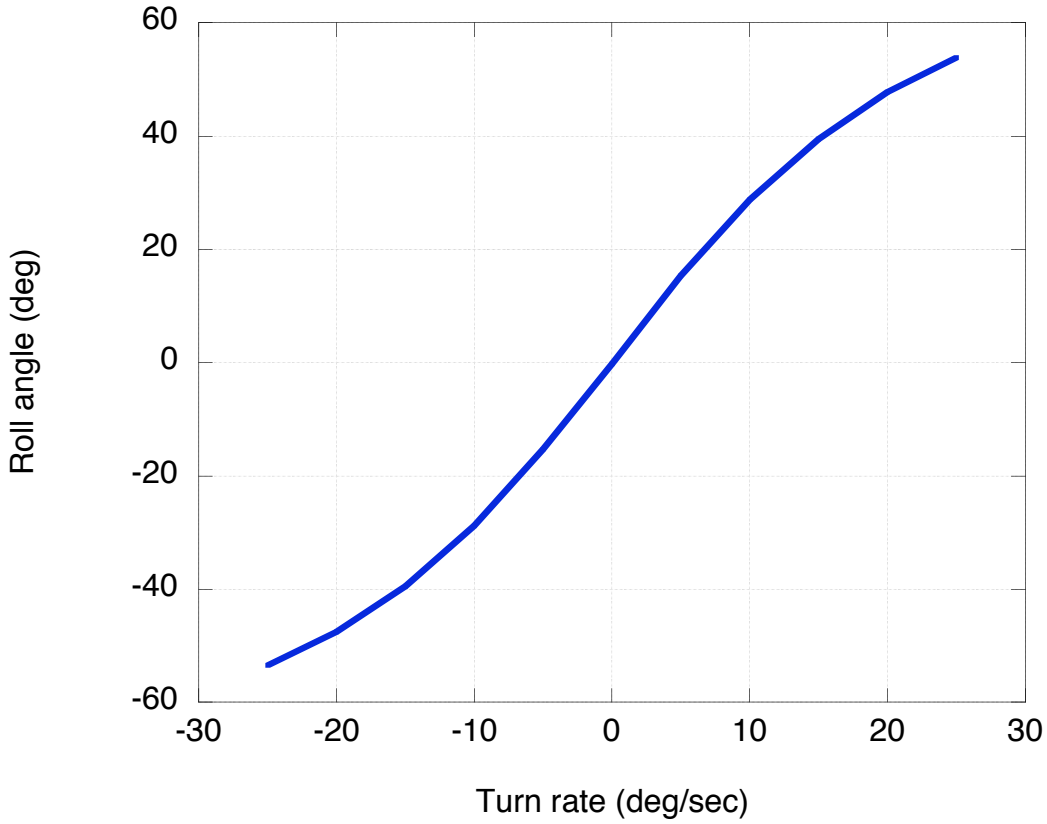

Figure 6.40: Relation between the roll angle, ϕ, and the turn rate, $\dot{\psi}$.

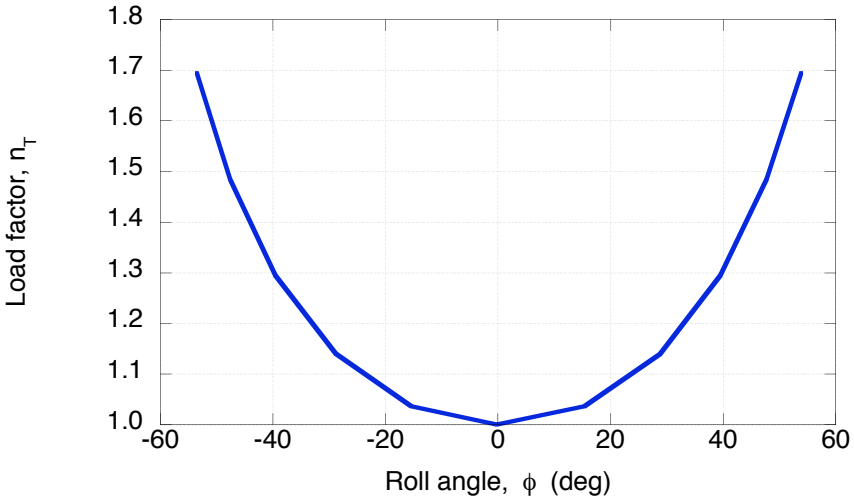

Figure 6.41: Relation between load factor n_T and bank angle ϕ.

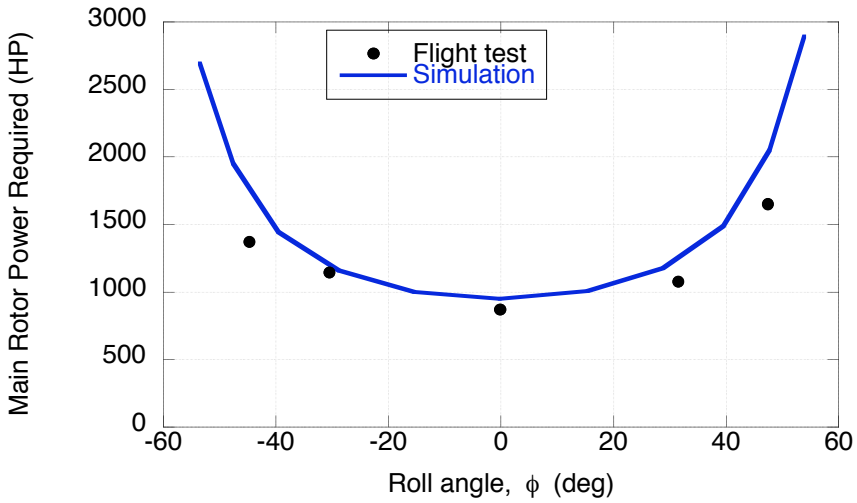

(a) Main rotor power required, Q_{MR}

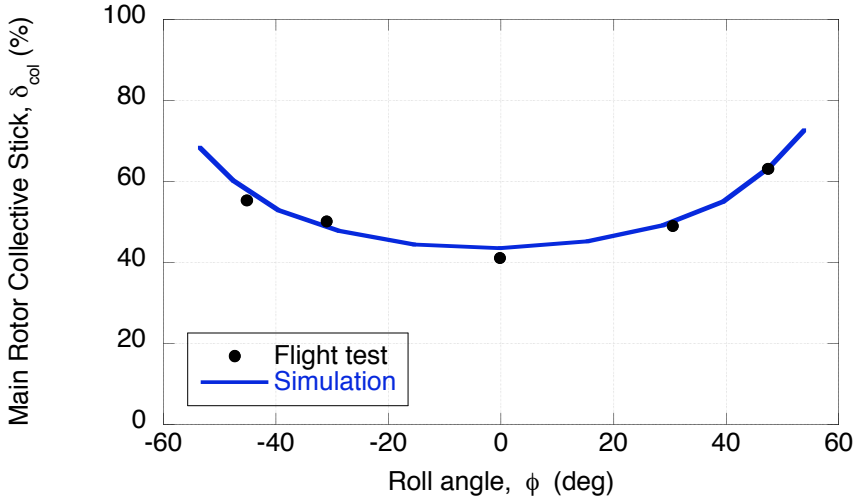

(b) Main rotor collective, δ_{col}

Figure 6.42: Main rotor power required, Q_{MR}, and collective, δ_{col}, as a function of roll angle ϕ.

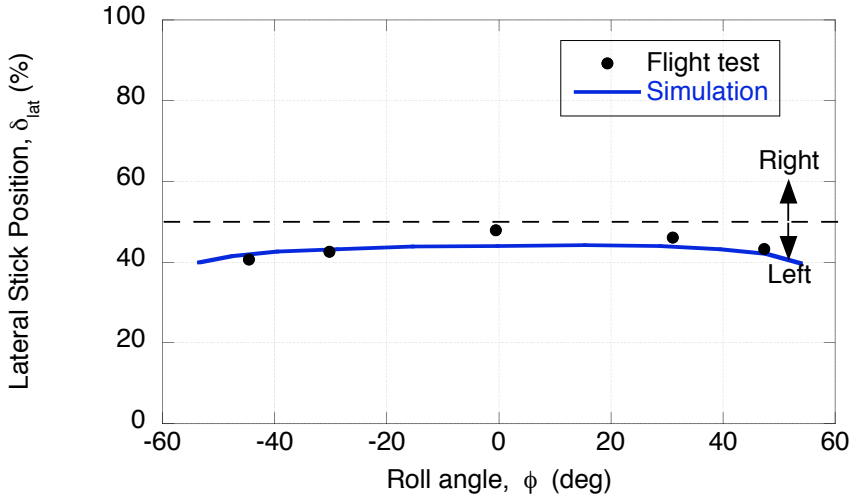

(a) Lateral stick position, δ_{lat}

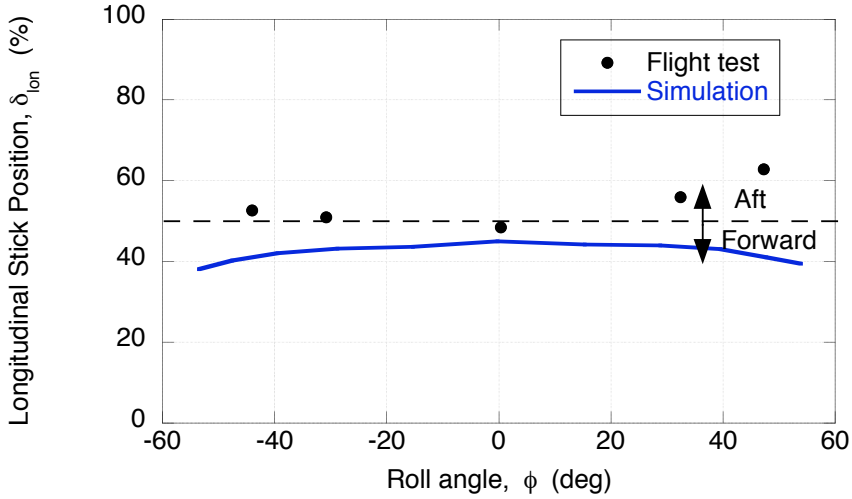

(b) Longitudinal stick position, δ_{lon}

Figure 6.43: Lateral stick position, δ_{lat}, and longitudinal stick position, δ_{lon}, as a function of roll angle ϕ.

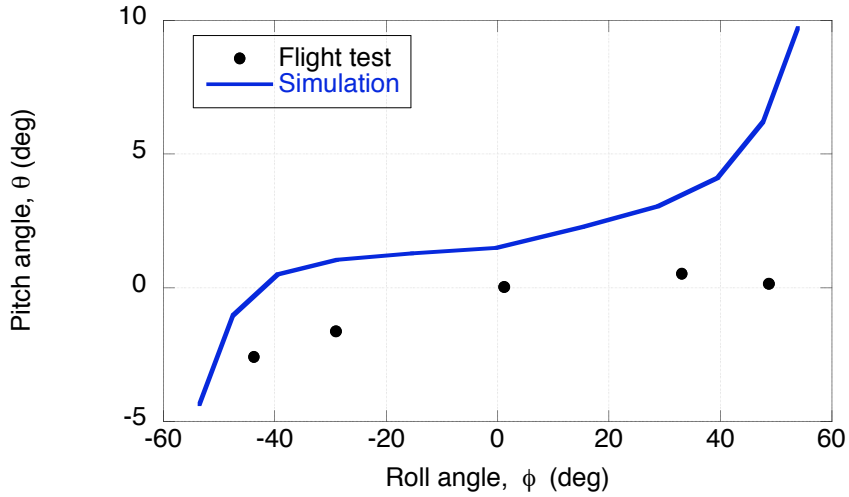

(a) Helicopter pitch angle, θ

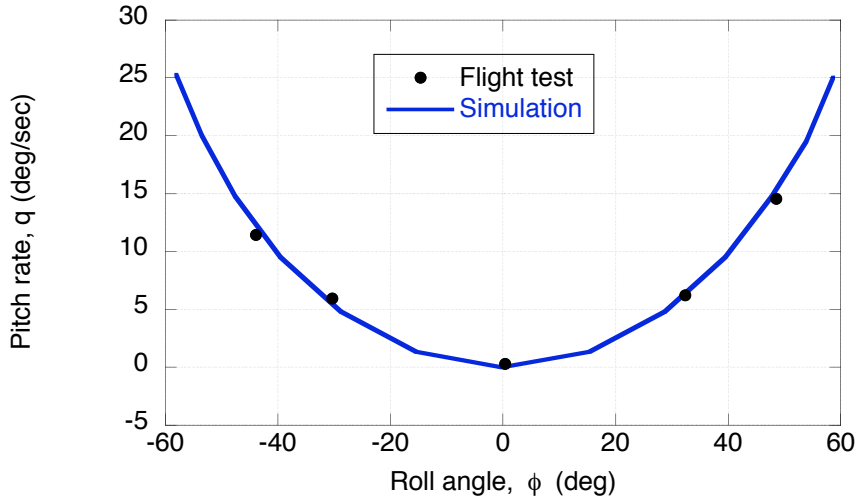

(b) Helicopter pitch rate, q

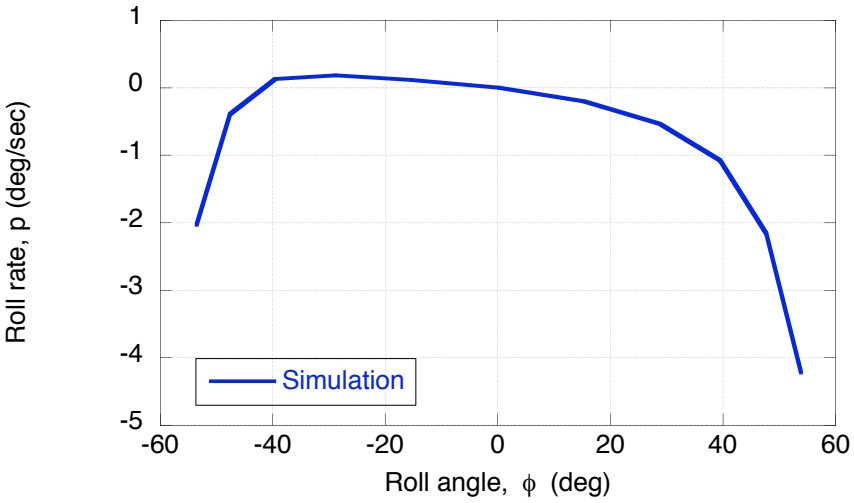

(c) Helicopter roll rate, p

Figure 6.44: Helicopter pitch angle, θ, pitch rate, q and roll rate, p, as a function of roll angle ϕ.

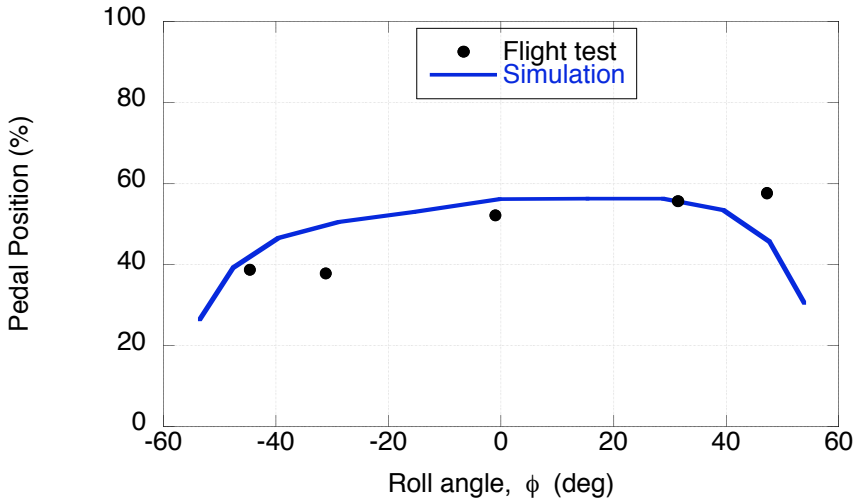

(a) Pedal position δ_{ped}

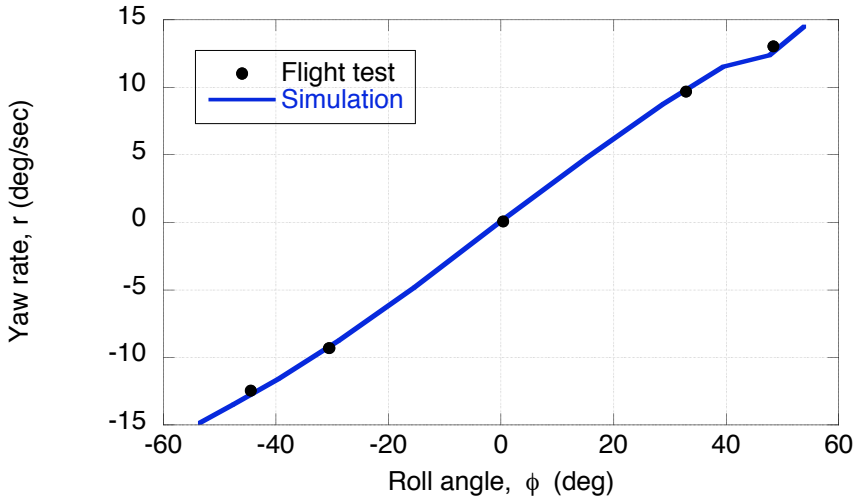

(b) Helicopter yaw rate, r

Figure 6.45: Pedal position δ_{ped}, and helicopter yaw rate, r, as a function of roll angle ϕ.

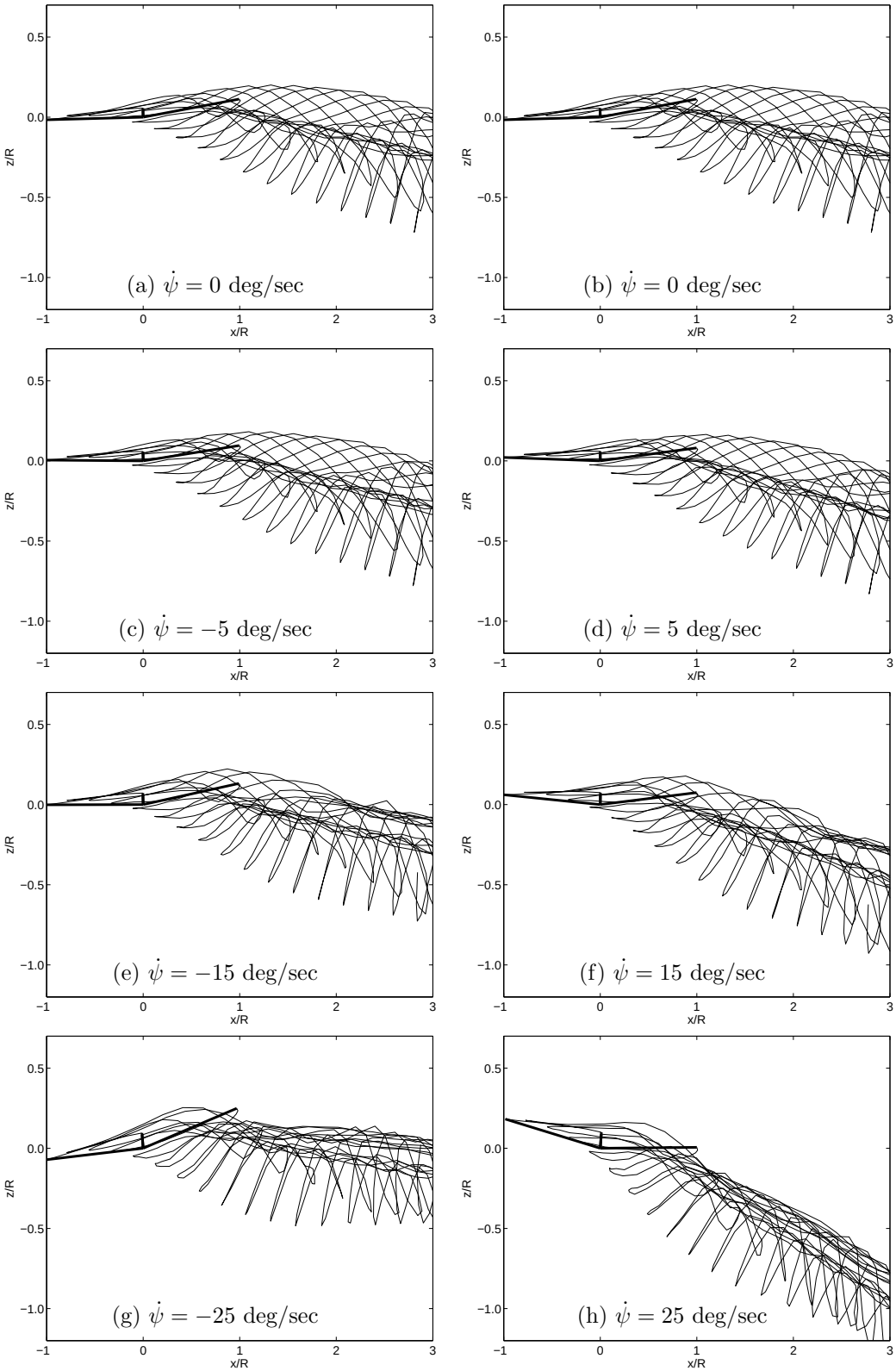

Figure 6.46: Side view of the free wake tip vortex for turns at $V = 60$ kts.

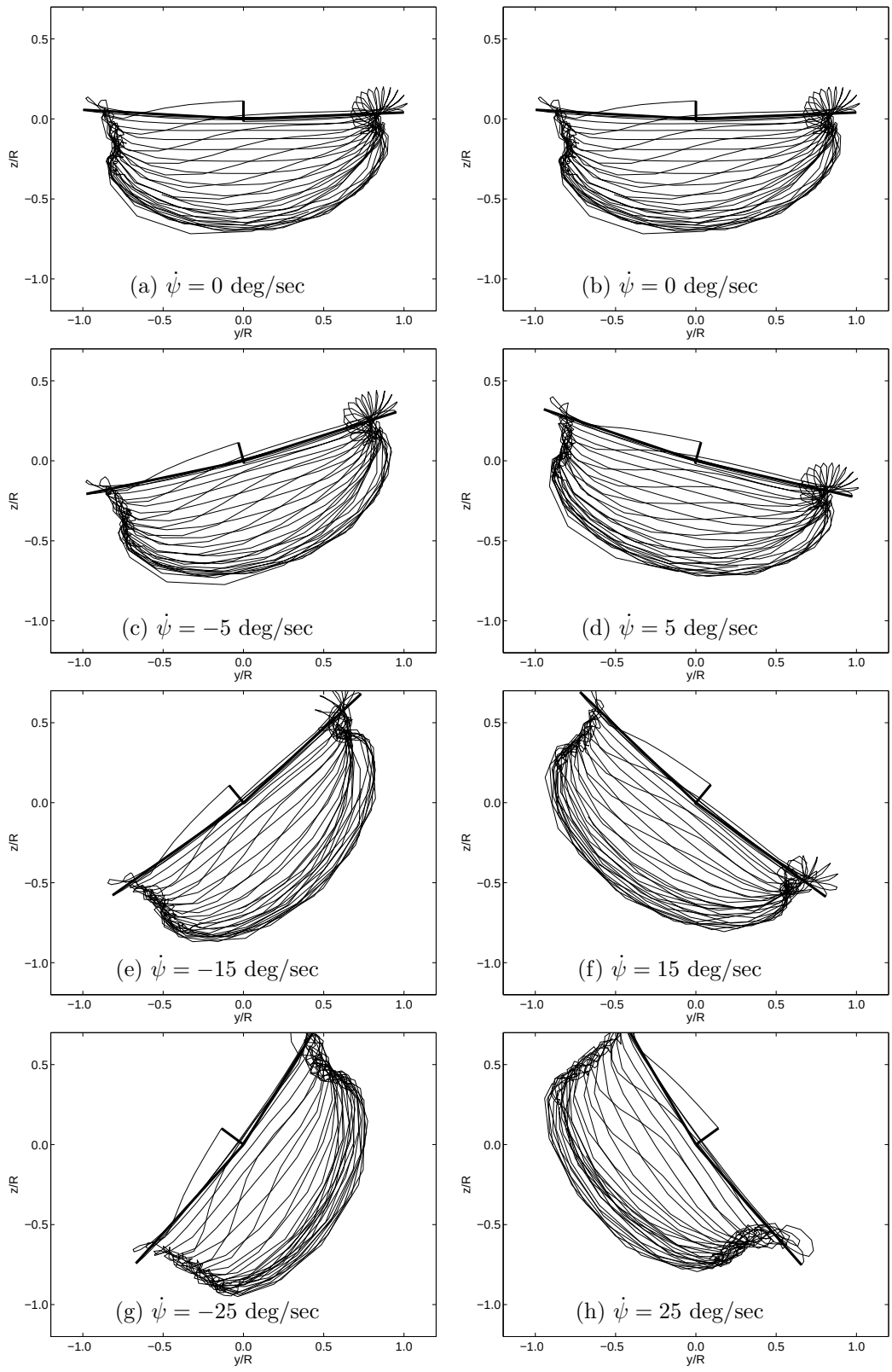

Figure 6.47: Rear view of the free wake tip vortex for turns at $V = 60$ kts.

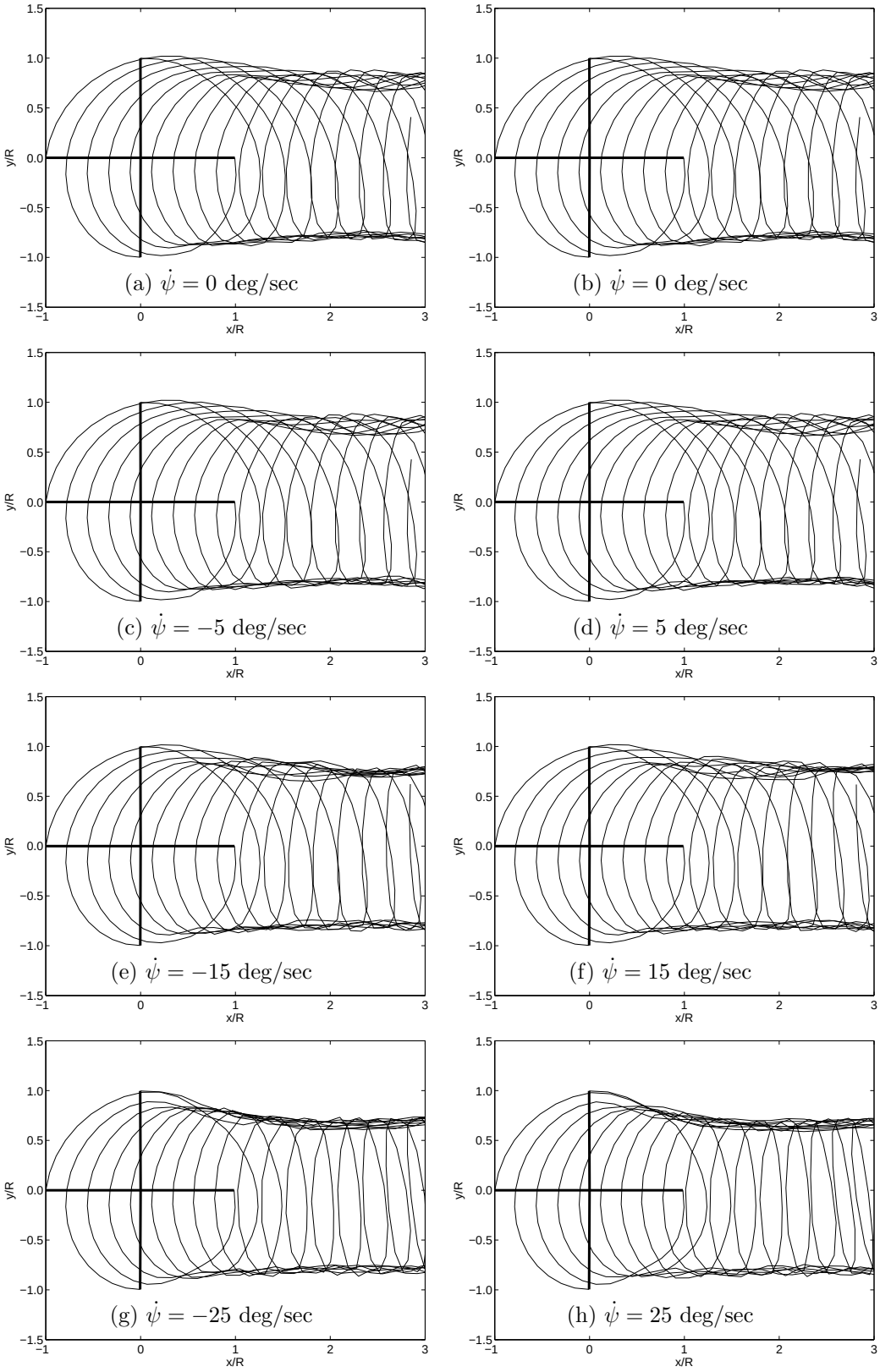

Figure 6.48: Top view of the free wake tip vortex for turns at $V = 60$ kts.

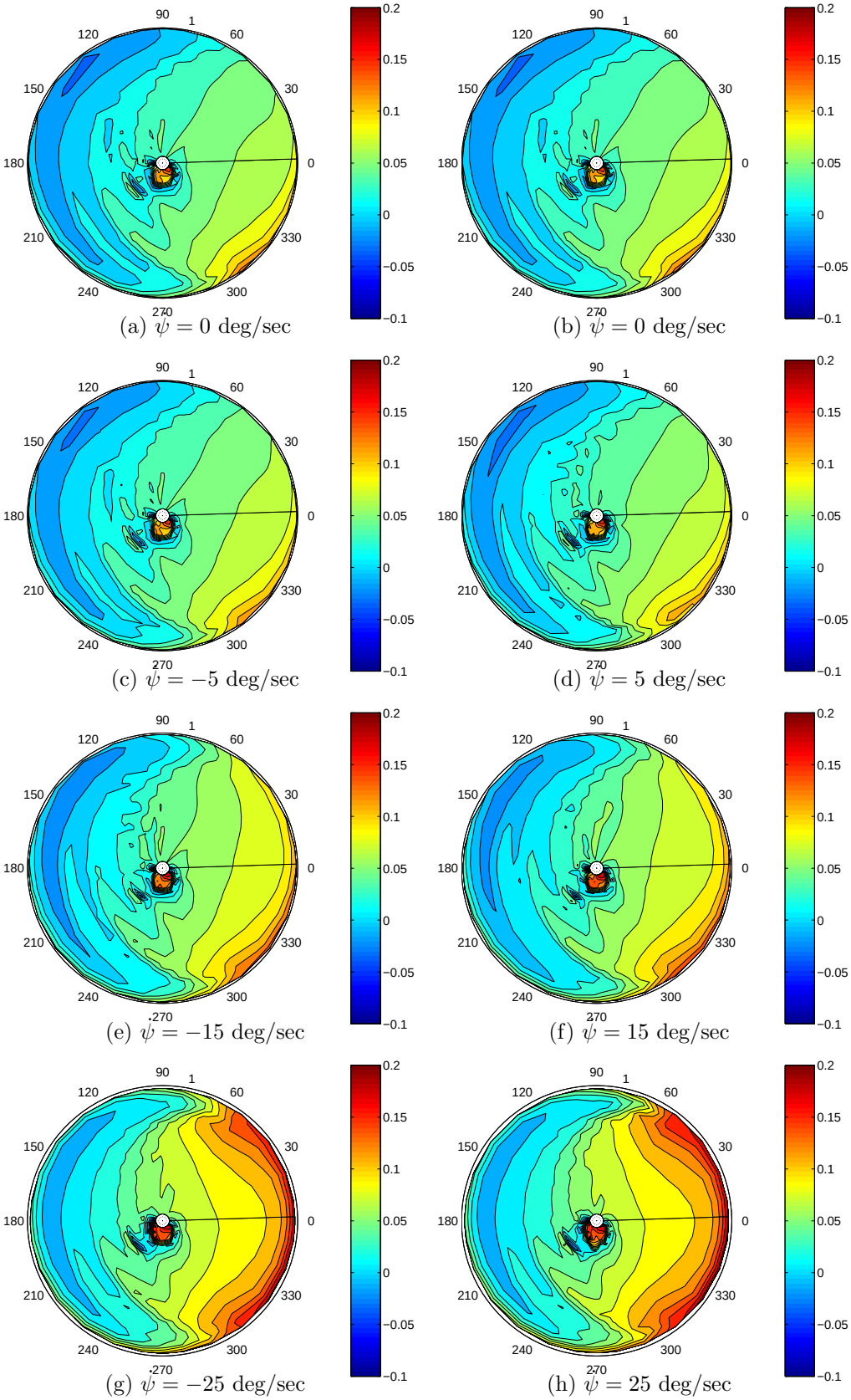

(a) $\dot{\psi} = 0$ deg/sec (b) $\dot{\psi} = 0$ deg/sec

(c) $\dot{\psi} = -5$ deg/sec (d) $\dot{\psi} = 5$ deg/sec

(e) $\dot{\psi} = -15$ deg/sec (f) $\dot{\psi} = 15$ deg/sec

(g) $\dot{\psi} = -25$ deg/sec (h) $\dot{\psi} = 25$ deg/sec

Figure 6.49: Inflow distribution for different turn rates at $V = 60$ kts.

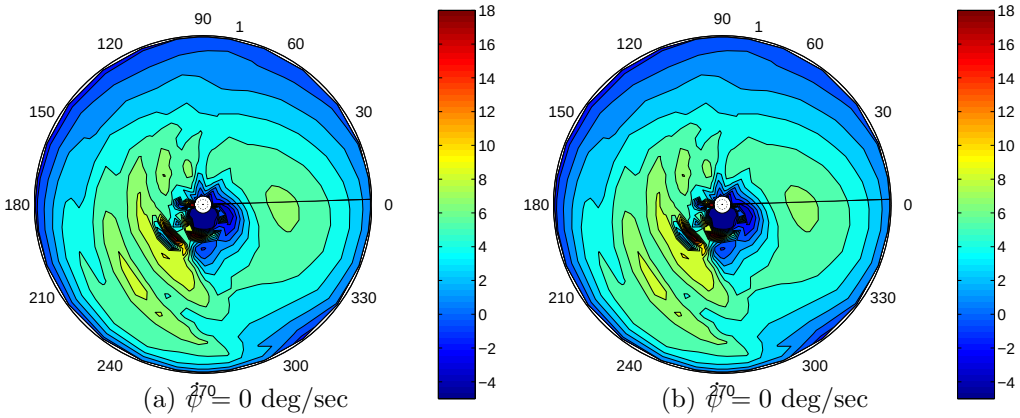

(a) $\dot{\psi}^{270} = 0$ deg/sec (b) $\dot{\psi}^{270} = 0$ deg/sec

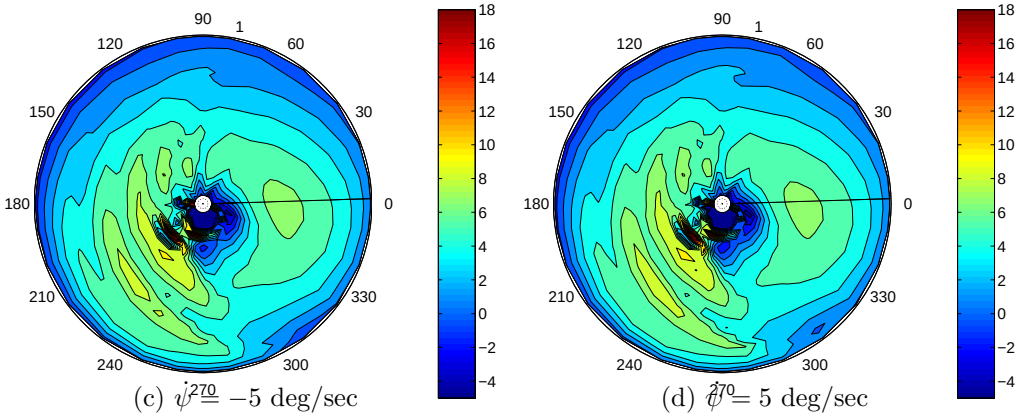

(c) $\dot{\psi}^{270} = -5$ deg/sec (d) $\dot{\psi}^{270} = 5$ deg/sec

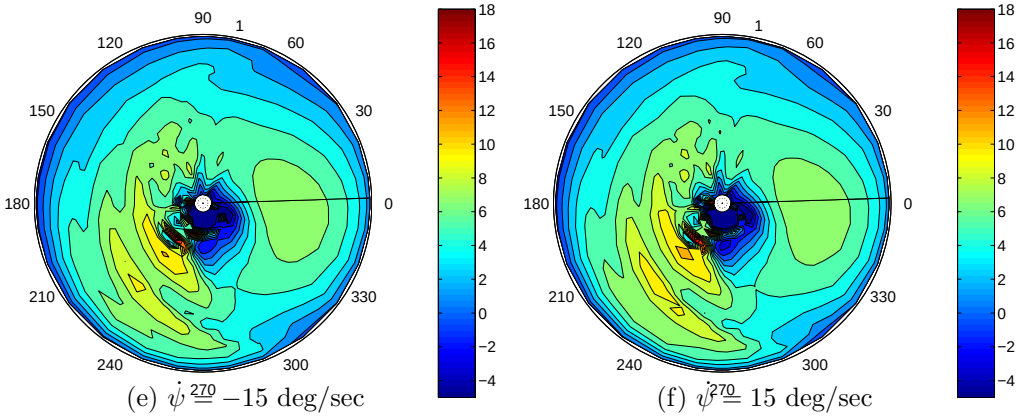

(e) $\dot{\psi}^{270} = -15$ deg/sec (f) $\dot{\psi}^{270} = 15$ deg/sec

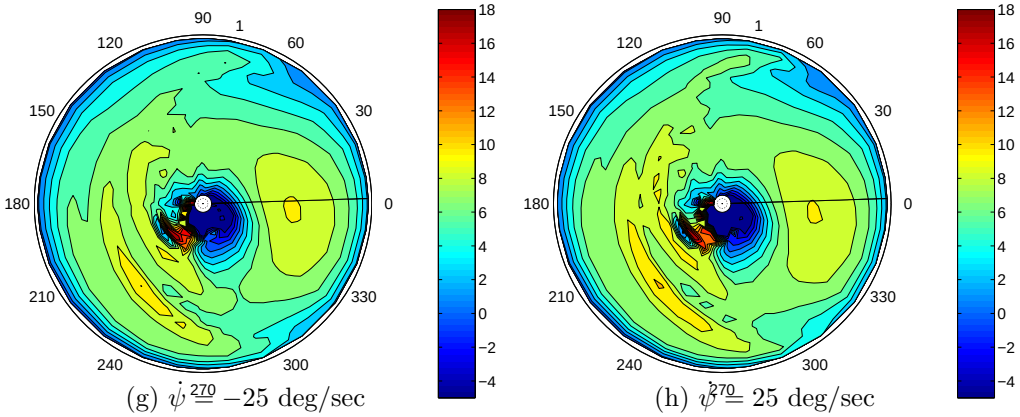

(g) $\dot{\psi}^{270} = -25$ deg/sec (h) $\dot{\psi}^{270} = 25$ deg/sec

Figure 6.50: Angle of attack distribution for different turn rates at $V = 60$ kts.

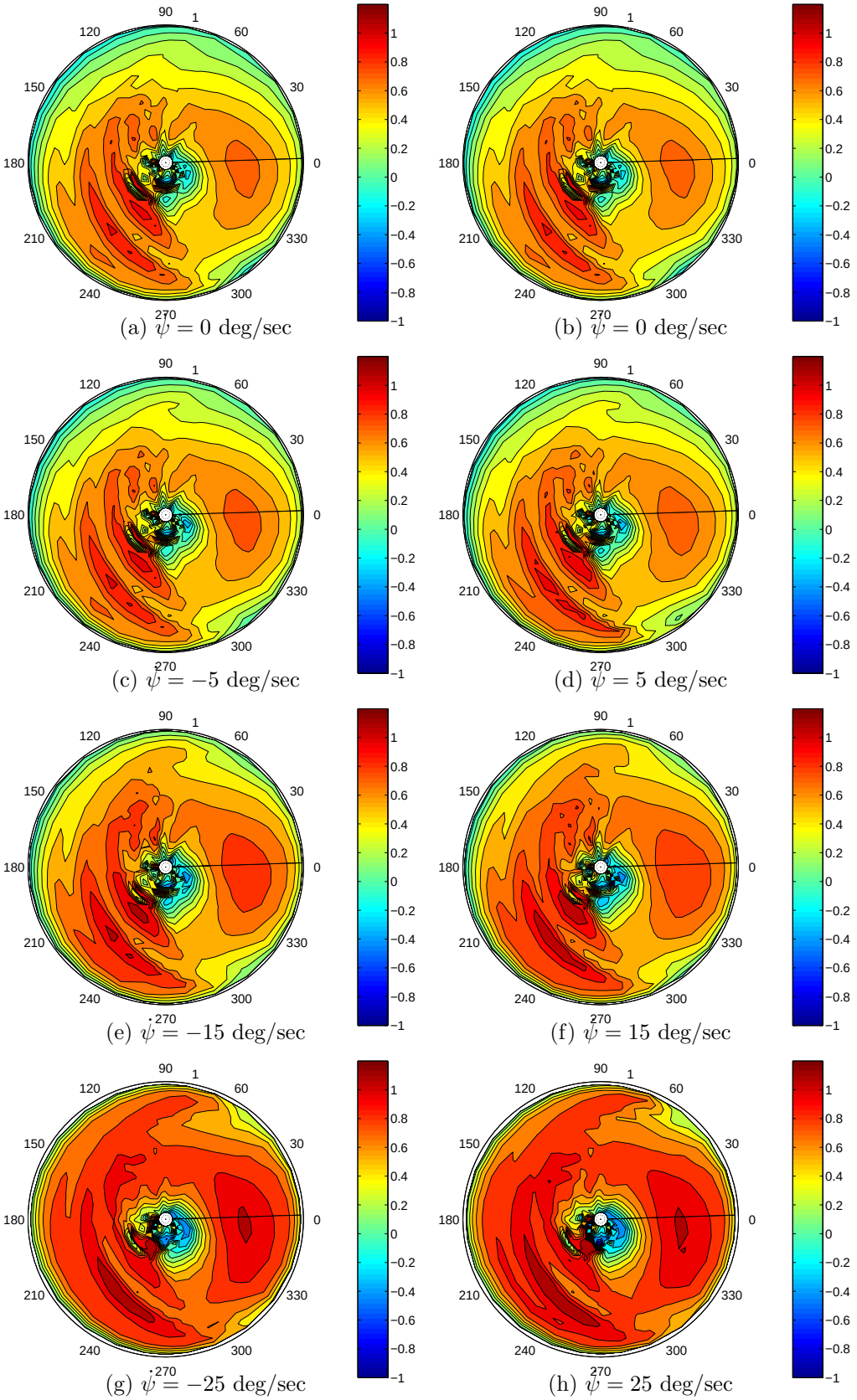

(a) $\dot{\psi} = 0$ deg/sec (b) $\dot{\psi} = 0$ deg/sec

(c) $\dot{\psi} = -5$ deg/sec (d) $\dot{\psi} = 5$ deg/sec

(e) $\dot{\psi} = -15$ deg/sec (f) $\dot{\psi} = 15$ deg/sec

(g) $\dot{\psi} = -25$ deg/sec (h) $\dot{\psi} = 25$ deg/sec

Figure 6.51: Lift coefficient distribution for different turn rates at $V = 60$ kts.

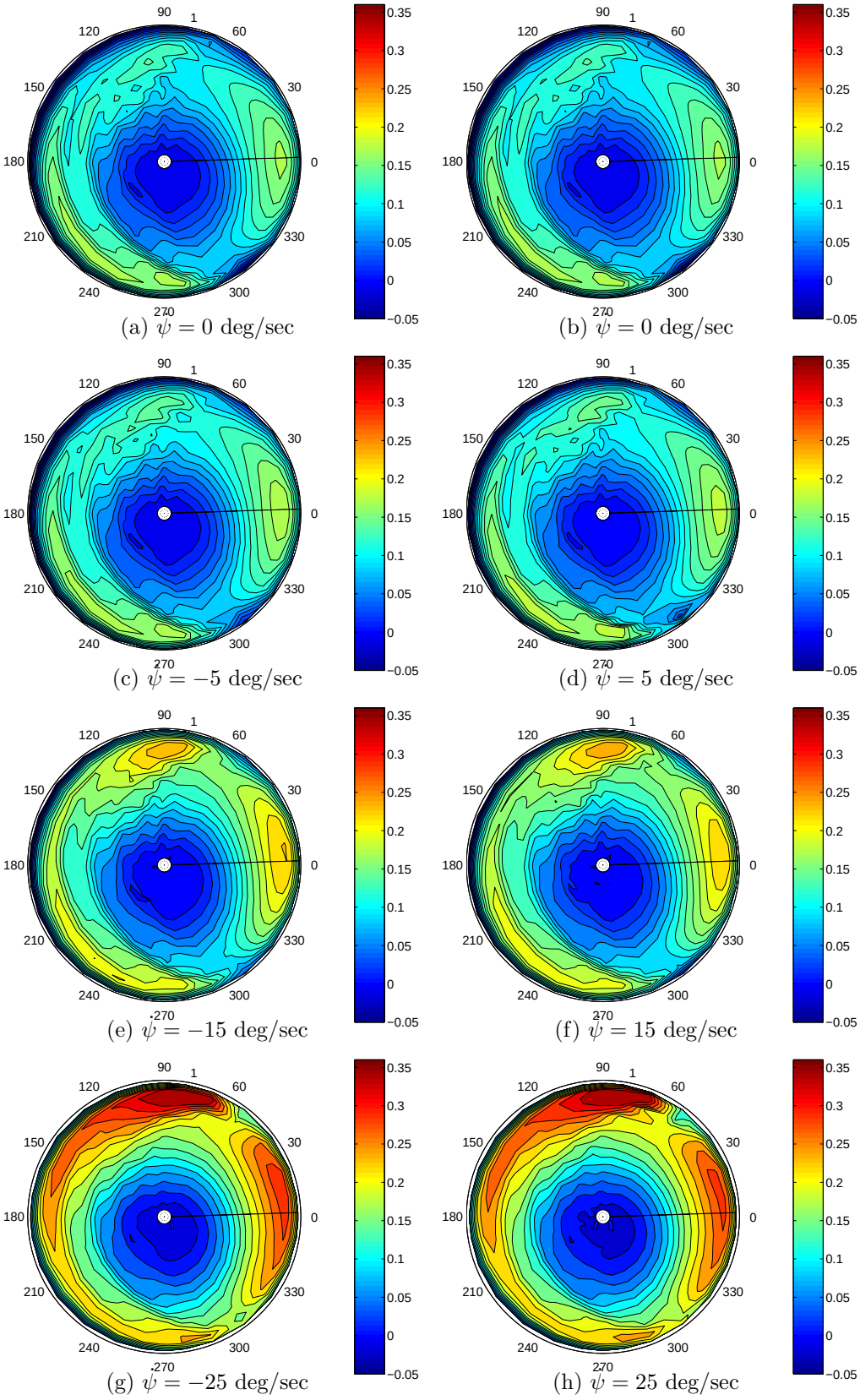

(a) $\dot{\psi} = 0$ deg/sec (b) $\dot{\psi} = 0$ deg/sec

(c) $\dot{\psi} = -5$ deg/sec (d) $\dot{\psi} = 5$ deg/sec

(e) $\dot{\psi} = -15$ deg/sec (f) $\dot{\psi} = 15$ deg/sec

(g) $\dot{\psi} = -25$ deg/sec (h) $\dot{\psi} = 25$ deg/sec

Figure 6.52: Elemental lift distribution for different turn rates at $V = 60$ kts.

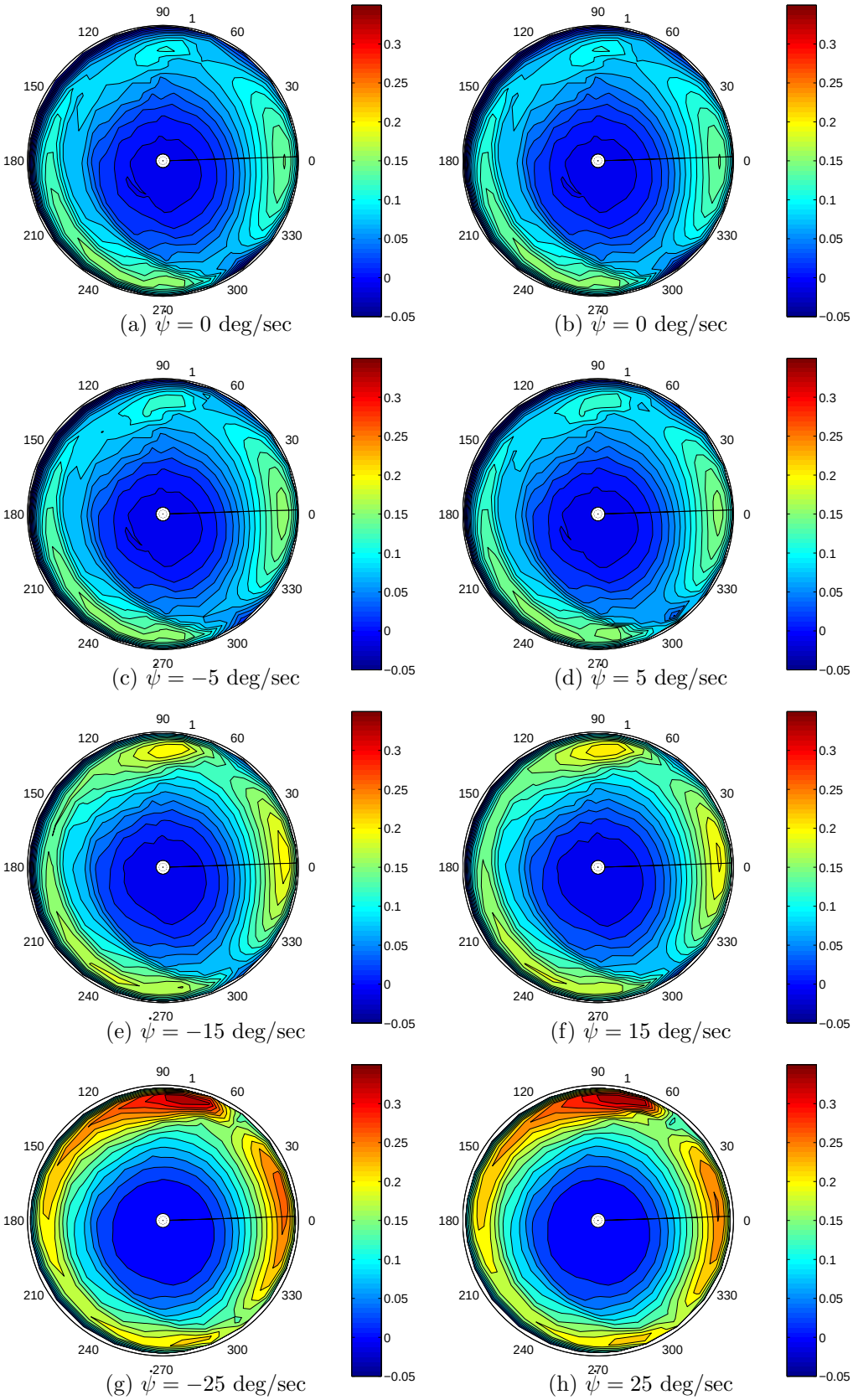

(a) $\dot{\psi} = 0$ deg/sec (b) $\dot{\psi} = 0$ deg/sec

(c) $\dot{\psi} = -5$ deg/sec (d) $\dot{\psi} = 5$ deg/sec

(e) $\dot{\psi} = -15$ deg/sec (f) $\dot{\psi} = 15$ deg/sec

(g) $\dot{\psi} = -25$ deg/sec (h) $\dot{\psi} = 25$ deg/sec

Figure 6.53: Local flap moment distribution for different turn rates at $V = 60$ kts.

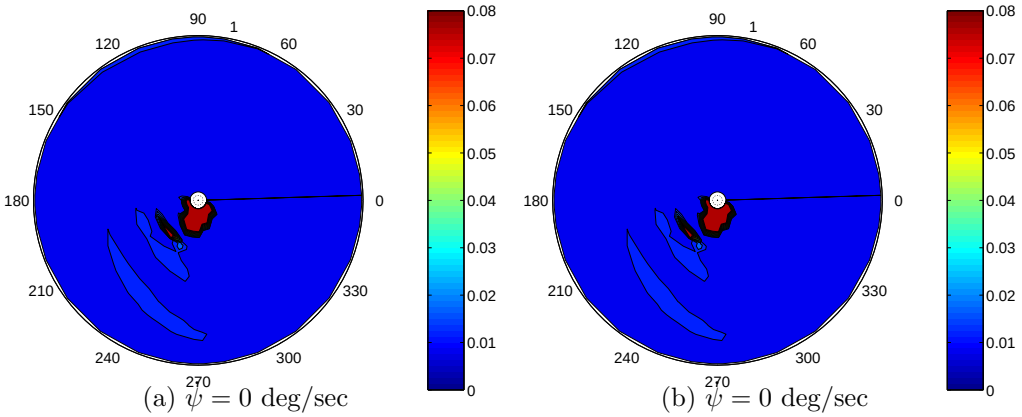

(a) $\dot{\psi} = 0$ deg/sec (b) $\dot{\psi} = 0$ deg/sec

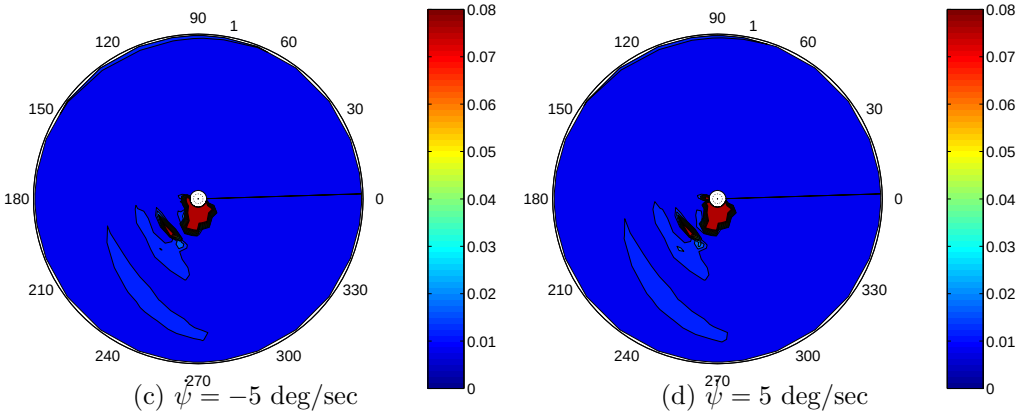

(c) $\dot{\psi} = -5$ deg/sec (d) $\dot{\psi} = 5$ deg/sec

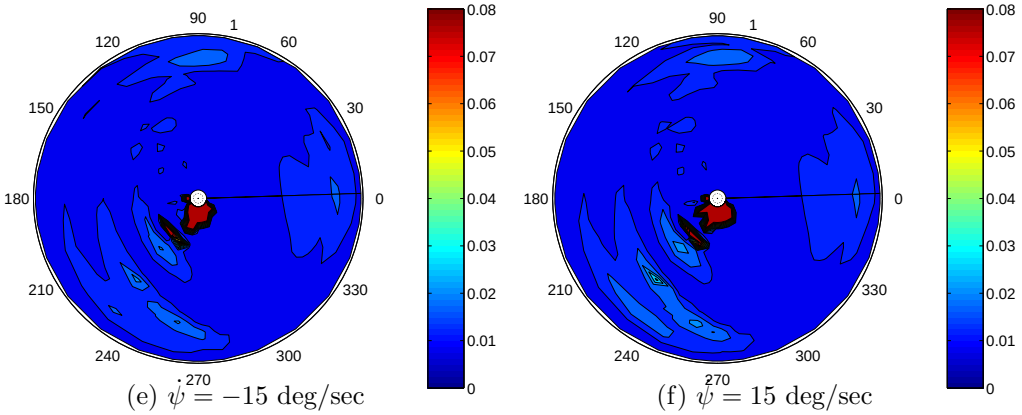

(e) $\dot{\psi} = -15$ deg/sec (f) $\dot{\psi} = 15$ deg/sec

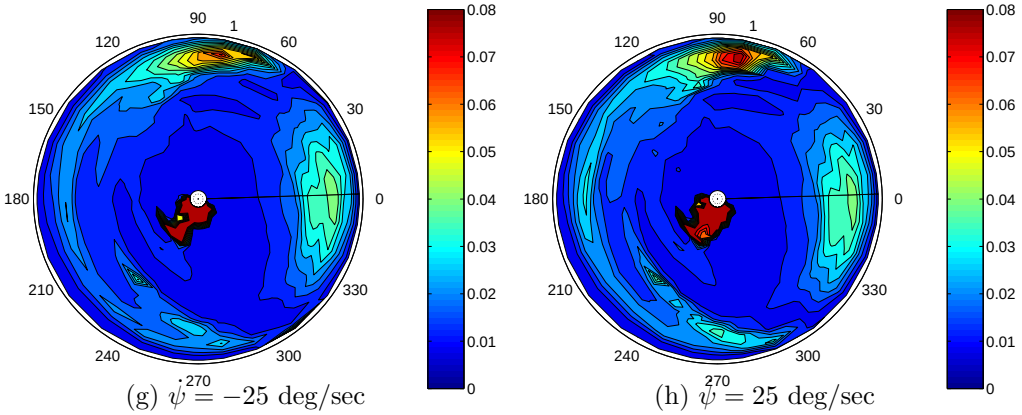

(g) $\dot{\psi} = -25$ deg/sec (h) $\dot{\psi} = 25$ deg/sec

Figure 6.54: Drag coefficient distribution for different turn rates at $V = 60$ kts.

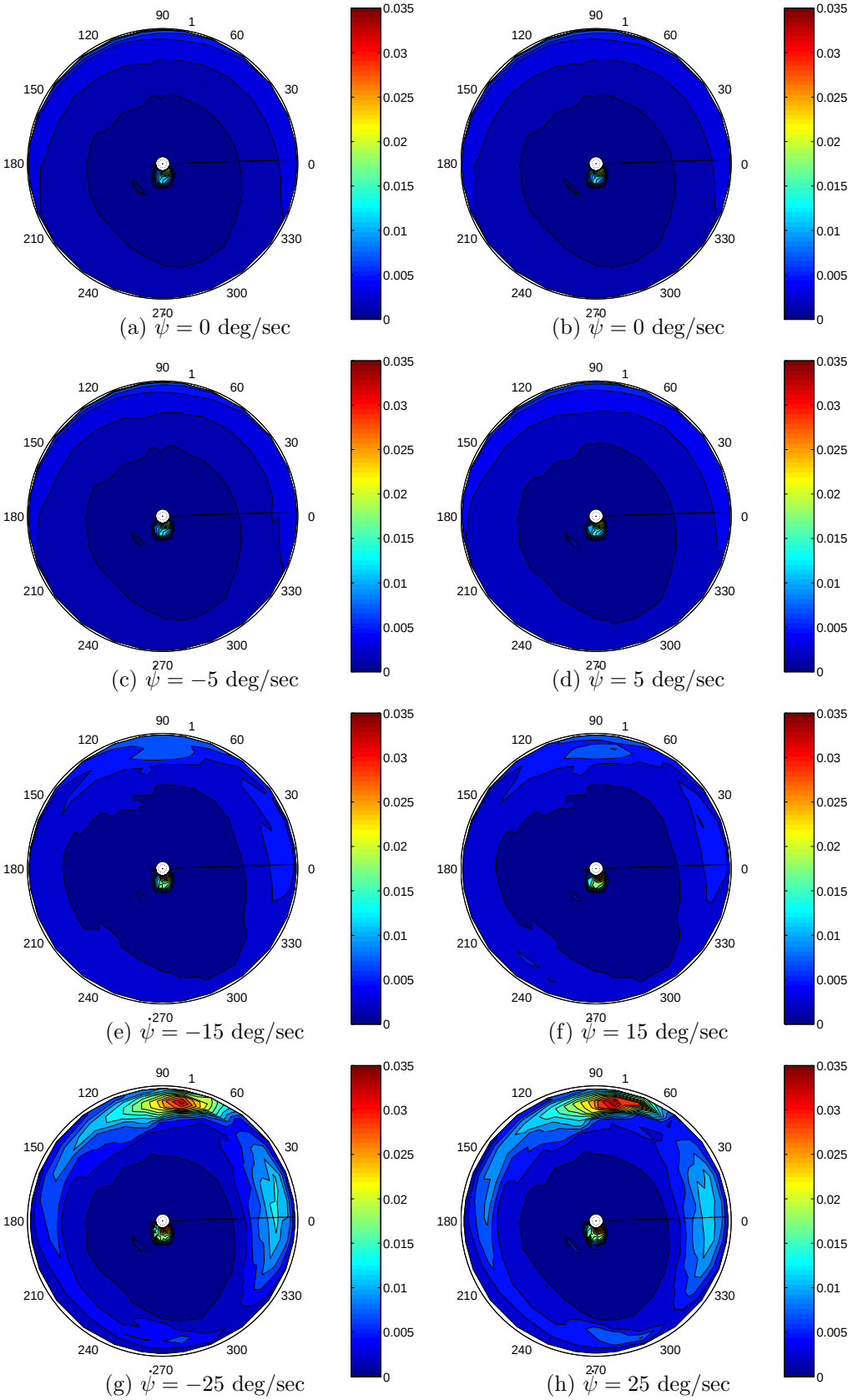

(a) $\dot{\psi} = 0$ deg/sec (b) $\dot{\psi} = 0$ deg/sec

(c) $\dot{\psi} = -5$ deg/sec (d) $\dot{\psi} = 5$ deg/sec

(e) $\dot{\psi} = -15$ deg/sec (f) $\dot{\psi} = 15$ deg/sec

(g) $\dot{\psi} = -25$ deg/sec (h) $\dot{\psi} = 25$ deg/sec

Figure 6.55: Elemental drag distribution for different turn rates at $V = 60$ kts.

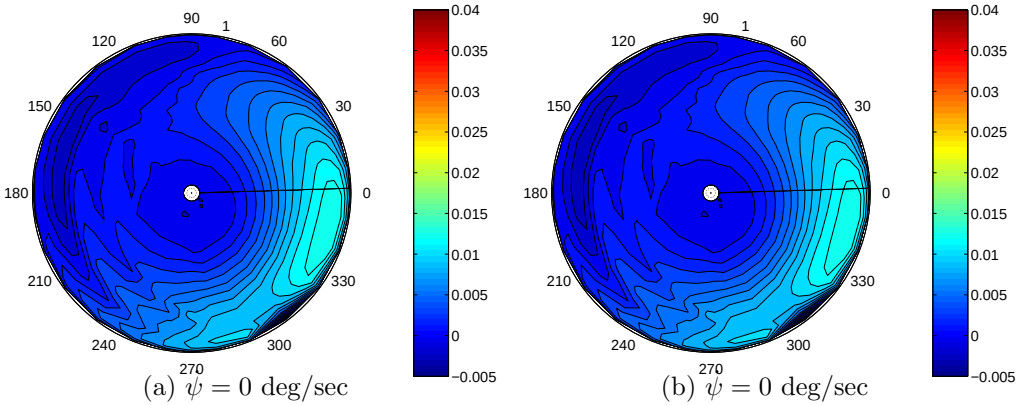

(a) $\dot{\psi} = 0$ deg/sec (b) $\dot{\psi} = 0$ deg/sec

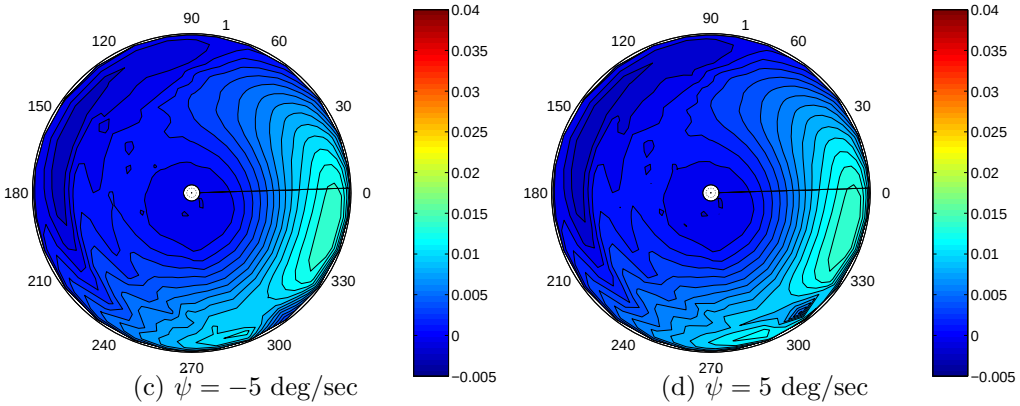

(c) $\dot{\psi} = -5$ deg/sec (d) $\dot{\psi} = 5$ deg/sec

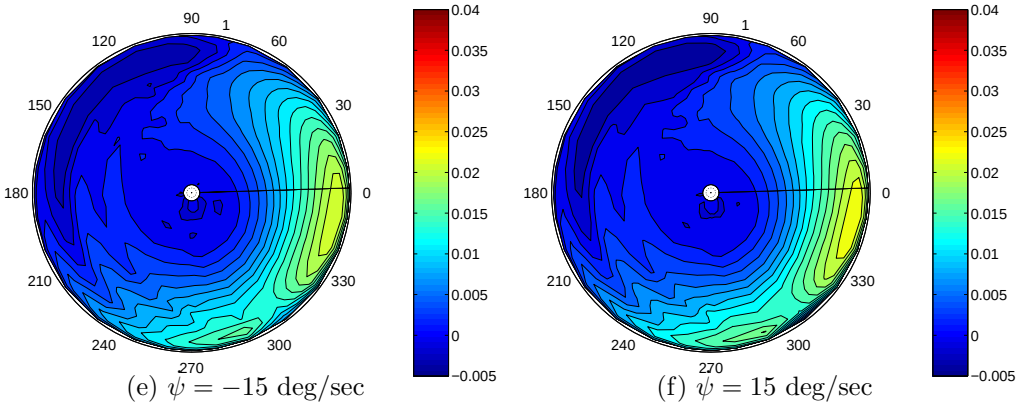

(e) $\dot{\psi} = -15$ deg/sec (f) $\dot{\psi} = 15$ deg/sec

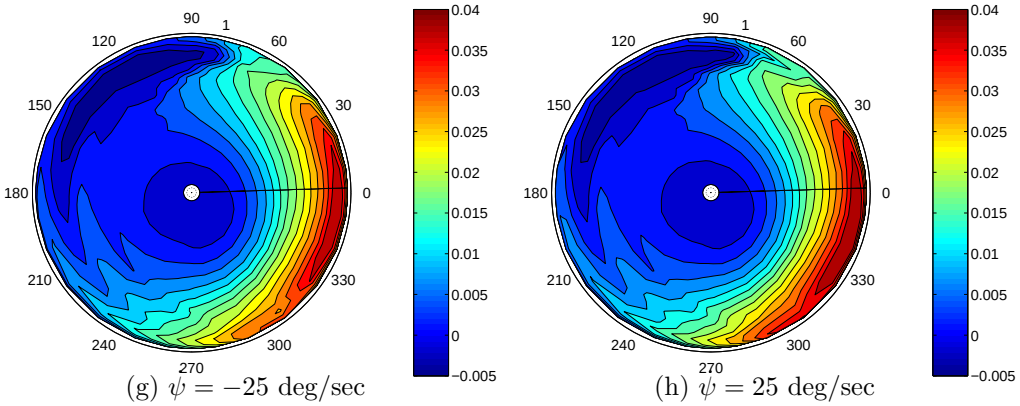

(g) $\dot{\psi} = -25$ deg/sec (h) $\dot{\psi} = 25$ deg/sec

Figure 6.56: Induced torque distribution for different turn rates at $V = 60$ kts.

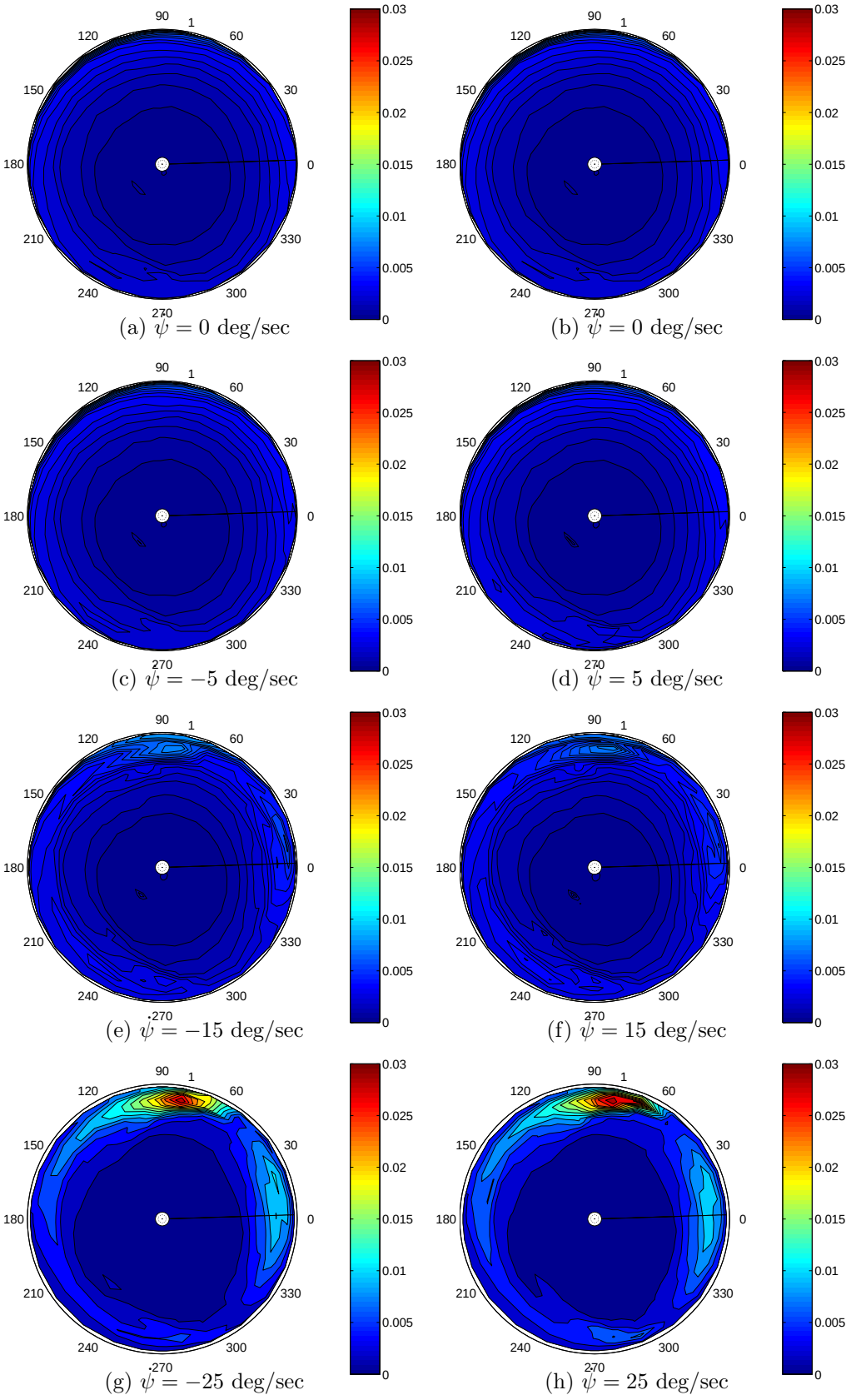

(a) $\dot{\psi} = 0$ deg/sec (b) $\dot{\psi} = 0$ deg/sec

(c) $\dot{\psi} = -5$ deg/sec (d) $\dot{\psi} = 5$ deg/sec

(e) $\dot{\psi} = -15$ deg/sec (f) $\dot{\psi} = 15$ deg/sec

(g) $\dot{\psi} = -25$ deg/sec (h) $\dot{\psi} = 25$ deg/sec

Figure 6.57: Profile torque distribution for different turn rates at $V = 60$ kts.

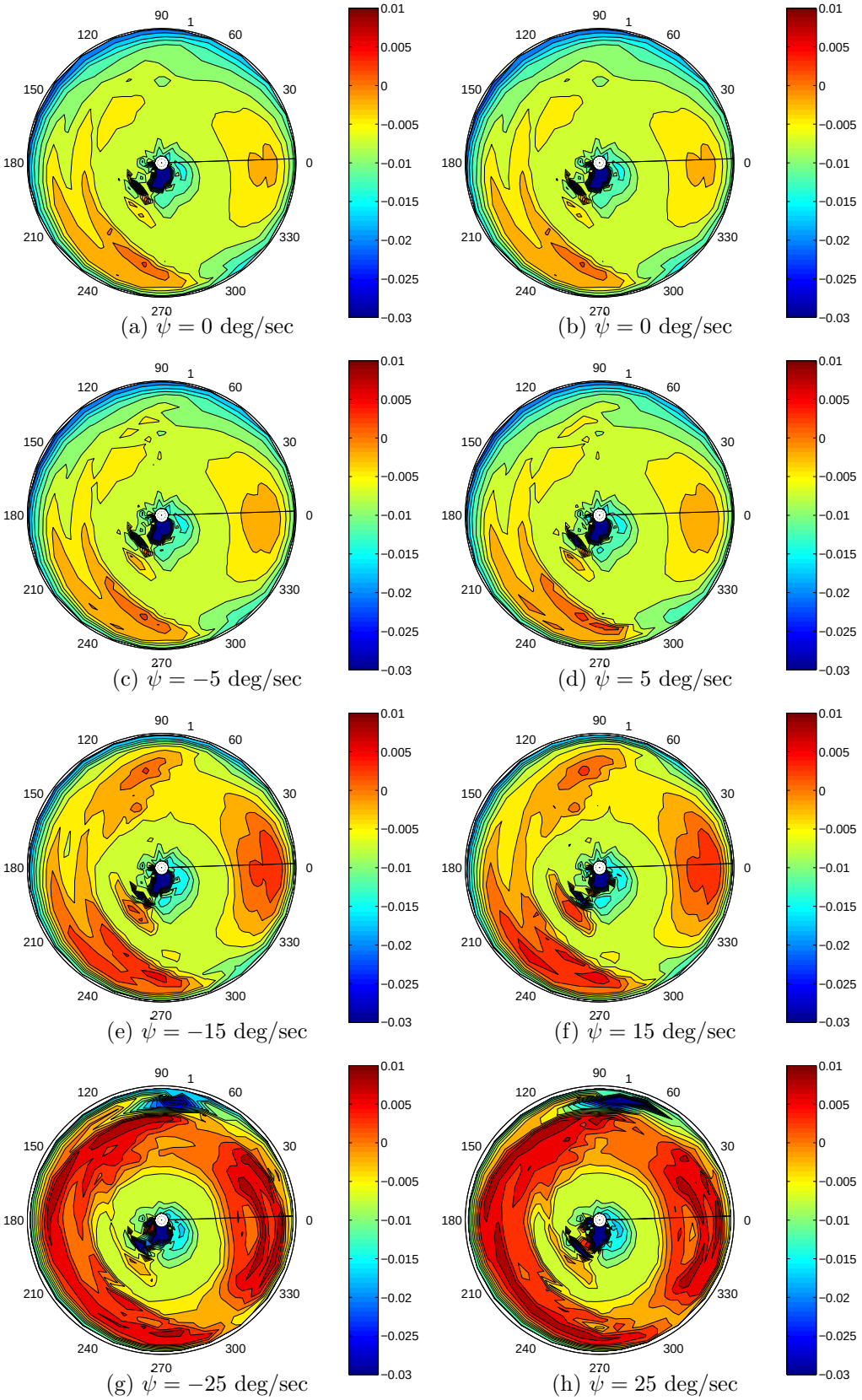

(a) $\psi = 0$ deg/sec (b) $\psi = 0$ deg/sec

(c) $\psi = -5$ deg/sec (d) $\psi = 5$ deg/sec

(e) $\psi = -15$ deg/sec (f) $\psi = 15$ deg/sec

(g) $\psi = -25$ deg/sec (h) $\psi = 25$ deg/sec

Figure 6.58: Moment coefficient distribution for different turn rates at $V = 60$ kts.

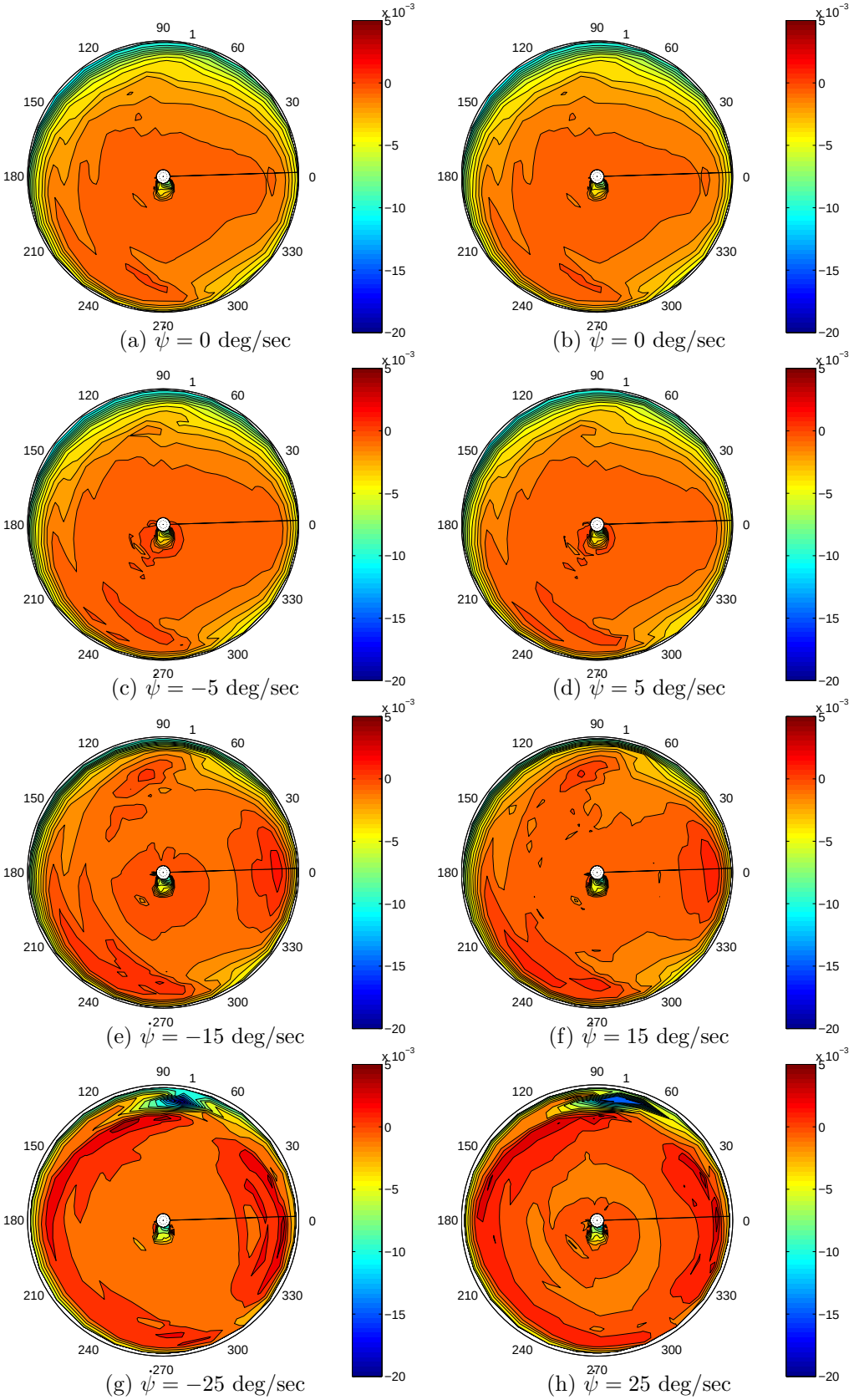

(a) $\dot{\psi} = 0$ deg/sec

(b) $\dot{\psi} = 0$ deg/sec

(c) $\dot{\psi} = -5$ deg/sec

(d) $\dot{\psi} = 5$ deg/sec

(e) $\dot{\psi} = -15$ deg/sec

(f) $\dot{\psi} = 15$ deg/sec

(g) $\dot{\psi} = -25$ deg/sec

(h) $\dot{\psi} = 25$ deg/sec

Figure 6.59: Elemental moment distribution for different turn rates at $V = 60$ kts.

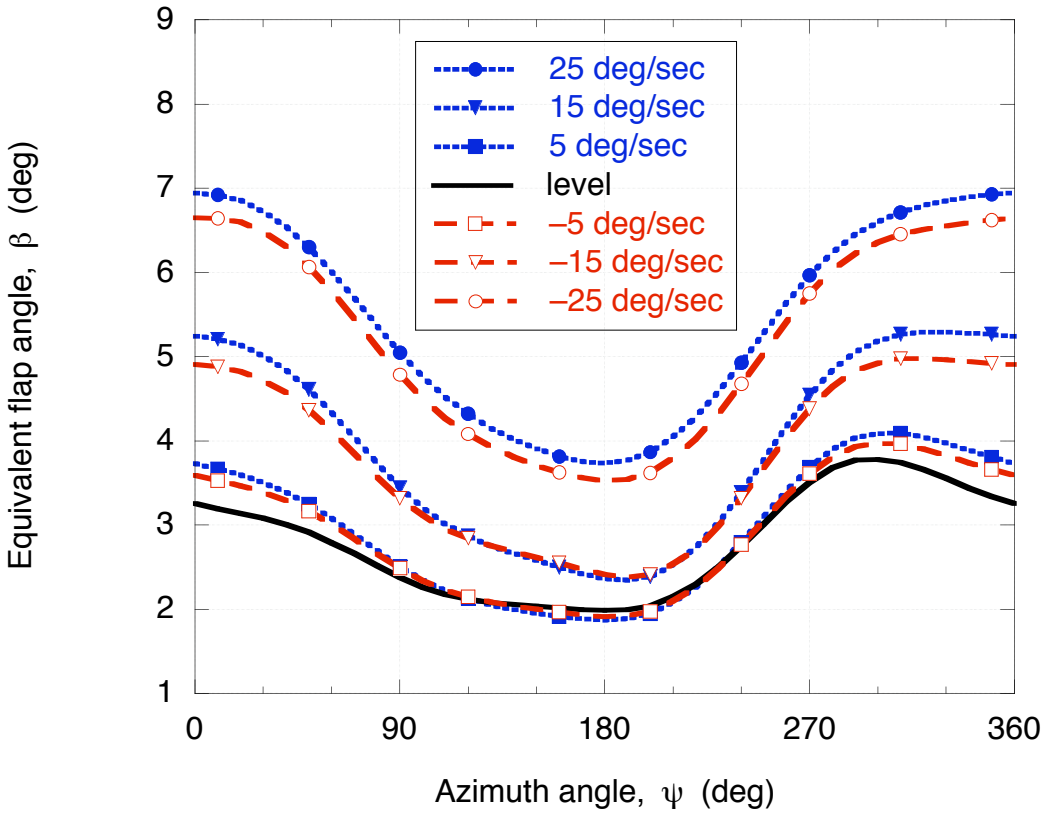

Figure 6.60: Equivalent flap angle distribution as a function of azimuth at various turn rates; $V = 60$ kts.

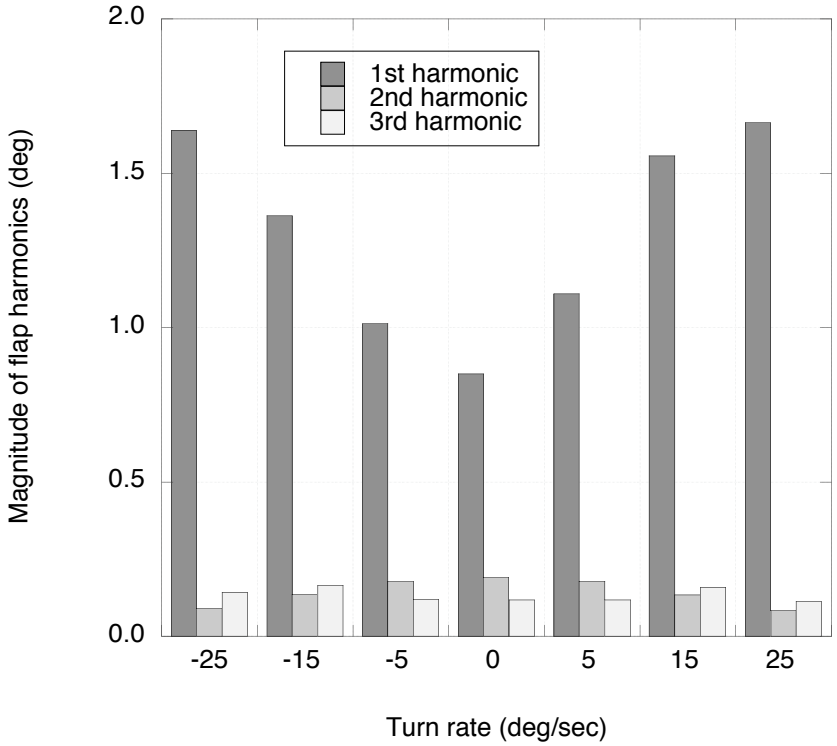

(a) Magnitude.

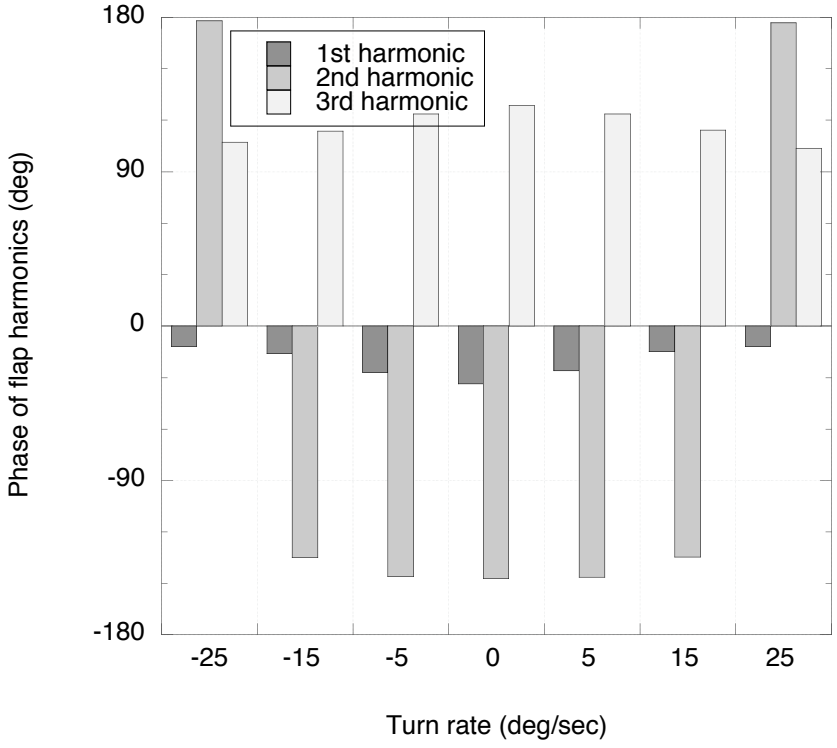

(b) Phase.

Figure 6.61: Magnitude and phase of the first three flap harmonics at various turn rates; $V = 60$ kts.

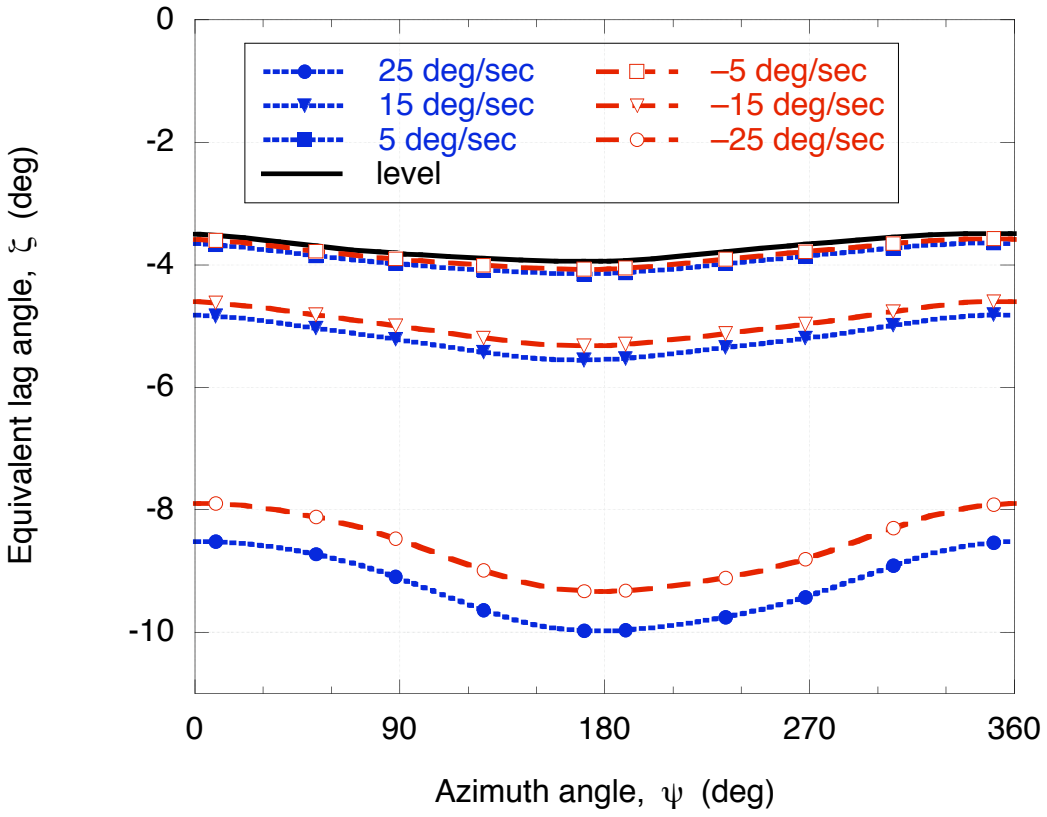

Figure 6.62: Equivalent lag angle distribution as a function of azimuth at various turn rates; $V = 60$ kts.

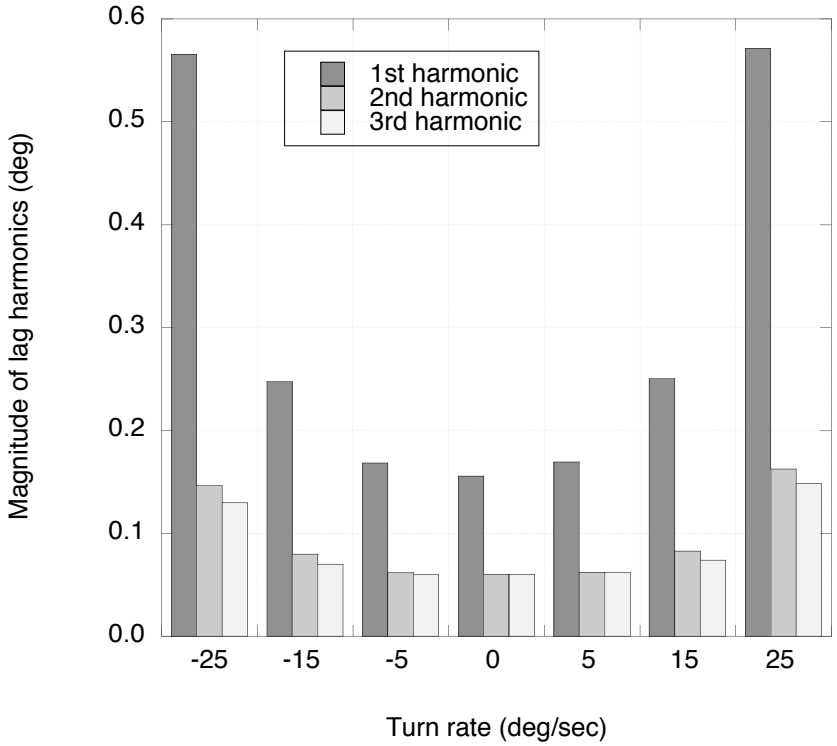

(a) Magnitude.

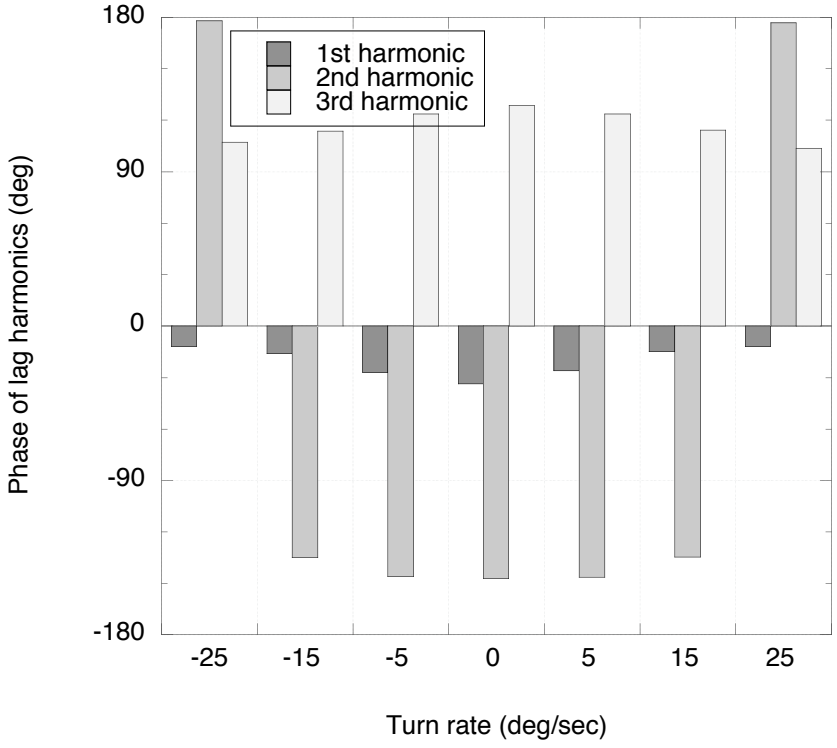

(b) Phase.

Figure 6.63: Magnitude and phase of the first three lag harmonics at various turn rates; $V = 60$ kts.

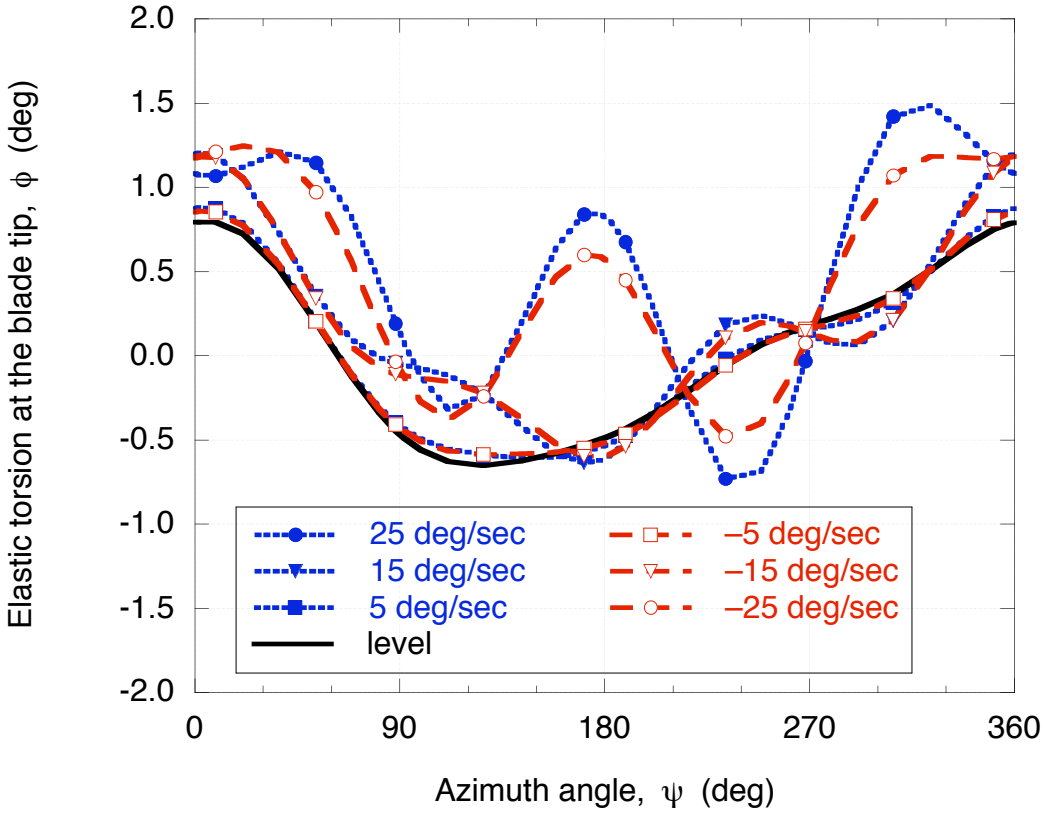

Figure 6.64: Blade tip elastic torsion versus azimuth angle at various turn rates; $V = 60$ kts.

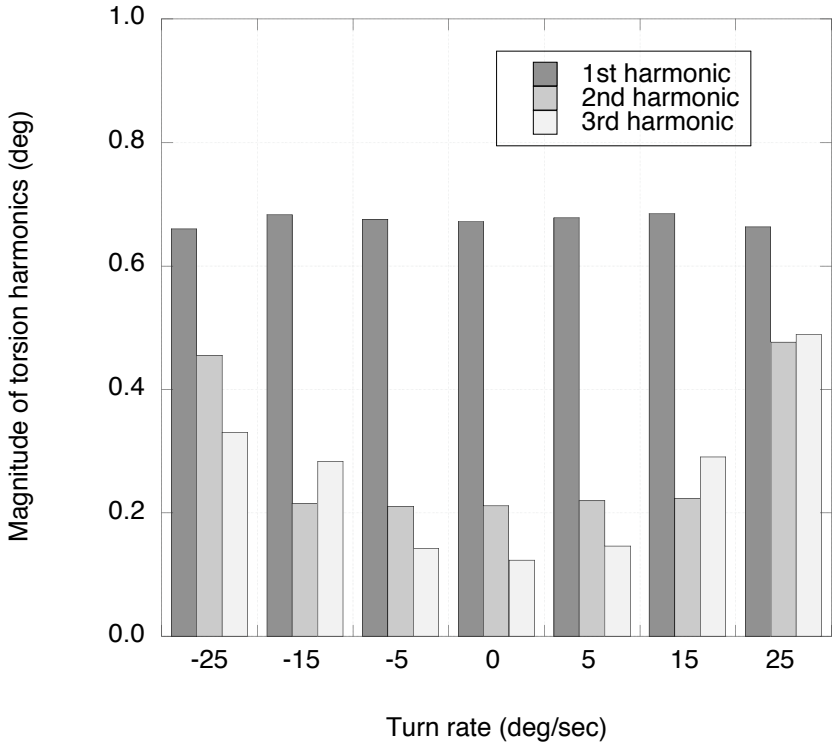

(a) Magnitude.

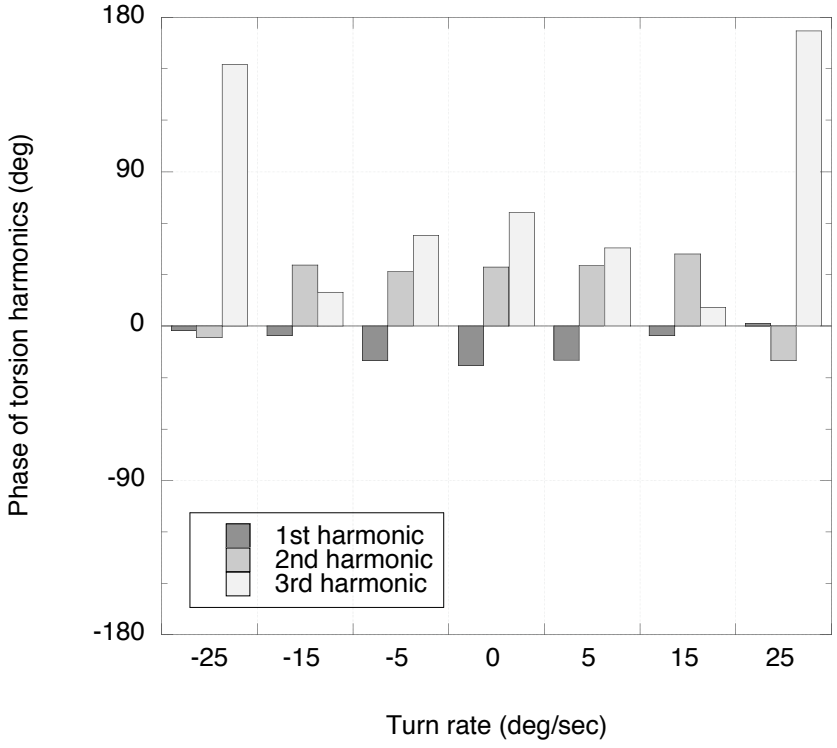

(b) Phase.

Figure 6.65: Magnitude and phase of the first three torsion harmonics at various turn rates; $V = 60$ kts.

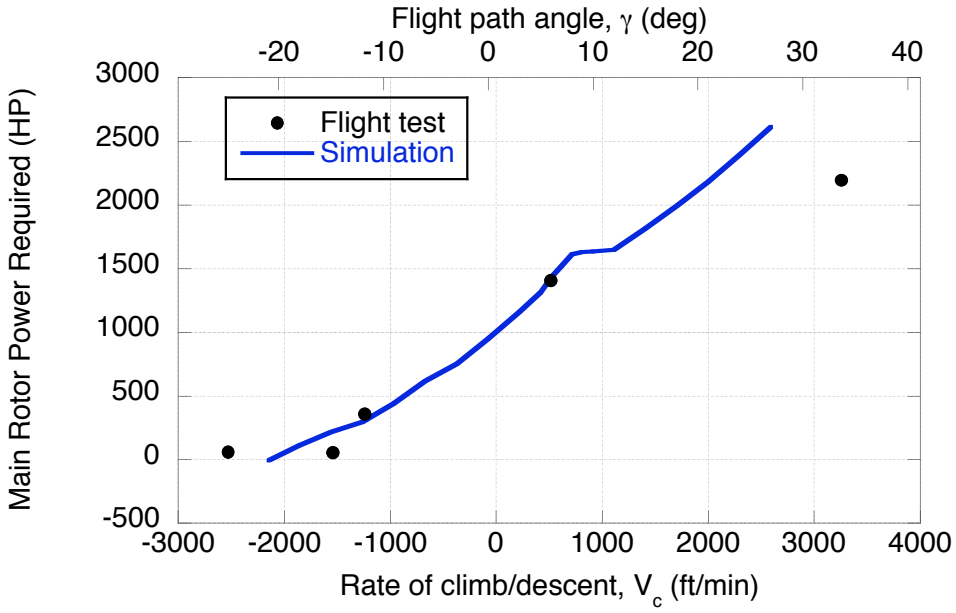

(a) Main rotor power required, Q_{MR}

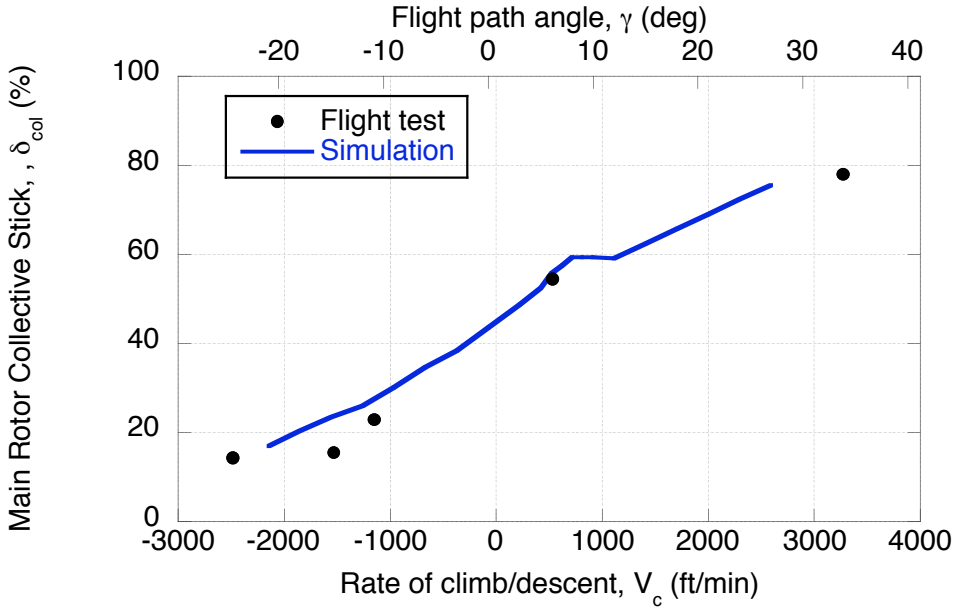

(b) Main rotor collective stick position, δ_{col}

Figure 6.66: Main rotor power required, Q_{MR}, and collective stick position, δ_{col}, as a function of flight path angle γ (or rate of climb/descent); $V = 60$ kts.

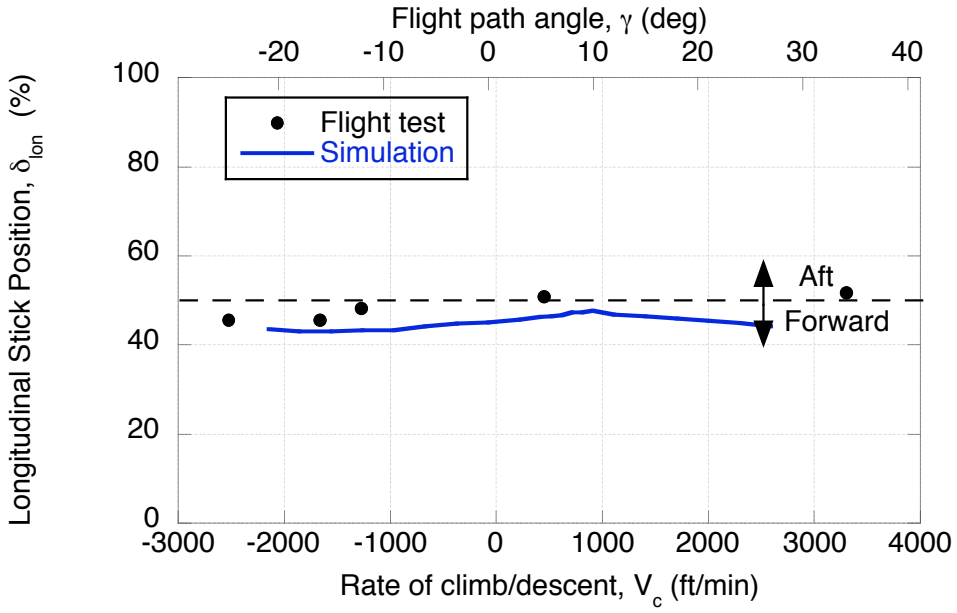

(a) Longitudinal stick position, δ_{lon}

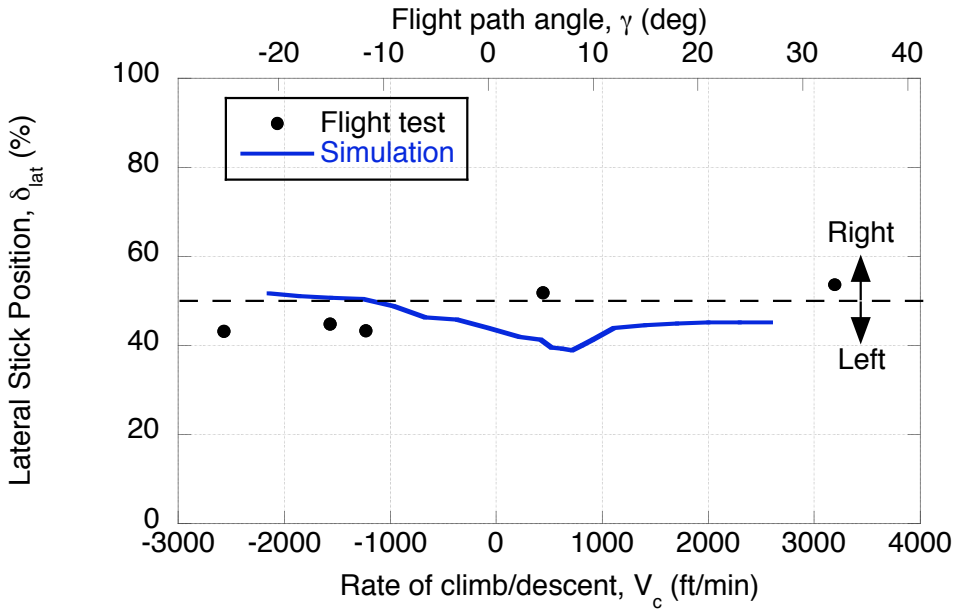

(b) Lateral stick position, δ_{lat}

Figure 6.67: Longitudinal stick position, δ_{lon}, and lateral stick position, δ_{lat}, as a function of flight path angle γ (or rate of climb/descent); $V = 60$ kts.

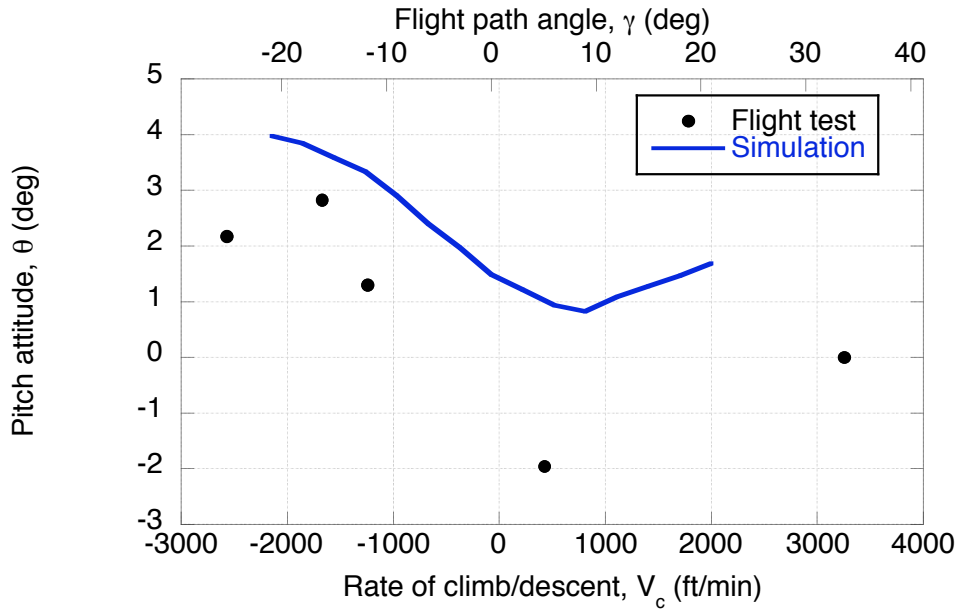

(a) Pitch attitude, θ

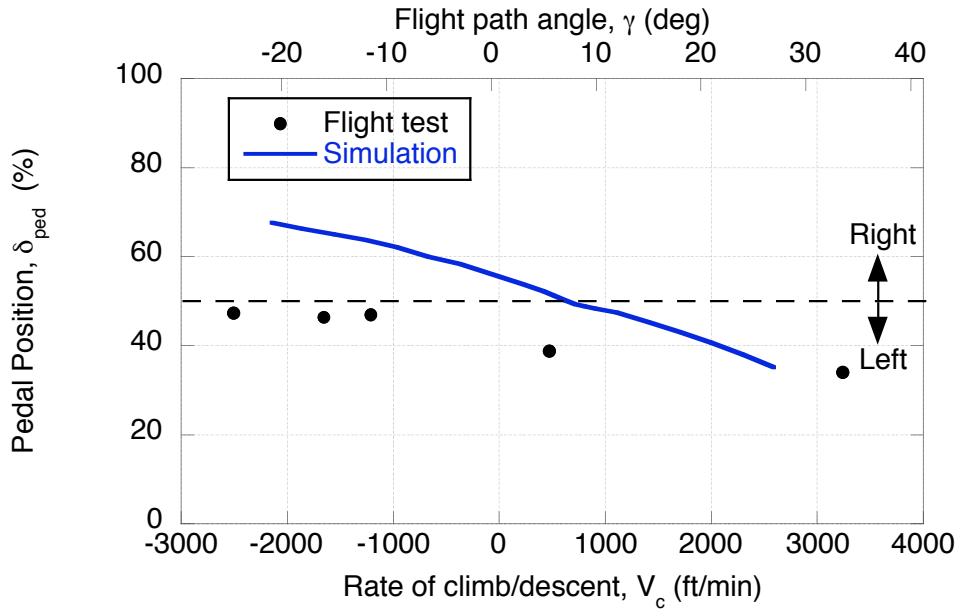

(b) Pedal setting, δ_{ped}

Figure 6.68: Helicopter pitch attitude, θ, and pedal setting, δ_{ped},as a function of flight path angle γ (or rate of climb/descent); $V = 60$ kts.

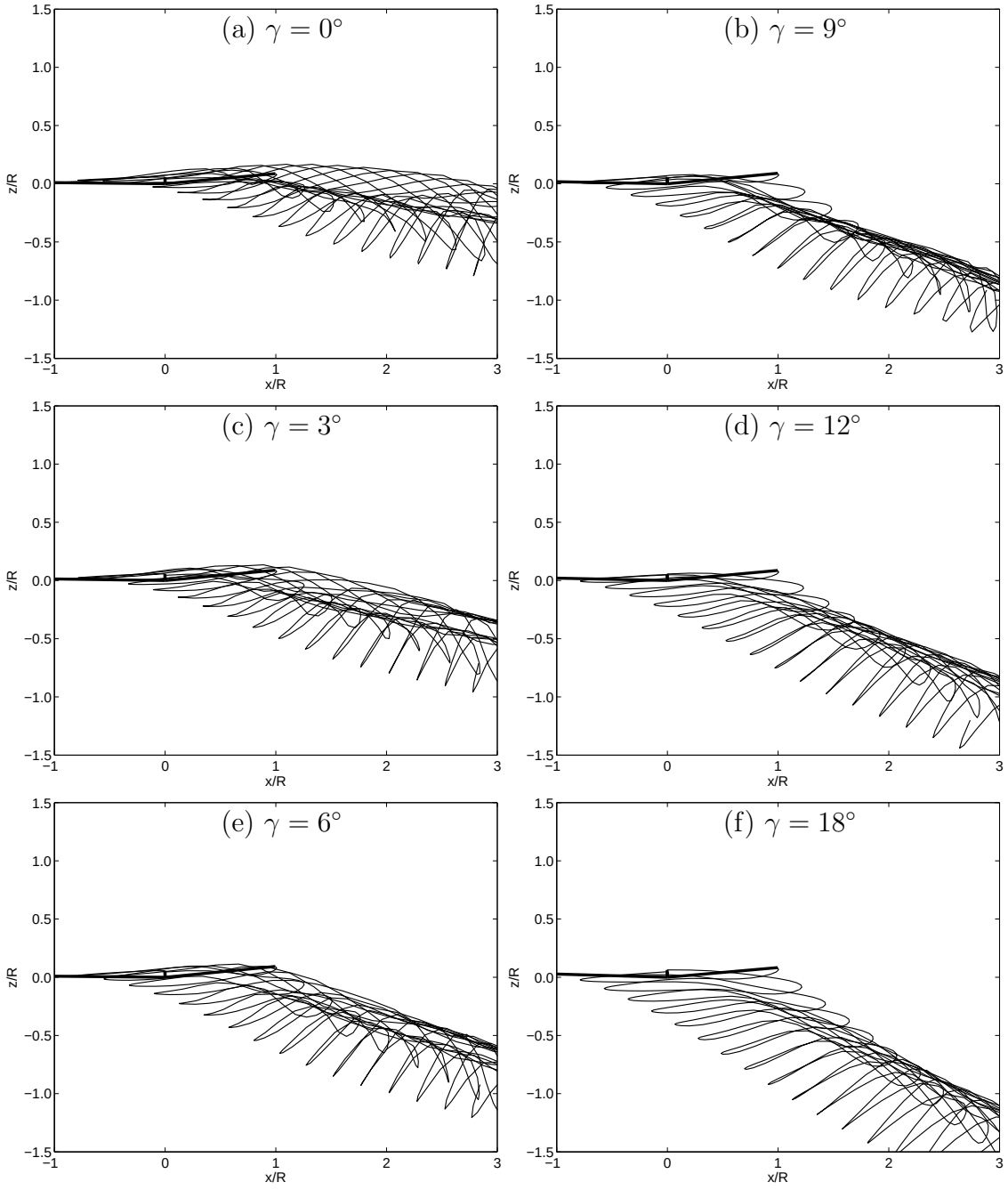

Figure 6.69: Side view of the wake geometry for different climb angles γ; $V = 60$ kts.

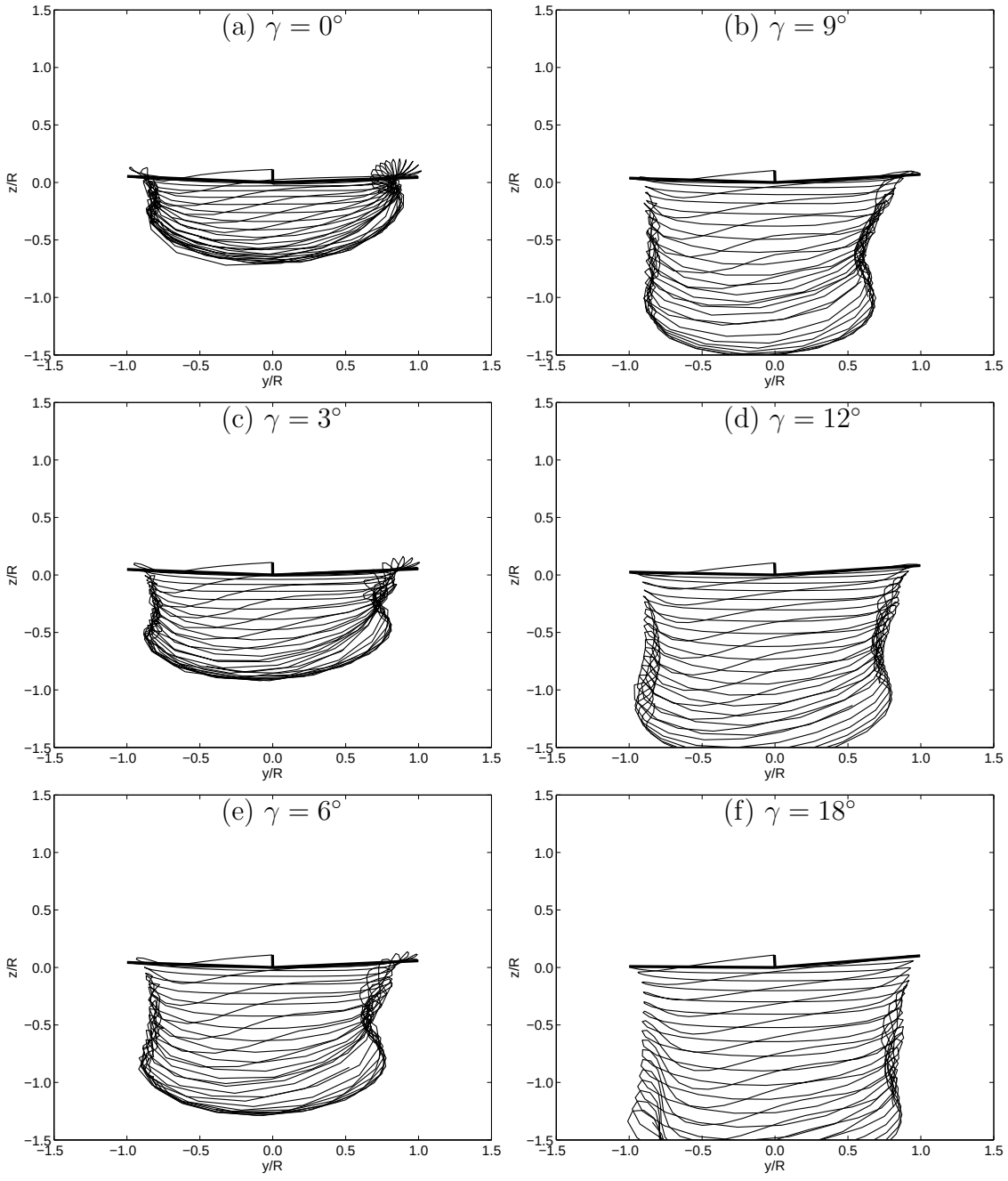

Figure 6.70: Rear view of the wake geometry for different climb angles γ; $V = 60$ kts.

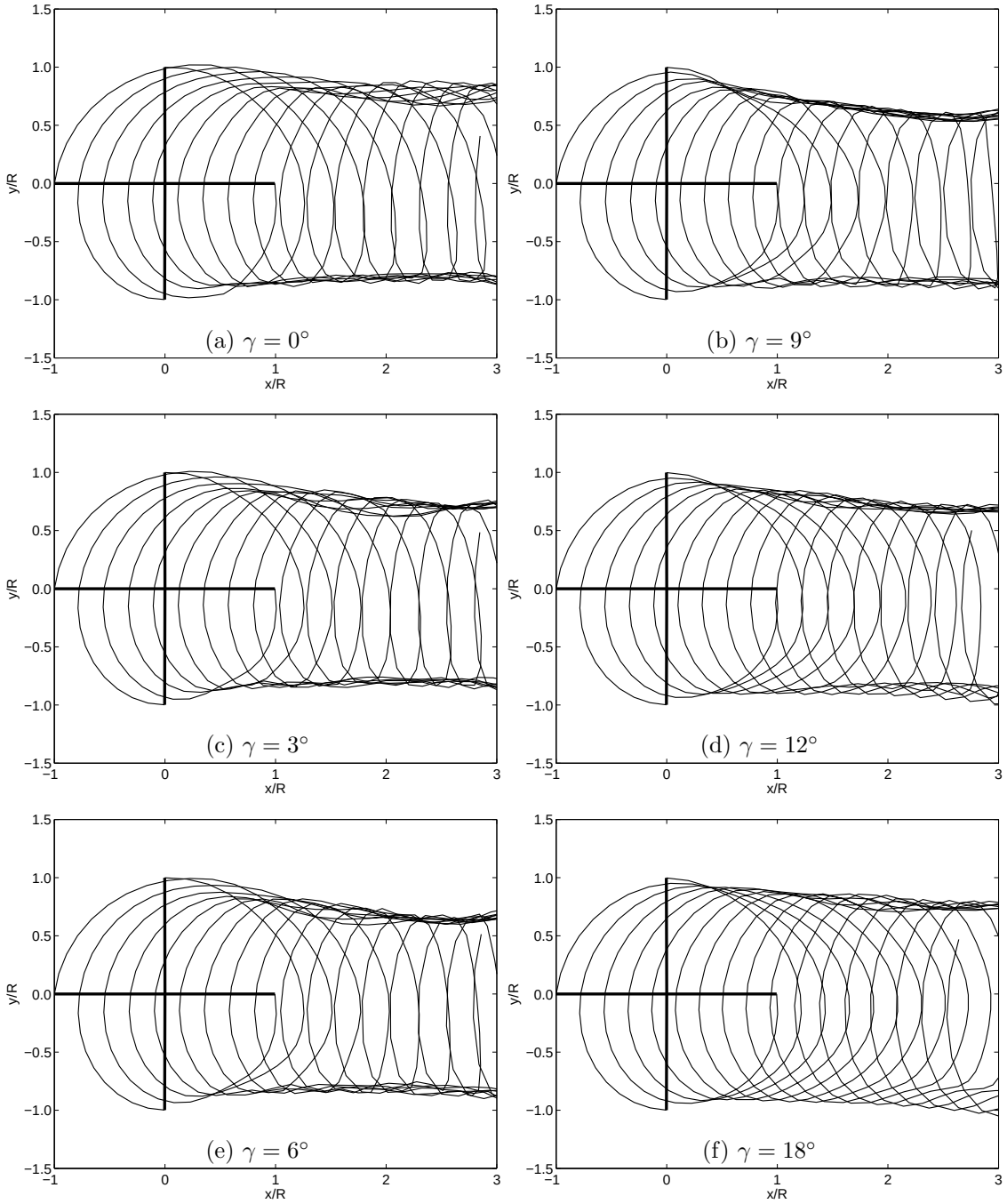

Figure 6.71: Top view of the wake geometry for different climb angles γ; $V = 60$ kts.

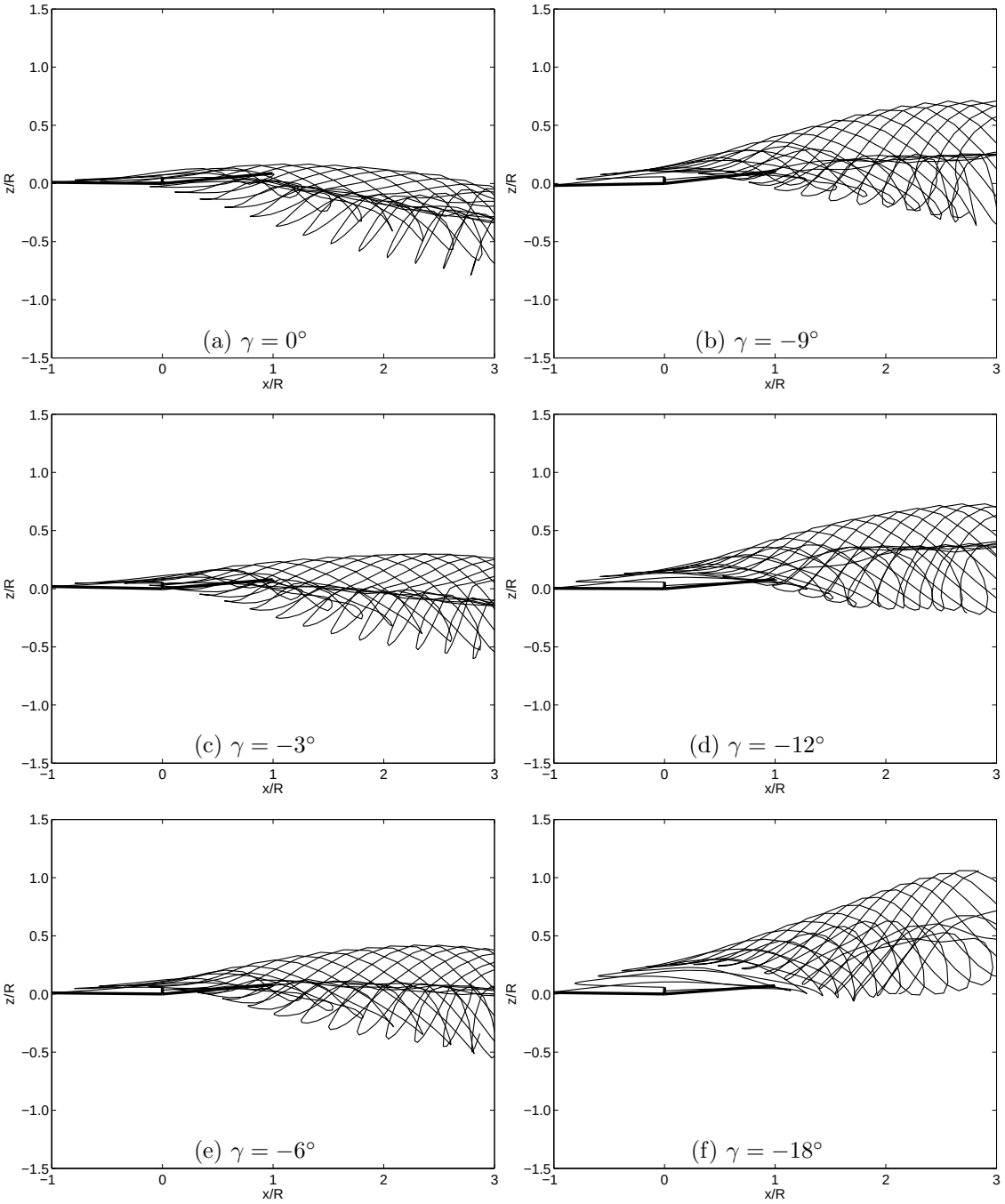

Figure 6.72: Side view of the wake geometry for different descent angles γ; $V = 60$ kts.

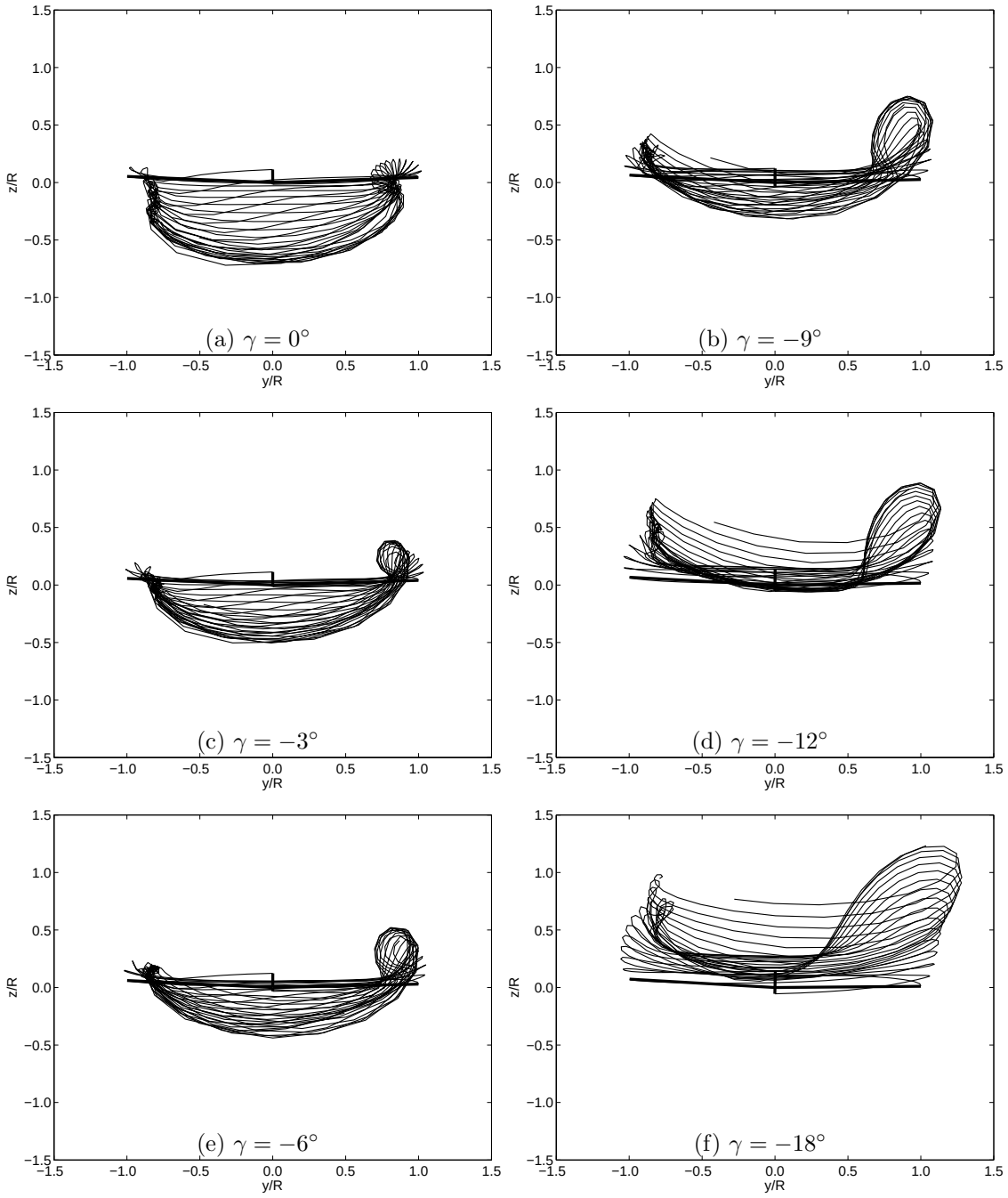

Figure 6.73: Rear view of the wake geometry for different descent angles γ; $V = 60$ kts.

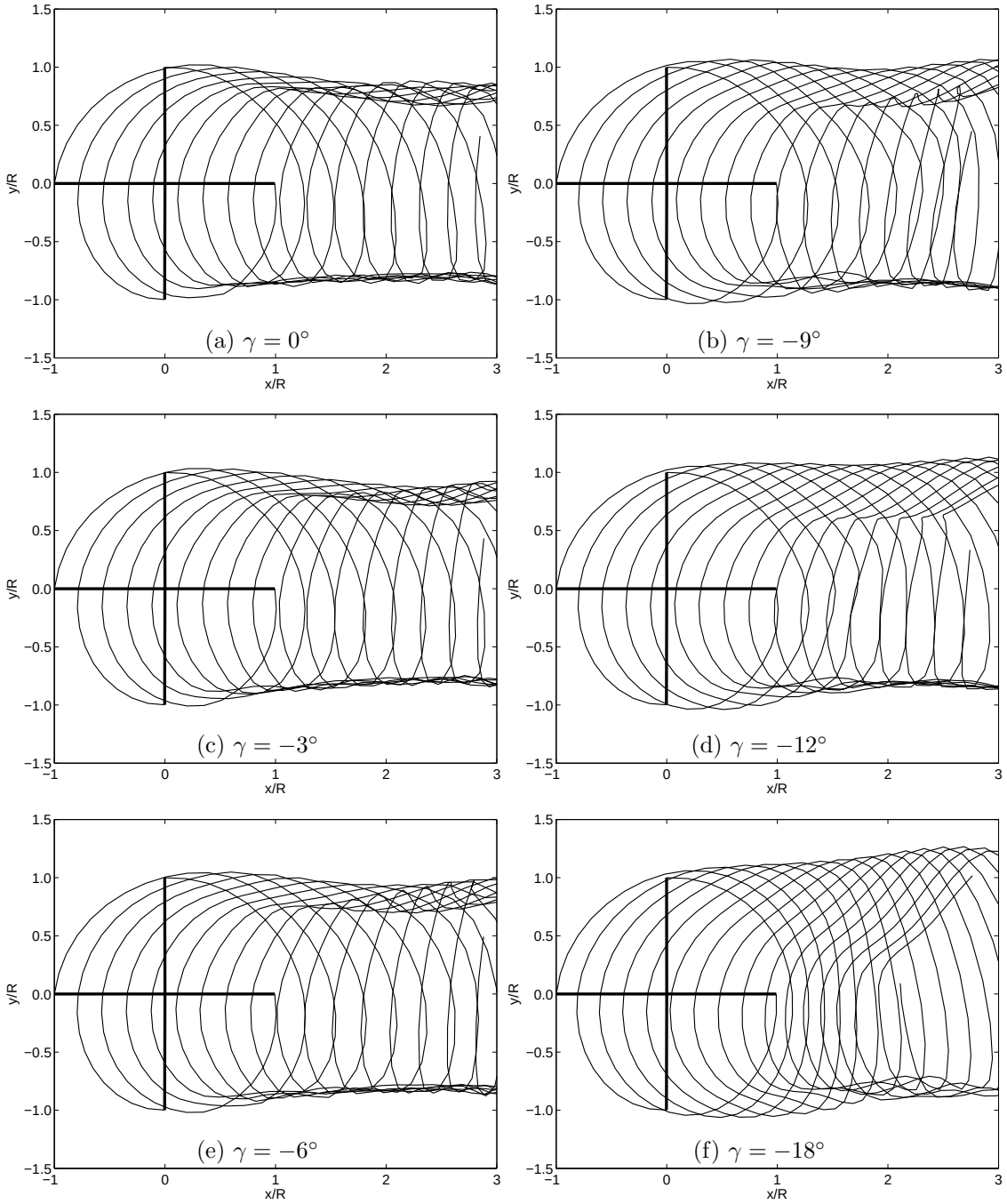

Figure 6.74: Top view of the wake geometry for different descent angles γ; $V = 60$ kts.

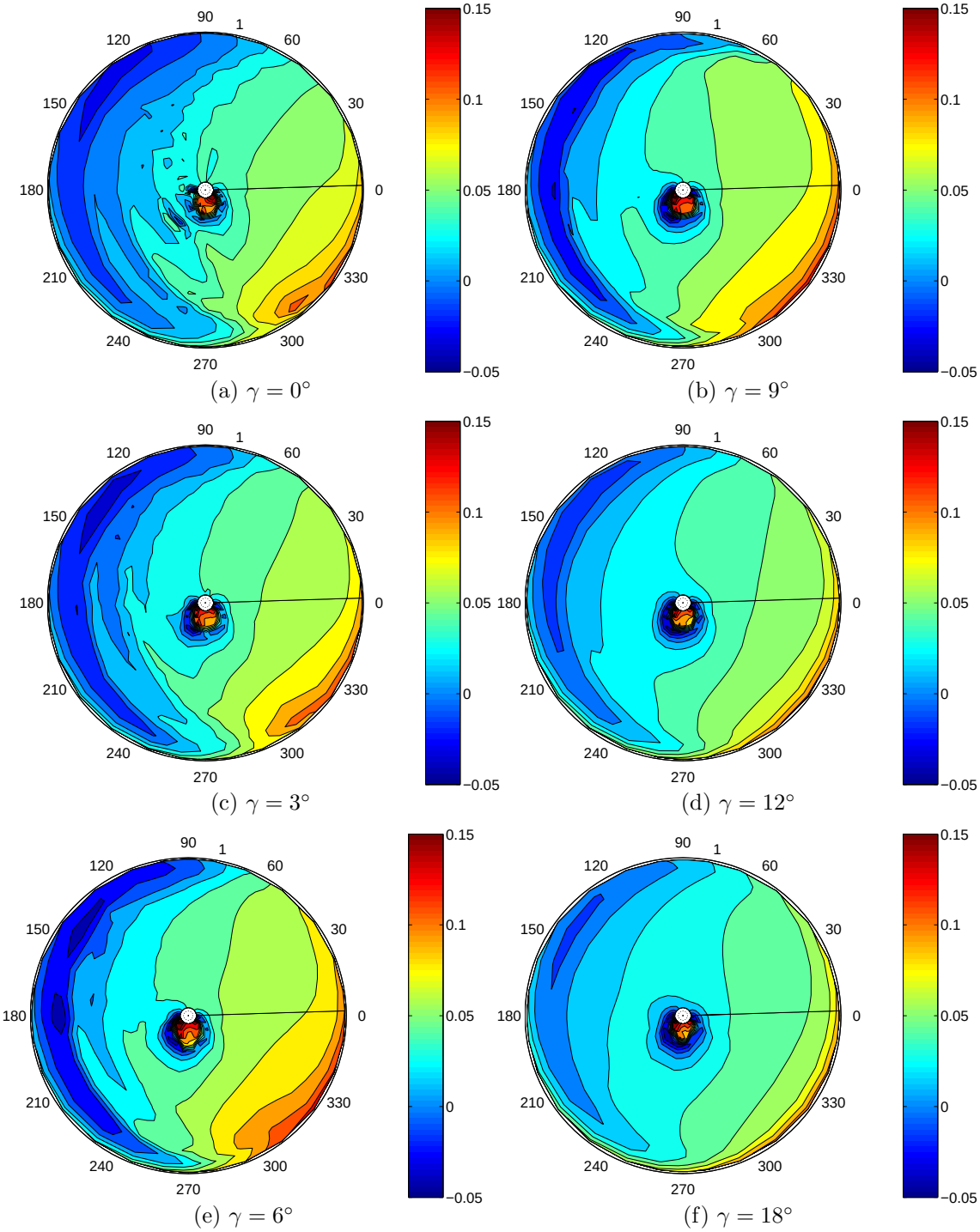

(a) $\gamma = 0°$ (b) $\gamma = 9°$

(c) $\gamma = 3°$ (d) $\gamma = 12°$

(e) $\gamma = 6°$ (f) $\gamma = 18°$

Figure 6.75: Inflow distribution for different climb angles γ; $V = 60$ kts.

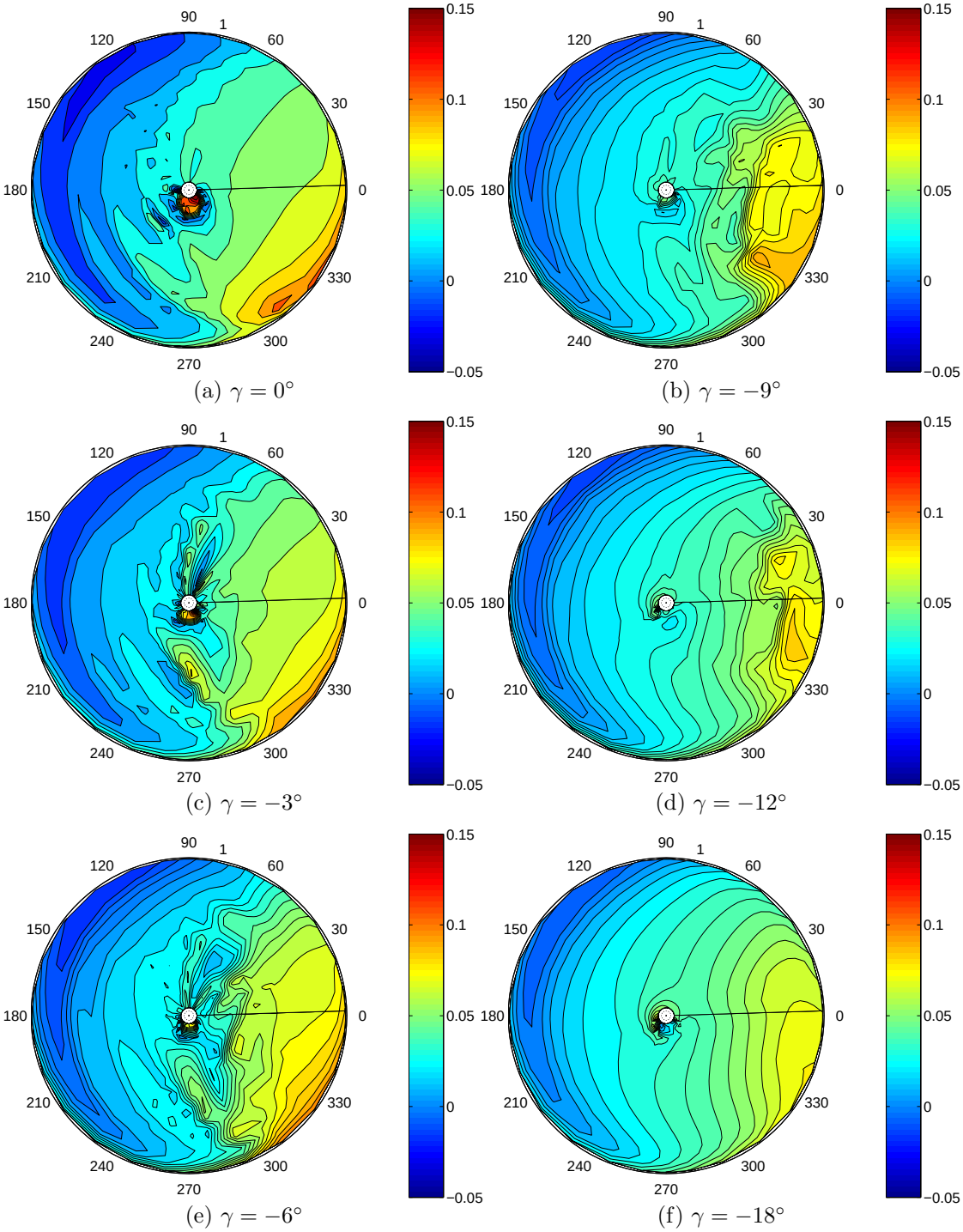

(a) $\gamma = 0°$ (b) $\gamma = -9°$

(c) $\gamma = -3°$ (d) $\gamma = -12°$

(e) $\gamma = -6°$ (f) $\gamma = -18°$

Figure 6.76: Inflow distribution for different descent angles γ; $V = 60$ kts.

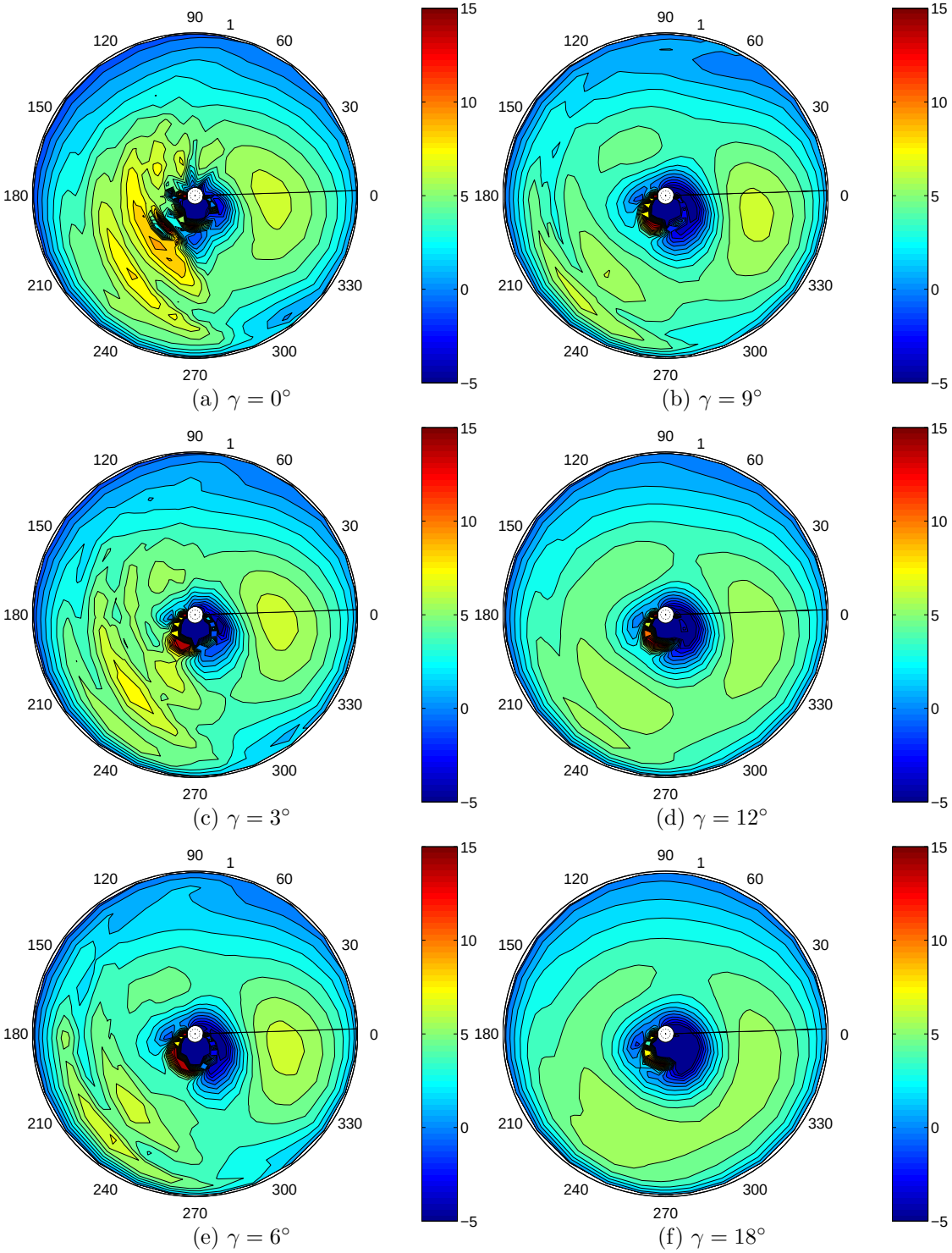

(a) $\gamma = 0°$ (b) $\gamma = 9°$

(c) $\gamma = 3°$ (d) $\gamma = 12°$

(e) $\gamma = 6°$ (f) $\gamma = 18°$

Figure 6.77: Angle of attack distribution for different climb angles γ; $V = 60$ kts.

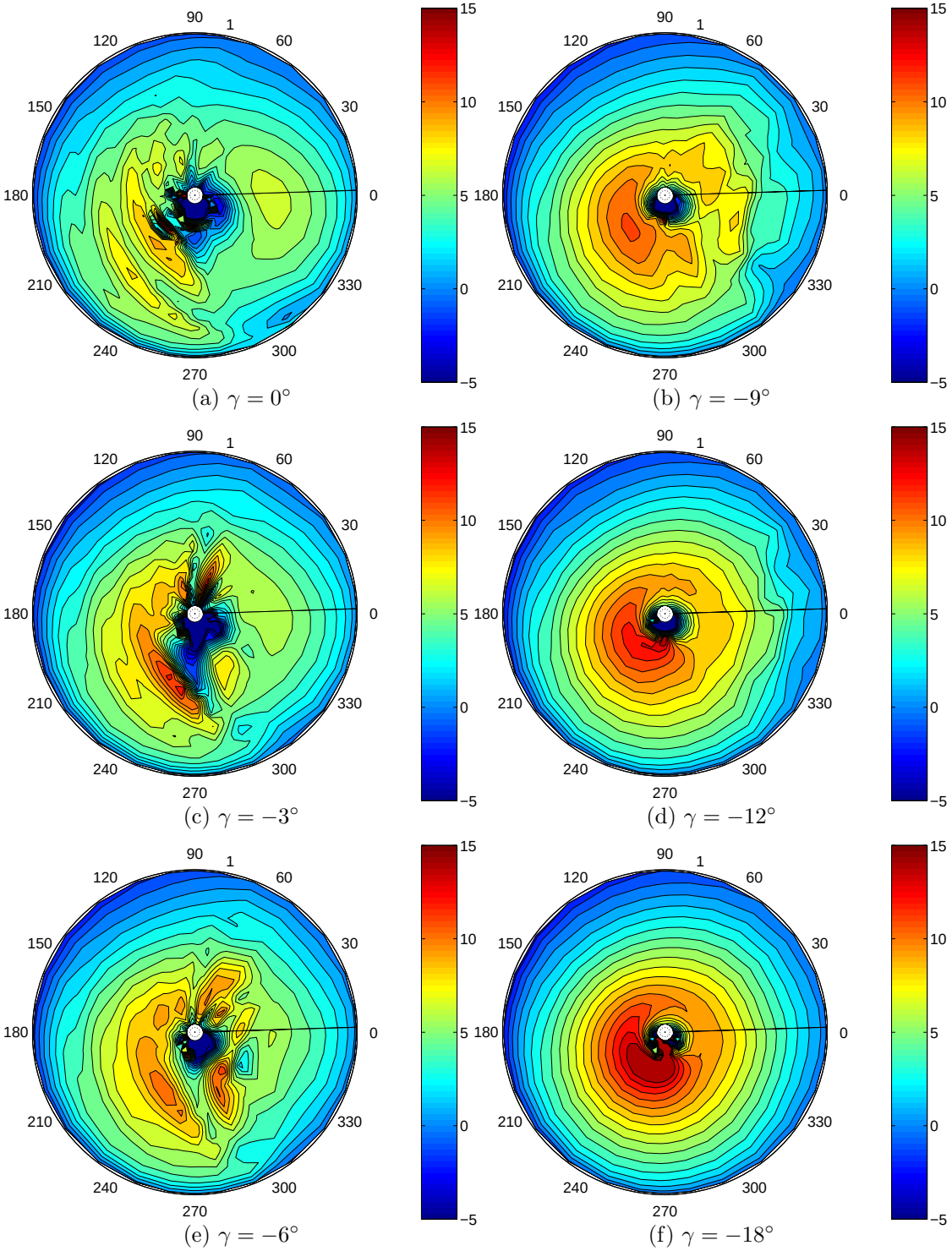

(a) $\gamma = 0°$ (b) $\gamma = -9°$

(c) $\gamma = -3°$ (d) $\gamma = -12°$

(e) $\gamma = -6°$ (f) $\gamma = -18°$

Figure 6.78: Angle of attack distribution for different descent angles γ; $V = 60$ kts.

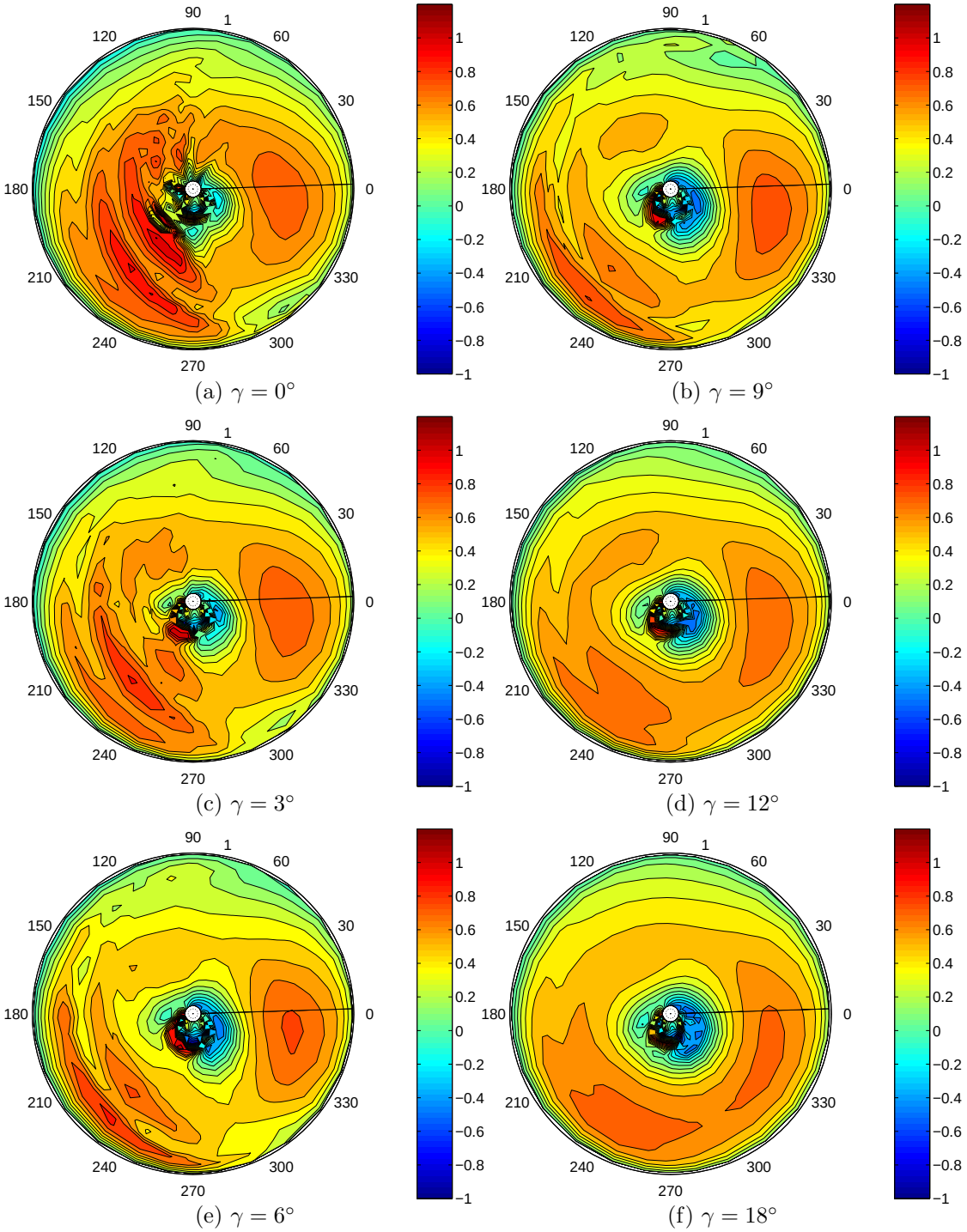

(a) $\gamma = 0°$ (b) $\gamma = 9°$

(c) $\gamma = 3°$ (d) $\gamma = 12°$

(e) $\gamma = 6°$ (f) $\gamma = 18°$

Figure 6.79: Lift coefficient distribution for different climb angles γ; $V = 60$ kts.

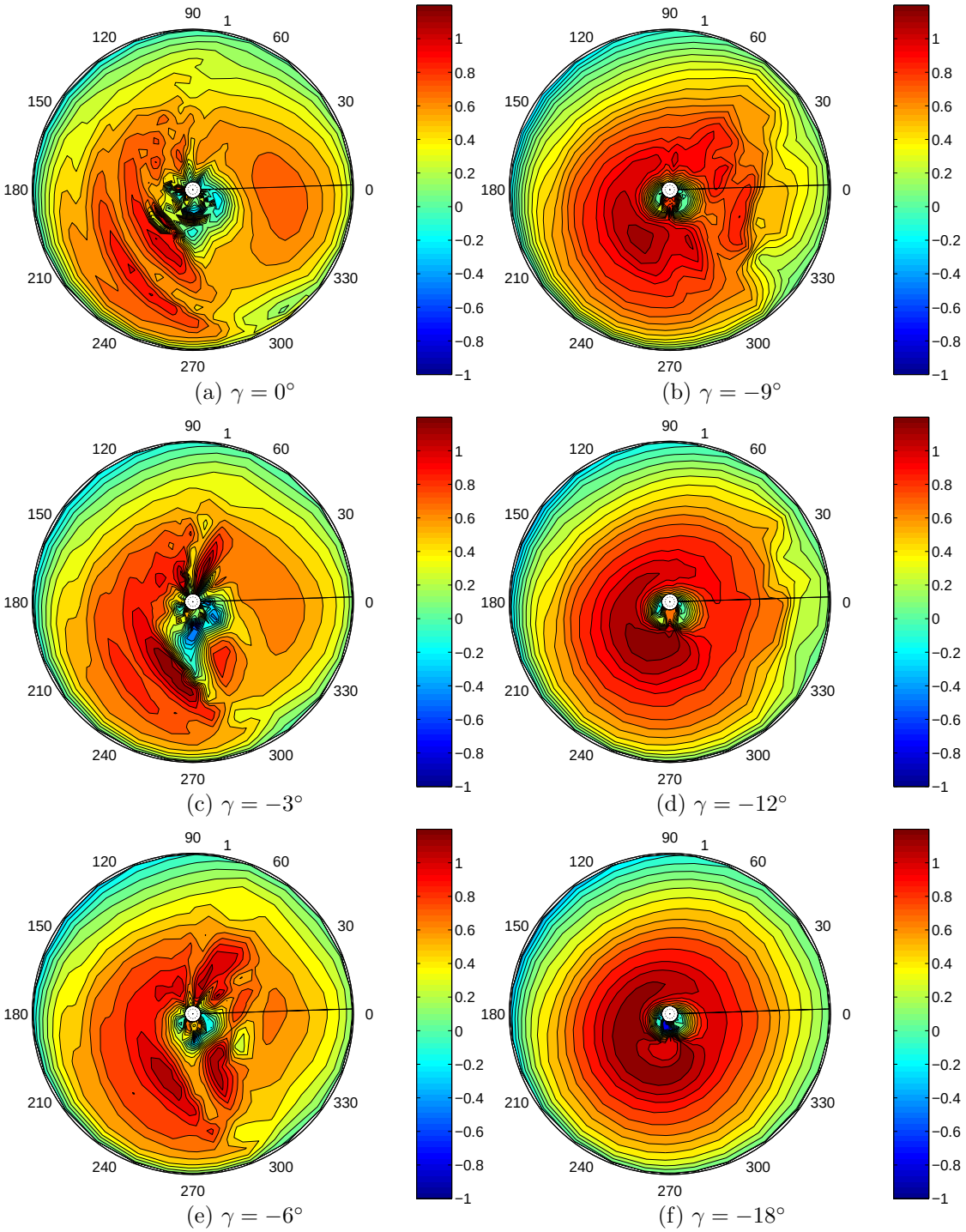

(a) $\gamma = 0°$ (b) $\gamma = -9°$

(c) $\gamma = -3°$ (d) $\gamma = -12°$

(e) $\gamma = -6°$ (f) $\gamma = -18°$

Figure 6.80: Lift coefficient distribution for different descent angles γ; $V = 60$ kts.

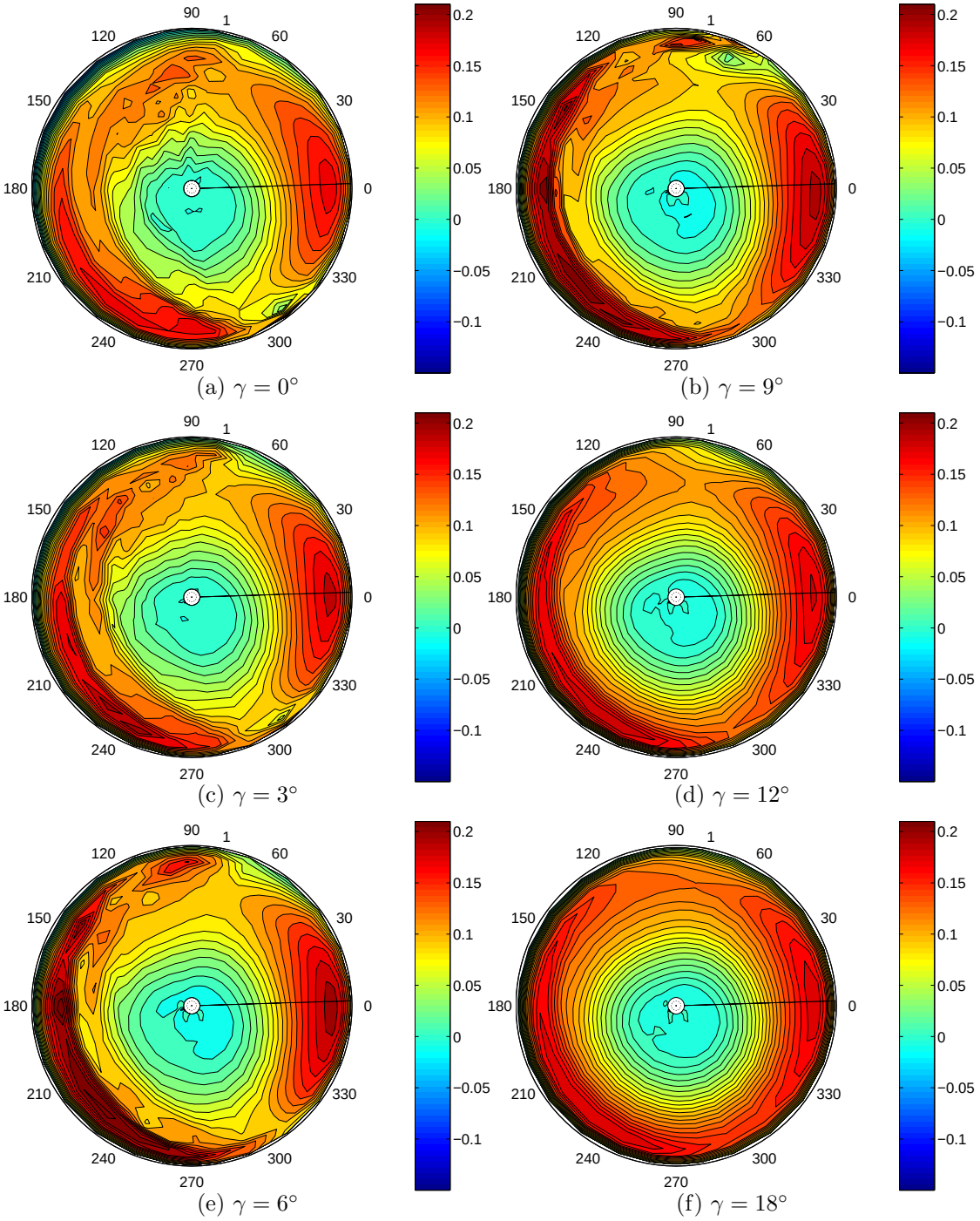

(a) $\gamma = 0°$ (b) $\gamma = 9°$

(c) $\gamma = 3°$ (d) $\gamma = 12°$

(e) $\gamma = 6°$ (f) $\gamma = 18°$

Figure 6.81: Elemental lift distribution for different climb angles γ; $V = 60$ kts.

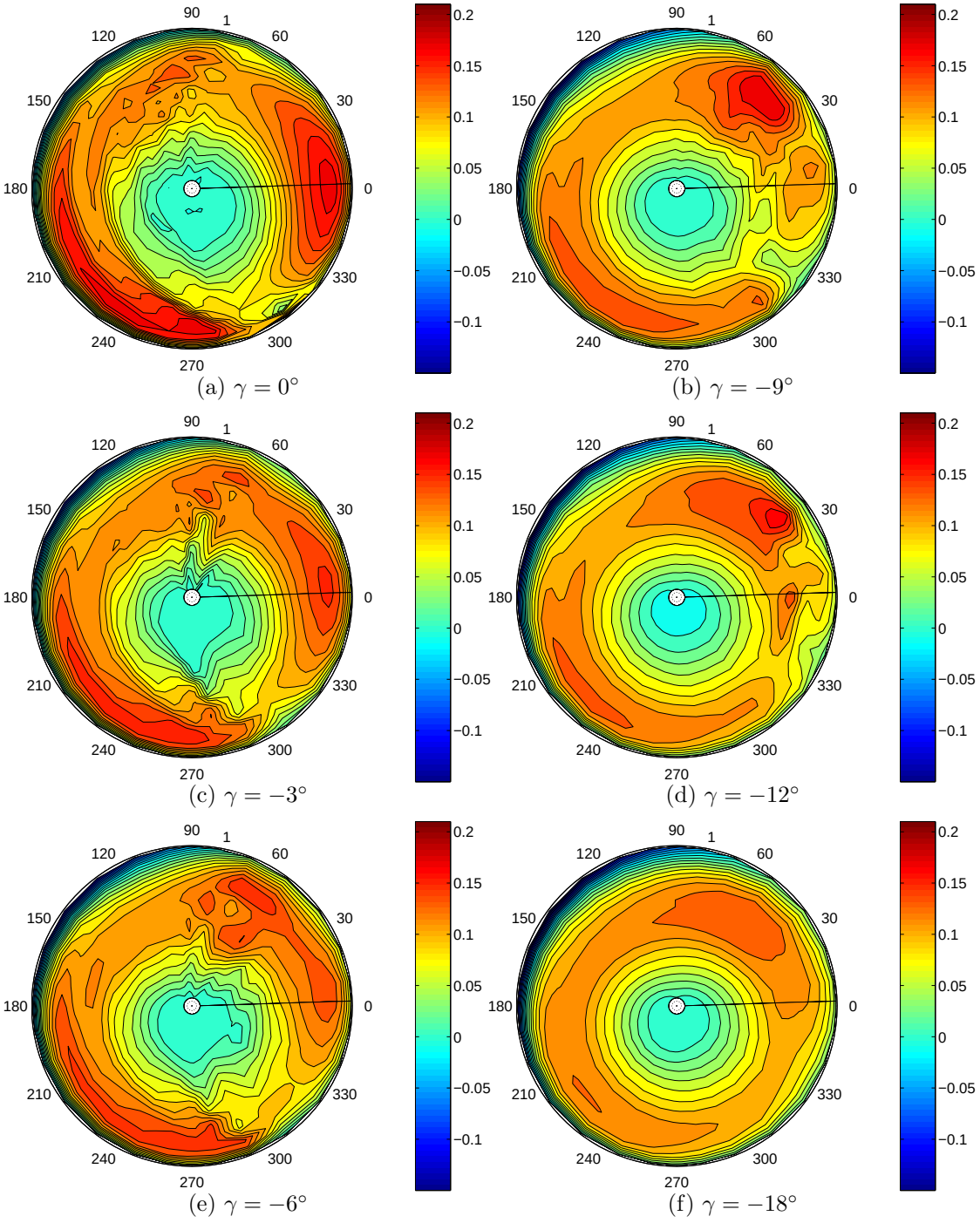

(a) $\gamma = 0°$ (b) $\gamma = -9°$

(c) $\gamma = -3°$ (d) $\gamma = -12°$

(e) $\gamma = -6°$ (f) $\gamma = -18°$

Figure 6.82: Elemental lift distribution for different descent angles γ; $V = 60$ kts.

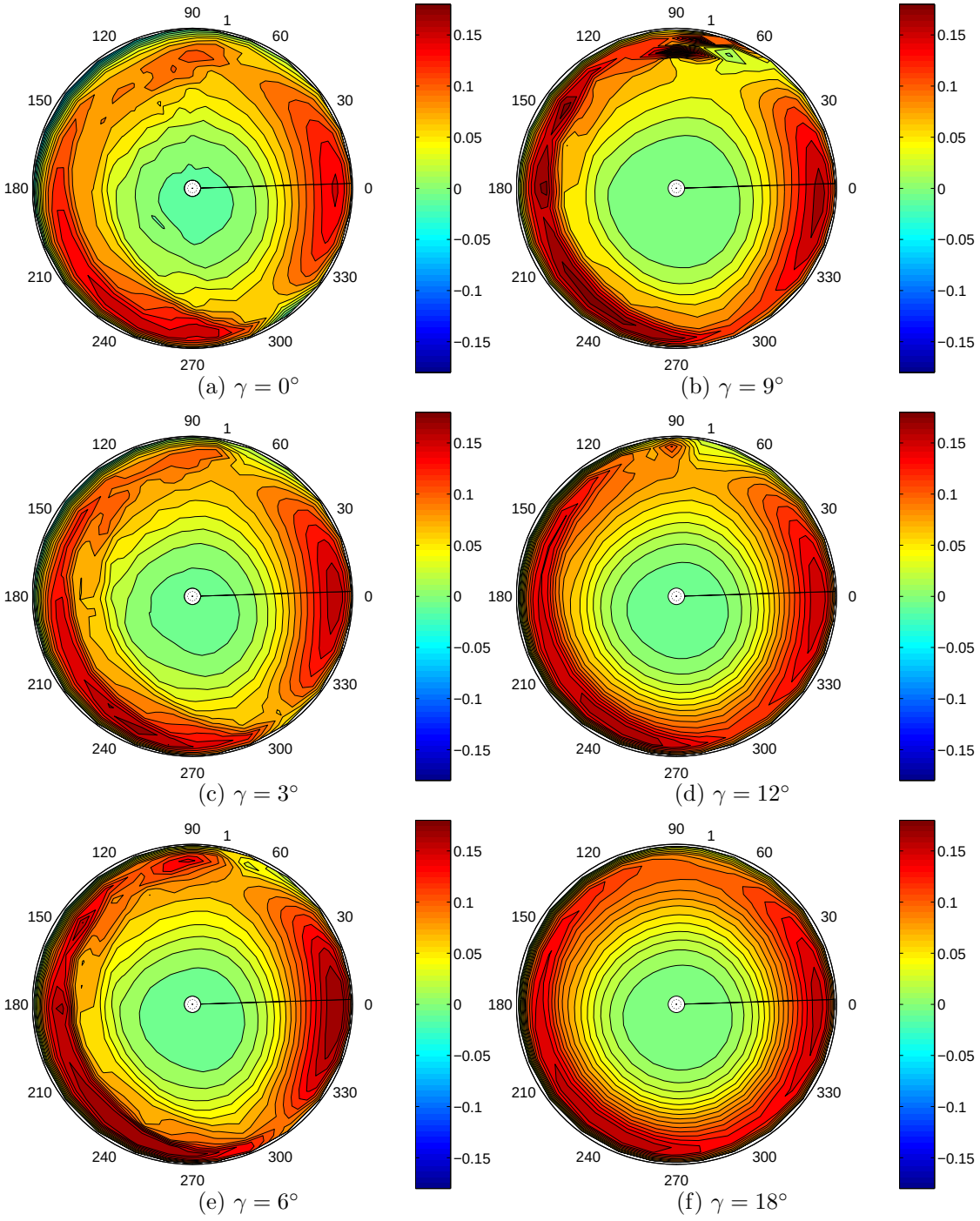

(a) $\gamma = 0°$ (b) $\gamma = 9°$

(c) $\gamma = 3°$ (d) $\gamma = 12°$

(e) $\gamma = 6°$ (f) $\gamma = 18°$

Figure 6.83: Local flap moment for different climb angles γ; $V = 60$ kts.

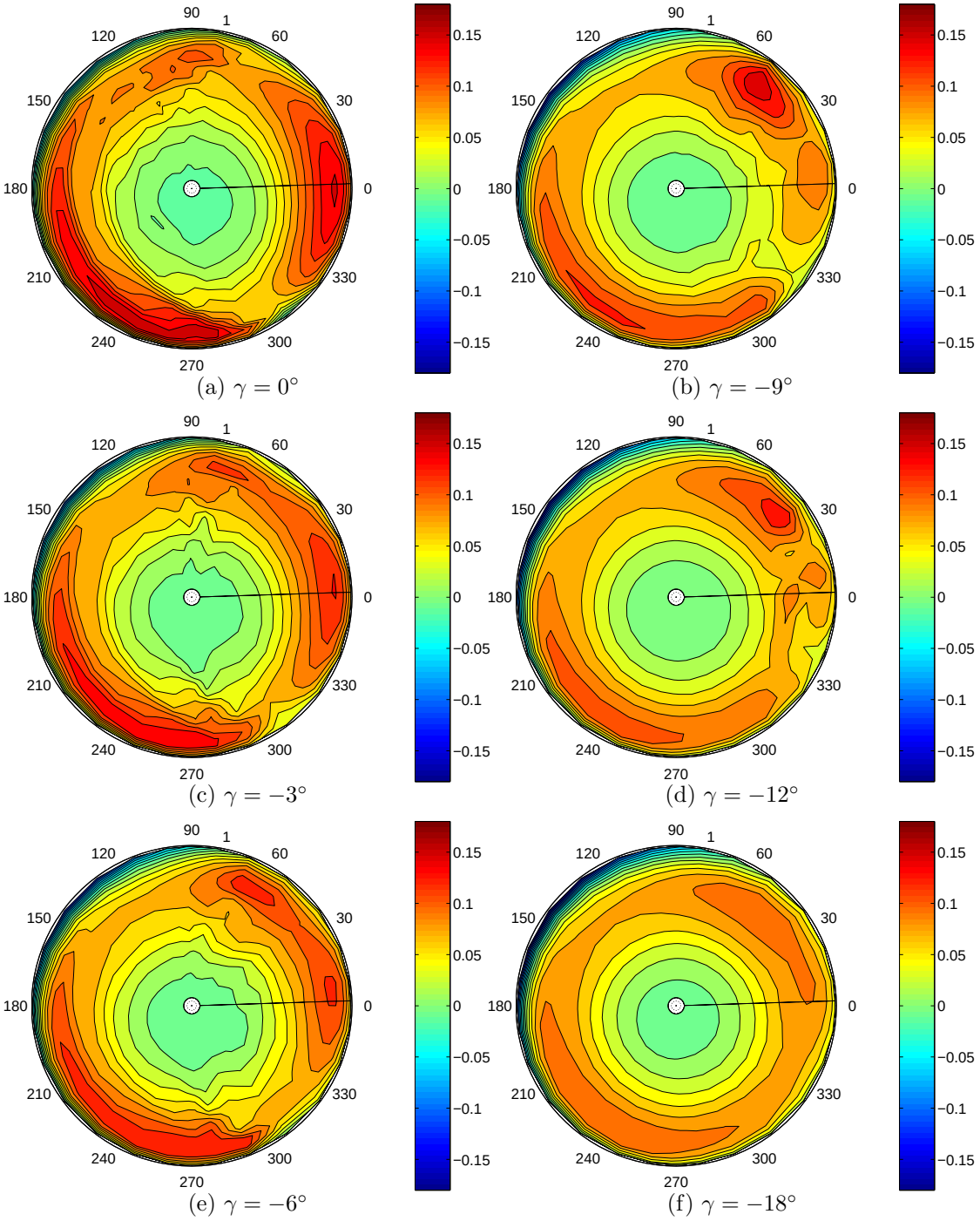

(a) $\gamma = 0°$ (b) $\gamma = -9°$

(c) $\gamma = -3°$ (d) $\gamma = -12°$

(e) $\gamma = -6°$ (f) $\gamma = -18°$

Figure 6.84: Local flap moment for different descent angles γ; $V = 60$ kts.

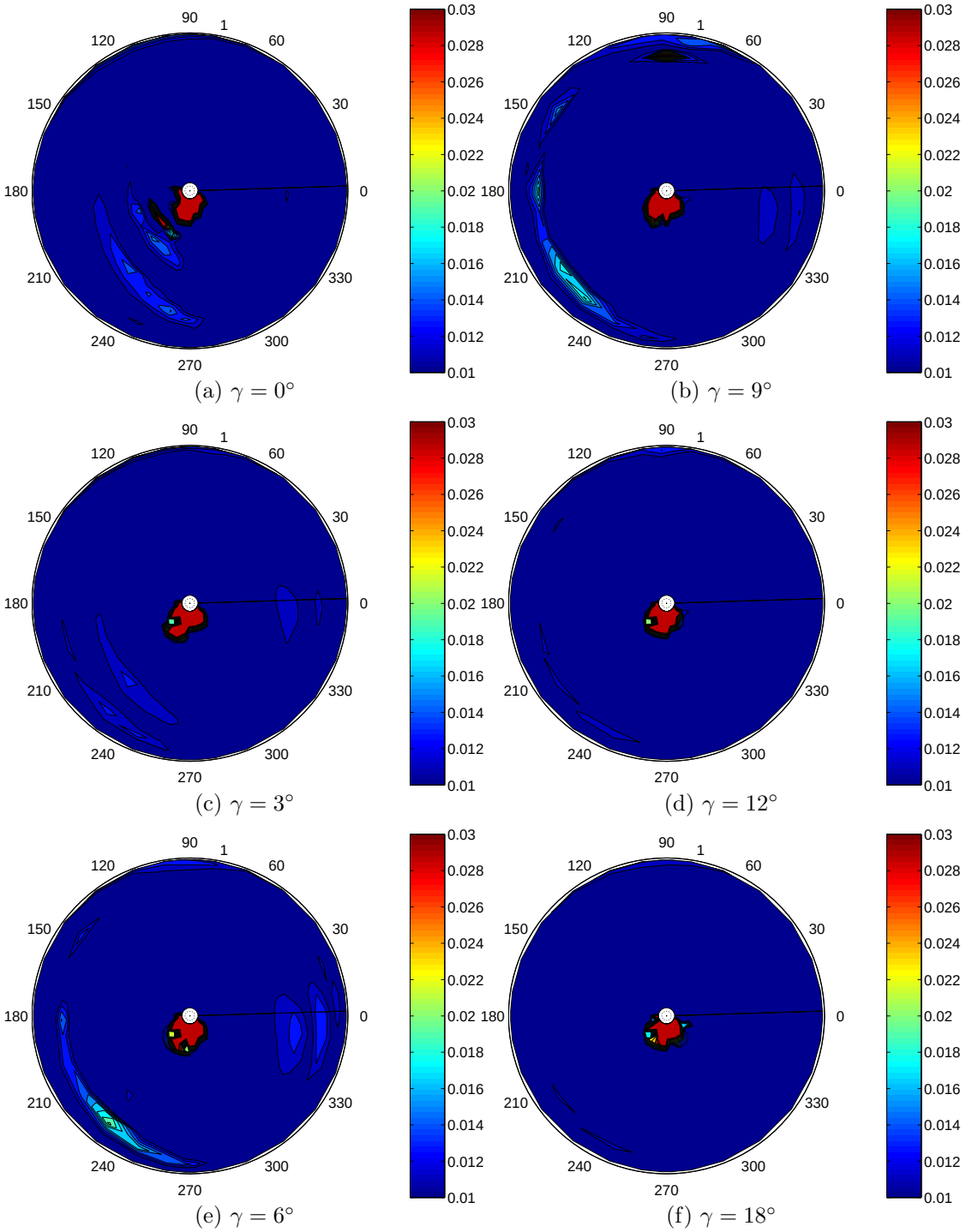

(a) $\gamma = 0°$ (b) $\gamma = 9°$

(c) $\gamma = 3°$ (d) $\gamma = 12°$

(e) $\gamma = 6°$ (f) $\gamma = 18°$

Figure 6.85: Drag coefficient distribution for different climb angles γ; $V = 60$ kts.

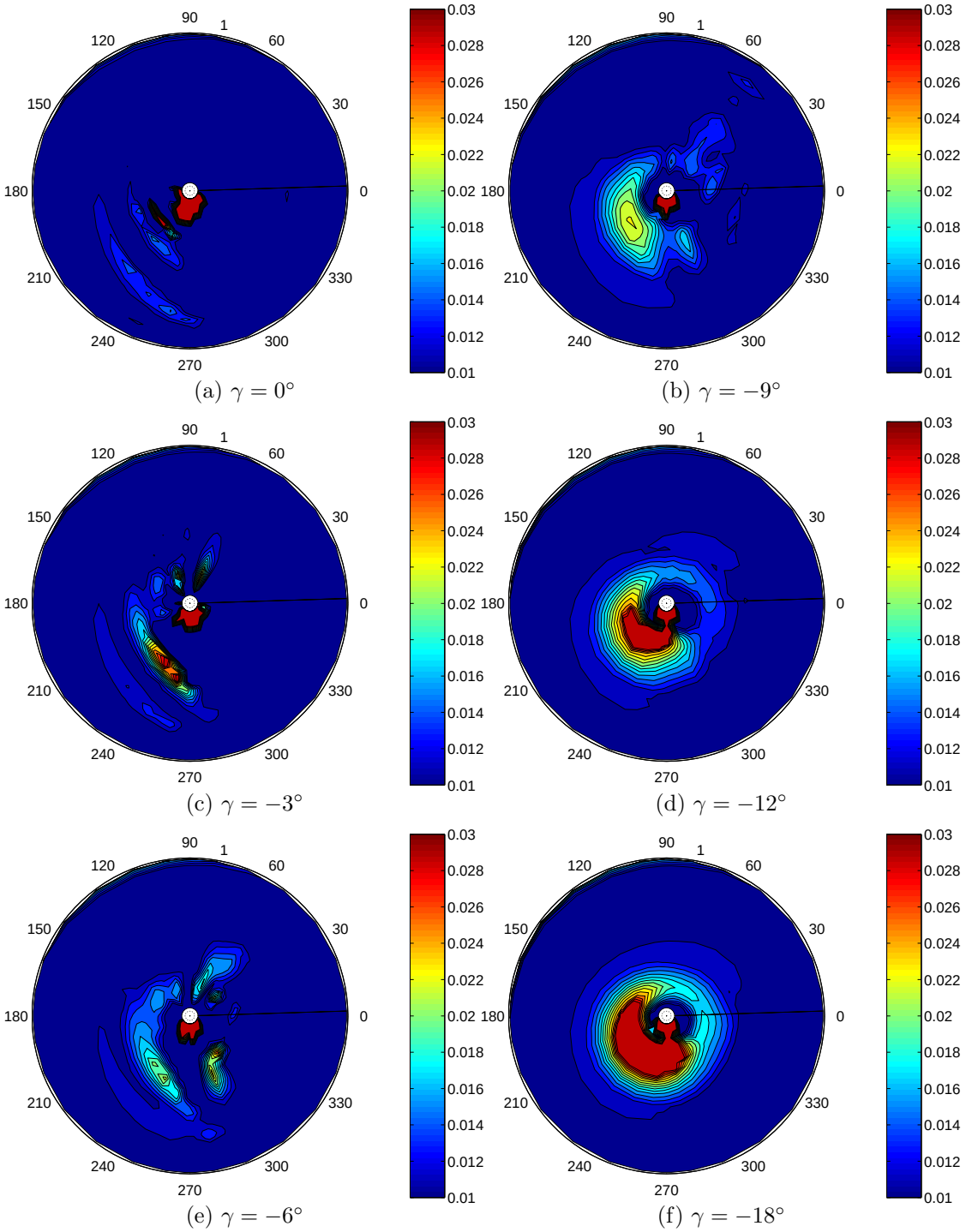

(a) $\gamma = 0°$ (b) $\gamma = -9°$

(c) $\gamma = -3°$ (d) $\gamma = -12°$

(e) $\gamma = -6°$ (f) $\gamma = -18°$

Figure 6.86: Drag coefficient distribution for different descent angles γ; $V = 60$ kts.

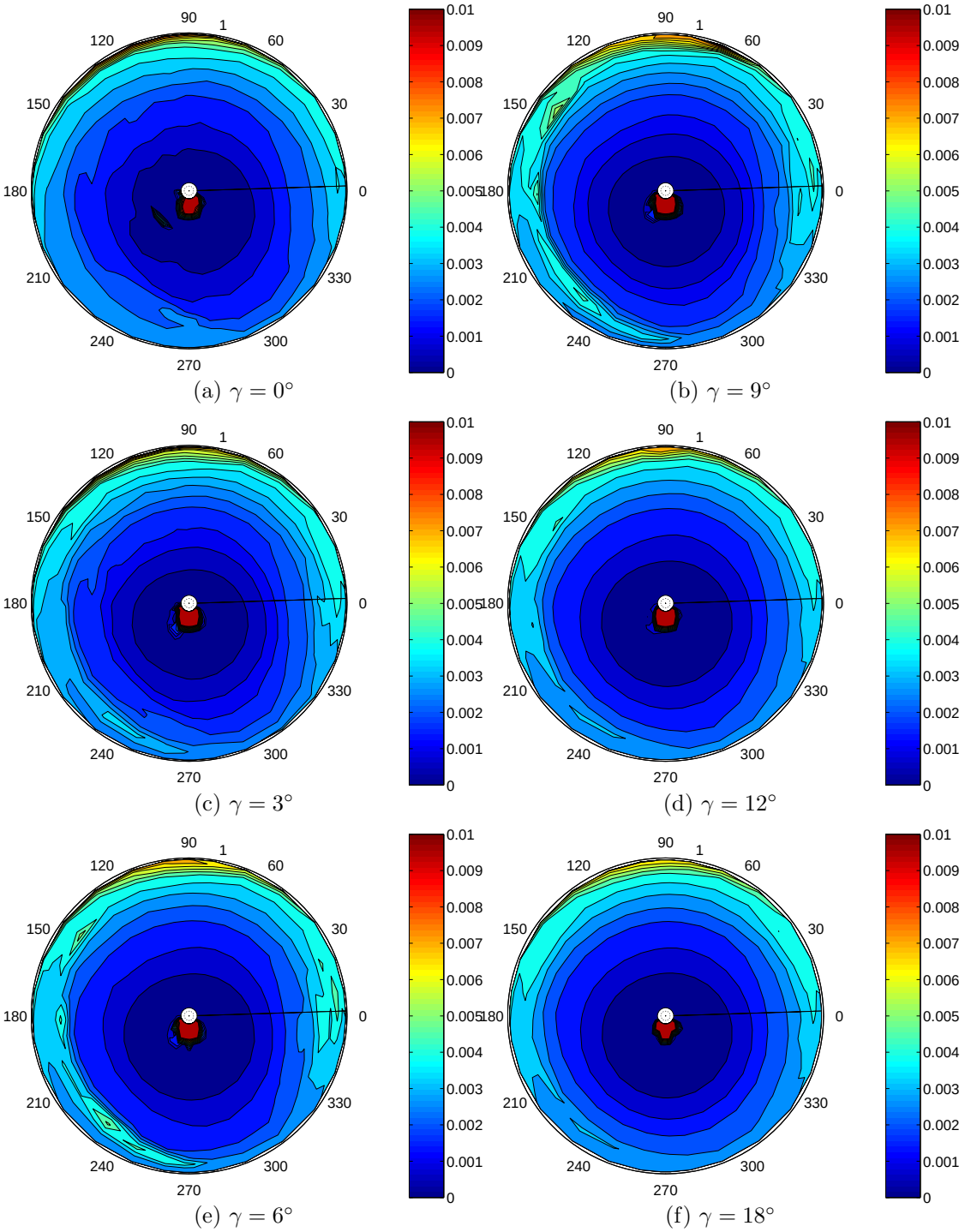

(a) $\gamma = 0°$ (b) $\gamma = 9°$

(c) $\gamma = 3°$ (d) $\gamma = 12°$

(e) $\gamma = 6°$ (f) $\gamma = 18°$

Figure 6.87: Elemental drag distribution for different climb angles γ; $V = 60$ kts.

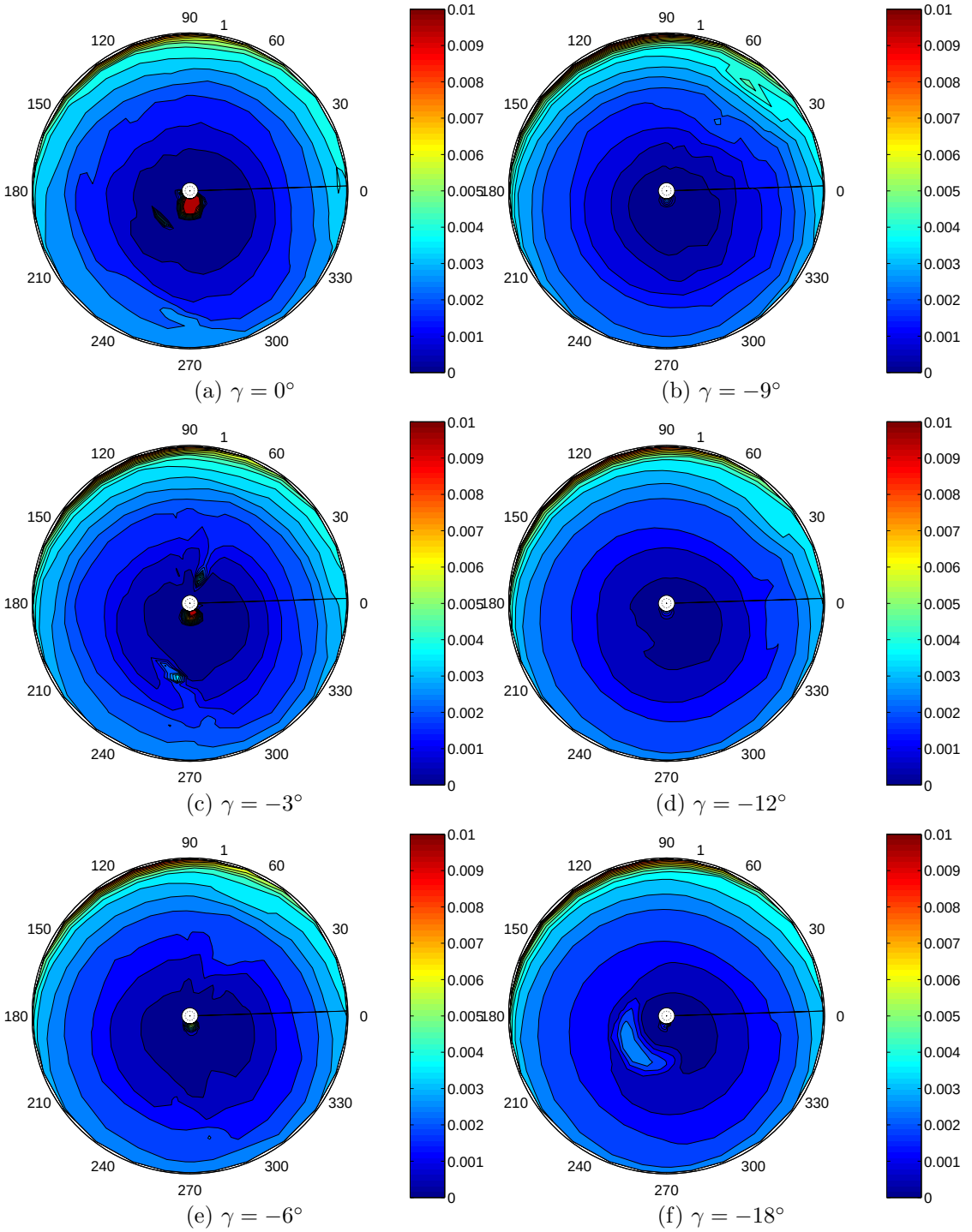

(a) $\gamma = 0°$ (b) $\gamma = -9°$

(c) $\gamma = -3°$ (d) $\gamma = -12°$

(e) $\gamma = -6°$ (f) $\gamma = -18°$

Figure 6.88: Elemental drag distribution for different descent angles γ; $V = 60$ kts.

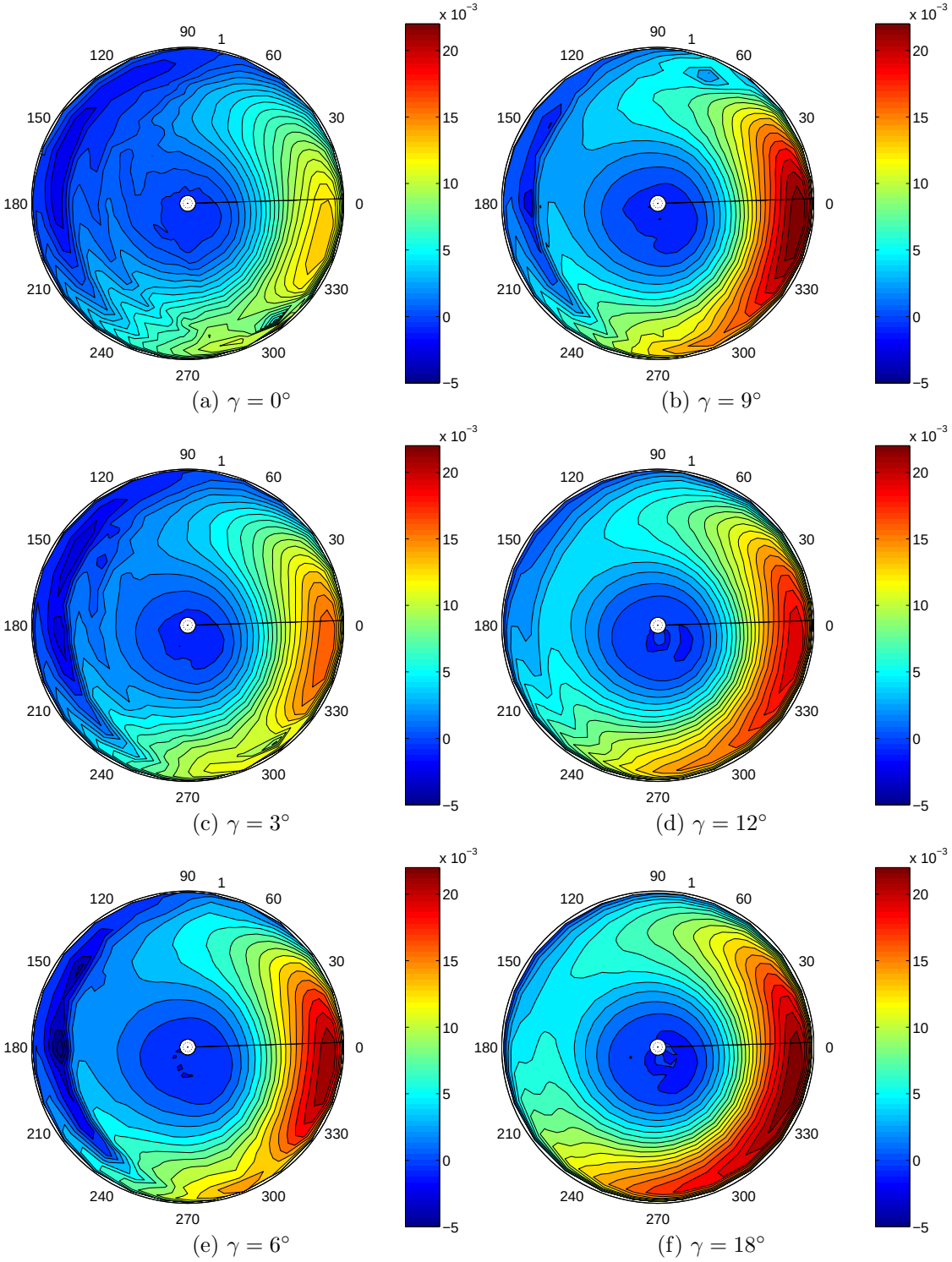

(a) $\gamma = 0°$ (b) $\gamma = 9°$

(c) $\gamma = 3°$ (d) $\gamma = 12°$

(e) $\gamma = 6°$ (f) $\gamma = 18°$

Figure 6.89: Elemental induced torque for different climb angles γ; $V = 60$ kts.

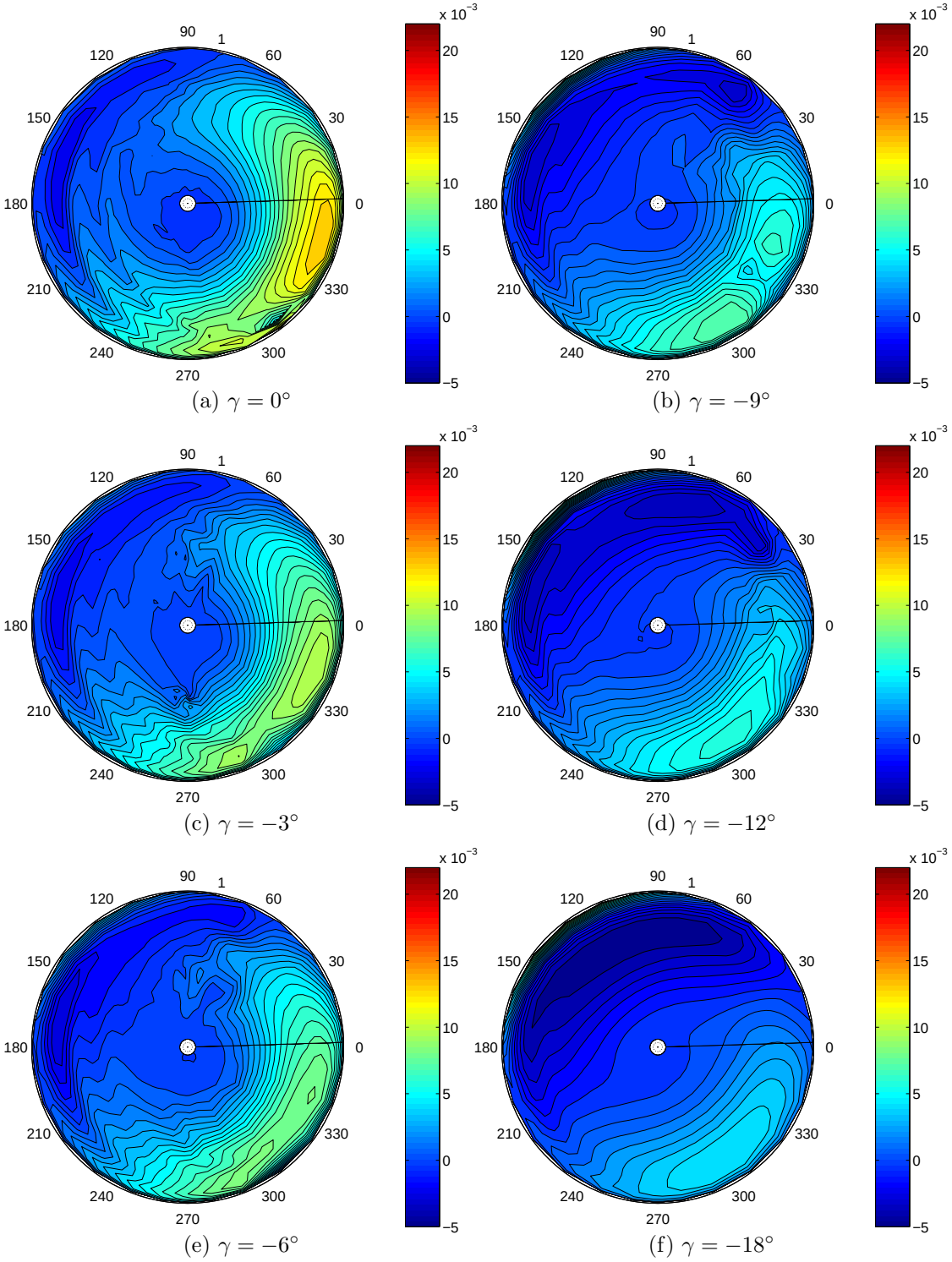

(a) $\gamma = 0°$ (b) $\gamma = -9°$

(c) $\gamma = -3°$ (d) $\gamma = -12°$

(e) $\gamma = -6°$ (f) $\gamma = -18°$

Figure 6.90: Elemental induced torque for different descent angles γ; $V = 60$ kts.

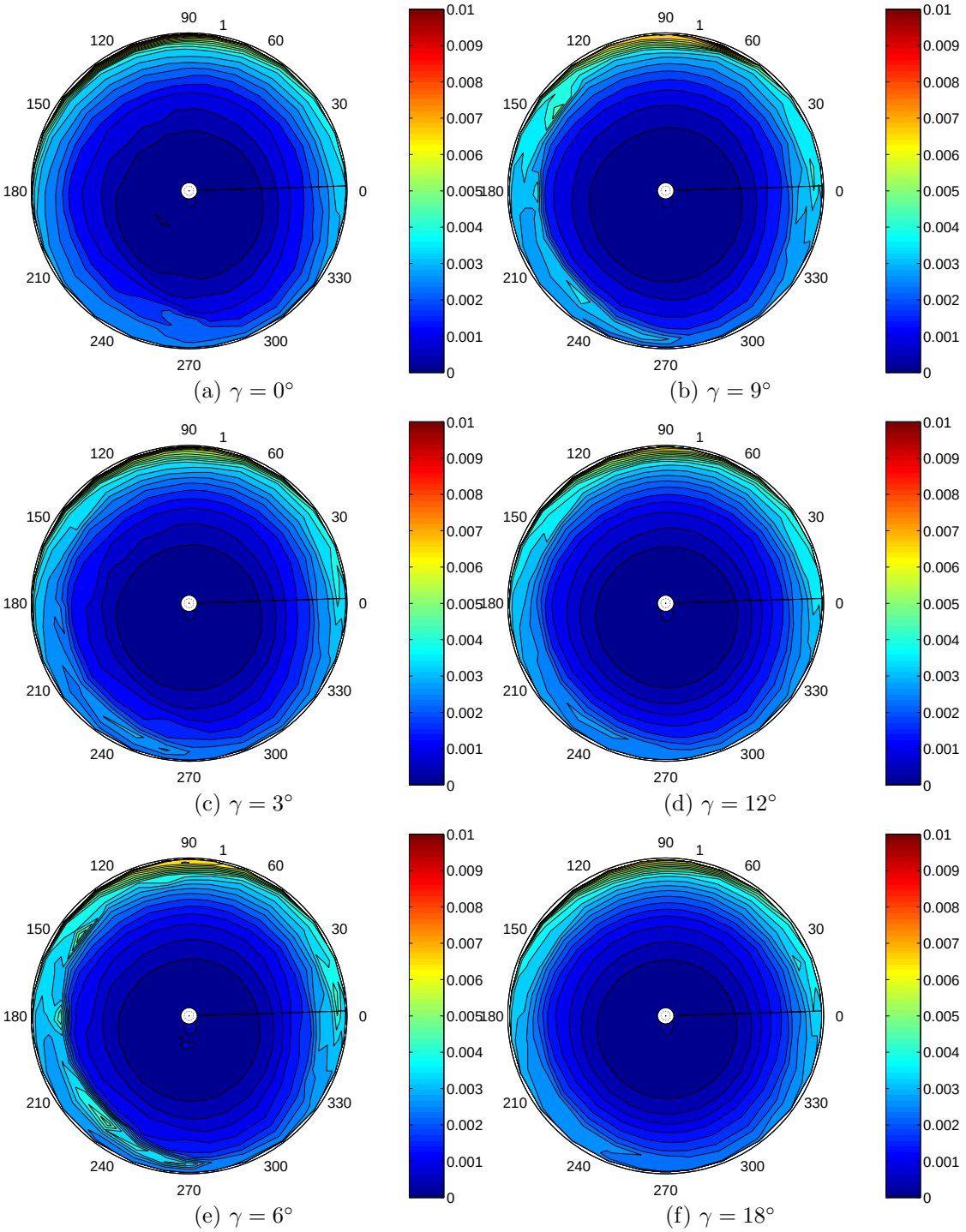

(a) $\gamma = 0°$ (b) $\gamma = 9°$

(c) $\gamma = 3°$ (d) $\gamma = 12°$

(e) $\gamma = 6°$ (f) $\gamma = 18°$

Figure 6.91: Elemental profile torque for different climb angles γ; $V = 60$ kts.

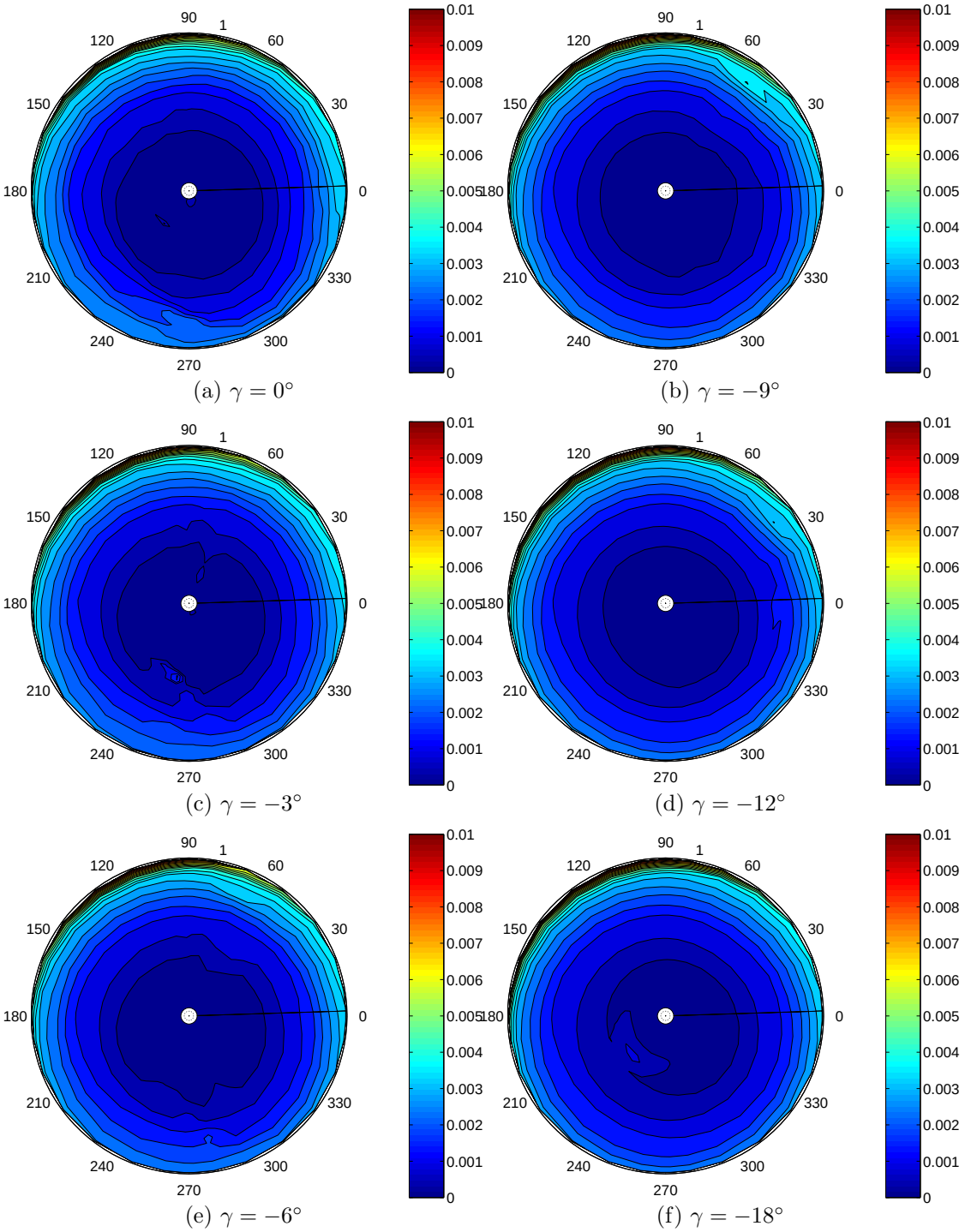

(a) $\gamma = 0°$ (b) $\gamma = -9°$

(c) $\gamma = -3°$ (d) $\gamma = -12°$

(e) $\gamma = -6°$ (f) $\gamma = -18°$

Figure 6.92: Elemental profile torque for different descent angles γ; $V = 60$ kts.

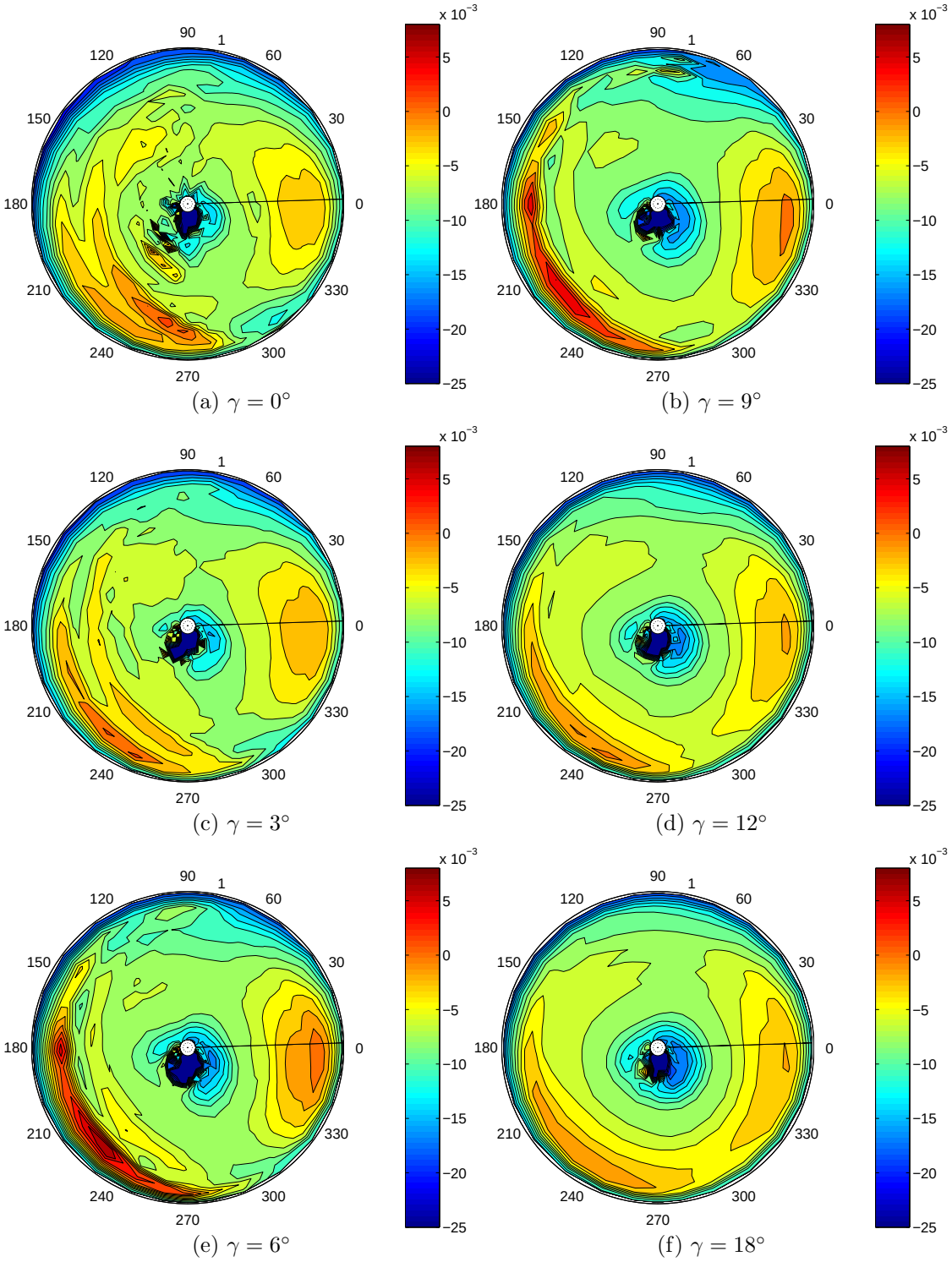

(a) $\gamma = 0°$ (b) $\gamma = 9°$

(c) $\gamma = 3°$ (d) $\gamma = 12°$

(e) $\gamma = 6°$ (f) $\gamma = 18°$

Figure 6.93: Moment coefficient distribution for different climb angles γ; $V = 60$ kts.

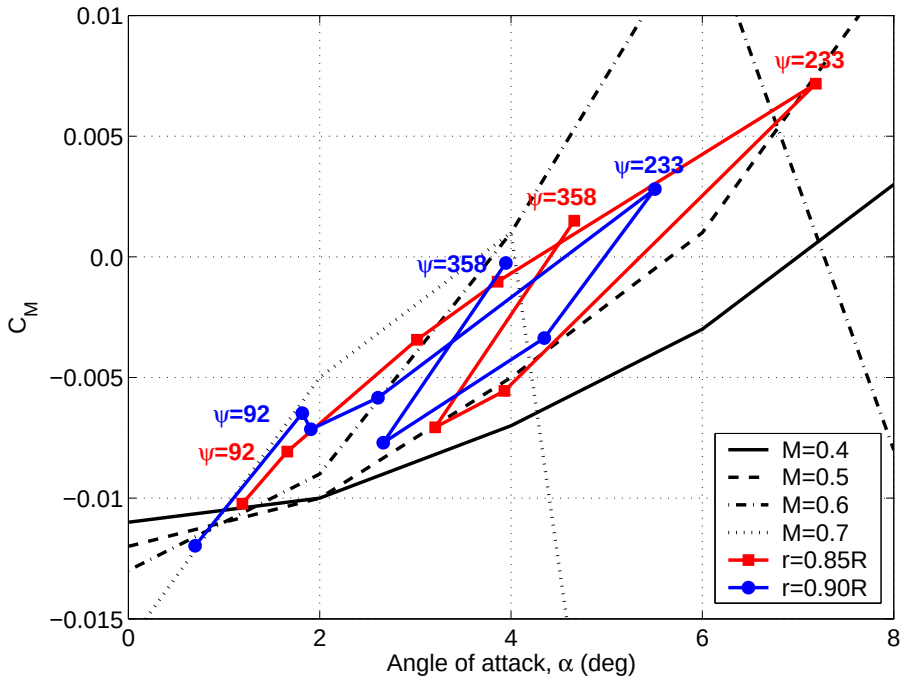

(a) $\gamma = 6°$

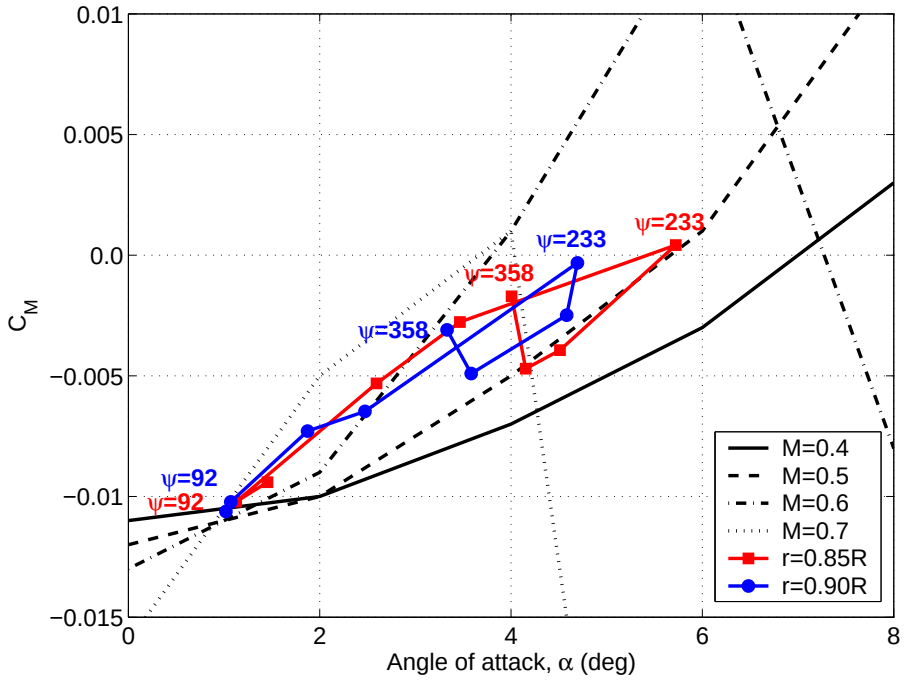

(b) $\gamma = 12°$

Figure 6.94: Moment coefficient at two radial locations, $r = 0.85R$ and $r = 0.90R$, for $\gamma = 6°$ and $\gamma = 12°$; $V = 60$ kts.

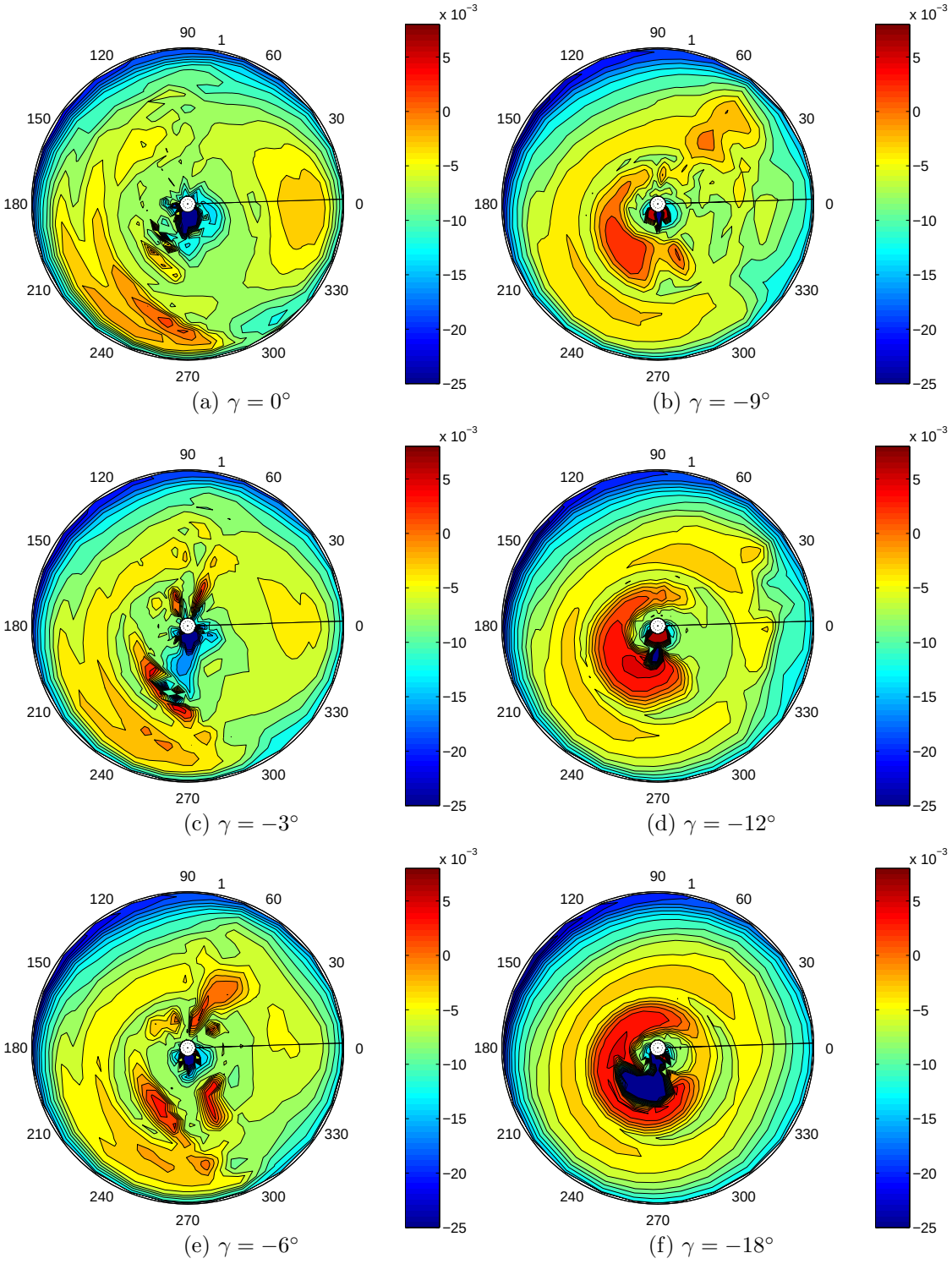

(a) $\gamma = 0°$ (b) $\gamma = -9°$

(c) $\gamma = -3°$ (d) $\gamma = -12°$

(e) $\gamma = -6°$ (f) $\gamma = -18°$

Figure 6.95: Moment coefficient distribution for different descent angles γ; $V = 60$ kts.

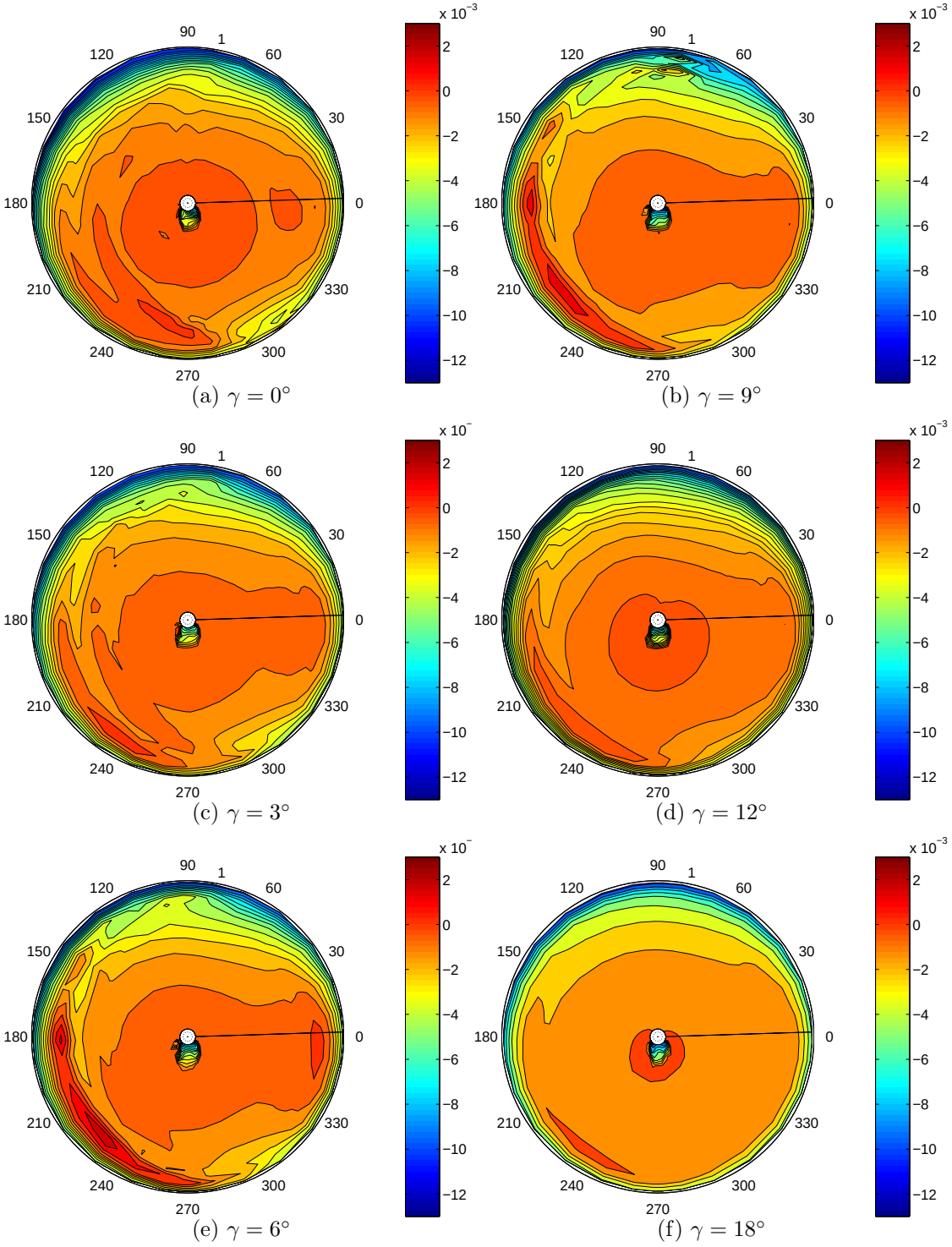

(a) $\gamma = 0°$ (b) $\gamma = 9°$

(c) $\gamma = 3°$ (d) $\gamma = 12°$

(e) $\gamma = 6°$ (f) $\gamma = 18°$

Figure 6.96: Elemental moment distribution for different climb angles γ; $V = 60$ kts.

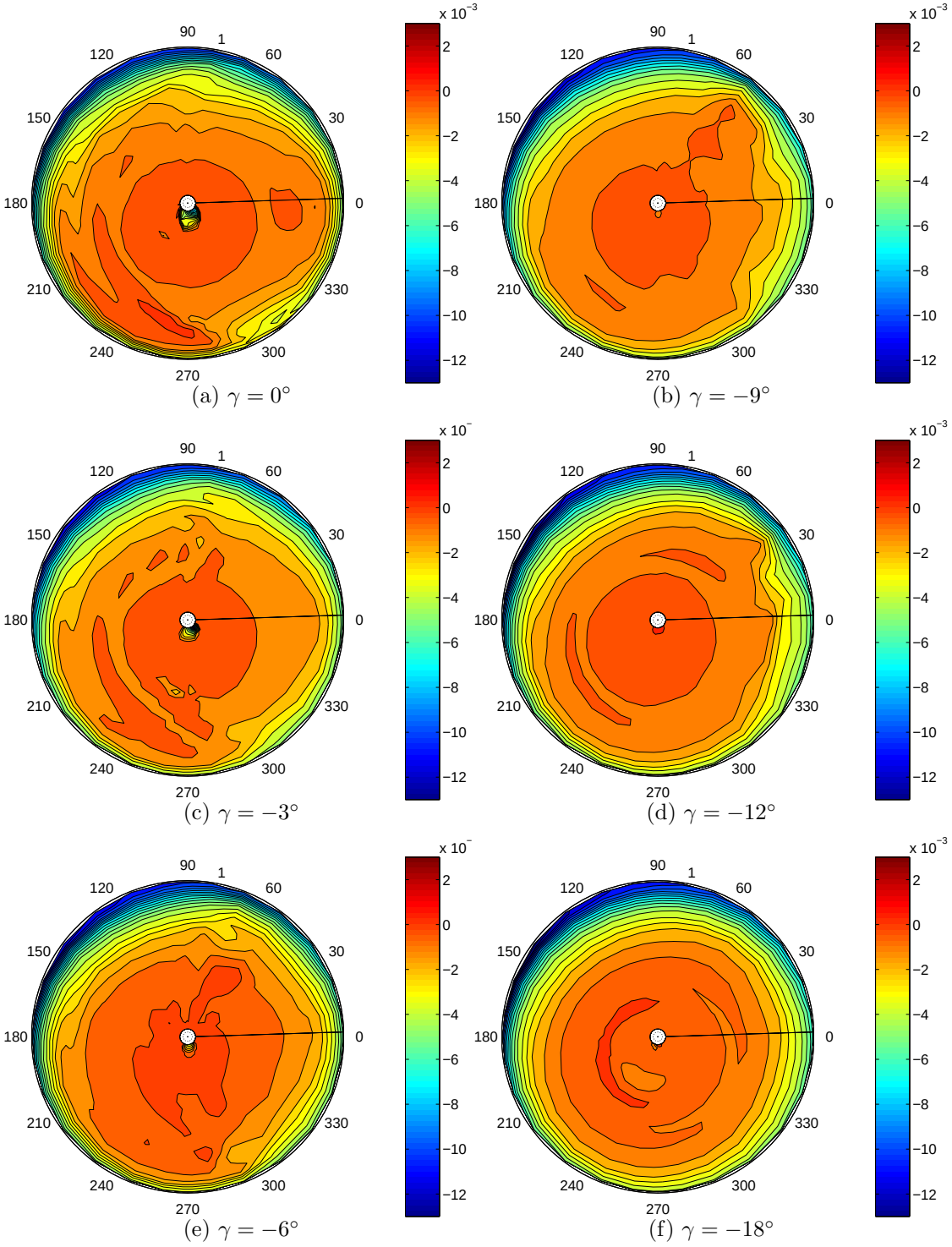

(a) $\gamma = 0°$ (b) $\gamma = -9°$

(c) $\gamma = -3°$ (d) $\gamma = -12°$

(e) $\gamma = -6°$ (f) $\gamma = -18°$

Figure 6.97: Elemental moment distribution for different descent angles γ; $V = 60$ kts.

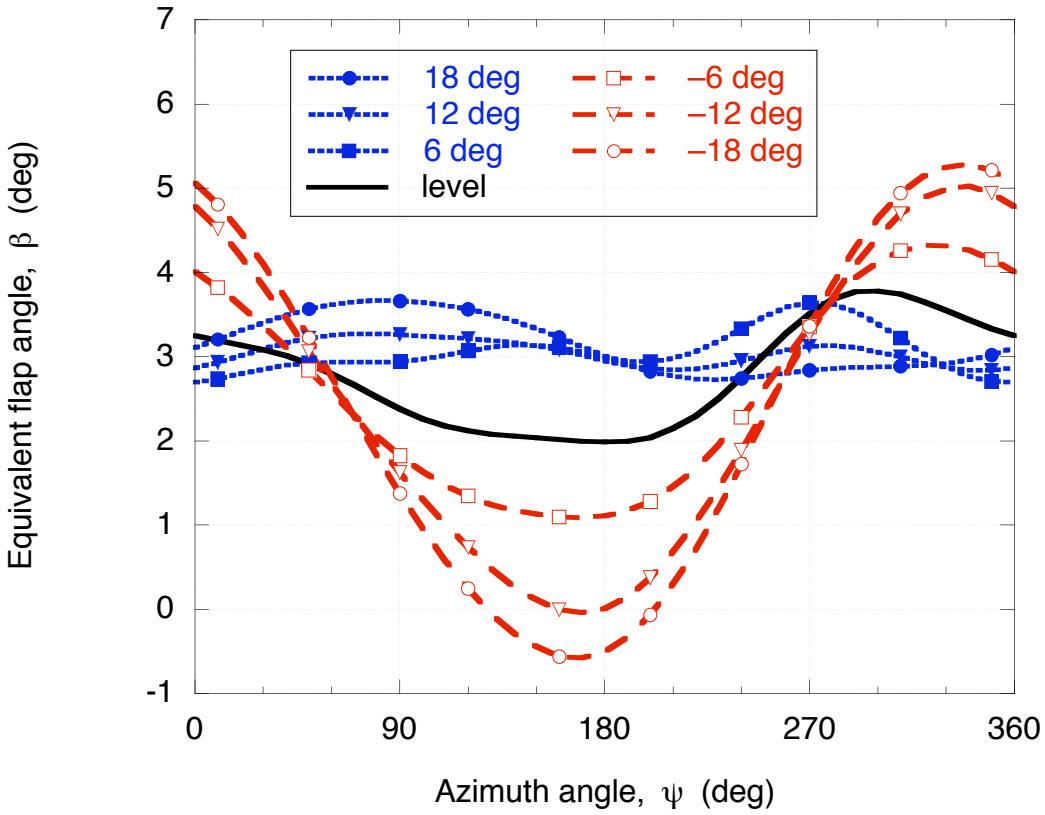

Figure 6.98: Blade tip equivalent flapping angle versus azimuth angle in climbs and descents; $V = 60$ kts.

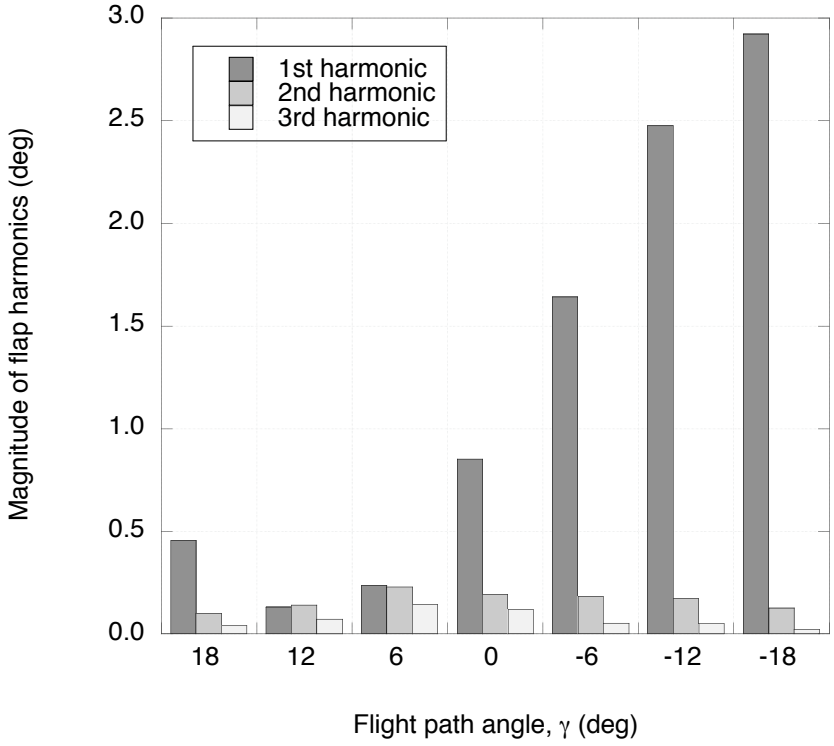

(a) Magnitude.

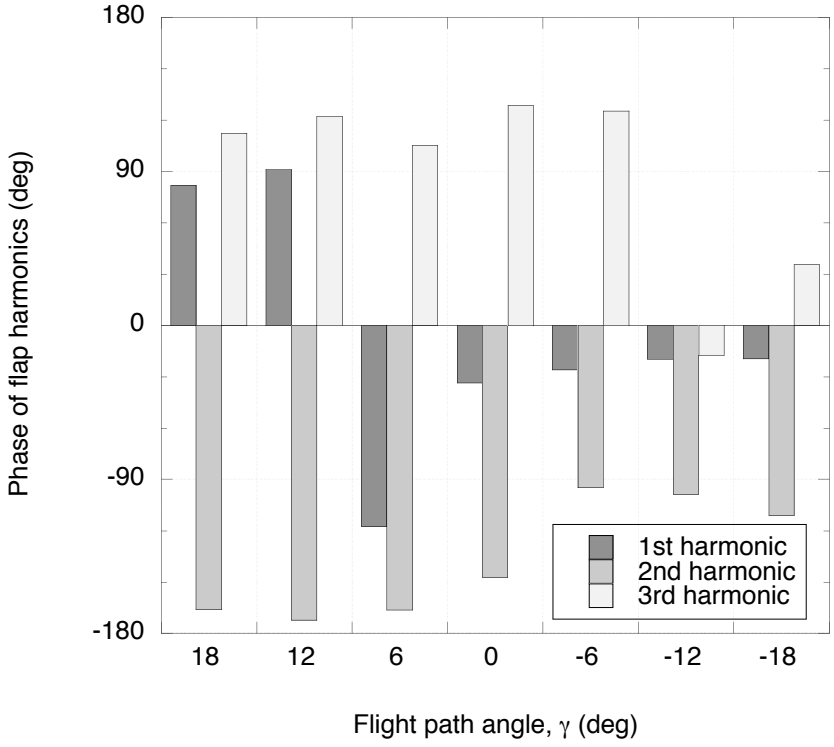

(b) Phase.

Figure 6.99: Magnitude (top) and phase (bottom) of the first three flap harmonics in climbs and descents; $V = 60$ kts.

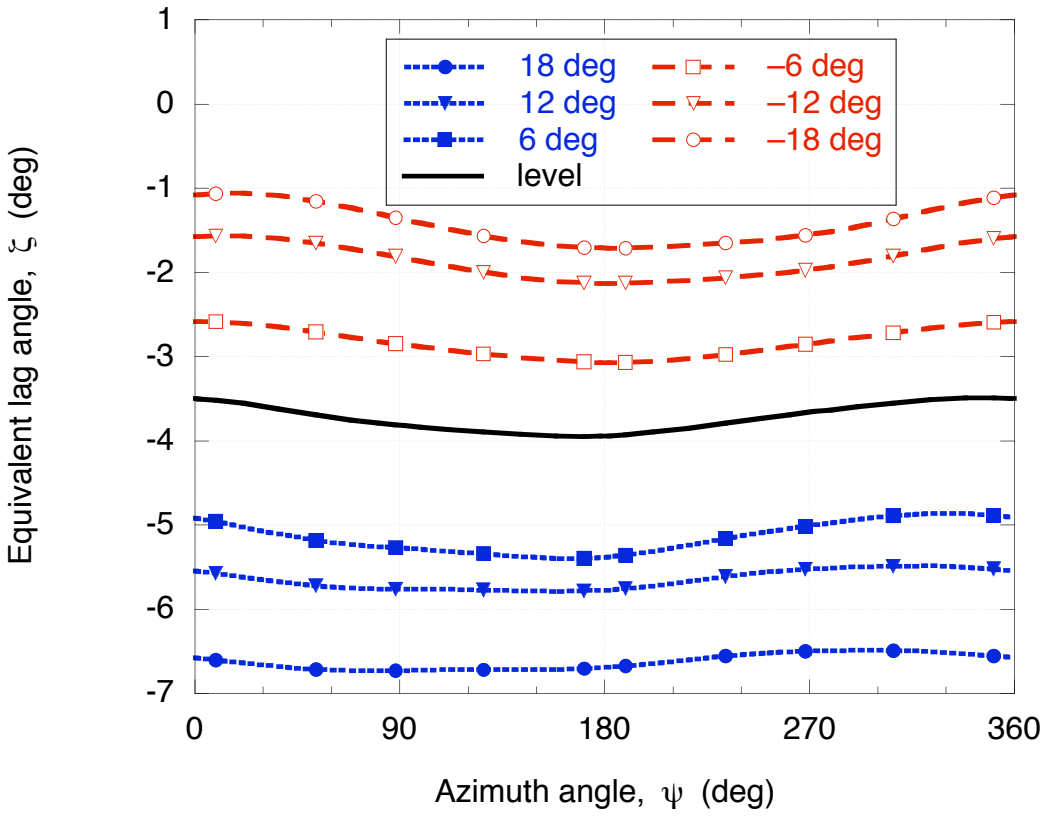

Figure 6.100: Blade tip equivalent lag angle versus azimuth angle in climbs and descents; $V = 60$ kts.

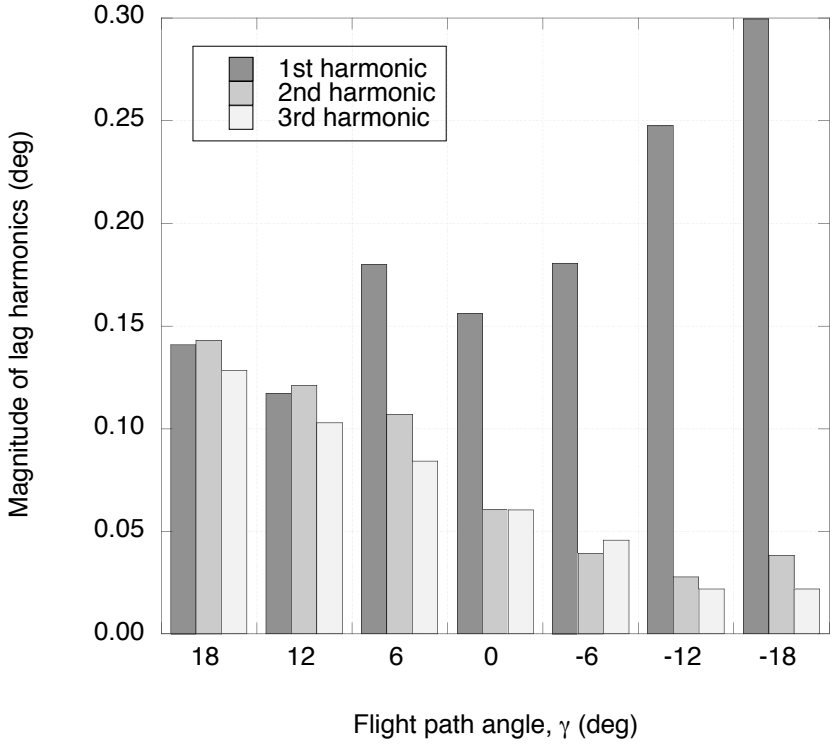

(a) Magnitude.

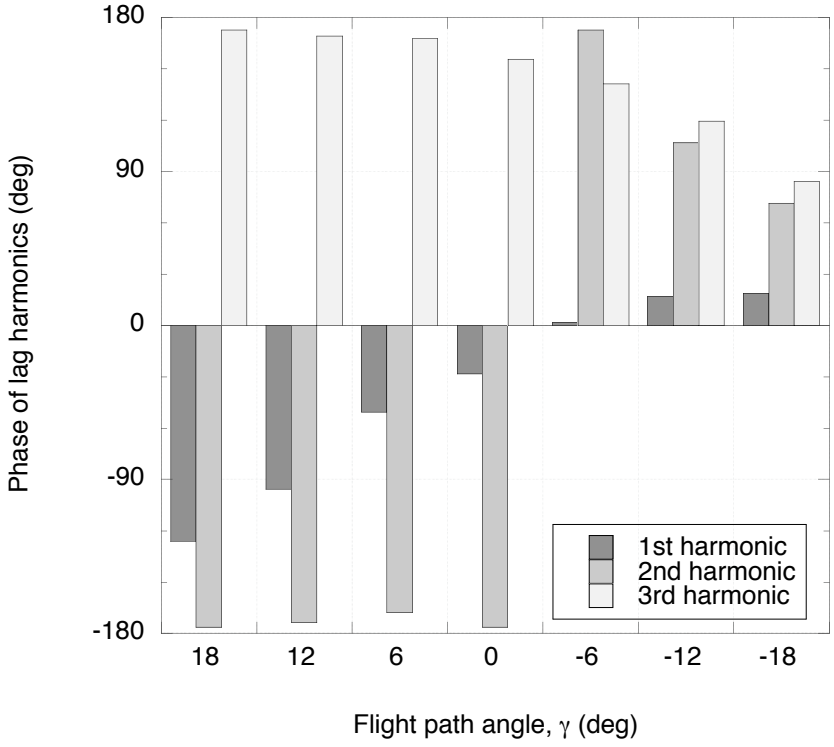

(b) Phase.

Figure 6.101: Magnitude (top) and phase (bottom) of the first three lag harmonics in climbs and descents; $V = 60$ kts.

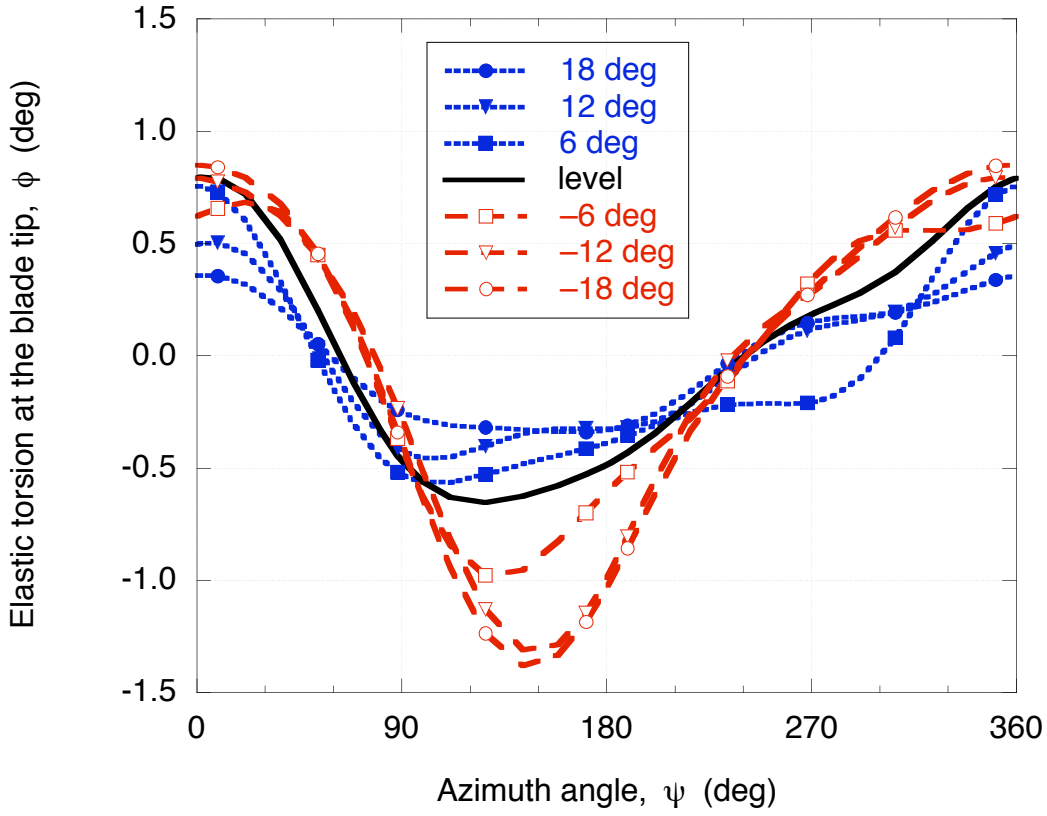

Figure 6.102: Blade tip elastic torsion versus azimuth angle in climbs and descents; $V = 60$ kts.

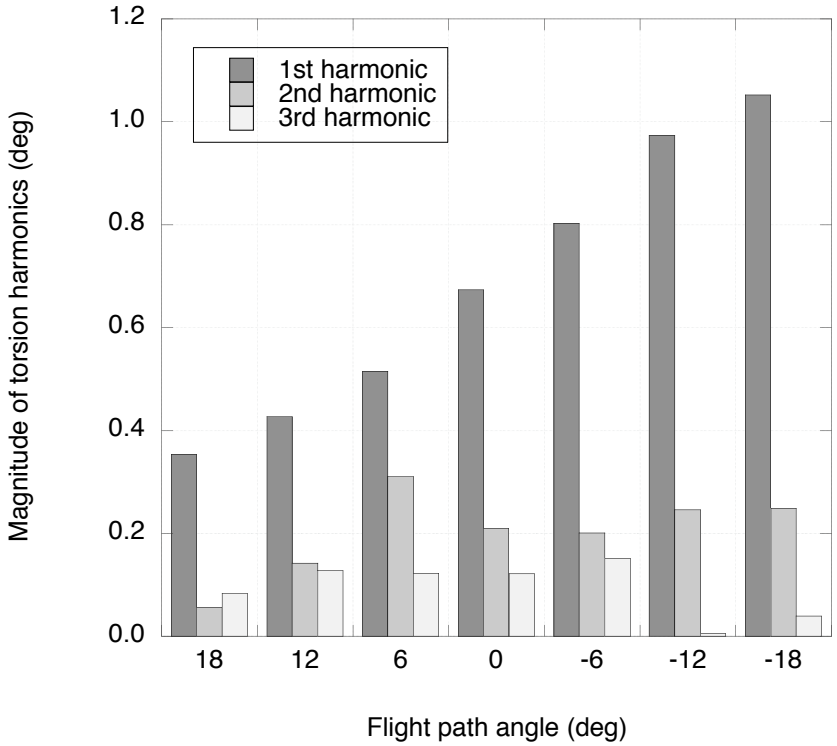

(a) Magnitude.

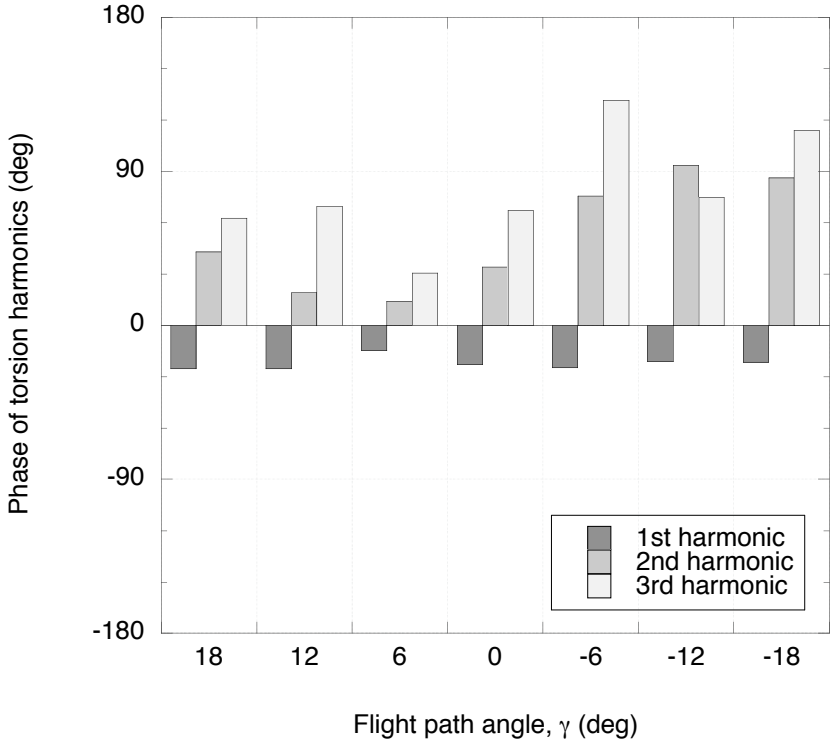

(b) Phase.

Figure 6.103: Magnitude and phase of the first three torsion harmonics in climbs and descents; $V = 60$ kts.

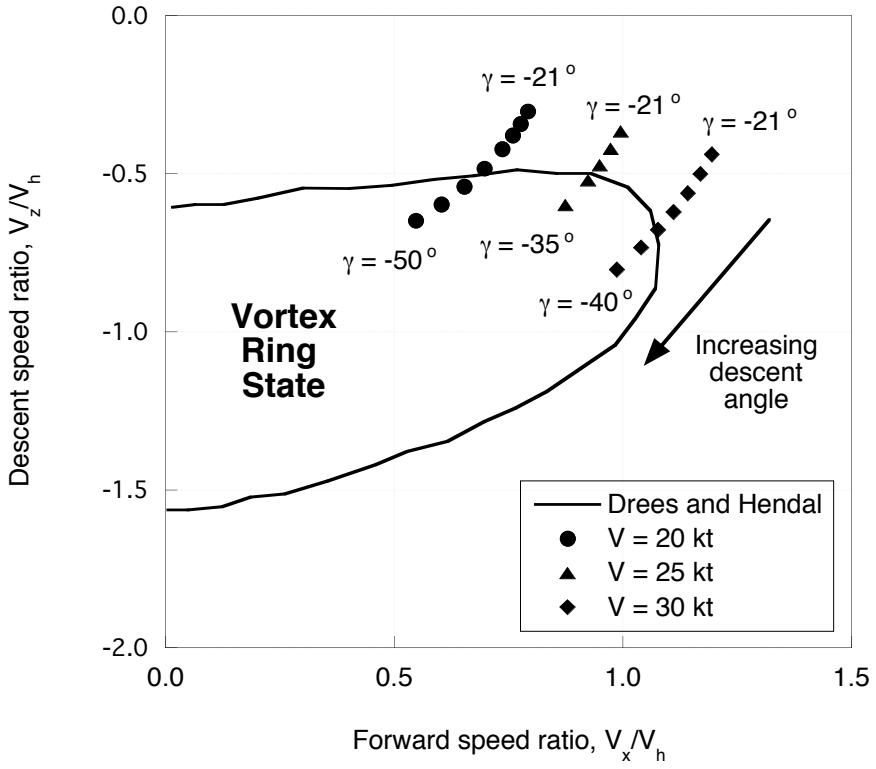

Figure 6.104: Vortex ring state boundary from the experiments of Drees and Hendal (Ref. 1); the markers indicate the flight conditions analyzed in this study.

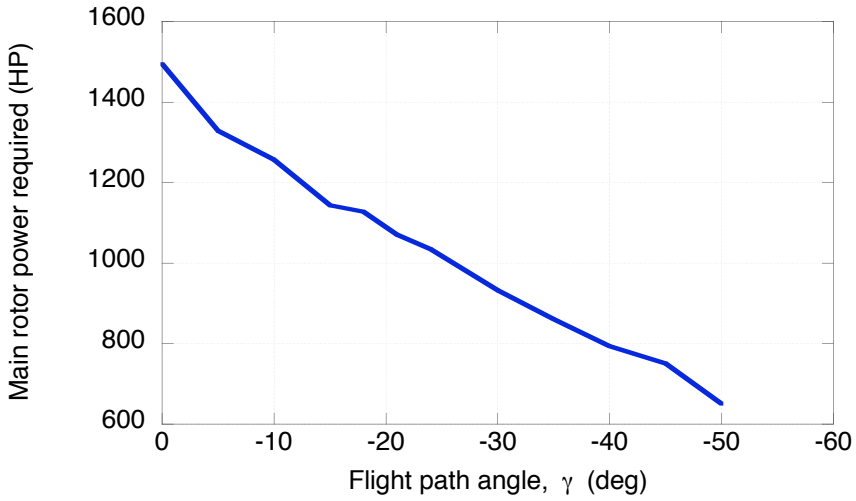

(a) Power

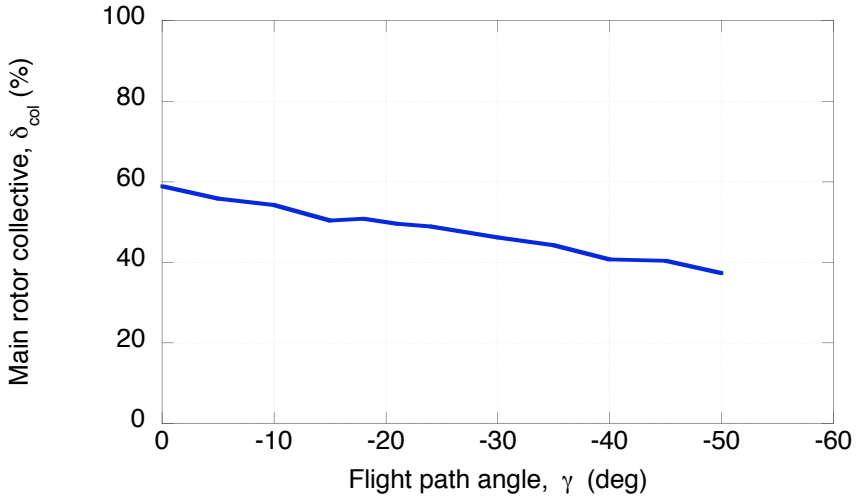

(b) Collective.

Figure 6.105: Main rotor power required and collective for different descent angles γ; $V = 20$ kts.

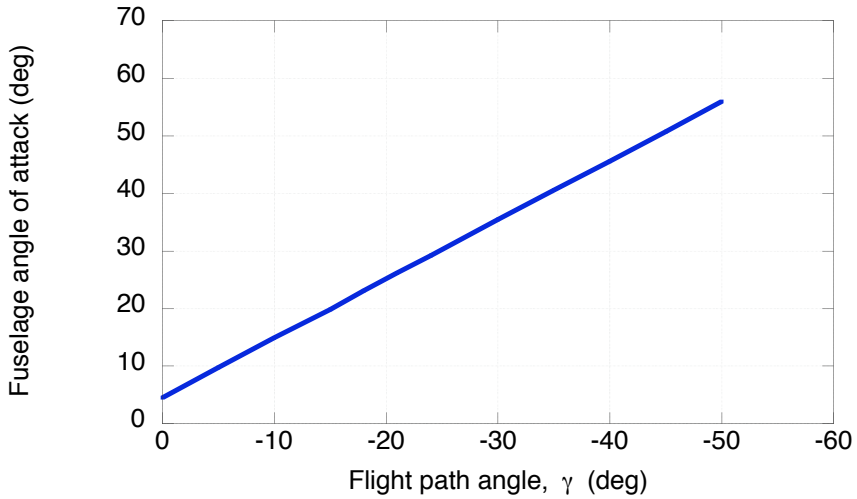

(a) Fuselage angle of attack.

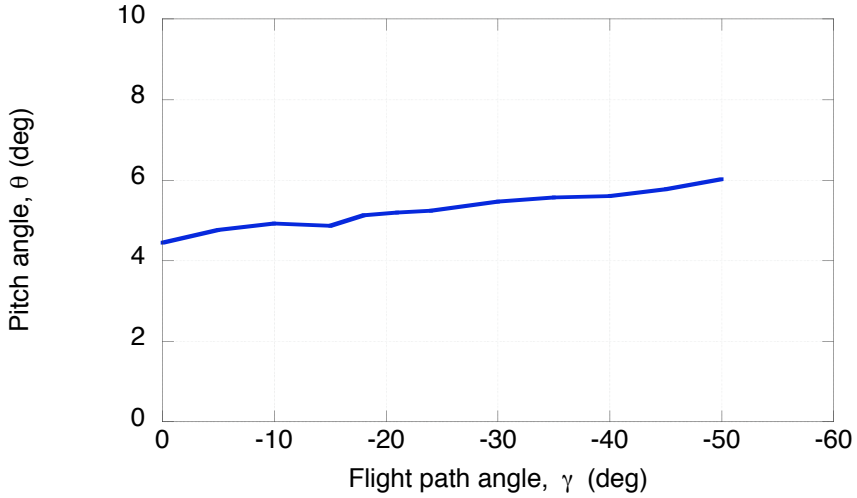

(b) Fuselage pitch angle.

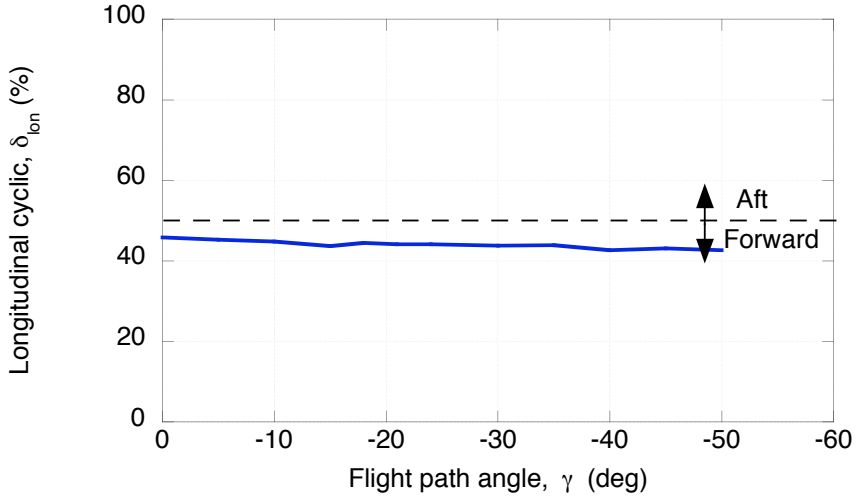

(c) Longitudinal cyclic.

Figure 6.106: Fuselage angle of attack and pitch angle, and main rotor longitudinal cyclic for different descent angles γ; $V = 20$ kts.

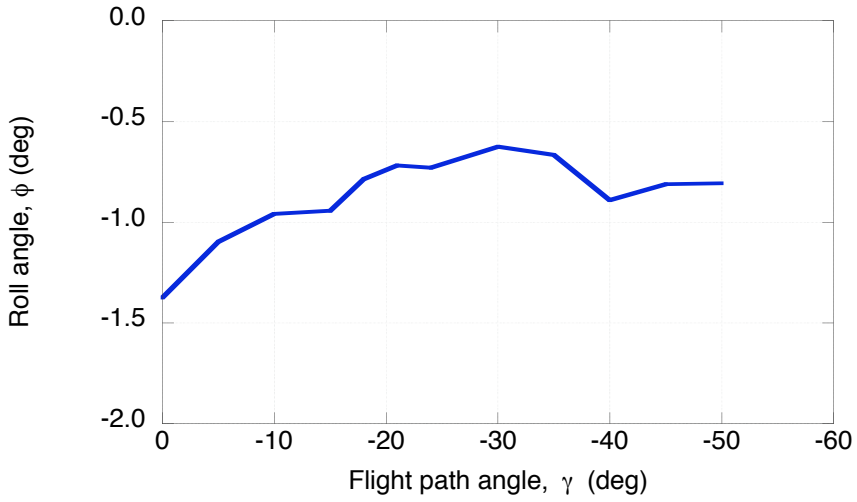

(a) Fuselage roll angle.

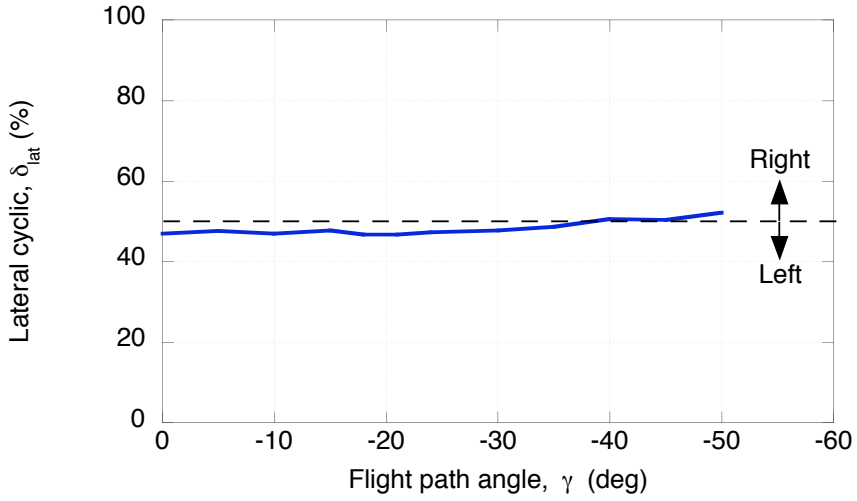

(b) Lateral cyclic.

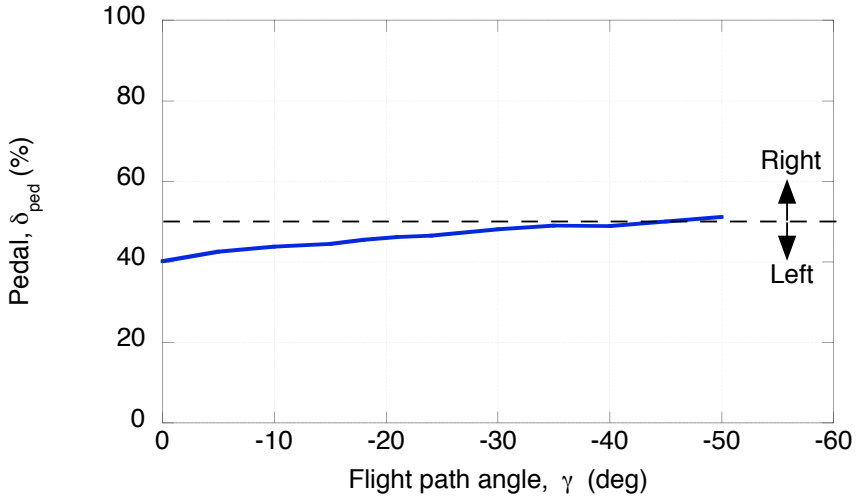

(c) Pedal.

Figure 6.107: Fuselage roll angle, main rotor lateral cyclic and pedal setting for different descent angles γ; $V = 20$ kts.

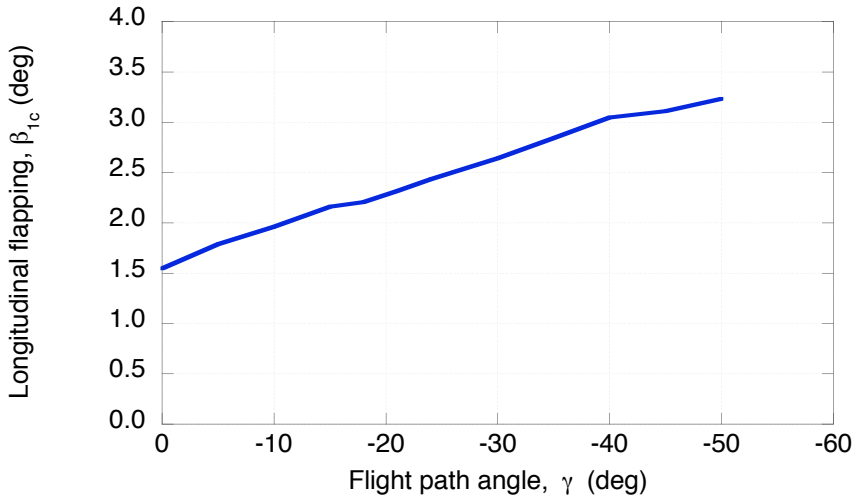

(a) Longitudinal flapping.

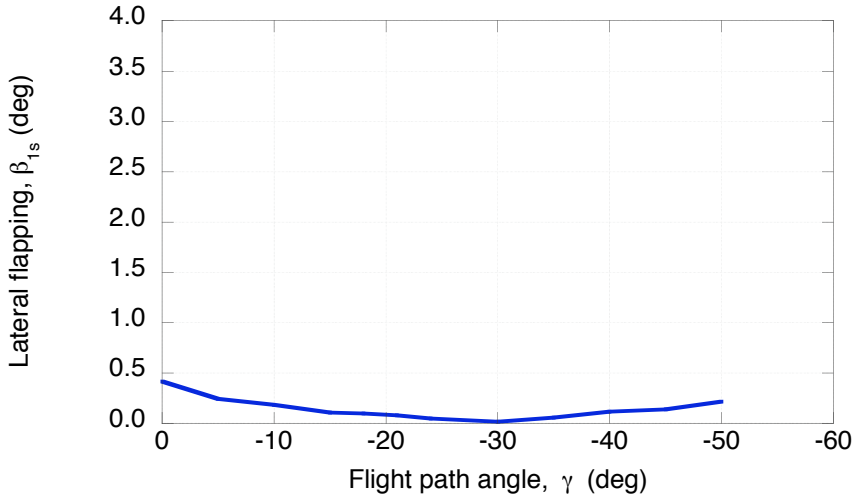

(b) Lateral flapping.

Figure 6.108: Main rotor longitudinal and lateral flapping coefficients for different descent angles γ; $V = 20$ kts.

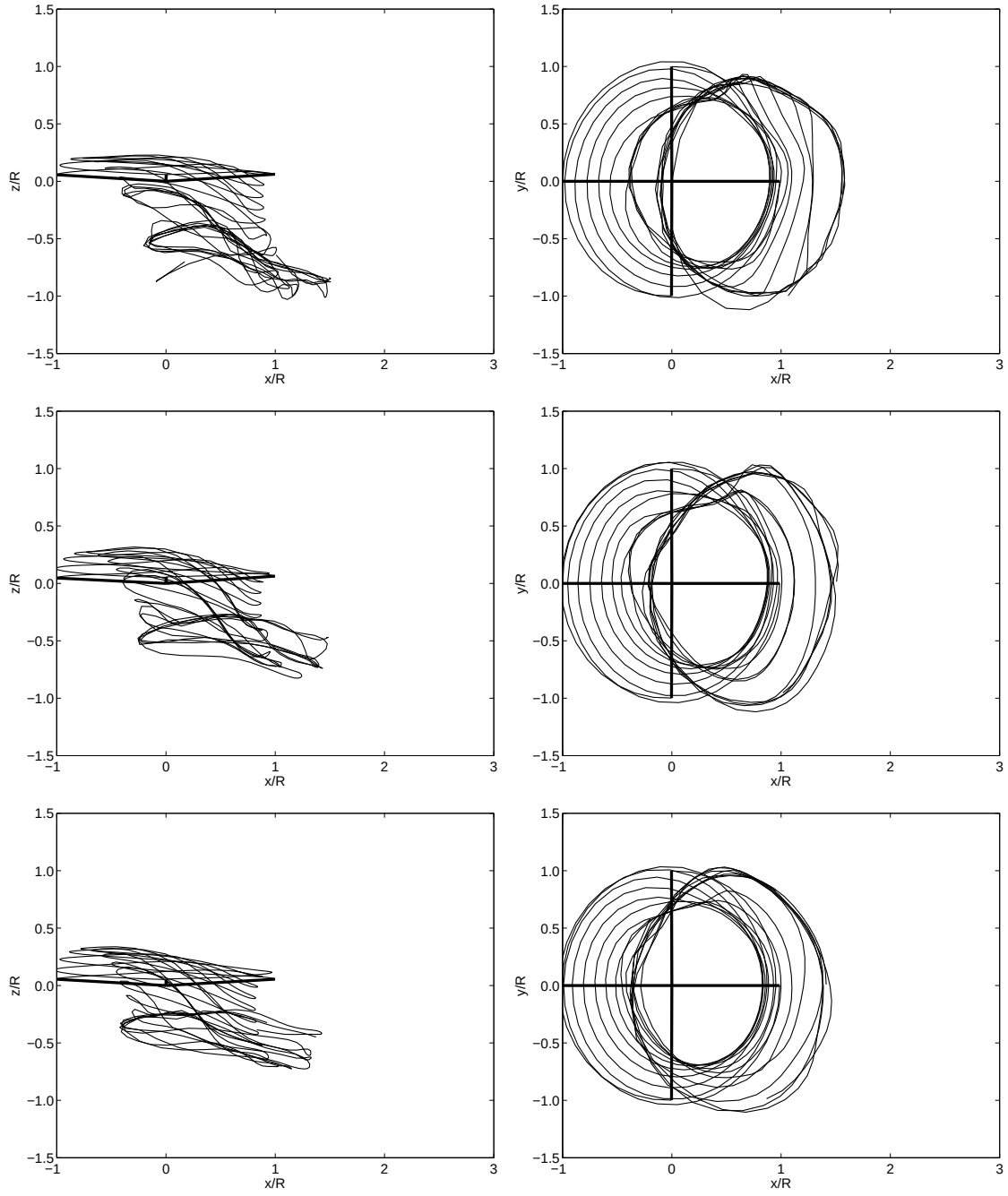

Figure 6.109: Side and top views of the wake geometry for $\gamma = -30°$ (top), $\gamma = -40°$ (middle) and $\gamma = -50°$ (bottom) at $V = 20$ kts.

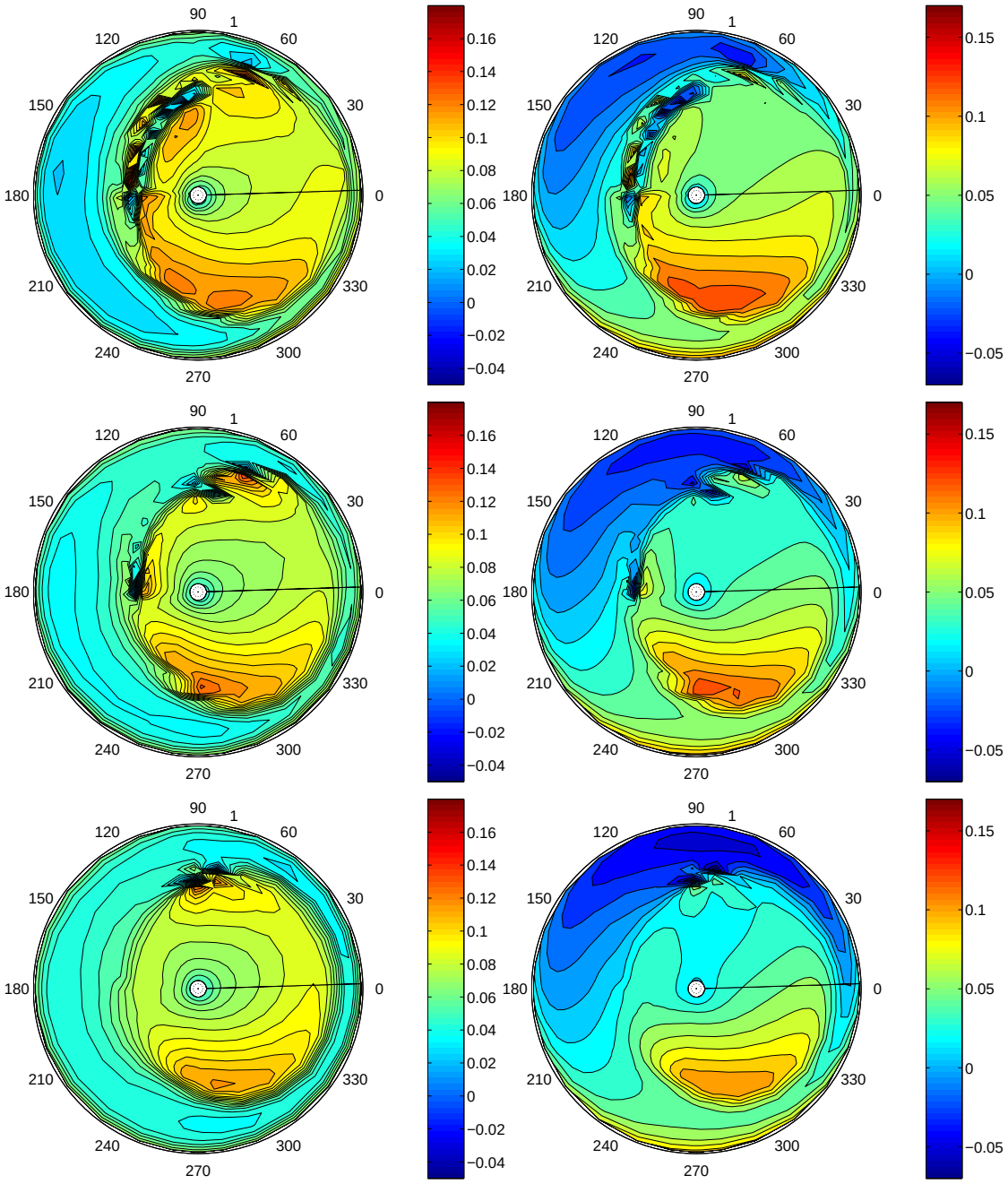

Figure 6.110: Inflow and perpendicular velocity distribution for $\gamma = -30°$ (top), $\gamma = -40°$ (middle) and $\gamma = -50°$ (bottom) at $V = 20$ kts.

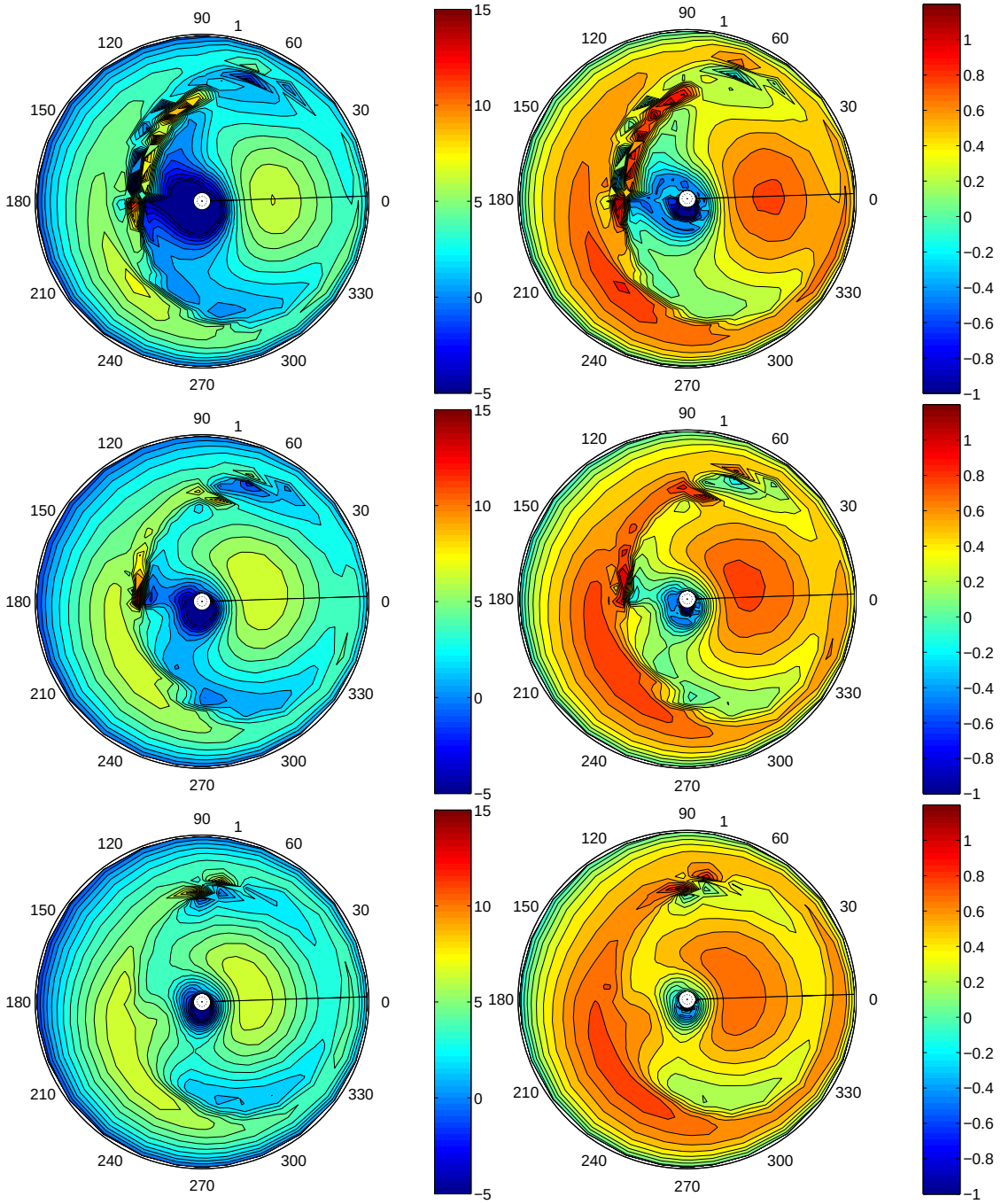

Angle of attack C_L

Figure 6.111: Angle of attack and lift coefficient distribution for $\gamma = -30°$ (top), $\gamma = -40°$ (middle) and $\gamma = -50°$ (bottom) at $V = 20$ kts.

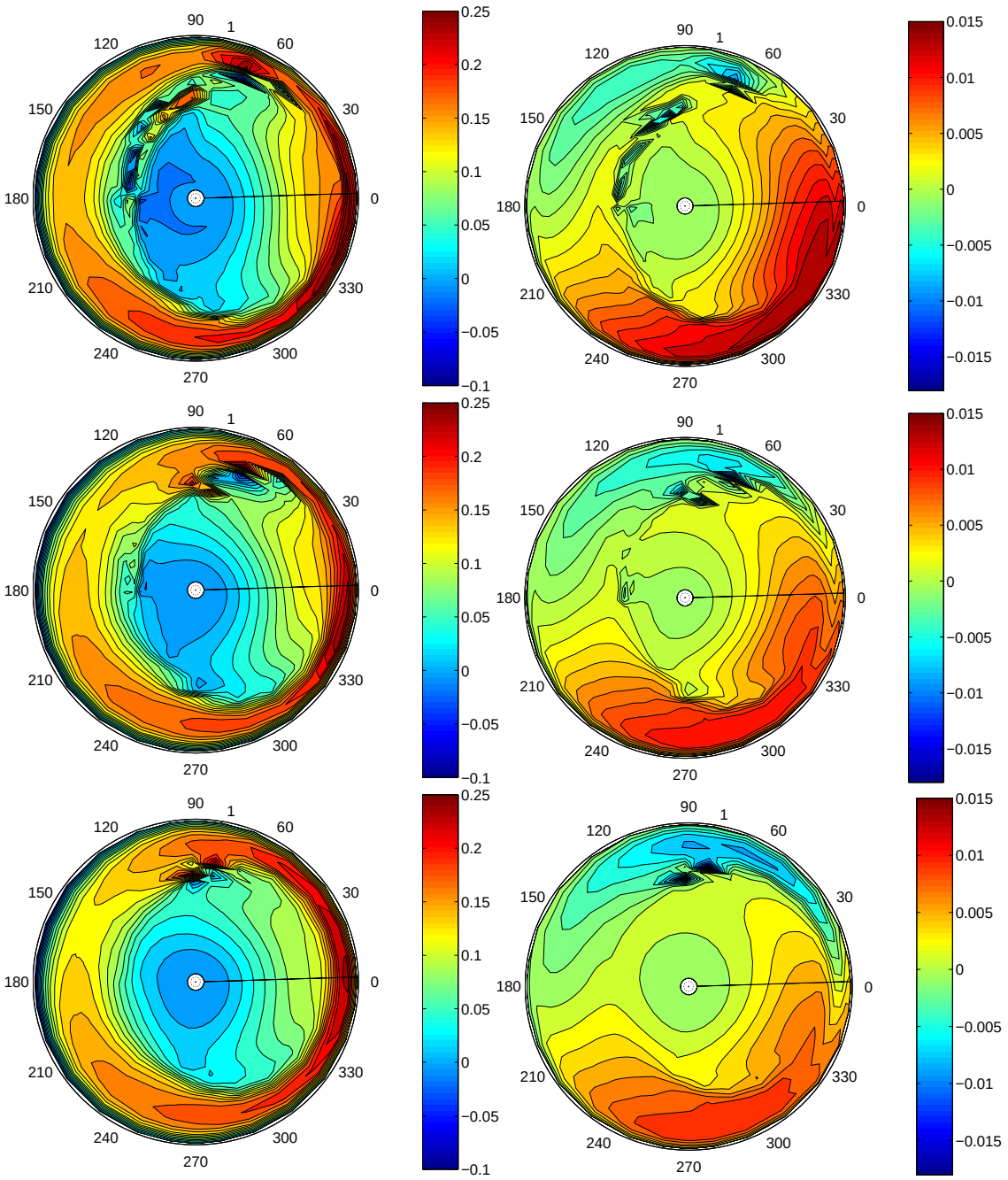

Figure 6.112: Elemental lift coefficient and elemental induced torque distribution for $\gamma = -30°$ (top), $\gamma = -40°$ (middle) and $\gamma = -50°$ (bottom) at $V = 20$ kts.

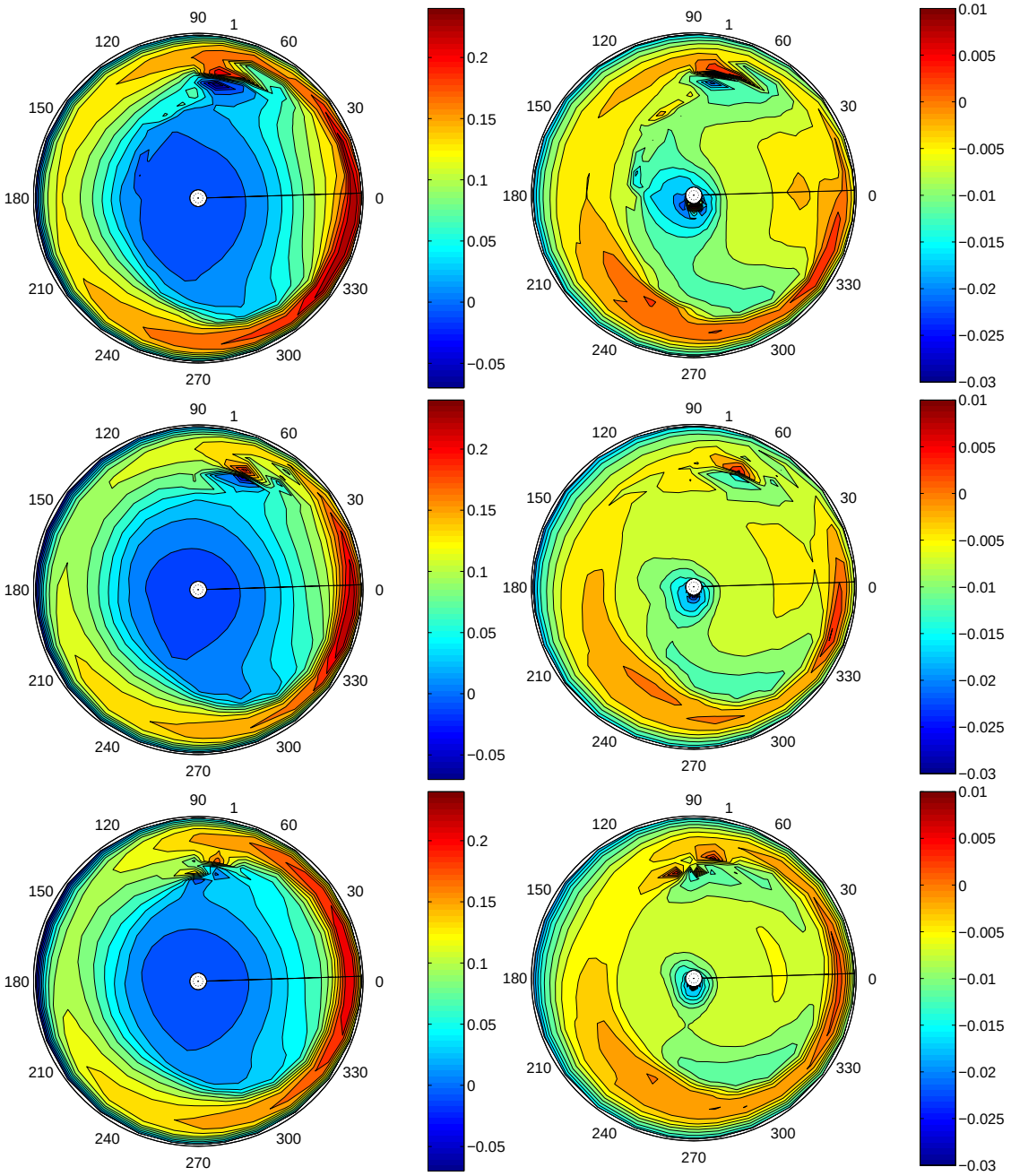

Figure 6.113: Local flap moment rC_LM^2 and moment coefficient C_M for $\gamma = -30°$ (top), $\gamma = -40°$ (middle) and $\gamma = -50°$ (bottom) at $V = 20$ kts.

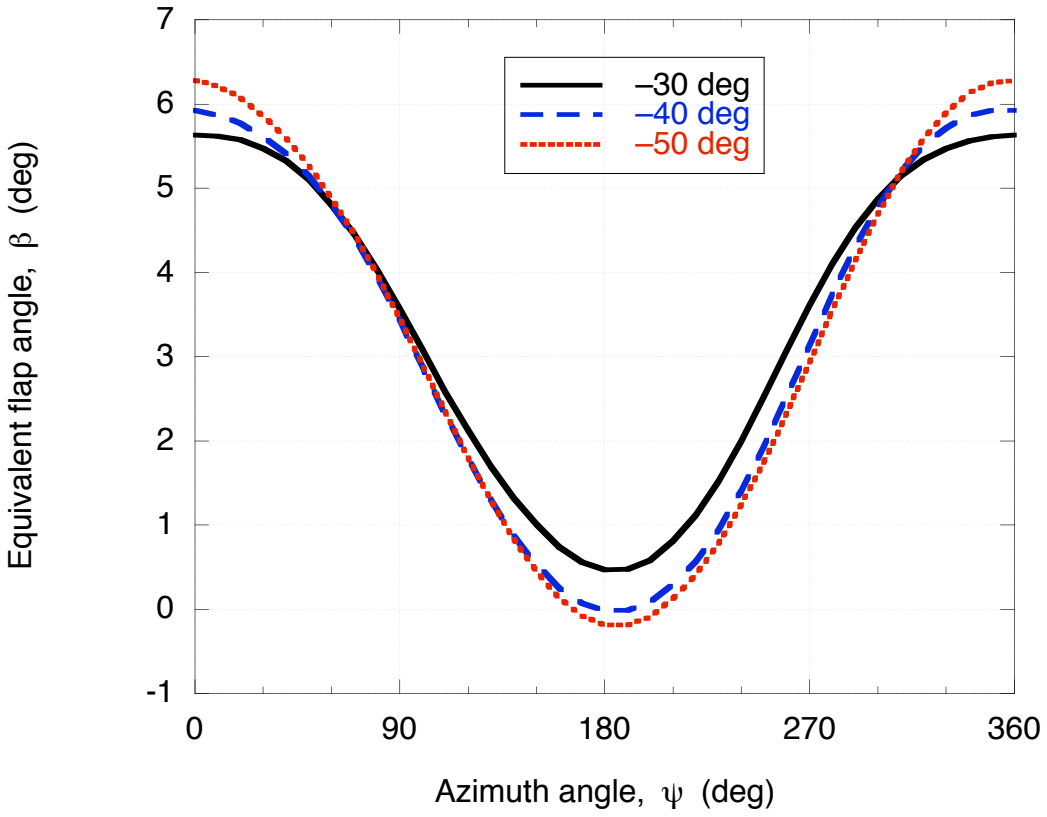

Figure 6.114: Blade tip equivalent flapping angle versus azimuth angle for $\gamma = -30°$, $\gamma = -40°$ and $\gamma = -50°$ at $V = 20$ kts.

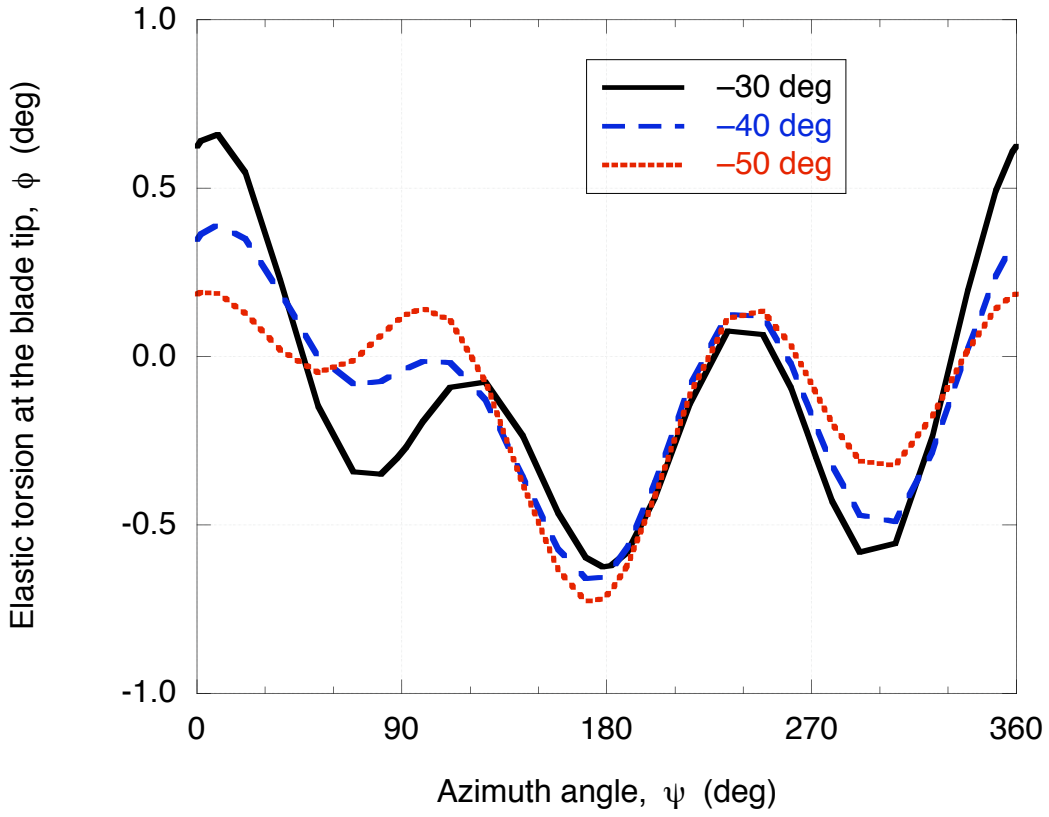

Figure 6.115: Blade elastic torsion angle versus azimuth displacement for $\gamma = -30°$, $\gamma = -40°$ and $\gamma = -50°$ at $V = 20$ kts.

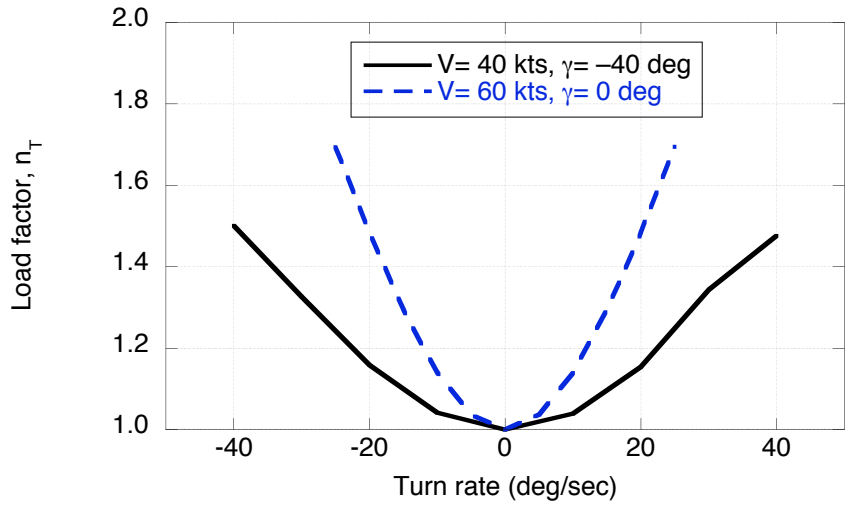

(a) Load factor, n_T

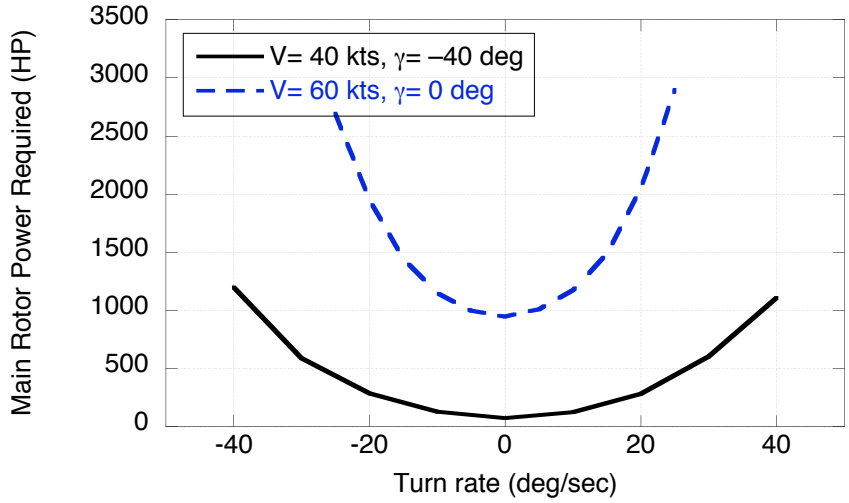

(b) Main rotor power required, Q_{MR}

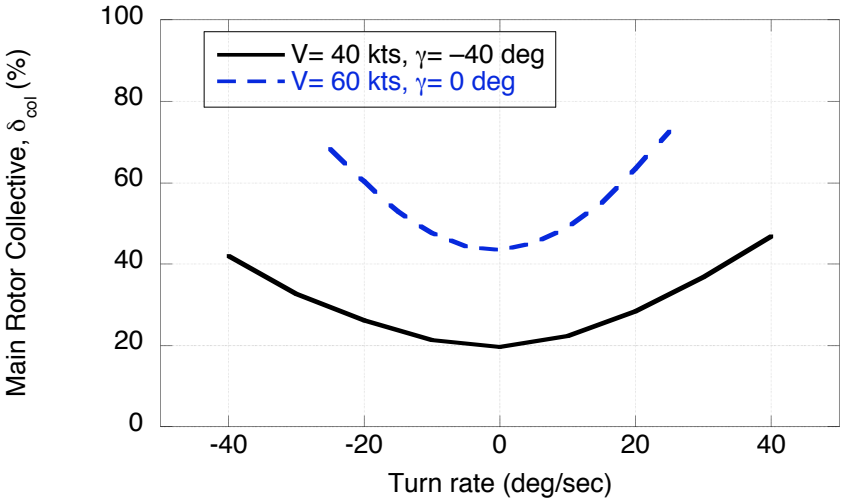

(c) Main rotor collective, δ_{col}

Figure 6.116: Load factor, n_T, main rotor power required, Q_{MR}, and collective, δ_{col}, for $\dot{\psi} = 0$ deg/sec to $\dot{\psi} = \pm 40$ deg/sec, $V = 40$ kts and $\gamma = -40°$.

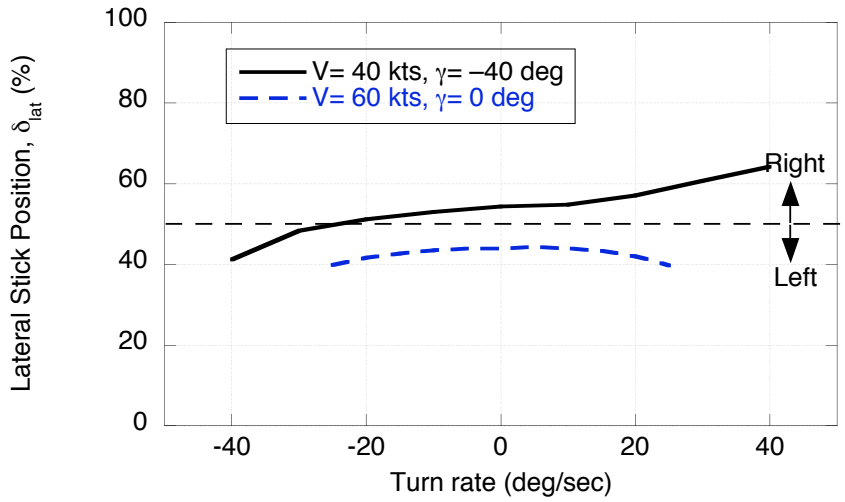

(a) Lateral stick position, δ_{lat}

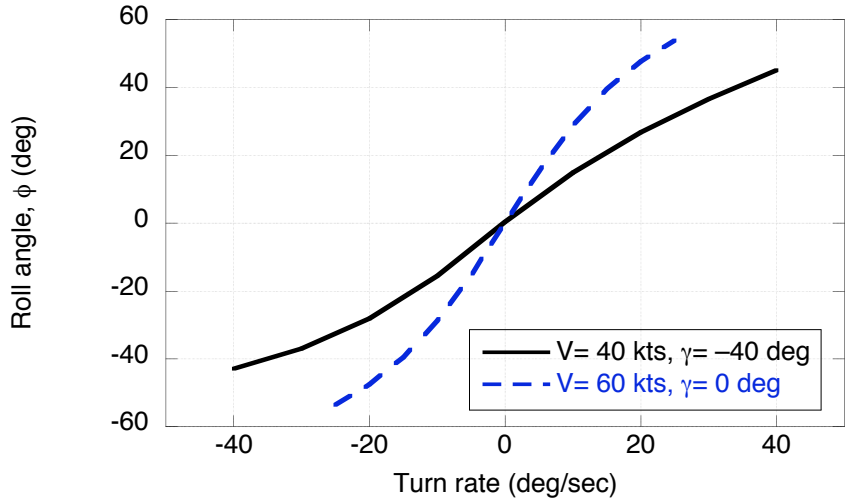

(b) Helicopter roll angle, ϕ

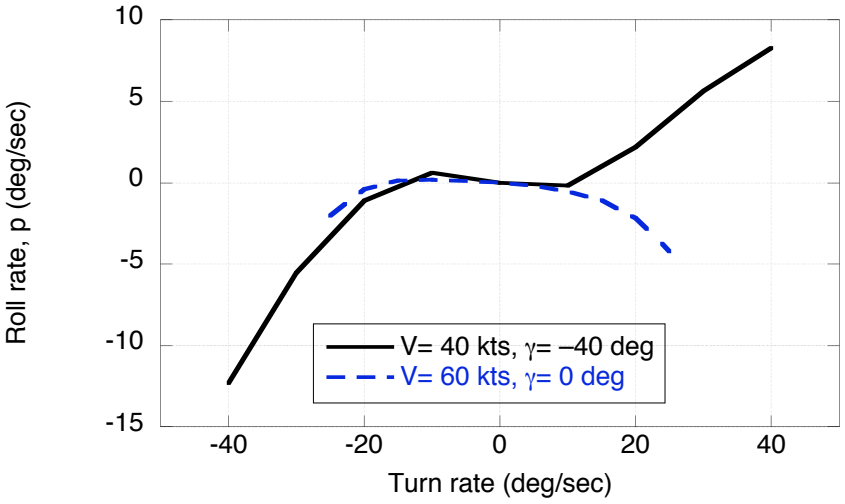

(c) Helicopter roll rate, p

Figure 6.117: Lateral stick position, δ_{lat}, helicopter roll angle, ϕ and roll rate p, for $\dot{\psi} = 0$ deg/sec to $\dot{\psi} = \pm 40$ deg/sec, $V = 40$ kts and $\gamma = -40°$.

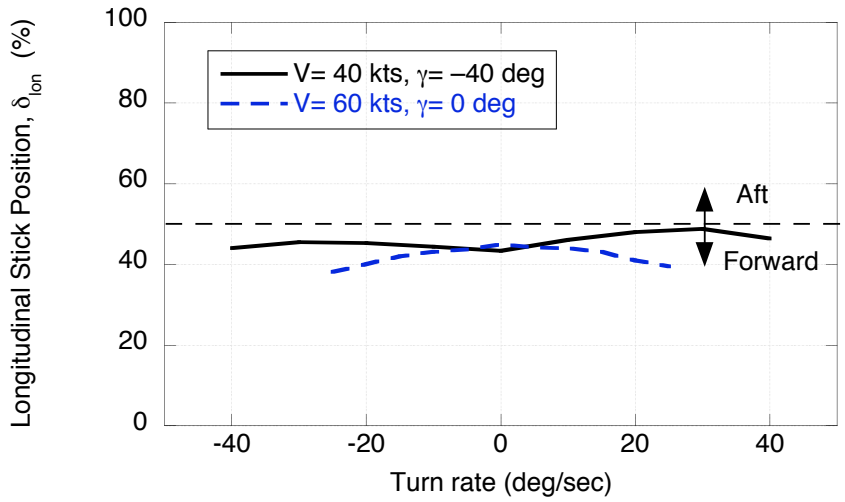

(a) Longitudinal stick position, δ_{lon}

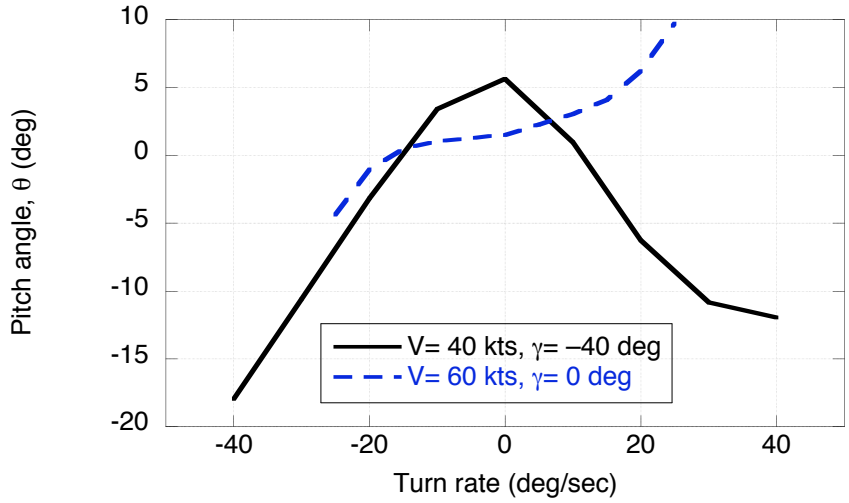

(b) Helicopter pitch angle, θ

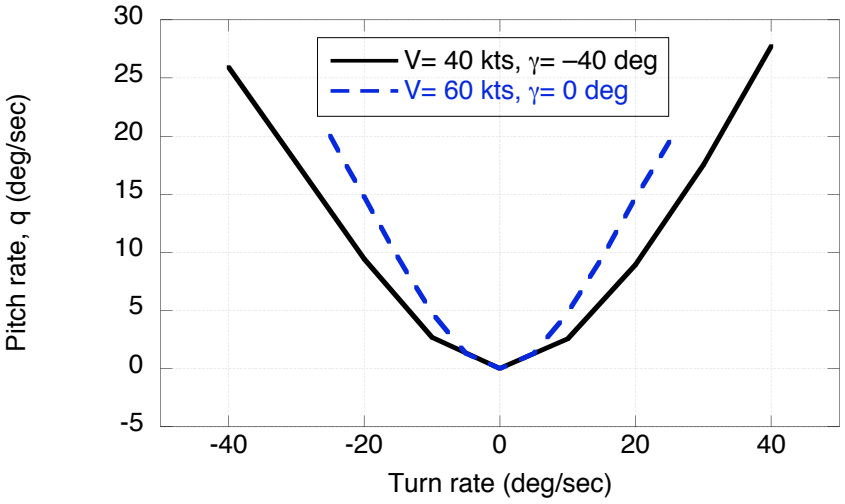

(c) Helicopter pitch rate, q

Figure 6.118: Longitudinal stick position, δ_{lon}, helicopter pitch angle, θ, and pitch rate, q, for $\dot{\psi} = 0$ deg/sec to $\dot{\psi} = \pm 40$ deg/sec, $V = 40$ kts and $\gamma = -40°$.

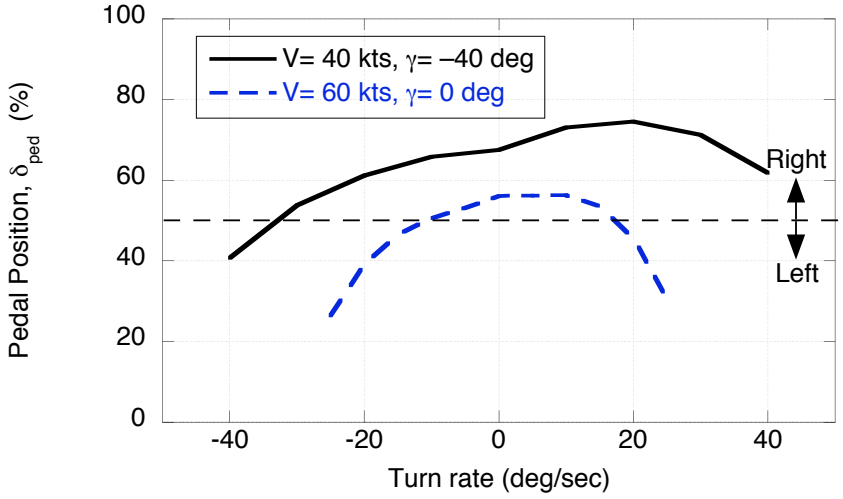

(a) Pedal position δ_{ped}

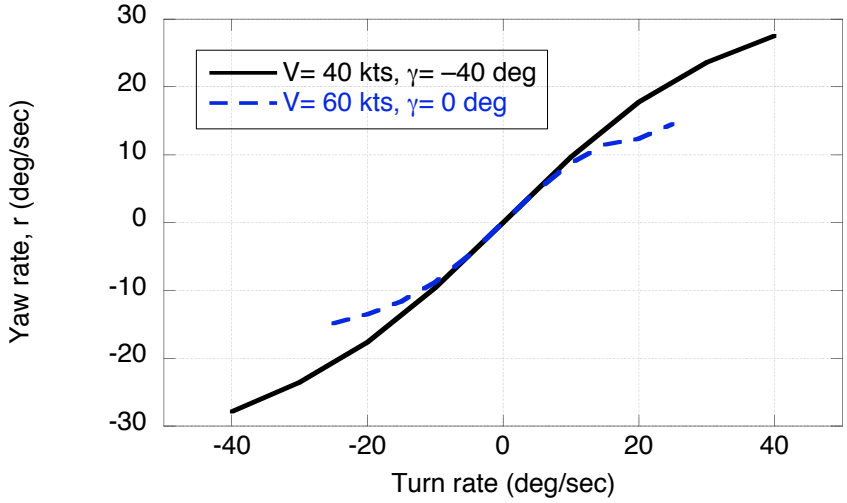

(b) Helicopter yaw rate, r

Figure 6.119: Pedal position δ_{ped}, and helicopter yaw rate, r, for $\dot{\psi} = 0$ deg/sec to $\dot{\psi} = \pm 40$ deg/sec, $V = 40$ kts and $\gamma = -40°$.

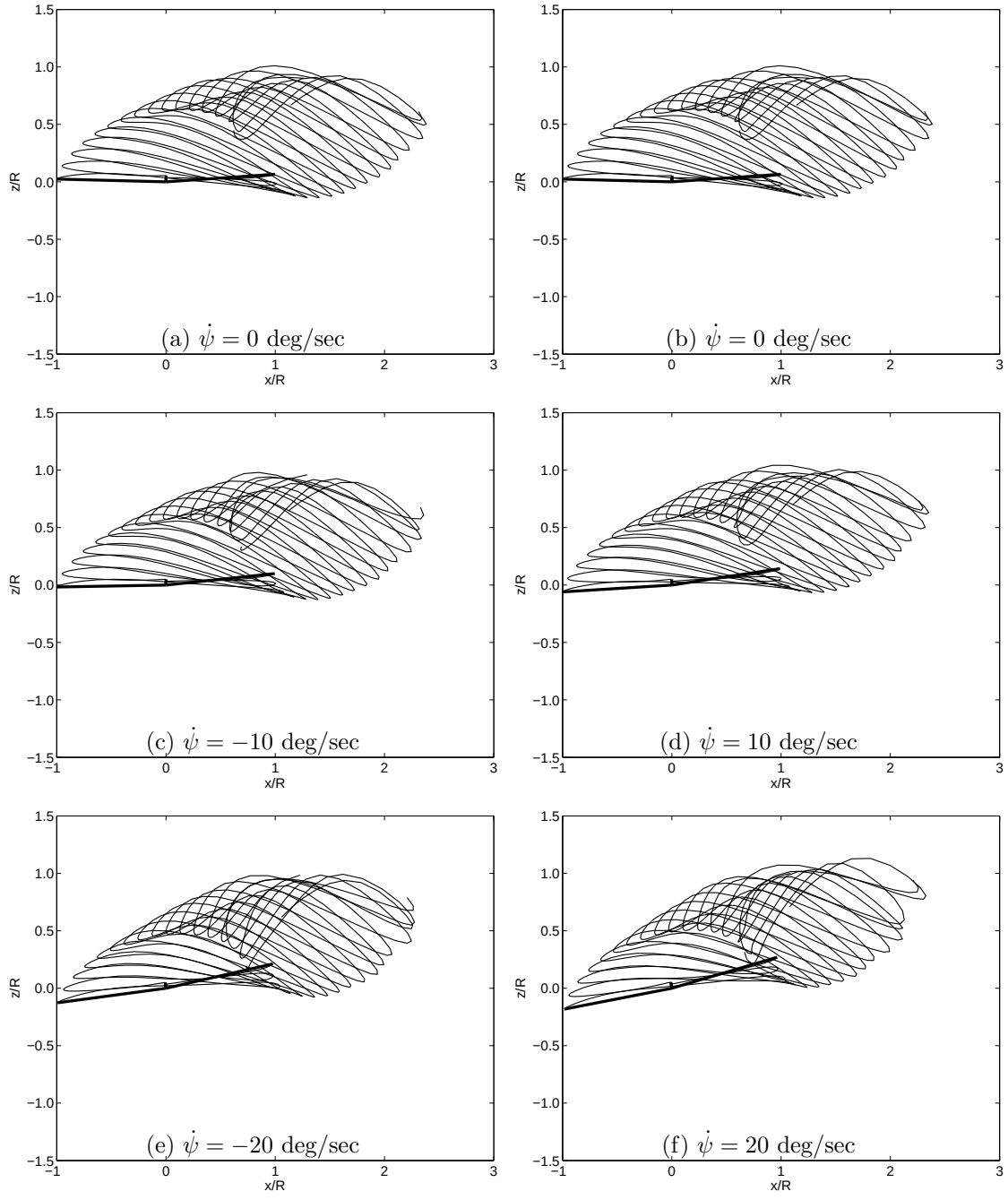

Figure 6.120: Side view of the free wake tip vortex geometry for turn rates from $\dot{\psi} = 0$ deg/sec to $\dot{\psi} = \pm 20$ deg/sec, $V = 40$ kts and $\gamma = -40°$.

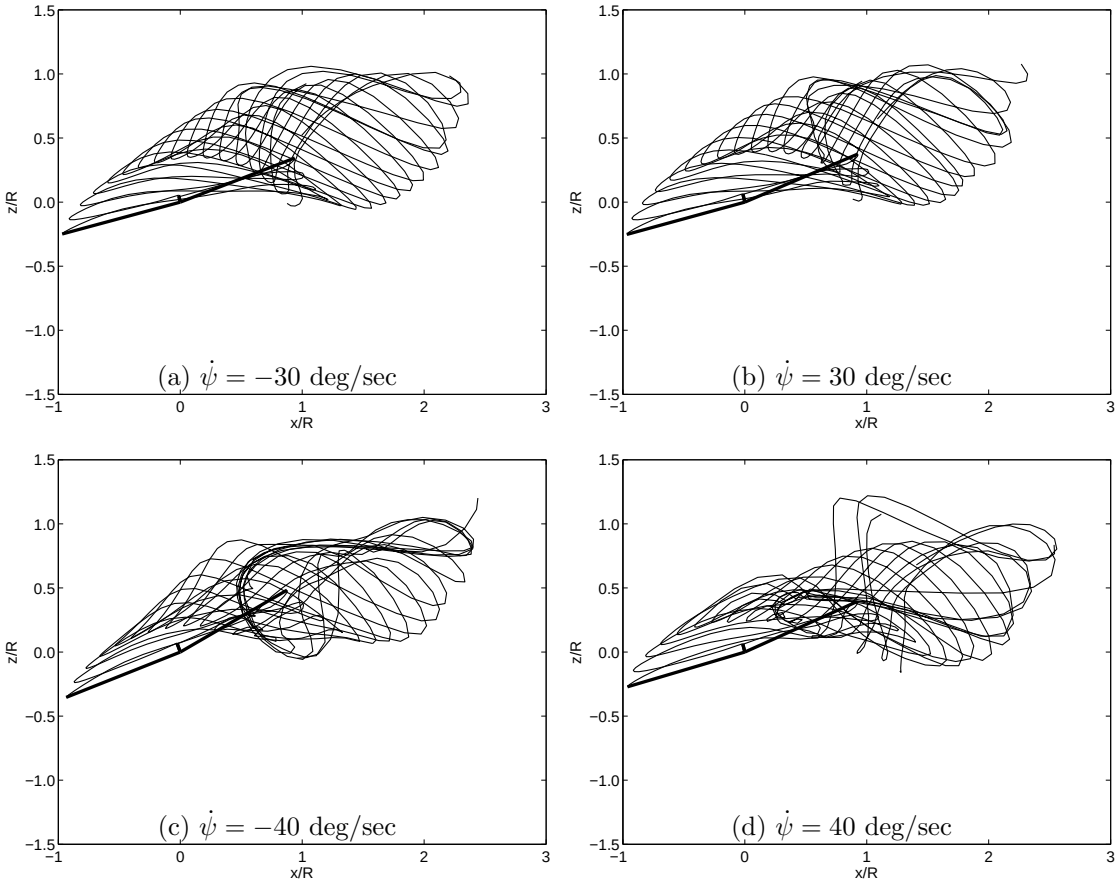

Figure 6.121: Side view of the wake geometry for turn rates from $\dot{\psi} = \pm 30$ deg/sec to $\dot{\psi} = \pm 40$ deg/sec, $V = 40$ kts and $\gamma = -40°$.

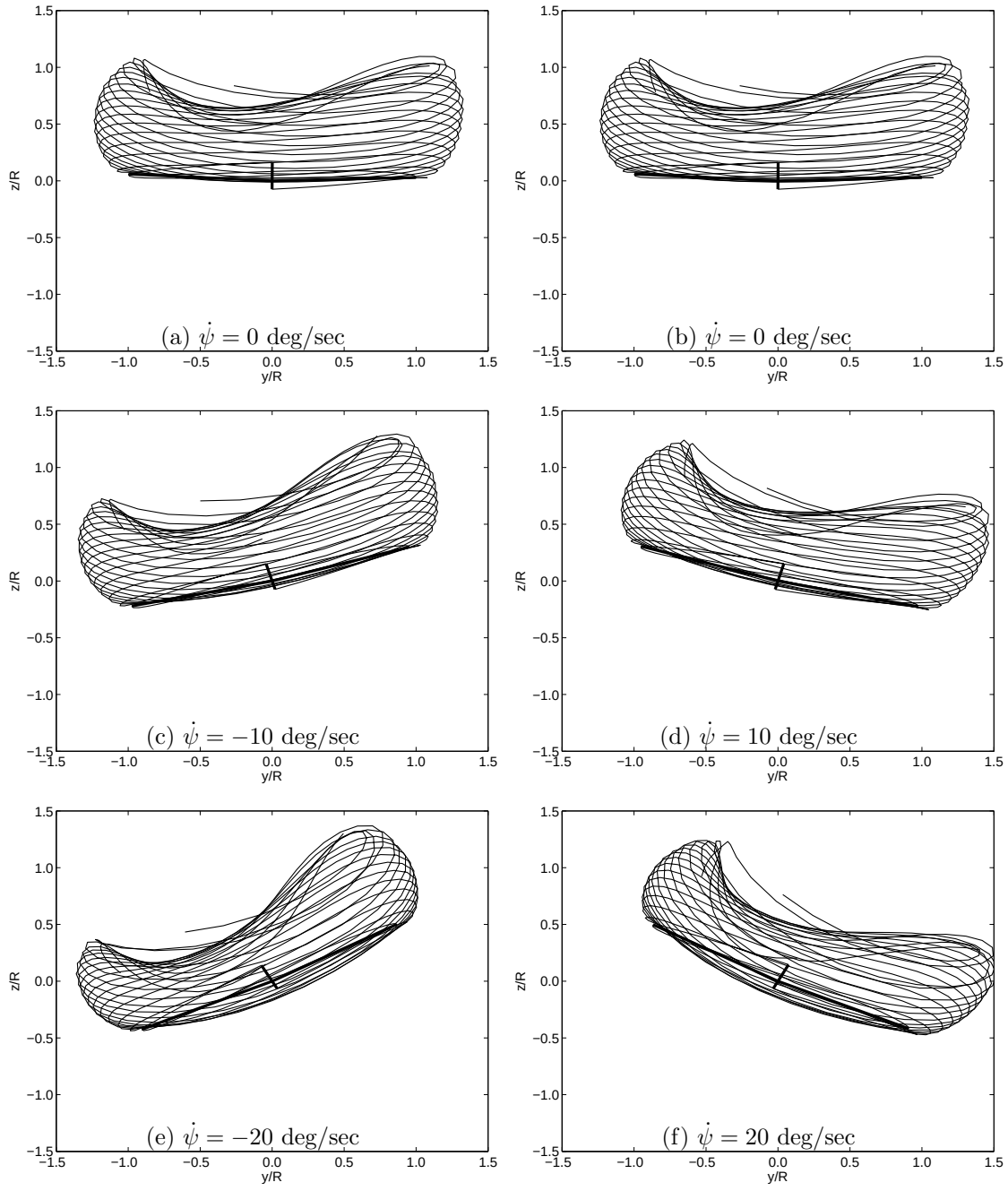

Figure 6.122: Rear view of the wake geometry for turn rates from $\dot{\psi} = 0$ deg/sec to $\dot{\psi} = \pm 20$ deg/sec, $V = 40$ kts and $\gamma = -40°$.

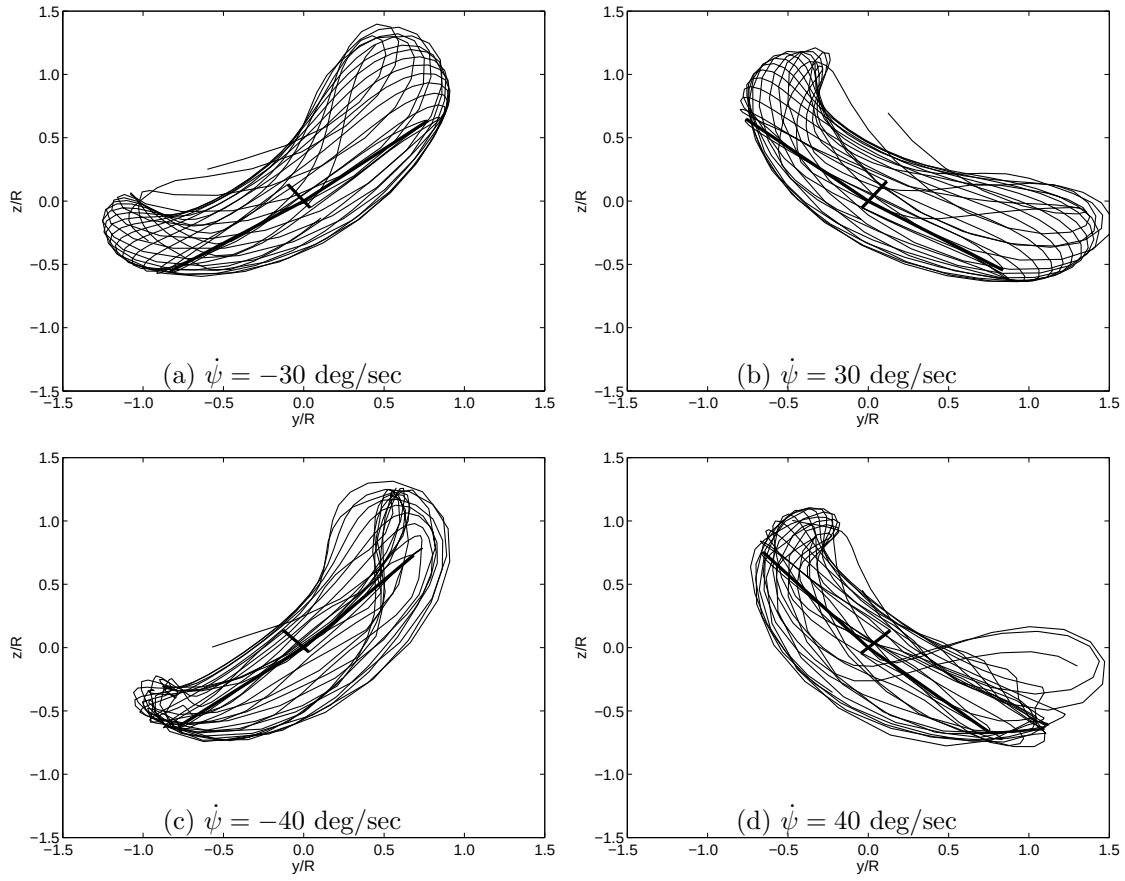

Figure 6.123: Rear view of the wake geometry for turn rates from $\dot{\psi} = \pm 30$ deg/sec to $\dot{\psi} = \pm 40$ deg/sec, $V = 40$ kts and $\gamma = -40°$.

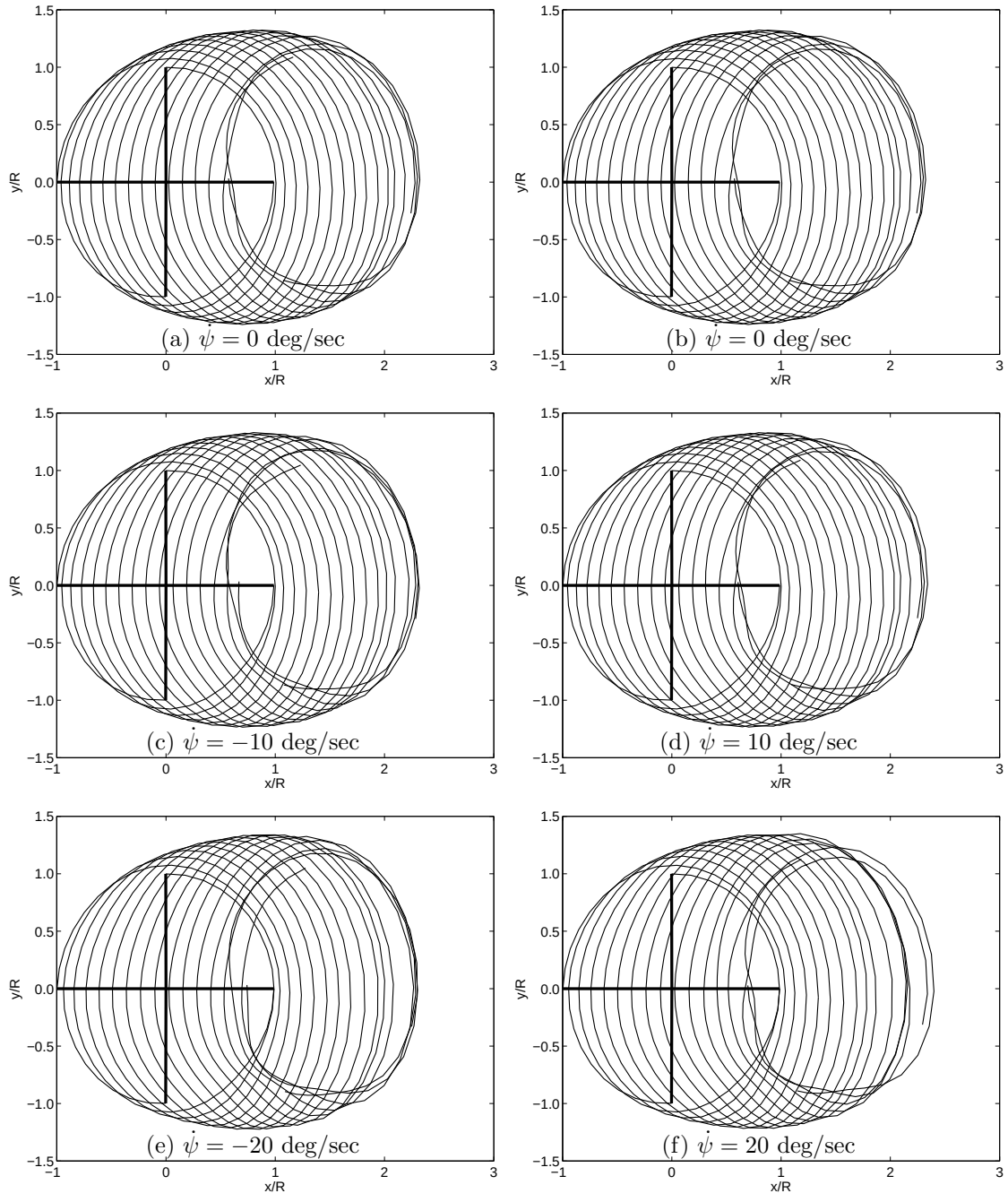

Figure 6.124: Top view of the wake geometry for turn rates from $\dot{\psi} = 0$ deg/sec to $\dot{\psi} = \pm 20$ deg/sec, $V = 40$ kts and $\gamma = -40°$.

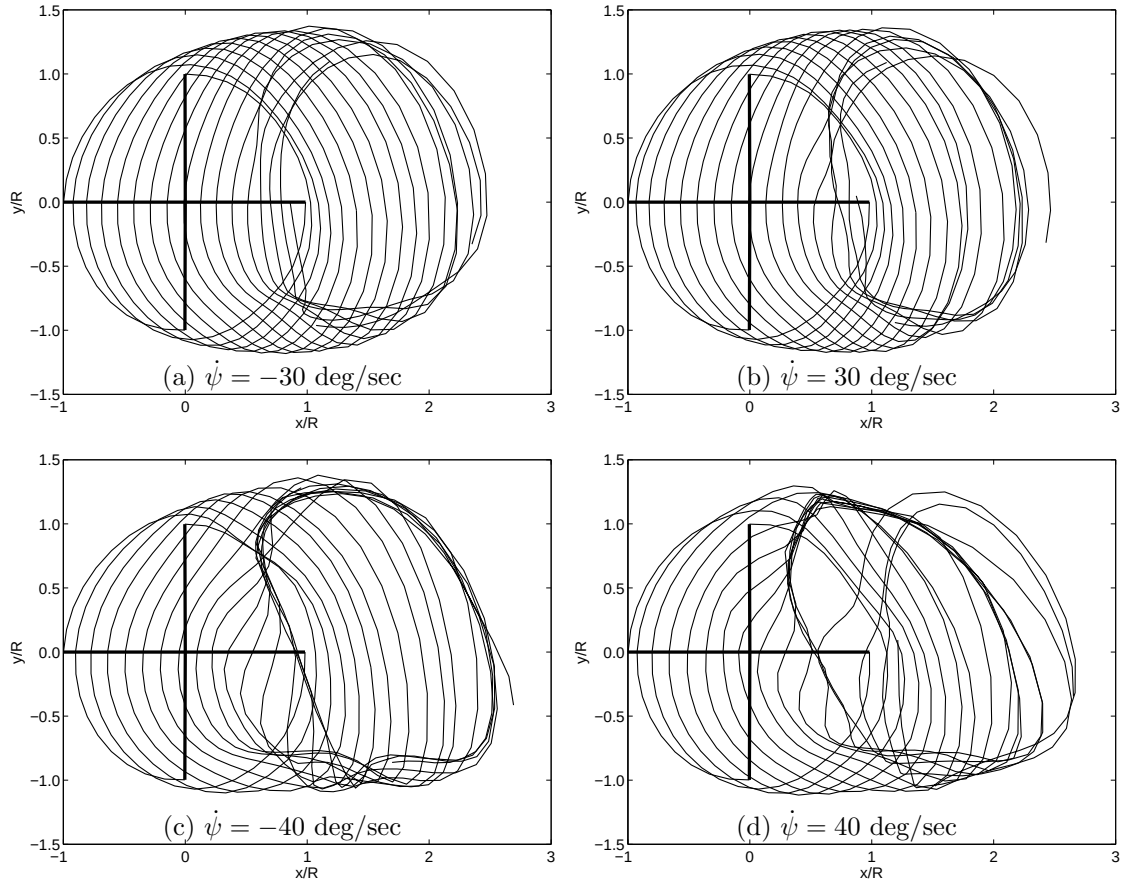

Figure 6.125: Top view of the wake geometry for turn rates from $\dot{\psi} = \pm 30$ deg/sec to $\dot{\psi} = \pm 40$ deg/sec, $V = 40$ kts and $\gamma = -40°$.

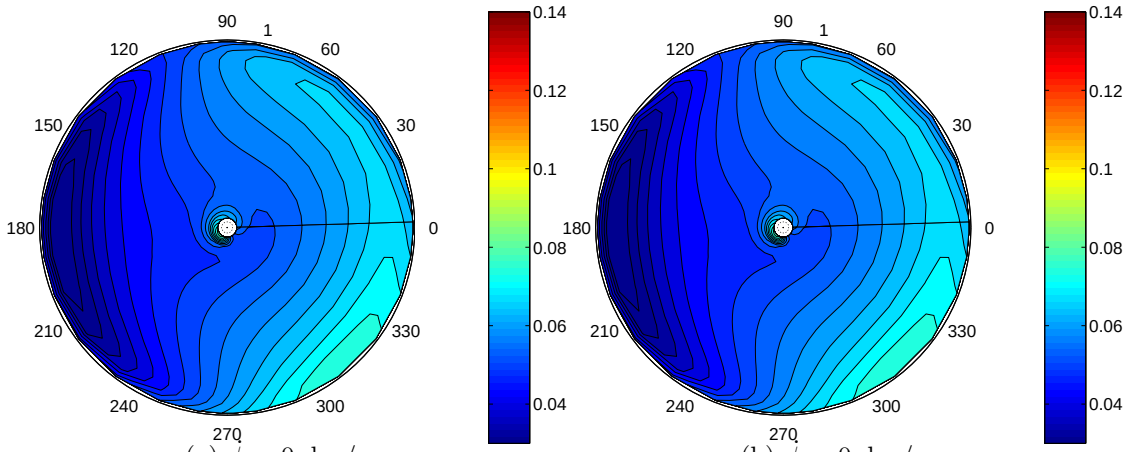

(a) $\dot{\psi} = 0$ deg/sec (b) $\dot{\psi} = 0$ deg/sec

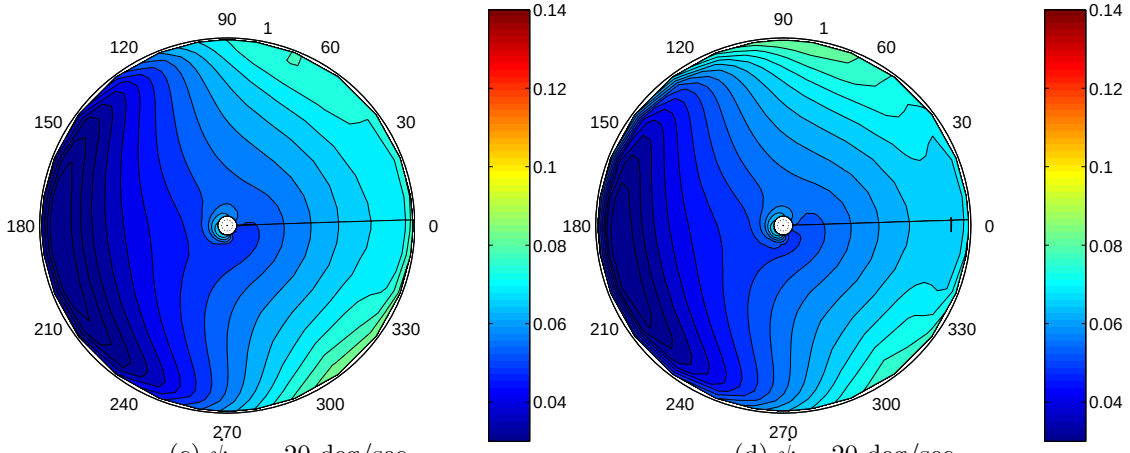

(c) $\dot{\psi} = -20$ deg/sec (d) $\dot{\psi} = 20$ deg/sec

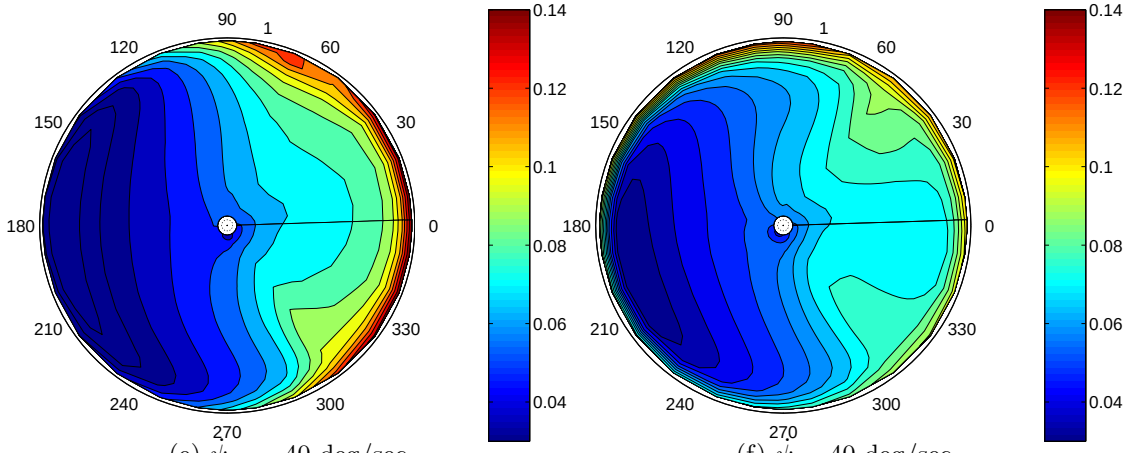

(e) $\dot{\psi} = -40$ deg/sec (f) $\dot{\psi} = 40$ deg/sec

Figure 6.126: Inflow distribution for turn rates at $\dot{\psi} = 0$ deg/sec, $\dot{\psi} = \pm 20$ deg/sec and $\dot{\psi} = \pm 40$ deg/sec, $V = 40$ kts and $\gamma = -40°$.

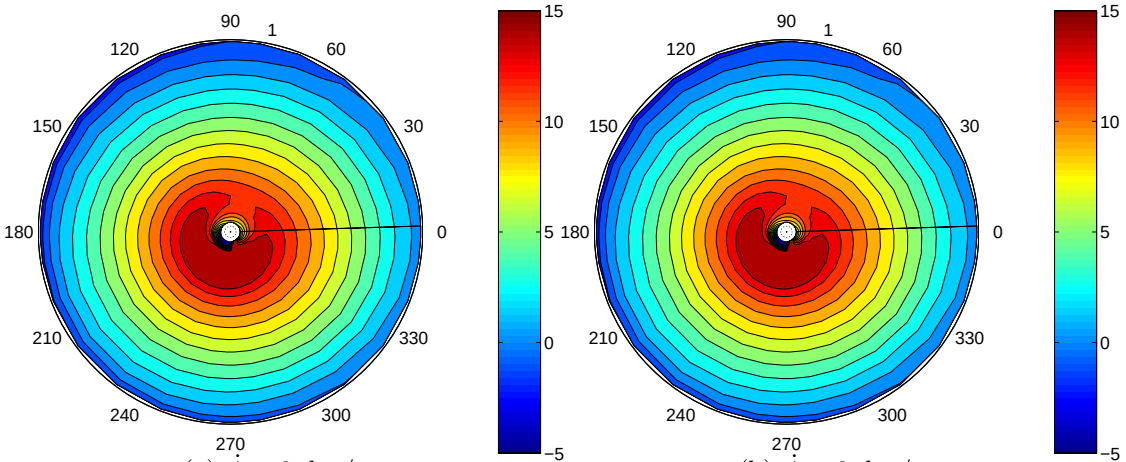

(a) $\dot{\psi} = 0$ deg/sec (b) $\dot{\psi} = 0$ deg/sec

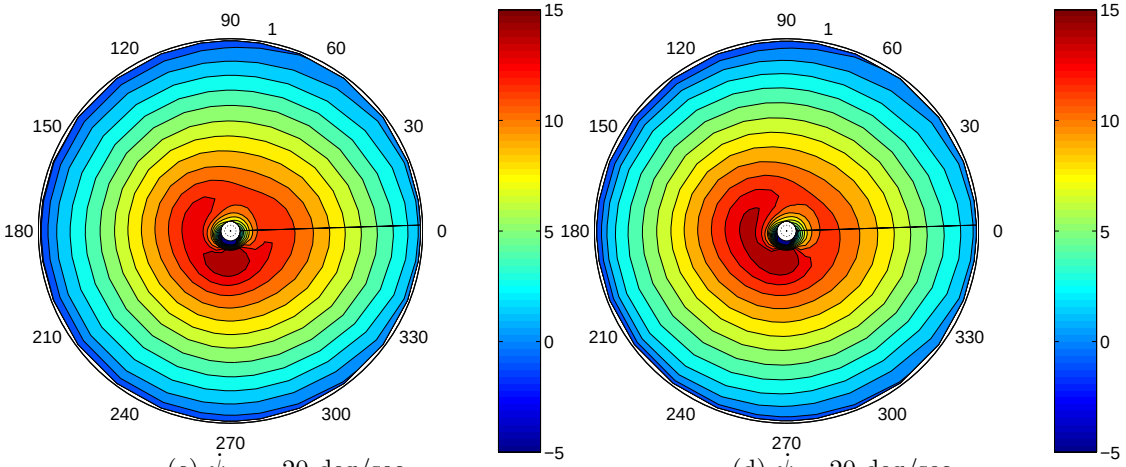

(c) $\dot{\psi} = -20$ deg/sec (d) $\dot{\psi} = 20$ deg/sec

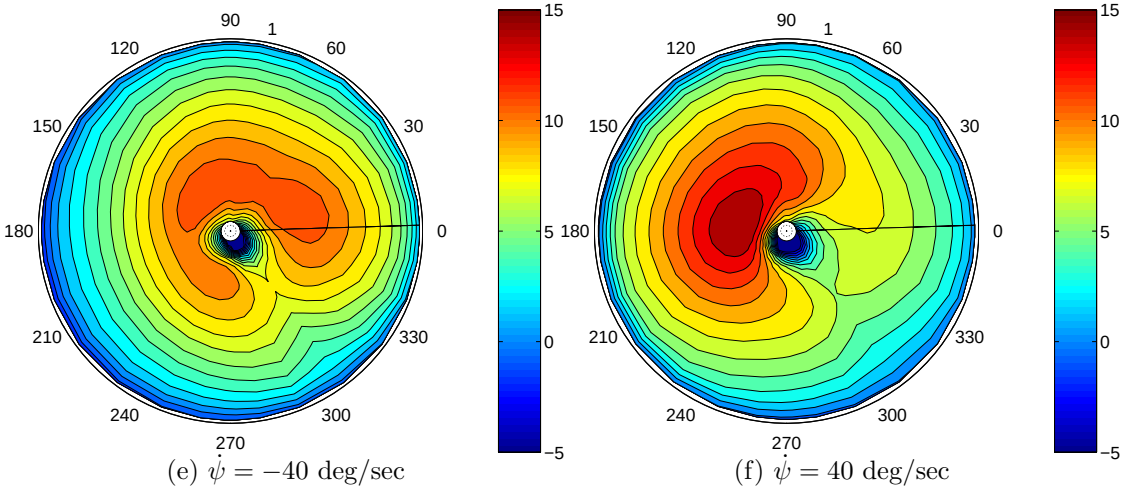

(e) $\dot{\psi} = -40$ deg/sec (f) $\dot{\psi} = 40$ deg/sec

Figure 6.127: Angle of attack distribution for turn rates at $\dot{\psi} = 0$ deg/sec, $\dot{\psi} = \pm 20$ deg/sec and $\dot{\psi} = \pm 40$ deg/sec, $V = 40$ kts and $\gamma = -40°$.

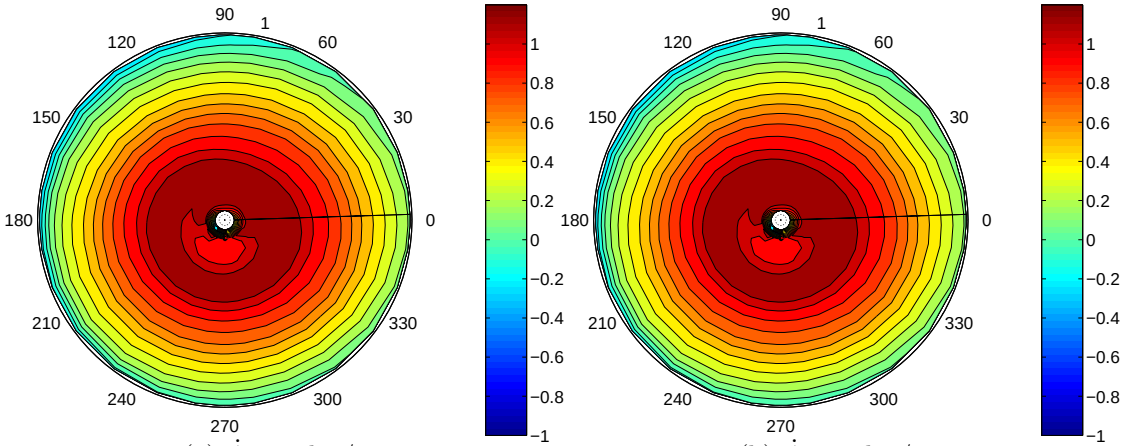

(a) $\dot{\psi} = 0$ deg/sec

(b) $\dot{\psi} = 0$ deg/sec

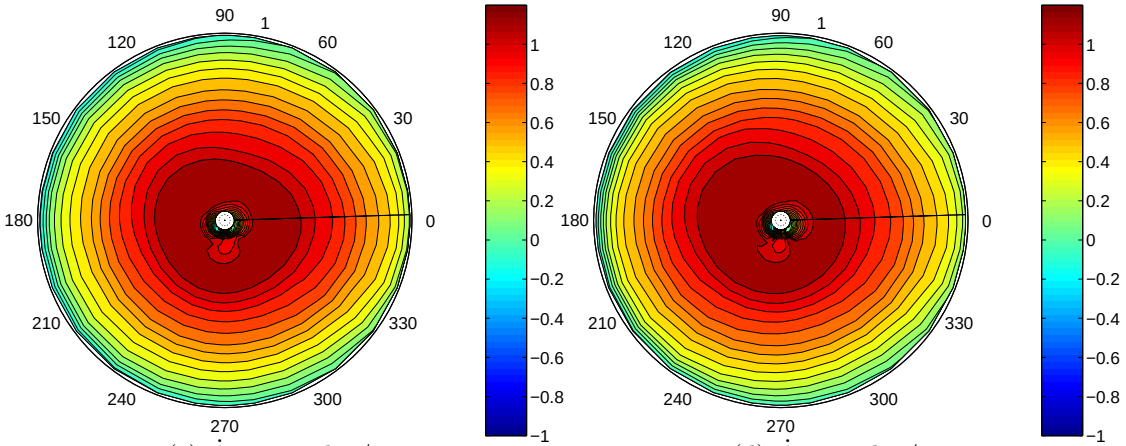

(c) $\dot{\psi} = -20$ deg/sec

(d) $\dot{\psi} = 20$ deg/sec

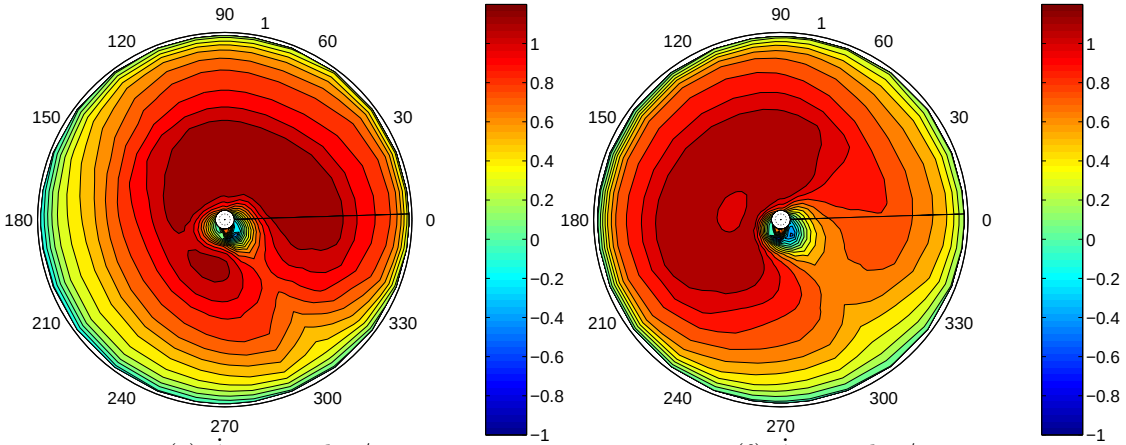

(e) $\dot{\psi} = -40$ deg/sec

(f) $\dot{\psi} = 40$ deg/sec

Figure 6.128: Lift coefficient distribution for turn rates at $\dot{\psi} = 0$ deg/sec, $\dot{\psi} = \pm 20$ deg/sec and $\dot{\psi} = \pm 40$ deg/sec, $V = 40$ kts and $\gamma = -40°$.

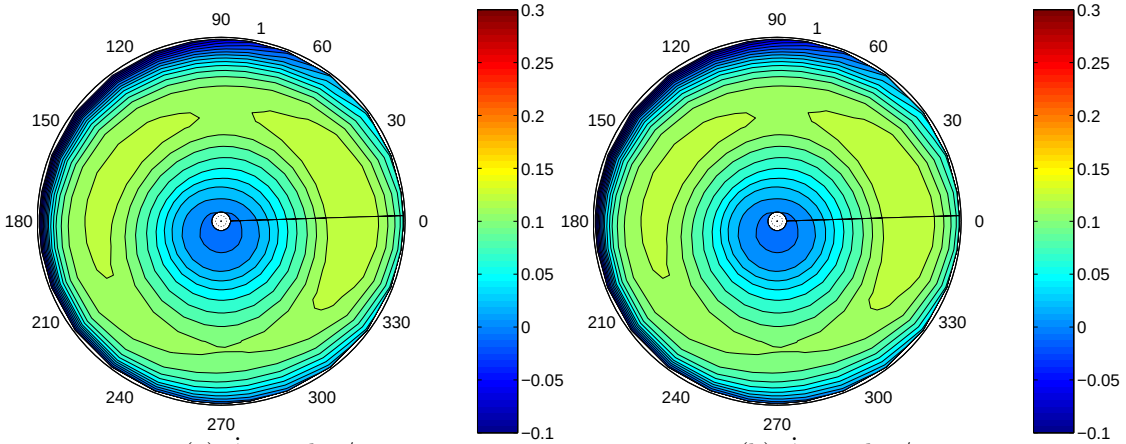

(a) $\dot{\psi} = 0$ deg/sec (b) $\dot{\psi} = 0$ deg/sec

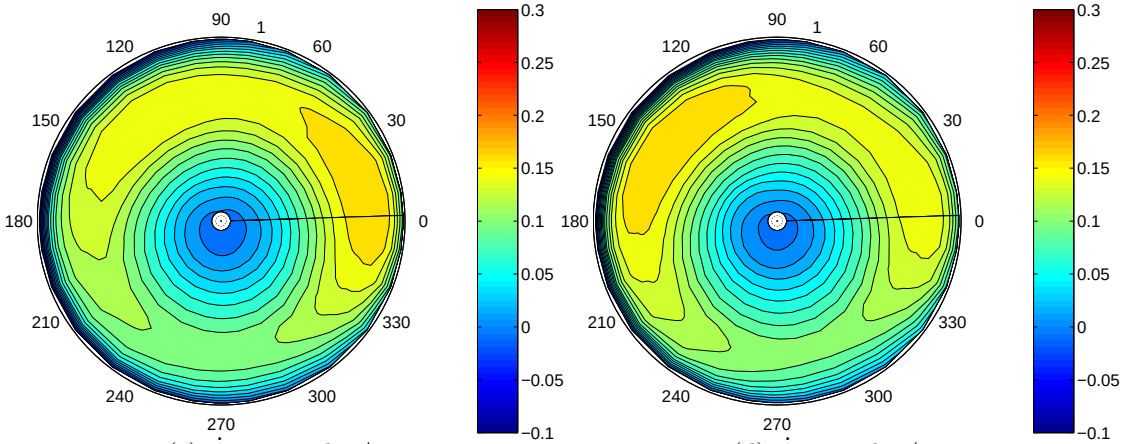

(c) $\dot{\psi} = -20$ deg/sec (d) $\dot{\psi} = 20$ deg/sec

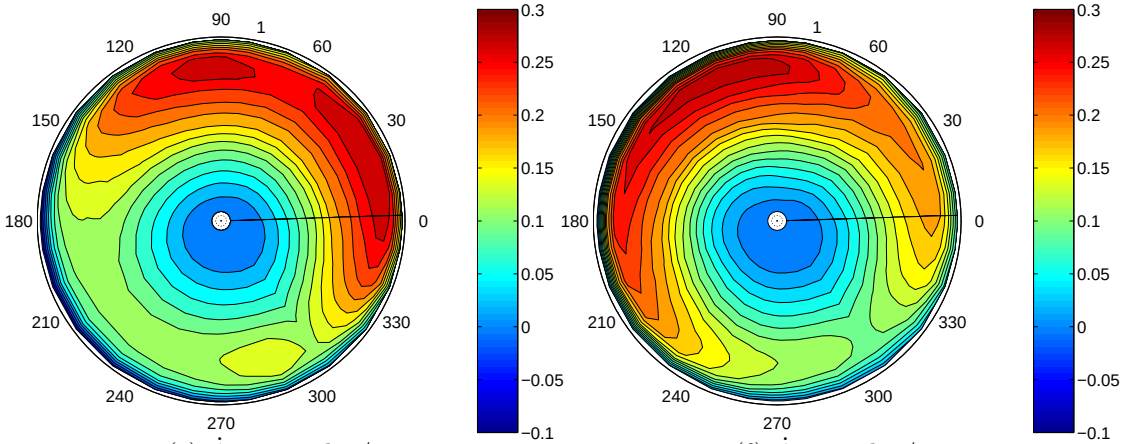

(e) $\dot{\psi} = -40$ deg/sec (f) $\dot{\psi} = 40$ deg/sec

Figure 6.129: Elemental lift distribution for turn rates at $\dot{\psi} = 0$ deg/sec, $\dot{\psi} = \pm 20$ deg/sec and $\dot{\psi} = \pm 40$ deg/sec, $V = 40$ kts and $\gamma = -40°$.

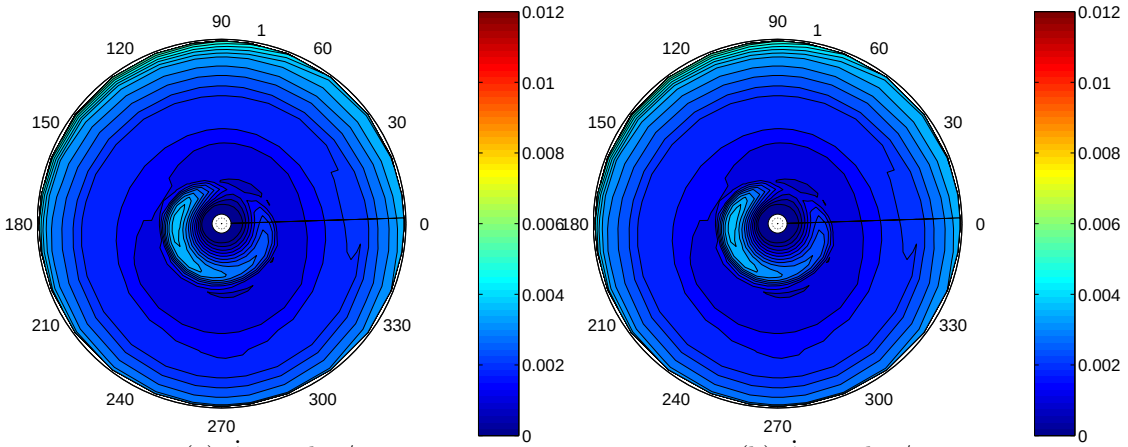

(a) $\dot{\psi} = 0$ deg/sec

(b) $\dot{\psi} = 0$ deg/sec

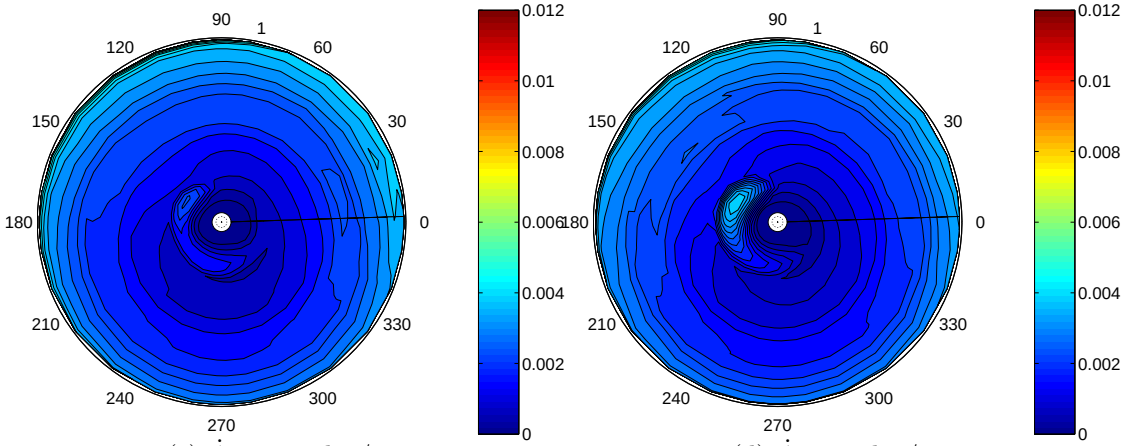

(c) $\dot{\psi} = -20$ deg/sec

(d) $\dot{\psi} = 20$ deg/sec

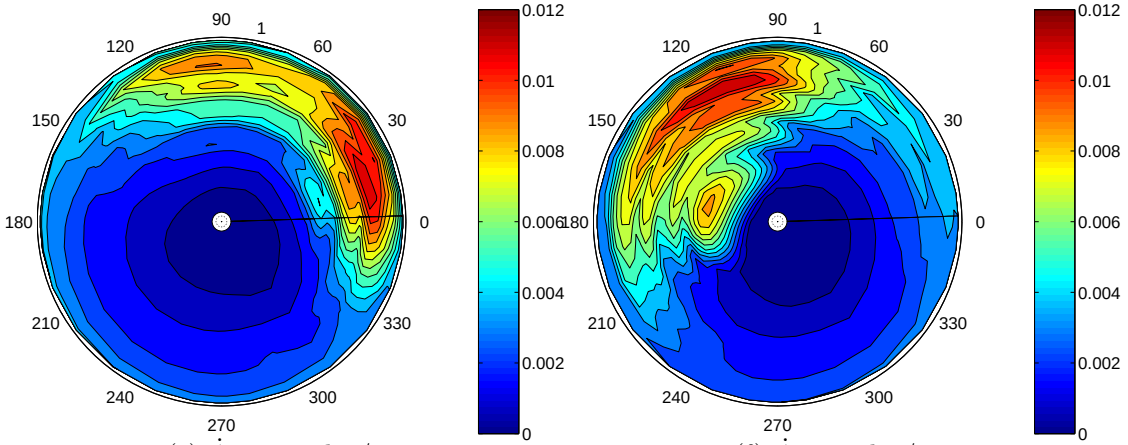

(e) $\dot{\psi} = -40$ deg/sec

(f) $\dot{\psi} = 40$ deg/sec

Figure 6.130: Elemental drag distribution for turn rates at $\dot{\psi} = 0$ deg/sec, $\dot{\psi} = \pm 20$ deg/sec and $\dot{\psi} = \pm 40$ deg/sec, $V = 40$ kts and $\gamma = -40°$.

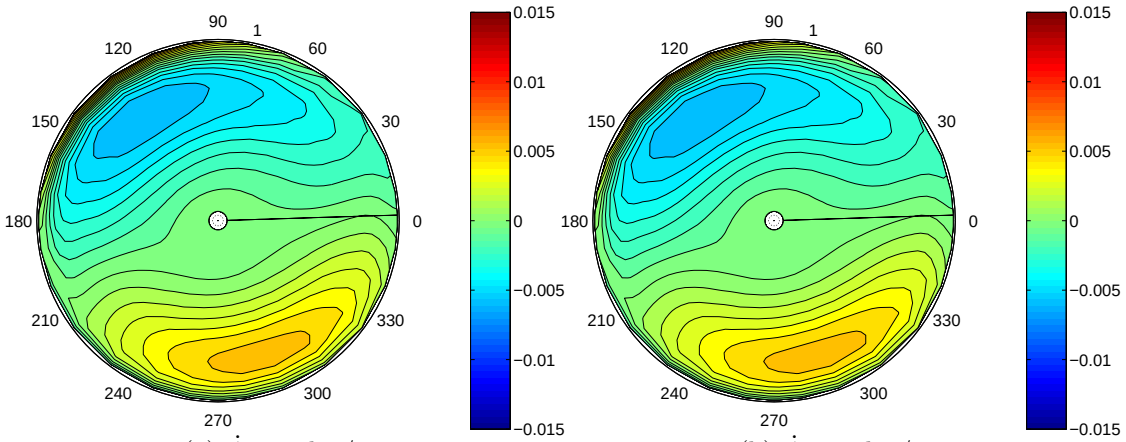

(a) $\dot{\psi} = 0$ deg/sec (b) $\dot{\psi} = 0$ deg/sec

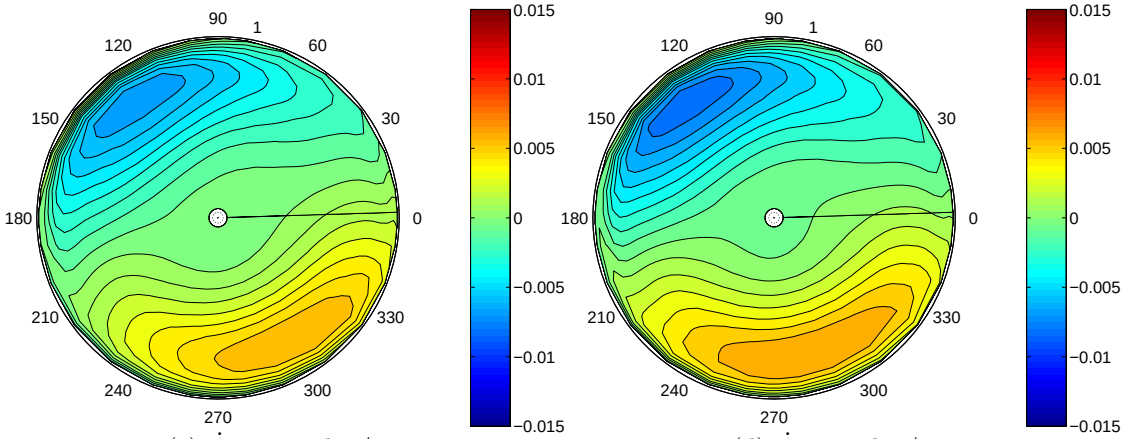

(c) $\dot{\psi} = -20$ deg/sec (d) $\dot{\psi} = 20$ deg/sec

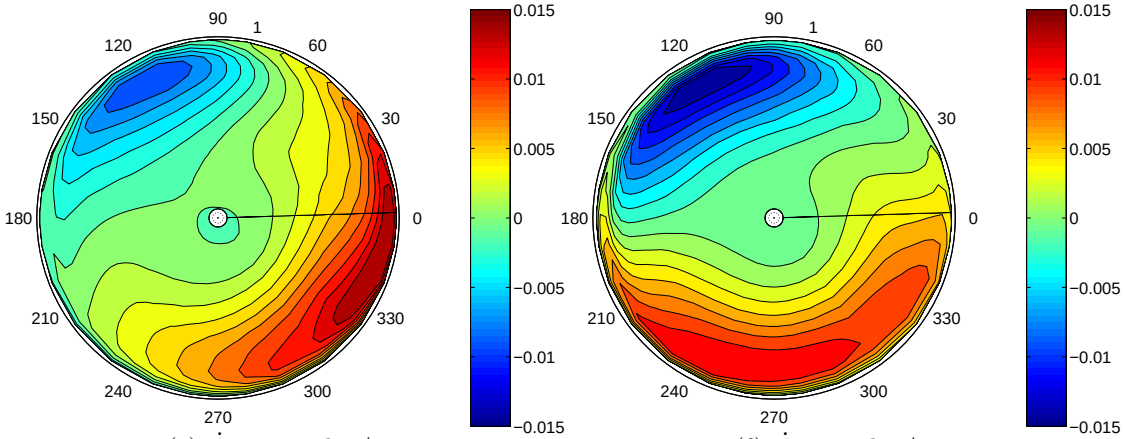

(e) $\dot{\psi} = -40$ deg/sec (f) $\dot{\psi} = 40$ deg/sec

Figure 6.131: Elemental induced torque for turn rates at $\dot{\psi} = 0$ deg/sec, $\dot{\psi} = \pm 20$ deg/sec and $\dot{\psi} = \pm 40$ deg/sec, $V = 40$ kts and $\gamma = -40°$.

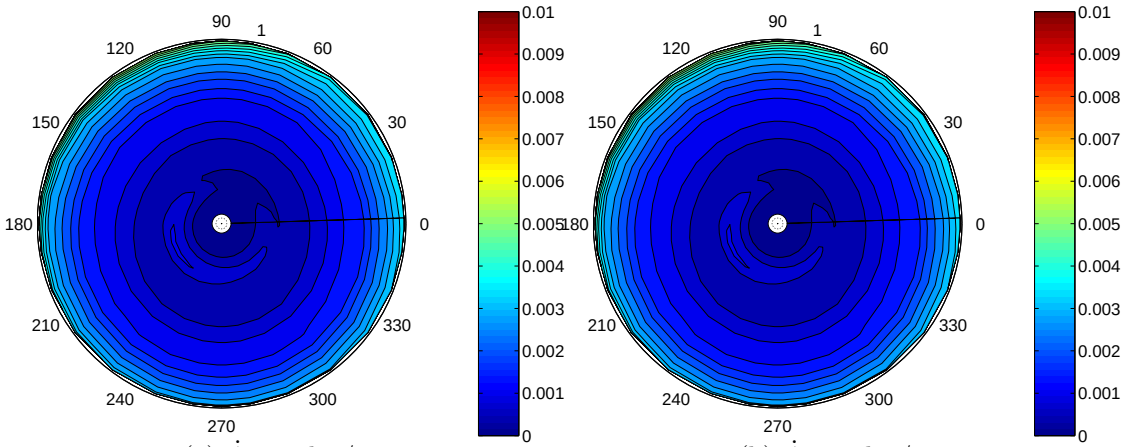

(a) $\dot{\psi} = 0$ deg/sec

(b) $\dot{\psi} = 0$ deg/sec

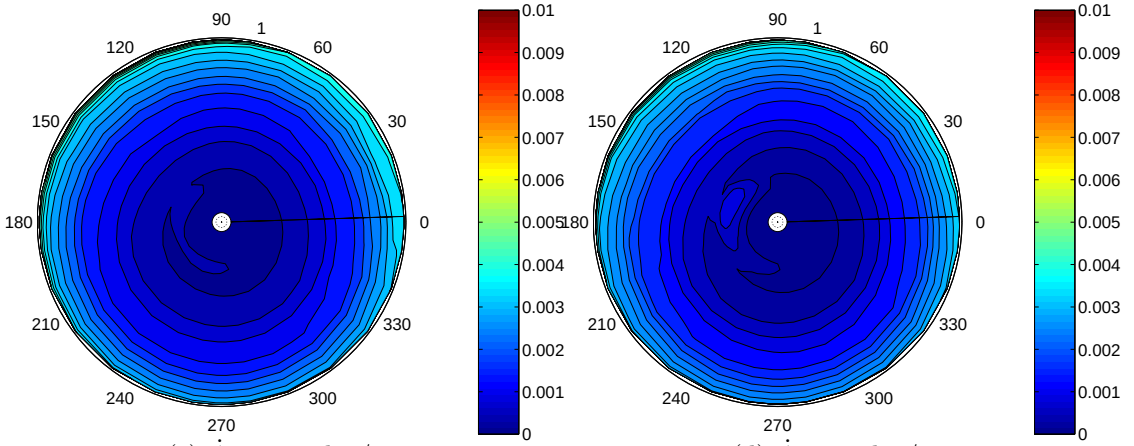

(c) $\dot{\psi} = -20$ deg/sec

(d) $\dot{\psi} = 20$ deg/sec

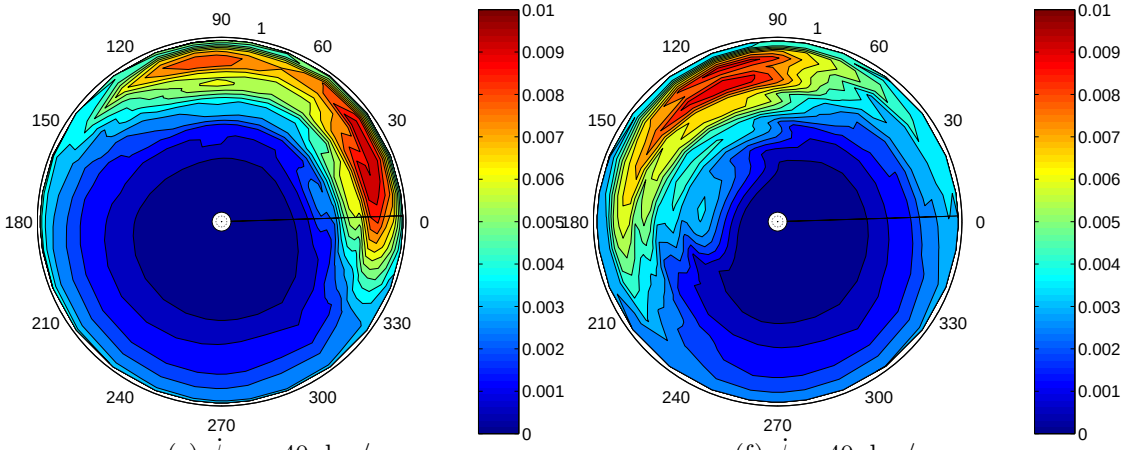

(e) $\dot{\psi} = -40$ deg/sec

(f) $\dot{\psi} = 40$ deg/sec

Figure 6.132: Elemental profile torque for turn rates at $\dot{\psi} = 0$ deg/sec, $\dot{\psi} = \pm 20$ deg/sec and $\dot{\psi} = \pm 40$ deg/sec, $V = 40$ kts and $\gamma = -40°$.

Chapter 7

Time integration results

This chapter presents the results of the flight dynamics simulation model during unsteady maneuvers. The free flight dynamic response for several maneuvers is calculated, and compared to flight test data when available.

First, the response to a lateral stick deflection from hover is simulated and compared to flight test data. Next, an axial descent from hover is simulated, which causes the rotor to go into the vortex ring state (VRS). No flight test data are available, but the simulation serves to illustrate the behavior of that flight condition. Finally, lateral stick input is applied to simulate a roll-reversal.

All these simulations are performed with a UH-60A helicopter, whose characteristics are described in Chapter 5, with flexible blades, based on the importance of blade flexibility concluded from the trim results shown in Section 6.2.4 and the results of Ref. 6 as well, which show that not including the bending and torsion of the blade significantly worsens the predicted response of the helicopter.

The integration procedure is described in Section 4.6. As explained previously, the solver used for the simulation is a variable-step solver; however, it is necessary to choose a step size $\Delta\psi$ at which to synchronize the flight dynamics simulation and

the free wake, which is solved separately. The simulation is advanced in steps of variable size chosen by the solver algorithm, but the solver stops every $\Delta\psi = 10°$, time at which the wake is advanced to the new position and the induced velocities updated. The step used to advance the free wake model needs not be the same as the time step of the simulation, $\Delta\psi$. If the free wake azimuthal discretization, $\Delta\psi_{FW}$, is smaller than $\Delta\psi$, several free wake time steps take place to advance to $\Delta\psi$. The present study uses the same wake azimuthal discretization $\Delta\psi_{FW}$ and time step $\Delta\psi_{FW}$ (10 degrees), and thus only one free wake step is taken for each time step of the simulation.

7.1 Lateral maneuver from hover

In this section, the results of the simulation of the free flight response to a mostly lateral cyclic input are presented. The control deflections for the trim solution specified by the pilot are shown in Fig. 7.1(a). The maneuver starts mainly with a lateral cyclic input, but as time progresses the other controls are applied, particularly after 4 seconds from the start of the simulation, to prevent the helicopter from reaching dangerous attitudes. The results are obtained at a gross weight of 16,000 lbs and an altitude of 5250 ft, starting from near hover, and are compared with the flight test data from Ref. 136.

7.1.1 Rigid body response

Figure 7.1(b) shows the time history of the roll rate, p. The roll rate represents the "on-axis" response for this pilot input. During the first stage of the maneuver, the prediction of the roll rate is very good, with the exception of a small overshoot of slightly less than 2 deg/sec at the point of maximum lateral control deflection. Beyond 4 seconds, the correlation worsens, but for another 2-3 seconds the experimental trends are still followed. Beyond 8 seconds the simulation diverges from the experimental values.

The results show that the prediction of the roll rate starts to deteriorate at around the time that a significant pedal input is applied. Recall that in the trim results shown in Chapter 6, some of the largest discrepancies between theory and experiment had been observed for the pedal settings. This seems to indicate that the modeling of the yaw dynamics is not sufficiently accurate.

The roll attitude, ϕ, like the roll rate, is captured correctly for the first part of the maneuver, as seen in Fig. 7.1(c). Beyond 5 seconds, the roll attitude starts to decrease, in a similar manner as the experimental results, only earlier by 1 second. Beyond 7 seconds, however, the response diverges, as seen in the previous figures, and the agreement with the flight test data deteriorates.

The time history of the pitch rate, q, which constitutes the "off-axis" response for this maneuver, is shown in Fig. 7.2(b). For the first few fractions of a second after the application of the lateral step, the predicted pitch rate stays constant as in the flight test. Then, the experimental values decrease slightly by 1.5 deg/sec before

increasing to a peak of 5.3 deg/sec at around the sixth second of the maneuver. However, the simulation does not decrease at all and instead starts the increasing trend ahead of the experimental values, to reach a similar maximum, only a bit sooner than in flight test. Beyond 6 seconds, the predicted values do not correlate at all with the experimental ones.

Figure 7.2(c) shows the pitch attitude θ in response to the maneuver in question. The initial response for the first two seconds of the simulation, which includes the application of the lateral control, follows the flight test data closely. After 2 seconds, however, the simulation the predicted pitch angle starts to increase, anticipating the actual helicopter response by 2 seconds. The behavior is somewhat captured, but with the wrong timing in the response. Beyond 6 seconds, the correlation worsens considerably.

The time histories of the yaw rate, r, and the yaw angle, ψ, are shown in Figs. 7.3(b) and 7.3(c). Both the yaw attitude and the yaw rate correlate well with flight test data for the majority of the maneuver.

7.1.2 Rotor Response

Figure 7.4 shows the time history of the flap motion coefficients, β_0, β_{1c} and β_{1s}. The constant flap coefficient, β_0, in Fig. 7.4(b), does not change significantly following the application of the lateral cyclic step, although it drifts off when there rest of the controls are applied.

The lateral flapping, β_{1s}, shown in Fig. 7.4(d), decreases by more than 0.5

degrees following the application of the lateral cyclic input. The positive lateral stick input δ_{lat} produces a negative control deflection at the swashplate, θ_{1c}, producing an initial decrease in β_{1s}, which tilts the rotor to the right. However, there is an overshoot in δ_{lat} beyond the desired steady value of 0.5 inches, and the corrective decrease in δ_{lat} increases β_{1s}, which remains at about 1.5° for remaining of the first half of the maneuver.

The longitudinal flapping, β_{1c}, shown in Fig. 7.4(c), is only perturbed very slightly when the lateral motion is applied, but it remains fairly constant up to 4-5 seconds of the maneuver, at which point β_{1c} increases considerably, tilting the rotor forward, in response to the negative longitudinal cyclic applied, and counteracting the nose up pitch attitude of the helicopter that has developed.

Figure 7.5 shows the time history of the lag coefficients ζ_0, ζ_{1c} and $\zeta 1s$. As in flap, the constant lag coefficient ζ_0, shown in Fig. 7.5(b), is not affected by the application of the lateral control input.

The cosine and sine lag coefficients, ζ_{1c} and ζ_{1s}, shown in Figs. 7.5(c) and 7.5(d) respectively, are much smaller in magnitude than the constant lag coefficient. ζ_{1c} shows an initial spike at the time the control deflection is first applied, but it quickly goes down to the same value, and then it grows gradually as the maneuver progresses, although always staying at much lower values than ζ_0. ζ_{1s} has a negative spike in value at the same time as ζ_{1c}, although then it remains constant for the majority of the maneuver.

7.1.3 Wake response

Figure 7.6 shows the side and rear views of the wake geometry for three instants in the maneuver ($t = 1.40, 2.79$ and 4.19 seconds) corresponding to the end of the $6^{th}, 12^{th}$ and 18^{th} revolutions. In all figures, the trim geometry of the wake is also shown, as if it had remained frozen and attached to the tip path plane. This allows an appreciation of the wake geometry distortions caused by the maneuver. At $t = 1.40$ seconds, the lateral control δ_{lat} has produced the maximum roll rate p to the right. While the size of the peak value of p is not high enough to produce large deformations in the geometry, some effects of the maneuver can be appreciated. In the advancing side, the vortex filaments move closer the rotor, while the retreating side does not change change almost at all. In the far wake, the new proximity at which the vortex filaments find themselves with increasing roll rate produces some vortex pairing. Even though the roll rate has reached its first peak, the roll angle has not changed much at this time, and therefore the orientation is unchanged. The pitch rate has barely changed at this point, and therefore the side view does not show any changes in the geometry until the vortices start pairing up in the far wake. At $t = 2.79$ seconds, the roll angle has increased to almost 17 degrees, but the roll rate has decreased in magnitude and the deformation of the wake in the advancing side is not as pronounced. The pitch rate and angle start to pick up, but are still small and hard to appreciate in the geoemetry. Finally, at $t = 4.19$ seconds, the roll rate is almost zero although the roll angle reaches a value of about 25 degrees, so the wake is tilted but hardly deformed from the roll maneuver. However, both

the pitch angle and pitch rate are noticeable, with a positive orientation of about 11 degrees and a slight deformation of the wake due to the nose up pitch.

The induced velocities for the same three instants of the maneuver are shown in Fig. 7.7 (left column), along with the inflow difference (right column) from the beginning of the maneuver, which corresponds to a hover condition, which is shown in Fig. 6.11(a). Because the angular rates are so small and they barely affect the geometry, the induced velocity distributions are very similar. In the first instant, corresponding to $t = 1.40$ seconds, the inflow increases mostly on the front of the rotor near the tips, with a bias towards the front advancing side, while in the rear of the rotor it decreases by a similar amount. This corresponds with the change in the wake geometry, which gets closer to the rotor plane on the front and advancing sides, as seen in Fig. 7.6. In the next instant, at $t = 2.79$ seconds, the values of the inflow increase similarly towards the tip of the blade all around the rotor, although slightly larger in the front. The inflow values remain the same in the second quadrant of the rotor (front advancing side) but are significantly lower in the fourth quadrant. At $t = 4.19$ seconds, the inflow is higher at the tip of the blades in the front of the rotor, but much lower on the retreating side.

As explained previously, the higher inflow increases the perpendicular velocity U_P, which decreases the angle of attack α, and vice versa, as seen in Eq.(2.56). Figure 7.8 shows the perpendicular component of the velocity at each blade section and the corresponding angle of attack distributions for the 3 instants considered above, corresponding to the 6^{th}, 12^{th} and 18^{th} rotor revolutions after the start of the maneuver. At $t = 1.40$ seconds, the perpendicular component of the velocity

U_P increases over most of the rotor, with the exception of the region near the tip on the advancing side, although the increase is larger in the retreating side, despite the inflow decreasing in the retreating side, which should decrease the total value of U_P. At this instant, the roll rate achieved in this maneuver is maximum, and its effect on U_P consists of increasing the perpendicular velocity on the retreating side, while decreasing it on the advancing side. The increase on the retreating side is larger than the reduction in induced velocities. On the advancing side, U_P increases inboard of the blade, where the effect of the roll rate is lower and the induced velocities are larger, although towards the tip the effect of the roll rate is dominant. The angle of attack α increases on the front-advancing side with respect to the hover condition, shown in Fig. 6.12(a), and decreases in the retreating side towards the rear of the rotor, causing the actual nose-up pitch that can ben seen in the pitch rate time history (Fig. 7.2(b)). In the next instant, at $t = 2.79$ seconds, the perpendicular velocity U_P is slightly higher on the advancing side, despite the inflow not changing, as the roll rate has decreased, while on the retreating side it decreases due to the decrease in induced velocities and the lower roll rate. The angle of attack reflects the lower values of U_P on the retreating side, which tilt the rotor to the starboard in the continuation of the roll maneuver, and increases in the front with a bias towards the advancing side, maintaining the nose up pitch rate. Finally, at $t = 4.19$ seconds, the higher induced velocities near the tips in the front half of the rotor contribute, to larger values of U_P and lower values of the angle of attack α in that region. As the roll rate continues to decrease, U_P becomes slightly larger on the advancing side and although it remains the same on the retreating side, due to the lower induced

velocities there.

Figure 7.9 shows the lift coefficient C_L and elemental lift $C_L M^2$ at the instants corresponding to the 6^{th}, 12^{th} and 18^{th} rotor revolutions after the start of the maneuver. The lift coefficient is a function of the angle of attack α and the Mach number M, as shown in Fig. 5.1. In hover, the Mach number increases axi-symmetrically with the radius. For the speeds and angles of attack observed in this maneuver, an increase in angle of attack at a fixed M increases C_L, and a higher value of M at a given α also increases the lift coefficient slightly. At $t = 1.40$ seconds, the higher angle of attack α in the front of the rotor increases the lift coefficient C_L from the hover values, shown in Fig. 6.13(a), decreasing on the rear half of the rotor where α is lower. At $t = 2.79$ seconds, the C_L decreases from the values achieved immediately after the application of the maneuver, particularly on the rear-retreating side where the decrease in angle of attack is higher, and the higher values of C_L shift slightly from the front to the front-advaincing side. Two seconds later, the lift coefficient is a little lower, and the shift of the highest values towards the advancing side continues.

In hover, the lift distribution is nearly axi-symmetric, with a slight bias towards the rear of the rotor, producing a slight forward tilt of rotor of a little under 2° After the application of the lateral cyclic, the lift coefficient increases in the front of the rotor reducing the longitudinal flapping β_{1c} by almost 1° for the first half of the maneuver. At $t = 4.79$ seconds, however, the lift in the front of the rotor decreases more significantly, as the maximum lift shifts towards the advancing side, and this lower lift produces a larger forward tilt of the rotor, as reflected in the increasing

values of β_{1c} in the second half of the maneuver.

The drag coefficient C_D and elemental drag $C_D M^2$ are shown in Fig. 7.10. As in the case of the lift coefficient, the drag coefficient is a function of the angle of attack α and the Mach number M, as shown in Fig. 5.2. For low Mach numbers, as those found inboard of the blade, the drag coefficient is constant for up to $\alpha = 10°$, i.e., for the entire range of angles of attack found in this case. At the Mach numbers observed at the tip, around $M = 0.65$, the drag coefficient for angles of attack below 5° is quite constant, but beyond 5°, each degree of angle of attack produces a significantly larger drag coefficient. From the start in hovering conditions, shown in Fig. 6.16(a), till $t = 1.40$ seconds, the increase in angle of attack in the front of the rotor translates into a much larger drag coefficient there. As the angles of attack in that region are around 5°, a small change in α results in a high increase in drag, which raises from 0.015 to 0.020. The lower angle of attack in the rear of the rotor results in slightly lower drag. At $t = 2.79$ seconds, the drag is only slightly lower than at the previous instant, but a shift occurs in the maximum values from the front of the rotor towards the front-advancing side, where the angles of attack are higher. At $t = 4.19$ seconds, the overall drag decreases, as the angle of attack decreases, but the highest drag values continue to shift towards the advancing side of the rotor.

The contribution of the local lift to the pitch and roll moments, which is the elemental lift $C_L M^2$ times the moment arm to the longitudinal axis in the case of the roll moment, or $r \sin \psi$, and to the lateral axis for the pitch moment, or $r \cos \psi$. At $t = 1.40$ seconds, the contribution to the roll moment decreases on the

advancing side and increases on the retreating side with respect to the beginning of the maneuver, as the maximum roll rate to the right is achieved, as seen in Fig. 7.1(b). As the maneuver progresses, the contribution on the advancing side does not change considerably, while it decreases on the retreating side, as the roll rate starts to decrease gradually from its peak value. In the "off-axis" direction, at $t = 1.40$ seconds, the contribution of the lift to the pitch moment decreases slightly both in the front and rear halves of the rotor, and the pitch rate does not change at this time, as seen in Fig. 7.2(b). In the next two instants considered, the lift contribution to pitch does not change significantly on the front half of the rotor, but it decreases slightly in the rear half, producing a moderate but increase nose-up pitch moment, reflected in an increase of the pitch rate.

7.1.4 Effect of swept tip modeling

This section studies the effect of the tip sweep modeling on the transient response of the helicopter. It was shown in Ref. 6 that the couplings between the pitch and flap degrees of freedom due to the swept tip may lead to an improved prediction in the on-axis response, and in a more limited way in the off-axis response as well. The present work includes a new rigorous model of the swept tip of the UH-60A helicopter (unlike the results in Ref. 6, in which the swept tip is approximated by simply shifting the center of gravity of the points on the swept part of the blade), with a finite element assigned to the swept tip and the loads calculated as explained in Section 2.4.7. Because of that, the same 5 lowest modes can be kept, same as in

the straight blade model, and the blade is allowed to deform in flap, lag and torsion.

Figure 7.12(b) shows the time history of the roll rate in response to the lateral maneuver from hover with the tip sweep modeled in the aeroelastic blade. The first and foremost observation is that the over-prediction of the roll rate at the point of maximum lateral deflection is reduced significantly with the increased sophistication of the blade model. The results are much closer to the flight test data for up to 4 seconds of the maneuver. Beyond that point, the swept blade model also starts to differ from the experimental values in the same way as the straight blade model did, but with slightly lesser error.

The prediction of the off-axis response also improves slightly. Figure 7.13(b) shows the pitch rate as a function of time in response to the controls of Fig. 7.1(a) with the blade model that has tip sweep. The prediction follows the experimental data for a bit longer than the results modeled with a straight blade, capturing the direction of the response with slightly better accuracy. For the second part of the maneuver, the solution with the swept blades also deteriorates, although like in the case of the roll rate, the error with the swept blade model is lesser than with the straight blade.

Figure 7.12(c) shows the predicted roll attitude in response to the same maneuver both with the straight blade and swept blade configurations. The prediction improves considerably up to 5 seconds of the maneuver, capturing very accurately the experimental values of the roll attitude for this maneuver. Beyond 5 seconds, both blade models give similar results up to 8 seconds, from which point the prediction worsens considerably for both models. The pitch attitude's improvement

with the swept blade model mirrors that of the pitch rate, as seen in Fig. 7.13(c), although the improvement is of lesser magnitude than in the case of the pitch rate.

7.1.5 Effect of the pedal modeling

It has been observed that prediction of the response to the maneuver in Fig. 7.1(a) appears to worsen at the time in which some pedal input is applied. Moreover, it has been noted that the trim results presented in Chapter 6 all had very poor correlation of the pedal values predicted at all flight conditions compared to flight test data.

This section attempts to look at what the effect of the pedal input is in the current maneuver by removing that particular input from the simulation. The simulation was therefore repeated under the same conditions but only with lateral, longitudinal and collective control inputs, and zero pedal deflection from the trim value.

Figure 7.14(b) shows the time history of the roll rate in response to the input controls of Fig. 7.1(a) excluding the pedal input. An improvement in the response after the pedal input would have been applied is clearly seen, particularly between the forth and seventh seconds of the maneuver. Beyond this point, the simulation worsens in both cases.

The pitch rate for the same case above is shown in Fig. 7.15(b). Like for the case of the roll rate, some improvement can be found of eliminating the pedal control input, and while the positive divergence of the pitch rate starts and the same point

(also missing the initial slightly negative pitch rate), the response is closer to the actual flight test data.

The roll and pitch attitude are shown, respectively, in Figs. 7.14(c) and 7.15(c), The roll attitude is also predicted better without the pedal input than with it, up to $t = 7$ seconds, in the similar manner to the roll rate. The pitch attitude, on the other hand, presents an interesting behavior. While it does not capture the initial nose-down attitude of the flight test, it does not diverge with positive values either. Instead, it remains flat until the fifth second of the maneuver. Beyond this point, it misses completely the nose-up pitch attitude that the helicopter attains towards the end of the maneuver.

The yaw rate and attitude are presented in Figs. 7.16(b) and 7.16(c) for the same maneuver. Eliminating the pedal of the simulation causes a total miss-prediction of the directional values, which in both cases start at the point in which the pedal should have been applied.

The conclusions that can be drawn from this little experiment is that, while the pedal needs to be modeled in the maneuver to accurately capture the yaw rate and heading of the helicopter, there are indications that the way it is implemented affects the longitudinal and lateral response in a negative way. Since the tail rotor is canted at an angle, it is definitely coupled with the longitudinal degree of freedom, and to some extent with the lateral degree of freedom as well. An investigation of both the modeling of the tail rotor and the control mixer is recommended.

7.2 Axial descent and the Vortex Ring State

This section presents the results of a free flight simulation starting from a near hover condition ($V = 1$ kt), at 16,000 lbs and at an altitude of 5,250 ft, for a decrease of collective of 5 inches over 1 second, shown in Fig. 7.19(a), which starts an axial descent into the vortex ring state (VRS). Although no flight test data is available for this maneuver, and only the collective control is perturbed (thus the maneuver is not a perfectly axial descent), this simulation is a great tool to analyze the behavior of the rotor through the VRS.

7.2.1 Rigid body response

The time history of the pitch attitude θ of the helicopter for this maneuver is shown in Fig. 7.17(b). Two seconds into the maneuver, a large nose-up pitch angle develops, which reaches a maximum value of 14 degrees. After this peak, which occurs in the fourth second into the maneuver, the pitch angle decreases to -5 degrees, and then oscillates about a mean value of 5 degrees.

The history of the pitch rate q is shown in Fig. 7.17(c). The pitch rate shows fairly large oscillations with a maximum amplitude of 15 degrees, which last throughout the entire maneuver.

Figure 7.18(b) shows the time history of the roll attitude ϕ. At the beginning of the maneuver, the helicopter rolls slightly to the starboard. Then, after approximately 5 seconds, the helicopter starts a sharp roll to the left, reaching a maximum roll attitude $\phi = -26$ degrees after 5.77 seconds. After that, the helicopter attitude

returns slowly to a nearly wings-level steady state value.

The roll rate p, in Fig. 7.18(c), has a small variation around $p = 0$ deg/sec until $t = 5$ seconds, at which time a large, doublet-like behavior occurs, followed, around $t = 7$ sec, by a return to a near zero steady value.

Figure 7.19(b) shows the time history of the thrust coefficient C_T. The thrust coefficient decreases with the lowering of the collective at the beginning of the maneuver. After the initial decrease, C_T stars to recover, and its value increases gradually during the next two seconds. There is a progressive loss of thrust between $t = 3$ and $t = 5$ seconds of the maneuver, typical of the lift losses associated with the "vortex ring" going through the rotor, followed by a spike in thrust coefficient. Eventually, the thrust goes back to a constant value as the wake restructures into a helical pattern again and the helicopter descents at a constant rate of descent. The presence of these thrust fluctuations has been documented before in the literature, from experiment (Refs. 137, 138) and in numerical analysis (Refs. 84, 135).

The main rotor power required as a function of time is shown in Fig. 7.19(c). The power decreases initially with the application of the step down of collective, and soon after that the continuing increase in the rate of descent brings the power requirement to almost zero. However, at that point the onset of the vortex ring state occurs, accompanied by large fluctuations of the power required. As the helicopter gets deeper into the vortex ring state condition, some very large and negative power values are predicting, as low as -1000 hp, indicating that the rotor is drawing power from the wind, in an autorotative condition. These power requirements, although not realistic, are a numerical solution that depends on the limitations of the model.

In a real free flight situation, the first observation would be an increase in the rotor rpm. Negative power occurs because the driving region is larger than the driven region, which would increase the rpm. However, the model does not include the rotor speed as a degree of freedom, and therefore it is fixed at a constant value of 27 rad/sec, which is not physical in a situation like this. Potential engine and structural failure is not modeled either, therefore the excessive power being drawn from the wind is not limited in any way by the model, and therefore it can reach unrealistic quantities. In reality, the large torque spikes would ove-rtorque the engine, leading to mechanical failure. An adept pilot could, to avoid such problems, de-clutch the engine and push the control stick forward to get some forward speed. However, the present simulation is limited to a single collective stick deflection, and the rest of the controls are not modeled. Eventually, the power requirement remains constant and slightly negative, indicating that the helicopter would be in autorotation for the remainder of the simulation.

The time histories of the forward and heave translational velocities u and w are shown in Figs. 7.20(b) and 7.20(c). The initial pitch up of the helicopter (Fig. 7.17(b)) produces a backward tilt of the thrust vector, which induces a backward motion of the helicopter, reaching a rearward speed of about $u = -15$ ft/sec. As the rotor reacts with a nose-down tip-path-plane tilt and a nose-down pitching moment, the helicopter accelerates forward up to about $u = 15$ ft/sec, eventually reaching a fairly steady forward velocity $u \approx 10$ ft/sec. The heave velocity w is shown in Fig. 7.20(c). The application of the collective step input is followed by a downward acceleration, with $w \approx 30$ ft/sec at about one second after the perturba-

tion collective reaches its final value. It should be noted that, at this point, the ratio of the climb speed V_c, which is the negative of the vertical velocity in body axes, and the hover induced velocity $v_h = \sqrt{C_T/2}$, which is 0.0549 in non-dimensional form, or 39.78 ft/sec, is about $V_c/v_h = -0.75$, which in the literature is associated with a rotor operating in the vortex ring state (Ref. 84). The helicopter then continues its downward acceleration due to the thrust losses associated with the approach and crossing of the vortex ring through the tip path plane. A maximum value of $w = 67$ ft/sec is reached 5.33 sec into the maneuver, corresponding to a ratio $V_c/v_h = 1.68$. As the maneuver progresses, the vertical speed reaches a steady value of approximately 63 ft/sec. This corresponds to a ratio $V_c/v_h = 1.58$, which is not quite the value $|V_c| > 2v_h$ theoretically required for a windmill brake state based on momentum theory, although conditions typical of windmill break state can already observed in the behavior of the wake. It should also be noted that at this point the maneuver is no longer purely axial, and therefore the transition velocities for axial flight are not precisely applicable.

Figure 7.21(b) shows the time history of the lateral translational velocity v. The roll attitudes that develop for $t > 5$ sec produce a corresponding increase in the sideward velocity, which reaches almost $v = -40$ ft/sec, and eventually settles at a nearly steady value of approximately $v = -25$ ft/sec. This results in a total velocity component in the $x-y$ body axis plane, i.e., not including the descent rate, of 27 ft/sec and a sideslip of -27 deg. Because the controls are assumed to be fixed during the entire maneuver, except for the initial collective input, the resultant flight condition is clearly not a purely axial descent, but a steep descent with a

total velocity $V = 68.5$ ft/sec, a sideslip angle of $\beta_F = 21$ deg and a flight path angle of $\gamma = -81$ deg. The simulation of a purely axial descent would require a coordination of all four pilot inputs to constrain all other motions of the helicopter. Also, because no pedal is applied to counteract the effects of the reduction of the required main rotor torque, the heading of the helicopter, shown in Fig. 7.21(c) changes considerably during the maneuver. At the end of the 15 seconds of the simulation, the helicopter has turned a full 90 degrees to the left from the initial orientation. The change in heading is slower than the decrease in torque and power required by the main rotor, but it follows a similar pattern.

7.2.2 Rotor response

The time history of the rotor flapping response in shown in Fig. 7.22. Figure 7.22(b) shows the time history of the collective flap β_0. The collective input produces an immediate decrease of about 3 degrees. Then, β_0 oscillates about a mean value of about 1.5 deg up to $t = 6$ sec approximately, at which point it increases very quickly to a peak value of $\beta_0 = 4$ deg, before settling to a steady value of abot $\beta_0 = 2.5$.

The longitudinal and lateral flapping coefficients (arising from the Multi-blade Coordinate Transformation) are shown as a function of time in Figs. 7.22(c) and 7.22(d), respectively. Both β_{1c} and β_{1s} initially decrease, i.e., the rotor tilts back and to the right, by about 2° in the case of the longitudinal and slightly less than 1° for the lateral flapping. After the first second, β_{1c} shows large oscillations throughout the descent, with an amplitude up to 6° and a maximum value of 8°

around $t = 6\,\text{sec}$. These longitudinal oscillations are cause for the large variations in the fuselage pitch angle and rate observed in Fig. 7.17. The lateral coefficient β_{1s} also oscillates during the first five seconds of the maneuver, although both the mean value, 0.5° and the amplitude of the oscillations, about 1°, are not as large. At $t = 6$ seconds, however, β_{1s} drops very fast to $-4°$, although it recovers within a second before settling at a steady value around $-1°$.

Figure 7.23 shows the rotor lag response. The collective lag ζ_0, shown in Fig. 7.23(b), increases by 4° in one second as the collective is decreased, i.e., the magnitude average lag displacement is reduced substantially (recall that the lag angle ζ is negative for a backward displacement in the lead-lag direction). After the rapid initial increase, ζ_0 continues to increase more slowly, until it becomes positive (effectively a lead angle). At around $t = 6$ seconds, there is a rather sudden drop in ζ_0 of about 1.5 degrees, and from that point it slowly evolves towards a steady value of around $\zeta_0 = 1$ deg.

The mean values of the cosine and sine lag coefficients, ζ_{1c} and ζ_{1s}, shown in Figs. 7.23(c) and 7.23(d), are much smaller in magnitude than the constant coefficient ζ_0, with values close to zero. However, between $t = 3$ and $t = 7$ second, both the cosine and sine coefficients show a high frequency oscillation, with an amplitude that is fairly random, with a maximum of about 1.5°.

The time history of the torsional coefficients are shown in Fig. 7.24. The collective torsion ϕ_0, shown in Fig. 7.24(b), starts at a value of $-1°$ in hover, indicating a slight nose-down twist. The decrease in collective increases ϕ_0 by 1° in the first 3 seconds of the maneuver. Between $t = 3$ and $t = 5$ seconds, ϕ_0 decreases to $-3°$,

at which time it increases rapidly to a zero twist angle, that remains for the rest of the maneuver.

The longitudinal and lateral torsion components, ϕ_{1c} and ϕ_{1s}, in Figs. 7.24(c) and 7.24(d) respectively, start with values of 0° in hover, as the loading is nearly axisymmetric, and remain at about that value, except during the period corresponding to the passage of the vorticity ring through the rotor disk, during which large, high-frequency oscillations occur.

Clearly, the most notable feature of the rotor response is the reaction to the wake vorticity as it progressively bundles below the rotor disk, crosses it, and is convected above it. The vortex ring has an irregular, nonaxisymmetric geometry and this, coupled with the linear and angular motions that the helicopter progressively develops, generate lateral and longitudinal components of the rotor response. The interaction between the rotor and the vortex ring manifests itself with substantial unsteadiness in the rotor response. The magnitude of this transient response is high, especially in flap and torsion.

7.2.3 Wake response

Figure 7.25 shows the side view of the free wake tip vortex filament at 6 time points during the descent. The nose of the helicopter points to the left of the figure. When the helicopter starts descending, the wake filaments are not convected as far downstream as they do in hover, and the increased proximity of the vortex filaments causes the vortices to start to "bundle". At time $t = 1.40$ sec (corresponding to 6

full revolutions after the start of the maneuver), time at which the collective has been decreased by the full 5 inches from the hover trim value, two vortex bundles are already visible, one in the far wake and one approaching the rotor. In addition, the vortex filaments start to move above the rotor tip-path-plane . At $t = 2.56$ sec (11 revolutions), the vortex filaments are first convected above the tip-path-plane , and the vortex bundle previously part of the far wake is now approaching the plane of the rotor. Six revolutions later, at $t = 3.96$ sec, the entire wake is bundled around the plane of the rotor, forming the actual vortex ring, a toroidal vortex bundle that characterizes and defines the phenomenon. Notice that the vortex ring is not evenly aligned with the tip-path-plane , and the uneven loads produced on the rotor cause the helicopter to pitch up. At $t = 4.89$ sec (21 revolutions), the vortex ring begins to separate from the rotor, starting from the rear portion of the disk, but still remains very close to the tip-path-plane . After 25 revolutions, corresponding to $t = 5.82$ seconds, the upward flow generated by the increasing rate of descent pushes the vortex bundle above the rotor. The wake geometry starts to reorganize itself above the rotor, although the vortex bundle remains still close to the tip-path-plane . Eventually, the wake becomes again periodic and forms a clean helical pattern above the rotor. At this point the helicopter is operating in the windmill-brake state, and is extracting power from the airflow.

The larger nose-up pitch angle that is observed in the sequence of wake geometries of Fig. 7.25 is seen to reach nearly 14 degrees in Fig. 7.17(b). When the vortex ring crosses the rotor and the uneven loading that caused the pitching moment on the helicopter disappears, the pitch attitude is reduced, but does not return

immediately to a steady value, instead it oscillates about its mean value of 5 degrees.

The rear view of the free wake geometry is shown for the same instants in the maneuver in Fig. 7.26. The rear view at $t = 1.40$ sec is very similar to the side view, with the vortex filaments first convecting over the rotor and the bundles forming downstream of the wake. Rear and side views are also very similar at next two instants shown in the figure, i.e., at $t = 2.56$ and $t = 3.96$ sec, except that the nose up pitch produced by the vortex bundle is less visible in the rear view. . At $t = 4.89$ seconds, it is observed that the helicopter starts to roll to the left or port side. The "vortex ring" goes through the advancing side first, but remains across the rotor in the retreating side. The uneven loading on the rotor is the primary cause of the roll and pitch motions of the helicopter, which are evident in this figure and the previous one. At $t = 5.82$ sec the vortex bundle starts to be convected above the rotor, with a distorted shape that is only very roughly parallel to the tip-path-plane . Eventually, the upwash flow reorganizes the wake above the rotor into a more regular and axisymmetric geometry and the helicopter roll and pitch motions are consequently reduced.

Figure 7.18(b) shows the time history of the roll attitude ϕ of the helicopter for the entire axial descent. At the beginning of the maneuver, the helicopter rolls slightly to the starboard (barely appreciated in the second snapshot of Fig. 7.26 due to the small magnitude and the fact that the initial trim position was a slightly negative bank angle). However, as the "vortex ring" goes through the rotor the helicopter starts to roll to the left, reaching a maximum roll attitude of -26 degrees after 5.77 seconds. After that, the helicopter attitude returns slowly to a steady

state value.

The induced velocities at the rotor plane at each of the instants explored before for the geometry are shown in Fig. 7.27 (note that larger scales will often be used for the quantities at $t = 4.89$ sec and $t = 5.82$ sec, where the strong perturbations generated by the vortex bundle are most visible: if the same scale had been used for all six cases, many interesting features at the other time points would have been very difficult to identify). Compared to the trim hover condition, shown in Fig. 6.11(a), reducing the collective first has an effect of reducing the inflow all over the rotor by an average of 0.03 (N-D). As the maneuver progresses and the wake filaments get closer to the wake, the inflow increases slightly towards the tips, but remains the same inboard of the blade. However, as the vortex ring forms around $t = 3.96$ seconds, the inflow distribution changes dramatically. The effects of the vortex ring intersecting the tip-path-plane can be clearly seen in the rear portion of the disk, where the vortex ring generates a strong upwash, with a strong downwash just inboard of it. The bias towards the rear is due to the fact that at this particular instant, the vortex ring is starting to separate from the tip-path-plane in the front, while it remains still close in the rear. A plot at a fraction of a second earlier (omitted here) would have revealed the same behavior in the induced velocities in the front of the rotor as the bundled vortex crossed the rotor plane there. As time progresses to $t = 4.89$ sec and the vortex ring starts to be convected above the rotor, the induced velocities slowly return to a more regular distribution, although on the left, or retreating side of the disk the influence of the bundled vortices is still clearly visible, as seen in Figs. 7.25 and 7.26. At this time point, the induced velocity

reaches both its largest and the lowest value. A region of upwash remains in the rear of the rotor towards the tip, but the inflow distribution is dominated by the large downwash on the advancing side. A second later, $t = 5.82$ seconds, the vortex ring has completely separated from the rotor, and while moving upstream of the wake structure, still exerts some influence over the front of the rotor. As the wake reorganizes itself into a clean helical structure above the rotor, $t = 9.31$ seconds, the inflow again becomes almost uniform.

Figure 7.28 shows the perpendicular blade sectional velocity, U_P, which includes the effects of inflow, descent speed, and blade flapping. The U_P component decreases with the initial application of the collective step, both because of the decrease in induced velocities associated with the lower thrust level, and because the descent of the helicopter produces an upwash through the rotor that decreases U_P (positive for a downward flow). But as the "vortex ring" forms around the rotor tips, it is the influence of the induced velocities that dominates the distribution of U_P, despite the continually increasing descent velocities. At $t = 3.96$ seconds, the wake induced upwash is particularly large in the rear of the rotor towards the tip. The area inboard of the formation of the vortex ring experiences positive values of U_P due to the large inflow there, which counteracts the velocities due to the continuing descent. The same can be said about the next instant, $t = 4.89$ seconds, at which the velocity reaches very large positive values due to the large downwash in the retreating side. Eventually, the wake reorganizes and U_P becomes again dominated by the upwash due to the descent.

The evolution of the angle of attack α over the rotor for the same six instants

during the axial maneuver are shown in Fig. 7.29. As described in Chapter 6, the angle of attack at any given section is given by the difference between the geometric angle of attack, which is composed of the pitch of the blades due to the applied controls, the built-in twist and the elastic deformation of the blade in torsion, and the induced angle of attack ϕ, defined as $\phi = \tan^{-1} U_P/U_T$. The changes in α depend primarily on three factors: (i) the decrease in collective pitch, which affects the total geometric angle of attack; (ii) the upward flow through the rotor disk due to the descent velocity; and (iii) the change in induced velocities. Figure 7.29 indicates the following sequence of events. The initial step down in collective is followed by a general decrease in α despite the initially smaller U_P, because of the lower geometric pitch angle. However, as the rate of descent continues to increase following the lower thrust setting, the angle of attack increases thanks to the higher values of the upwash through the rotor, specially in the inboard blade region. At the "vortex ring" approaches and then crosses over the rotor, the concentrations of vorticity encountered by the blades are associated with load fluctuations and areas of very high and very low angles of attack, often in close proximity of each other. While some areas of the rotor are near or in stall conditions, other areas produce negative lift. As the descent progresses towards the windmill break state, the areas of negative angle of attack disappear, but the angle of attack in the descent remains much higher than during hover due to the decreased value of U_P caused by the high speed descent achieved.

Figure 7.30 shows the lift coefficient C_L at different instants during the axial descent. Recall that C_L is a function of the angle of attack α and the Mach

number M. Initially, the lift decreases (compared with the hover values, shown in Fig. 6.13(a)), because of the lower collective. At $t = 2.56$ seconds the upwash generated by the descent is already increasing C_L over the entire rotor disk. first approaches and then crosses the rotor plane, $t = 3.96$ and $t = 4.89$ seconds, areas of stall or near stall appear, while other parts of the rotor inboard of the vortex ring formation produce negative lift as the angle of attack becomes negative due to the high induced velocities found there. This behavior of the angle of attack and the lift coefficient is typical of the vortex ring state, and has been observed previously, both in simulation (Ref. 135) as in experiment (Ref. 137).

The initial decrease in angle of attack and therefore lift coefficient associated with the lower collective translate into a sudden decrease in the net thrust produced, as observed in Fig. 7.19(b). As the maneuver continues and the high rate of descent increases the angle of attack and lift, the thrust is seen to increase slowly. However, the large regions of negative lift that occur at $t = 4.89$ seconds produce the thrust losses previously shown. At $t = 5.82$ seconds, however, the lift increases considerably all over the rotor, which produces a very large thrust coefficient.

Figure 7.31 shows distribution of $C_L M^2$, which is proportional to the elemental lift, at the same time points. The distribution of $C_L M^2$ loosely resembles that of C_L in Fig 7.30, but some areas of high C_L, especially in the inboard portions of the disk do not translate into large $C_L M^2$ because the local Mach number is low.

Figure 7.32 shows the distribution of $rC_L M^2$, which is proportional to the local contribution to the flapping moment. The distribution is nearly axisymmetric, with the important exception of the period during which the vortex ring first approaches

and then crosses the rotor plane. The evolution of rC_LM^2 helps explain the flapping behavior observed in Fig. 7.22. For example, the reduction of flapping moment at the beginning of the maneuver, while keeping an axisymmetric distribution, justifies the corresponding reduction in coning. As the vortex bundle approaches the plane of the rotor, the unsteady airloads associated with it translate into some oscillations in the flapping response. At $t = 3.96$ seconds, the flap moment is very large on the rear of the rotor and, because of the nearly 90 deg lag in flapping response, produces a large lateral tilt of the tip path plane, and the peak of β_{1s}. As the maneuver continues and the vortex ring goes through the rotor significantly large spikes and fluctuations occur (Ref. 84). At $t = 4.89$ seconds, there is still a strong positive flap moment region in the rear portion of the disk, which sustains the strong lateral flapping. The picture is less clear on the retreating side, especially between 240 and 300 deg, where simultaneous regions of strong positive and negative contributions to flap moment are visible. The net result is a reduction of longitudinal flapping. At $t = 5.82$ seconds, the effects of the vortex ring begin to diminish, the distribution of rC_LM^2 begins to take again a more regular shape, and the oscillations of longitudinal and lateral flapping begin to subside.

Figure 7.33 shows the distribution of elemental profile drag, C_DM^2. At the beginning of the descent, the drag decreases from the initial hovering condition (Fig. 6.17(a)) with the decrease in collective, reaching very low values, as both the angle of attack α and the Mach number M are low. However, as the vortex ring goes through the rotor, the regions of very high and very low angles of attack previously observed cause large values of C_D (Fig. 5.2). At $t = 3.96$ seconds, a concentrated

band of very high drag begins to appear in the tip regions on the rear portions of the rotor. As the maneuver continues to $t = 4.89$ seconds and the "vortex ring" continues to cross the rotor disk, this region is larger and extends over the outer portions of the fourth quadrant of the rotor, where the vortex ring still affects strongly the inflow distribution. At $t = 5.82$ seconds, , the drag is returning to a more uniform distribution decrease, with only an elevated area on the retreating side around $\psi = 270°$. As the maneuver continues and the wake returns to an organized helical structure, the values of the drag return to normal, although slightly higher than in hover.

The decrease in drag following the reduction in collective clearly justifies the decrease in the lag angle seen in Fig. 7.23(b). As the maneuver continues, the "vortex ring" goes through the rotor producing large gradients of angle, regions of high drag, and pronounced unsteadiness, which in turn cause the development of longitudinal and lateral lag components, and pronounced lag vibrations.

The distribution of the moment coefficient C_M is shown in Fig. 7.34. The moment coefficient is a function of both the angle of attack α and the Mach number M, and their relationship is shown in Fig. 5.3. At the range of angles of attack and Mach numbers found at the beginning of the maneuver, the decrease of α due to the lower collective reduces the moment coefficient slightly in the first instant. At $t = 2.56$ seconds, the α increases a little and so does C_M. At $t = 3.96$ seconds, the area of high angle of attack near the tip in the rear of the rotor, where the Mach number is also high, produces some positive values of C_M, including some very large, near 0.02 around $\psi = 30°$, although the negative α encountered slightly inboard of

this region produces some very low and negative values of C_M. At $t = 4.89$ seconds, the angle of attack reaches values lower than $-10°$ in the fourth quadrant of the rotor, which increase the moment coefficient into large nose-up values, along with some very low values further towards the tip, where α reaches values higher than $20°$. As the "vortex ring" leaves the plane of the rotor, the lower angle of attack that occurs in the outer half of the rotor disk is associated with mild nose-down moments, although some high nose-down pitching moments are found near the root, where the angle of attack is much higher.

The large decrease in the constant torsion coefficient shown in Fig. 7.24(b), is associated with the lower nose down moment overall while in the vortex ring state, as the regions of very high nose-up C_M are cancelled by approximate regions of very low C_M. Before $t = 5$ seconds, the pitching moment coefficient near the rotor is very low, producing a decrease in the cosine torsion coefficient ϕ_{1c} (Fig. 7.24(c)). After $t = 5$ seconds, C_M increases in the rear of the rotor, producing an increase in ϕ_{1c}, before it settles in a steady value close to zero as the wake structure becomes helical again. The sine torsion coefficient, $\phi 1s$ increases to a maximum around $t = 5.82$ seconds, due to the large nose-down moments that occur on the retreating side.

The induced and profile torque distributions for this maneuver are shown, respectively, in Fig. 7.35 and 7.36. The induced torque, or $rC_L M^2 \sin\phi$, changes both with the local lift and with the induced angle of attack, which is the ratio of U_P over U_T. The lower lift caused by the decreasing angle of attack, along with lower U_P, decrease the induced torque of the rotor. The profile torque is generally much lower than the induced torque, although as the drag increases (Fig. 7.33),

some regions of localized high profile torque occur in the early stages of the vortex ring state, and at $t = 5.82$ seconds there is a large region of profile torque on the retreating side with values reaching up to 0.012, corresponding to the "vortex ring" crossing the rotor disk. The main rotor power required for this maneuver, shown in Fig. 7.19(c), decreases initially with the lower induced torque, although the high profile torque that occurs $t = 5.82$ seconds increases the power requirement.

Figures 7.37 and 7.38 show how the lift contributes to the roll and pitch moment respectively, by multiplying the local lift at each blade section, $C_L M^2$ times the moment arm to the longitudinal axis, $r \sin \psi$, in the case of the roll moment, and to the lateral axis, $r \cos \psi$. During the first part of the maneuver, the contribution to the roll moment on both the left and right sides of the rotor is very similar, although slight variations cause some oscillations in the roll rate p during the first five seconds (Fig. 7.18(c)). At around $t = 5$ seconds, however, the large unsteady loads produce a large negative contribution on the left side which causes a rapid roll to the left, and when the negative loads disappear, the rotor reacts with another rapid roll to the right before returning to $p = 0$ deg/sec. The pitch contribution is shows regions of both positive and negative values, both in the front and the rear of the rotor, and as a result the pith rate q (Fig. 7.17(c)) oscillates between positive and negative values as the larger contribution shifts from the front to the rear of the rotor.

In summary, the application of a decrease in collective setting starting from hover brings the helicopter into an axial descent, and it soon enters the vortex ring state. The formation of the concentrated vortex toroidal structure is clearly visible

in the geometry of the wake, and its influence can be seen in the rotor loading, in the orientation of the helicopter, and it the thrust and flap fluctuations that occur due to the aerodynamic losses that accompany the formation of the "vortex ring" at the plane of the rotor.

7.3 Roll reversal maneuver

This section presents the results to a roll reversal maneuver in response to a lateral only control deflection. There is no flight test data available for this maneuver, the magnitude of which was selected arbitrarily and might not be realistic. But it is included here because the high rates of this maneuver are typical of military tactics and the capability to capture the wake dynamics during such conditions is very desirable.

The baseline flight condition for this maneuver is a straight and level flight at $v = 80$ kts, at a weight of 16,000 lbs and an altitude of 5250 ft. The maneuver is performed without any stability augmentation, in order to better understand the actual couplings occurring in the fully modeled helicopter, as opposed to an isolated rotor configuration (Ref. 5). In comparing the present results with those of Ref. 5 one must also keep in mind that the present work only keeps 4 full turns of the wake beneath the rotor, while Ref. 5 uses 6 turns, which makes the far wake roll up more obvious and more dramatic. Moreover, Ref. 5 uses a very small discretization of the free wake, with steps of only 2.5 degrees to capture the BVI, while the present study uses a 10 degree discretization.

7.3.1 Rigid body response

The applied lateral control deflection δ_{lat} for this maneuver is shown in Fig. 7.42(a). The maneuver consists of a 1.5 inch deflection of the lateral cyclic to the right, followed by a deflection of twice that magnitude in the opposite direction at the same rate, another step of 3 inches to the right again and a return to the original position after 8 seconds. The pilot does not apply any other control for this idealized maneuver, and therefore the inherent couplings of the helicopter system produce additional longitudinal motion in addition to the roll reversal that follows the application of the lateral cyclic input.

Figure 7.39(b) shows the time history of the roll rate p of the helicopter following the application of the lateral stick input of Fig. 7.42(a). As δ_{lat} increases, p increases to almost 40 deg/sec to the right. As the lateral stick shift to the left, the roll rate follows, reaching almost -60 deg/sec (to the left). The inverse stick deflection produces a roll to the right reaching a peak roll rate of about 30 dg/sec, and it decreases as soon as δ_{lat} returns to zero.

The roll angle ϕ is shown in Fig. 7.39(c). The roll rate p causes an increase in the roll angle to the right, which raises continuously until the roll rate starts to decrease at around $t = 3$ seconds, at which point $\phi = 70°$ to the right. The negative roll rate decreases the roll angle which reaches a maximum value of about 15° to the left. The increasing roll rate in the opposite direction does not allow the roll angle to decrease any further, and ϕ starts to increase again, reaching another maximum of about 50°.

The off-axis response is shown in Fig. 7.40. The pitch rate, q, shown in Fig. 7.40(b), increases slowly with the application of the right lateral stick deflection, up to $q = 10$ deg/sec, at which moment the reversal into a left roll produces a large nose down moment, which decreases the pitch rate more rapidly than in the first part of the maneuver, reaching a low around $q = -20$ deg/sec. The application of a lateral stick deflection to the right does not immediately affect the pitch rate, although with some delay it increases q in a short period of time. The pitch angle, shown in Fig. 7.40(c), does not change during the first roll to the right. However, the reversal into a left roll produces an increasingly large nose down pitch attitude, that does not stop until the pitch rate increases around $t = 8$ seconds as the maneuver deteriorates.

As no additional controls are applied to maintain the maneuver purely lateral as the helicopter continues to travel at high speed, the reaction of the helicopter translates into all three degrees of freedom due to the inherent couplings of the rotor-fuselage system. The velocities of the helicopter along the three body axes are shown in Fig. 7.41. The large nose-down pitch attitude that the helicopter adopts after the 4^{th} second of the maneuver accelerates the helicopter, which starts the maneuver at 135 ft/sec and increases its speed by 50 ft/sec in 5 seconds. The on-axis response of the velocity follows the roll attitude closely, as the change in the direction of the thrust vector causes an increase of the lateral velocity first to the right up to 40 ft/sec, followed by change to the left reaching a total speed of -40 ft/sec, to eventually increase again to the right. The vertical velocity also changes, as the collective is not adjusted to maintain altitude with the changes in the

direction of the thrust vector. First, the the helicopter starts a descent that peaks around the 4^{th} second (the z-axis is positive down), due to the the loss of vertical thrust due to the new bank angle. However, after the 4^{th} second, the increased thrust caused by the higher angle of attack and thus lift seen in the second part of the maneuver (Figs. 7.49 and 7.50), the helicopter enters into an effective climb, reaching a maximum rate of climb of 60 ft/sec. Notice that this is not the rate of climb in gravity axes, rather in the helicopter-based body axes, and because the orientation of the rotor and the high speed reached along the X-axis as well, the resultant flight condition may not appear like a climb at all. For instance, at around the 8^{th} second, the combination of the 3 body velocities and the nose-down pitch attitude of about -45 degrees results in a total velocity of about 180 ft/sec approximately, at an angle of -25 degrees below the horizon, which effectively has the helicopter losing altitude, although for the rotor it appears as a climb.

Figure 7.42 shows the main rotor power required and thrust coefficient C_T. The power decreases slightly and the helicopter rolls to the right, although the roll to the left increases the power to almost 2000 HP around $t = 4$ seconds. After that, the power starts to decrease, reaching a minimum of -400 HP at the point of maximum nose-down pitch angle, around $t = 8$ seconds. The power remains at all times below the maximum power available (2800 hp). C_T decreases slightly as the helicopter rolls to the right. For the left turn, more thrust is required and C_T increases, around $t = 3$ seconds, reaching 0.008. As the maneuver continues and the large nose-down pitching moment starts to develop, the thrust drops considerably into the negative values as the maneuver deteriorates and becomes unrealistic.

7.3.2 Rotor response

The time histories of the coefficients of the blade flap motion are shown in Fig. 7.43. Figure 7.43(b) shows the constant flap coefficient β_0, which decreases slightly from an initial starting value of 3° as the stick is deflected to the right in the first part of the maneuver. As δ_{lat} shifts to the left and the roll rate p starts to decrease, β_0 increases by more than 1°, with a peak at $t = 4$ seconds. After this time, β_0 decreases by more than 4° as the helicopter rolls to the left and pitches forward. The longitudinal flap coefficient β_{1c}, shown in Fig. 7.43(c), changes very little during the first 2 seconds of the maneuver, with a variation about 0.5° of no more tan 1° in amplitude. However, between $t = 2$ and $t = 4$ seconds of the maneuver, β_{1c} increases by more than 3°, tilting the rotor forward. This longitudinal tilt of the rotor plane are responsible for the nose-down pitch moment that follows. After this point, β_{1c} returns to values around zero, before increasing towards the end of the maneuver as it deteriorates. Figure 7.43(d) shows the lateral flap coefficient β_{1s}. β_{1s} does not change significantly over the first 2 seconds of the maneuver, except a slight tilt from an initial orientation slightly biased to the left to a $\beta_{1s} = 0°$. After 3 seconds, however, there is a short positive spike in β_{1s} followed by a large decrease around $t = 4$ seconds, which produces a lateral tilt of the rotor to the right, which increases p despite that the lateral stick is not removed from its leftmost position until 1 second later. After this point, β_{1s} oscillates between a slight tilt to the left and a neutral position for the remainder of the maneuver.

Figure 7.44 shows the time history of the different lag coefficients of the blade

lag motion. Figure 7.44(b) shows the constant lag coefficient ζ_0, which increases over the first two seconds of the maneuver, which effectively signifies a reduction in the lag angle (as the in-plane angle is negative for a lag displacement). The cosine and sine lag coefficients, ζ_{1c} and ζ_{1s}, shown in Figs. 7.44(c) and 7.44(d) respectively, are much smaller in magnitude, and oscillate about zero during the first two seconds of the maneuver. After $t = 3$ seconds, the average lag angle increases (ζ_0 decreases by 3° rapidly. At the same time, both the cosine and sine lag coefficients increase, particularly ζ_{1c}, which reaches a value of about 0.8°. After this time, ζ_0 increases gradually as the helicopter rolls to the right, ζ_{1s} returns fast to oscillations about its mean zero value, and ζ_{1c} also shows a more gradual return to zero.

The time histories of the coefficients of the blade torsional elastic deformation are shown in Fig. 7.45. The constant torsion coefficient, ϕ_0, shown in Fig. 7.45(b), oscillates with a mean amplitude of about 0.2°. Its mean value decreases on the first turn to the right, increases to positive, nose up values on the left roll, and decreases again as the helicopter rolls to the right a second time. The longitudinal torsion coefficient, ϕ_{1c}, in Fig. 7.45(c), and the lateral coefficient ϕ_{1s}, in Fig. 7.45(d), both decrease on the right turns, indicating a decrease in the local pitching moment on the rear and advancing sides, and a nose-down moment occurs in the front and retreating side, while the opposite occurs in the left turn.

7.3.3 Wake response

The behavior of the rotor wake under the lateral maneuver of Fig. 7.42(a) is depicted in Fig. 7.46, which shows the rear view of the wake tip filaments for six instants in time, which correspond to times $t = 2.09, 3.02, 4.19, 5.58, 6.98$ and 8.14 seconds (and coincide with revolutions number 9, 13, 18, 24, 30 and 35 after the start of the maneuver). The first instant corresponds to the end of the stick deflection to the right, which produces the maximum roll rate. The helicopter has rolled considerably to the right, and the effects of the high roll rate achieved, as shown in Fig. 7.39(b), are visible in the geometry, which gets closer to the rotor in the advancing side, and the roll up moves further downstream of the wake. The wake filaments on the retreating side, on the other hand, move further away from the rotor. At the next instant depicted, at $t = 3.02$ seconds, the lateral cyclic has been applied in the opposite direction, which is followed by a decrease in the roll rate, however the roll attitude continues to increase reaching its maximum at this instant, as seen in Fig. 7.39(c). So, while the geometry is rolled all the way to the way to the right, the roll rate is already negative and the wake geometry shows signs of it, such as a more compressed filaments in the retreating side as the rotor folds unto that part of the wake, and a tighter roll-up on the advancing side. At $t = 4.19$ seconds, the helicopter has reached its maximum roll rate to the left, yet it maintains a slightly positive roll attitude, as it has not recovered from the right roll. The geometry shows that the maximum negative roll rate increases the roll up in the retreating side. Moreover, notice that the entire wake is a lot closer to the plane of the rotor.

With a delay of about 1.4 seconds, the helicopter reaches its maximum bank angle in the port direction, but as the lateral cyclic has already been applied in the opposite direction, the maximum left bank is much lower than the maximum right bank, despite the deflections in both directions being of equal magnitude. The inversion of the roll rate eliminates the roll-up on the retreating side, and the wake starts getting closer to the rotor in the advancing side. Continuing the roll to the right shows the wake structure stretching away from the rotor, and no roll up occurs in neither the advancing nor the retreating side. The high roll rates are still obvious in the wake geometry dynamics, which shows the filaments are much closer together in the advancing side.

The side view of the wake geometry at the same instants during the roll reversal maneuver are shown in Fig. 7.47, and it helps understand the behavior of the wake during the maneuver. The first two instants shown of the side view of the rotor wake have signs of a positive pitch rate, although at this point the rates are still small in magnitude, as seen in Fig. 7.40(b). At the third instant, however, the pitch rate has past its maximum, which has brought the far wake closer to the plane of the rotor, as was appreciated from the rear view at the same instant, and has reverted signs with a high negative angular acceleration. The helicopter reacts with a nose-down pitch attitude, as seen in Fig. 7.40(c), and the wake starts to deform with the negative pitch rate. Soon after the pitch attitude becomes more and more negative, while the pitch rate remains constant at a very low negative value. This negative pitch rate brings the wake closer to the front of the rotor.

The distribution of induced velocities, shown in Fig. 7.48 for the same instants

depicted earlier, and its effect on the lift distribution can help us understand the effect of the wake dynamics on the response of the helicopter, both on-axis and off-axis. As the helicopter starts to roll to the right, the wake vortices get closer to the rotor in the advancing side, increasing the induced velocities in that part of the rotor. The second instant corresponds to the maximum roll attitude to the right, however the roll rate has already started to reverse direction, while some positive (nose-up) pitch rate. The combination of both brings the wake closer to the rotor, which increases the induced velocities overall, specially in the rear of the rotor near the tips. The following instants in the maneuver sequence produce a large nose down pitching moment as the wake rolls to the left, which push the wake filaments further away from the rotor, reducing the inflow to really low values all over the rotor.

The angle of attack distribution at the same times in the maneuver is shown in Fig. 7.49. The angle of attack decreases with increasing inflow, and vice-versa. However, there are several other factors affecting the angle of attack in this maneuver, as applied lateral input and the coupled longitudinal reaction produce large velocities in all three directions. For this reason, both U_P and U_T change considerably during the maneuver. In addition to this, the lateral cyclic changes considerably, which affects the geometric angle of attack cyclic in a sinusoidal manner. The first instant considered sees an increase in the angle of attack in the front, where the induced velocities are lowest, while it is lower in the rear of the rotor, despite the inflow decreasing in that region as well. The reason for the decrease is that the lateral cyclic applied is maximum at this point. Notice that an in increase in the lateral stick de-

flection corresponds to a decrease of the lateral cyclic at the swashplate. Therefore, the blade pitch is lowest at $\psi = 0$ and the rotor tilts to the right. Based on this, the maximum lateral stick deflection reached at this instant in the maneuver decreases the angle of attack in the rear of the rotor, despite the higher inflow there, and increases it in the front. In the next instant, the inflow increases slightly over the whole rotor, which decreases the angle of attack. At the same time, the lateral stick is almost deflected at the maximum left position, which decreases the angle of attack further in the front, and decreases it in the back of the rotor. At the next instant, at $t = 4.19$ seconds, the lateral stick still remains at the maximum left deflection, which increases the angle of attack in the rear and decreases it in the back, in spite of the induced velocities having the opposite effect. In addition, the roll maneuver starts to develop important translational and rotational velocities at this point that affect the velocities in all three directions. For this reason, both U_P and U_T start to play an important role in the angle of attack that at times dominates the effect of the induced velocities. In the next three instants, in which the inflow becomes low as the filaments are pushed far from the rotor plane, the angle of attack becomes dominated be the other effects just mentioned.

Figure 7.50 shows the distribution of elemental lift, $C_L M^2$, at the times considered previously. The non-dimensional lift shown increases proportionally to the angle of attack and the Mach number. At $t = 2.09$ seconds, the higher angle of attack seen in the front of the rotor produces an area of higher lift, increasing considerably more on the second quadrant of the rotor, although $C_L M^2$ decreases in the rear of the rotor, where α is lower. The net effect of the increase in the front and

decrease in the back is a slight reduction in overall lift produced, which decreases the average flap β_0, in Fig. 7.43(b), while the shift of the region of higher lift from the retreating side to the front of the rotor increases β_{1s} (Fig. 7.43(d)). The net thrust produced in this first right turn therefore decreases, as seen in Fig. 7.42. As the angle of attack decreases considerably in the front of the rotor in the next instant, the lift is also reduced in that area. However, both α and $C_L M^2$ start to increase in the rear half of the rotor over the next 2 seconds, slightly biased to the advancing side, which increases the overall flap of the blades and thrust produced. This shift to the rear-retreating side of the area of highest lift increases the longitudinal flapping, β_{1c} (Fig. 7.43(c)), tilting the rotor forward, and decreases β_{1s}, which tilts the tip path plane to the right. As the maneuver progresses beyond $t = 4$ seconds, the magnitude of the overall lift produced decreases continuously, and so does the thrust coefficient, reducing the average flapping β_0, and the area of higher lift moves gradually towards the front, reducing the nose-down moment and returning β_{1c} to a neutral position.

The drag coefficient C_D at different times of the maneuver is shown in Fig. 7.51. Initially, the higher values of α in the front of the rotor increase the drag forces, which produce pockets of particularly high drag coefficient, where both the angle of attack and the Mach number are high. However, C_D decreases over the rest of the rotor, effectively reducing the lag angle. As the maneuver reaches the maximum left δ_{lat} around $t = 4$ seconds, the higher values of the angle of attack on the retreating and rear sides produce a region of very high C_D (notice that a different scale is used to help visualize the new range in values), particularly in the rear of the rotor disk.

After this time, the drag decreases considerably, although some high values remain towards the tip of the advancing side. This reduced drag decreases the overall lag angle, although as the higher values occur on the advancing side, ζ_{1c} decreases very slowly.

How the actual lift distribution affects pitch and roll motion can be seen by multiplying the value at each point on the rotor by the moment arm with respect to the 0-180 degree axis, $r \sin\psi$, for the contribution to the roll moment and to the 90-270 degree axis, $r \cos\psi$, for the pitch contribution. Figure 7.53 shows the distribution of the lift contribution to the roll moment, $rC_L M^2 \sin\psi$, at the different times on the roll reversal maneuver considered earlier. At the first instant, the higher values on the retreating side (negative because the sign of the moment arm, $r \sin\psi$ is negative on the retreating side) contribute to the roll towards the starboard. The next two instants, in the transition and full roll to the left, clearly show that the lift contribution is higher in the advancing side, producing the rolling moment that turns the helicopter. The next instant is quite neutral, as it is reflected in a transition roll rate between the port and starboard rolls. Finally, the last two instants show an area of negative contribution in the advancing side, and the net effect is the second roll to the starboard of the maneuver. The lift contribution to the off-axis degree of freedom, $rC_L M^2 \cos\psi$, is shown in Fig. 7.52. In the first time considered, the lift is evenly distributed between the front and the back halves of the rotor. The next instant sees a slightly higher contribution in the front half, which develops into the slight nose-up pitch rate seen in Fig. 7.40(b). However, in the next instant sees an inversion of the area of higher influence, which then switches to the rear half

of the rotor, contributing to a large nose-down pitching moment. The following two instants maintain the nose-down moment, and in the final time considered, a reverse is seen again with a large area of higher contribution to pitch in the front half, producing the fast change to a positive pitch rate seen in Fig. 7.40(b).

In summary, the application of a sequence of right-left-right-level lateral stick input deflections produces a roll reversal maneuver with large roll rates that follow the application of the lateral cyclic. Some important roll angles are produced in the right turns. The left turn does not develop as large a roll angle because there is a lag in the reaction between the application of the lateral cyclic and the roll attitude and the application of the lateral input in the opposite direction occurs before the left roll angle has time to develop. The roll rate brings the wake filaments closer to the rotor in the side that it is turning into, the advancing side in the starboard roll and the retreating side in the port roll. As a consequence the induced velocities increase with the proximity of the vortices and that affects the angle of attack and lift distribution. Moreover, the off-axis response was also analyzed. An initial nose-up pitch rate develops with the first turn to the right, although the longitudinal orientation of the helicopter is not greatly affected. The inversion of the roll, to the port side, produces a larger nose-down pitch rate which develops a large nose-down pitch attitude. As a consequence, the rotor operates in an effective climb, despite the fact that the helicopter is losing altitude slightly, which pushes the wake vortices away from the rotor plane and affects the overall angle of attack and lift distribution as well.

7.4 Numerical characteristics

The inclusion of a vortex model to predict the induced velocities is associated with much higher computational costs than other simpler inflow models, such as dynamic inflow (Refs. 24, 36) (see Section 6.6).

However, the cost of the integration of the equations of motion with the time-marching free wake model is remarkably lower than in trim. The main reason is that the free wake model only needs to be evaluated for the current time-step, instead of being converged at every call of the free wake. This is a significant improvement computationally over the use of a relaxation free wake model (Ref. 6), which required the inflow and circulation to converge at each revolution of the maneuver.

As mentioned in Section 6.6, the results in the present study were obtained using a 2.5 GHz Quad G5 (two dual core PowerPC processors) Macintosh computer with 1GB of RAM, although the code is not designed to run in multiple processors and the resultant effect was that of running in a single PowerPC processor at 2.5 GHz. In such a machine, it takes about 2.18 minutes to complete the equivalent time of a full revolution (1 rotor revolution is completed in approximately 0.24 seconds at a rotational speed of 27 rad/sec), which translates into 3.6 seconds per 10-degree time step. Compared to a 3-state dynamic inflow model (Ref. 36), which needs approximately 43 seconds on average on the same machine to complete a revolution (and thus taking about 1.2 seconds per 10-degree time step), the time-marching free wake only takes about 3 times longer than dynamic inflow, which is a lot less than one would expect for a vortex-method.

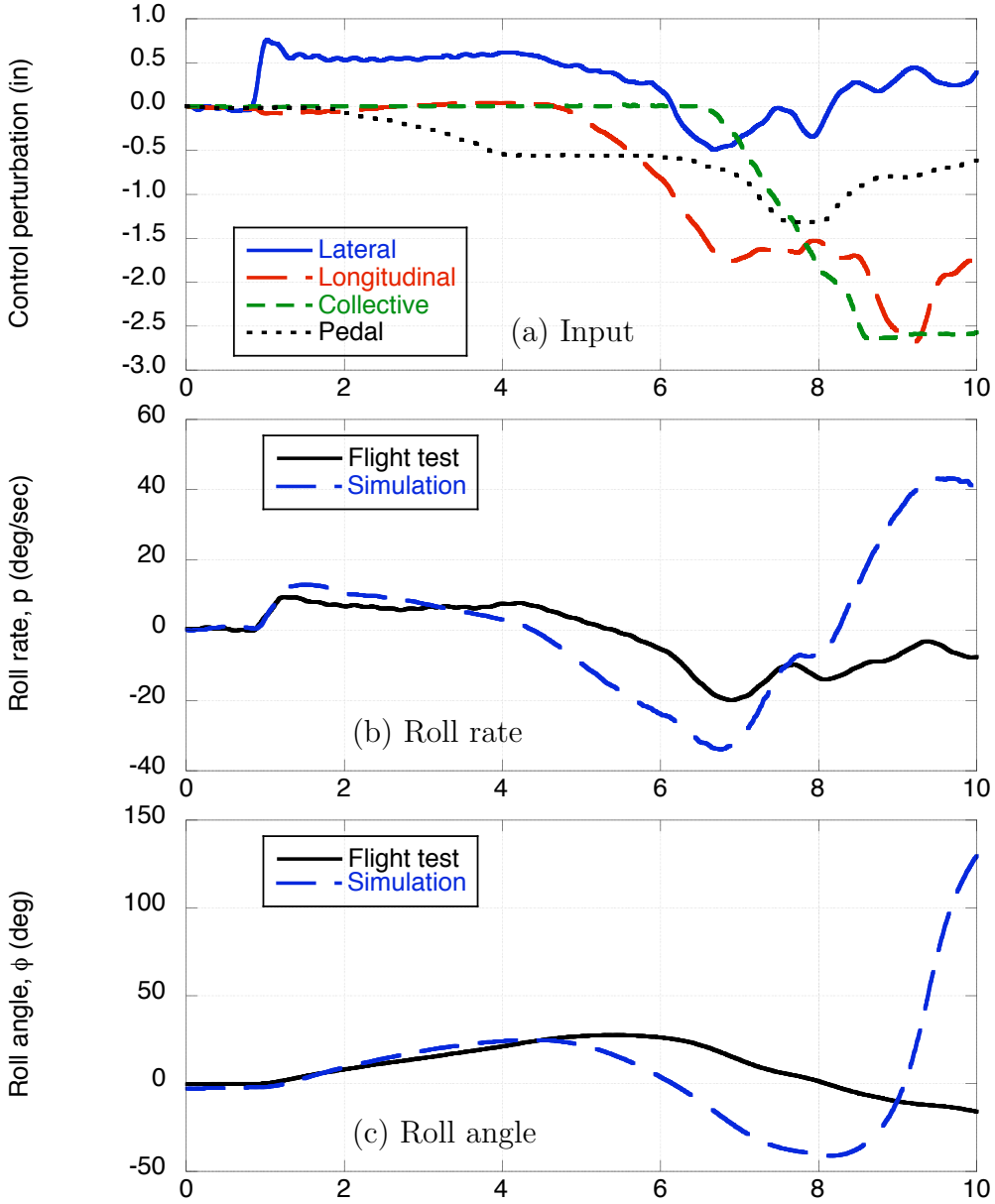

Figure 7.1: Time history of the control input, roll rate p, and roll angle ϕ, for a lateral maneuver; $V = 1$ kt.

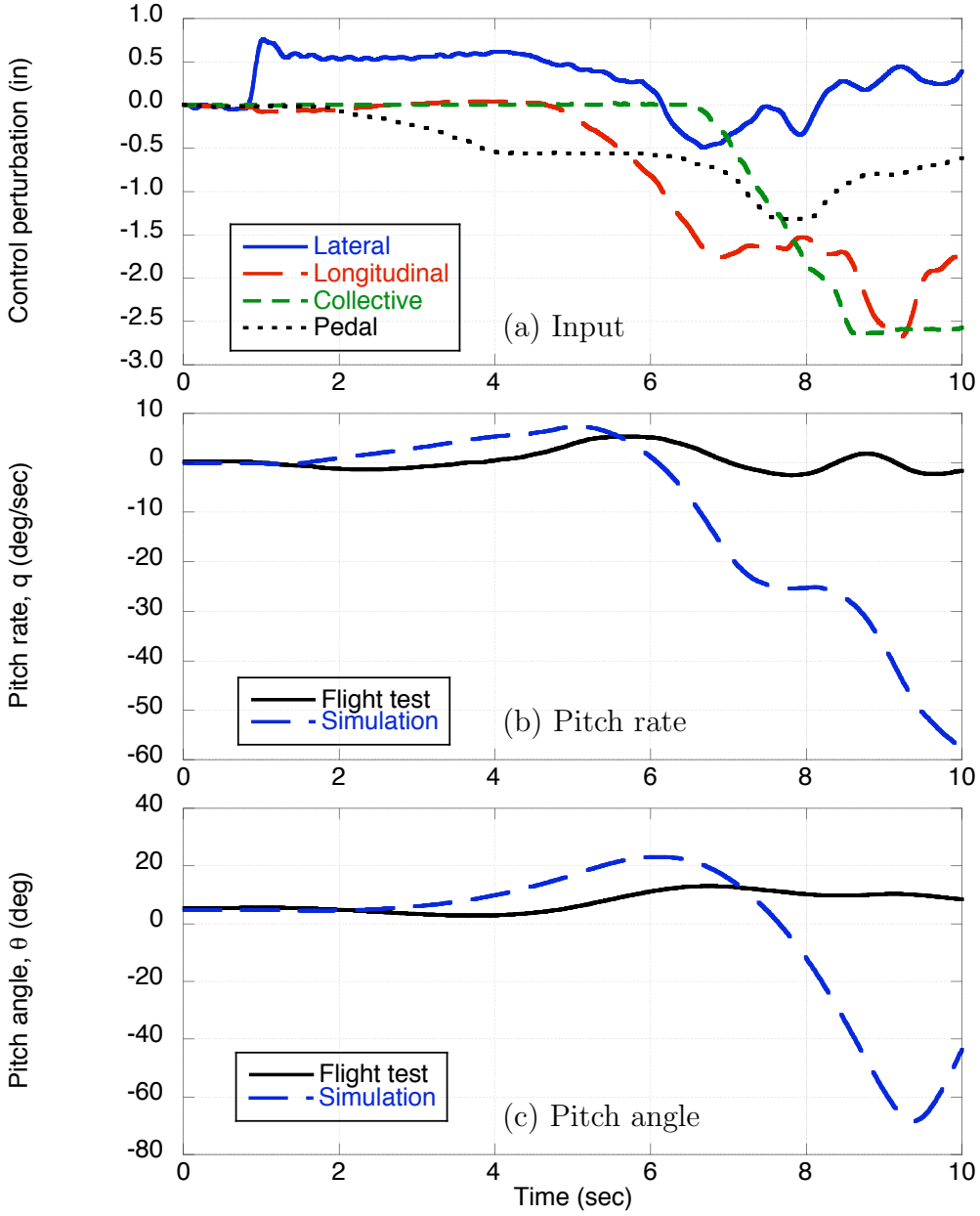

Figure 7.2: Time history of the control input, pitch rate q, and pitch angle θ for a lateral maneuver; $V = 1$ kt.

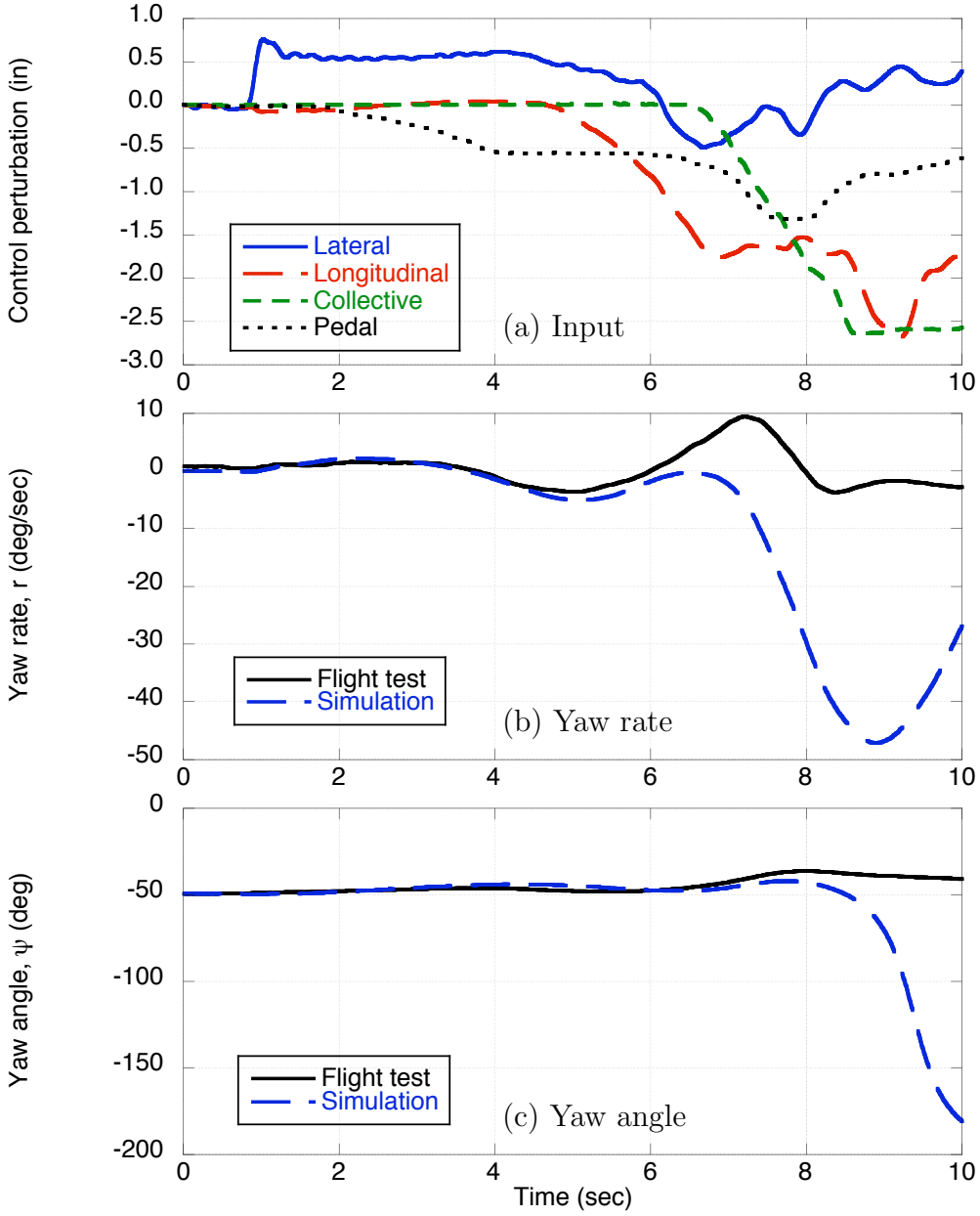

Figure 7.3: Time history of the control input, yaw rate r and yaw angle ψ for a lateral maneuver; $V = 1$ kt.

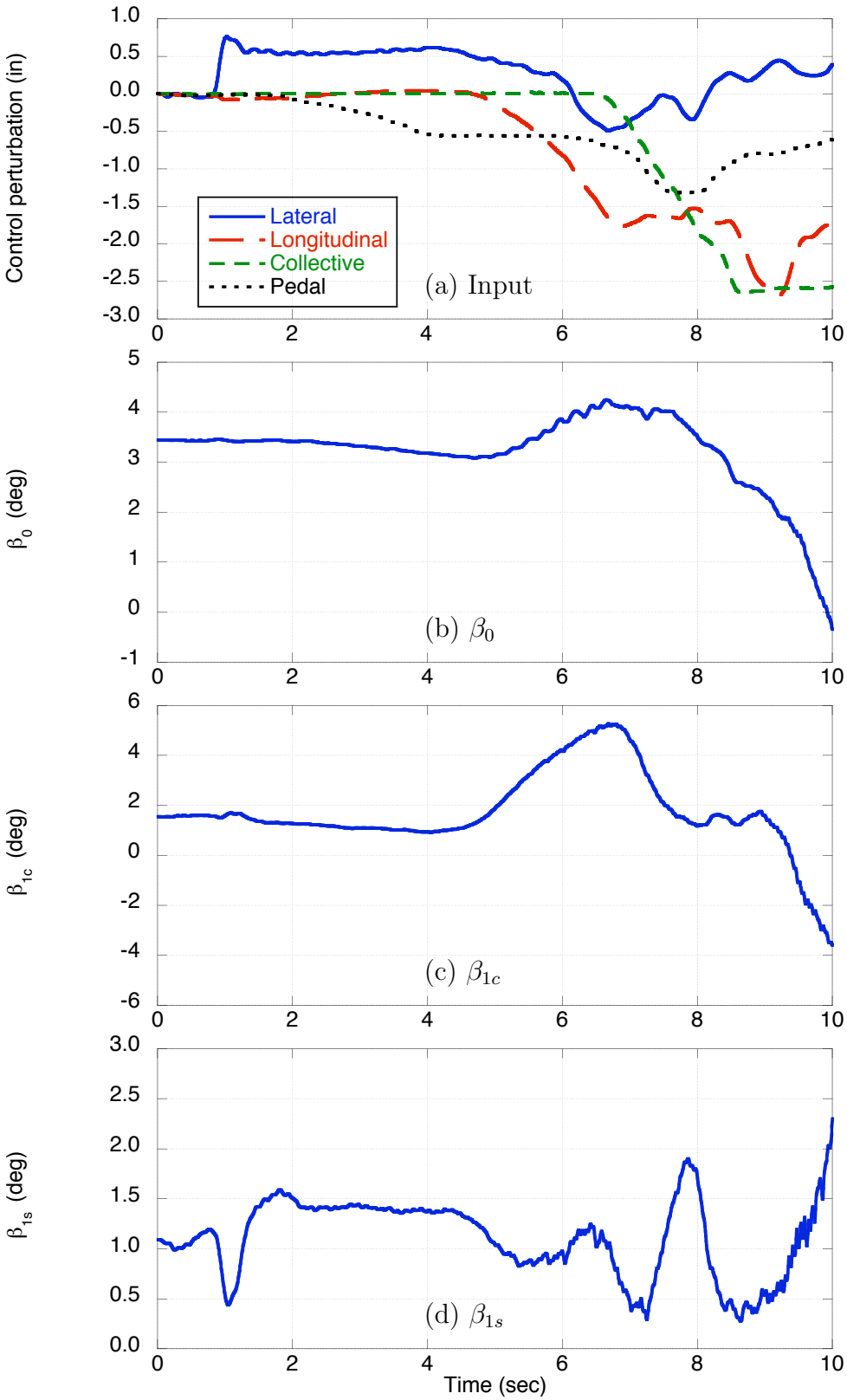

Figure 7.4: Time history of the control input and flap coefficients, β_0, β_{1c} and β_{1s} for a lateral maneuver; $V = 1$ kt.

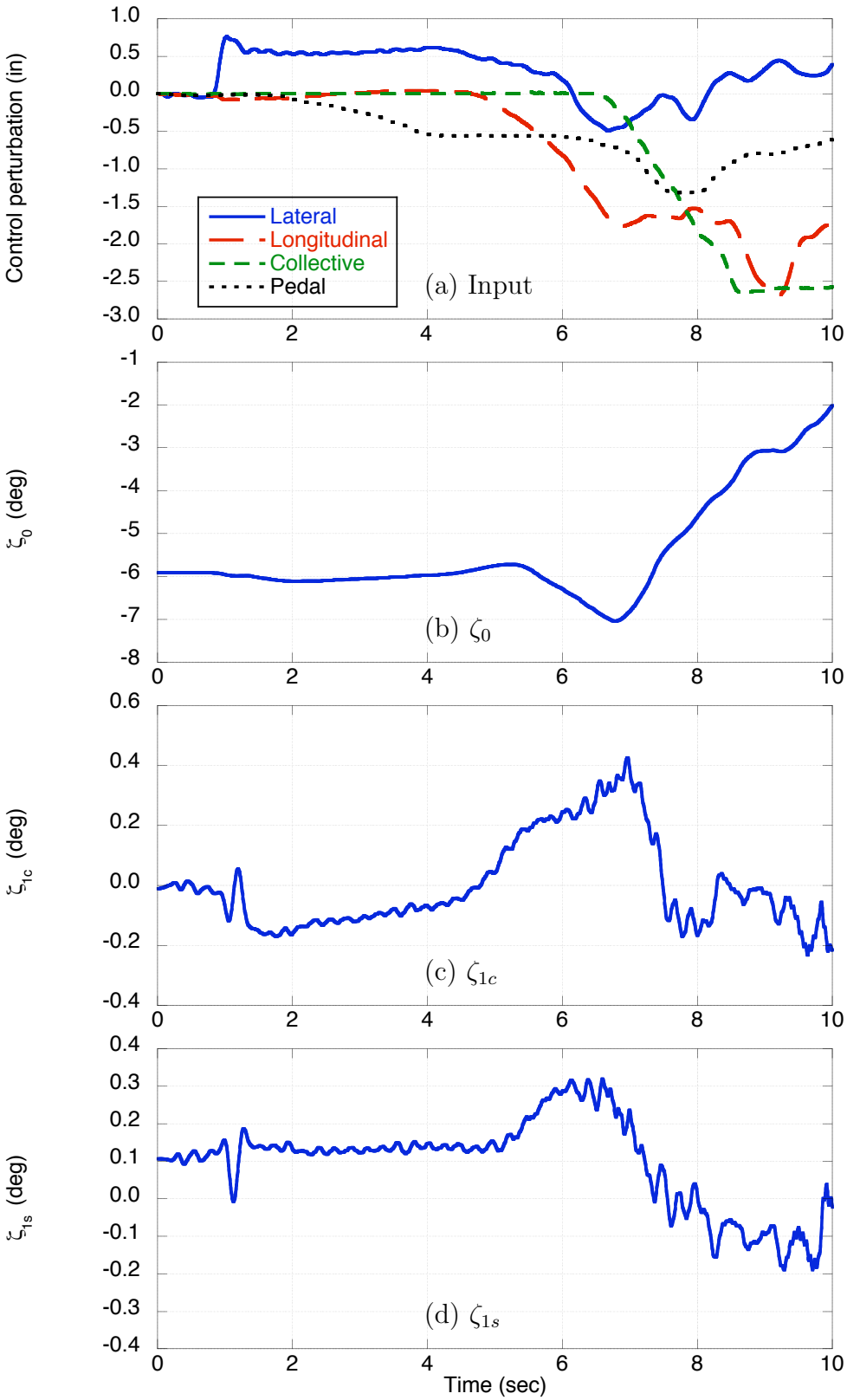

Figure 7.5: Time history of the control input and lag coefficients, ζ_0, ζ_{1c} and ζ_{1s} for a lateral maneuver; $V = 1$ kt.

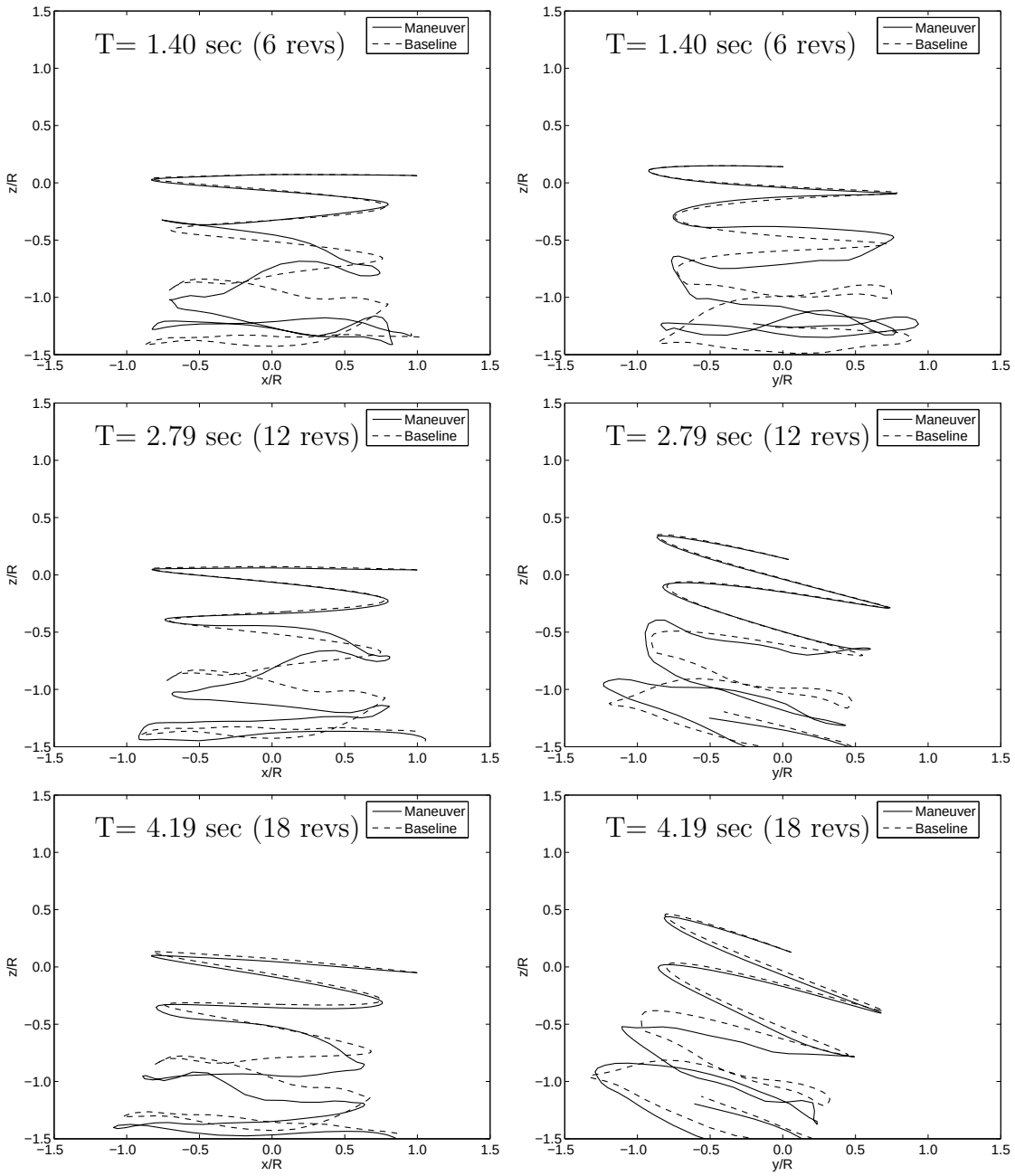

Figure 7.6: Side (left) and rear (right) views of the wake geometry at different times for a lateral maneuver compared to the baseline starting condition; $V = 1$ kt.

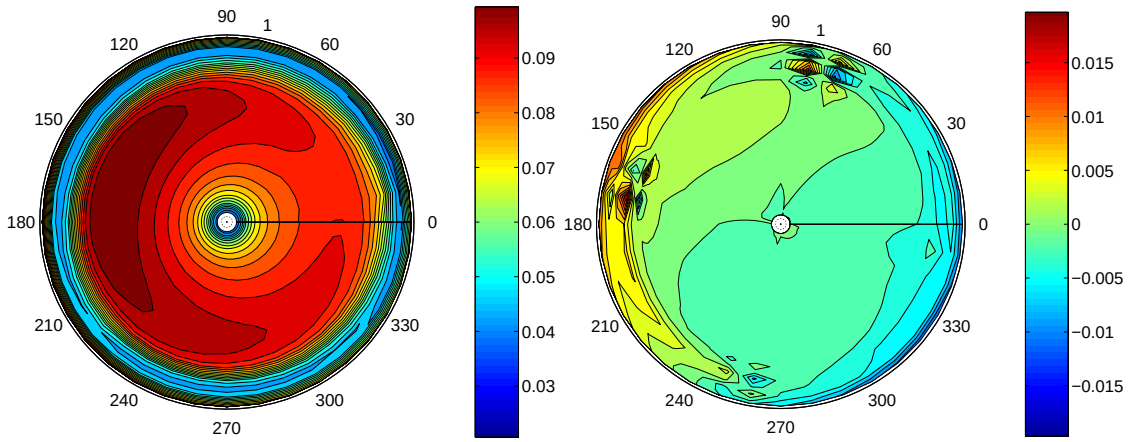

(a) T= 1.40 sec (6 revs) (b) T= 1.40 sec (6 revs)

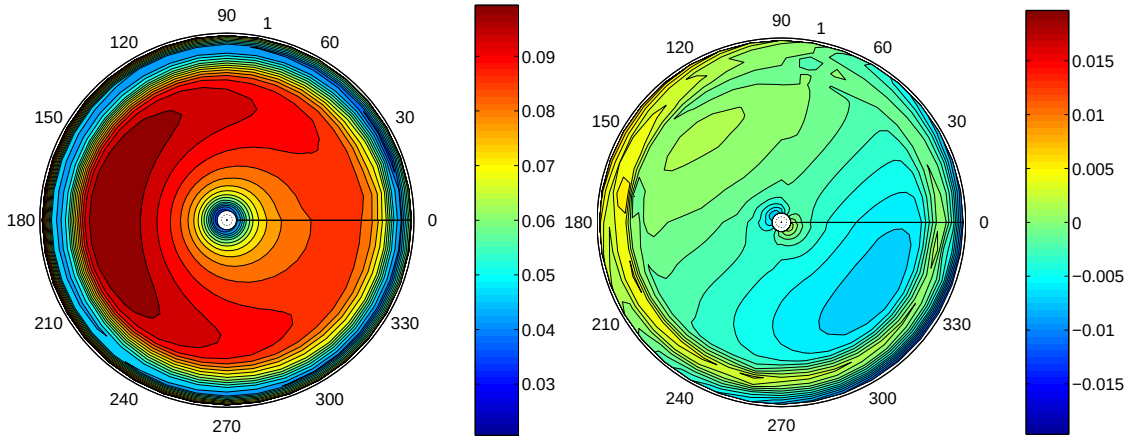

(c) T= 2.79 sec (12 revs) (d) T= 2.79 sec (12 revs)

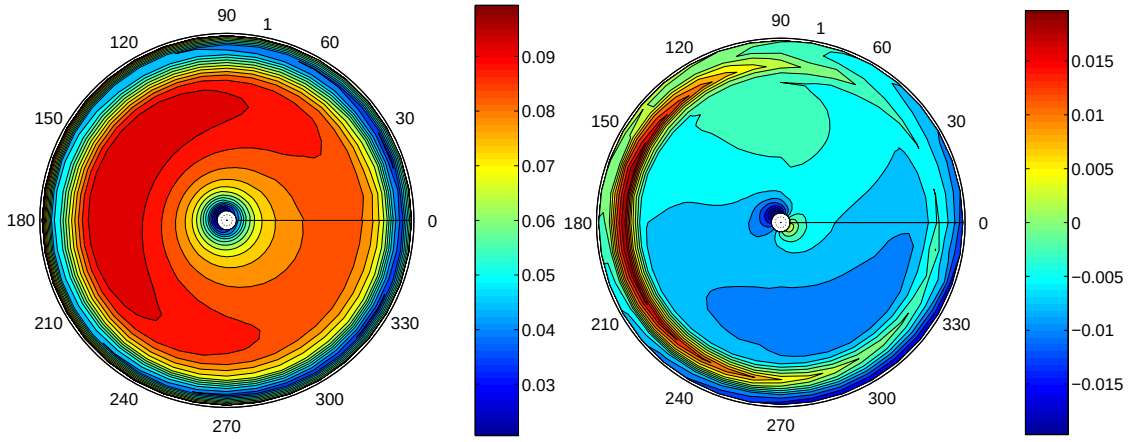

(e) T= 4.19 sec (18 revs) (f) T= 4.19 sec (18 revs)

λ $\Delta\lambda$

Figure 7.7: Inflow λ (left) and inflow difference (since the beginning of the maneuver) $\Delta\lambda$ (right) at different times for a lateral maneuver; $V = 1$ kt.

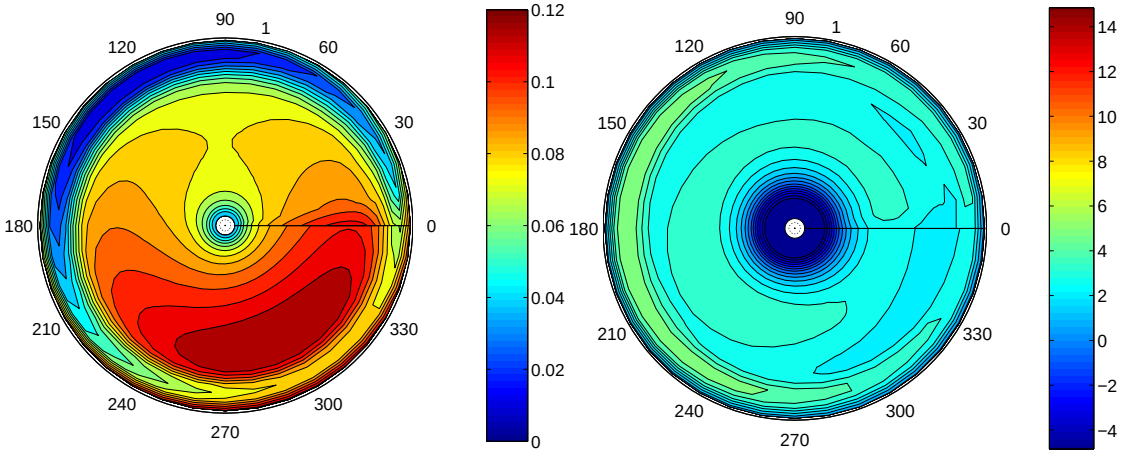

(a) T= 1.40 sec (6 revs) (b) T= 1.40 sec (6 revs)

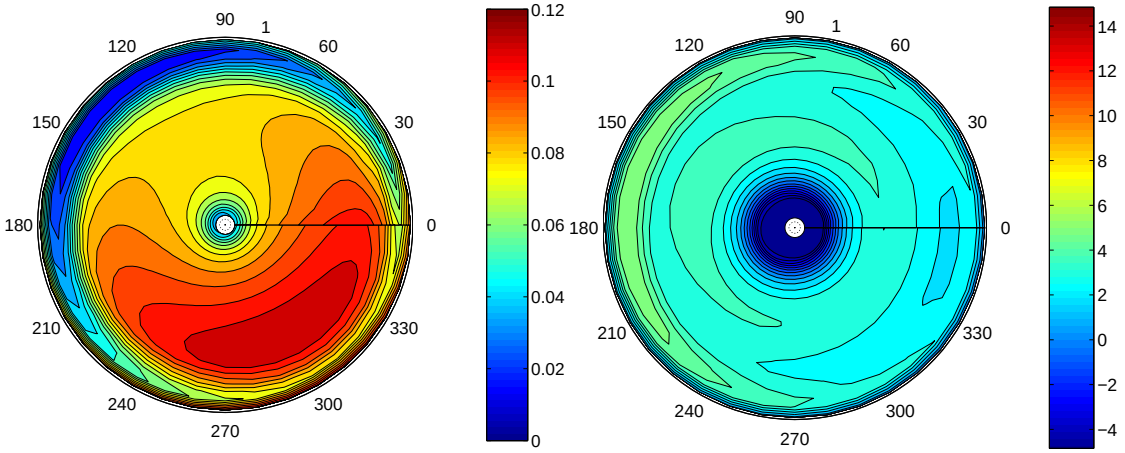

(c) T= 2.79 sec (12 revs) (d) T= 2.79 sec (12 revs)

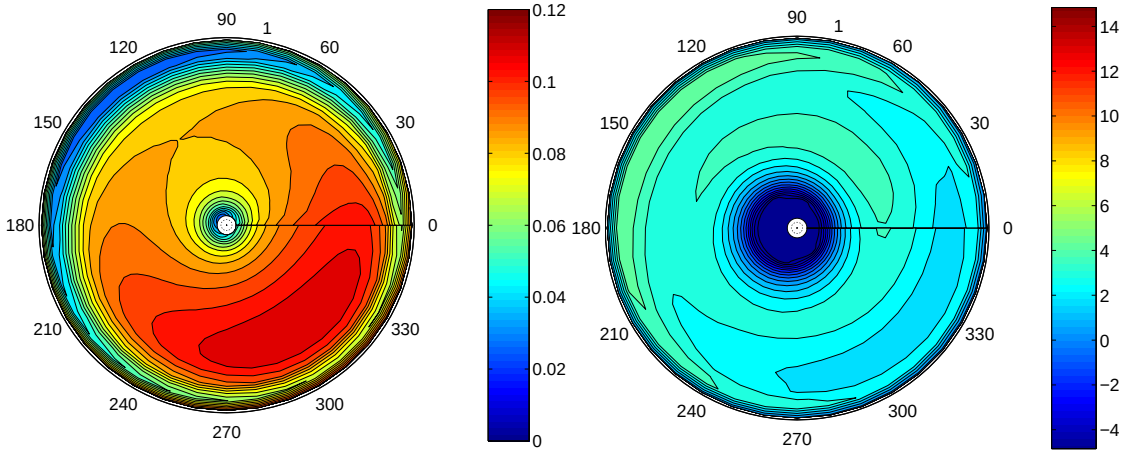

(e) T= 4.19 sec (18 revs) (f) T= 4.19 sec (18 revs)

U_P α

Figure 7.8: Perpendicular sectional velocity U_P (left) and angle of attack α (right) distribution at different times for a lateral maneuver; $V = 1$ kt.

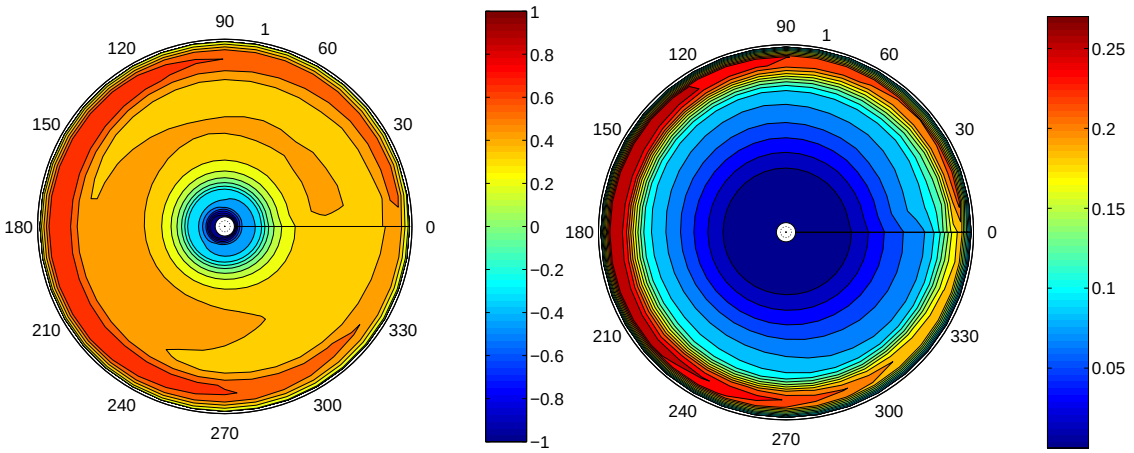

(a) T= 1.40 sec (6 revs) (b) T= 1.40 sec (6 revs)

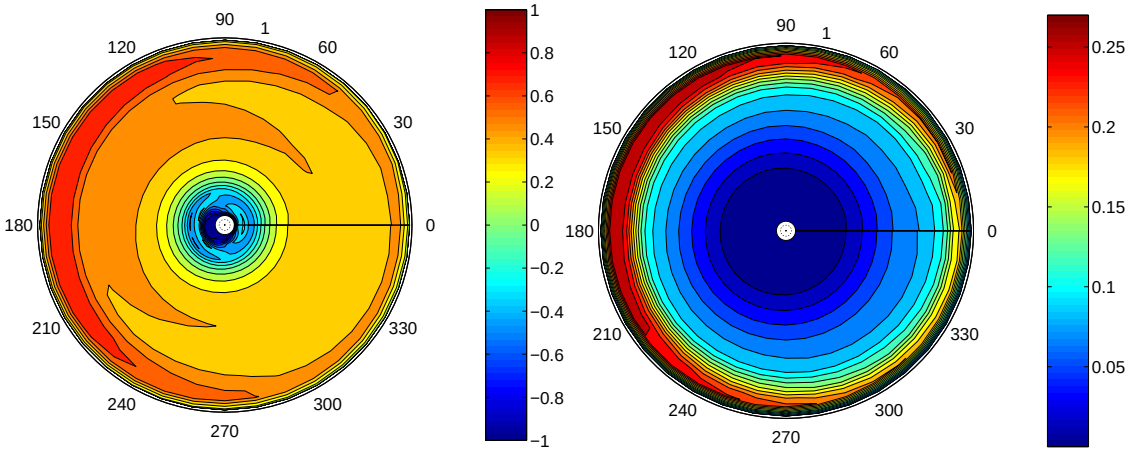

(c) T= 2.79 sec (12 revs) (d) T= 2.79 sec (12 revs)

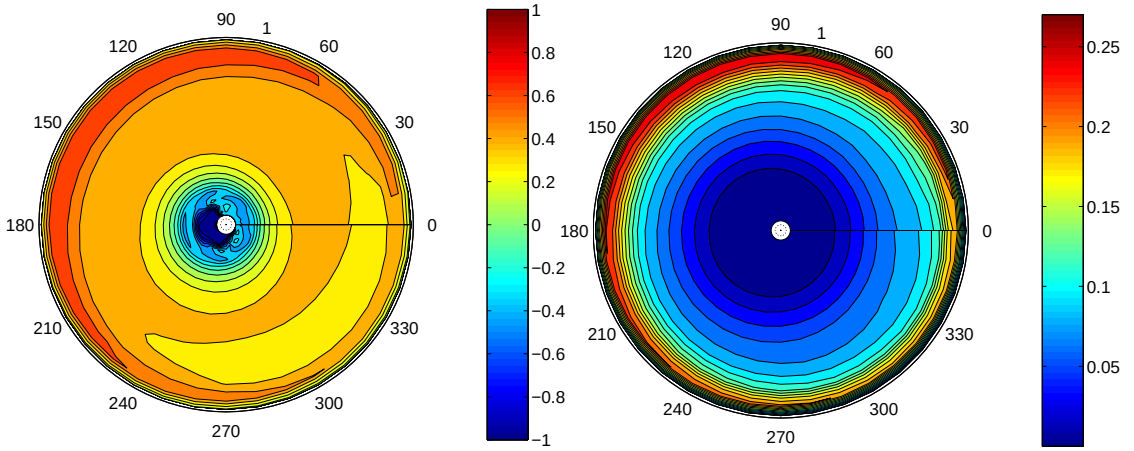

(e) T= 4.19 sec (18 revs) (f) T= 4.19 sec (18 revs)

C_L $C_L M^2$

Figure 7.9: Distribution of lift coefficient C_L (left) and elemental lift $C_L M^2$ (right) distribution at different times for a lateral maneuver; $V = 1$ kt.

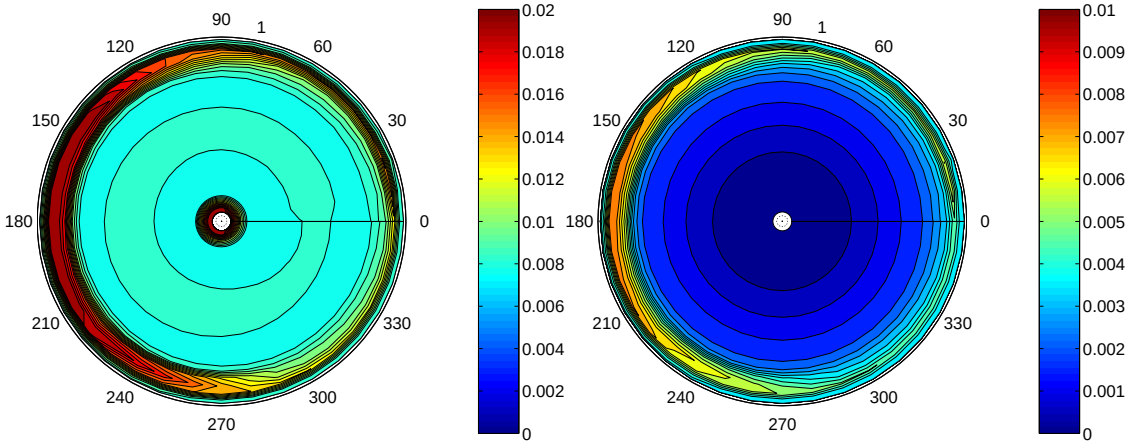

(a) T= 1.40 sec (6 revs)

(b) T= 1.40 sec (6 revs)

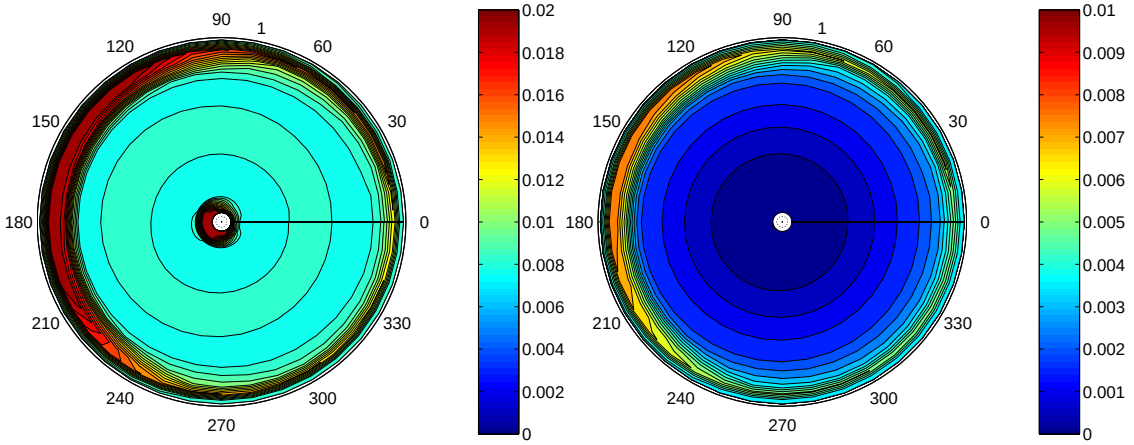

(c) T= 2.79 sec (12 revs)

(d) T= 2.79 sec (12 revs)

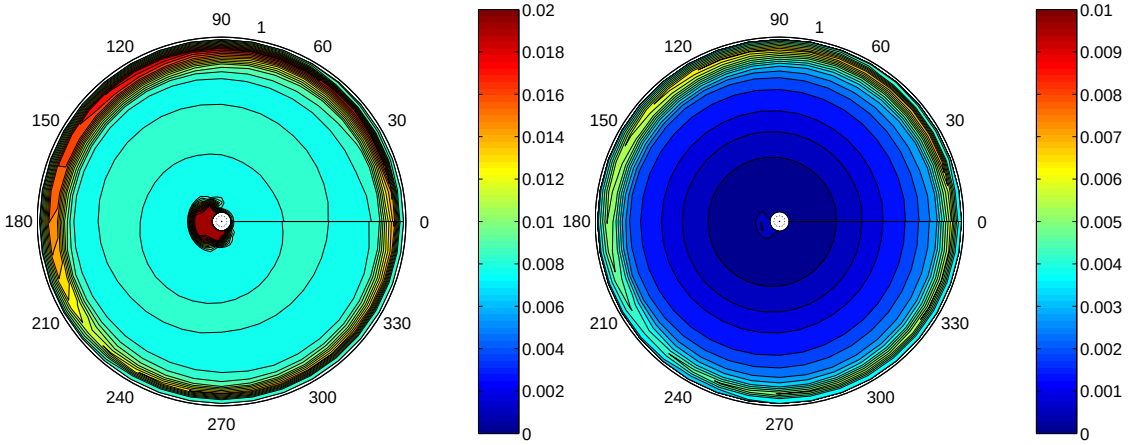

(e) T= 4.19 sec (18 revs)

(f) T= 4.19 sec (18 revs)

C_D

$C_D M^2$

Figure 7.10: Distribution of drag coefficient C_D (left) and elemental drag $C_D M^2$ (right) distribution at different times for a lateral maneuver; $V = 1$ kt.

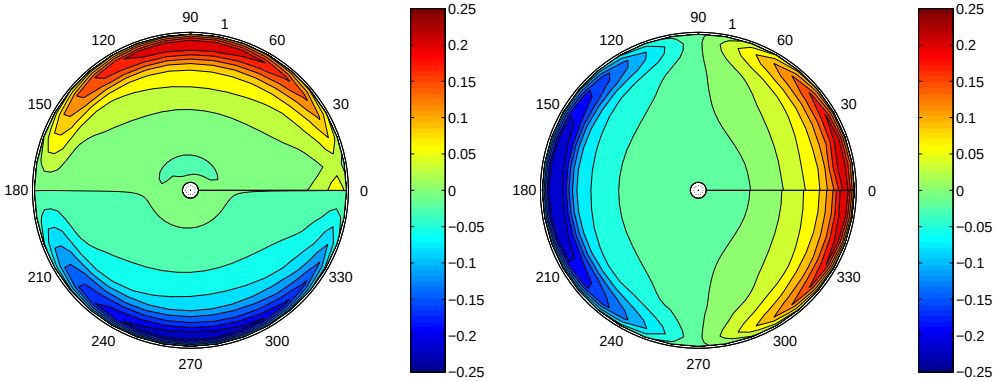

(a) T= 0.24 sec (1 rev)

(b) T= 0.24 sec (1 rev)

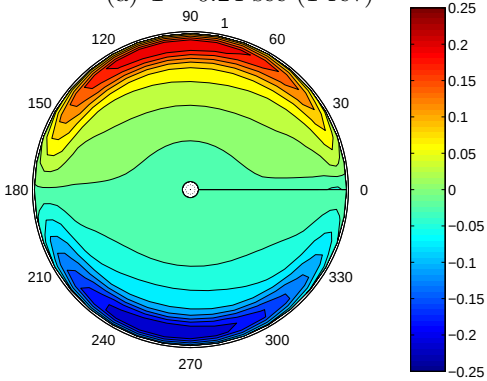

(c) T= 1.40 sec (6 revs)

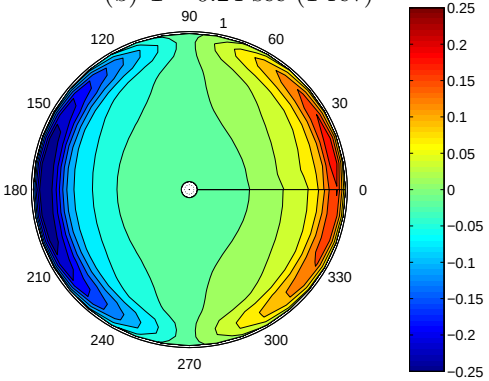

(d) T= 1.40 sec (6 revs)

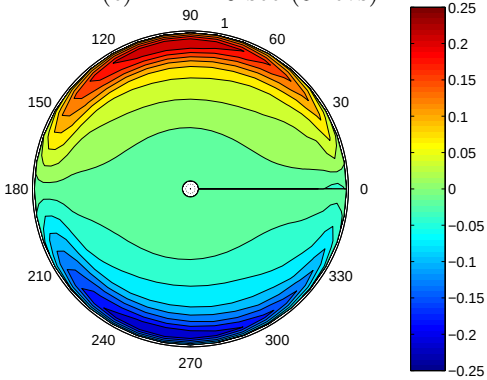

(e) T= 2.79 sec (12 revs)

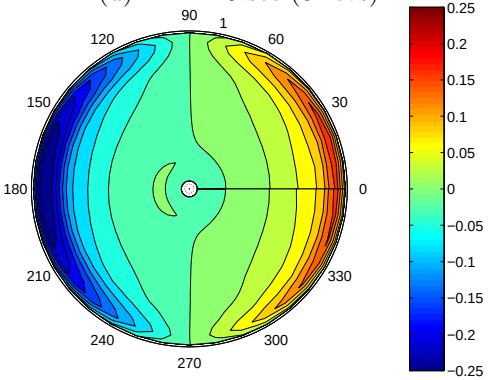

(f) T= 2.79 sec (12 revs)

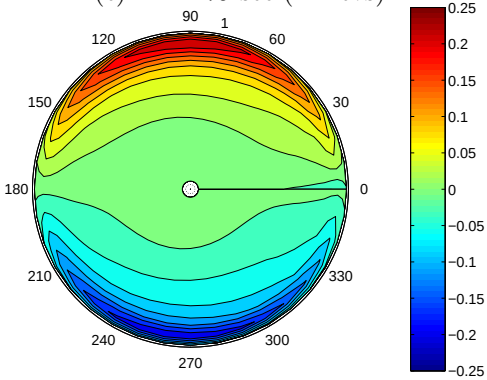

(g) T= 4.19 sec (18 revs)

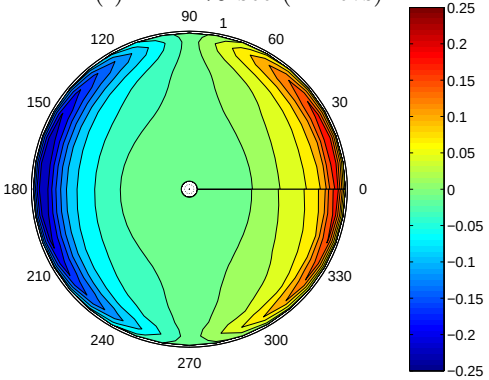

(h) T= 4.19 sec (18 revs)

Figure 7.11: Lift contribution to roll (left) and pitch (right) for a lateral maneuver; $V = 1$ kt.

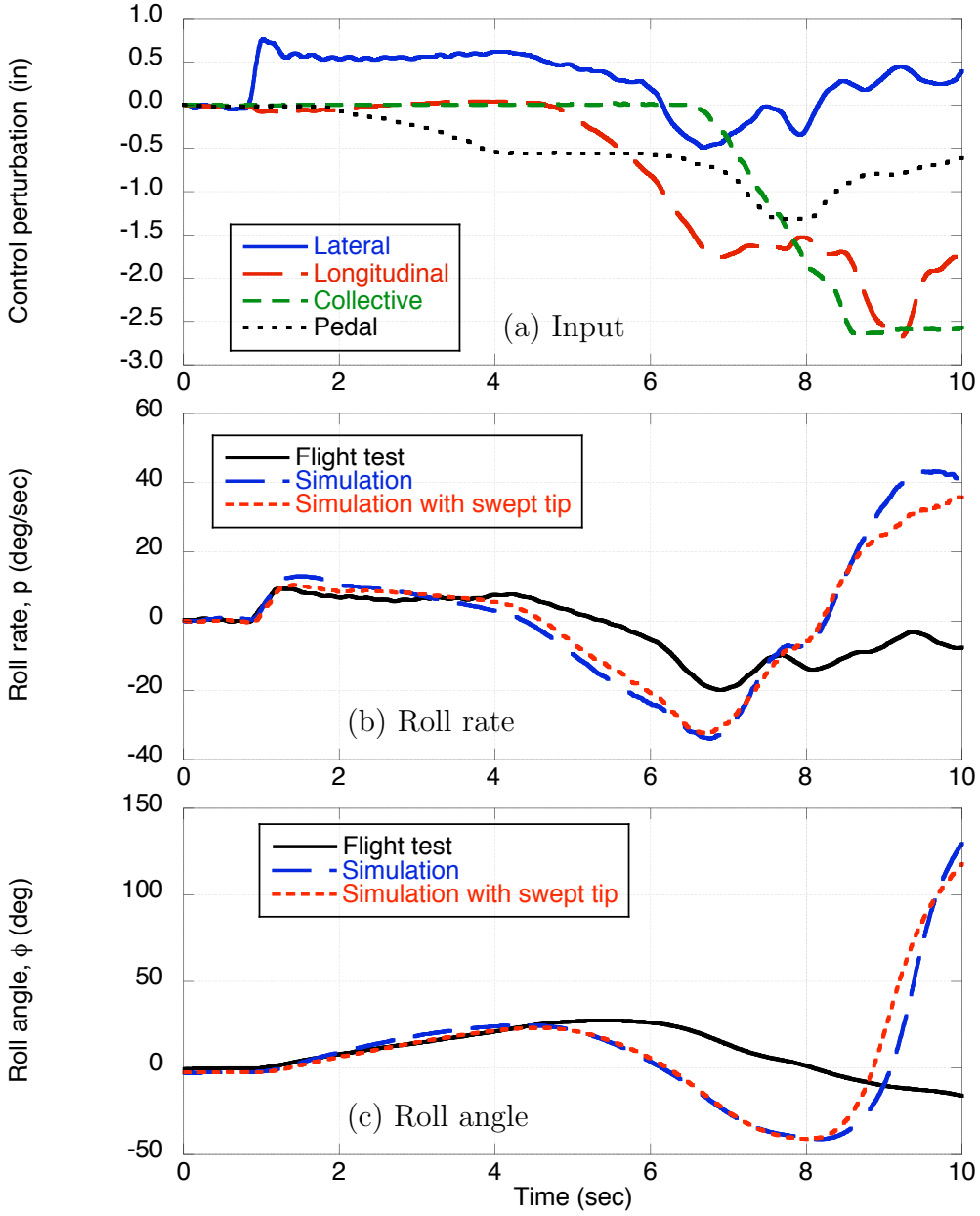

Figure 7.12: Time history of the control input, roll rate p and roll angle ϕ for a lateral maneuver with the swept tip modeled in the blade; $V = 1$ kt.

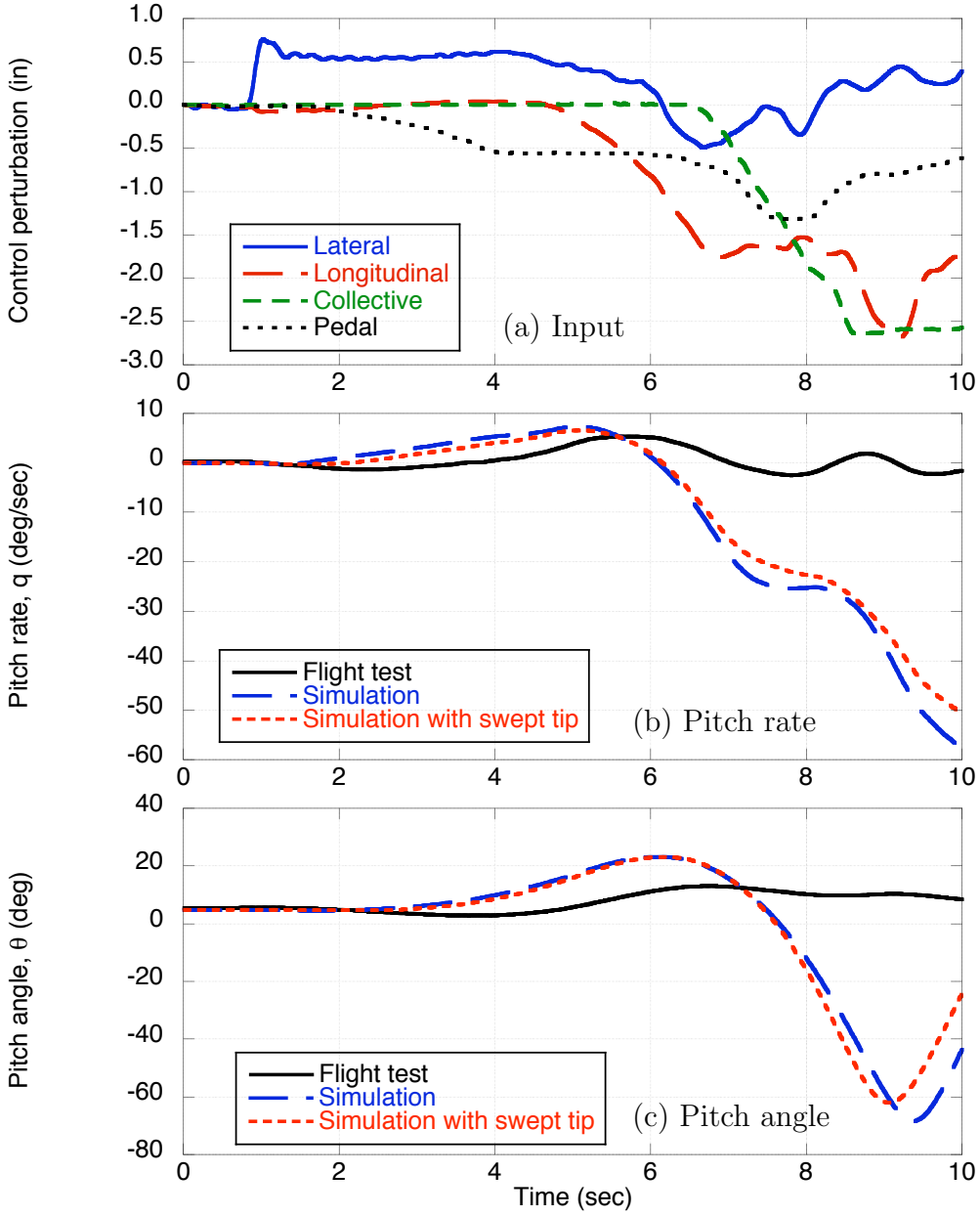

Figure 7.13: Time history of the control input, pitch rate q and pitch angle θ for a lateral maneuver with the swept tip modeled in the blade; $V = 1$ kt.

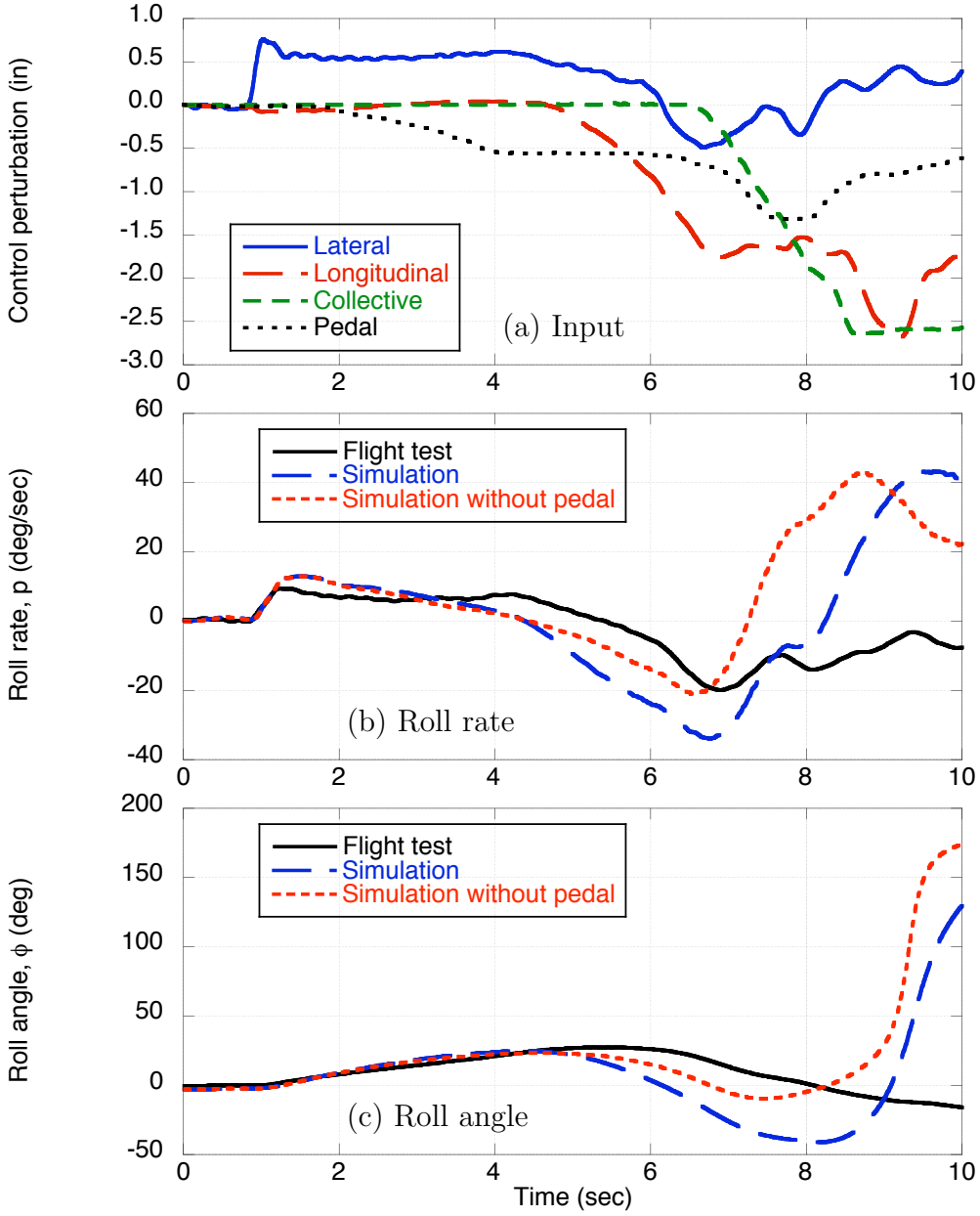

Figure 7.14: Time history of the control input, roll rate p and roll angle ϕ for a lateral maneuver with no pedal input; $V = 1$ kt.

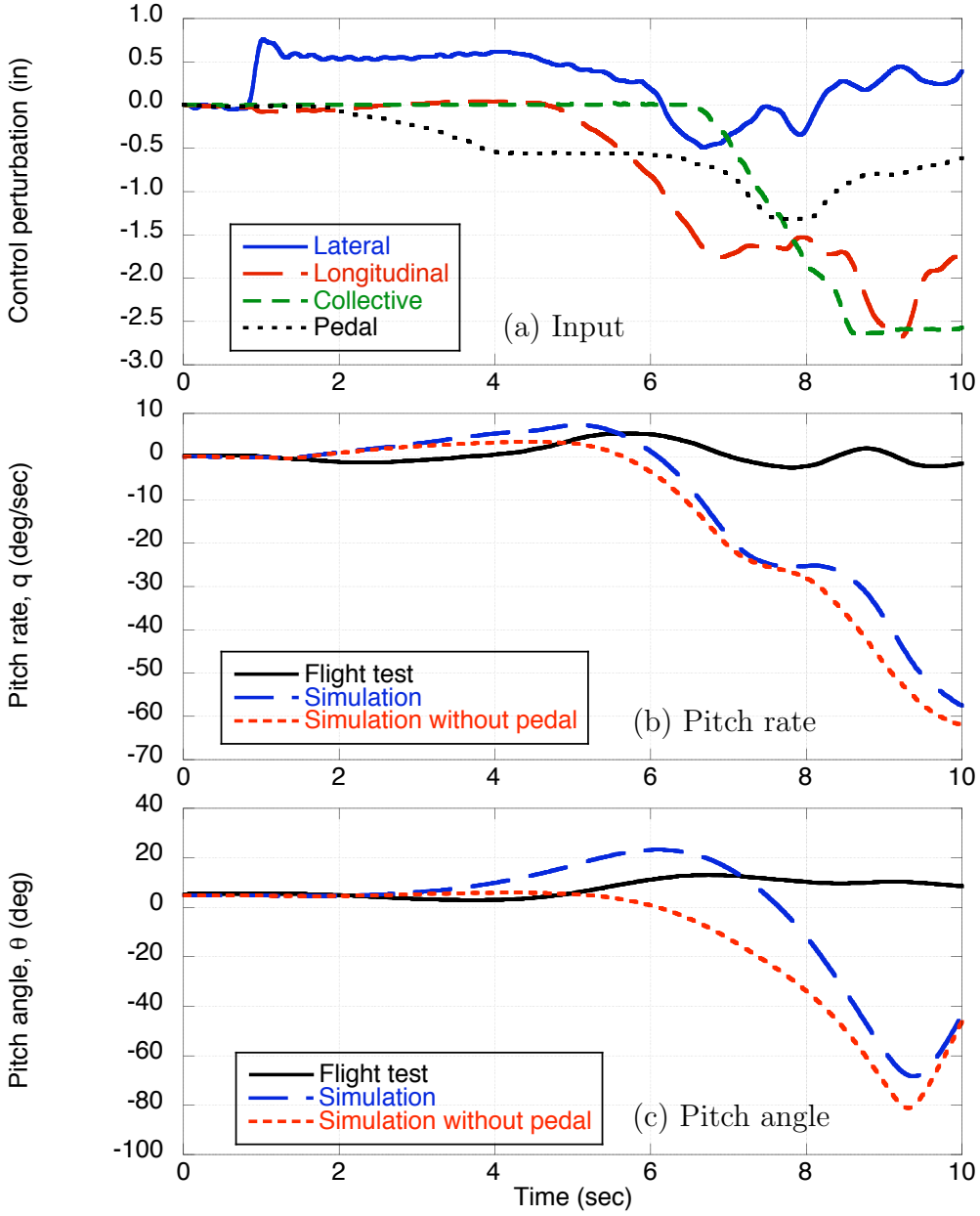

Figure 7.15: Time history of the control input, pitch rate q and pitch angle θ for a lateral maneuver with no pedal input; $V = 1$ kt.

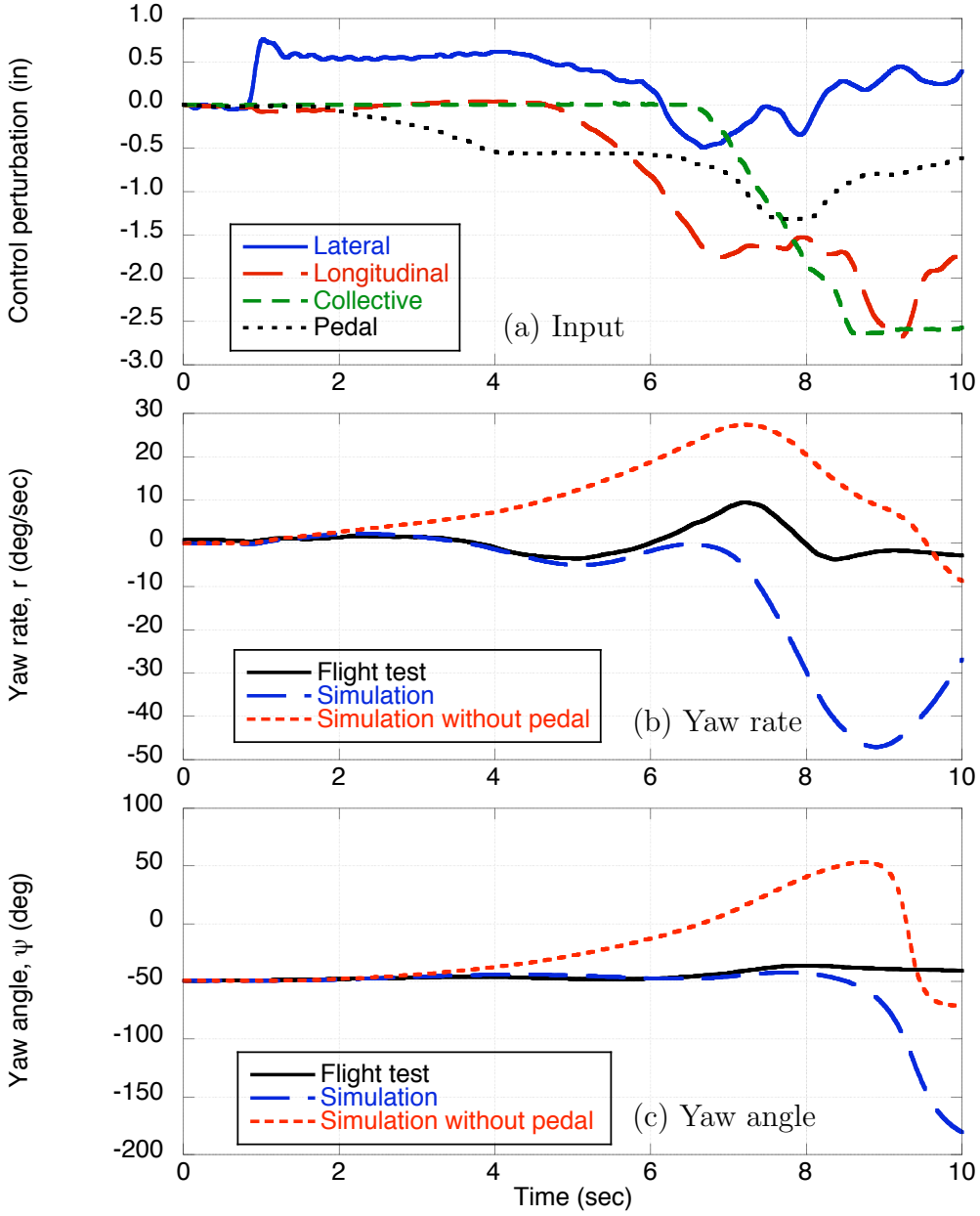

Figure 7.16: Time history of the control input, yaw rate r and yaw angle ψ for a lateral maneuver with no pedal input; $V = 1$ kt.

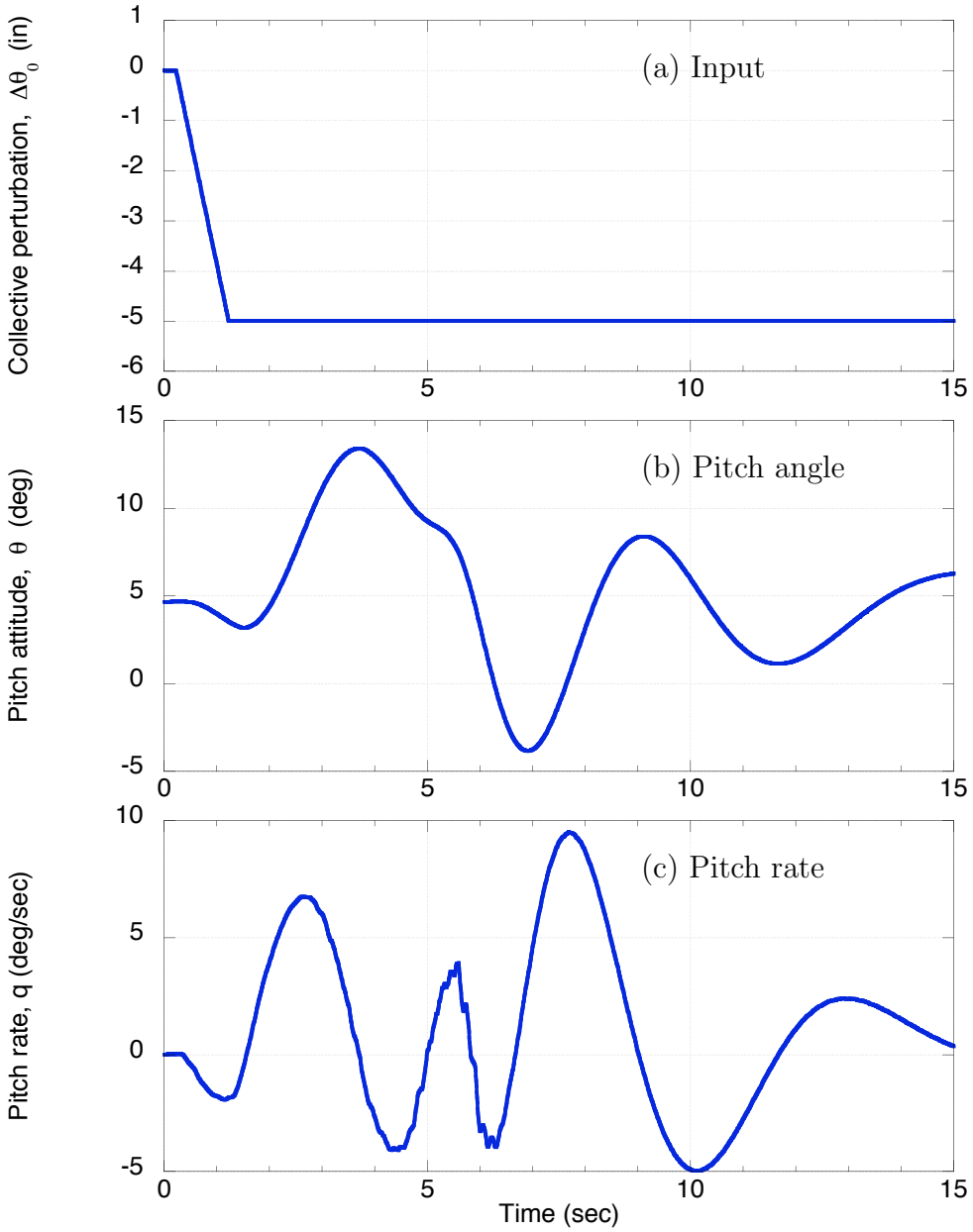

Figure 7.17: Time history of the control input, pitch angle θ and pitch rate q for an axial descent; $V = 1$ kt.

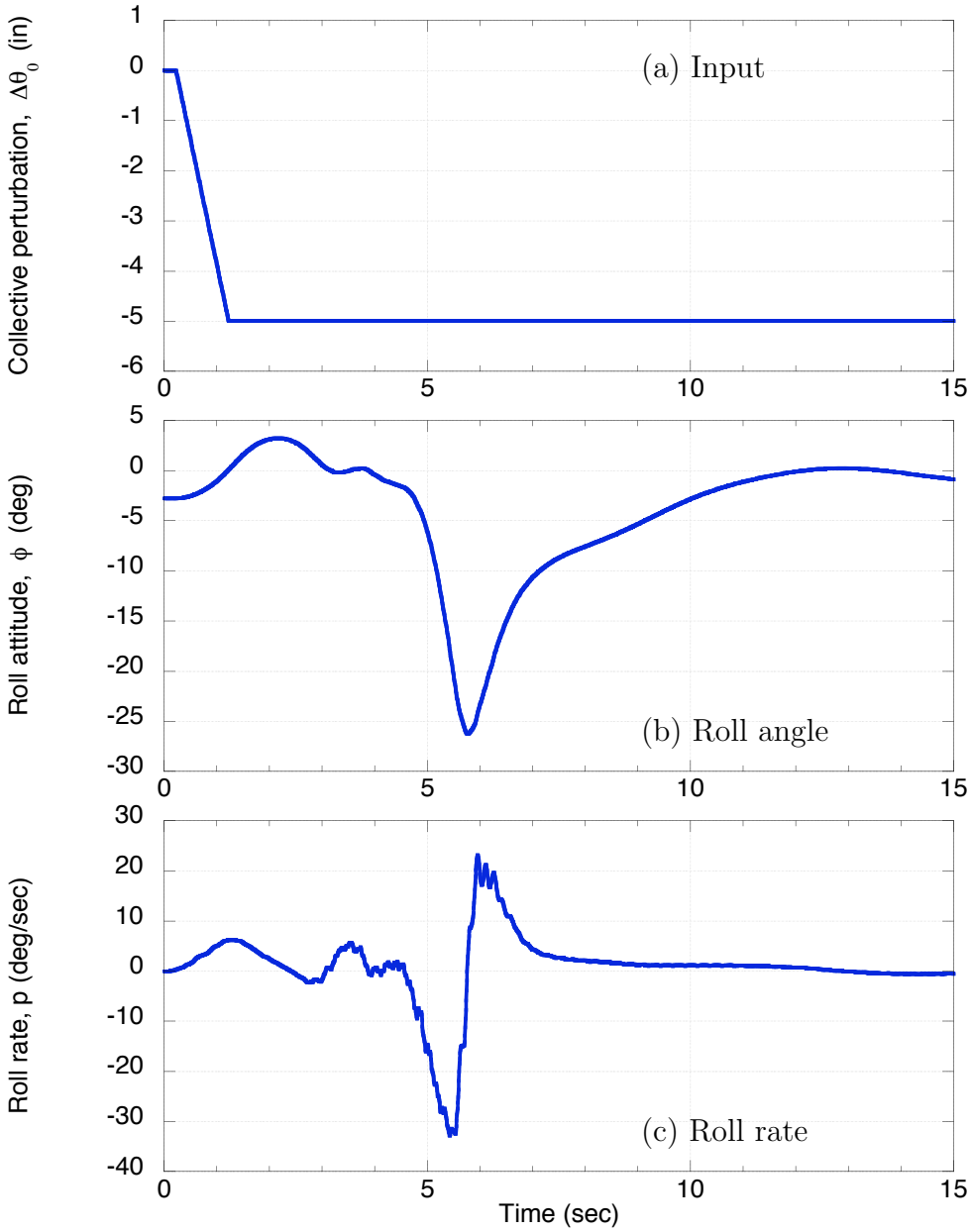

Figure 7.18: Time history of the control input, roll angle ϕ and roll rate p for an axial descent; $V = 1$ kt.

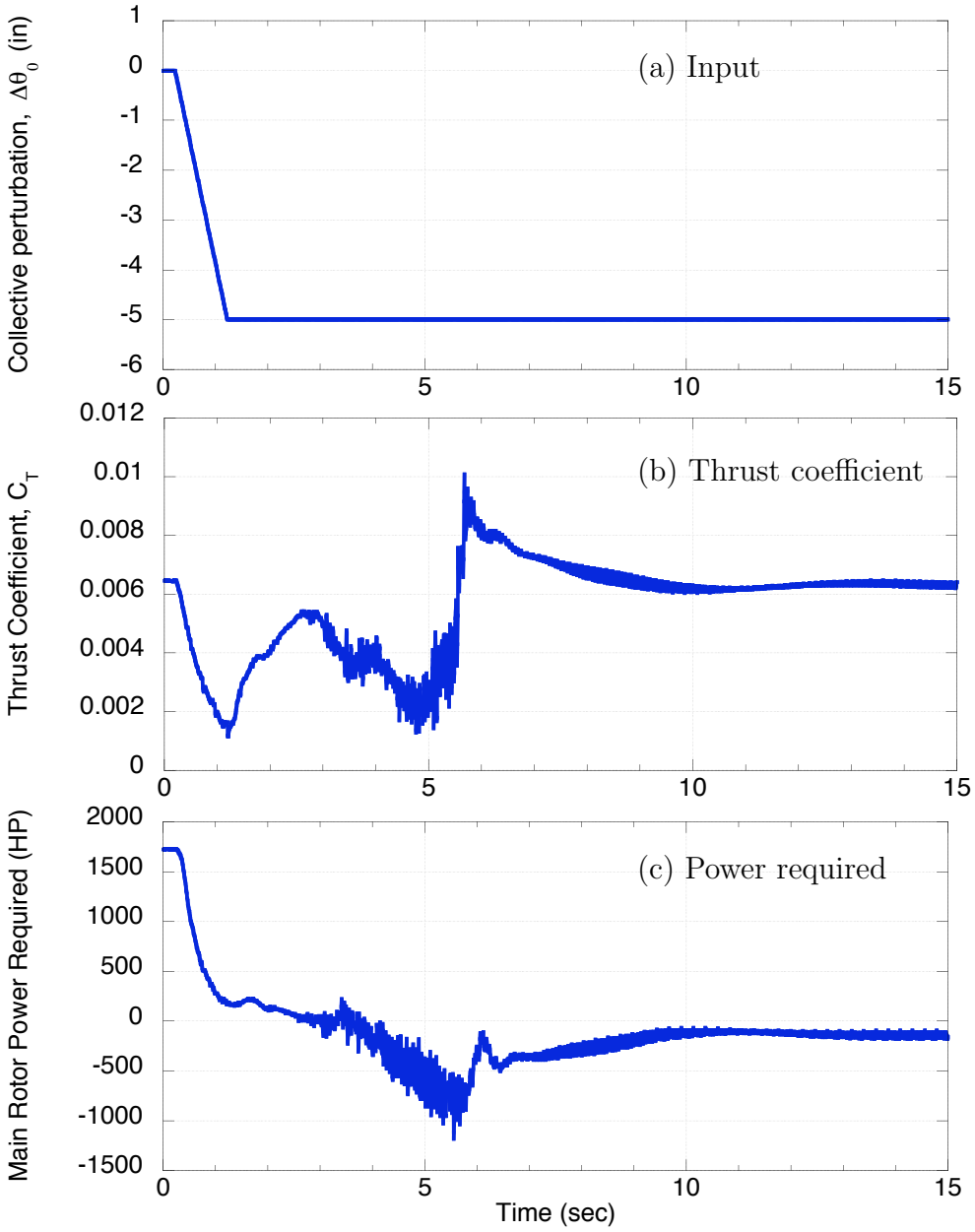

Figure 7.19: Time history of the control input, thrust coefficient C_T and main rotor power required Q_{MR} for an axial descent; $V = 1$ kt.

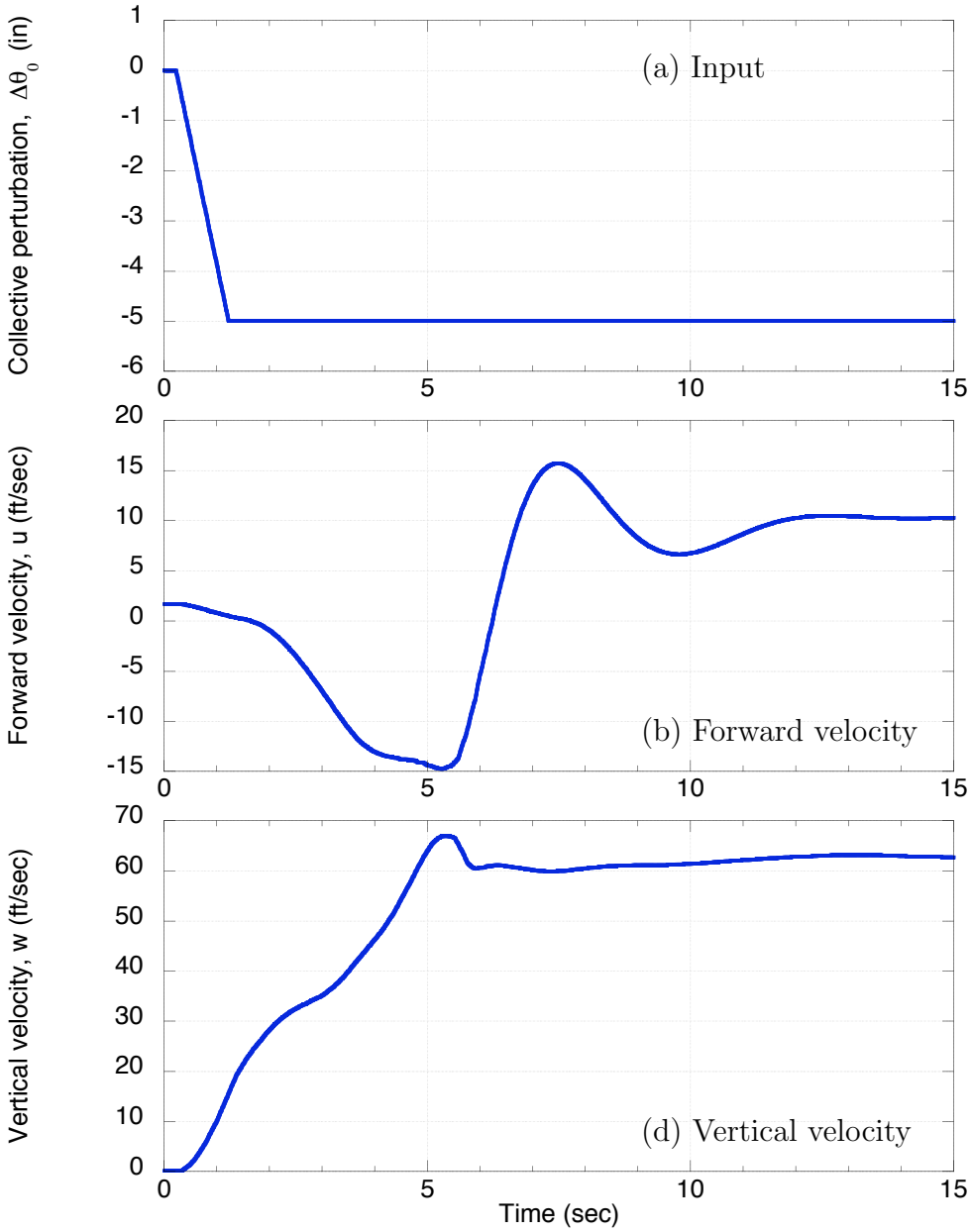

Figure 7.20: Time history of the control input and forward and vertical velocities, u and w respectively, for an axial descent; $V = 1$ kt.

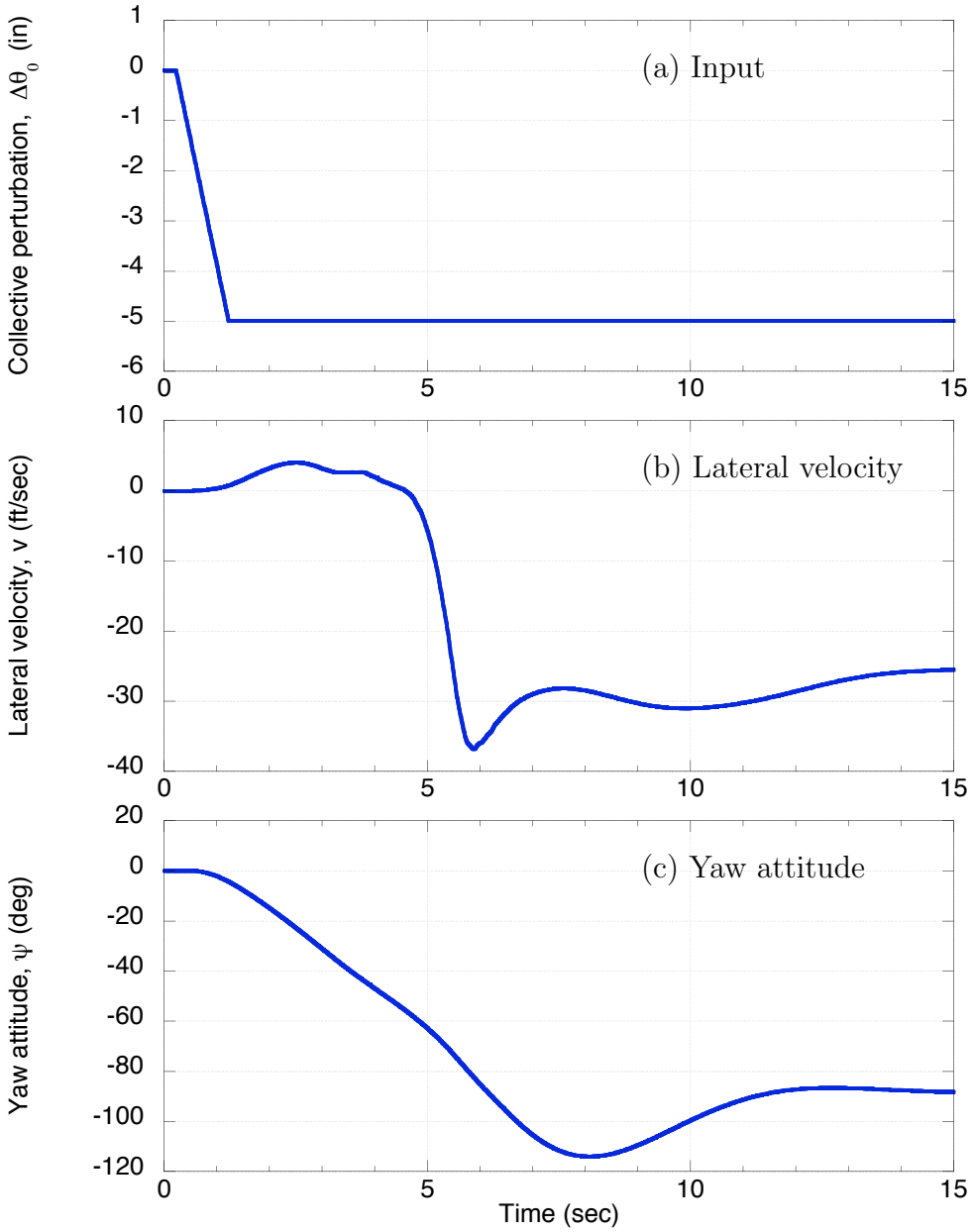

Figure 7.21: Time history of the control input and the lateral velocity v yaw angle ψ for an axial descent; $V = 1$ kt.

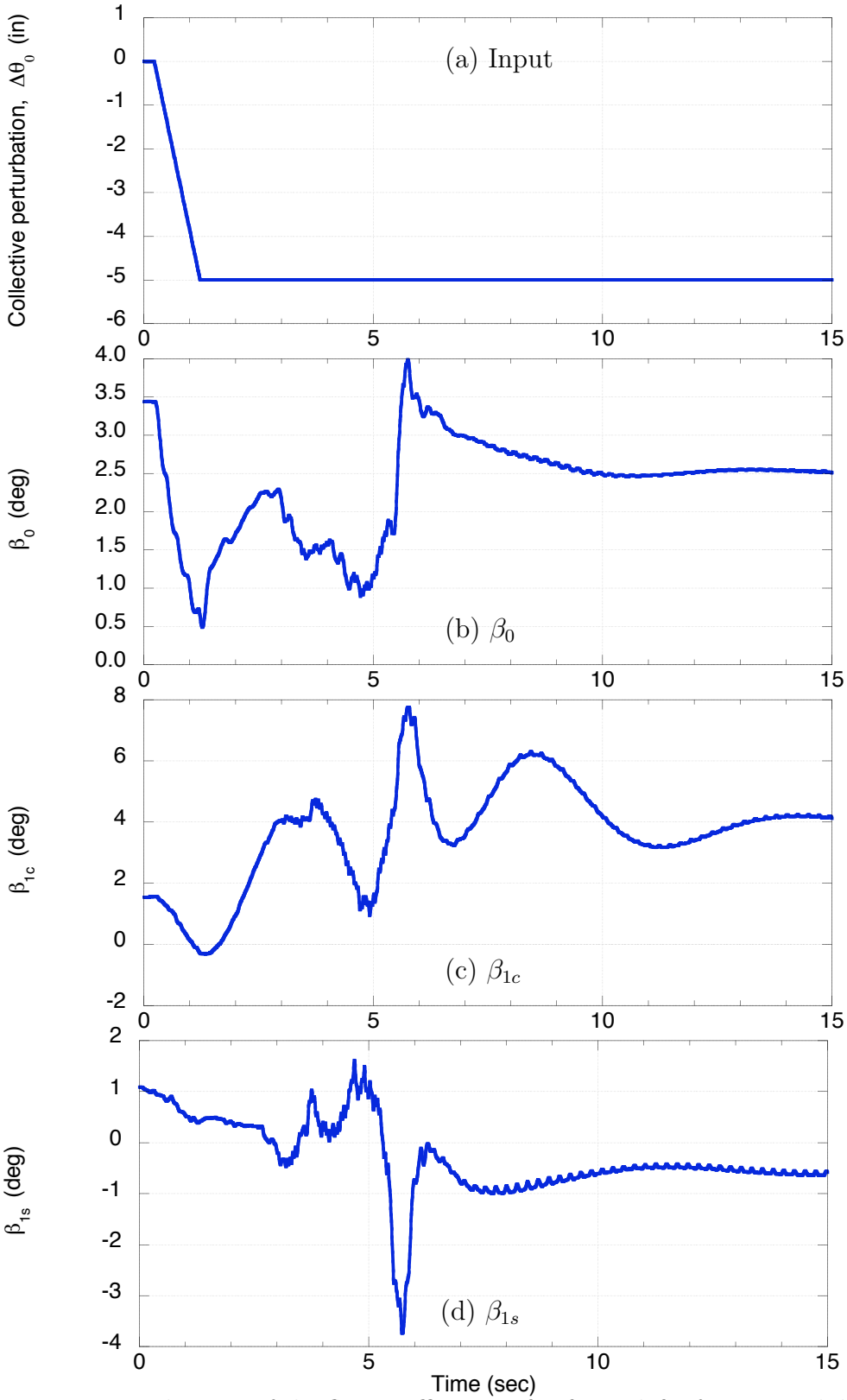

Figure 7.22: Time history of the flap coefficients, β_0, β_{1c} and β_{1s} for an axial descent; $V = 1$ kt.

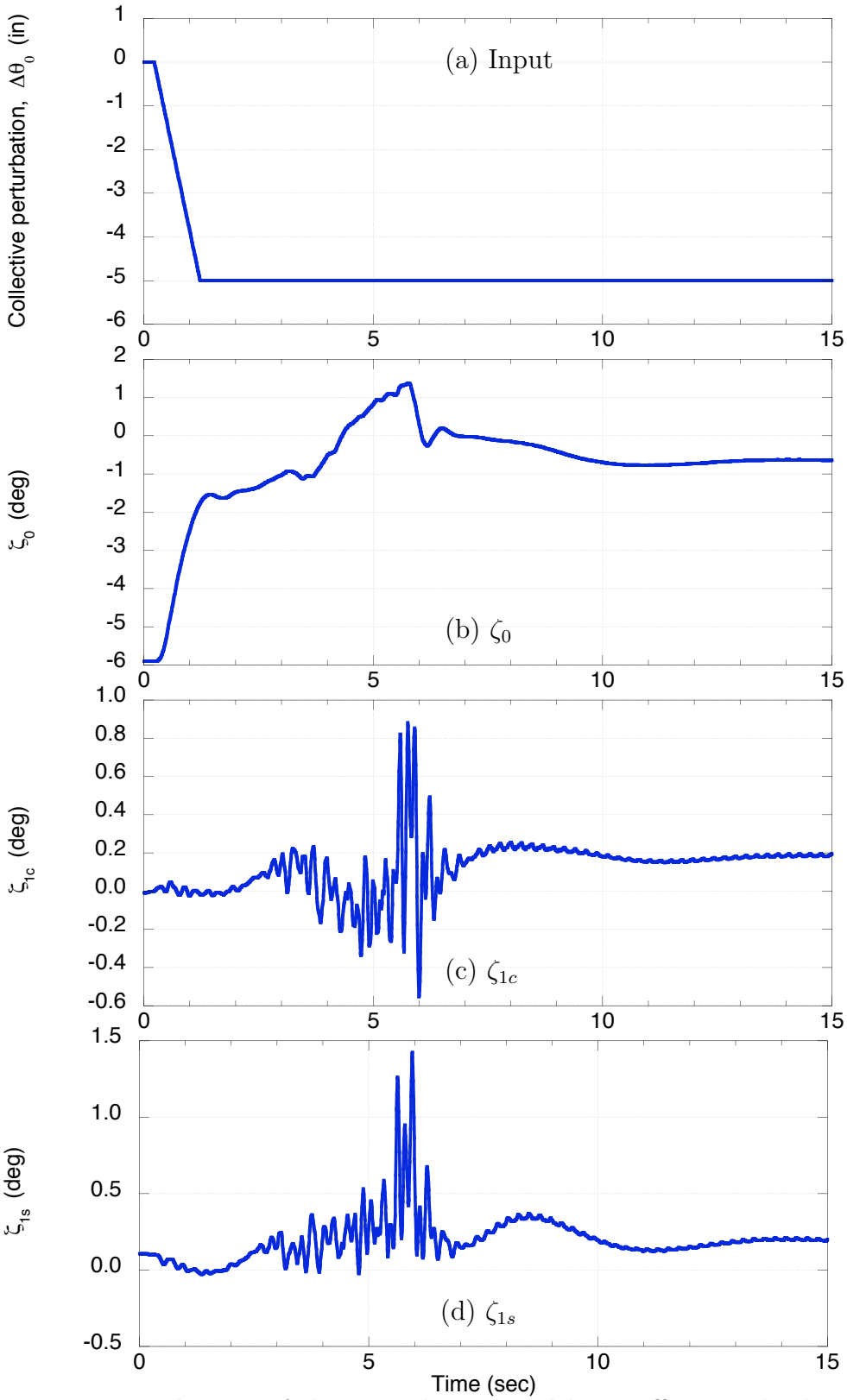

Figure 7.23: Time history of the control input and lag coefficients, ζ_0, ζ_{1c} and ζ_{1s} for an axial descent; $V = 1$ kt.

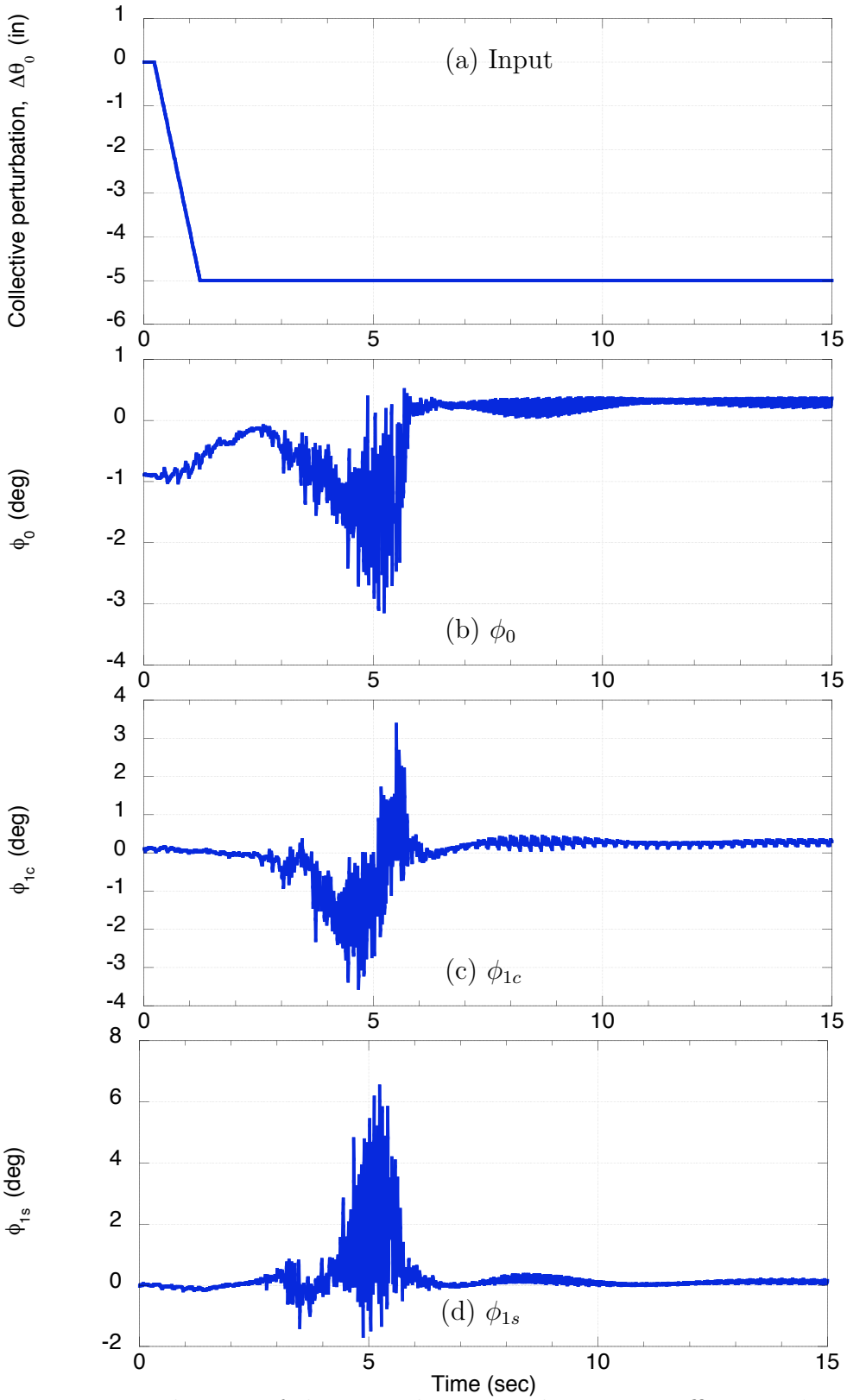

Figure 7.24: Time history of the control input and torsion coefficients, ϕ_0, ϕ_{1c} and ϕ_{1s} for an axial descent; $V = 1$ kt.

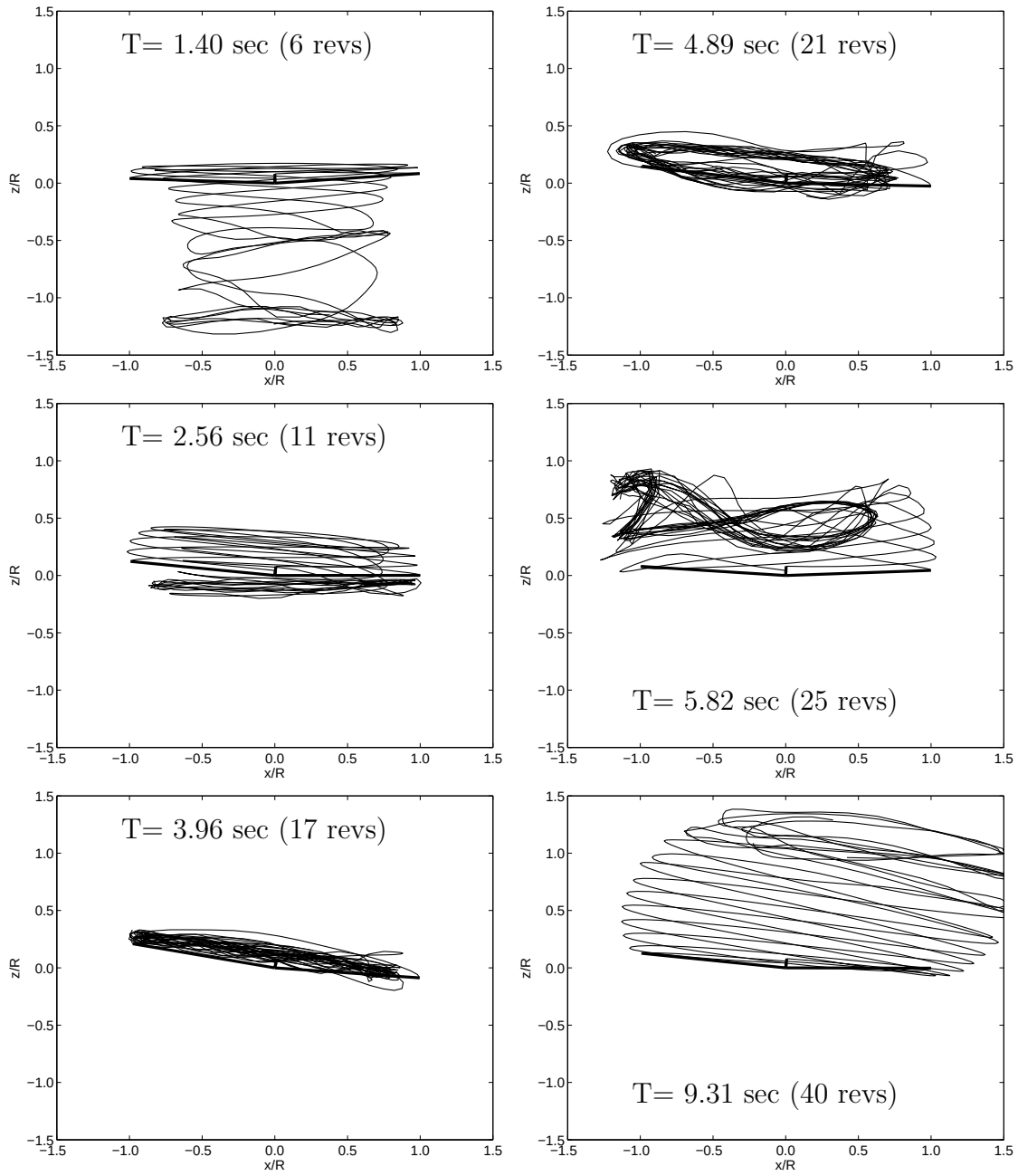

Figure 7.25: Side view of the free wake tip vortex geometry at different times for an axial descent; $V = 1$ kt.

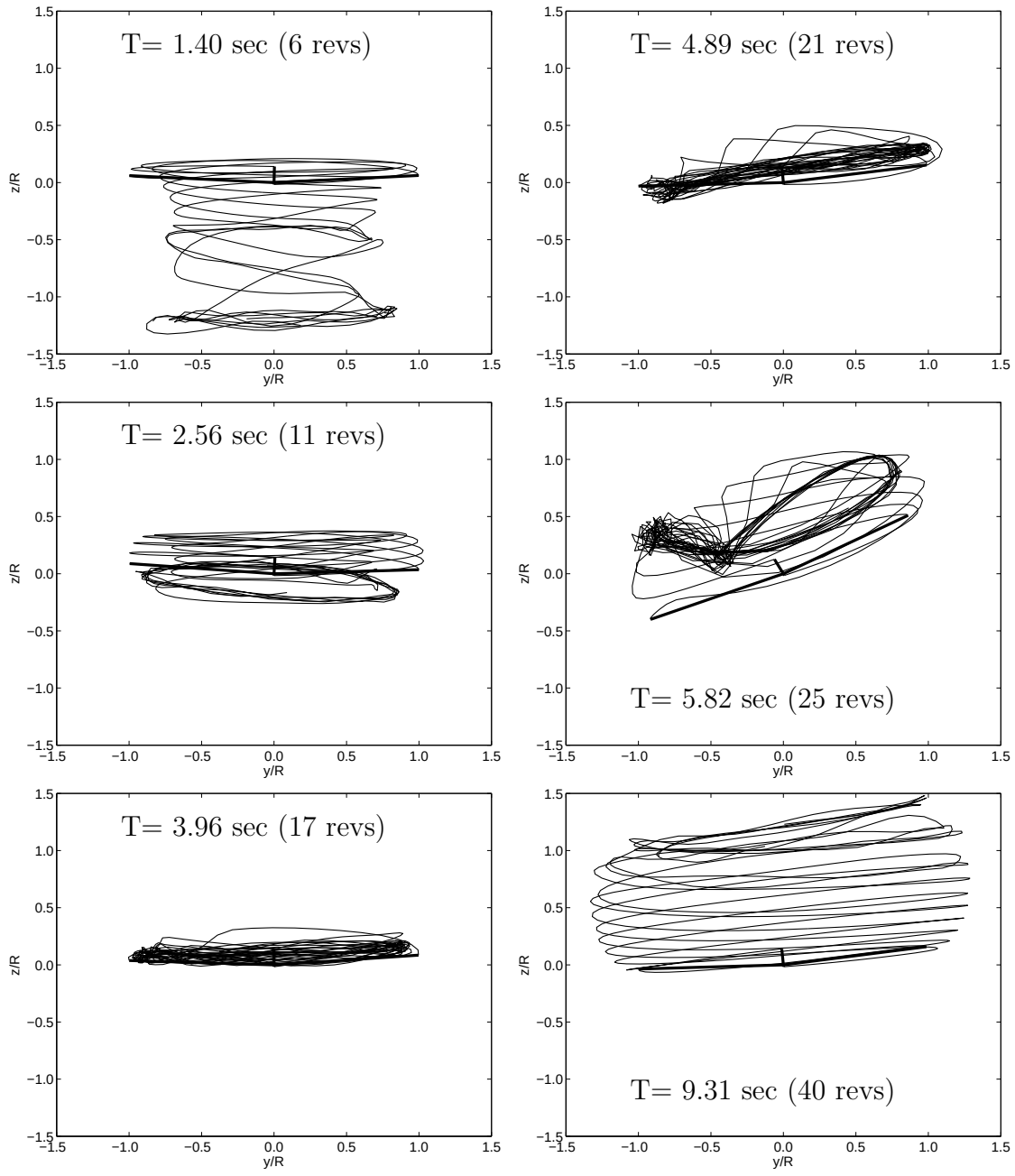

Figure 7.26: Rear view of the free wake tip vortex geometry at different times for an axial descent; $V = 1$ kt.

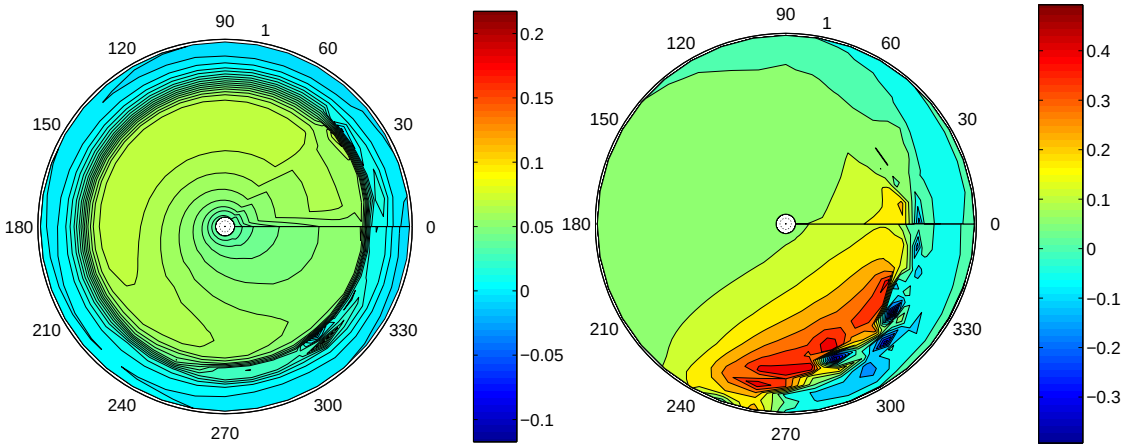

(a) T= 1.40 sec (6 revs)

(b) T= 4.89 sec (21 revs)

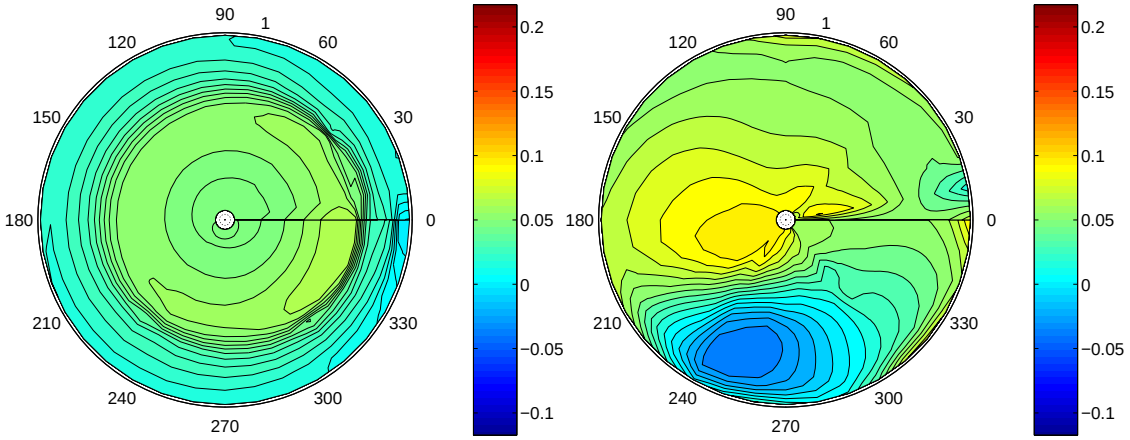

(c) T= 2.56 sec (11 revs)

(d) T= 5.82 sec (25 revs)

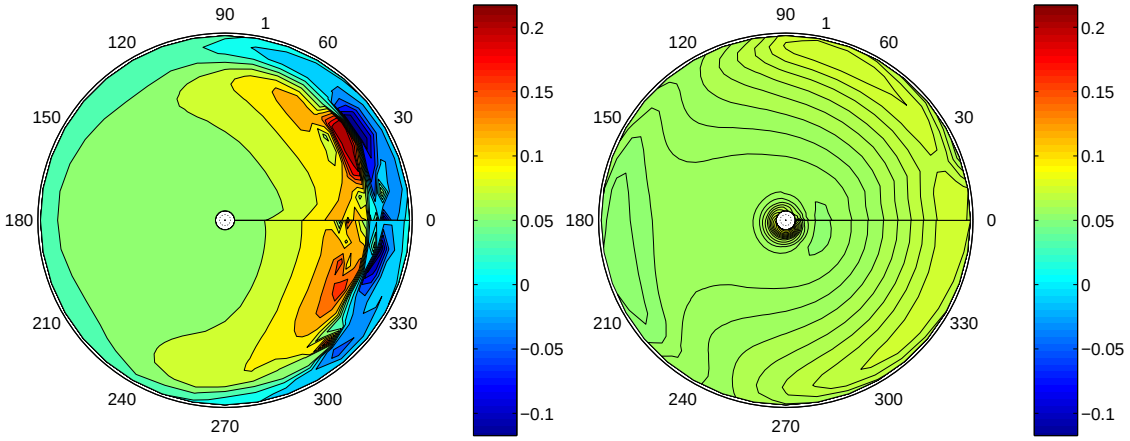

(e) T= 3.96 sec (17 revs)

(f) T= 9.31 sec (40 revs)

Figure 7.27: Distribution of induced velocities at different times for an axial descent; $V = 1$ kt.

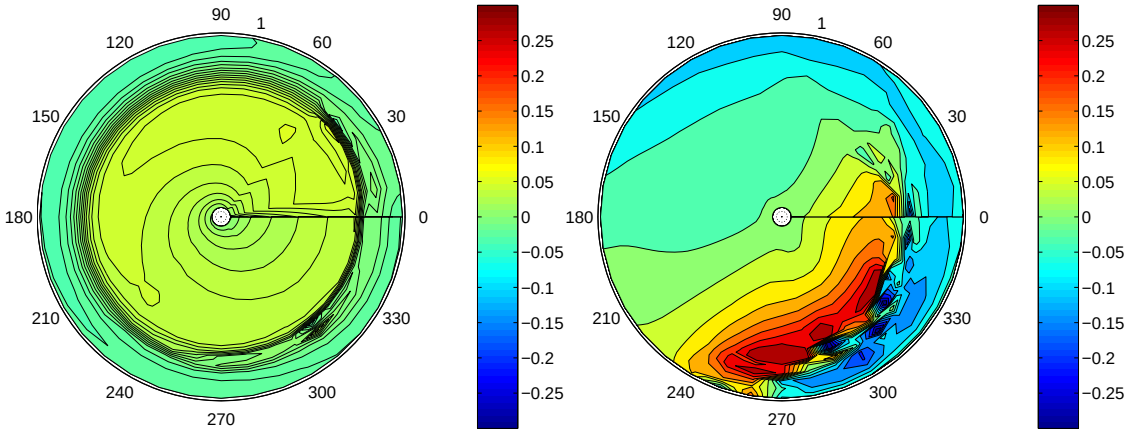

(a) T= 1.40 sec (6 revs)

(b) T= 4.89 sec (21 revolutions)

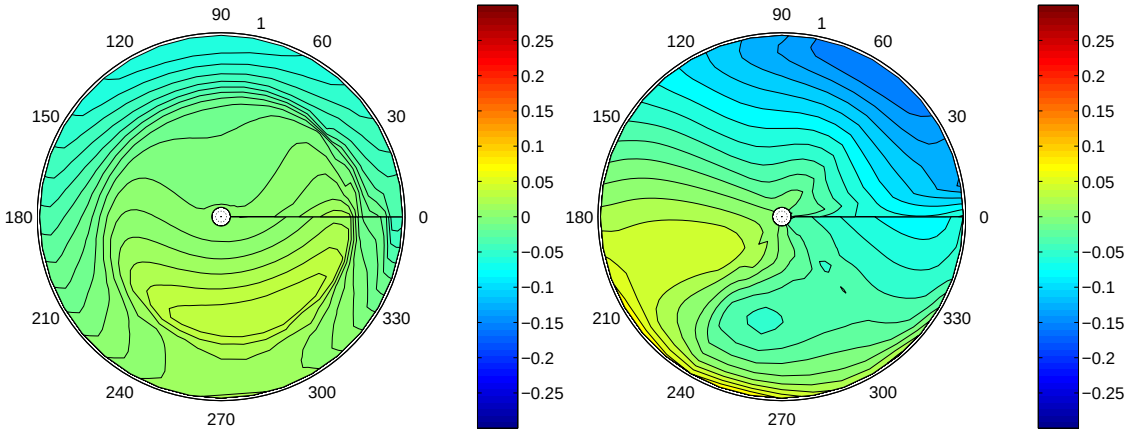

(c) T= 2.56 sec (11 revs)

(d) T= 5.82 sec (25 revs)

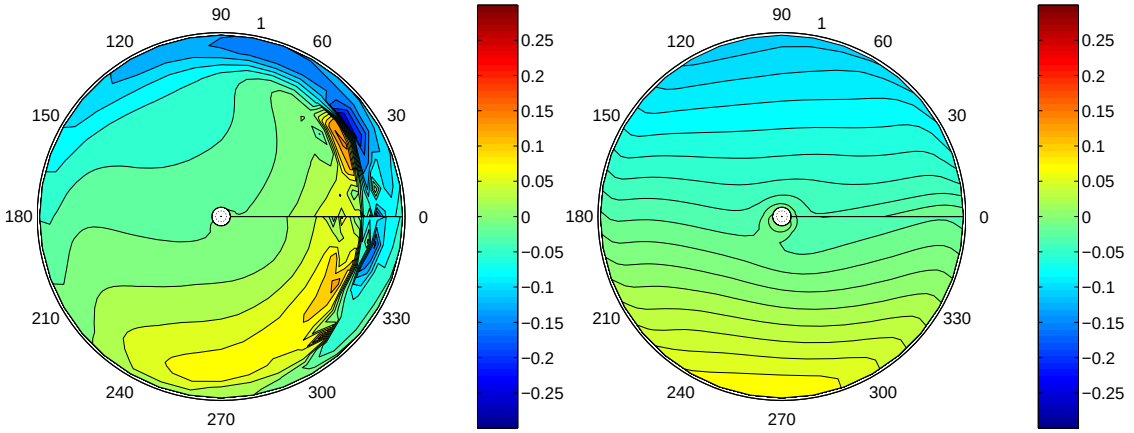

(e) T= 3.96 sec (17 revs)

(f) T= 9.31 sec (40 revs)

Figure 7.28: Distribution of blade sectional perpendicular velocity at different times for an axial descent; $V = 1$ kt.

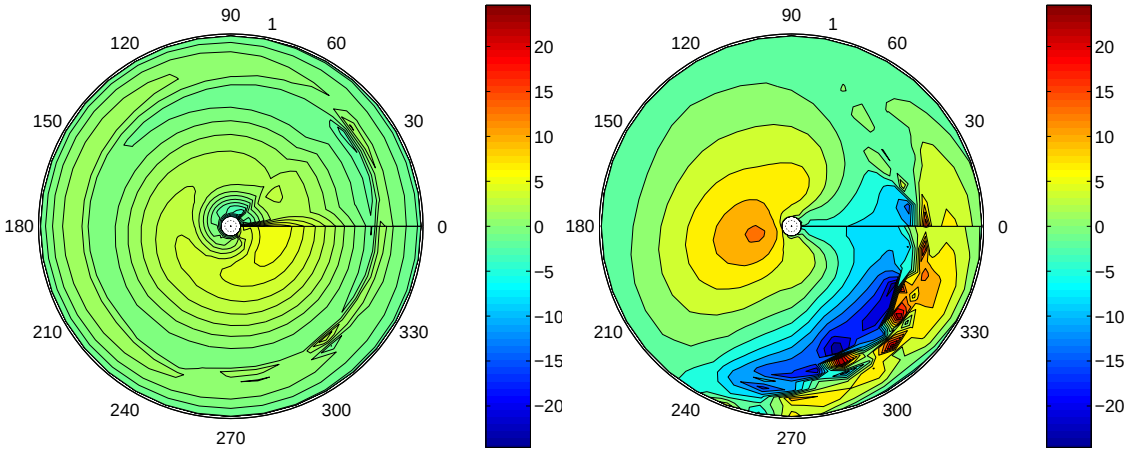

(a) T= 1.40 sec (6 revs)

(b) T= 4.89 sec (21 revs)

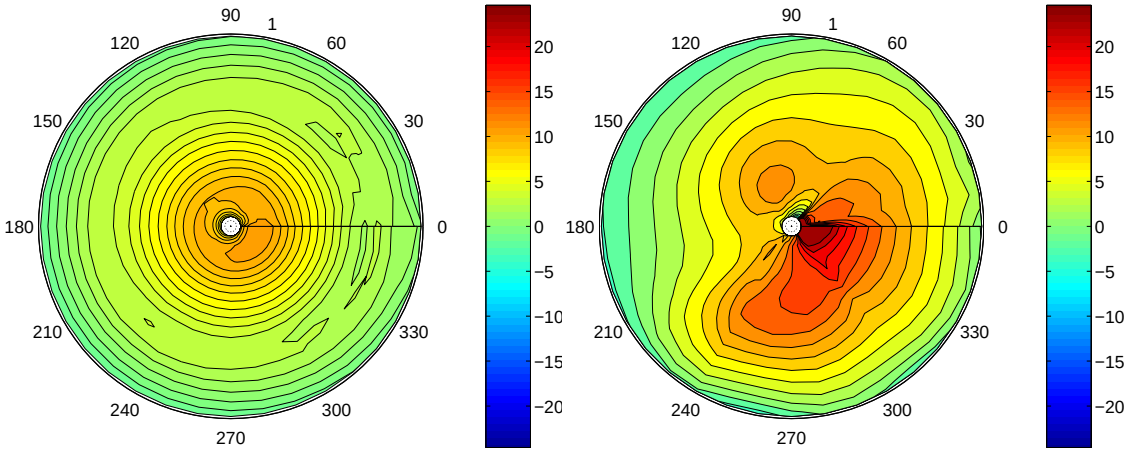

(c) T= 2.56 sec (11 revs)

(d) T= 5.82 sec (25 revs)

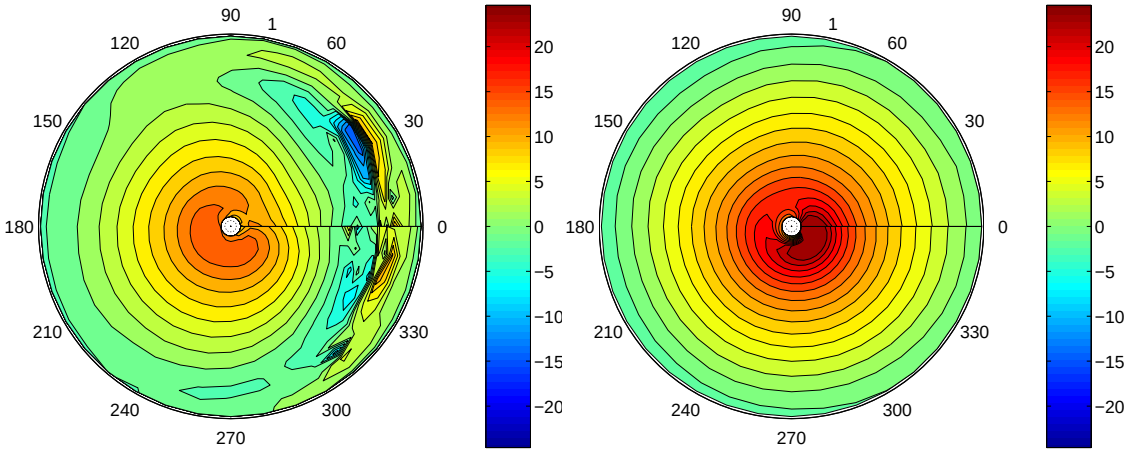

(e) T= 3.96 sec (17 revs)

(f) T= 9.31 sec (40 revs)

Figure 7.29: Distribution of sectional angle of attack at different times for an axial descent; $V = 1$ kt.

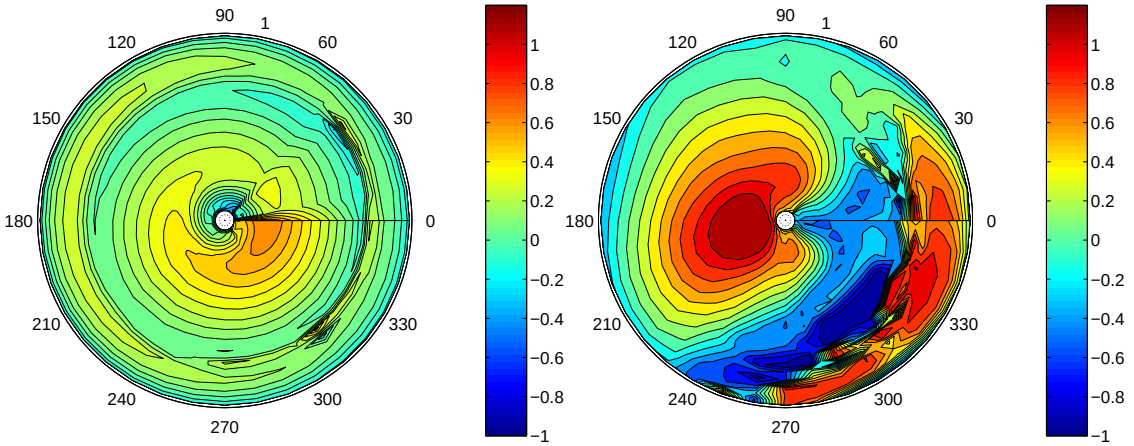

(a) T= 1.40 sec (6 revs)

(b) T= 4.89 sec (21 revs)

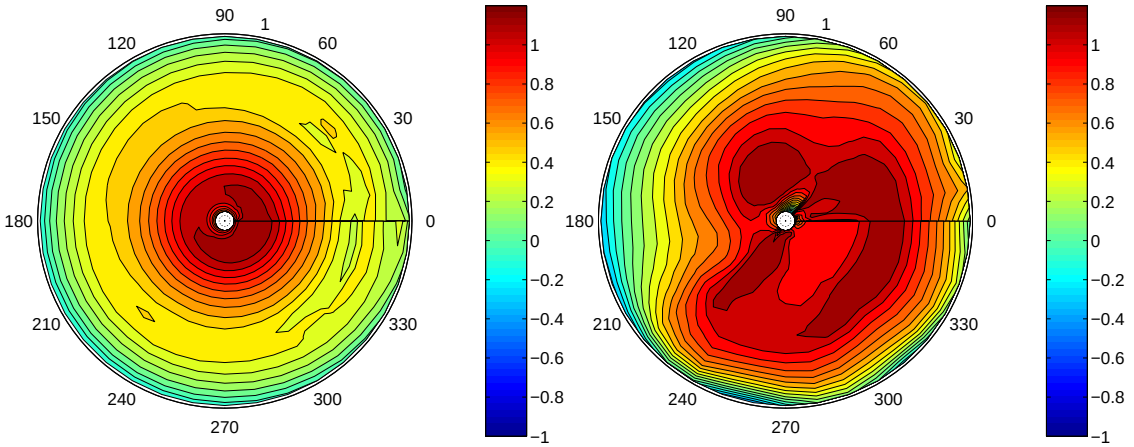

(c) T= 2.56 sec (11 revs)

(d) T= 5.82 sec (25 revs)

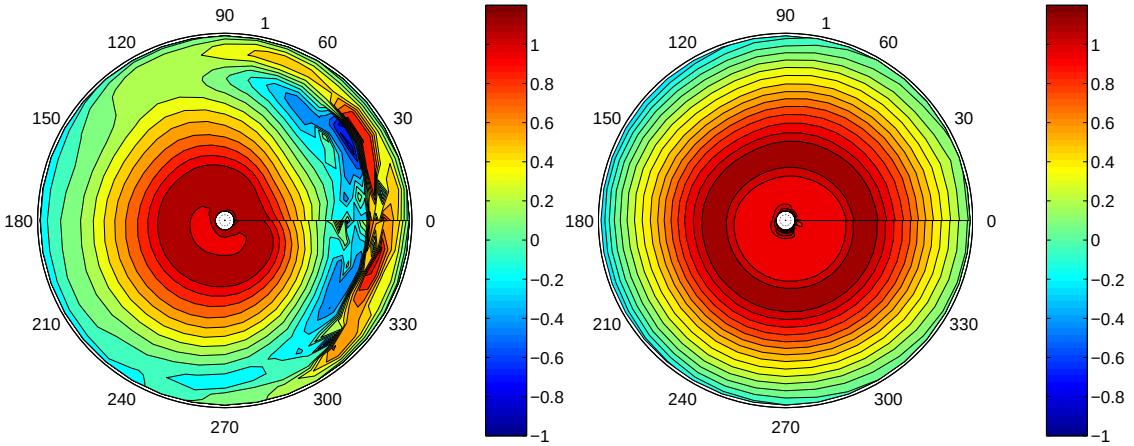

(e) T= 3.96 sec (17 revs)

(f) T= 9.31 sec (40 revs)

Figure 7.30: Distribution of lift coefficient C_L at different times for an axial descent; $V = 1$ kt.

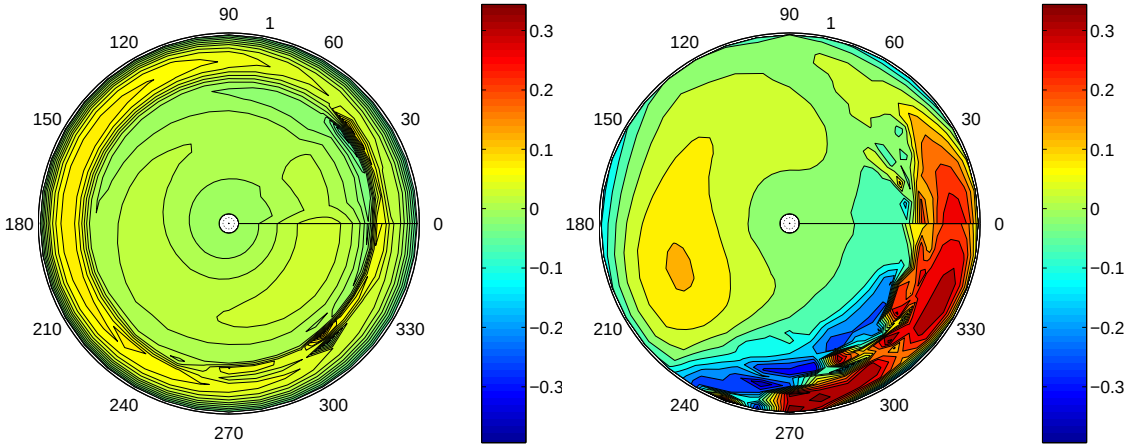

(a) T= 1.40 sec (6 revs)

(b) T= 4.89 sec (21 revs)

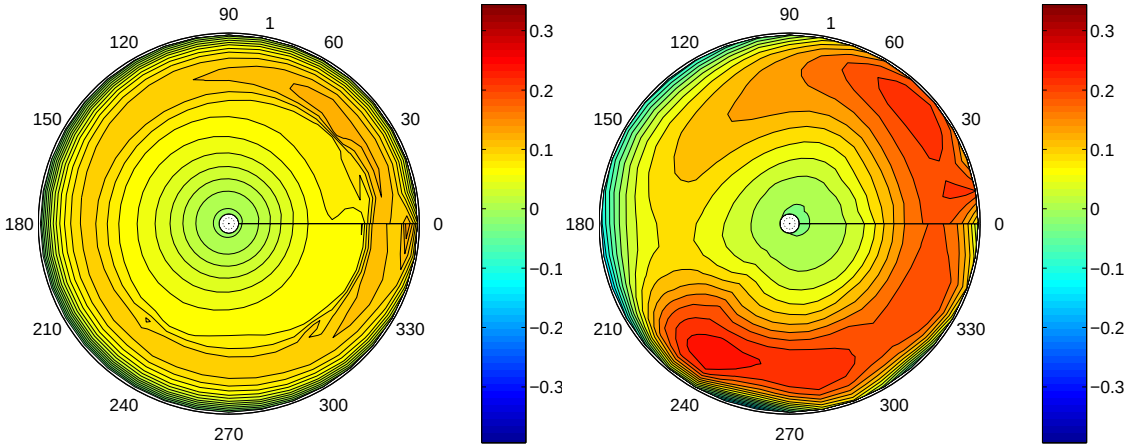

(c) T= 2.56 sec (11 revs)

(d) T= 5.82 sec (25 revs)

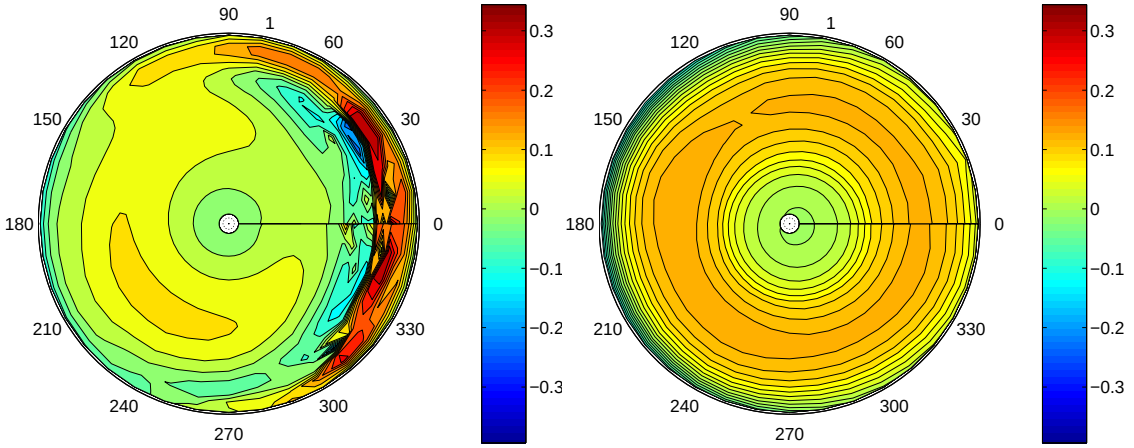

(e) T= 3.96 sec (17 revs)

(f) T= 9.31 sec (40 revs)

Figure 7.31: Distribution of non-dimensional lift $C_L M^2$ at different times for an axial descent; $V = 1$ kt.

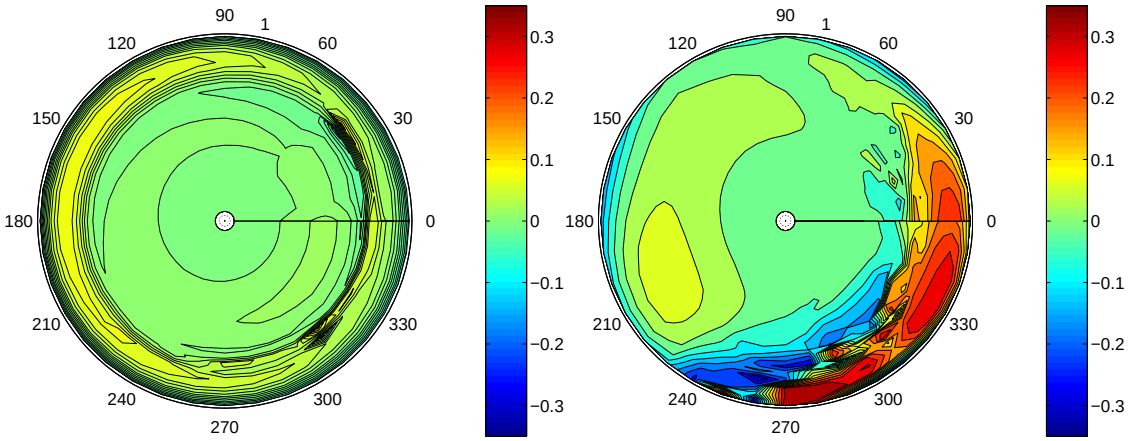

(a) T= 1.40 sec (6 revs)

(b) T= 4.89 sec (21 revs)

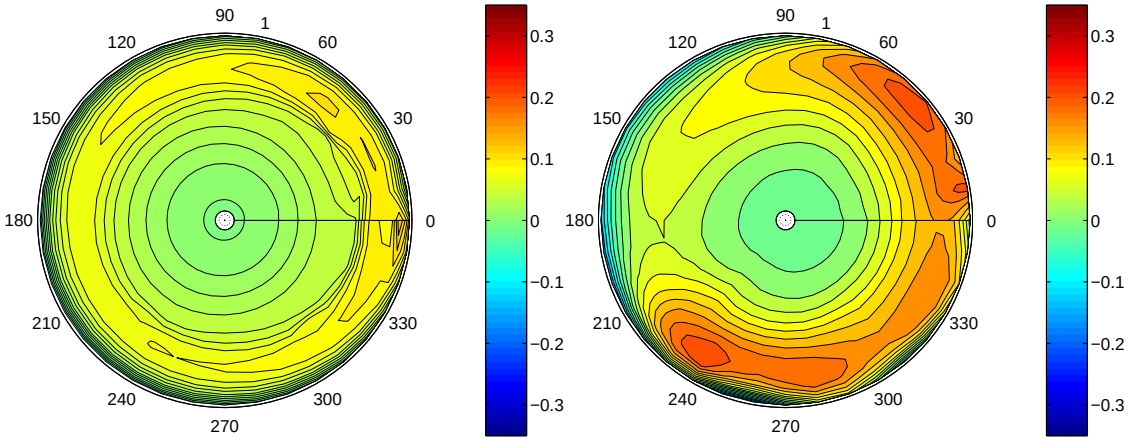

(c) T= 2.56 sec (11 revs)

(d) T= 5.82 sec (25 revs)

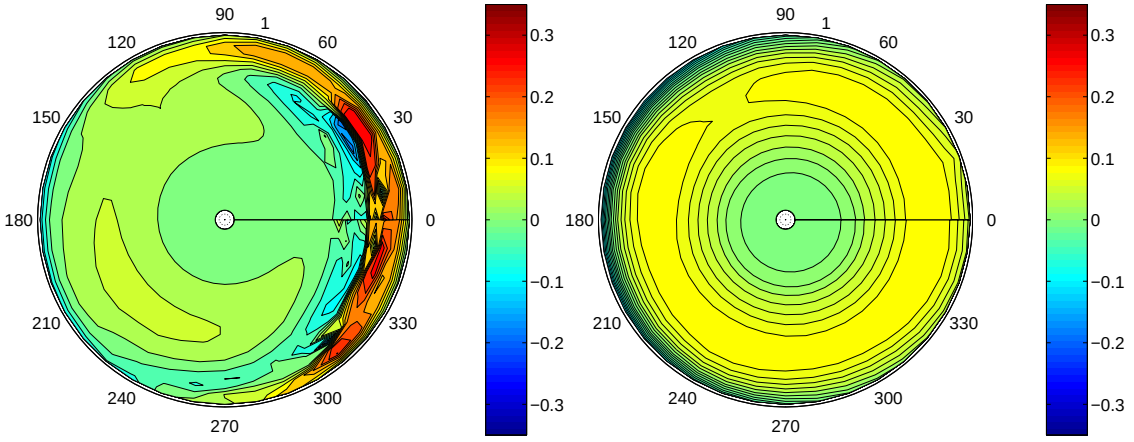

(e) T= 3.96 sec (17 revs)

(f) T= 9.31 sec (40 revs)

Figure 7.32: Distribution of flap moment $rC_L M^2$ at different times for an axial descent; $V = 1$ kt.

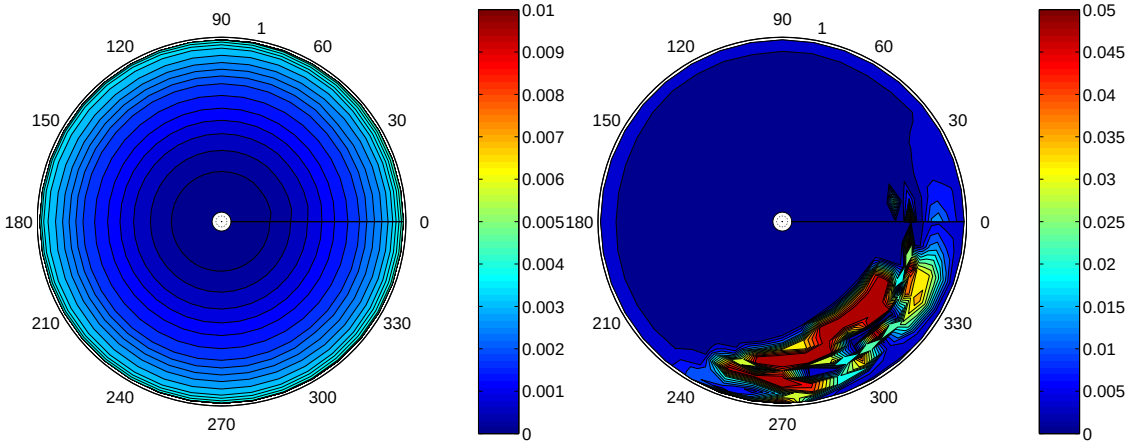

(a) T= 1.40 sec (6 revs)

(b) T= 4.89 sec (21 revs)

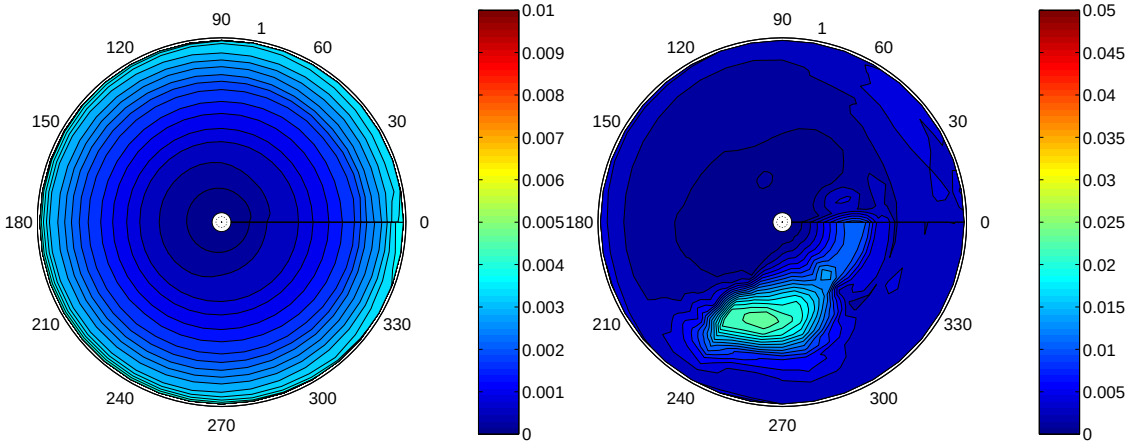

(c) T= 2.56 sec (11 revs)

(d) T= 5.82 sec (25 revs)

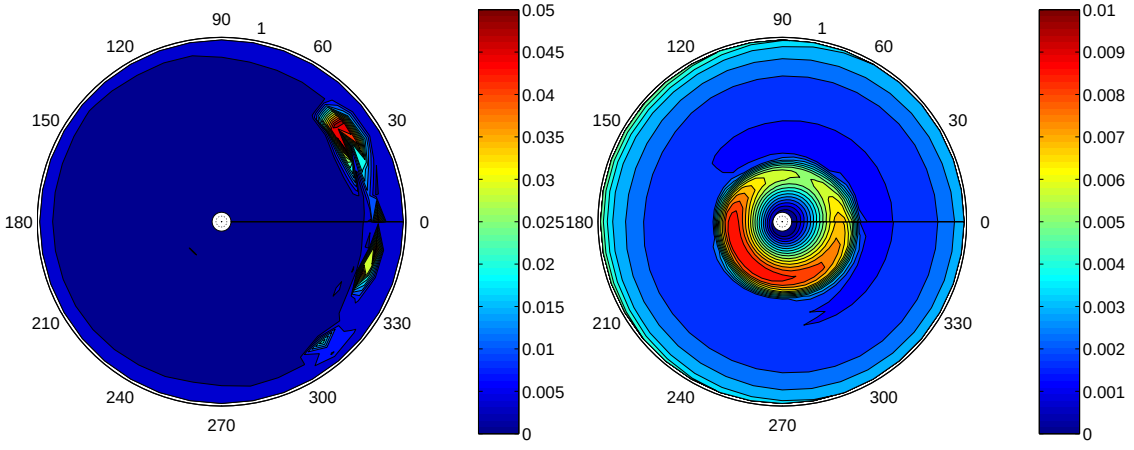

(e) T= 3.96 sec (17 revs)

(f) T= 9.31 sec (40 revs)

Figure 7.33: Distribution of elemental drag $C_D M^2$ at different times for an axial descent; $V = 1$ kt.

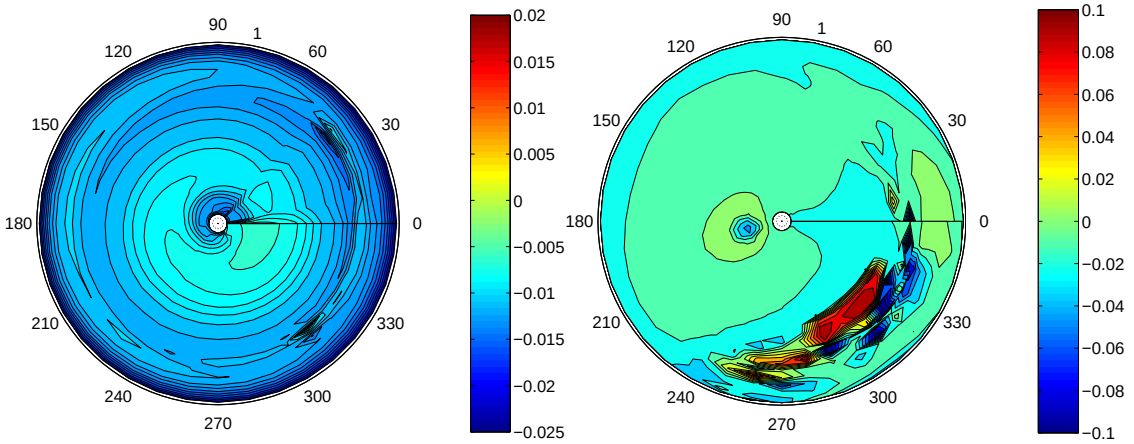

(a) T= 1.40 sec (6 revs)

(b) T= 4.89 sec (21 revs)

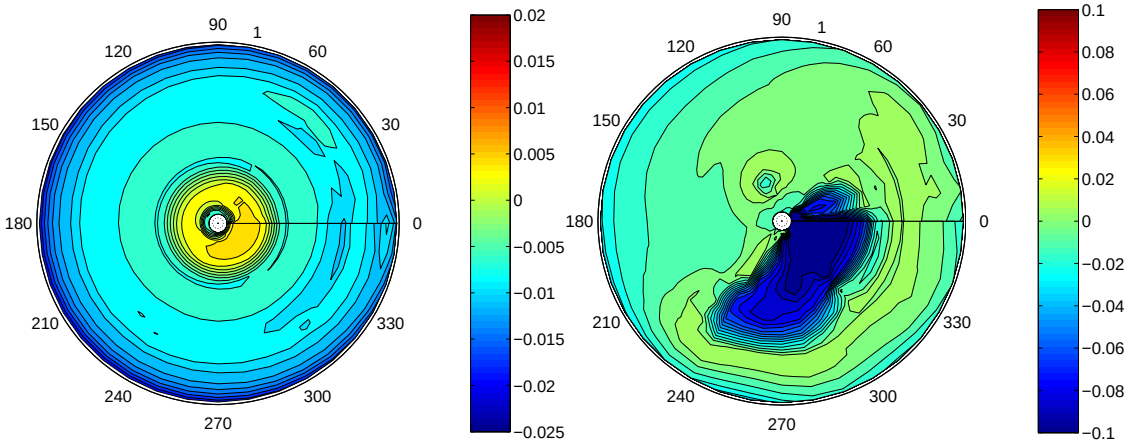

(c) T= 2.56 sec (11 revs)

(d) T= 5.82 sec (25 revs)

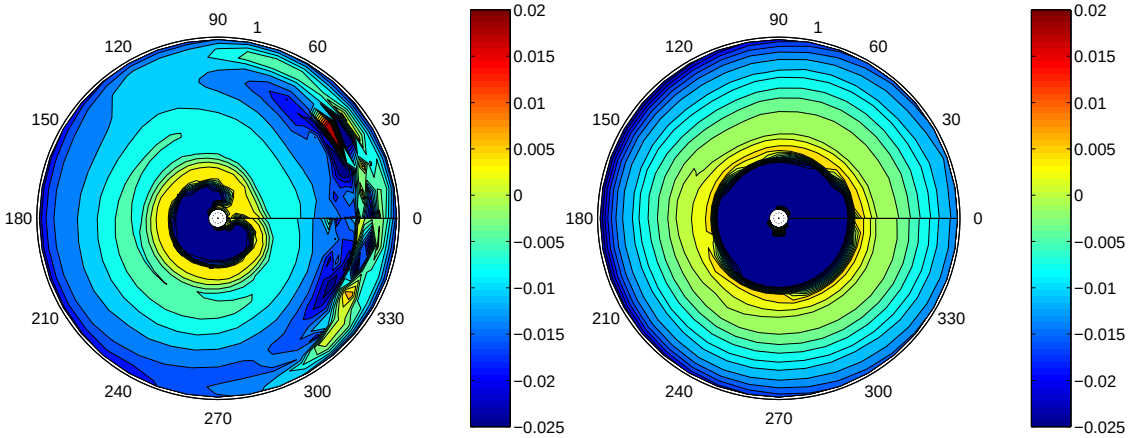

(e) T= 3.96 sec (17 revs)

(f) T= 9.31 sec (40 revs)

Figure 7.34: Distribution of moment coefficient C_M at different times for an axial descent; $V = 1$ kt.

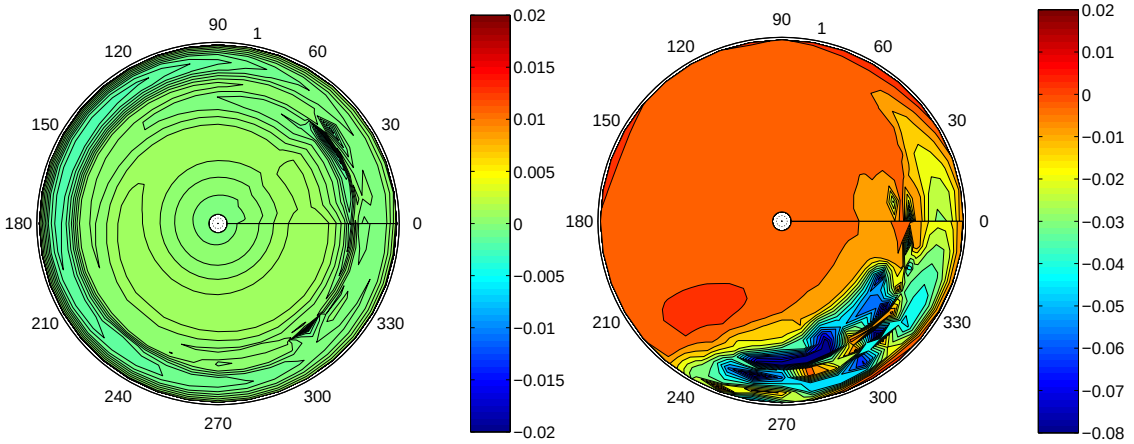

(a) T= 1.40 sec (6 revs)

(b) T= 4.89 sec (21 revs)

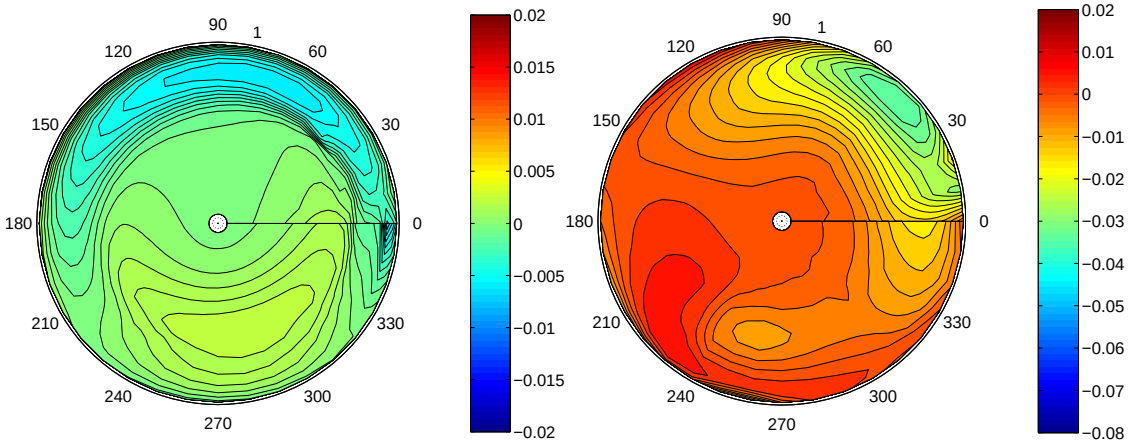

(c) T= 2.56 sec (11 revs)

(d) T= 5.82 sec (25 revs)

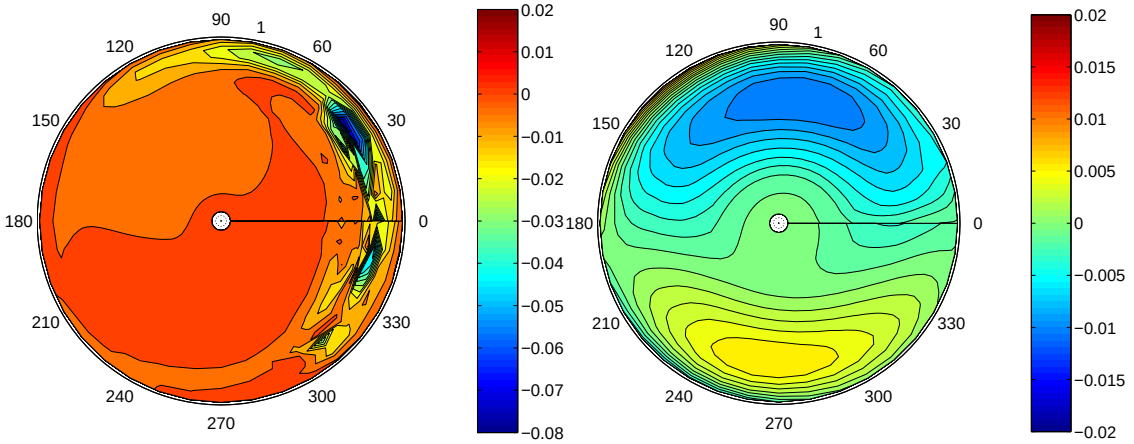

(e) T= 3.96 sec (17 revs)

(f) T= 9.31 sec (40 revs)

Figure 7.35: Distribution of induced torque $rC_L M^2 \sin\phi$ at different times for an axial descent; $V = 1$ kt.

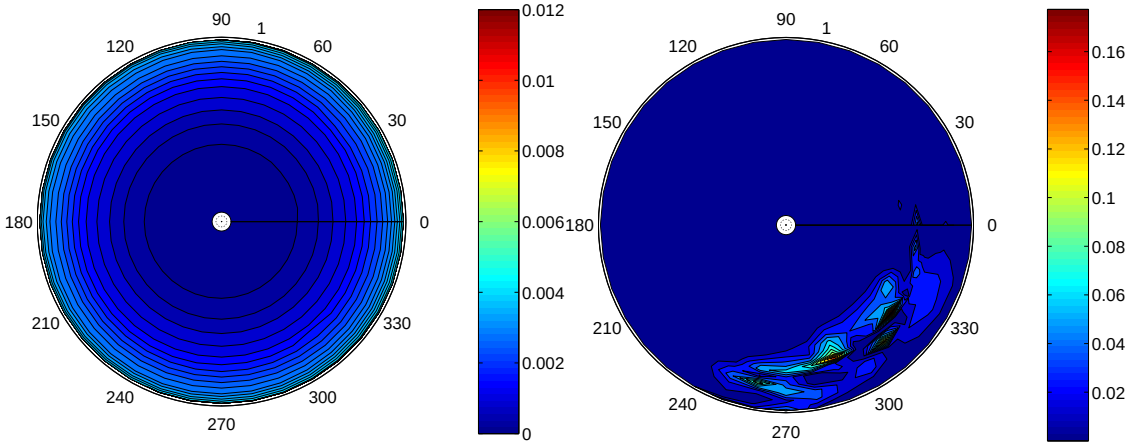

(a) T= 1.40 sec (6 revs)

(b) T= 4.89 sec (21 revs)

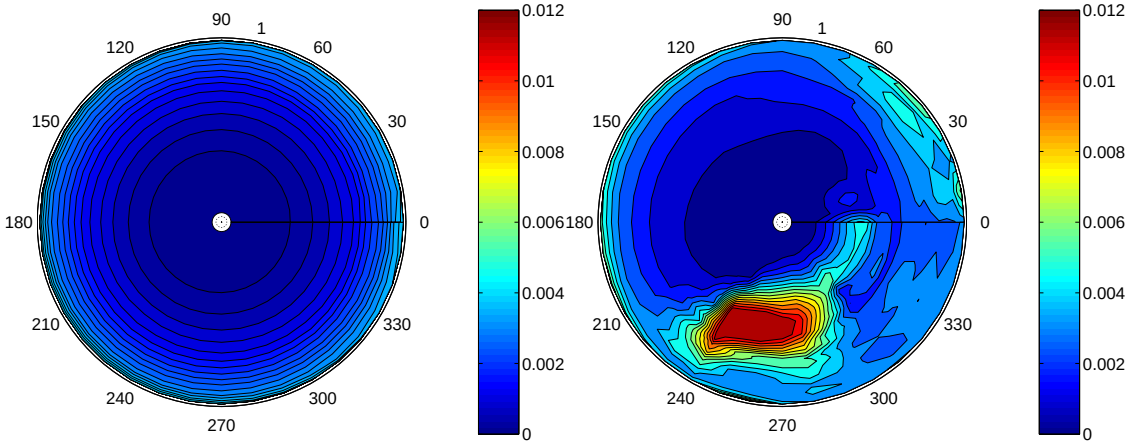

(c) T= 2.56 sec (11 revs)

(d) T= 5.82 sec (25 revs)

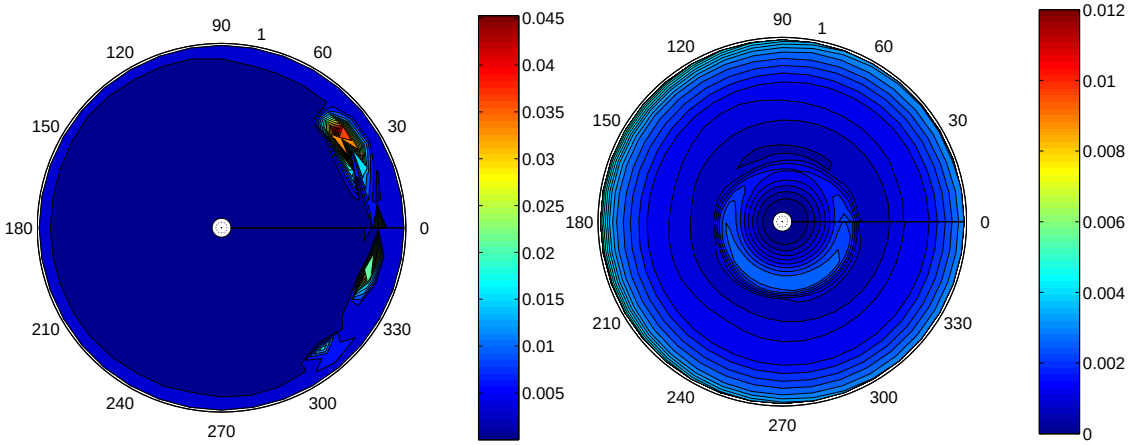

(e) T= 3.96 sec (17 revs)

(f) T= 9.31 sec (40 revs)

Figure 7.36: Distribution of profile torque $rC_D M^2 \cos\phi$ at different times for an axial descent; $V = 1$ kt.

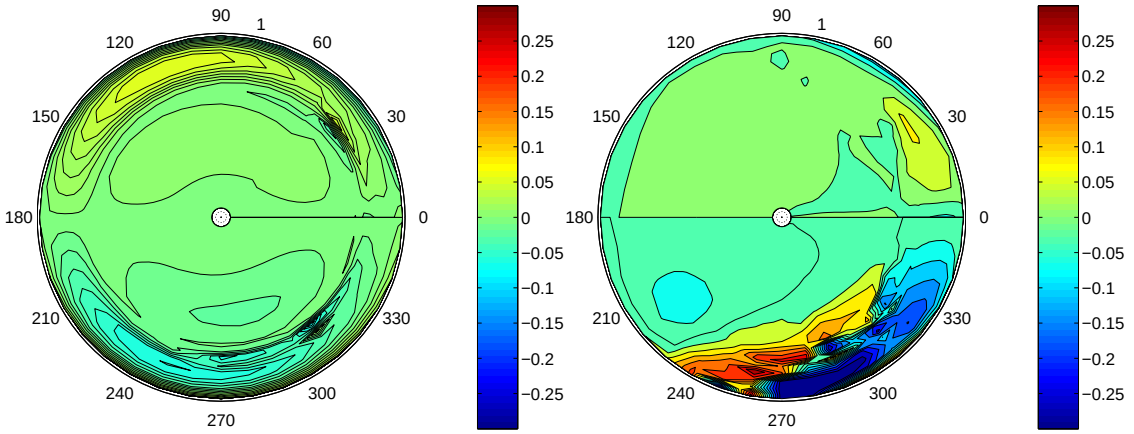

(a) T= 1.40 sec (6 revs)

(b) T= 4.89 sec (21 revs)

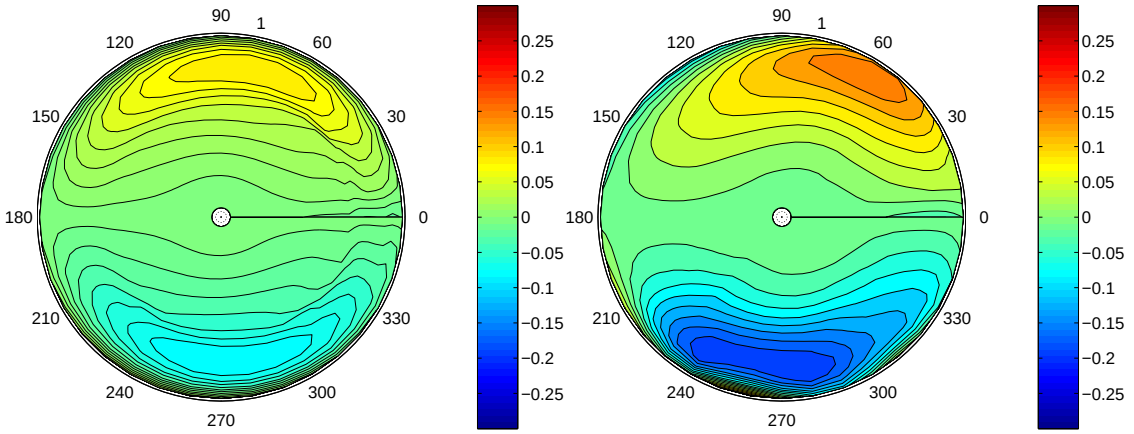

(c) T= 2.56 sec (11 revs)

(d) T= 5.82 sec (25 revs)

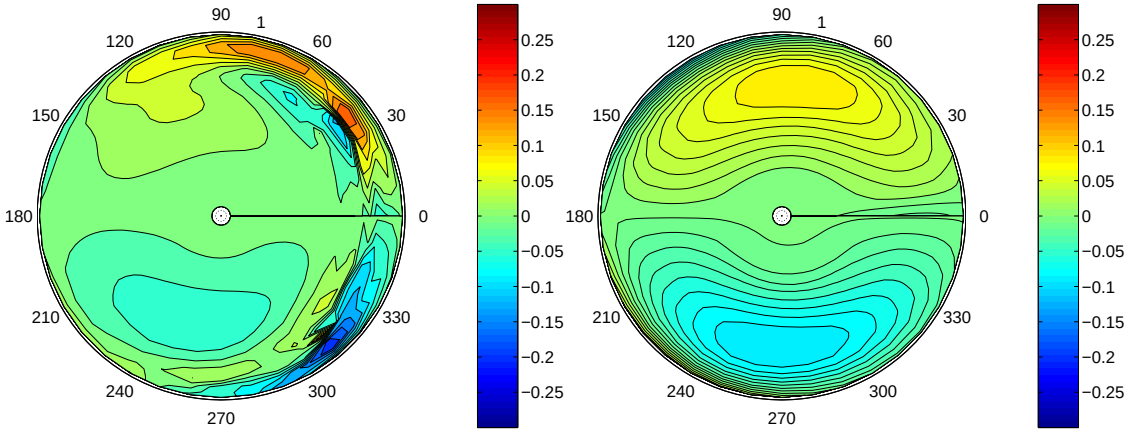

(e) T= 3.96 sec (17 revs)

(f) T= 9.31 sec (40 revs)

Figure 7.37: Lift contribution to roll moment $rC_L M^2 \sin\psi$ at different times for an axial descent; $V = 1$ kt.

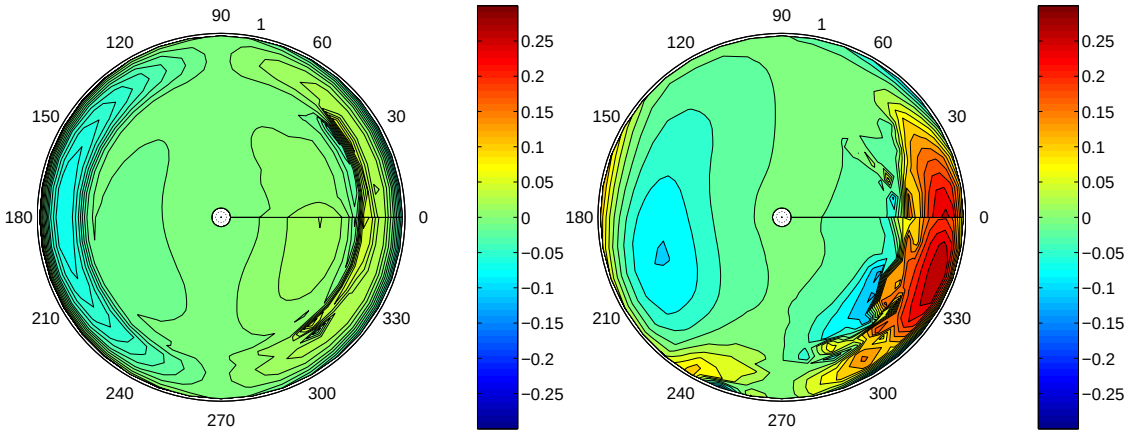

(a) T= 1.40 sec (6 revs)

(b) T= 4.89 sec (21 revs)

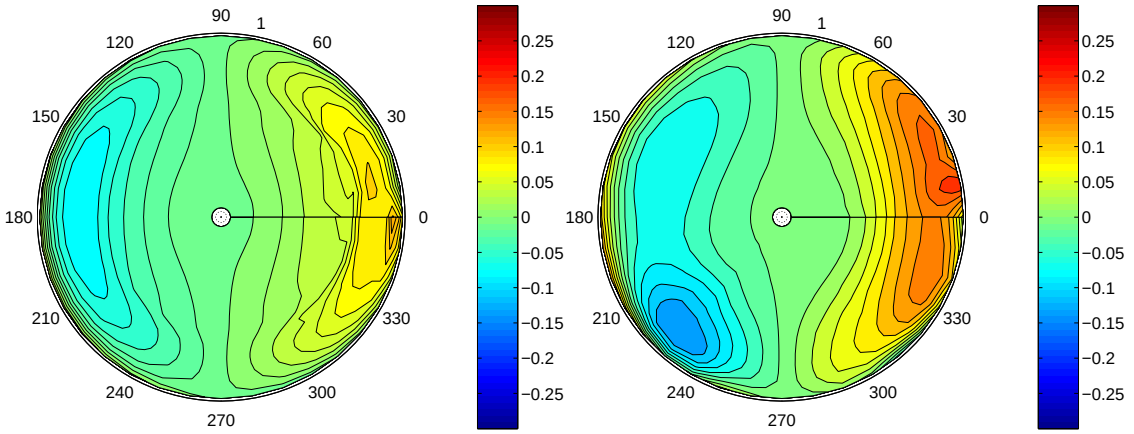

(c) T= 2.56 sec (11 revs)

(d) T= 5.82 sec (25 revs)

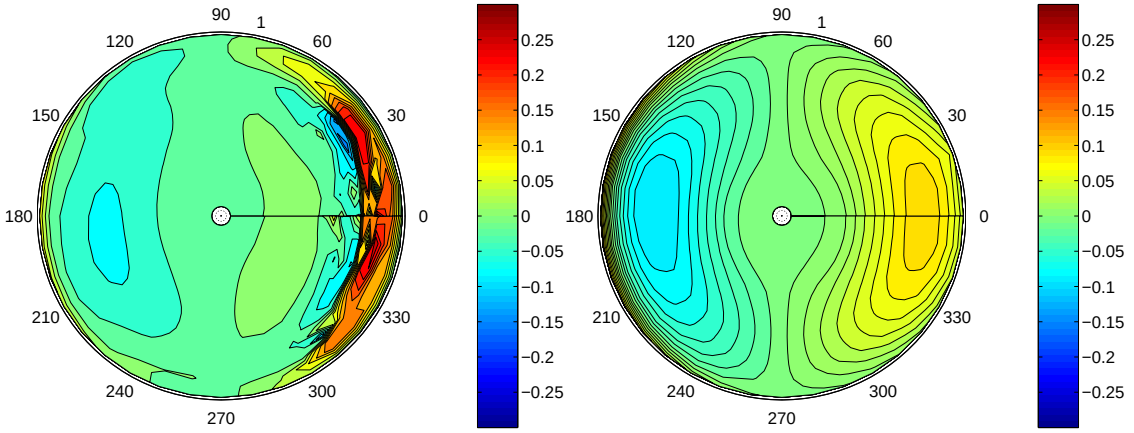

(e) T= 3.96 sec (17 revs)

(f) T= 9.31 sec (40 revs)

Figure 7.38: Lift contribution to pitch moment $rC_L M^2 \cos\psi$ at different times for an axial descent; $V = 1$ kt.

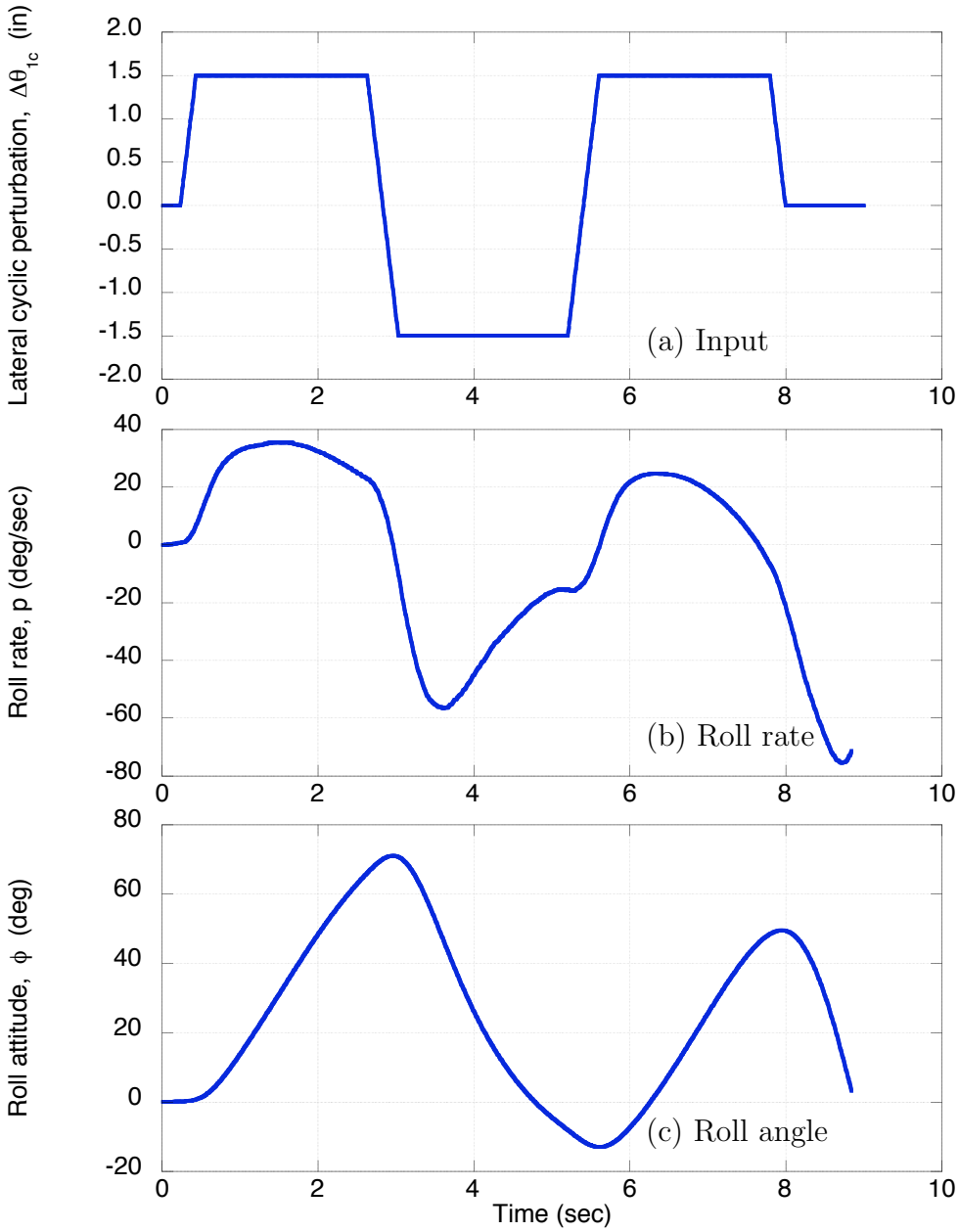

Figure 7.39: Time history of the control input, roll rate p and roll angle ϕ for a roll reversal maneuver; $V = 80$ kts.

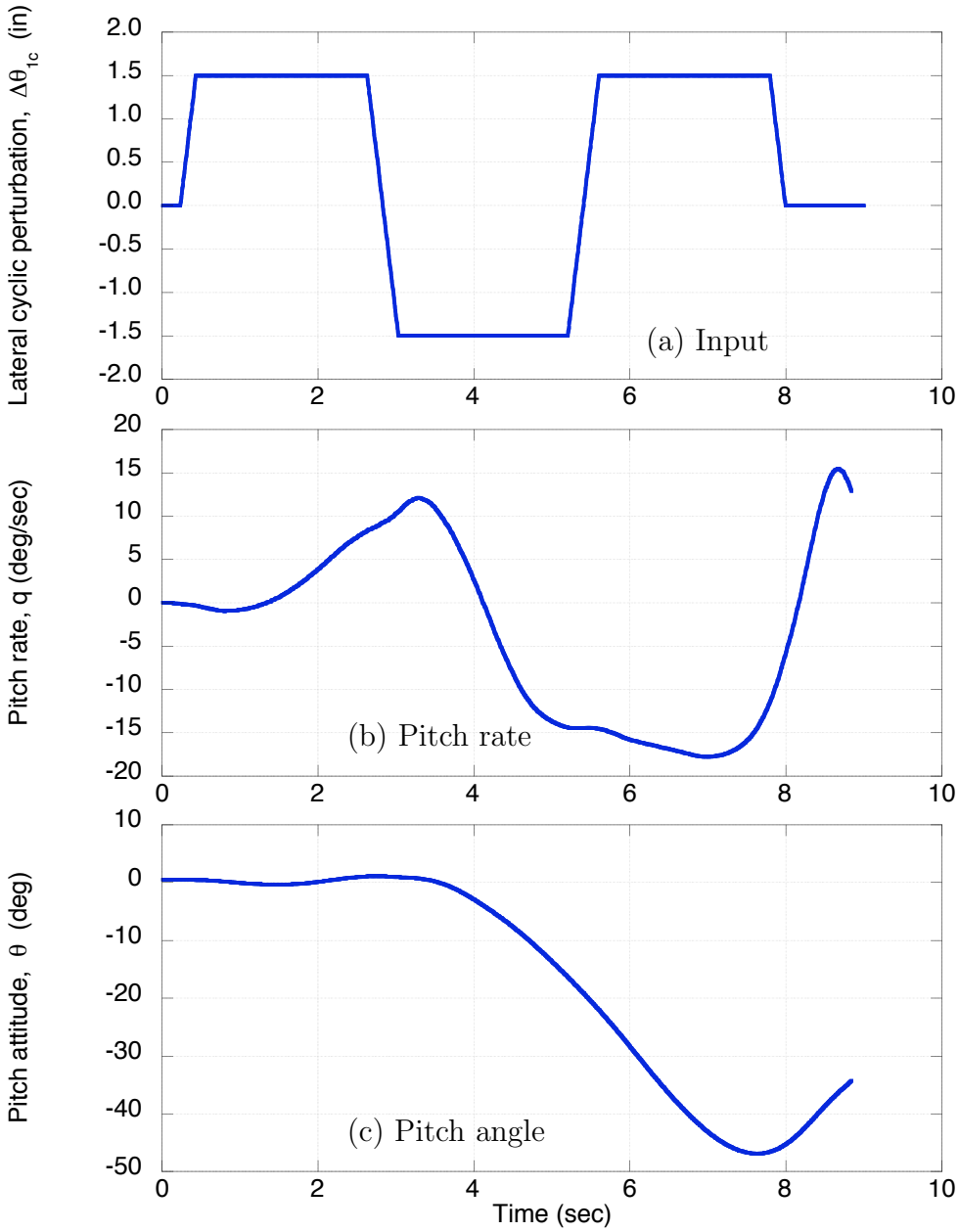

Figure 7.40: Time history of the control input, pitch rate q and pitch angle θ for a roll reversal maneuver; $V = 80$ kts.

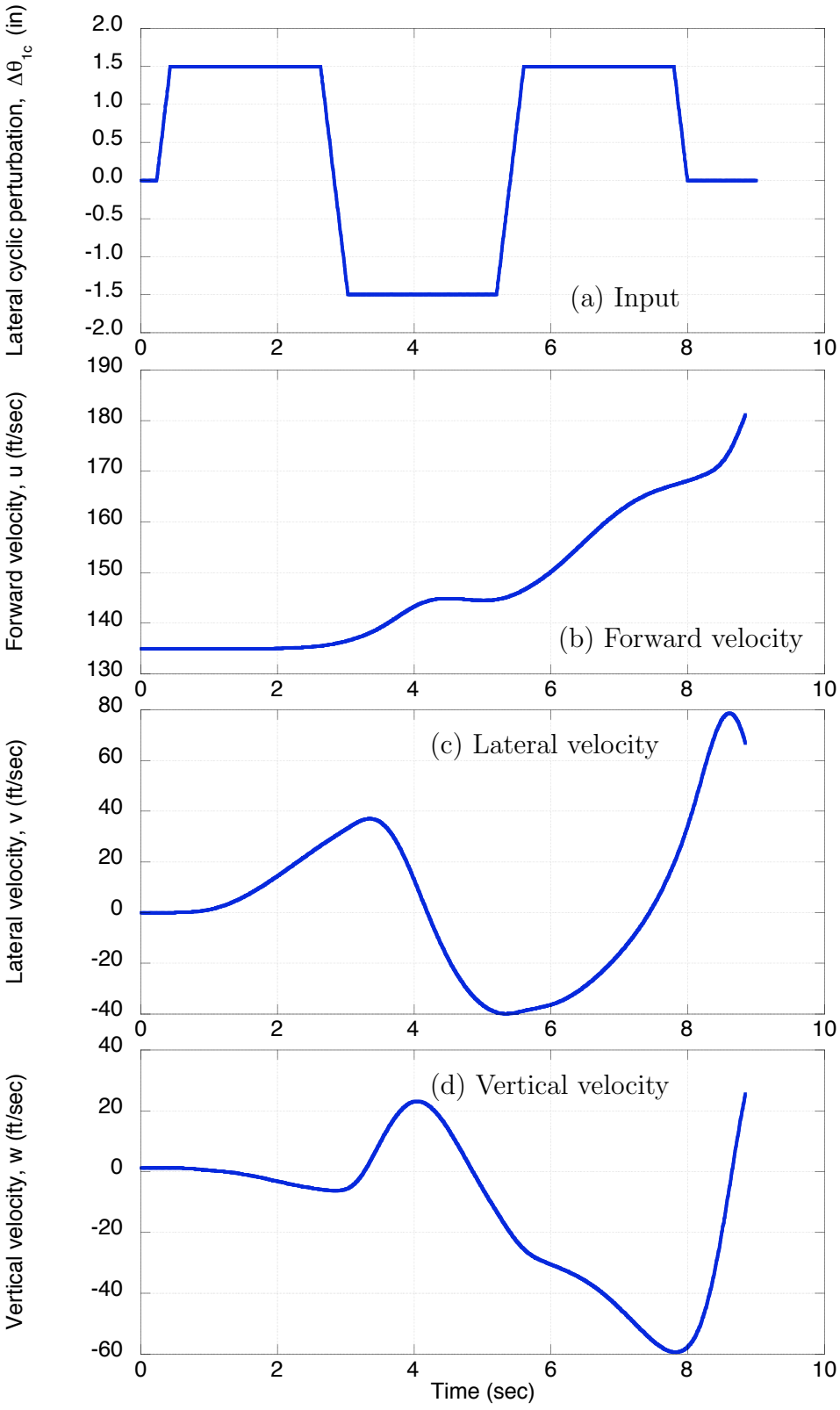

Figure 7.41: Time history of the control input and forward, lateral and vertical velocities, u, v and w respectively, for a roll reversal maneuver; $V = 80$ kts.

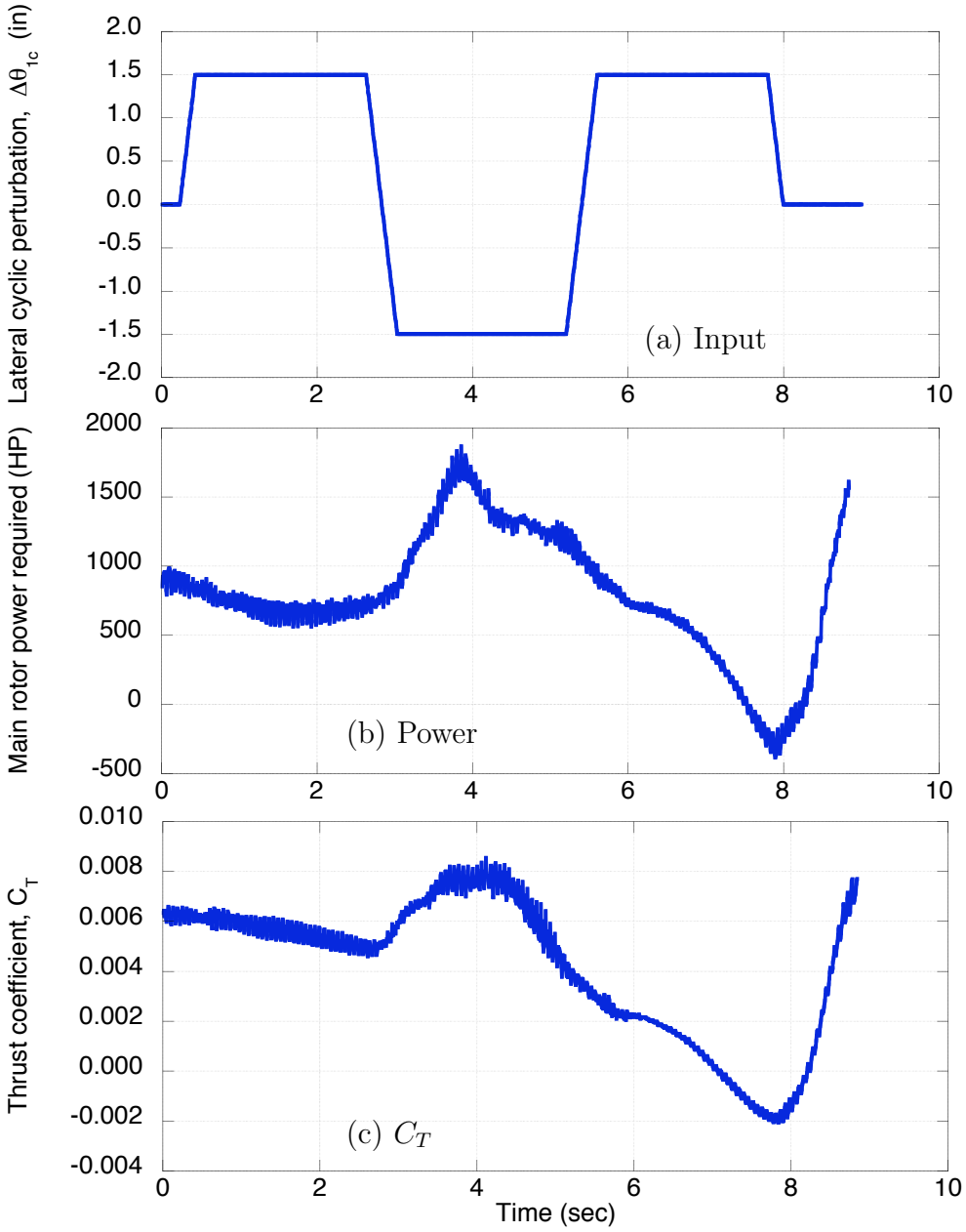

Figure 7.42: Time history of the control input, main rotor power required Q_{MR} and thrust coefficient C_T for a roll reversal maneuver; $V = 80$ kts.

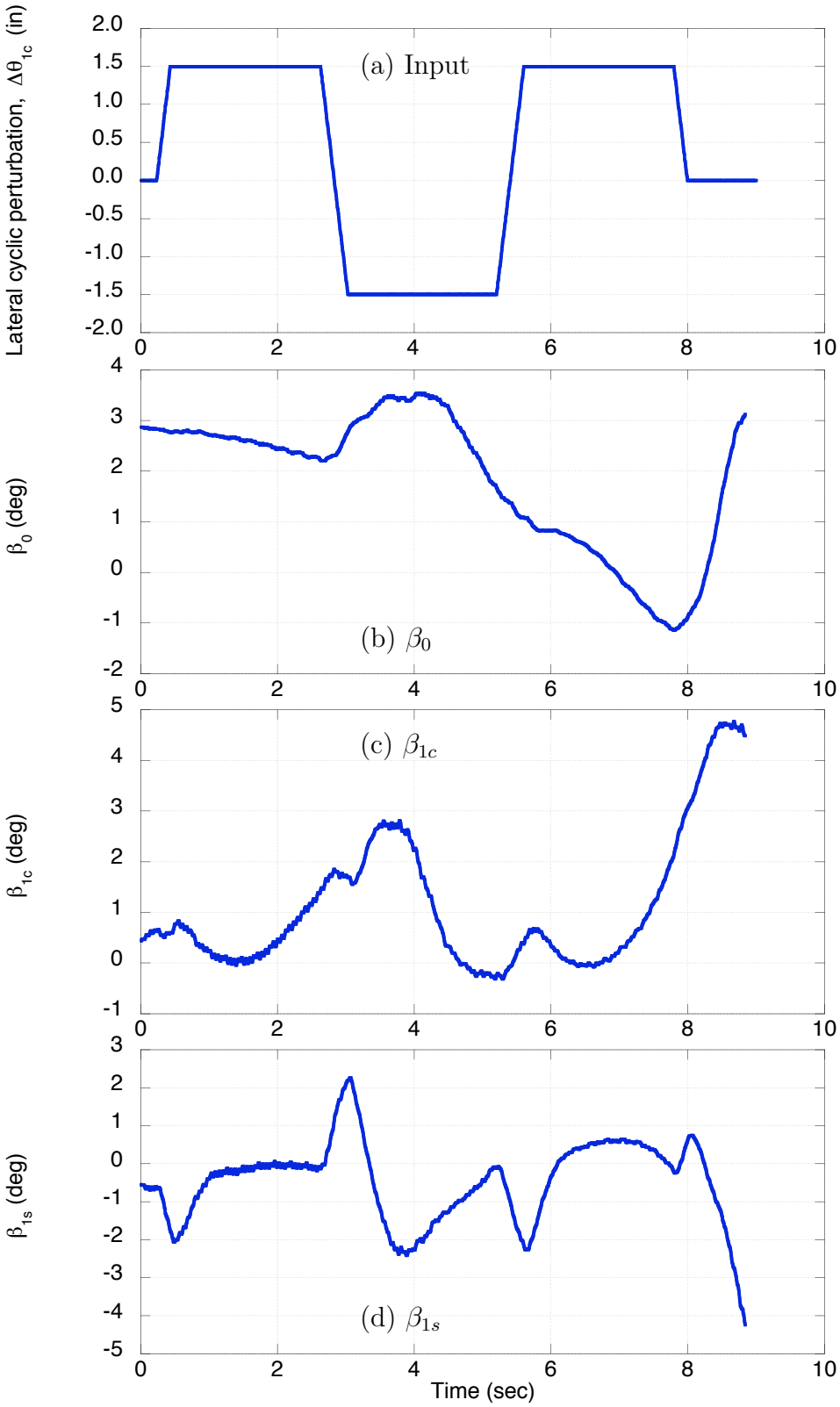

Figure 7.43: Time history of the control input and flap coefficients, β_0, β_{1c} and β_{1s} for a roll reversal maneuver; $V = 80$ kts.

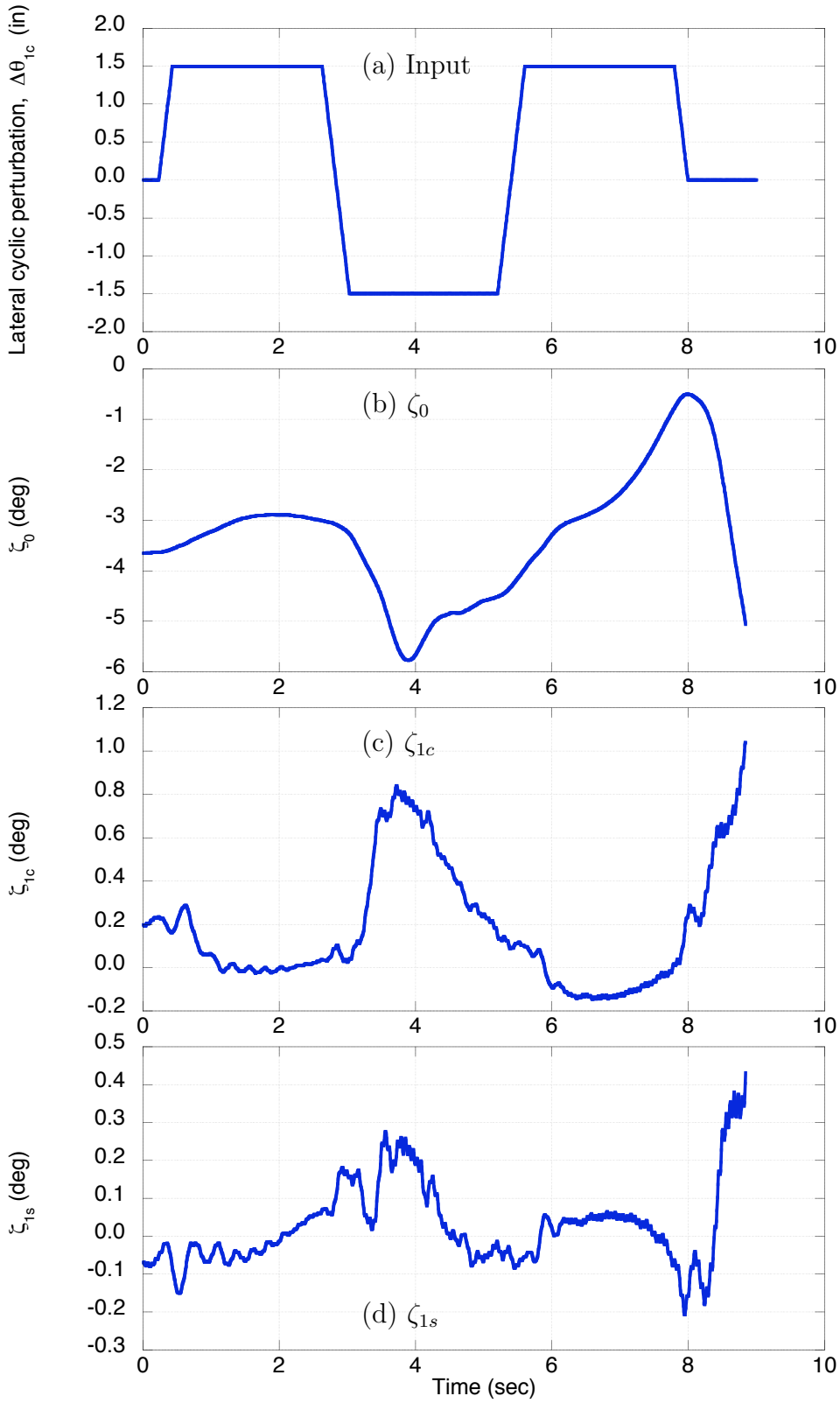

Figure 7.44: Time history of the control input and lag coefficients, ζ_0, ζ_{1c} and ζ_{1s} for a roll reversal maneuver; $V = 80$ kts.

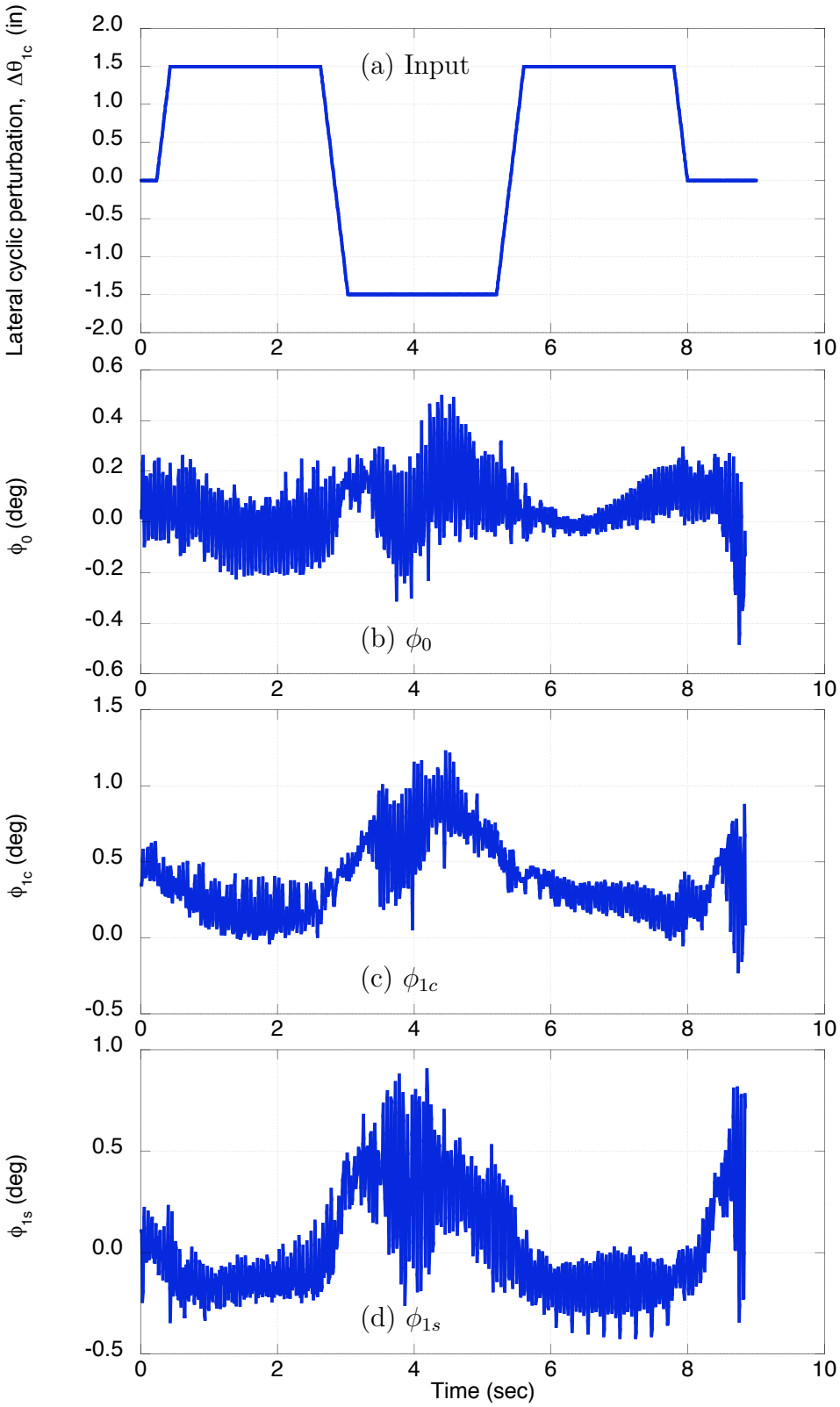

Figure 7.45: Time history of the control input and torsion coefficients, ϕ_0, ϕ_{1c} and ϕ_{1s} for a roll reversal maneuver; $V = 80$ kts.

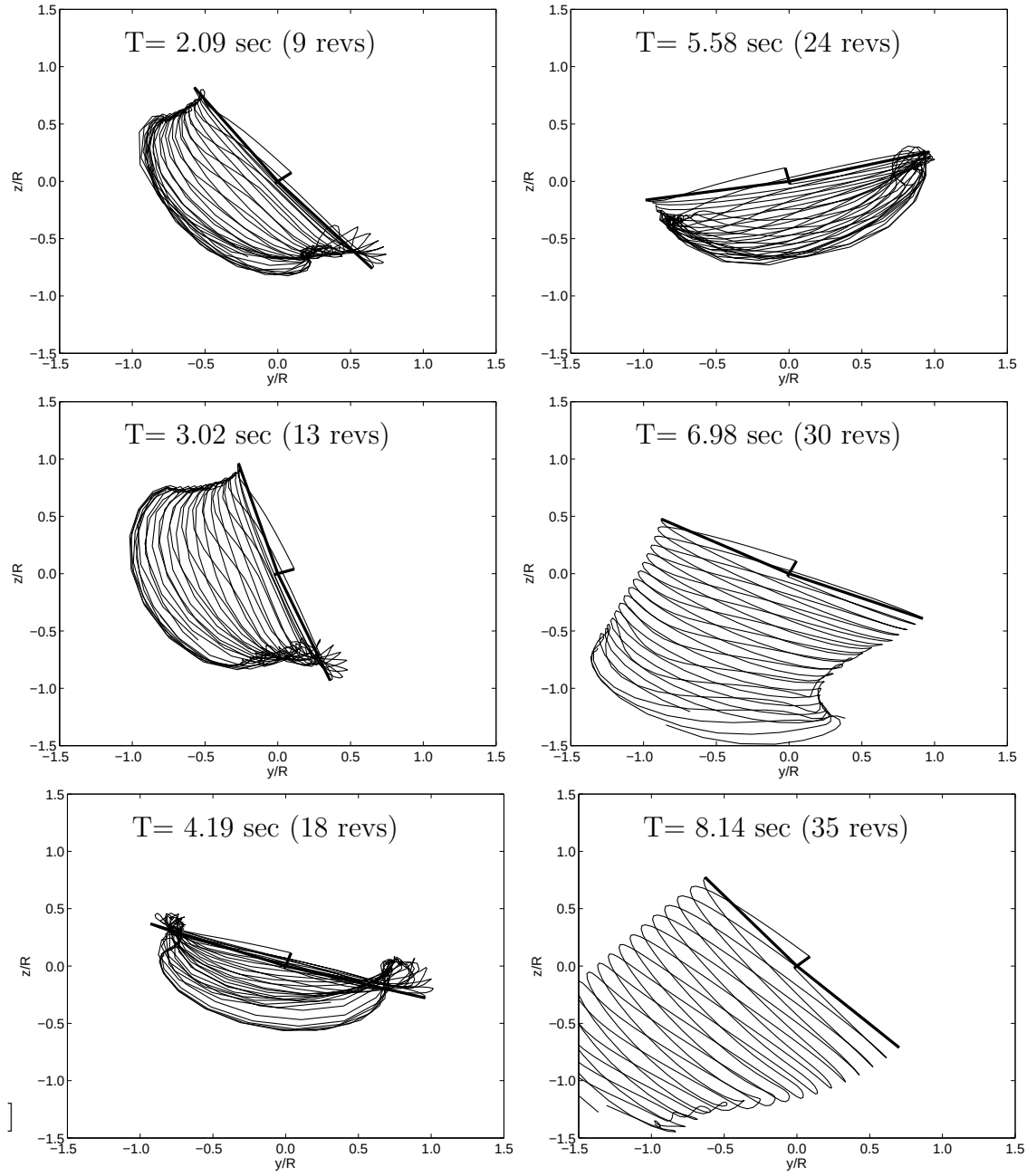

Figure 7.46: Rear view of the wake geometry at different times for a roll reversal maneuver; $V = 80$ kts.

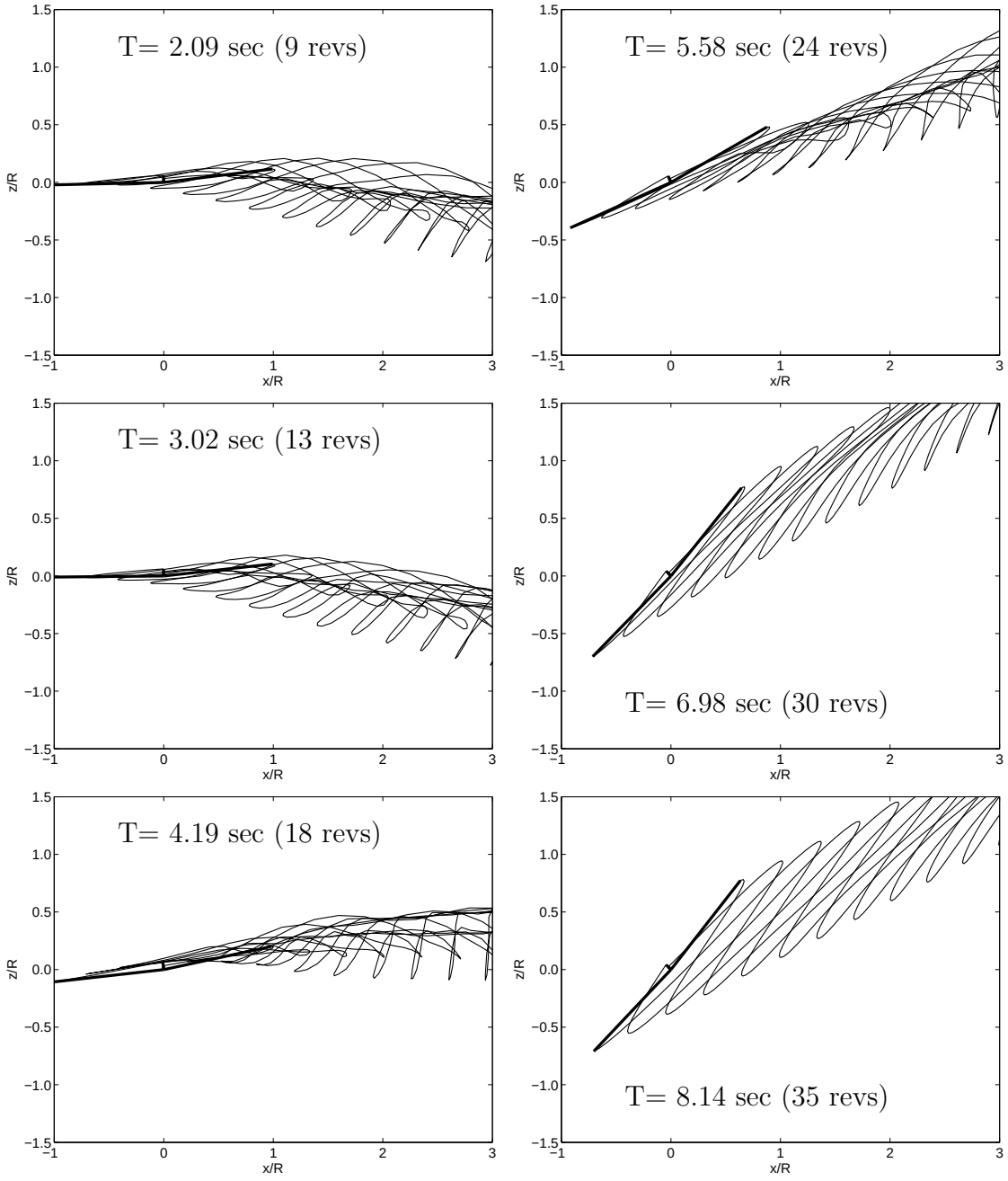

Figure 7.47: Side view of the wake geometry at different times for a roll reversal maneuver; $V = 80$ kts.

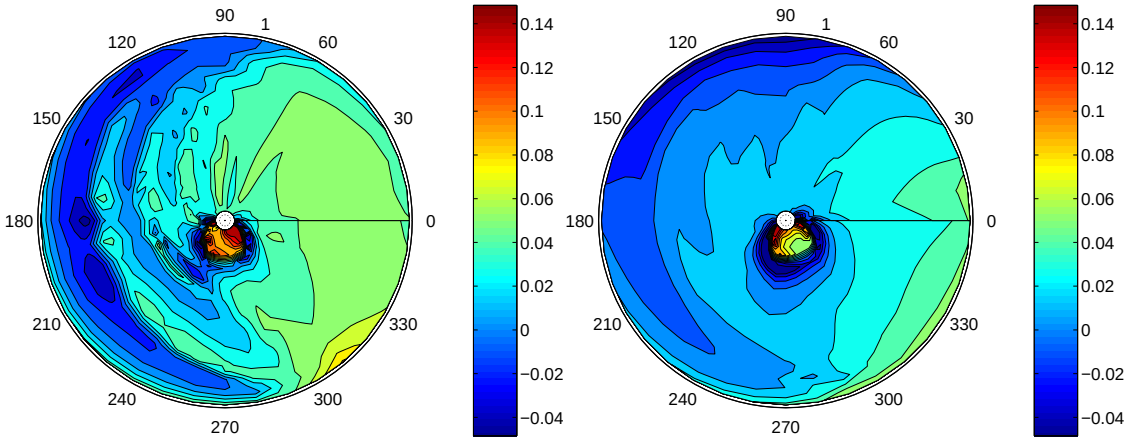

(a) T= 2.09 sec (9 revs)

(b) T= 5.58 sec (24 revs)

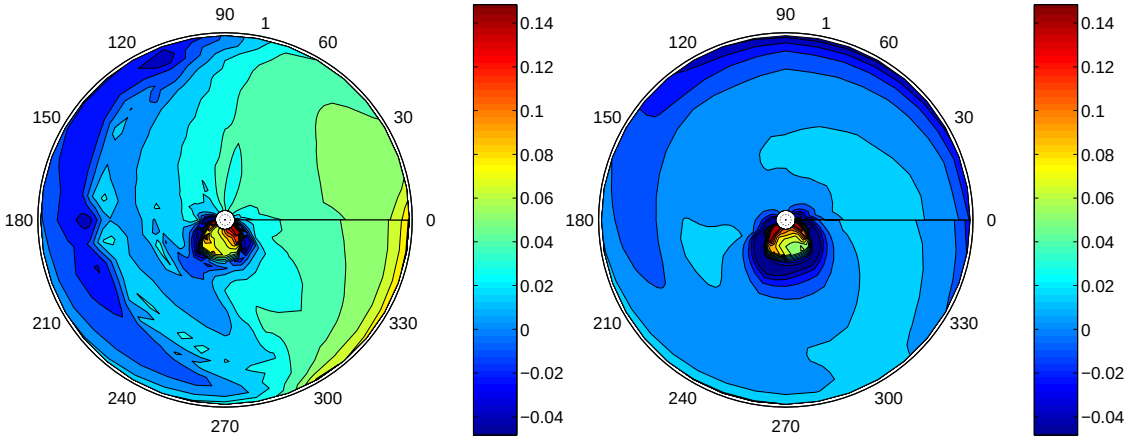

(c) T= 3.02 sec (13 revs)

(d) T= 6.98 sec (30 revs)

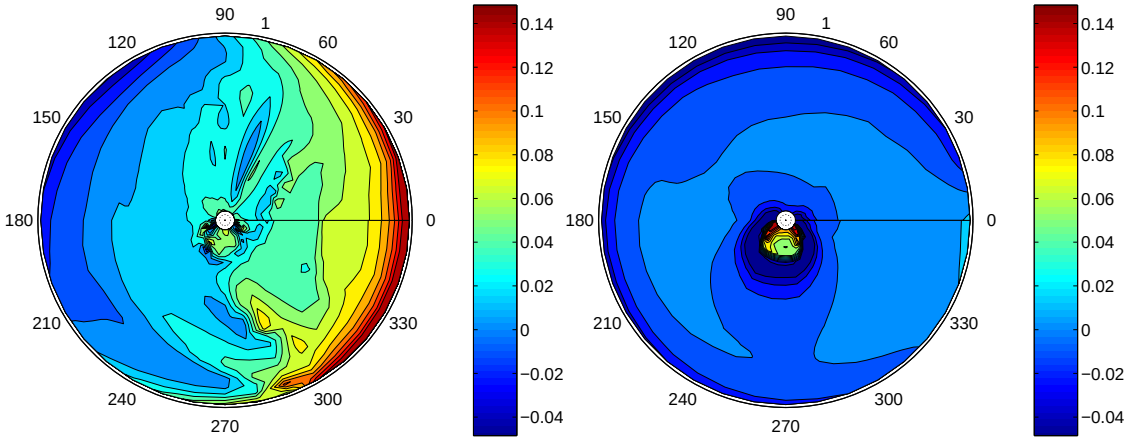

(e) T= 4.19 sec (18 revs)

(f) T= 8.14 sec (35 revs)

Figure 7.48: Distribution of induced velocities over the rotor at different times for a roll reversal maneuver; $V = 80$ kts.

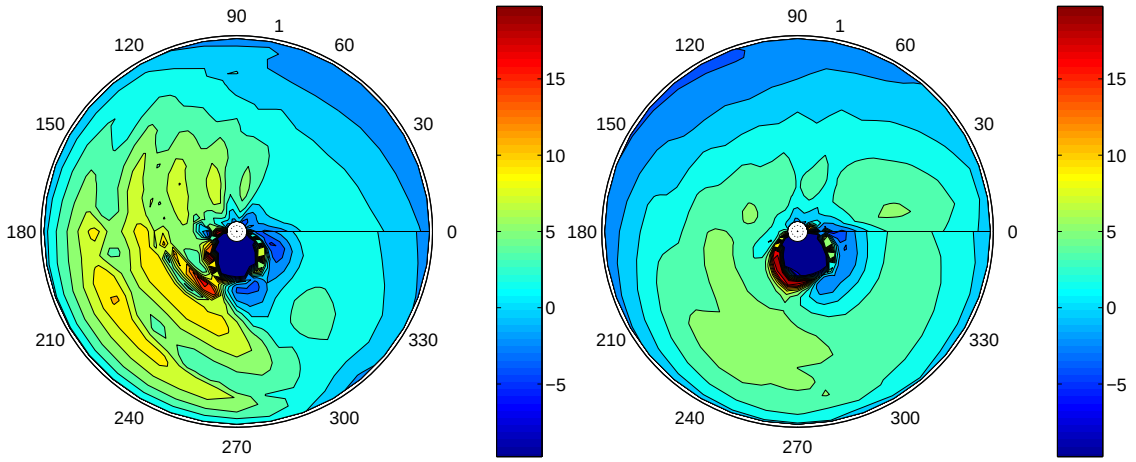

(a) T= 2.09 sec (9 revs)

(b) T= 5.58 sec (24 revs)

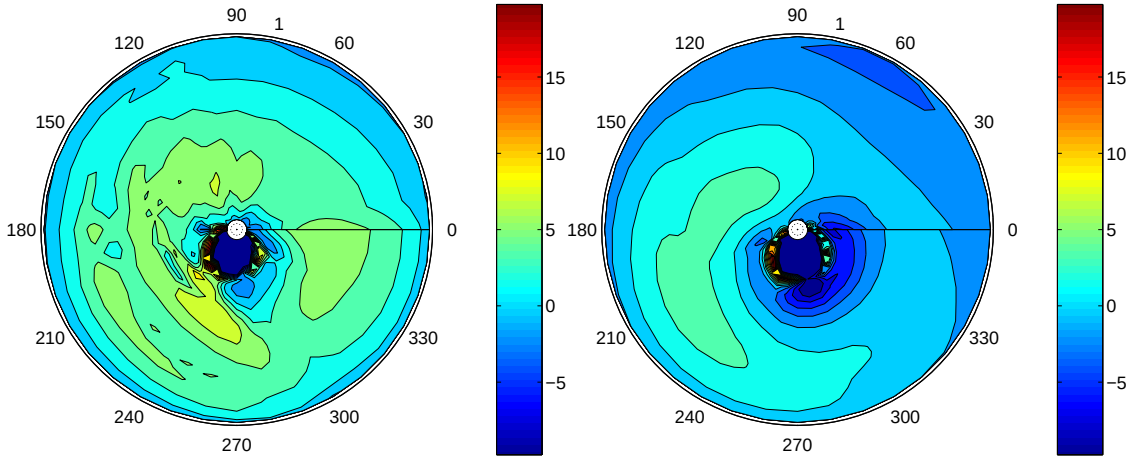

(c) T= 3.02 sec (13 revs)

(d) T= 6.98 sec (30 revs)

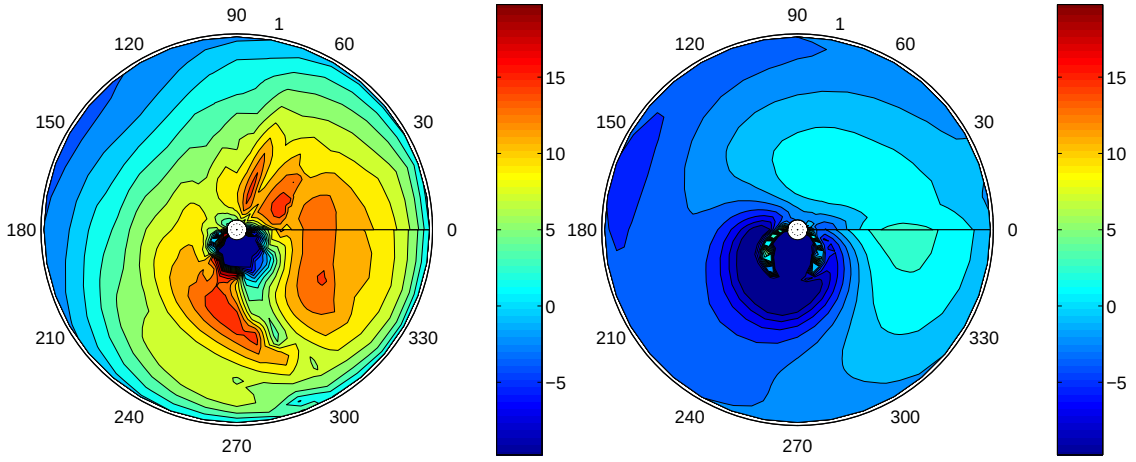

(e) T= 4.19 sec (18 revs)

(f) T= 8.14 sec (35 revs)

Figure 7.49: Distribution of angle of attack over the rotor at different times for a roll reversal maneuver; $V = 80$ kts.

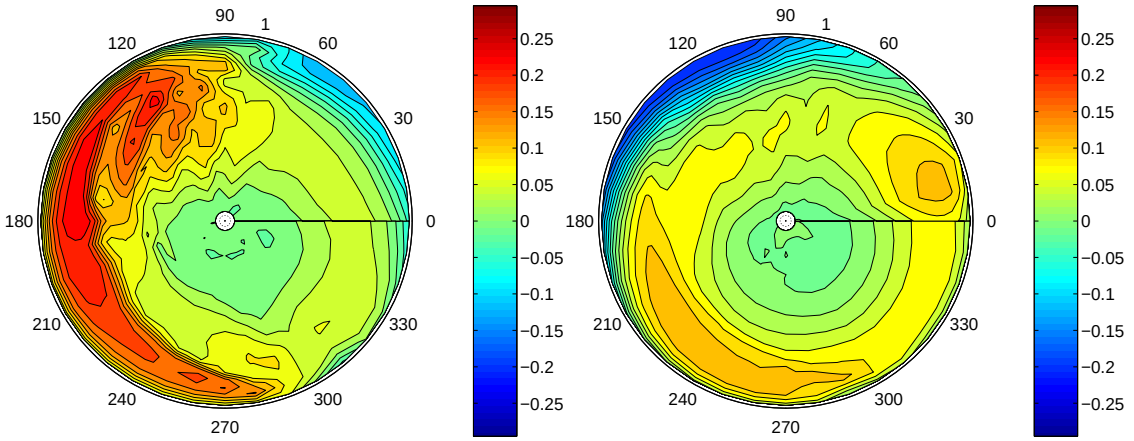

(a) T= 2.09 sec (9 revs)

(b) T= 5.58 sec (24 revs)

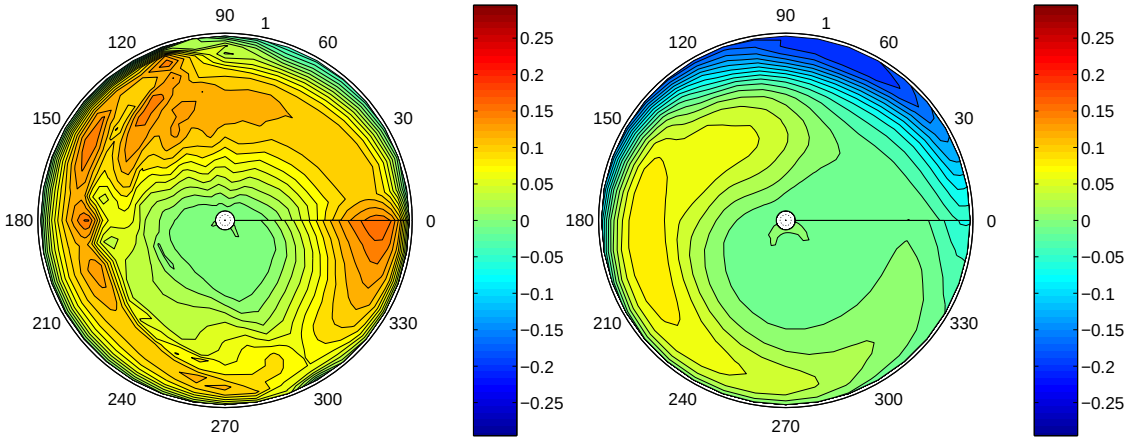

(c) T= 3.02 sec (13 revs)

(d) T= 6.98 sec (30 revs)

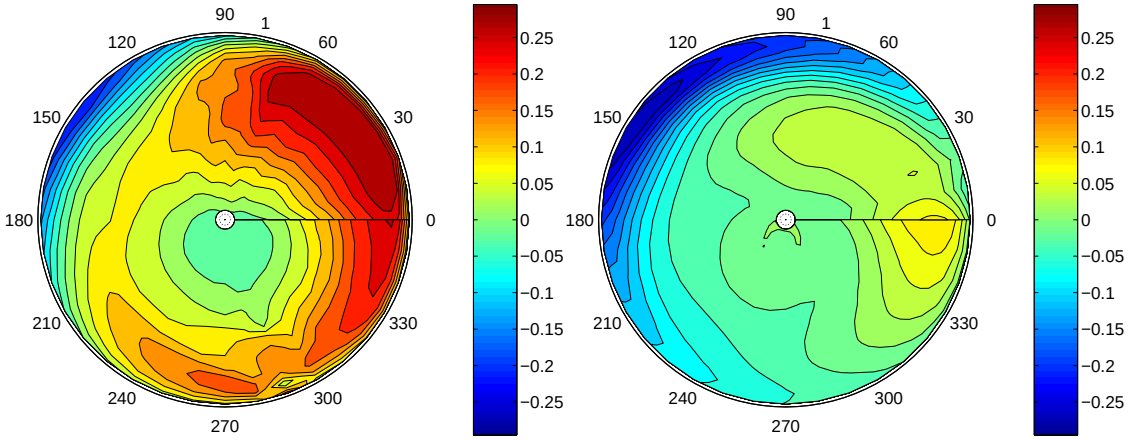

(e) T= 4.19 sec (18 revs)

(f) T= 8.14 sec (35 revs)

Figure 7.50: Distribution of non-dimensional elemental lift, $C_L M^2$, over the rotor at different times for a roll reversal maneuver; $V = 80$ kts.

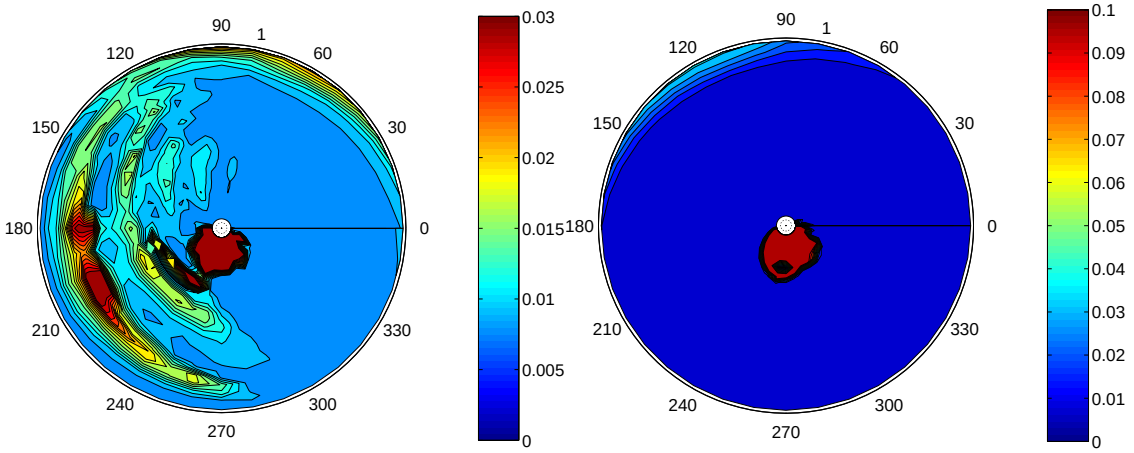

(a) T= 2.09 sec (9 revs)

(b) T= 5.58 sec (24 revs)

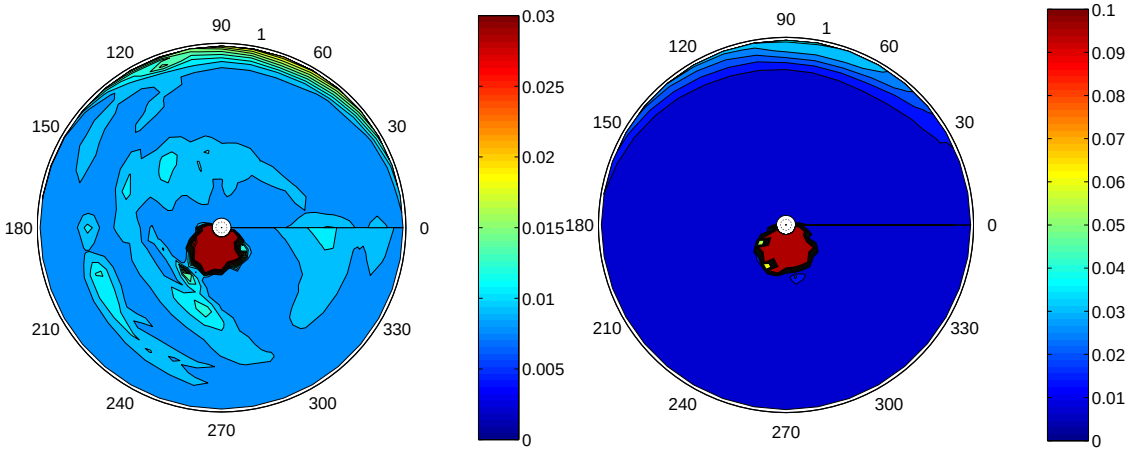

(c) T= 3.02 sec (13 revs)

(d) T= 6.98 sec (30 revs)

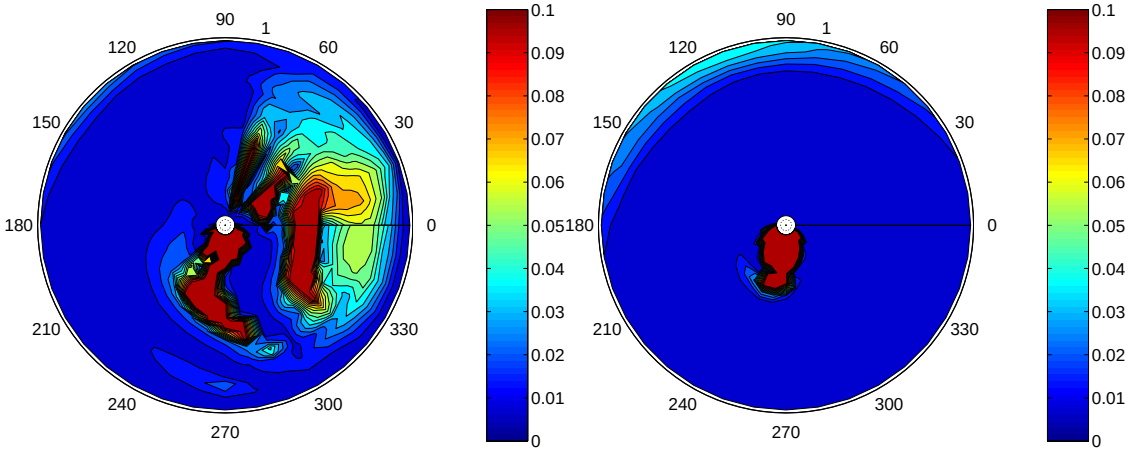

(e) T= 4.19 sec (18 revs)

(f) T= 8.14 sec (35 revs)

Figure 7.51: Distribution of drag coefficient, C_D, over the rotor at different times for a roll reversal maneuver; $V = 80$ kts.

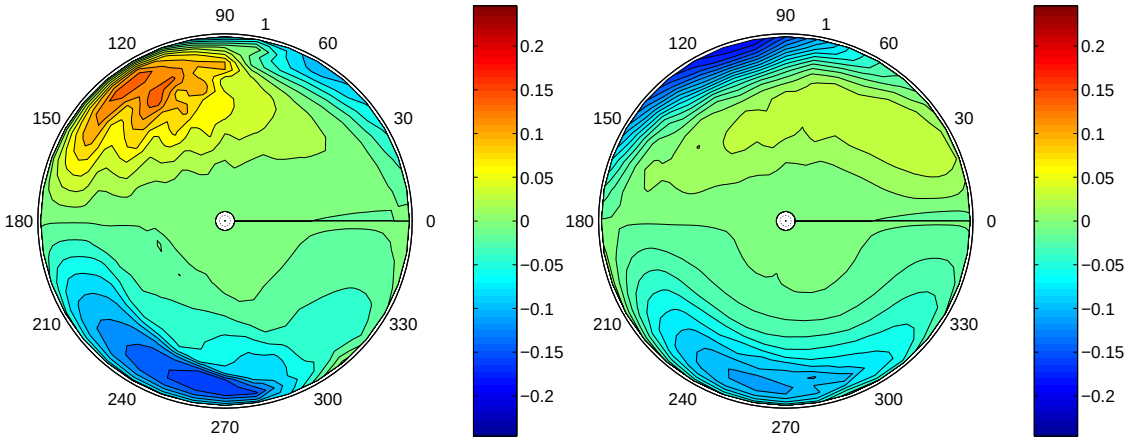

(a) T= 2.09 sec (9 revs)

(b) T= 5.58 sec (24 revs)

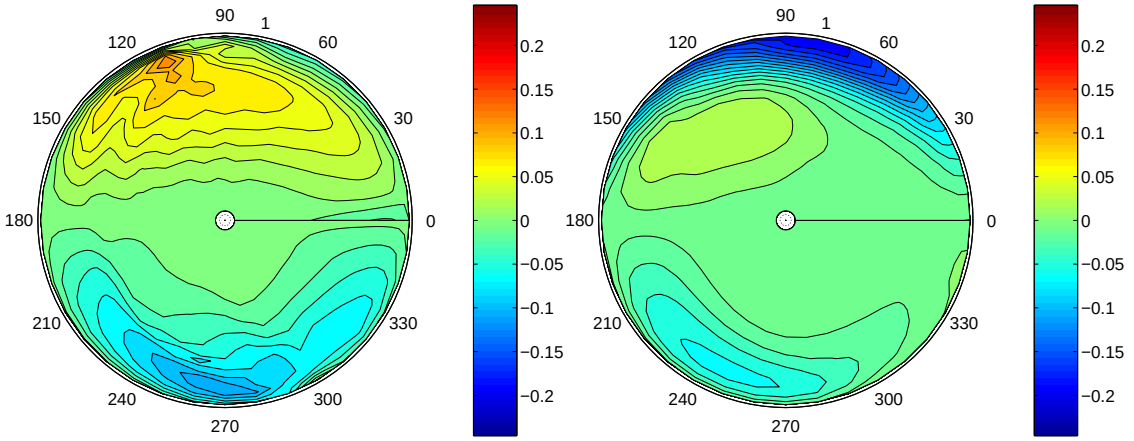

(c) T= 3.02 sec (13 revs)

(d) T= 6.98 sec (30 revs)

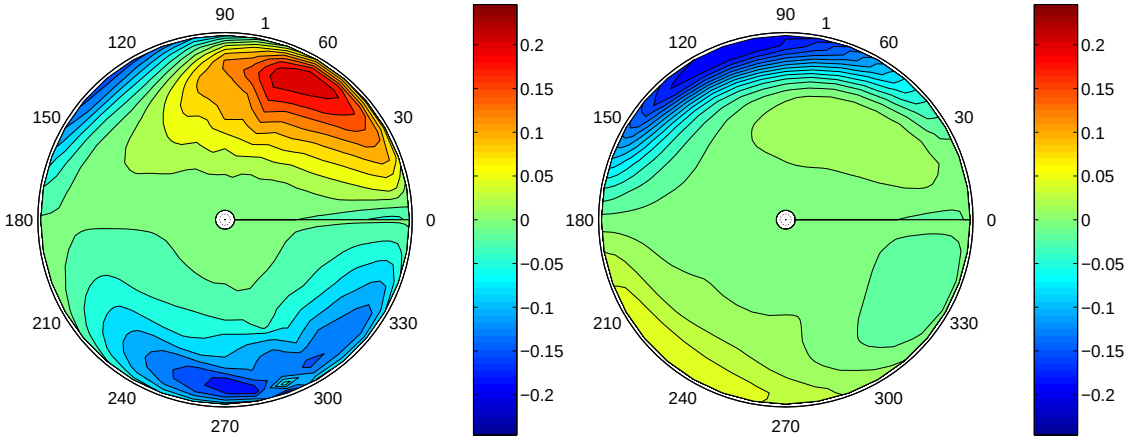

(e) T= 4.19 sec (18 revs)

(f) T= 8.14 sec (35 revs)

Figure 7.52: Distribution of lift contribution to roll moment $rC_L M^2 \sin\psi$, over the rotor at different times for a roll reversal maneuver; $V = 80$ kts.

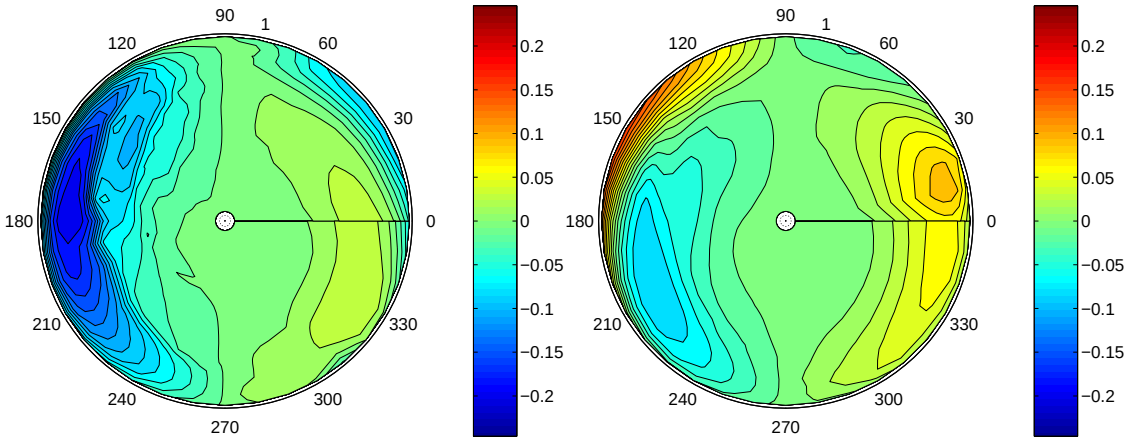

(a) T= 2.09 sec (9 revs)

(b) T= 5.58 sec (24 revs)

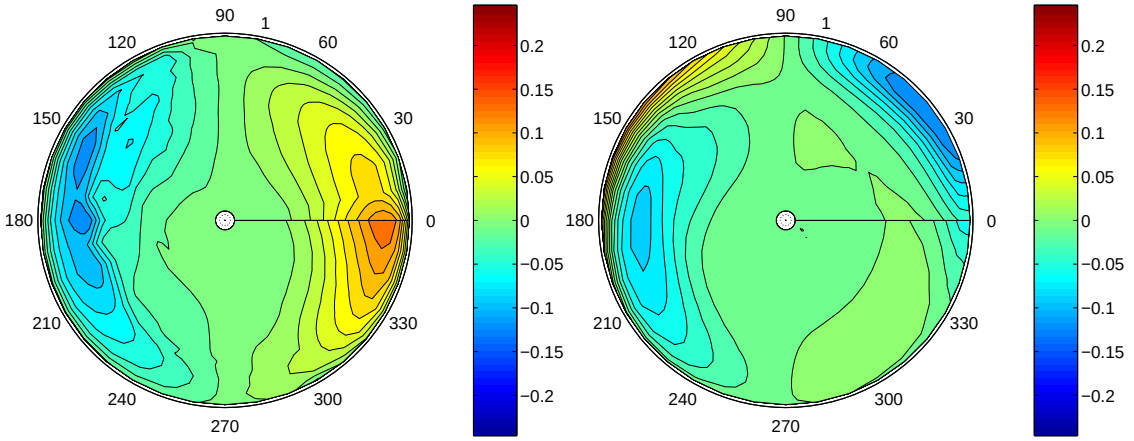

(c) T= 3.02 sec (13 revs)

(d) T= 6.98 sec (30 revs)

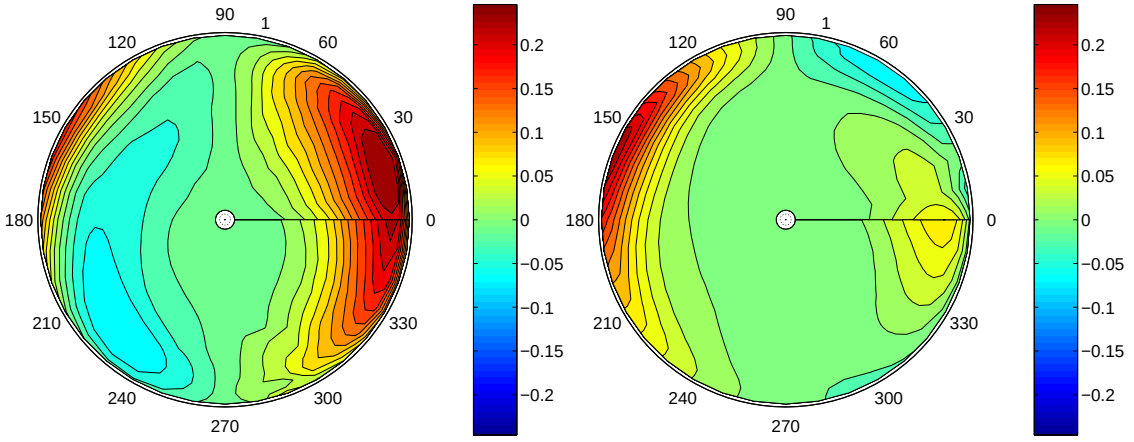

(e) T= 4.19 sec (18 revs)

(f) T= 8.14 sec (35 revs)

Figure 7.53: Distribution of lift contribution to pitch moment $rC_L M^2 \cos\psi$, over the rotor at different times for a roll reversal maneuver; $V = 80$ kts.

Chapter 8

Summary and Conclusions

8.1 Summary

This dissertation has described and validated the coupling of a flight dynamics model that includes a flexible blade model with a time-marching free wake model capable of capturing maneuvering flight.

The flight dynamics model is based on a system of coupled nonlinear rotor-fuselage differential equations in first-order, state-space form. It models the rigid body dynamics of the helicopter with the non-linear Euler equations. The aerodynamic characteristics of the fuselage and empennage are included in the form of look-up tables as a function of angle of attack and sideslip. The dynamics of the rotor blades are modeled with coupled flap, lag and torsion, a finite element discretization and a modal coordinate transformation to reduce the number of degrees of freedom. There is no limitation on the magnitudes of the hub motions. In particular, the effects of large rigid body motions on the structural, inertia, and aerodynamic loads acting on the flexible blades are rigorously taken into account.

The free wake model used uses time-accurate scheme to solve the wake equa-

tions, and therefore it can be used rigorously to obtain the transient response of the helicopter to pilot inputs, while it can also model steady state conditions by simply stepping the equations until the induced velocities or the geometry converge below certain threshold. Moreover, this wake model can capture the effect of maneuvering and can, therefore, be used to model turns and other maneuvers of arbitrary amplitude.

The coupled model was used to solve for steady equilibrium conditions and to integrate the equations of motion to obtain the response of the helicopter to pilot inputs. The flight conditions which have hitherto proven a challenge to most flight dynamics codes can be successfully simulated using the new coupled time-marching free wake-flight dynamics code. Regarding trim, the flight conditions studied and validated with experimental data were straight and level flight, steady turns at 60 kts and climbs and descents, also at 60 kts. Some steep descents at very low speed and descending turns were also simulated in trim and investigated. Besides validation with flight test data when available, the effects of different model parameters were also considered, like blade flexibility or the implementation of the swept tip of the UH-60A. In terms of transient response, the model was compared with available flight test data for a lateral stick deflection starting from hover conditions. Moreover, the model was used to simulate a descent into the vortex ring state and a roll reversal maneuver.

8.2 Conclusions

After presenting the results obtained with the present model, the following are the conclusions obtain in this dissertation.

With regards to the general coupling of the model and computational considerations, the following can be said:

1. The non-linear algebraic equation solver builds a Jacobian matrix of derivatives by perturbing each of the unknowns and approximating the derivative with a forward difference approximation. It was shown that the free wake model was insensitive to the perturbation used to build the Jacobian, and therefore converging the free wake for each call to build the Jacobian matrix was a waste of computational time. The process was updated to use a baseline inflow calculated only once to build the derivatives, while the free wake is updated normally in every evaluation of the equations of motion needed by the solver towards a solution.

2. The new approach to calculate the bound circulation with the Weissinger-L method is not only more accurate than the previous calculation with two-dimensional lift theory without consideration for tip loss effects, but also, being integrated with the free wake model, it can be updated within each step in the calculation of the free wake model, inverting the circulation-inflow loop in a more accurate and computationally efficient manner.

3. The new approach for the integration of the equations of motion with the time-

marching free wake model is more rigorous that the previous implementation with a relaxation free wake model, as the time-accurate wake model can provide updated and accurate inflow at each step of the simulation. Moreover, not having to look for a trim-like convergence of the free wake for every revolution during the calculation of the response is computationally more efficient.

4. Most importantly, the tightly coupled resulting simulation model is very robust, having been used to model quite extreme flight conditions where numerical instabilities may occur, no computational difficulties were observed.

As for the straight and level flight trim results, the following conclusions can be drawn:

1. The Bhagwat–Leishman free wake model significantly improves the trim prediction results over previous inflow methodologies used. The induced velocities obtained with the time-marching free wake improve the correlation of the power required results and the predicted values of collective. The lack of interference effects between the rotor wake and the fuselage and empennage affects the prediction of the longitudinal and lateral cyclic and pitch and roll attitudes at the transition speeds, although in hover and high speed they both correlate well with flight test data. The pedal setting is predicted poorly for the entire flight range.

2. The effect of the accurate inflow distribution on the blade dynamics during trim was also studied. The blade flapping response depends greatly on the

distribution of angle of attack, which in turn is largely determined by the induced velocities. In hover, a perfectly axially symmetric angle of attack distribution contributes to a 1-harmonic sinusoidal flapping response. As the speed increases, the angle of attack variation over the rotor excites the higher harmonics of the flapping response. The variation in lag is determined with the in-plane forces, and as the drag increases on the advancing side with speed, the lag angle changes parallelly. The elastic torsion of the blade can also be explained with the changes in the pitching moment at each blade station over the azimuth due to changes in the lift distribution, which is in turn determined to a great extent by the non-linear inflow obtained with the time-marching free wake model.

3. The effect of blade flexibility was analyzed by comparing the trim results with a rigid blade and the elastic blade with 5 coupled flap, lag and torsion. The rigid blade model under-predicts the power required by 10% because the lack on torsion dynamics reduces the collective needed to produce the same overall thrust.

4. The inclusion of the swept tip in the blade model decreases the profile torque, and thus the power, in high speeds, improving the correlation with flight test data. However, the swept tip model also increases the overall induced velocities and thus the induced torque, and this effect is dominant at speeds between 40 and 100 kts, in which the extra induced torque causes an over-prediction of the main rotor power required. As the free wake model has not been investigated

for such a blade planform, it becomes unclear whether the approach used to model the swept tip with the free wake is the most appropriate, and further study is required.

Regarding the coordinated turns and the steady climbs and descents modeled, specific conclusions were:

1. The coordinated turns performed at a speed of 60 kts and with turn rates of -25 to 25 deg/sec compared positively with flight test data. The collective showed excellent correlation, and the power required by the main rotor did so as well with the exception of the highest rates of turn, at which the profile torque increased the power dramatically. While the lateral cyclic was captured with great accuracy, the longitudinal cyclic prediction was very poor, as was the pitch attitude prediction. However, there is a trade-off in the miss-prediction of the longitudinal cyclic and the fuselage pitch attitude. This indicates again that the wake-fuselage interaction is necessary to accurately predict the longitudinal equilibrium conditions, as well as the effects of the interaction between the main rotor and the tail rotor. The pitch and yaw rates show excellent agreement with the experimental values, while the pedal is poorly predicted.

2. The agreement of the power predictions with the flight test measurements was good, except at high rates of descent where, however, the general trends were still well predicted. A slight anomaly observed in the trend with flight path angle of the power required to climb at 60 kts, was seen both in the

experimental data and in the simulation results, and could be explained with the particular geometry of the wake in the transition to climb and the induced velocities such geometries produce.

3. The tip path plane tilts forward more significantly during descents because of a region of high angle of attack in the retreating side caused by higher induced velocities there. In climbing flight there is more than one region of increased angle of attack, which results in an additional 2/rev excitation of the flapping response.

4. The analysis of the blade tip elastic torsion distribution for different climb and descent angles shows than, similarly to the flapping response, in descents the high lift in the retreating side produces a region of nose up pitching moments. This causes the blade to twist nose-up in the rear of the rotor. The reverse occurs on the advancing side/front of the rotor. In climb, the 2/rev excitation described for the flap degree of freedom also affects the time histories of the torsional deflections of the blade tip.

5. The near-vortex ring state wake characteristics observed experimentally and predicted with isolated rotor models were also observed in this coupled rotor-fuselage-wake simulation, including: wake convection over the plane of the rotor, vortex bundling downstream of the wake approaching the rotor with increasing rate of descent, and high lift coefficient and near-stall condition in the inboard section of the blade.

The simulation of the transient response to several maneuvers provided the

following conclusions:

1. The use of a time-accurate free wake model, coupled rigorously with the time integration procedure, improves the prediction of the on-axis response to a lateral cyclic deflection of 1 inch to the right from an initial hover condition, as compared with a relaxation free wake model. The off-axis response does not capture the initial pitch-down trend, even though the induced velocities would contribute to that being captured correctly. The following trend of pitch rate is captured correctly, but anticipated. However, it is believed that the fact that this response is relatively small in amplitude and that the rotor wake influence on the fuselage and empennage is not modeled are the cause for the poor off-axis response, despite the accurate inflow modeling.

2. The inclusion of the swept tip in the modeling of the blade improves the on-axis response further, with a decrease of the overshoot of the roll rate predicted immediately after the application of the lateral cyclic step. The off-axis response improves slightly, although the presence of other issues affecting the off-axis response remains. Therefore, improved blade modeling has a positive effect on the flight dynamics calculations.

3. It was observed that the response to the lateral cyclic maneuver from hover deteriorated after the application of some pedal by the pilot. Given that the pedal setting had been predicted poorly throughout the trim results, it was believed that the problems in the modeling of the pedal would also affect the response to a pedal input. Indeed, removing the pedal input improved the

response obtained with the simulation model, both in the longitudinal and lateral directions.

4. An axial descent from hover was simulated with the intention of investigating the effects of going through the vortex ring state. The time-marching free wake can capture the formation of the vortex accumulation in a toroidal shape at the plane of the rotor, and the consequences that have been observed previously in the literature. As the vortex forms at the plane of the rotor, large changes in attitude are observed, both in pitch (nose-down) and roll (port side). A look at the geometry of the wake during the formation and evolution of the VRS shows that the vortex ring does not cross the rotor plane uniformly, but does so unevenly with the consequential distributed aerodynamic loads producing large nose-down and port side moments.

5. The lift losses associated with the "vortex ring" crossing the rotor produce large thrust fluctuations, an increase in power, visible despite the lower power requirements associated with the descent, and flap fluctuations. These effects have been documented before in experimental studies.

6. A roll reversal was simulated to see the effect of larger angular rates on the wake geometry and the effect of those changes in the overall simulation. The maneuver-induced wake deformations influence the inflow distribution, which in turn affects the aerodynamic loading. The initial roll to the right produces a large bank angle, and a slight nose-up pitching moment due to the cross-couplings. The roll to the left does not reach such a high bank angle because

there is a delay between the roll attitude and the roll rate, and the next deflection to the right is applied before the left bank angle can develop. However, the left turn is accompanied by a large nose-down pitching moment and attitude. This, combined with the high speed of the helicopter, translates into an effective climb for the rotor, even though the helicopter is slightly descending as it pitches down and rolls back to the right.

As a closing remark, the new flight dynamics simulation with a time-marching free-vortex wake model shows that the assumptions on which simpler momentum theory or dynamic inflow based models rely on are not correct. A correct representation of the wake deformations has been shown to be critical to be able to describe the behavior of the helicopter in free flight accurately. The wake does not behave in an organized skewed helicoidal shape, as some simpler models assume, and the actual deformations it suffers are asymmetric and time-dependant. Moreover, the present model also shows that the wake behavior depends greatly on the flight condition. Parametric extensions to the simpler inflow models are limited to the flight conditions for which the tuning coefficients were developed, but cannot be applied to other flight conditions in which the wake behaves differently. The present model overcomes those limitations, with the capability of accurately describing both steady and transient maneuvers without imposing conditions on the behavior of the rotor wake.

8.3 Recommendations for future work

The many limitations, assumptions or approximations that the present study has faced are all encouraging suggestions for future work. On many occasions, a particular problem encountered was deemed to be beyond the scope of the current work, which otherwise would have lengthen beyond the reasonable. This does not mean that the problem was not considered worthy of attention, and thus this sections will recommend areas in which to further the development of the model.

In summary, the following are recommendations for future work:

1. It was soon found that the simple method to include the downwash of the rotor on the fuselage that is used with dynamic inflow did not allow for convergence of the model with the free wake. The present study was carried without including such effects, but without disregarding their importance. In particular, the effect of the moments caused by such interference would be expected to improve the prediction of the body attitudes, which were not always captured correctly. An better implementation of the influence of the rotor wake on the fuselage and empennage, as well as the interaction between the main rotor and tail rotor wakes is therefore highly recommended. Such implementation would ideally take advantage of the knowledge of the exact location of the vortex wake that is available from the free wake model.

2. Throughout the present work, the prediction of the pedal setting has been poor for all the flight conditions considered. It is recommendable to dedicate some effort to the modeling of the tail rotor as well as the control mixer in the

model.

3. The induced velocities with the free wake model and the swept blade were found to be larger than with the straight blade configuration. The Bhagwat–Leishman free wake model (Ref. 9) has not been studied specifically for such particular blade configuration. Before conclusions can be drawn with a coupled rotor-fuselage-free wake model, the behavior of the free wake with swept tips and the most appropriate way to model it should be investigated.

4. The availability of such a model capable of describing descending flight through the vortex ring state and into autorotation conditions is a great advantage to helicopter pilots who can simulate a wide range of situations in which entering autorotation might be necessary. This tool can be used to explore that flight regime further and increase safety and opperability.

5. The Bhagwat–Leishman time-marching free wake model has been validated in a wide range of configurations and for several applications, from ground effect (Ref. 40), to aeroacustic work (Ref. 73), including tandem (Ref. 83) and coaxial (Ref. 139) configurations. Some of that validation has been simulated similarly in the present work (Ref. 5). However, some of the other applications, like the aeroacustic calculations, would greatly benefit from being studied with a coupled rotor-fuselage-free wake model such as the one of the present study.

Appendix A

Additional swept tip coordinate transformation matrices

A.1 Local-to-global velocities and accelerations

The transformation between the local and the global coordinate systems of the velocity and acceleration of the rotational degrees of freedom is given by the following relations:

$$\begin{Bmatrix} \dot{\phi}_L \\ \dot{w}_{,xL} \\ \dot{v}_{,xL} \end{Bmatrix} = \left([T_\Lambda]^T + \left[T_\Lambda^{CR} \right] \right) \begin{Bmatrix} \dot{\phi}_G \\ \dot{w}_{,xG} \\ \dot{v}_{,xG} \end{Bmatrix} \tag{A.1}$$

$$\begin{Bmatrix} \ddot{\phi}_L \\ \ddot{w}_{,xL} \\ \ddot{v}_{,xL} \end{Bmatrix} = \left([T_\Lambda]^T + \left[T_\Lambda^{CR} \right] \right) \begin{Bmatrix} \ddot{\phi}_G \\ \ddot{w}_{,xG} \\ \ddot{v}_{,xG} \end{Bmatrix} + \left[T_\Lambda^{MR} \right] \begin{Bmatrix} \dot{\phi}_G \\ \dot{w}_{,xG} \\ \dot{v}_{,xG} \end{Bmatrix} \tag{A.2}$$

The non-zero elements of matrices $\left[T_{\Lambda}^{CR}\right]$ and $\left[T_{\Lambda}^{MR}\right]$ are:

$$
\begin{aligned}
ccc T_{\Lambda}^{CR}(3,1) &= w_{,xG}\left(\sin^2\Lambda + v_{,xG}\sin\Lambda\cos\Lambda\right) && \text{(A.3)}\\
T_{\Lambda}^{CR}(3,2) &= \phi_G\left(\sin^2\Lambda + v_{,xG}\sin\Lambda\cos\Lambda\right) && \text{(A.4)}\\
T_{\Lambda}^{CR}(3,3) &= w_{,xG}\phi_G\sin\Lambda\cos\Lambda && \text{(A.5)}\\
T_{\Lambda}^{MR}(3,1) &= 2\dot{w}_{,xG}\left(\sin^2\Lambda + v_{,xG}\sin\Lambda\cos\Lambda\right) + 2w_{,xG}\dot{v}_{,xG}\sin\Lambda\cos\Lambda && \text{(A.6)}\\
T_{\Lambda}^{MR}(3,2) &= 2\phi_G\dot{v}_{,xG}\sin\Lambda\cos\Lambda && \text{(A.7)}
\end{aligned}
$$

A.2 Global-to-local coordinate transformation

The global-to-local coordinate transformation for the vector of nodal degrees of freedom of the swept-tip element can be written in the form:

$$\left\{\mathbf{y}_G^t\right\} = \left[\Lambda_{GL}\right]\left\{\mathbf{y}_L^t\right\} \tag{A.8}$$

where $\{\mathbf{y}_L^t\}$ and $\{\mathbf{y}_G^t\}$ are given by Eqs.(4.28) and (4.29) respectively.

Combining Eqs.(2.29), (2.32) and (A.8), and comparing this to Eq.(2.17), the following relation can be stablished:

$$\left[T_{DP}\right]_G = \left[T_{\Lambda}\right]^T\left[T_{DP}\right]_L\left[T_{\Lambda}\right] \tag{A.9}$$

The transformation of the rotational degrees of freedom can be obtained by comparing elements $(1,2)$, $(1,3)$ and $(2,3)$ of Eq.(A.9):

$$\left\{\begin{array}{c}\phi_G\\ w_{,xG}\\ v_{,xG}\end{array}\right\} = \left(\left[T_{\Lambda}\right] + \left[T_{\Lambda}^{KR}\right]\right)\left\{\begin{array}{c}\phi_L\\ w_{,xL}\\ v_{,xL}\end{array}\right\} \tag{A.10}$$

The matrix $\left[T_{\Lambda}^{KR}\right]$ contains the nonlinear elements of the transformation between the rotational degrees of freedom in both frames. For the case of sweep only, the only nonlinear terms appear in the lag equation, and the only non-zero element of nonlinear transformation matrix is $T_{\Lambda}^{KR}(3,1)$, given by:

$$T_{\Lambda}^{KR}(3,1) = w_{,xL}\left(\sin^2\Lambda - v_{,xL}\sin\Lambda\cos\Lambda\right) \tag{A.11}$$

With the transformation of both the translational and rotational degrees of freedom known, the total transformation matrix $[\Lambda_{GL}]$ can be assembled:

One can similarly construct the inverse transformation matrix, which is:

$$[\Lambda_{GL}] = \begin{bmatrix} [\Lambda_{LL}] & [0] & \left[\Lambda_{NL}^{R}\right] \\ [0] & [\Lambda_{FF}] & -[\Lambda_{FT}] \\ [0] & -[\Lambda_{TF}] & [\Lambda_{TT}] \end{bmatrix} \tag{A.12}$$

The only new matrix in Eq.(A.12) is the nonlinear contribution, which for the reverse transformation becomes:

$$\left[\Lambda_{NL}^{R}\right] = \begin{bmatrix} 0 & 0 & 0 \\ w_{,xJ}\left(\sin^2\Lambda - \sin\Lambda\cos\Lambda v_{,xJ}\right) & 0 & 0 \\ 0 & 0 & 0 \\ 0 & 0 & 0 \end{bmatrix} \tag{A.13}$$

Appendix B

Coupling methodology with a relaxation free wake model in trim and a time-marching free wake model for the integrated response

The overall schematic of the coupling of the Bhagwat-Leishman time-accurate wake with the rotor-fuselage model to obtain the transient response of the helicopter after having obtained the trim solution with the Bagai-Leishman relaxation free wake model is described in Fig. B.1. There are two basic phases, namely, trim and transient analysis. As far as the transient analysis is concerned, the coupling is "loose". The rotor-fuselage equations are integrated for a specific time interval (e.g., 10° of azimuth angle) for constant inflow. The free wake is then advanced over the same time interval, with the time history of the rotor-fuselage states just calculated. The inflow at the end of the time interval is then held constant while the rotor-fuselage equations are integrated for another time interval, then the wake is recalculated, and so on (Ref. 128).

In theory, the relaxation free wake model could be used to compute the trim

solution. Then, because the underlying mathematical model is essentially the same as that of the time-accurate wake, the geometry obtained using relaxation would be the same as that of the time-accurate wake. If a subsequent time-marching simulation was desired, this geometry would provide the correct initial conditions. In practice, however, the relaxation solution is close but not identical to a steady-state solution for the time-accurate wake, mostly because of the different numerical schemes used for the solution. As a consequence, in switching from the former to the latter numerical transients still appear, with the same problems previously mentioned.

The solution involves an intermediate "convergence" phase between the trim calculation with the relaxation wake and a subsequent time-marching simulation using the time-accurate wake. With the rotor-fuselage states and controls fixed at their trim values, the time-marching free wake is run until all the numerical transients disappear. Then the rotor-fuselage states and controls are released, and the time-marching simulation can start with the correct wake geometry and no numerical transients.

After trimming the helicopter with the relaxation free wake model, and before computing the transient response with a time-marching free wake, the intermediate convergence phase needs to be introduced. The details of the process are described in Fig. B.2. Starting from the trim solution, obtained with a relaxation free wake, and fixing the states and controls at their trim values, the flap angles and the blade velocities are calculated and passed to the time-marching free wake model. With these, the circulation distribution is calculated with the Weissinger-L method and

the time-marching process is started. At every step of the time-marching solution, the circulation is updated with the most recent inflow. The process is repeated until convergence is reached, or for a number of revolutions long enough such that all the numerical transients have disappeared. After that, the integration of the equations of motion with the time-accurate free wake can start, with an initial geometry free of the numerical transients caused by the two different numerical schemes.

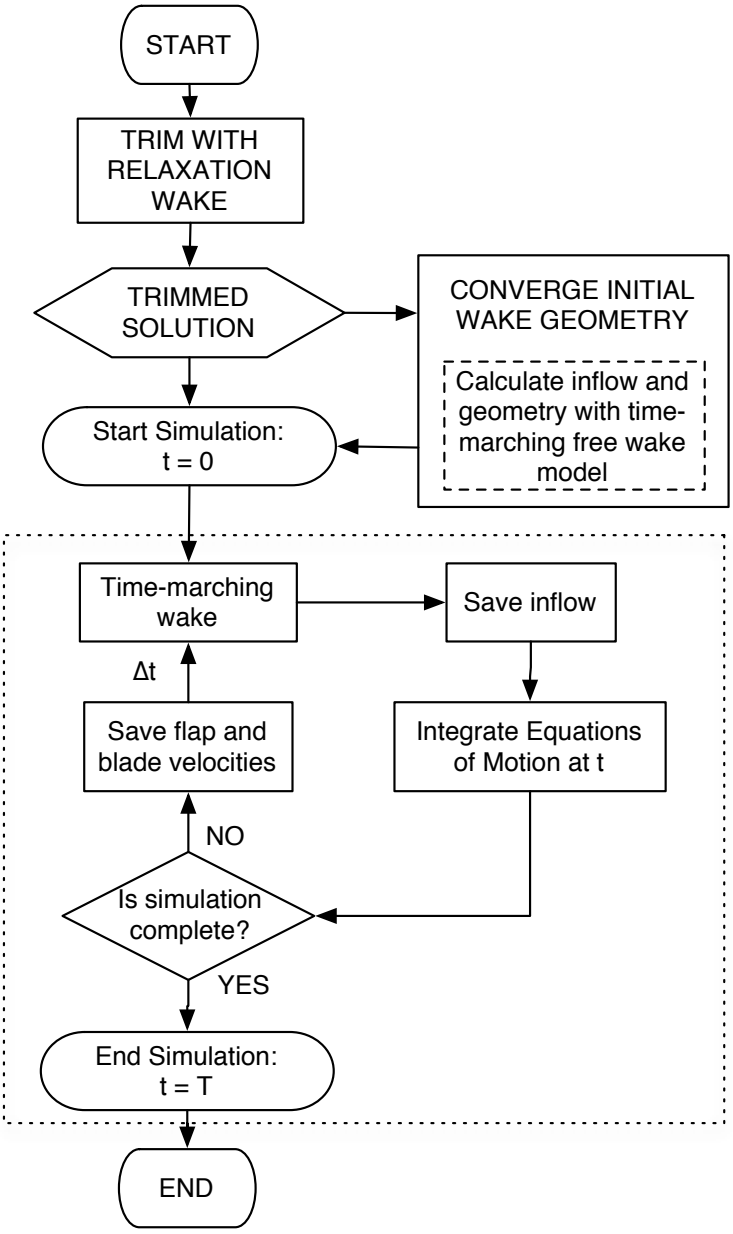

Figure B.1: Time integration procedure for the coupling of a time-accurate wake model to the flight dynamics simulation after obtaining the trim solution with a relaxation free wake model.

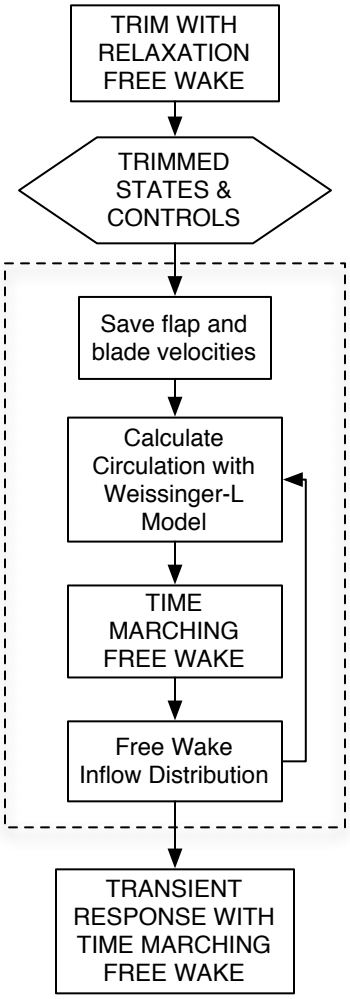

Figure B.2: Schematic of the free wake convergence phase between trimming with the relaxation free wake and integrating the transient response with the time-marching free wake.

Appendix C

Trim precedure in previous studies

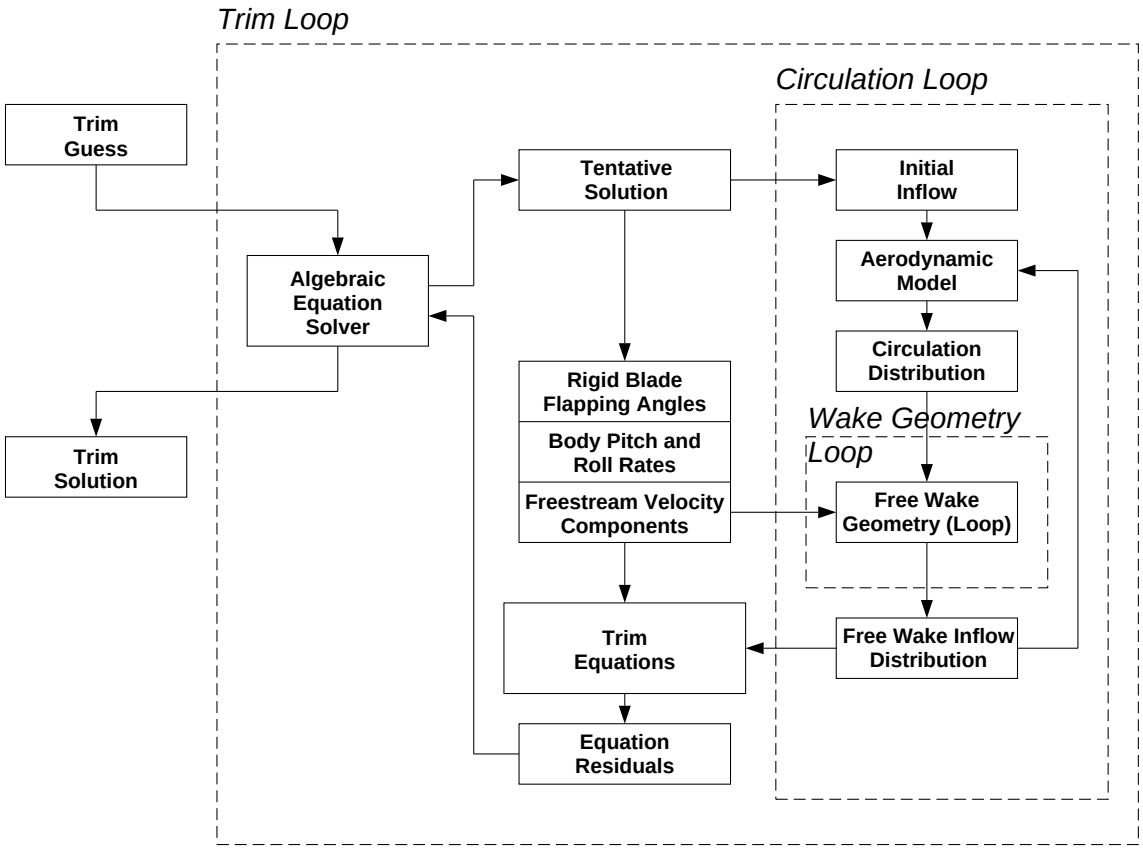

Figure C.1: Schematic of the trim procedure with the Bagai-Leishman free wake as used by Theodore (Ref. 6).

BIBLIOGRAPHY

[1] Drees, J. M. and Hendal, W. P., "The Field of Flow Through a Helicopter Rotor Obtained from Wind Tunnel Smoke Tests," Versl. Nat. Luchtvlab,, February 1950. Also, Journal of Aircraft Engineering, Vol. 23, No. 266, pp. 107–111.

[2] Shevell, R. S., *Fundamentals of Flight*. Prentice Hall, 2nd ed., 1988.

[3] Leishman, J. G., *Principles of Helicopter Aerodynamics*. New York: Cambridge University Press, 2000.

[4] Padfield, G. D., *Helicopter Flight Dynamics: The Theory and Application of Flying Qualities and Simulation Modeling*. AIAA, 1996.

[5] Ananthan, S. and Leishman, J. G., "Helicopter Rotor Wake Dynamics During Tactical Maneuvers," in *Proceedings of the* 60th *Annual Forum of the American Helicopter Society International*, (Baltimore, MD), June 7 – 10 2004.

[6] Theodore, C. R., Helicopter Flight Dynamic Simulation with Refined Aerodynamic Modeling, Ph.D. Dissertation, University of Maryland, 2000.

[7] Leishman, J. G., Bhagwat, M. J., and Bagai, A., "Free-Vortex Filament Methods for the Analysis of Helicopter Rotor Wakes," *Journal of Aircraft*, Vol. 39, No. 5, September-October 2002, pp. 759–775.

[8] Friedmann, P. P., "Rotary-Wing Aeroelasticity - Current Status and Future Trends," in *39th AIAA Aerospace Sciences Meeting and Exhibit*, (Reno, NV), AIAA, January 2001.

[9] Bhagwat, M. J. and Leishman, J. G., "Stability, Consistency and Convergence of Time Marching Free-Vortex Rotor Wake Algorithms of Time-Marching Free-Vortex Rotor Wake Algorithms," *Journal of the American Helicopter Society*, Vol. 46, No. 1, January 2001, pp. 59–71.

[10] Ballin, M. G., "Validation of a Real-Time Engineering Simulation of the UH-60A Helicopter," NASA TM-88360, 1987.

[11] Johnson, W., "Technology Drivers in the Development of CAMRAD II," *Proceedings of the American Helicopter Society Aeromechanics Specialists Conference*, San Francisco, California, January 1994.

[12] Bagai, A., Contributions to the Mathematical Modeling of Rotor Flow-Fields using a Pseudo-Implicit Free-Wake Analysis, Ph.D. Dissertation, University of Maryland, 1995.

[13] Heyson, H. H., "A Momentum Analysis of Helicopters and Autogyros in Inclined Descent, with Comments on Operational Restrictions," NASA, October 1975.

[14] Rosen, A. and Isser, A., "A Model of the Unsteady Aerodynamics of a Hovering Rotor That Includes Variations of the Wake Geometry," *Journal of the American Helicopter Society*, Vol. 40, No. 3, July 1995, pp. 6–16.

[15] Bhagwat, M. J., Transient Dynamics of Helicopter Rotor Wakes Using a Time-Accurate Free-Vortex Method, Ph.D. Dissertation, Department of Aerospace Engineering, University of Maryland, College Park, MD, 2001.

[16] Johnson, W., "Wake Model for Helicopter Rotors in High Speed Flight," NASA, November 1988.

[17] Scully, M. P., "A Method of Computing Helicopter Vortex Wake Distortion," Massachusetts Institute of Technology, June 1967.

[18] Wachspress, D. A., Quackenbush, T. R., and Boschitsch, A. H., "Rotorcraft Interactional Aerodynamics with Fast Vortex/Fast Panel Methods," *Journal of the American Helicopter Society*, October 2003, pp. 223–235.

[19] Wachspress, D. A., Quackenbush, T. R., and Boschitsch, A. H., "First-Principles Free-Vortex Wake Analysis for Helicopters and Tiltrotors," in *Proceedings of the 59th Annual Forum of the American Helicopter Society*, (Phoenix, AZ), May 2003.

[20] Yen, J. G., Corrigan, J. J., Schillings, J. J., and Hsieh, P. Y., "Comprehensive Analysis Methodology at Bell Helicopter: COPTER," *Proceedings of the American Helicopter Society Aeromechanics Specialists Conference*, San Francisco, California, January 1994.

[21] DuVal, R., "A Real-Time Blade Element Helicopter Simulation for Handling Qualities Analysis," *Proceedings of the 15th Annual European Rotorcraft Forum*, Amsterdam, The Netherlands, September 1989.

[22] Peters, D. A., Boyd, D. D., and He, C. J., "Finite-State Induced-Flow Model for Rotors in Hover and Forward Flight," *Journal of the American Helicopter Society*, Vol. 34, No. 4, October 1989, pp. 5–17.

[23] Benoit, B., Dequin, A. M., Kampa, K., von Grünhagen, W., Basset, P. M., and Gimonet, B., "HOST, a General Helicopter Simulation Tool for Germany and France," in *Proceedings of the 56th Annual American Helicopter Society Forum for Rotorcraft Acoustics and Aerodynamics*, (Virginia Beach, VA), May 2-4 2000.

[24] Pitt, D. M. and Peters, D. A., "Theoretical Prediction of Dynamic Inflow Derivatives," *Vertica*, Vol. 5, No. 1, 1981, pp. 21–34.

[25] Basset, P. M. and Tchen-Fo, F., "Study of the Rotor Wake Distortion Effects on the Helicopter Pitch-Roll Cross-Coupling," *Proceedings of the 24nd Annual European Rotorcraft Forum*, Marseilles, France, September 1998.

[26] Ormiston, R. A., Rutkowski, M. J., Ruzicka, G. C., Saberi, H., and Jung, Y., "Comprehensive Aeromechanics Analysis of Complex Rotorcraft Using 2GCHAS," *Proceedings of the American Helicopter Society Aeromechanics Specialists Conference*, San Francisco, California, January 1994.

[27] Saberi, H., Khoshlahjeh, M., Ormiston, R. A., and Rutkowski, M. J., "Overview of RCAS and Application to Advanced Rotorcraft Problems," in *Proceedings of the AHS Fourth Decennial Specialists' Conference on Aeromechanics*, (San Francisco, CA), January 2004.

[28] Bagai, A. and Leishman, J. G., "Rotor Free-Wake Modeling Using a Relaxation Technique - Including Comparisons with Experimental Data," *Journal of the American Helicopter Society*, Vol. 40, No. 3, July 1995, pp. 29–41.

[29] Shultz, L. A., Panda, B., Tarzanin, F. J., Derham, R. C., Oh, B. K., and Danone, L., "Interdisciplinary Analysis For Advanced Rotors – Approach, Capabilities and Status," *Proceedings of the American Helicopter Society Aeromechanics Specialists Conference*, San Francisco, California, January 1994.

[30] Drees, J. M., "A Theory of Airflow Through Rotors and Its Application to some Helicopter Problems," *Journal of the Helicopter Association of Great Britian*, Vol. 3, No. 2, July 1949.

[31] Bir, G. and Chopra, I., "Status of University of Maryland Advanced Rotorcraft Code (UMARC)," *Proceedings of the American Helicopter Society Aeromechanics Specialists Conference*, San Francisco, California, January 1994.

[32] Howlett, J. J., "UH-60A Black Hawk Engineering Simulation Program - Volume II - Mathematical Model," NASA CR-166309, December 1981.

[33] Gaonkar, G. H. and Peters, D. A., "Effectiveness of Current Dynamic Inflow Models in Hover and Forward Flight," *Journal of the American Helicopter Society*, Vol. 31, No. 2, April 1986, pp. 47–57.

[34] Gaonkar, G. H. and Peters, D. A., "Review of Dynamic Inflow Modeling for Rotorcraft Flight Dynamics," *Vertica*, Vol. 12, No. 3, 1988, pp. 213–242.

[35] Chen, R. T. N., "A Survey of Nonuniform Inflow Models for Rotorcraft Flight Dynamics and Control Applications," *Proceedings of the 15th Annual European Rotorcraft Forum*, Amsterdam, The Netherlands, September 1989.

[36] Peters, D. A. and He, C. J., "Correlation of Measured Induced Velocities with a Finite-State Wake Model," *Journal of the American Helicopter Society*, Vol. 36, No. 3, July 1991, pp. 59–70.

[37] Prasad, J., Zhao, J., and Peters, D. A., "Helicopter Rotor Wake Distortion Models for Maneuvering Flight Wake Distortion Models for Maneuvering Flight," in *Proceedings of the 28th European Rotorcraft Forum*, (Bristol, UK), Sep 2002.

[38] Zhao, J., Prasad, J. V. R., and Peters, D. A., "Investigation of Wake Curvature Dynamics for Helicopter Maneuvering Flight Simulation," in *Proceedings of the 59th Annual Forum of the American Helicopter Society*, (Phoenix, AZ), May 2003.

[39] He, C. J., Lee, C., and Chen, C. W., "Finite State Induced Flow Model in Vortex Ring State," *Journal of the American Helicopter Society*, Vol. 45, No. 4, October 2000, pp. 318–320.

[40] Ananthan, S., Analysis of Rotor Wake Aerodynamics During Maneuvering Flight Using a Free-Vortex Wake Methodology, Ph.D. Dissertation, University of Maryland, 2006.

[41] Landgrebe, A. J., "The Wake Geometry of a Hovering Helicopter Rotor and Its Influence on Rotor Performance," *Journal of the American Helicopter Society*, Vol. 17, No. 4, October 1972, pp. 3–15.

[42] Kocurek, J. D. and Tangler, J. L., "A Prescribed Wake Lifting Surface Hover Performance Analysis," *Journal of the American Helicopter Society*, Vol. 22, No. 1, January 1977, pp. 24–35.

[43] Egolf, T. A. and Landgrebe, A. J., "Helicopter Rotor Wake Geometry and its Influence in Forward Flight, Vol. 1 — Generalized Wake Geometry and Wake Effects in Rotor Airloads and Performance," NASA, October 1983.

[44] Beddoes, T. S., "A Wake Model for High Resolution Airloads," in *Proceedings of the 2nd International Conference on Basic Rotorcraft Research*, (Triangle Park, NC), 1985.

[45] Quackenbush, T. R., Wachspress, D. A., and Boschitsch, A. H., "Computation of Rotor Aerodynamic Loads with a Constant Vorticity Contour Free Wake Model," in *AIAA Paper 91-3229, 9th AIAA Applied Aerodynamics Conference*, (Baltimore, MD), September 1991.

[46] Lee, D. J. and Na, S. U., "High Resolution Free Vortex Blob Method for Highly Distorted Vortex Wake Generated From a Slowly Starting Rotor Blade in Hover," in *Twenty First European Rotorcraft Forum*, (Saint Petersburg, Russia), August 30–September 1, 1995.

[47] Clark, D. R. and Leiper, A. C., "The Free Wake Analysis – A Method for Prediction of Helicopter Rotor Hovering Performance," *Journal of the American Helicopter Society*, Vol. 15, No. 1, January 1970, pp. 3–11. Also presented at the American Helicopter Society 25th Annual Forum, May 1969.

[48] Scully, M. P., "Computation of Helicopter Rotor Wake Geometry and Its Influence on Rotor Harmonic Loads," Massachusetts Institde of Technology, Aeroelastic and Structures Research Laboratory, Cambridge, MA, March 1975.

[49] Johnson, W., "A Comprehensive Analytical Model of Rotorcraft Aerodynamics and Dynamics, Part I: Analytical Development," NASA, 1980.

[50] Miller, R. H., "A Simplified Approach to the Free Wake Analysis of a Hovering Rotor," *Vertica*, Vol. 6, 1982, pp. 89–95.

[51] Weissinger, J., "The Lift Distribution of Swept-Back Wings," NASA TM-1120, March 1947.

[52] Bliss, D. B., Quackenbush, T. R., and Bilanin, A. J., "A New Methodology for Helicopter Free-Wake Analyses," in *American Helicopter Society 39*$^{\text{th}}$ *Annual National Forum*, (St. Louis, MO), May 9–11, 1983.

[53] Bliss, D. B., Washspress, D. A., and Quackenbush, T. R., "A New Approach to the Free Wake Problem for Hovering Rotors," in *American Helicopter Society 41*st *Annual National Forum*, (Fort Worth, TX), May 15–17, 1985.

[54] Miller, W. O. and Bliss, D. B., "Direct Periodic Solutions of Rotor Free Wake Calculations," in *American Helicopter Society 46*$^{\text{th}}$ *Annual National Forum*, (Washington, DC), May 21–23, 1990.

[55] Crouse, Jr., G. L. and Leishman, J. G., "A New Method for Improved Rotor Free Wake Convergence," in *31*st *AIAA Aerospace Sciences Meeting and Exhibit*, (Reno, NV), January 1993.

[56] Crimi, P., "Theoretical Prediction of the Flow in the Wake of a Helicopter Rotor," Cornell Aeronautical Laboratory, Buffalo NY, September 1965.

[57] Clark, D. R. and Leiper, A. C., "The Free Wake Analysis: A Method for the Prediction of Helicopter Hovering Peformance," in *American Helicopter Society 25th Annual National Forum*, (Washington, DC), May 14–16, 1969.

[58] Landgrebe, A. J., "An Analytical Method for Predicting Rotor Wake Geometry," in *Presented at the AIAA/AHS VTOL Research, Design & Operations Meeting*, (Atlanta, GA), February 1969.

[59] Sadler, S. G., "A Method for Predicting Helicopter Wake Geometry, Wake-Induced Inflow and Wake Effects on Blade Airloads," in *American Helicopter Society 27th Annual National Forum*, (Washington, DC), May 1971.

[60] Bliss, D. B., Teske, M. E., and Quackenbush, T. R., "A New Methodology for Free Wake Analysis using Curved Vortex Elements," NASA, December 1987.

[61] Bliss, D. B., Dadone, L., and Wachspress, D. A., "Rotor Wake Modeling for High Speed Applications," in *American Helicopter Society 43th Annual National Forum*, (St. Louis, MO), May 18–20, 1987.

[62] Egolf, T. A., "Rotor Wake Modeling for High Speed Applications," in *American Helicopter Society 44th Annual National Forum*, (Washington, DC), June 16–18, 1988.

[63] Brown, R. E., "Rotor Wake Modeling for Flight Dynamic Simulation of Helicopters," *AIAA Journal*, Vol. 38, No. 1, 2000, pp. 57–63.

[64] Line, A. J. and Brown, R. E., "High Resolution Wake Modeling Using A Semi-Lagrangian Adaptive Grid Formulation," in 29^{th} *European Rotorcraft Forum*, (Friedrichshafen, Germany), September 16–18 2003.

[65] Toro, E. F., "A Weighted Average Flux Method for Hyperbolic Conservation Laws," in *Proceedings of the Royal Society of London, Series A: Mathematical and Physical Sciences*, Vol. 423, pp. 401–418, 1989.

[66] Fletcher, J. W. and Tischler, M. B., "Improving Helicopter Flight Mechanics Models with Laser Measurements of Blade Flapping," in *Proceedings of the 53rd Annual Forum of the American Helicopter Society*, (Virginia Beach, VA), pp. pp. 1467–1994, Apr 1997.

[67] Rosen, A., Yaffe, R., Mansur, M. H., and Tischler, M. B., "Methods for Improving the Modeling of Rotor Aerodynamics for Flight Mechanics Purposes," in *Proceedings of the 54th Annual Forum of the American Helicopter Society*, (Washington D.C.), pp. pp. 1337–1355, May 1998.

[68] Mansur, M. H. and Tischler, M. B., "An Empirical Correlation Method for Improving Off-Axis Response in Flight Mechanics Helicopter Models," *Journal of the American Helicopter Society*, Vol. 43, No. 2, April 1998, pp. 94–102.

[69] Bagai, A., Leishman, J. G., and Park, J., "Aerodynamic Analysis of a Helicopter in Steady Maneuvering Flight Using a Free-Vortex Rotor Wake Model," *Journal of the American Helicopter Society*, Vol. 44, No. 2, April 1999, pp. 109–120.

[70] Spoldi, S. and Ruckel, P., "High Fidelity Helicopter Simulation using Free Wake, Lifting Line Tail, and Blade Element Tail Rotor Models," in *Proceedings of the 59th Annual Forum of the American Helicopter Society*, May 2003.

[71] Kothmann, B. D., Lu, Y., DeBrun, E., and Horn, J. F., "Perspectives on Rotorcraft Aerodynamic Modeling for Flight Dynamics Applications," in *Proceedings of the AHS Fourth Decennial Specialists' Conference on Aeromechanics*, (San Francisco, CA), 2004.

[72] Brentner, K. S., Lopes, L., H.-N., C., and Horn, J. F., "Near Real-Time Simulation of Rotorcraft Acoustics and Flight Dynamics," in *Proceedings of the 59th Annual Forum of the American Helicopter Society*, (Phoenix, AZ), May 2003.

[73] Hennes, C. C., Chen, H., Brentner, K. S., S, A., and Leishman, G. J., "Influence of Transient Flight Maneuvers on Rotor Wake Dynamics and Noise Radiation," in *AHS* 4^{th} *Decennial Specialist's Conference on Aeromechanics*, (San Francisco, CA), January 21–23 2004.

[74] Theodore, C. and Celi, R., "Helicopter Flight Dynamic Simulation with Refined Aerodynamic and Flexible Blade Modeling," *Journal of Aircraft*, Vol. 39, No. 4, July-August 2002, pp. 577–586.

[75] Newman, S. J., Brown, R., Perry, J., Lewis, S., Orchard, M., and Modha, A., "Comparative Numerical and Experimental Investigations of the Vortex Ring

Phenomenon in Rotorcraft," in *Proceedings of the* 57th *Annual Forum of the American Helicopter Society International*, 2001.

[76] Johnson, W., "Model for Vortex Ring State Influence on Rotorcraft Flight Dynamics," in *Proceedings of the AHS Fourth Decennial Specialists' Conference on Aeromechanics*, 2004.

[77] Wolkovitch, J., "Analytical Prediction of Vortex-Ring Boundaries for Helicopters in Steep Descents," *Journal of the American Helicopter Society*, Vol. 17, No. 3, 1972, pp. 13–19.

[78] Peters, D. A. and Chen, S.-Y., "Momentum Theory, Dynamic Inflow, and the Vortex Ring State," *Journal of the American Helicopter Society*, Vol. 27, No. 3, July 1982, pp. 18–24.

[79] Chen, C., Prasad, J. V. R., and Basset, P. M., "A Simplified Inflow Model of a Helicopter Rotor in Vertical Descent," in *Proceedings of the* 60th *Annual Forum of the American Helicopter Society International*, 2004.

[80] Chen, C. and Prasad, J. V. R., "Theoretical Investigations of a Helicopter Rotor in Steep Descent," in *Collection of Technical Papers - AIAA Modeling and Simulation Technologies Conference*, 2005.

[81] Peters, D. A. and He, C., "Modification of Mass-Flow Parameter to Allow Smooth Transition Between Helicopter and Windmill States," *American Helicopter Society*, Vol. 51, No. 3, July 2006, pp. 275–278.

[82] Prasad, J. and Chen, C., "Prediction of Vortex Ring State using Ring Vortex Model for Single-Rotor and Multi-Rotor Configurations," No. AIAA Paper No. 2006-6632, (Keystone, CO), August 21-24 2006.

[83] Leishman, J. G., Bhagwat, M. J., and Ananthan, S., "Free-Vortex Wake Predictions of the Vortex Ring State for Single Rotor and Multi-Rotor Configurations," in *Proceedings of the* 58^{th} *Annual Forum of the American Helicopter Society International*, (Montréal Canada), 2002.

[84] Leishman, J. G., Bhagwat, J. G., and Ananthan, S., "The Vortex Ring State as a Spatially and Temporally Developing Wake Instability," in *American Helicopter Society International Aerodynamics Meeting*, (San Francisco, CA), January 2002.

[85] Brown, R. E., Line, A. J., and Ahlin, G. A., "Fuselage and Tail-Rotor Interference Effects on Helicopter Wake Development in Descending Flight," in *Proceedings of the* 60^{th} *Annual Forum of the American Helicopter Society International*, 2004.

[86] Houson, S. S. and Brown, R. E., "Rotor-Wake Modeling for Simulation of Helicopter Flight Mechanics in Autorotation," *Journal of Aircraft*, Vol. 40, No. 5, September-October 2003.

[87] Thibert, J. J. and Phillippe, J. J., "Etudes de Profils et D'Extremites de Pales D'Helicoptere'," in *AGARD Conference Proceedings No. 334*, pp. 3–1/3–14, May 1982.

[88] Phillippe, J. J. and Vuillet, A., "Aerodynamic Design of Advanced Rotors With New Tip Shapes," in *Proceedings of the 39th Annual Forum of the American Helicopter Society*, (Saint Louis, MO), pp. 58–71, May 1983.

[89] Desopper, A., Lafon, P., Ceroni, P., and Phillippe, J. J., "10 Years of Rotor Flow Studies at ONERA - State of the Art and Future Studies," in *Proceedings of the 42nd Annual Forum of the American Helicopter Society*, (Washington D.C.), pp. 267–277, June 1986.

[90] Tarzanin, F. J. J. and Vlaminck, R. R., "Investigation of the Effect of Blade Sweep on Rotor Vibratory Loads," NASA, 1983.

[91] Celi, R., Aeroelasticity and Structural Optimization of Helicopter Rotor Blades with Swept Tips, Ph.D. Dissertation, Mechanical, Aerospace and Nuclear Engineering Department, University of California, Los Angeles, 1987.

[92] Celi, R. and Friedmann, P. P., "Rotor Blade Aeroelasticity in Forward Flight with an Implicit Formulation," *AIAA Journal*, Vol. 26, No. 12, December 1988.

[93] Celi, R. and Friedmann, P. P., "Aerolastic Model of Swept Tip Rotor Blades Using Finite Elements," *Journal of the American Helicopter Society*, Vol. 33, No. 2, April 1988, pp. 43–52.

[94] Shamie, J. and Friedmann, P. P., "Effect of Moderate Deflections on the Aeroelastic Stability of a Rotor Blade in Forward Flight," *Proceedings of the 3rd An-*

nual European Rotorcraft and Powered Lift Aircraft Forum, Aixen-Provence, France, September 1977.

[95] Friedmann, P. P. and Straub, F. K., "Application of the Finite Element Method to Rotary-Wing Aeroelasticity," *Journal of the American Helicopter Society*, Vol. 25, No. 1, January 1980.

[96] Straub, F. K. and Friedmann, P. P., "A Gelerkin Type Finite Element Method for Rotary-Wing Aeroelasticity in Hover and Forward Flight," *Vertica*, Vol. 5, 1981, pp. 75–98.

[97] Panda, B., "Technical Note: Assembly of Moderate-Rotation Finite Elements Used in Helicopter Rotor Dynamics," *Journal of the American Helicopter Society*, Vol. 32, No. 4, 1987, pp. 63–69.

[98] Benquet, P. and Chopra, I., "Calculated Dynamic Response and Loads for an Advanced Tip Rotor in Forward Flight," in *Proceedings of the 15th Annual European Rotorcraft Forum*, pp. 50.1–50.25, 1989.

[99] Kim, K. C. and Chopra, I., "Aeroelastic Analysis of Swept, Anhedral, and Tapered Tip Rotor Blades," *Journal of the American Helicopter Society*, Vol. 37, No. 1, 1992, pp. 15–30.

[100] Bir, G. S. and Chopra, I., "Aeromechanical Stability of Rotorcraft with Advance Geometry Blades," in *Proceedings of the 34th AIAA/ASME/ASCE/AHS/ASC Structures, Structural Dynamics and Materials Conference* (AIAA, ed.), (La Jolla, CA), pp. 38–62, AIAA, April 1993.

[101] Yuan, K. A. and Friedmann, P. P., "Aeroelasticity and Structural Optimization of Composite Helicopter Rotor Blades with Swept Tips," NASA, 1995.

[102] Friedmann, P. P., Yuan, K. A., and de Terlizzi, M., "An aeroelastic model for composite rotor blades with straight and swept tips. Part I: Aeroelastic stability in hover," *International Journal of Non-linear Mechanics*, Vol. 37, No. 4-5, June 2002, pp. 967–986.

[103] de Terlizzi, M. and Friedmann, P. P., "Active Control of BVI Induced Vibrations Using a Refined Aerodynamic Model and Experimental Correlation," in *Proceedings of the 55th Annual American Helicopter Society Forum*, (Montreal, Canada), May 25-27 1999.

[104] Ballin, M. G. and Dalang-Secretan, M. A., "Validation of the Dynamic Response of a Blade-Element UH-60 Simulation Model in Hovering Flight," *Proceedings of the 46th Annual American Helicopter Society Forum*, Washington D.C., May 1990.

[105] Kim, F. D., Celi, R., and Tischler, M. B., "High-Order State Space Simulation Models of Helicopter Flight Mechanics," *Journal of the American Helicopter Society*, Vol. 38, No. 4, October 1993, pp. 16–27.

[106] Peters, D. A. and HaQuang, N., "Dynamic Inflow for Practical Applications," *Journal of the American Helicopter Society*, Vol. 33, No. 4, October 1988, pp. 64–68.

[107] Turnour, S. R. and Celi, R., "Modeling of Flexible Rotor Blades for Helicopter Flight Dynamics Applications," *Journal of the American Helicopter Society*, Vol. 41, No. 1, January 1996, pp. 52–66; Correction in Vol. 41, No. 3, July 1996, pp. 191–194.

[108] Celi, R., "Helicopter Rotor Blade Aeroelasticity in Forward Flight with an Implicit Structural Formulation," *AIAA Journal*, Vol. 30, No. 9, September 1992, pp. 2274–2282.

[109] Leishman, J. G. and Nguyen, K. Q., "State Space Representation of Unsteady Airfoil Behavior," *AIAA Journal*, Vol. 28, No. 5, May 1990, pp. 836–844.

[110] Bagai, A. and Leishman, J. G., "Rotor Free-Wake Modeling using a Relaxation Technique – Including Comparisons with Experimental Data," *Proceedings of the 50th Annual American Helicopter Society Forum*, Washington D.C., May 1994.

[111] Fusato, D., Design Sensitivity Analysis and Optimization for Helicopter Handling Qualities Improvement, Ph.D. Dissertation, University of Maryland, 2002.

[112] Cheng, R. P., Helicopter Dynamics with Advanced Rotor Control, Ph.D. Dissertation, University of Maryland, 2003.

[113] Lovera, M., Colaneri, P., Malpica, C. A., and Celi, R., "Closed-Loop Aeromechanical Stability of a Hingeless Rotor Helicopter with Higher Harmonic Con-

trol," *Journal of Guidance, Control, and Dynamics*, Vol. 29, No. 1, January-February 2006, pp. 179–189.

[114] Turnour, S. R., Flight Dynamics Modeling of Hingeless and Bearingless Rotor Helicopters, Ph.D. Dissertation, Department of Aerospace Engineering, University of Maryland, College Park, MD, 1996.

[115] Rosen, A. and Friedmann, P. P., "Nonlinear Equations of Equilibrium for Elastic Helicopter or Wind Turbine Blades Undergoing Moderate Deflections," NASA CR-159478, December 1978.

[116] Bailey, F. J. Jr., "A Simplified Theoretical Method of Determining the Characteristics of a Lifting Rotor in Forward Flight," NACA Rep. 716, 1941.

[117] Ananthan, S. and Leishman, J. G., "Role of Filament Strain in the FreeVortex Modeling of Rotor Wakes," *Journal of the American Helicopter Society*, Vol. 49, No. 2, April 2004, pp. 176–191.

[118] Bhagwat, M. J. and Leishman, J. G., "Time-Accurate Modeling of Rotor Wakes Using A Free-Vortex Wake Method," *Journal of Aircraft*, Vol. 39, No. 5, September/October 2002, pp. 759–775.

[119] Ramasamy, M. and Leishman, J. G., "A Generalized Model for Transitional Blade Tip Vortices," in *Proceedings of the 60th Annual Forum of the American Helicopter Society International*, (Baltimore, MD), June 7-10 2004.

[120] Lewis, R. I., *Vortex Element Methods for Fluid Dynamic Analysis of Engineering Systems,*. New York, NY: Cambridge University Press, 1991.

[121] Zienkiewicz, O. C. and Taylor, R. L., *The finite element method*, Vol. 15. Boston, MA: Butterworth-Heinemann, 5th ed., 2000.

[122] Celi, R., "Helicopter Rotor Dynamics in Coordinated Turns," *Journal of the American Helicopter Society*, Vol. 36, No. 4, October 1991, pp. 39–47.

[123] Kim, F. D., Celi, R., and Tischler, M. B., "Forward Flight Trim Calculation and Frequency Response Validation of a High-Order Helicopter Simulation Model," *Journal of Aircraft*, Vol. 30, No. 6, November-December 1993, pp. 854–863.

[124] More, J. J., Garbow, B. S., and Hillstrom, K. E., *User's Guide for MINPACK-1.* Argonne National Laboratory, Report ANL-80-74, August 1980.

[125] Powell, M. J. D., *A Hybrid Method for Nonlinear Equations. Numerical Methods for Nonlinear Algebraic Equations.* Gordon and Breach, 1970.

[126] Celi, R., "Implementation of Rotary-Wing Aeromechanical Problems Using Differential-Algebraic Equation Solvers," *Journal of the American Helicopter Society*, Vol. 45, No. 4, October 2000, pp. 253–262.

[127] Brenan, K. E., Campbell, S. L., and Petzold, L. R., *The Numerical Solution of Initial Value Problems in Differential-Algebraic Equations.* New York: Elsevier Science Publishing Co., 1989.

[128] Ribera, M. and Celi, R., "Simulation Modeling of Unsteady Maneuvers Using a Time-Accurate Free Wake," in *Proceedings of the 60th Annual Forum of the American Helicopter Society*, 2004.

[129] Ribera, M. and Celi, R., "Simulation Modeling in Steady Turning Flight with Refined Aerodynamics," in *Proceedings of the* 31$^{\text{th}}$ *European Rotorcraft Forum*, 2005.

[130] Datta, A., Fundamental Understanding, Prediction and Validation of Rotor Vibratory Loads in Steady Level Flight, Ph.D. Dissertation, University of Maryland, 2004.

[131] Caradonna, F., Hendley, E., Silva, M., Huang, S., Komerath, N., Reddy, U., Mahalingam, R., Funk, R., Wong, O., Ames, R., Darden, L., Villareal, L., and Gregory, J., "An Experimental Study of a Rotor in Axial Flight," in *Proceedings of the AHS Technical Specialists' Meeting for Rotorcraft Acoustics and Aerodynamics*, (Williamsburg, VA), October 28–30, 1997.

[132] Caradonna, F., Hendley, E., Silva, M., Huang, S., Komerath, N., Reddy, U., Mahalingam, R., Funk, R., Wong, O., Ames, R., Darden, L., Villareal, L., and Gregory, J., "Performance Measurement and Wake Characteristics of a Model Rotor in Axial Flight," *Journal of the American Helicopter Society*, Vol. 44, No. 2, 1999, pp. 101–108. (Errata, Vol. 44, No. 3).

[133] Martin, P. B., Bhagwat, M. J., and Leishman, J. G., "Strobed Laser-Sheet Visualization of a Helicopter Rotor Wake," *Journal of Flow Visualization & Image Processing*, Vol. 9, No. 1, 2001, pp. 31–50.

[134] Bhagwat, M. J. and Leishman, J. G., "Stability Analysis of Helicopter Rotor Wakes in Axial Flight," *Journal of the American Helicopter Society*, Vol. 45,

No. 3, 2000, pp. 165–178.

[135] Brown, R. E., Newman, S. J., Leishman, J. G., and Perry, F. J., "Blade Twist Effects on Rotor Behaviour in the Vortex Ring State," in *Proceedings of the* 28th *European Rotorcraft Forum*, 2002.

[136] Abbott, W. Y., Benson, J. O., Oliver, R. G., and Williams, R. A., "Validation Flight Test of a UH-60A for Rotorcraft Systems Integration Simulator (RIRS)," U.S. Army Aviotion Engineering Flight Activity, July 1082.

[137] Betzina, M. D., "Tiltrotor Descent Aerodynamics: A Small-Scale Experimental Investigation of Vortex Ring State," in *Proceedings of the* 57th *Annual Forum of the American Helicopter Society International*, (Washington, D.C.), May 9–11 2001.

[138] Washizu, K., Azuma, A., Kōo, J., and Oka, T., "Experiments on a Model Helicopter Rotor Operating in the Vortex Ring State," *Journal of Aircraft*, Vol. 3, No. 3, May-June 1966, pp. 225–230.

[139] Leishman, J. G. and Ananthan, S., "Aerodynamic Optimization of a Coaxial Proprotor," in *Proceedings of the 62nd Annual Forum of the American Helicopter Society*, (Phoenix, AZ), May 2006.